NASA/CP-2001-210827

Microgravity Materials Science Conference 2000

Edited by
Narayanan Ramachandran
Universities Space Research Association
Huntsville AL

Nancy Bennett
Universities Space Research Association
Huntsville AL

Dannah McCauley
University of Alabama in Huntsville
Huntsville AL

Karen Murphy
Morgan Research Corporation
Marshall Space Flight Center
Huntsville AL

Samantha Poindexter
Universities Space Research Association
Huntsville AL

Proceedings of a conference sponsored by the
Microgravity Research Division, NASA Headquarters
and held at Huntsville, Alabama, June 6-8, 2000

March 2001

Main Menu

The NASA STI Program Office…in Profile

Since its founding, NASA has been dedicated to the advancement of aeronautics and space science. The NASA Scientific and Technical Information (STI) Program Office plays a key part in helping NASA maintain this important role.

The NASA STI Program Office is operated by Langley Research Center, the lead center for NASA's scientific and technical information. The NASA STI Program Office provides access to the NASA STI Database, the largest collection of aeronautical and space science STI in the world. The Program Office is also NASA's institutional mechanism for disseminating the results of its research and development activities. These results are published by NASA in the NASA STI Report Series, which includes the following report types:

- TECHNICAL PUBLICATION. Reports of completed research or a major significant phase of research that present the results of NASA programs and include extensive data or theoretical analysis. Includes compilations of significant scientific and technical data and information deemed to be of continuing reference value. NASA's counterpart of peer-reviewed formal professional papers but has less stringent limitations on manuscript length and extent of graphic presentations.

- TECHNICAL MEMORANDUM. Scientific and technical findings that are preliminary or of specialized interest, e.g., quick release reports, working papers, and bibliographies that contain minimal annotation. Does not contain extensive analysis.

- CONTRACTOR REPORT. Scientific and technical findings by NASA-sponsored contractors and grantees.

- CONFERENCE PUBLICATION. Collected papers from scientific and technical conferences, symposia, seminars, or other meetings sponsored or cosponsored by NASA.

- SPECIAL PUBLICATION. Scientific, technical, or historical information from NASA programs, projects, and mission, often concerned with subjects having substantial public interest.

- TECHNICAL TRANSLATION. English-language translations of foreign scientific and technical material pertinent to NASA's mission.

Specialized services that complement the STI Program Office's diverse offerings include creating custom thesauri, building customized databases, organizing and publishing research results…even providing videos.

For more information about the NASA STI Program Office, see the following:

- Access the NASA STI Program Home Page at ***http://www.sti.nasa.gov***

- E-mail your question via the Internet to help@sti.nasa.gov

- Fax your question to the NASA Access Help Desk at (301) 621–0134

- Telephone the NASA Access Help Desk at (301) 621–0390

- Write to:
  NASA Access Help Desk
  NASA Center for AeroSpace Information
  7121 Standard Drive
  Hanover, MD 21076–1320
  (301)621–0390

Available from:

NASA Center for AeroSpace Information
7121 Standard Drive
Hanover, MD 21076–1320
(301) 621–0390

National Technical Information Service
5285 Port Royal Road
Springfield, VA 22161
(703) 487–4650

Microgravity Materials Science Conference

Using This Document

SEARCH

Adobe® Acrobat® Online Guide

Additional Material

---

*The research reports are organized alphabetically by principal author.

Tips for Using this Document:

▸ Navigation through the document is primarily possible by the use of bookmarks (to open, go to Window → Show Bookmarks on the menubar or click the Bookmark icon on the toolbar). Buttons on the document pages, and, while within document sections, scrollbars, also allow you to reach specific pages quickly.

▸ The reports in the document have been separated into three sections, and arranged alphabetically by the primary author. Please look in Appendix A: Author Index for links and page references to work by specific authors and co-authors.

▸ For more information on using Adobe® Acrobat®, please review the Acrobat® Online Guide (go to Help → Acrobat Guide on the menubar or click the Adobe® Acrobat® Online Guide button on the Main Menu page), or check out a quick review of the Acrobat® Menu Bar Functions by clicking the Icons button below.

Main Menu

Icons

Contributor Websites

Abbaschian, Reza:
- http://www.eng.ufl.edu/home/pubs/Diamonds.htm
- http://www.grc.nasa.gov/Other_Groups/RT1998/6000/6712degroh.html
- http://science.nasa.gov/usmp4/daily/dec02_sciupdate.htm

Banish, R.M.: http://www.cmmr.uah.edu/banish/

Beckermann, C.:
- http://css.engineering.uiowa.edu/~becker/
- http://www.cco.caltech.edu/~atomic/snowcrystals/gallery98/snow98.htm

Debelak, Kenneth A.:
- http://www.vuse.vanderbilt.edu/~debelak/visanal.htm
- http://www.vuse.vanderbilt.edu/~debelak/gas_solid.html

Glicksman, Martin E.:
- http://science.nasa.gov/newhome/headlines/msad19feb99_1.htm
- http://www.digitalfootprint.com/engineering/hall/1994.html
- http://wwwssl.msfc.nasa.gov/USMP4/daily/nov20_sciupdate.htm
- http://mgnews.msfc.nasa.gov/IDGE/IDGE.html
- http://www.rpi.edu/locker/56/000756/index.html

Hofmeister, W.H.: http://www.vuse.vanderbilt.edu/~aesinfo/hofmeist.htm

Karma, Alain:
- http://css.engineering.uiowa.edu/~becker/
- http://www.circs.neu.edu/bio/karma_bio.html

Kelton, Kenneth: http://wuphys.wustl.edu/~kfk/

Koss, Matthew B.:
- http://mgnwww.larc.nasa.gov/spring97/spr97p3.html
- http://science.msfc.nasa.gov/newhome/headlines/msad16jul98_1.htm

Kou, Sindo:
- http://www.engr.wisc.edu/mse
- http://www.engr.wisc.edu/mse/faculty/kou_sindo.html
- http://www.engr.wisc.edu

Krishnan, Shankar: http://www.cs.unc.edu/~krishnas/

Larson, David J.: http://dol1.eng.sunysb.edu/larson/cgl.html

Matthiesen, David: http://mgnews.msfc.nasa.gov/winter98/mission.html

McFadden, Geoffrey B.: http://math.nist.gov/~GMcFadden/GMcFadden_Res.html

Megaridis, Constantine: http://www.me.uic.edu/combustion/index.html

Ostrogorsky, A.: http://www.cmmr.uah.edu/crystalgrowth/

Perepezko, John H.: http://wwwssl.msfc.nasa.gov/ssl/msad/dtf/immisci.htm

Regel, Liya L.:
- http://www.clarkson.edu/~regel/cover2.htm
- http://www.clarkson.edu/~regel/dia-pat.jpg
- http://www.clarkson.edu/~regel/research.htm

Sekerka, Robert F.:
- http://info.phys.cmu.edu/people/faculty/Sekerka/
- http://math.nist.gov/~GMcFadden/dendrite.html

Spaepen, Frans A.:
- http://www.deas.harvard.edu/faculty/spaepen.html
- http://www.deas.harvard.edu/matsci/index.html

Stefanescu, Doru: http://www.sciencedaily.com/releases/1997/11/971126052114.htm

Su, Ching-Hua: http://www.astrophysics.com/newhome/headlines/msad22mar99_1.htm

Szofran, Frank: http://www.proc.org/terracom/tc0198/german/html/science.htm

Trivedi, Rohit: http://www.mse.iastate.edu/people/trivedi.html

Voorhees, Peter:
- http://mgnwww.larc.nasa.gov/spring97/spr97lead.html
- http://zeta.lerc.nasa.gov/cslm/cslm.html

Wilcox, William: http://www.clarkson.edu/~wilcox/wilcox.htm

Main Menu

Microgravity Materials Science Conference

June 6 - 8, 2000

Organized by

Microgravity Materials Science Discipline Working Group

Sponsored by

Microgravity Research Division, NASA Headquarters, Washington, D. C.

Hosted by

NASA Marshall Space Flight Center, Huntsville, Alabama

Foreword

The 2000 Microgravity Materials Science Conference was held June 6-8 at the Von Braun Center, Huntsville, Alabama. It was organized by the Microgravity Materials Science Discipline Working Group, sponsored by the Microgravity Research Division (MRD) at NASA Headquarters, and hosted by NASA Marshall Space Flight Center and the Alliance for Microgravity Materials Science and Applications (AMMSA). It was the fourth NASA conference of this type in the microgravity materials science discipline. The microgravity science program sponsored approximately two hundred investigations, all of whom made oral or poster presentations at this conference. In addition, posters and exhibits covering NASA microgravity facilities, Advanced Technology Development projects sponsored by the NASA Microgravity Research Division at NASA Headquarters, and commercial interests were exhibited. The purpose of the conference was to inform the materials science community of research opportunities in reduced gravity and to highlight the spring 2001 release of the NASA Research Announcement (NRA) to solicit proposals for future investigations. It also served to review the current research and activities in materials science, to discuss the envisioned long-term goals, and to highlight new crosscutting research areas of particular interest to MRD. The conference was aimed at materials science researchers from academia, industry, and government. A workshop on In Situ Resource Utilization (ISRU) was held in conjunction with the conference with the goal of evaluating and prioritizing processing issues in Lunar and Martian-type environments. The workshop participation included invited speakers and investigators currently funded in the material science program under the Human Exploration and Development of Space (HEDS) initiative. The conference featured a plenary session every day with an invited speaker that was followed by three parallel breakout sessions in sub-disciplines. Attendance was close to three hundred and fifty people. Posters were available for viewing during the conference and a dedicated poster session was held on the second day. Nanotechnology, Radiation shielding materials, Space Station science opportunities, Biomaterials research and Outreach and Educational aspects of the program were featured in the plenary talks. This volume, the first to be released on CD-Rom for materials science, is comprised of the research reports submitted by the Principal Investigators at the conference.

Table of Contents

*Dr. Frans Spaepen is the Co-Principal Investigator on this project.

Main Menu

IN SITU MONITORING OF CRYSTAL GROWTH USING MEPHISTO

Reza Abbaschian[1], Y. Lian[1], H. de Groh III[2], V. Timchenko[3], P.Y.P. Chen[3], E. Leonardi[3], and G. de Vahl Davis[3]

[1]Materials Science and Engineering
[1]University of Florida, Gainesville, FL 32611
[2]NASA/Glenn Research Center at Lewis Field
Cleveland, OH 44135
[3]University of New South Wales, Sydney, Australia 2052

ABSTRACT

Experiments were carried out to study the morphological stability of Bi-1atomic% Sn alloys using the MEPHISTO directional solidification apparatus aboard Space Shuttle Columbia (STS-87, launched November 19, 1997). The research program involved collaboration of the University of Florida, Centre National d'Etudes Spatiales (France), NASA/Glenn Research Center, the National Institute of Standards and Technology, and the University of New South Wales (Australia). The experiments made use of the Seebeck technique to measure the interface temperature, the resistance change across the sample for determination of the interface velocity, and Peltier current pulsing for demarcation of the interface shape. These data were obtained in real-time during various melting/solidification cycles, and the experiments were controlled via telecommands.

The Seebeck signal and temperature measurements in the space experiments, as well as morphological behavior of the solid/liquid interface, were found to be significantly different than those obtained from ground-based studies. For the space-based experiments, interface breakdown was observed at growth velocities of 6.7, 27, and 40 μm/s, but not at 1.8 and 3.3 μm/s. The results further indicate that the morphological stability threshold for some grain orientations is significantly enhanced, resulting in a staggered planar to cellular transition front. This report summarizes some of these findings.

This work was supported by NASA/Grant/Contract #NASA NCC3-476.

I. Background

The formation of dendrites generally follows morphological instability of a planar solid/liquid interface [1]. The morphological stability criterion of Mullins and Sekerka [2] can be utilized to predict the onset of instability in planar interfaces. The criterion determines the conditions for the growth or decay of a perturbation on a planar interface under a given steady state condition. More recent theoretical models indicate that anisotropic interfacial properties play a role in the morphological stability of planar interfaces, as well as the evolution of cellular and dendritic structures, this has been predicted theoretically by Coriell and Sekerka [3] and Coriell *et al.* [4] by extending the linear stability analysis of Mullins and Sekerka [2], and by Young *et al.* [5] in the weakly nonlinear regime. These treatments indicate that such anisotropies tend to stabilize the growth of a planar

Main Menu

interface. Experimental observations reported by Tiller and Rutter [6] for lead-tin alloys and by Trivedi [7] and Trivedi *et al.* [8] for transparent organic systems have been found to be generally consistent with the theoretical predictions.

The influence of anisotropic interfacial kinetics on the morphological stability threshold was recently demonstrated by the present investigators for solidification of Bismuth alloyed with 0.1% Sn [9,10]. The experiments were conducted under microgravity conditions during the STS-62 flight of the space shuttle Columbia, using the MEPHISTO directional solidification facility. Similar to the USMP-4 experiments, the experiments yielded 15 cm of three parallel-processed samples, each grown directionally at six velocities ranging from 1.85 to 40 μm/s. The microstructural evaluation of the space grown samples indicated that for 1.85, 3.4 and 6.7 μm/s interface velocities, the growth occurred in a planar mode. The microstrutural evolution at a higher velocity of 13.3 μm/s appeared to be cellular in one grain, and planar in another, whereas for 26.9 and 40 μm/s velocities, cellular/dendritic morphologies were observed in both grains. The most interesting aspect of the planar-cellular transition at 26.9 μm/s velocity was the existence of distinct preferential breakdown in one grain versus the other. The upper grain became cellular approximately 0.6 mm after the initiation of growth, forming cells which were tilted about 6.5° with respect to the heat flow and growth directions. The neighboring grain on the other hand, continued with planar growth about 12.2 mm until it became cellular, with cells parallel to the growth direction. The cell spacing within the two grains were approximately the same, 265 and 276 μm, respectively.

II. Experimental Facility and Techniques

The MEPHISTO hardware is shown schematically in Figure 1 [9,11]. The apparatus is capable of simultaneous processing of three rod shaped samples, each of which is approximately 900 mm in length and 6 mm in diameter. The central part of MEPHISTO consists of two furnaces each with a neighboring heat sink, which is cooled by a refrigerant. One of the furnace-heat sink structures is stationary, while the other is on a moving platform. Between these heaters special reflectors and insulation are used to maintain a nearly uniform temperature. In the experiments to be described the furnaces were heated to 750° C, while the cold zones were kept near 50° C, resulting in a molten zone in the middle of each as illustrated in Figure 1. When the movable furnace-heat sink structure is translated away from the fixed furnace, the extent of the hot zone is lengthened, increasing the extent of the molten zone in the sample. Near the solid-liquid interfaces, which are located between each furnace and its accompanying heat sink, a temperature gradient on the order of 200° C/cm is established. The furnace heaters are in contact with cylindrical thermal diffusers made of graphite and are regulated using thermocouples within the diffusers. The graphite diffusers have three holes to accommodate the samples. The uniform temperature field produces a very similar thermal profile for the three samples. In order for the heat sinks to efficiently remove the heat from the samples, a metal seal of a low melting point (45° C) alloy was utilized. When the heat sink reached its operating temperature, the liquid alloy made a direct contact between the heat sink and the outer quartz wall of the samples.

The alloy used for the experiments was Bi with 1 atomic % Sn. As shown in Figure 2, Bi and Sn form a simple eutectic diagram, with a maximum solubility of 1.63 atomic % Sn at the eutectic temperature of 140° C. The distribution coefficient for Sn in Bi is measured to be around 0.03. Schematics of the three samples inserted into the MEPHISTO apparatus and their dimensions are shown in Figure 3. Each of the three samples, which will be referred to as the "Quenching," "Peltier," and "Seebeck," has a special

purpose in the study of alloy solidification. A 2 mm ID, 3 mm OD quartz capillary is located on the moving furnace side, which extends about 250 mm into the sample. Thin capillaries (approximately 0.6 mm OD) for the thermocouples were also inserted for the thermocouples in the Peltier and Quenching samples. The 3mm OD were filled with the alloy during sample preparation. The samples used in the ground-based processing were similar except the capillaries were about 40 mm shorter.

The Quenching sample was used to measure the rate of solidification using the resistance change across the sample during processing and to produce a short section of quenched interface at the end of the experiments. To achieve the latter, the sample is attached to a mechanism which quickly pulls the sample about 2 cm towards the cold zone and freezes the sample. The Quenching sample was electrically connected for the resistance measurements, and was used to calculate the solidification rate. The Peltier sample has connections to allow marking the sample with short electrical pulses which cause heating or cooling at the solid-liquid interface.

The Seebeck sample is used to measure the difference between the temperature of the stationary and moving solid-liquid interfaces. The relationship between the measured Seebeck signal and the temperature of the moving interface, T_C, and the temperature of the stationary interface, T_D, will be discussed together with the experimental results. Details of Seebeck interface temperature measurement can be found elsewhere [12].

III. Experiments and Growth Conditions

The flight experiments were performed with the help of Société Européene de Propulsion (SEP) by telecommanding. The experiments were initiated by heating the movable and stationary furnaces to 750°C. This established a liquid zone approximately 340 mm long as depicted in Figure 1. Melting and solidification experiments were performed by commanding the apparatus to move the mobile furnace/heat sink structure. The fully open position was referenced as 1 mm and the fully closed 150 mm. Increasing the furnace position corresponded to freezing and decreasing the furnace position to melting. Figure 4 is a plot of the MEPHISTO movable furnace position during the USMP-4 mission. Many of the experiments consisted of a freezing period where the furnace was moved forward, a hold period where the furnace was kept stationary, and a melt period where the furnace was moved back to the original position for the cycle with the opposite velocity of the freezing period. Figure 5 is an example with a start position of 115 mm, freezing for 15 mm at 13.5 μm/s, and a hold period of 30 minutes, and then melting back to the 115 mm position at 13.5 μm/s. As shown in Figure 4, the experiments included thirty-five freeze-hold-melt cycles during the mission and eleven periods of final directional solidification. The experiments were performed over a range of solidification rates from 0.74 to 40 μm/s. All of the flight experiments were commanded and controlled via telemetry from the NASA-Marshall Payload Operational Control Center.

IV. Microstructural and Data Analysis

The micrographs in Figures 6(a)-(b) show the successive development of the microstructure as a function of the distance and the growth velocity for the Seebeck sample. Figure 7 shows schematically a summary of processing lengths and velocities as well as the microstructure in each section. Also shown is the successive development of the microstructure as a function in the growth velocity. For solidification at velocities below V2 the growth occurs in a planer mode, while cellular morphology is seen at V3

through V6 velocities. The planar to cellular transition reveal many important aspects of the solidification of faceted materials in microgravity as discussed in more detail in the following section. The initial (Earth grown) microstructure of the samples is shown in Figure 8. The samples were produced from a homogeneous liquid through quenching. The optical micrograph in Figure 8 shows relatively uniform microstructure with a faceted cellular/dendritic morphology.

The development of a plane-front microstructure is illustrated in Figures 9(a)-(c) which show the transition from a facet cellular/dendritic structure of the Earth-grown portion of the samples to a plane-front morphology at the moving furnace interface. At all three interfaces, the initial cellular to plane-front transition interface was sharply delineated. The optical micrographs show that only a few dominant orientations emerge from the initial microstructure, which was found to be a common feature of all three samples. The microstructure is characterized by a complete absence of the Sn-rich second phase indicating plane-front solidification. It was found that the interface was associated with a sharp compositional change, detected via electron microprobe analysis as presented later.

When an interface was revealed, for example during the interface breakdown, it was found that the interface was nearly flat, with a slight curvature near the s/l/crucible triple junction. Upon closer examination, the boundary across each grain appears to be fairly flat, with the small angles between them giving the appearance of an overall slight curvature of the interface, as shown by the micrograph of the interface where the sample was quenched in Figure 10.

Microstructural examination of the microgravity-processed sections indicated that those regions of samples grown at V3 through V6 velocities exhibited a morphological transition to a cellular growth mode. The microstructural appearance of the cellular breakdown of event 15, V5 (Peltier sample) is shown in Figure 11. A much narrower planar to cellular transition zone was seen at a higher growth velocity (V5, V6) than that at lower growth velocity V3. More detail of the morphological transition will be reported later.

The thermal profile in the MEPHISTO apparatus were monitored using nine thermocouples located in each of the furnace diffusers and heat sinks. Four thermocouples were also placed inside the small quartz capillaries within the Quenching and Peltier samples. The thermocouples in the heater and heat sink diffusers were used to control the overall thermal conditions of the furnace. The thermal profile of the samples, however, is not fully determined by the temperatures imposed by the diffusers, but also by the properties of the sample to be processed. Therefore, the temperature field in the samples was monitored using the four experimental thermocouples located within the samples. A typical thermal measurement by three of the thermal couples is shown in Figure 12. Also shown in the figure is the corresponding furnace position and the melting temperature. The temperature gradients in the solid and liquid near the interface were measured as 260 and 204 K/cm for growth within the 6 mm quartz tube.

Figure 13 gives the temperature profile for ground- and space-based experiments within the Peltier sample using thermocouple T4 in the ground-based experiment, and T4 and T6 in the space-based experiments. (The positions of these thermocouples are marked in Figure 3.) Note the temperature gradient for the space-based experiments within and outside the capillary for the space-based experiments are both about 260° C/cm. The thermal profile in the solid (below about 270° C) for the ground-based experiments is very similar to the space-based measurements. However, the average temperature gradient in the liquid for the ground-based mission is only about 100 °C/cm.

A non-intrusive technique for studying interfacial undercooling is to measure the Seebeck signal generated by a solid-liquid-solid structure [13,14,15]. The technique enables a quantitative investigation of interfacial undercooling including compositional and kinetic terms. For the current loop pictured in Figure 1, the Seebeck Voltage will be given by:

$$E_S = \int_A^F \eta\,(\phi\,(w), c\,(w), \theta\,(\vec{w}), T\,(w))\;\nabla T \bullet d\vec{w}$$

where w is the path, η is the Seebeck coefficient, and ∇T is the temperature gradient. Here we have assumed the Seebeck coefficient depends only on the phase of material, ϕ, the composition, c, and the crystallographic orientation, θ. For the equation to be valid, a necessary condition is that the integral does not depend on the path taken within the material. This could be violated, for example, if there are alternate paths through materials with different Seebeck coefficients. For the present setup, $T_A = T_F$ (where T refers to temperature, and the subscript the position), $T_B = T_E$, and the wires from A to B and F to E are the same material. (The MEPHISTO apparatus can monitor and control the end temperatures of the sample to within 0.01°C.) If it is assumed that the Seebeck coefficients for the solid and liquid do not vary with concentration, temperature or structure, the resulting signal for the simplified conditions will be:

$$E_S = \eta_S(T_C - T_B) + \eta_L\,(T_E - T_D) + \eta_S\,(T_E - T_D)$$

where η_S is the Seebeck coefficient for the solid, and η_L is the Seebeck coefficient for the liquid. Since $T_B = T_E$, this simplifies to $E_S = -(\eta_S - \eta_L)(T_D - T_C)$. If the Seebeck coefficient of the liquid and solid are known, then one can determine the difference in temperatures of the two solid-liquid interfaces. The temperature at the stationary interface, T_D, is given by the phase diagram in Figure 2. The equation simplifies to:

$$T_C = T_D + \frac{E_S}{\eta_S - \eta_L} = T_D + \frac{E_S}{\eta_{S/L}}$$

where $\eta_{S/L}$ is the difference in the Seebeck coefficient of the solid and liquid near the melting temperature.

Figure 5 gives the Seebeck signals acquired for a ground- and a space-based experiment. Each consisted of solidification, hold, and melt period as previously described. The Seebeck signal for the ground-based experiment rose during freezing, fluctuated around an average value for the hold, then decreased during melting. The fluctuations in the signal are due to hydrodynamic mixing in the liquid. It was observed that the magnitude of the fluctuations strongly depended on the maximum temperature of the melt. The signal for the space-based experiment had an initial increase, then decreased during freezing. After the furnace stopped, the signal increased due to the interface temperature increase caused by the exponential decay of solute at the interface. During melting the signal decreased, then increased back to near its initial value before the freeze-hold-melt cycle was begun. The differing behavior of the ground- and space-based Seebeck results may be due to the differences in the amount of solute build-up at the interfaces as well as structural changes in the solid. As such, the results can not be explained by the above mentioned simplified equation that is based on the assumption that structure and composition do not affect the Seebeck coefficient of the solid or the liquid. More accurate analysis of the Seebeck data can be found in Reference [16].

A mathematical model of heat, momentum and solute transfer during directional solidification of binary alloys in a Bridgman furnace has been developed by the Computational Fluid Dynamics Research Group at the University of New South Wales, Sydney, Australia. The results of the calculations are being compared with those of the experiments for the purpose of better interpretation of the data, as

well as the determination of the property values of bismuth. The model uses a fixed grid single domain approach (enthalpy method) to incorporate the effects of coupling with the phase diagram (a concentration-dependent melting temperature) and of thermal and solutal convection on segregation of solute, shape and position of the solid/liquid interface.

Two numerical approaches are being employed. In the first, the primitive variable equations are solved by a finite volume discretization, using a commercial flow code CFX 4.1. in the second, a finite difference/finite volume discretization of the vorticity-stream function formulation of the equation is solved by an in-house code SOLCON. Figure 15 compares results of one such calculation with the experimentally determined solute concentration at two velocities. The distribution of solute concentration in the solid along the center line of the sample is shown in Figure 15a. Numerical solutions were obtained from the experimental samples. Figure 15b shows the distribution of solute concentration across the solid. Both axial and transverse numerical distributions are in very agreement with the experimental results. More detailed comparison can be found in Ref erence [17].

V. Summary

Many of the parameters important for studying morphological instabilities were successfully measured during directional solidification of Bi 1 at % Sn. The Seebeck signals and calculated temperature gradient in the liquid for the ground- and space-based sets of experiments were significantly different. The differences are consistent with strong hydrodynamic mixing in the liquid during the ground-based experiments. The analysis of the Seebeck measurements indicate that for bismuth-based alloys, the structure and composition of the solid alloy have strong influences on the Seebeck signal generated. The microstructural examination of the directionally solidified samples reveals strong influences of interfacial kinetics and anisotropy on the morphological instability of the solid-liquid interface.

VI. Acknowledgments

The authors would like to thank CEA and the Société Européene de Propulsion, France for their support during ground-based experiments and flight preparations. We would also like to acknowledge the entire USMP-4 team, especially Philippe Beaugrand, Kirk Beatty, G. Cambon, Vincent Gounot, Philippe Le, Regis Rieu, Bill Foster, Gil Santoro, Mingwu Yao, Nick Barbosa, Jeff Clancy and Gordon Seuell. The financial support of the program by NASA is gratefully acknowledged.

REFERENCES

1. As reviewed in "Morphological Stability," S.R. Coriell and G.B. McFadden, Handbook of Crystal Growth, Vol.1, ed. D.T.J. Hurle, (Elsevier) 785.
2. W.W. Mullins and R.F. Sekerka, "Stability of a Planar Interface During Solidification of a Dilute Binary Alloy," *J. Appl. Phys*., (1964) 444.
3. S.R. Coriell and R.F. Sekerka, "The Effect of Anisotropy of Surface Tension and Interface Kinetics on Morphological Stability," *J. Crystal Growth*, 3 (1976) 157.
4. S.R. Coriell, B.T. Murray, and A.A. Chernov, "Kinetic Self-Stabilization of a Stepped Interface: Binary Alloy Solidification," *J. Cryst. Growth*, 141 (1994) 219.
5. G.W. Young, S.H. Davis and K. Brattkus, "Anisotropic Interface Kinetics and Tilted Cell Unidirectional Solidification," *J. Cryst. Growth*, 83 (1987) 560.

6. W.A. Tiller and J.W. Rutter, "The Effect of Growth Conditions Upon the Solidification of a Binary Alloy," *Can. J. Phys*., 34, (1956) 96.
7. R. Trivedi, "Effects of Anisotropy Properties on Interface Pattern Formation," *Appl. Mech. Rev*., 43 (5) Part 2, (1990) S79.
8. R. Trivedi, V. Seetharaman and M.A. Eshelman, "The Effects of Interface Kinetics Anisotropy on the Growth of Cellular Microstructures," *Met. Trans. A*, 22A (1991) 585.
9. R. Abbaschian, A.B. Gokhale, J.J. Favier, G. Combon, S.R. Coriell, H.C. de Groh III, and R.L. DeWitt, "A Study of Directional Solidification of Faceted Bi-Sn Alloys in Microgravity," (American Institute of Aeronautics and Astronautics, January 1995) AIAA 95-0608.
10. R. Abbaschian, A.B. Gokhale, and D.B. Allen, " A Study of Directional Solidification of Faceted Bi-Sn Alloys in Microgravity," *Solidification Science and Processing*, Edited by I. Ohnaka and D.M. Stefanescu, 1996, pp.73-84.
11. A. Rouzard, J.J. Favier and D. Thevenard, *Adv. Space*. *Res.* 8, (1988) p 49.
12. S.D. Peteves, Ph.D. Dissertation, University of Florida, (1985)
13. S.D. Peteves and R. Abbaschian, *Met. Trans*. A 22A (1991), 1259.
14. S.D. Peteves and R. Abbaschian, *Met. Trans*. A 22A (1991), 1271.
15. B.Sixou, A. Rouzaud, J.J. Favier, *J. Crystal Growth* 137 (1994) p. 605.
16. P.Y.P. Chen, V. Timchenko, E. Leonardi, G. de Vahl Davis, H.C. de Groh III and R. Abbaschian, "Seebeck Signals for Concentration Measurement During Solidification," to be published.
17. V. Timchenko, P.Y.P. Chen, E. Leonardi, G. de Vahl Davis, R. Abbaschian and H.C. de Groh III, "Solute Redistribution During Plane Front Solidification," to be published.

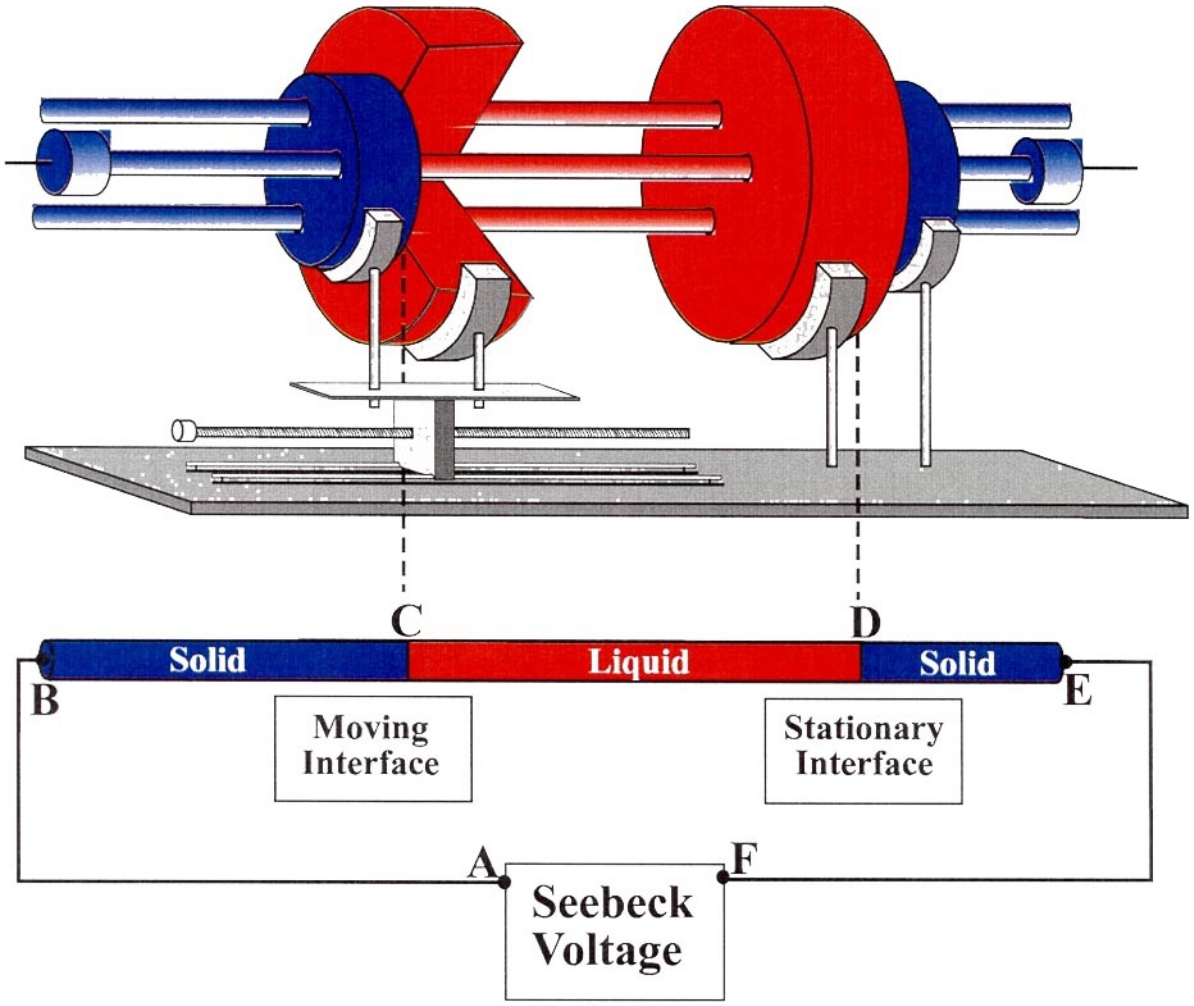

Figure 1. MEPHISTO Apparatus is shown with two furnace/heat sink structures. The three long cylinders going through the two furnace/heat sink structures are the Quenching, Peltier, and Seebeck Samples. The three samples are subjected to the same temperture field, except the Seeback sample has additional temperture regulation to maatch the temperature at its ends. The furnace/heat sink structure on the left can move, causing melting or solidification at the moving solid-liquid interface. In the schematic of the Seebeck sample the ends marked B and E while the solid-liquid interfaces are marked C and D. When solidifying/melting at the moving interface, the tempertures at C and D will not be the same due to compositional and kinetic undercooling/superheating.

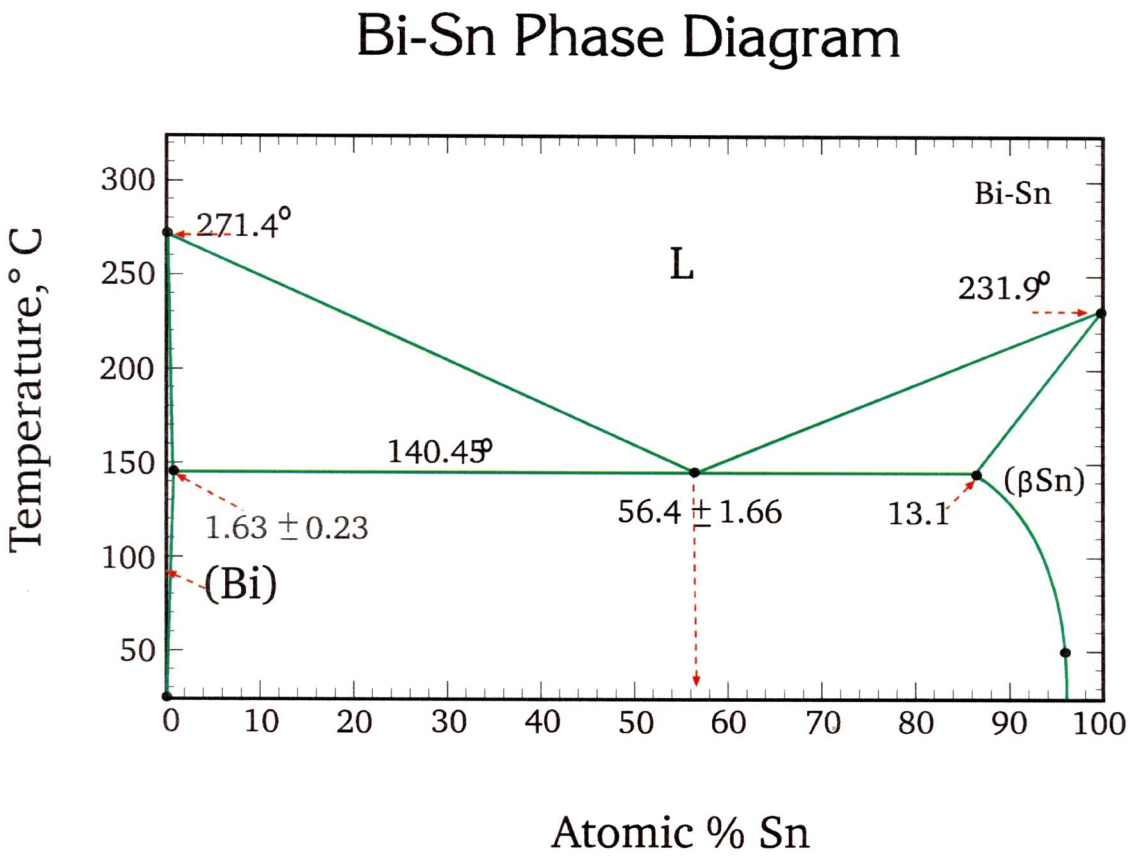

Figure 2. Phase Diagram for the bismuth-tin system.

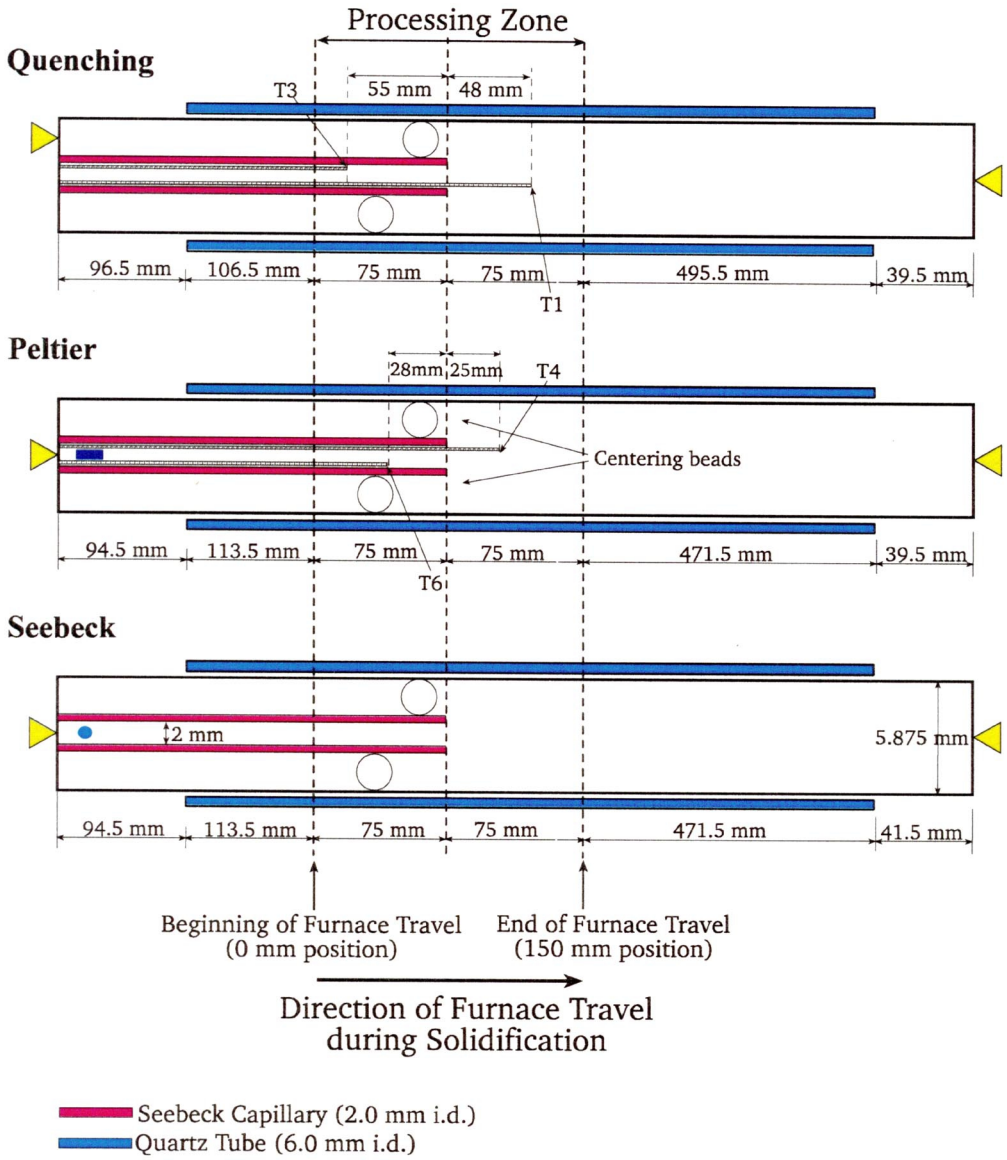

Figure 3. Configurations for the Quenching, Peltier, and Seebeck samples. The samples consist of 5.87 mm diameter cylinders of Bi-1 atomic % Sn alloy which are contained in quartz tubing. The four thermocouples (the Quenching and Peltier each has two) are labeled T1, T3, T4, and T6. The Seebeck capillary is a 2mm i.d quartz tube on the left of each sample. The triangles indicate position of electrical contacts. A small cut in the capillary tube for the Peltier sample allows current to flow in the alloy inside and outside the capillary.

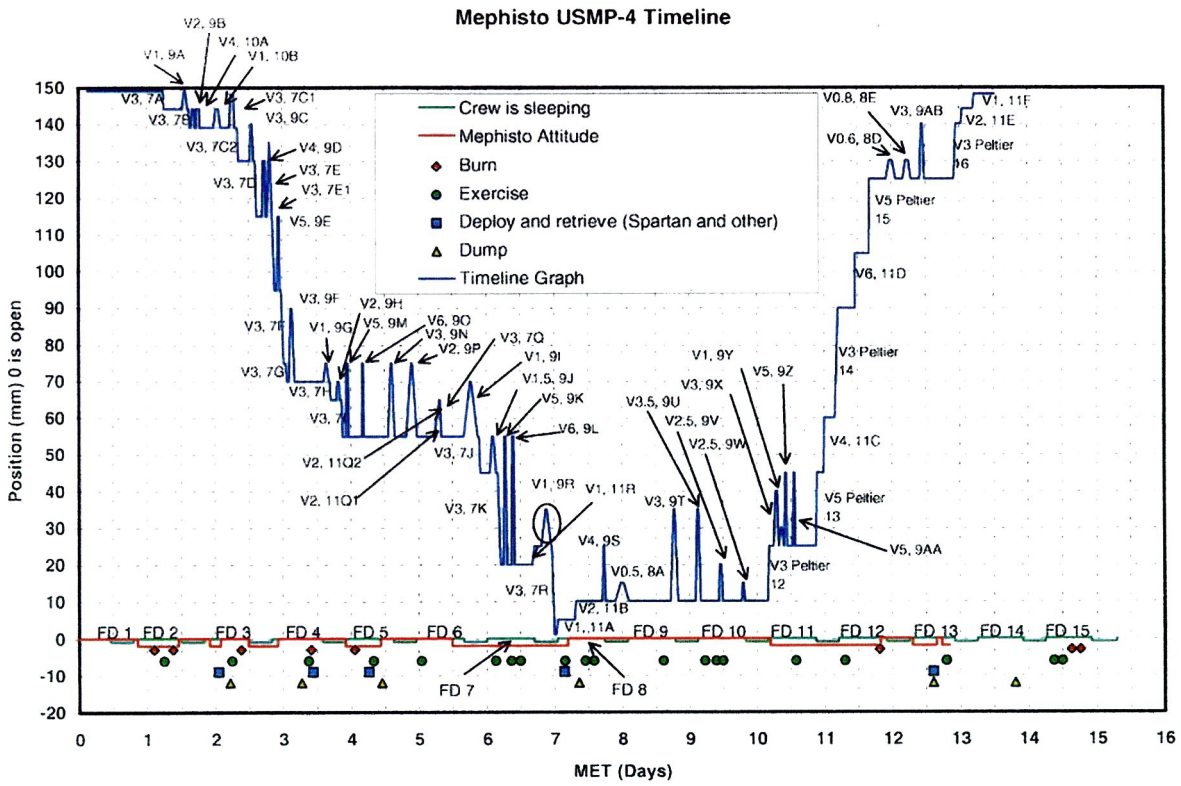

Figure 4. The MEPHISTO moving furnace position as a function of days into USMP-4 mission. The velocities for V0.5, V0.6, V0.8, V1.5, V2, V2.5, V3, V3.5, V4, V5, V6 are 0.74, 1.11, 1.48, 1.85, 2.59, 3.7, 5.2, 6.7, 10, 13.3, 26.7 and 40 µms/s respectively.

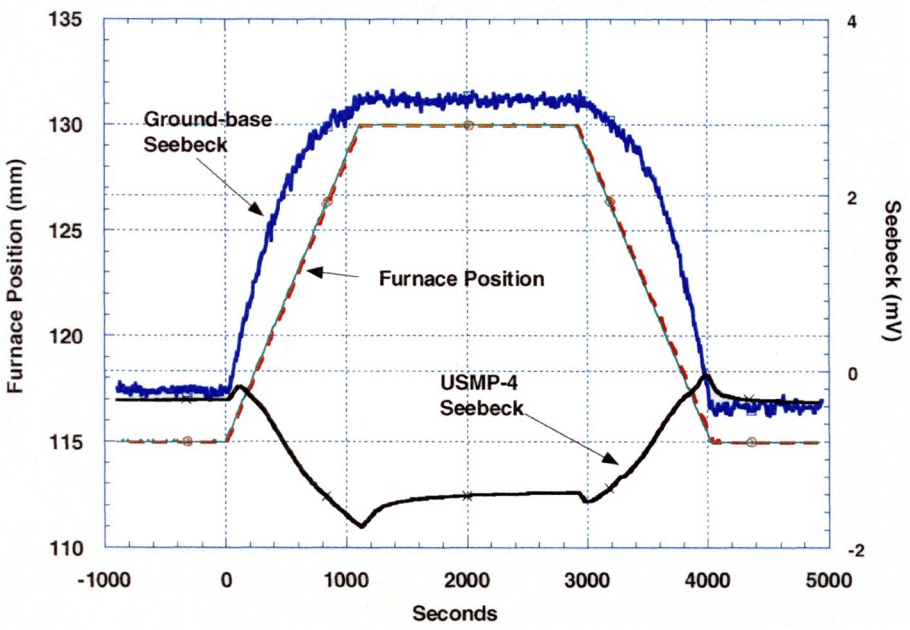

Figure 5. Seebeck signal and position for ground-and space-based experiments for solidification at 13.5 µm/s. The moving furnace position as a function of time into the experiment is very similar for the two experiments. The ground-based experiments have noticeable fluctuations inthe Seebeck signal, presumably from hydrodynamic mixing in the melt.

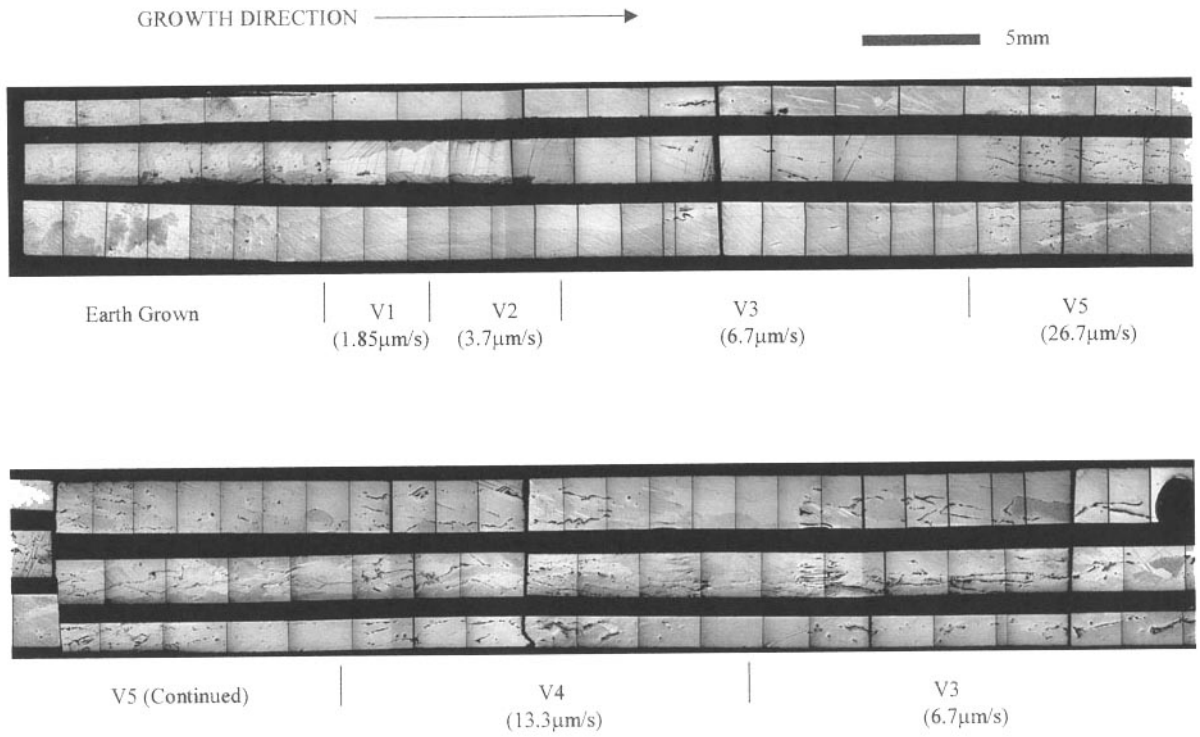

Figure 6a. Microstructural evolution of the Seebeck sample from the Earth grown material to growth in the capillary section.

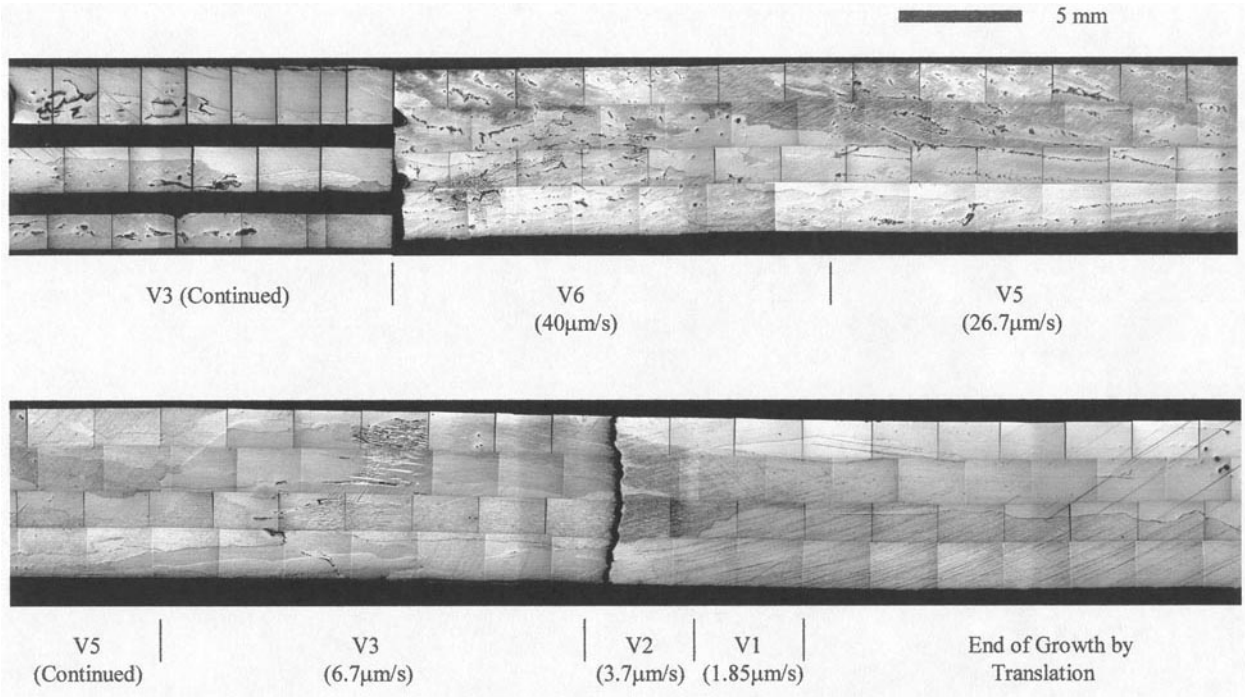

Figure 6b. Continued microstructure of the Seebeck sample extending into the section outside the capillary and finishing in the region where translation finished.

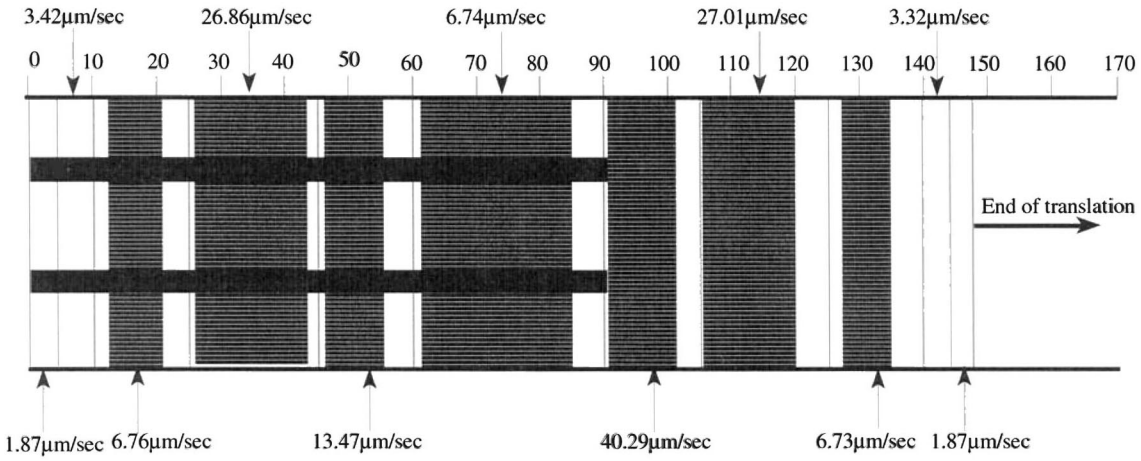

Figure 7: Summary of sample sections preserved during final solidification. Sections with horizontal lines indicate cellular breakdown.

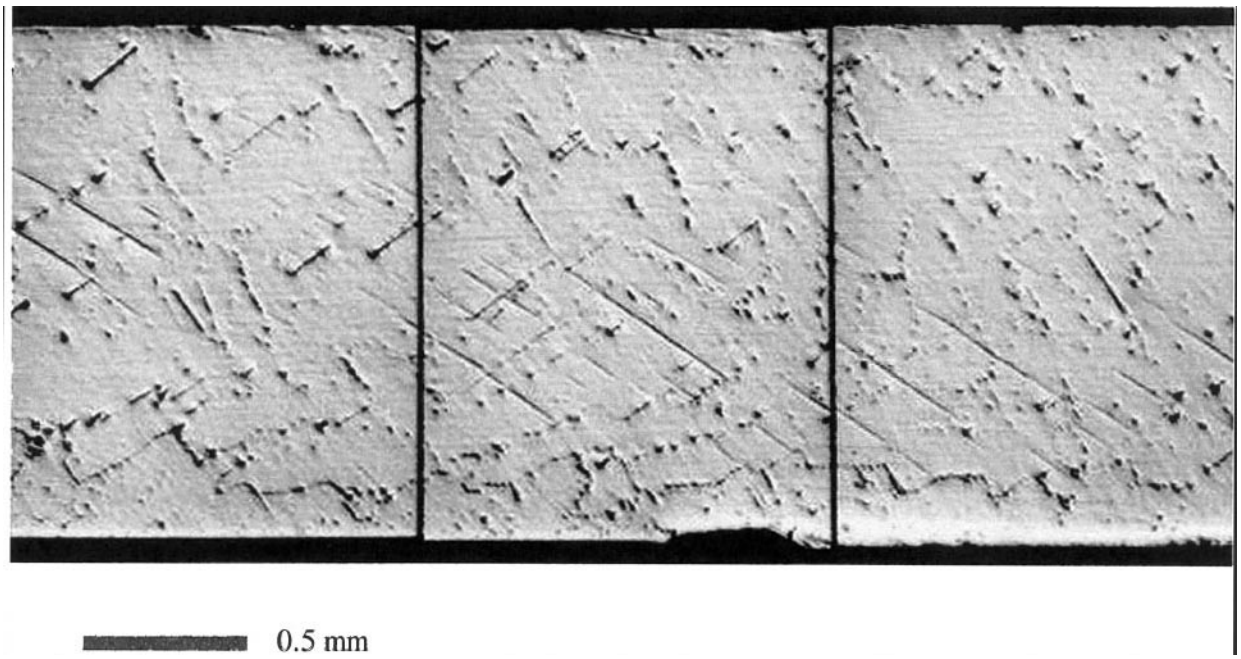

Figure 8: Detail of Earth-grown section showing a faceted cellular/dendritic structure.

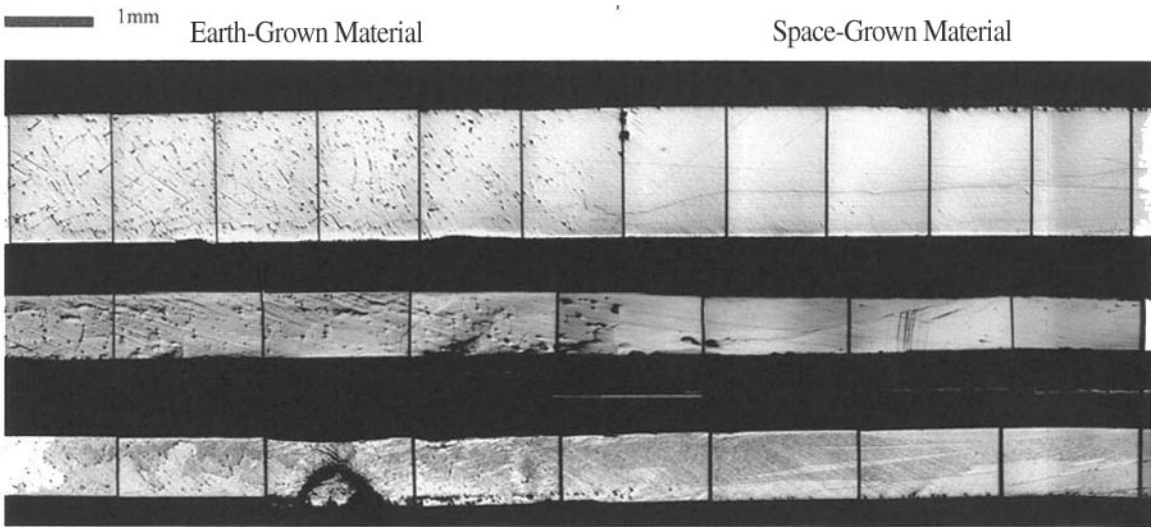

Figure 9a. Composite image of the initial growth of the quench sample. The initial Earth-grown structure on the left hand side shows a faceted cellular dendritic morphology. The transition to plane-front growth is visible in the space-grown material on the right hand.

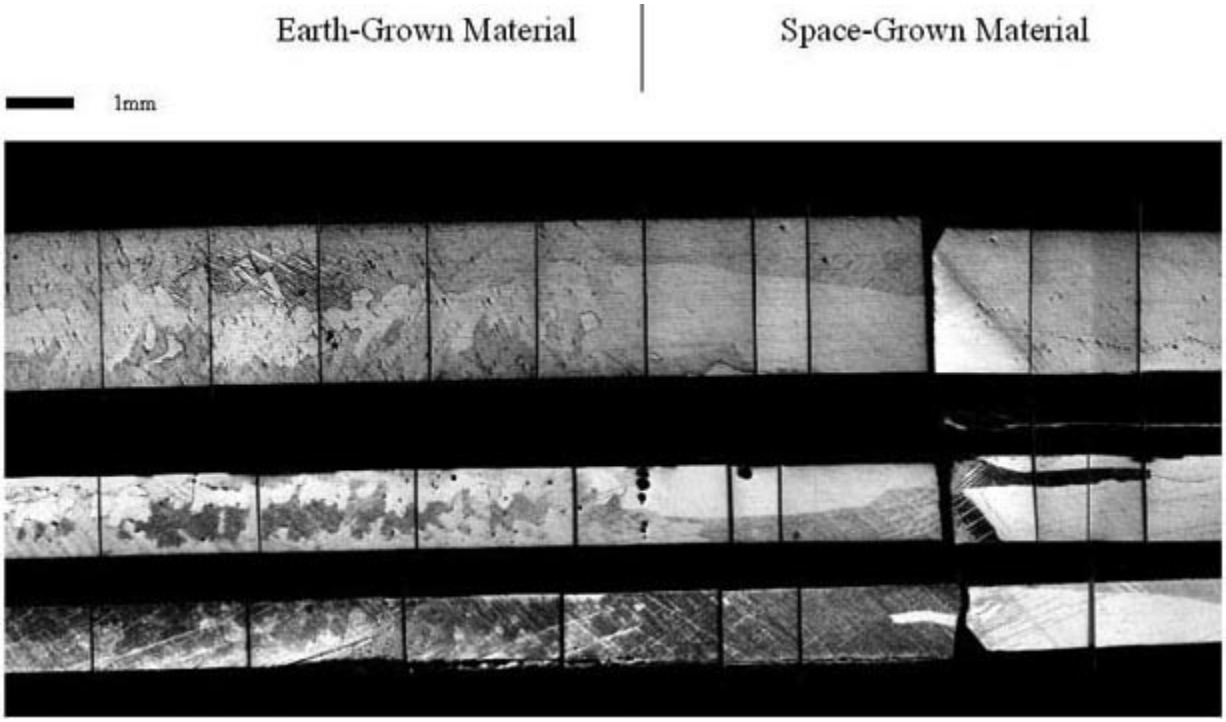

Figure 9b. Composite image of the initial growth of the Peltier sample showing structure to the quench sample. The break in the micrograph is where the sample was cross sectioned.

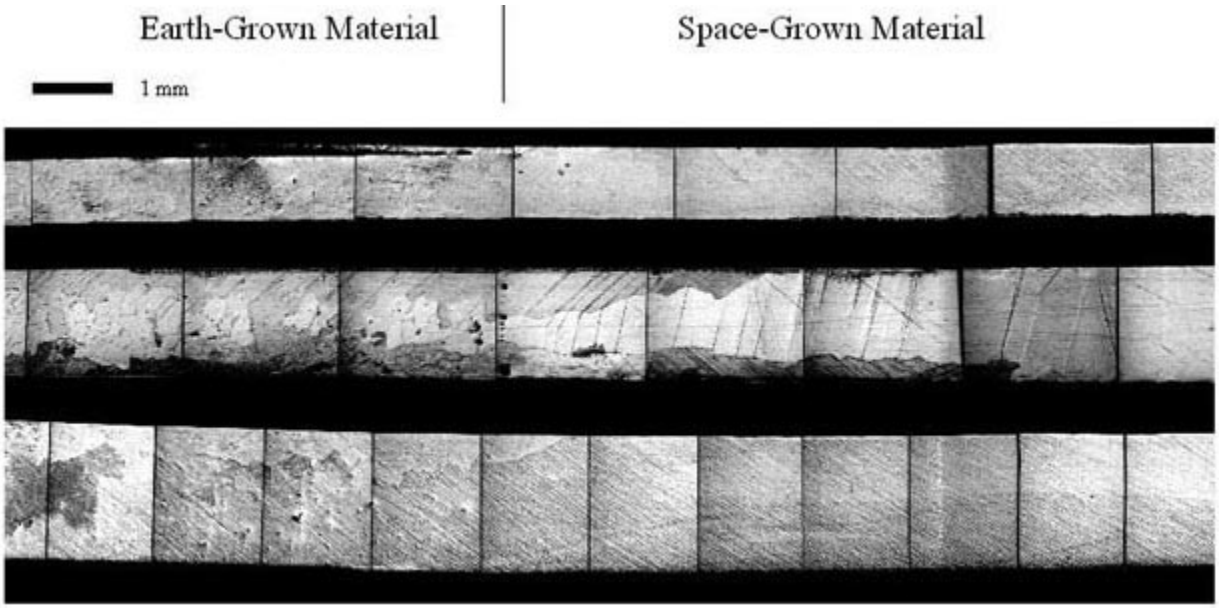

Figure 9c. Composite image of the initial growth of the Seebeck sample showing a similar structure to the previous samples. Twins are visible in the capillary section.

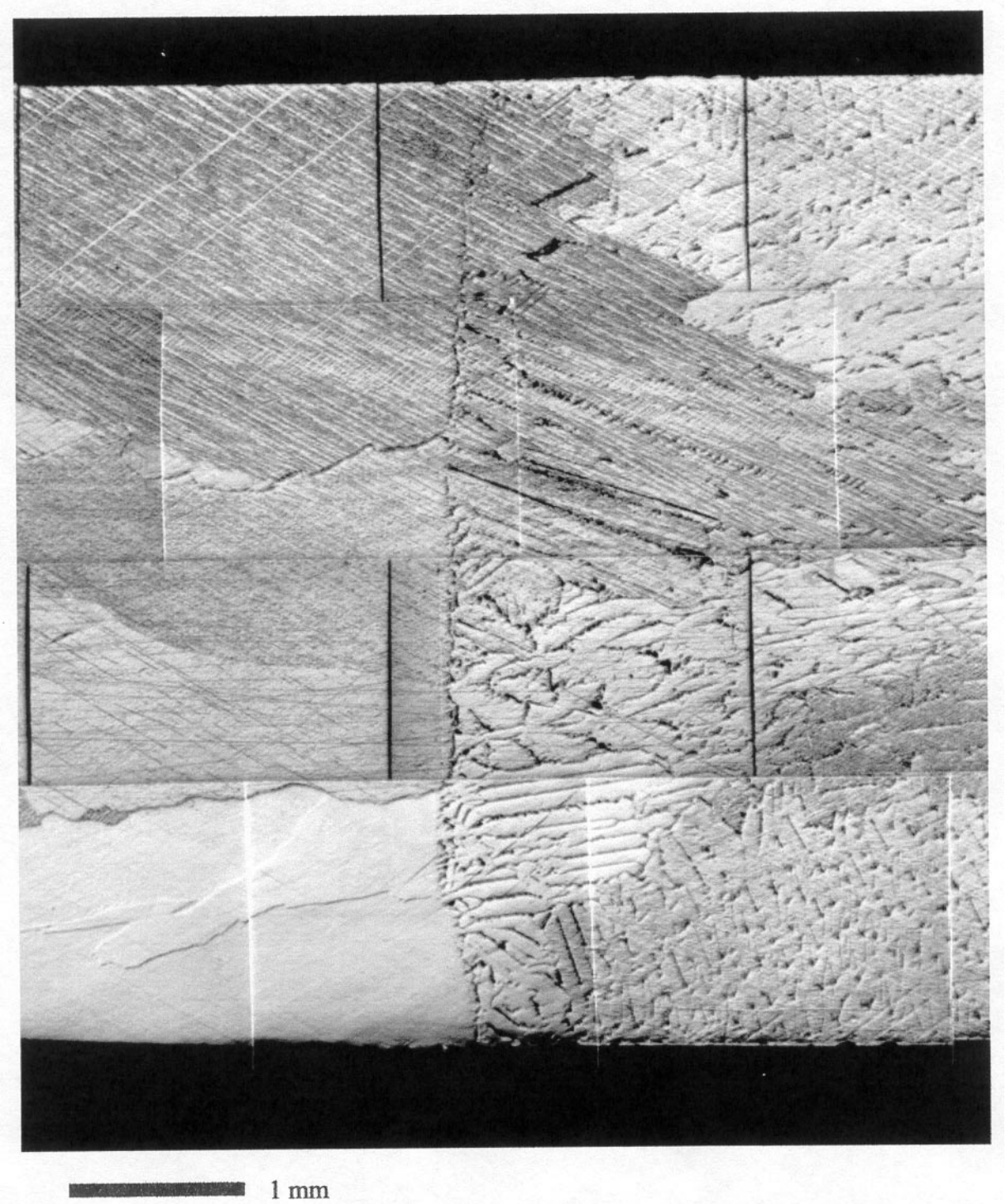

Figure 10. Composite micrograph of quenched section of the quench sample showing the S/L interface shape.

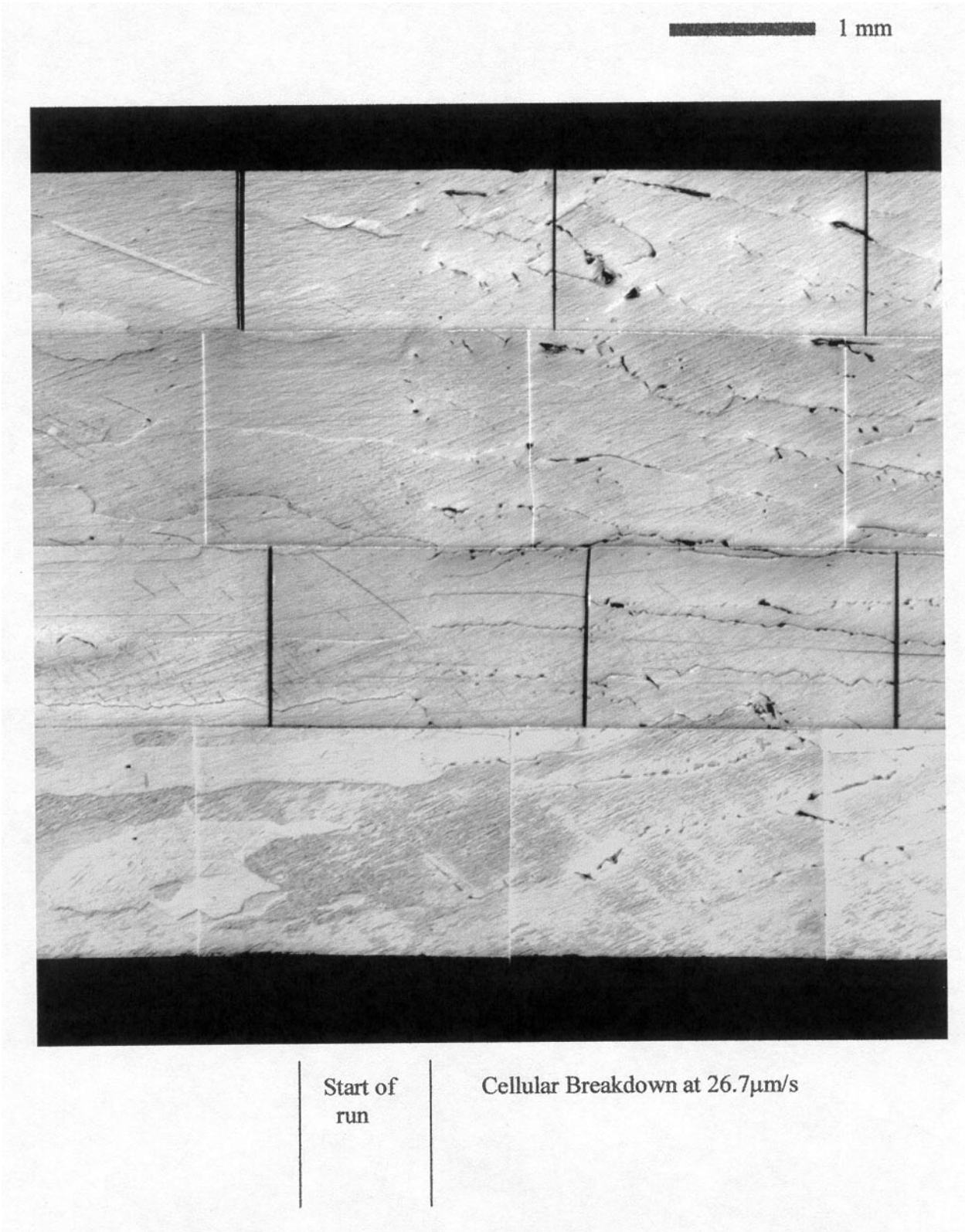

Figure 11. Detail of Peltier sample showing a V5 breakdown outside of the capillary region.

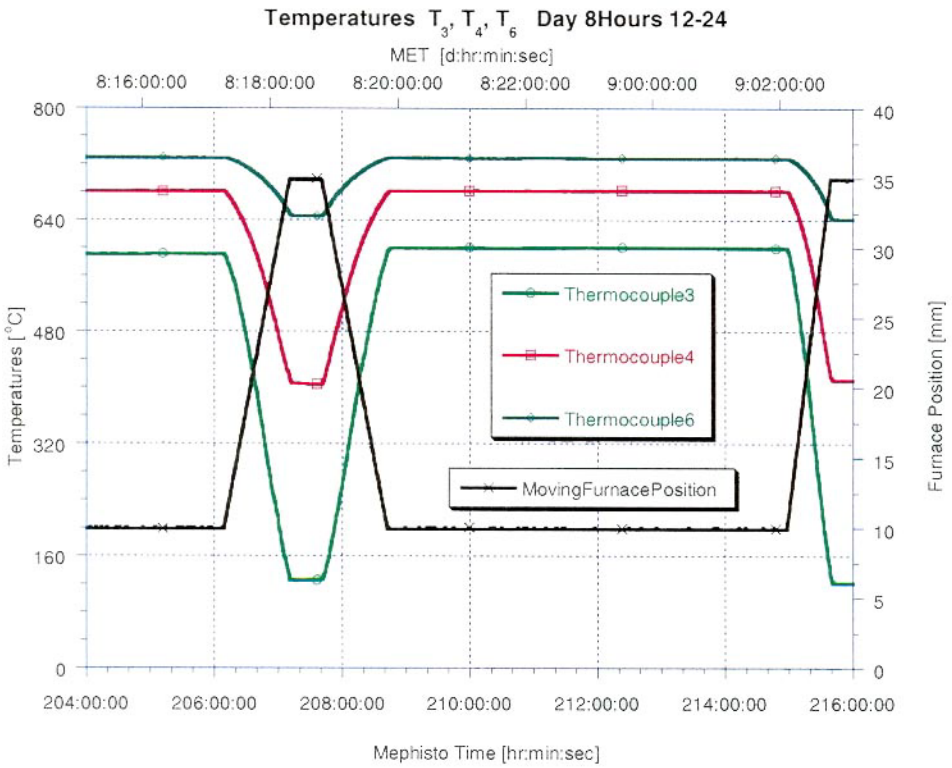

Figure 12. Thermal measurement by the three thermocouples.

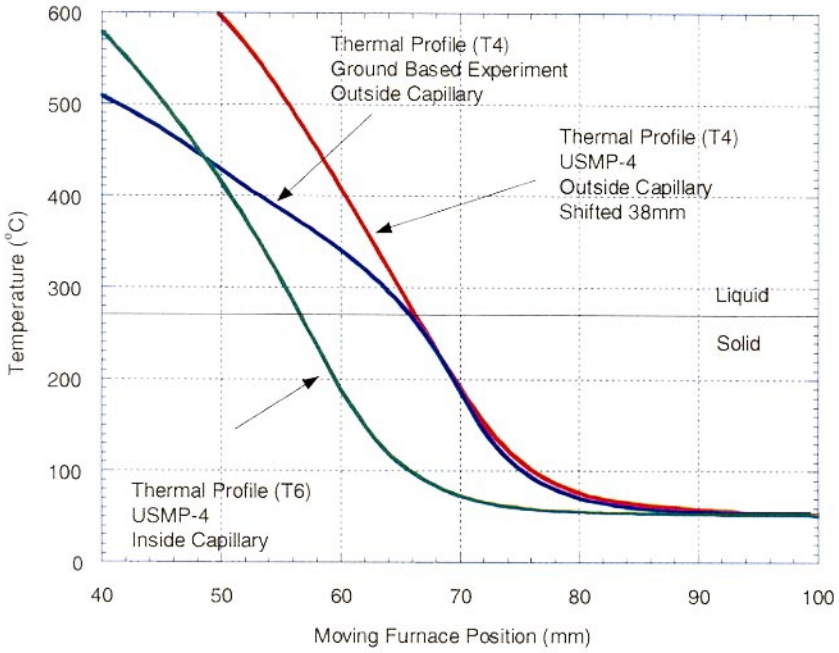

Figure 13. MEPHISTO thermal profile for ground and space based mission. Above the melting point of the liquid the temperature gradient for the ground-based experiments is significantly lower indicating convection. The profile is very similar inside and outside capillary on space-based experiments.

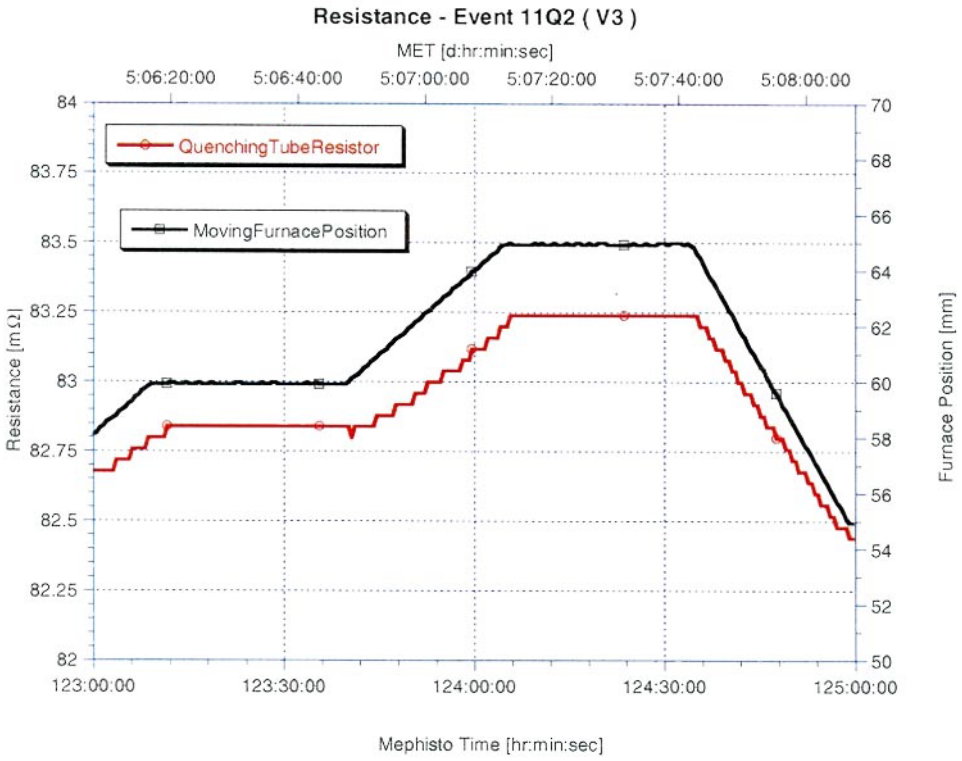

Figure 14. Resistance and furnace position change as a function of processing time during event 11Q2 in MEPHISTO experiment.

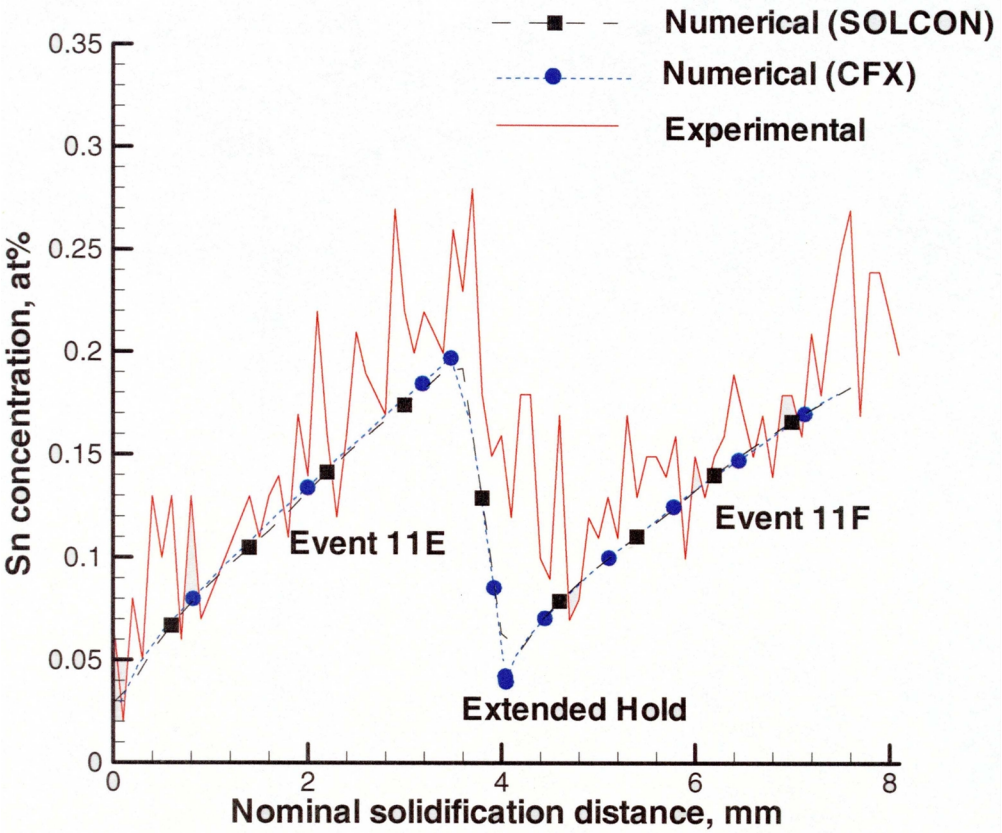

Figure 15 (a). Solute concentration in the solid along the center line.

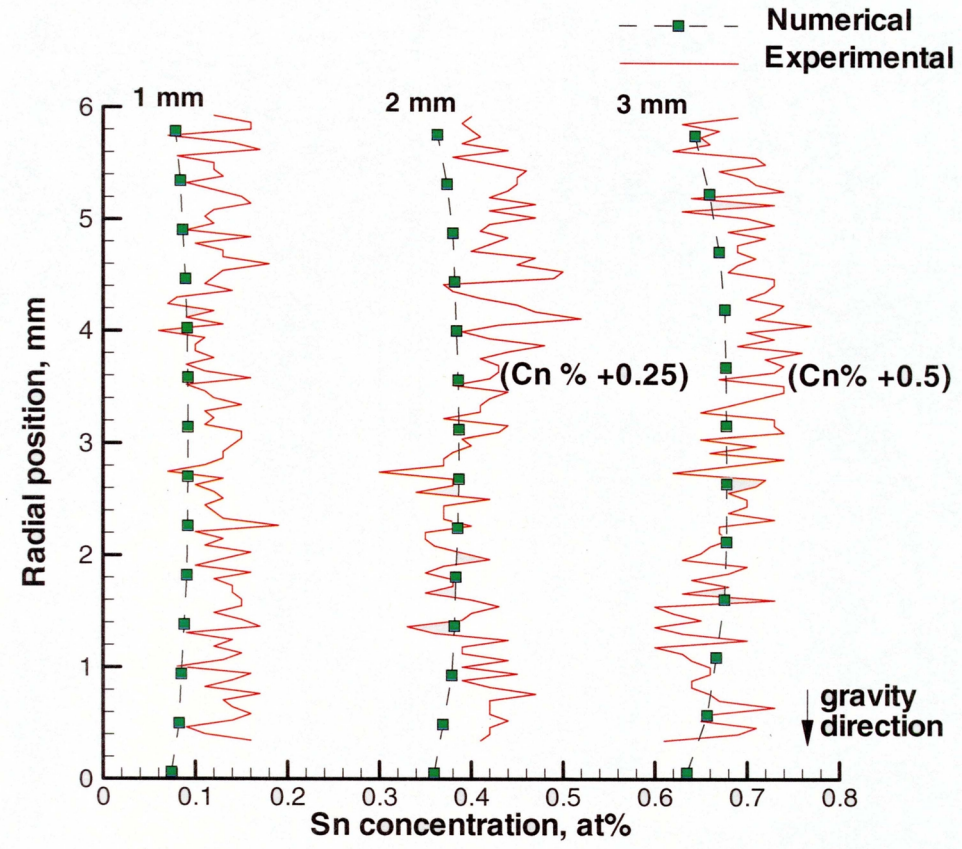

Figure 15 (b). Solute concentration in the solid along the vertical lines.

MORPHOLOGICAL STABILITY OF FACETED INTERFACES

R. Abbaschian[1], V. D. Golyshev[2], M. Gonik[2], V. Tsvetivsky[2], G. de Vahl Davis[3], and E. Leonardi[3]

[1]Department of Materials Science & Engineering, University of Florida
[2]Center of Thermophysical Research (CTR), Russia
[3]University of New South Wales, Australia

The major focus of this investigation is to study the fundamentals of layer spreading mechanisms during growth of doped Ge (a facet forming material), and to determine the conditions for morphological instability of vicinal solid-liquid interfaces. The investigation will also lead to the determination of the effect of dopants on the layer growth kinetics, step free energy, and dopant capture by the advancing ledges.

The theoretical treatment of growth of faceted interfaces indicates that the kinetics of a step on a growing vicinal interface considerably depends on its angle of inclination, the melt concentration, and characteristics of flow currents in the melt. The morphological stability of the interface also depends on these parameters, as well as on the density and spreading velocity of the steps. However, the treatment of the instability of the interface by the layer growth mechanism is rather difficult because it requires exact knowledge of the thermal and solutal fields, hydrodynamics of the melt, and supercooling at the interface. The results of recent space experiments of the principal investigator involving directional solidification of faceted Bi-Sn alloys have shown that the morphological stability of various crystallographic orientations is significantly affected by the anistropy in interfacial properties of the faceted alloy in general, and the interface kinetics in particular. These findings have also raised many important and fundamental questions, particularly with respect to the behavior of interfacial steps, which need to be addressed via additional ground-based and microgravity experiments.

For the present investigation we will use a novel crystal growth technique which provides axial heat flux close to the solid-liquid boundary. The Axial Heat Processing (AHP) technique allows for precise control and determination of the heat and mass transfer close to the crystallization front, and the establishment of a planar interface over the entire cross-section of the growing crystal.

The project began in June 2000, under NASA grant # NAG8-1673.

VIBRATIONS AND G-JITTER: TRANSPORT DISTURBANCES DUE TO RESIDUAL ACCELERATION DURING LOW GRAVITY DIRECTIONAL SOLIDIFICATION AND DIFFUSION EXPERIMENTS

J. Iwan D. Alexander[1,2 *], J. P. Kizito[2], and M. Kassemi[2]

[1] Department of Mechanical and Aerospace Engineering, Case Western Reserve University
[2]National Center for Microgravity Research on Fluids and Combustion

The proposed research involves a four-year program of ground-based research leading to the definition of a set of benchmark flight experiments. The experimental objectives are to characterize the response of heat and species transport in a directionally solidifying model transparent alloy system subject to well-characterized imposed vibrations and, ultimately, to spacecraft residual acceleration. The experiments will:

- Quantify the effects of residual acceleration on transport during directional solidification
- Investigate, as part of the flight experiment definition, modulated 1g convective transport in solidifying succinonitrile-ethanol (SCN-E) and succinonitrile-water (SCN-W) melts using high and low frequency translational and rotational vibrations
- Investigate single and two-liquid phase melt responses
- Compare thermo-solutal and dominantly thermal convective responses to vibration (facilitated by the weak dependence of SCN-W density on composition)
- Investigate the possibility of using vibration for transport control (*e.g.*, for melt homogenization or rehomogenization).

The candidate systems for carrying out the experiments are succinonitrile-ethanol (SCN-E) and succinonitrile-water (SCN-W). A generic phase diagram is shown in Figure 1. These systems have been chosen because, depending on composition, the melt can be single phase with two components, or can be composed of two liquid phases and are reasonable model systems for montectic metal alloys. Both systems have been the subject of previous holographic interferometric studies [1-4] in which flow regimes during solidification under terrestrial conditions were qualitatively characterized. For SCN-W, especially at temperatures in excess of 40°C, the change in density due to composition is insignificant in comparison to that caused by temperature. In contrast, compositional density changes are comparable to temperature induced density changes. (For example, a 10 wt.% change in ethanol concentration leads to density change of approximately 5% while a 10°C change can lead to between 1% and 10% density change depending on whether the melt is ethanol rich or SCN-rich. The Prandtl number for both systems is of the order 10^{-1}. Further details concerning the thermophysical properties of these systems can be found in References. [4-7].

* Corresponding author

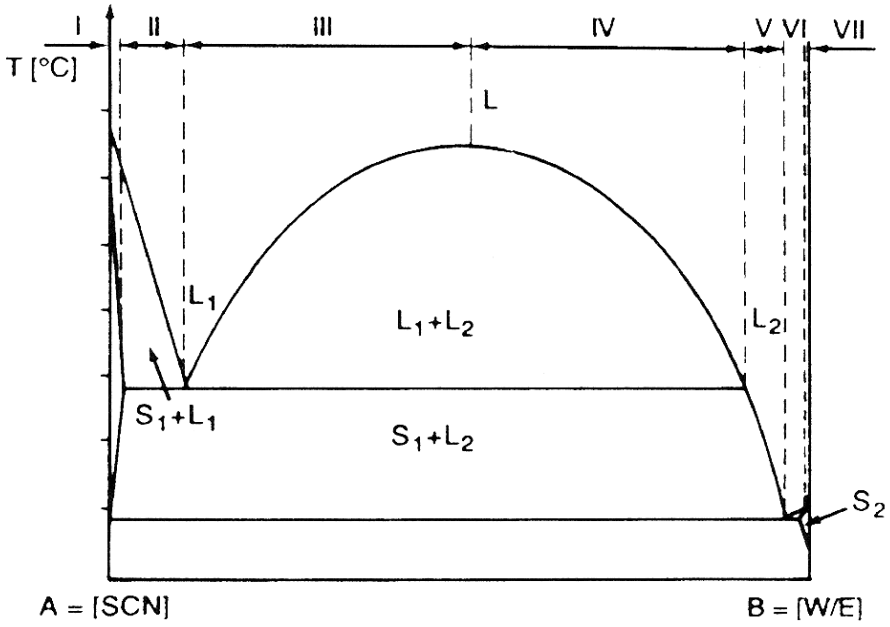

Figure 1. Generic Phase Diagram, SCN-[W/E] [4]

The rationale for choosing these systems is that they cover a range of fluid properties including a two-phase melt, one system exhibits a dominantly temperature dependent melt-density while the other depends strongly on both density and composition. For dilute SCN-rich or water (ethanol) rich systems (regions VII or I in Figure 1) this will allow comparison of the behavior of dominantly thermal and thermo-solutal convective effects. In the two-phase liquid regions, the effects of g-jitter (and thermocapillary driven motions) on liquid droplet and bulk transport will be investigated. Ground-based experiments will be conducted to determine the operating conditions suitable for the space experiments and, as far as possible characterize, the response to g-jitter type vibrations.

REFERENCES

1. A. Ecker, Simultaneous measurement of temperature and concentration in front of solidifying monotectic systems using the two wavelength holographic technique, Proc. 6th European Symposium on Materials Sciences under microgravity conditions, (ESA SP-256) 309-311 (1987)
2. A. Ecker, AIAA J. Thermophysics and Heat Trans., 2 193-96 (1988).
3. A. Ecker, D. O. Frazier and J.I.D. Alexander, Classification of fluid flow in front of solidifying monotectic alloys, Proc. 7th European Symposium on Materials and Fluid Sciences in Microgravity, (ESA SP-295) 115-119 (1990)
4. A. Ecker, D. O. Frazier and J.I.D. Alexander, Fluid flow in solidifying monotectic alloys, Met. Trans. A, 20, 2511-2517 (1989).
5. F. A. Schrinemakers, Z. Phys. Chem., 25 543-566 (1898).
6. L. M. Lacy, W.K. Witherow, B. R. Facemire and G.M. Nishioka, NASA Tech. Memo, NASA TM-82494, Marshall Space Flight Center, Huntsville, AL, June 1982.
7. J. E. Smith, D.O. Frazier and W.F. Kaukler, Scripta Metall., 94, 677-82 (1984).

THE EVOLUTION OF DENDRITE MORPHOLOGY DURING ISOTHERMAL COARSENING

Jens Alkemper and Peter Voorhees

Department for Materials Science and Engineering, Northwestern University
Evanston, Illinois, USA

The project studies the evolution of dendrites during isothermal coarsening for Sn-dendrites in a Pb-Sn matrix phase. The matrix is liquid during the coarsening process to ensure significant coarsening in a reasonable amount of time. This system has been chosen because it has been extensively studied in the past with respect to coarsening, particularly in the Coarsening in Solid-Liquid Mixtures (CSLM) project – see Reference [1].

The process of dendrite coarsening is crucial to all casting processes where dendrites are formed in the early stage of the cooling process. All dendrites subsequently coarsen until the structure is completely solidified. In order to study the effect of the coarsening process on the overall microstructure it is useful to design the experiments so that the coarsening happens isolated from the overall solidification but still involves a dendritic microstructure. Once the coarsening of dendrites has been studied it can be fed back into the understanding and simulation of casting processes. The results thus will provide new insights into dendritic coarsening as well as guide simulations of solidification processing with respect to coarsening.

Usually the coarsening of dendrites is evaluated using the secondary dendrite arm spacing determined from planar sections through the microstructure – see figure 1. It has been found, that the secondary dendrite arm spacing grows proportional to the time available for coarsening with an exponent of 1/3. This underlines the general similarity to particle coarsening.

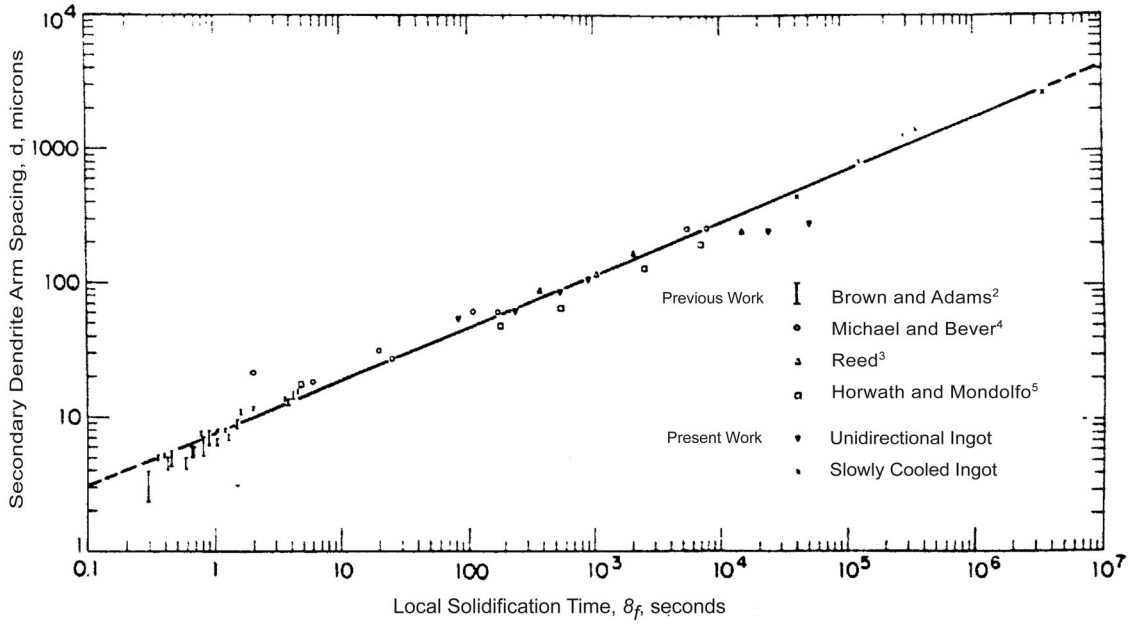

Figure 1. Secondary arm spacing versus local solidification time for Al-Cu from Bower *et al.* [2]

In this research the microstructures will be evaluated using a newly developed serial sectioning method. A similar method has been employed by Wolfsdorf *et al.* [3] for connected particle structures in the lead-tin system. Figure 2 shows an example from their research of a microstructure that was serial-sectioned and then reconstructed. It gives a good impression of the possibilities using such a method. The method, however, has been greatly improved since, allowing now to take sections as little as 2μm apart and at a rate of *ca*. 15-20 sections per hour.

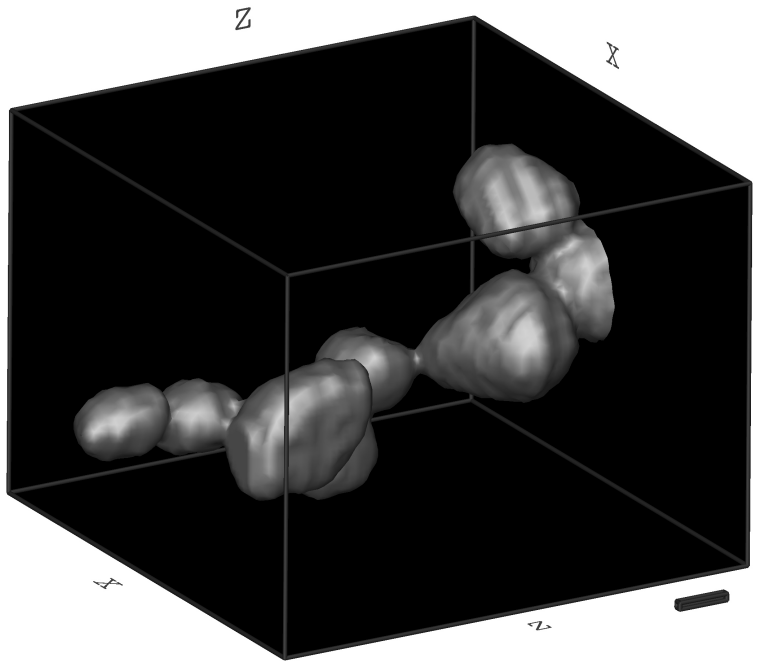

Figure 2. Tin particles reconstructed from 80 cross-sections. The sections were spaced apart *ca*. 20μm.

Measurements will be done with respect to the full three dimensional microstructure instead of the usual two-dimensional cross-sections. This allows us to evaluate the curvatures of the dendrite surface and the genus (see figure 3) per volume of the dendrites. The curvatures are of particular interest since they provide the driving force for the coarsening process due to the Gibbs-Thomson effect. The role of the genus with respect to coarsening is not clear, but it is important for the materials parameters after the process. Attempts have been made earlier to show the link between the curvature distribution of a dendrite surface to the overall coarsening process, but they were clearly limited by the experimental techniques available. The genus of dendritic microstructures has not been measured at this time. In order to compare the results to existing literature we will further determine the secondary dendrite arm spacing from two dimensional cross-sections.

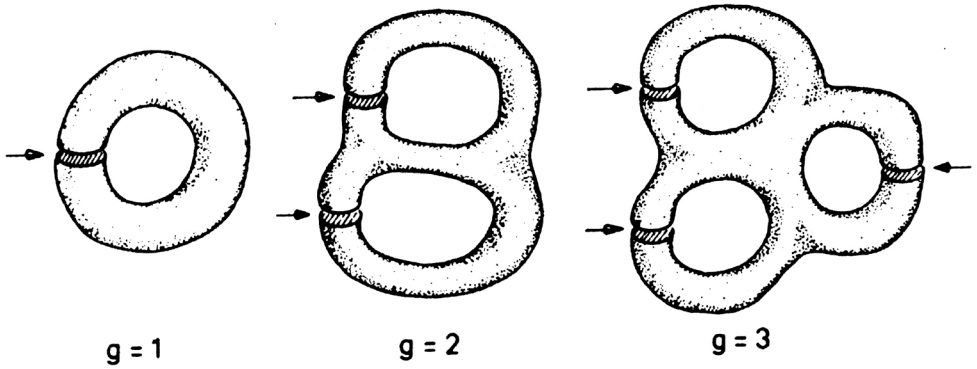

Figure 3. The topological genus of various tori is given by the number of cuts with closed curve that can be applied without splitting the torus into two parts (taken from *Stereological Methods* [4]).

REFERENCES

1. J.Alkemper, V.A.Snyder, N.Akaiwa, and P.W.Voorhees, *Dynamics of Late-Stage Phase Separation: A Test of Theory*, Phys. Rev. Let., Vol. 82, No.13, pp 2725-2728, (1999)
2. T.F. Bower, H.D. Brody, and M.C.Flemings, *Measurement of Solute Redistribution in Dendritic Solidification*, Transactions of the metallurgical society of AIME, Vol.236, pp 624-634, (1966)
3. T.L.Wolfsdorf, W.H.Bender, and P.W.Voorhees, *The Morphology of High Volume Fraction Solid-Liquid Mixtures: An Application of Microstructural Tomography*, Acta Mater. Vol.45, No.6 pp. 2279-2295, (1997)
4. E.R.Weibel, *Stereological Methods Vol.2: Theoretical Foundation*, Academic Press, (1980)

MICROGRAVITY IMPREGNATION OF FIBER PREFORMS

M. C. Altan[1 *], F.-C. Lai[1], B. P. Grady[2] and E. A. O'Rear[2]

[1]School of Aerospace and Mechanical Engineering
[2]School of Chemical Engineering and Materials Science
University of Oklahoma, Norman, OK 73019, U.S.A.

INTRODUCTION

Molding operations involving low-viscosity polymers are commonly used to manufacture net-shape components quickly and inexpensively. Molding is usually characterized by the displacement of air in a cavity by a polymeric resin which is either cooled or cured to form the final solid part. During filling the interface between the polymer and the air, referred to as the free surface, progresses through the cavity. The dynamics of this free surface can affect heat transfer as well as the curing rate in the mold, and thus the mechanical properties of the molded part. During mold filling the bottom of the fluid front may sag due to gravity, thus forming a nonsymmetric free surface.

The experimental and theoretical studies dealing with free surface shapes published in literature often do not approach the problem from a mold filling perspective. Those related to mold filling typically neglect gravity effects on the free surface. The most common approach in determining the free surface shapes in molding is to assume the capillary number is high and that viscous forces dominate surface forces. For instance Behrens *et al.* [1] calculated and experimentally measured axisymmetric free surface shapes. In reference [1], surface effects, such as those due to surface tension and contact angle, are ignored and the fluid front shape is completely dictated by the flow kinematics.

Other studies dealing with free surface shape include research on the motion of contact lines [2,3]. These address the issue of the viscous stress singularity and so called slip length used in the analysis of moving contact lines, but do not address the free surface shape over the entirety of the free surface. Closely related are investigations in determination of the dynamic contact angles [4-6]. Again, the focus of such studies is on the flow dynamics near the contact point. Blake investigated gravity effects on free surface shape in mold filling [7,8]; however this study involves a vertically aligned cavity in which gravity does not cause an asymmetric fluid front. Several studies have been performed which include gravity effects on the spreading of a liquid drop on a solid surface which do include gravity effects on the shape and motion of the free surface (*e.g.* Chen, *et al*. [9] and Hocking [10]), but not in a mold cavity.

The purpose of the current study is to experimentally study the effect of gravity on the free surface shape during the filling of a mold cavity. It is of particular interest to determine the important non-dimensional parameters governing the fluid front dynamics. Towards this end, mold filling experiments are performed to characterize the spreading of the fluid front during the filling of a disk-shaped cavity. The effects of Reynolds, Bond, and Capillary numbers on spreading are studied.

* Corresponding author

I. Effects of Gravity on Mold Filling

Spreading at a radial location in a centergated disk shaped cavity can be characterized by the Reynolds, Bond, Capillary numbers and by the contact angle, α, which is assumed constant in the current study. For the filling of a mold, the first three non-dimensional parameters can be expressed as,

$$\mathrm{Re}=\frac{\rho u L}{\mu}\ ;\ Ca=\frac{\mu u}{\sigma}\ ;\ Bo=\frac{\rho g L^2}{\sigma}, \tag{1}$$

where ρ, σ, and μ are the fluid properties density, surface tension, and viscosity; L is the gapwidth; and u is the average local velocity. These numbers are defined at the location of the first fluid front probe (R= 2.0 inches), thus the velocity, u, represents the average velocity at R = 2.0 inches. For macroscopic analysis, a Reynolds number to characterize the flow regime can be expressed in terms of the volume flow rate as

$$\mathrm{Re}_Q=\frac{\rho Q}{\mu L} \tag{2}$$

The dependence of spreading on Reynolds, Bond, Capillary numbers and contact angle needs to be fully understood through carefully designed experiments. Towards this end, the following physical parameters can be changed in filling experiments: gapwidth, L; volume flow rate, Q; viscosity of the fluid, μ, its density, ρ, and the surface tension, σ. For a given fluid and the mold surface the contact angle can be determined. Then two of the remaining three non-dimensional parameters need to be kept constant while changing the third one. This requires the adjustment of all the physical parameters (i.e., L, Q, ρ, σ, and μ) in a unique manner. In order to allow arbitrarily specified non-dimensional parameters, glycerol diluted with water is used as the filling fluid. Different volume fractions of glycerol, f, in the mixture yield variations in fluid properties. Additionally, the molding setup allows the gap width and flow rate to be varied, thus all the noted physical parameters can be controlled.

There are five unknown physical parameters for each specified set of non-dimensional values, thus the three equations in (1) are not sufficient to determine the required experimental conditions. However, three of the unknowns, *i.e.* ρ, σ, and μ, are related in that they are physical properties of the filling fluid. Experiments are performed to obtain the dependence of these on the volume fraction of glycerol in the mixture, and each are expressed as functions of f. The fluid properties are substituted into equations (1), and manipulated to yield a single equation, leaving the volume fraction, f, as the only unknown [11],

$$0=\left(\frac{\rho(f)Bo}{g}\right)^{1/4}\left(\frac{Ca}{\mathrm{Re}}\right)^{1/2}(\sigma(f))^{3/4}-\mu(f). \tag{3}$$

For a desired set of non-dimensional parameters, equation (3) is solved implicitly for f. The volume flow rate and gapwidth are subsequently found by using equations (1).

II. Experimental Setup

An experimental molding setup for observing and characterizing flow during the filling of a disk shaped cavity has been constructed. The experimental setup consists of the following components: an assembled mold cavity, a peristaltic pump and tubing system for fluid transfer, and a data acquisition system. The 9.0 inch radius centergated disk shaped mold cavity, depicted in figure1, is formed by placing spacer plates between 1.0 inch thick Plexiglas mold walls. Spacer plates are cut from 20x20-

inch aluminum or acrylic sheets with an 18-inch diameter disk shaped cut from its center. Several spacer plates with thicknesses ranging from 1/16 to 1/2 inch are fabricated and can be combined to provide gapwidths from 1/16 to 1 inch. Fluid is injected by the peristaltic pump at constant flow rate through an inlet gate with a diameter that can be varied from 0.125-0.375 inch. Figure 1 shows the radial locations of pressure transducers and fluid front sensors which are connected to the data acquisition system. Figure 2 provides a closer view of the fluid front sensors and how they detect spreading of the free surface. Figure 2a shows a typical fluid front as it might appear without spreading in the absence of gravity, while figure 2b shows a front which has sagged due to gravity. The sensors are mounted at three radial locations in the disk, $R = 2$, 4, and 6 inches, and each consists of two small pairs of terminals mounted on the top and bottom walls. Each has a power terminal and three numbered sensing terminals as illustrated in figure 2.

A sensing circuit in conjunction with the data acquisition system detects when the front contacts each sensing terminal by measuring a resistance drop. The three sharp voltage increases represent the fluid front contacting the three terminals. The derivation for obtaining spreading based on the fluid contact times and geometry has been calculated previously and will not be presented here [11]. It was shown that spreading S, is the difference between the radii R_c and R_b, and is calculated using the two known radii R_a and R_b and these three fluid front contact times t_1, t_2, and t_3 as

$$S = \sqrt{R_b^2 + \frac{(R_b^2 - R_a^2)(t_2 - t_1)}{(t_2 - t_3)}} - R_b . \tag{4}$$

III. Results

Spreading results for eleven sets of experiments in which the Reynolds and Bond number are varied are depicted in figure 3. Each experiment in a set is repeated between four and seven times to minimize statistical error. There are three groups of three curves, representing the three radii, R, at each of the three Bond numbers. The largest errors are observed near at $R = 6.0$ inches at the highest Bond number, where spreading is the highest. In all nine curves, spreading is seen to vary linearly over the range of Reynolds numbers studied. In most of these experiments, two orders of magnitude change in Reynolds number did not significantly affect spreading, as shown in figure 3. However, Bond number is observed to significantly affect spreading at all Reynolds numbers. Figure 3 shows that spreading increases by an order of magnitude due to a small increase in Bond number at all Reynolds numbers.

At Bo = 8.2, spreading is observed to be least near the inlet, and increases as the fluid decelerates radially through the cavity. At $Bo = 5.75$ however, spreading is nearly identical on the $R = 2$ and $R = 6$ in. lines, and noticeably higher at $R = 4$ inches. At $Bo = 4.35$ the same behavior is observed at $R = 4.0$ inches. The increase in spreading at $R = 4$ at these Bond numbers is pronounced enough to be visually observed through the Plexiglas mold walls. This phenomenon is believed to be due to inlet effects as spreading is measured to be at the order of inlet diameter.

Figures 4-6 contain sets of spreading data obtained from different mold radii as a function of Bond number. In these figures, the error bars are the same as in figure 3, thus they are not included for clarity. In each figure, the variation of spreading at different Bond numbers is shown for three different Reynolds numbers. In figure 4, inlet effects at $R = 2$ are observed for the lowest Reynolds number, *i.e.*, Re = 0.04. The spreading for Re = 1.0 and Re = 2.0 increases with Bond number and have a slightly negative radius of curvature. These curves demonstrate the previously observed trend that Reynolds number has minimal effect on spreading, in particular at low Bo numbers. The Re = 0.04 curve matches the others at the lower two Bond numbers as well, but is observed to deviate from the others as the Bond number is increased. This is due to the inlet effect where a very slow flow at a high Bond number runs

along the bottom mold wall before the fluid ever contacts the top mold wall. An interesting extension of this behavior is observed near this range of non-dimensional parameters, when the fluid spreads several inches along the bottom wall before the top touches, at which point the bottom of the fluid front slows down considerably for a brief instant while the top rapidly progresses ahead.

In figure 5, spreading measurements are shown at $R = 4.0$ inches, farther from the inlet. There is still a slight inlet effect visible for $Bo = 8.7$, but in general the curves have condensed and are similar for each Reynolds number. Spreading at this radius is observed to increase by almost an order of magnitude when the Bond number is doubled. The curves for these Reynolds numbers are nearly linear. The data from $R = 6.0$ inches, depicted in figure 6, exhibits a similar significant increase in spreading with Bond number, however in this case the curves are concave indicating around one-inch spreading at $R = 6.0$ inches.

Similar mold filling experiments are performed holding the Bond number constant at 5.75, and the Reynolds number constant at 1.0, while varying the Capillary number between 0.006 and 0.2. Results from these experiments are presented in figure 7, with the spreading measurements are drawn with a 95% confidence interval. Figure 7 displays the general trend that spreading decreases with increasing Capillary number. Increasing the Capillary number translates to increasing both the volume flow rate and the fluid viscosity in terms of physical parameters. The dependence of spreading on Capillary number is less pronounced than the dependence on Bond number. The reduction in spreading is approximately 50%, as Capillary number is increased nearly two orders of magnitude. The graphs of spreading vs. radius demonstrate the phenomena observed in the previous data set, where spreading increases from the inlet to a maximum at $R = 4$ in. at which point it begins to decrease again.

REFERENCES

1. Behrens, R.A., Crochet, M.J., Denson, C.D., and Metzner, A.B., "Transient Free-Surface Flows: Motion of a Fluid Advancing in a Tube," *AIChE Journal*, 33(7), pp. 1178-1186, 1987.
2. Jansons, K.M., "Moving Contact Lines at Non-Zero Capillary Number," *J. Fluid Mech.*, 167, pp. 393-407, 1986.
3. Dussan, E.B., and Davis, S.H., "On the Motion of a Fluid-Fluid Interface Along a Solid Surface," *J. Fluid Mech.*, 65(1), pp. 71-95, 1974.
4. Rame, E., and Garoff, S., "Microscopic and Macroscopic Dynamic Interface Shapes and the Interpretation of Dynamic Contact Angles," *J. Colloid and Interface Sci.*, 177, 234-244, 1996.
5. Gennes, P.G., Hua, X., and Levinson, P., "Dynamics of Wetting: Local Contact Angles," *J. Fluid Mech.*, 212, pp. 55-63, 1989.
6. Ström, G., Fredriksson, M., Stenius, P., and Radoev, B., "Kinetics of Steady State Wetting," *J. Colloid and Interface Sci.*, 134, 107-116, 1989.
7. Blake, J.W., "Studies in Reaction Injection Mold Filling," Ph.D. Thesis, University of Minnesota, 1987.
8. Blake, J.W., and Macosko, C.W., "The Kinematics of Fountain Flow in Mold-Filling," *AIChE Journal*, 33(7), pp. 1168-1177, 1987.
9. Chen, Q., Rame, E., and Garoff, S., "The Breakdown of Asymptotic Hydrodynamic Models of Liquid Spreading at Increasing Capillary Number," *Phys. Fluids*, 7(11), 2631-2639, 1995.
10. Hocking, L.M., "Rival Contact-Angle Models and the Spreading of Drops," *J. Fluid Mech.*, 239, pp. 671-681, 1991.
11. Olivero, K.A. and Altan, M.C., "Gravity Effects on Preform Impregnation During Resin Transfer Molding", 14th meeting of the Polymer Processing Society, PPS-14, 786-787, 1998.

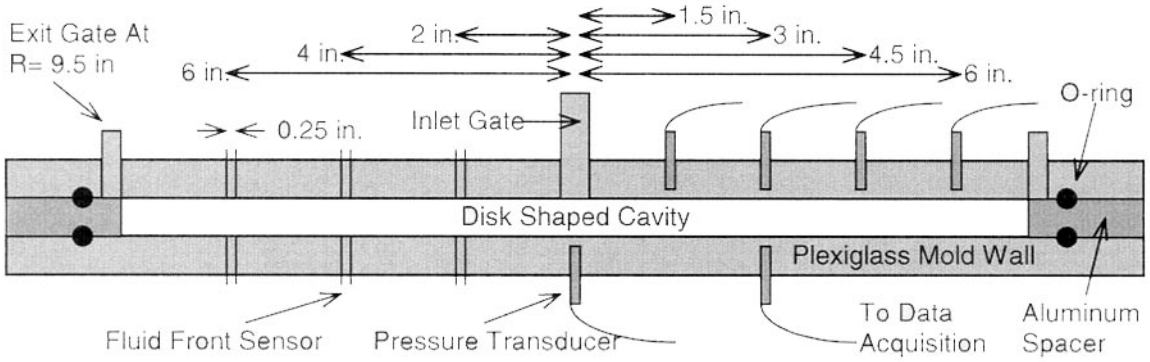

Figure 1. Cross section of experimental mold cavity.

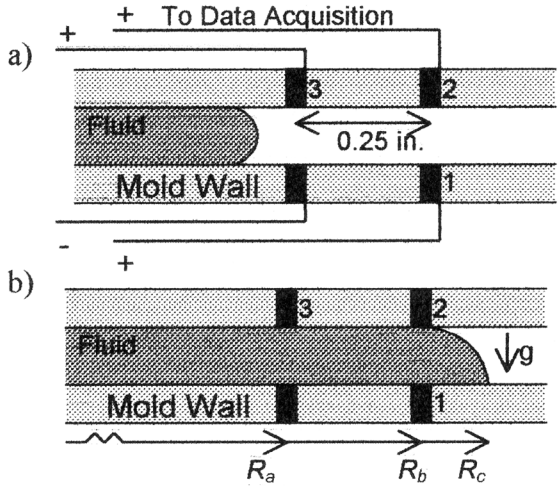

Figure 2. Schematic cross section of fluid front probe and a fluid front, a) without spreading; b) with spreading due to gravity.

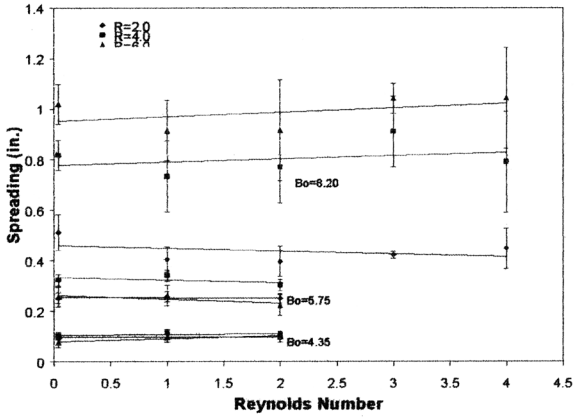

Figure 3. Spreading versus Reynolds Number at Each Radius for Three Bond Numbers with a 95% Confidence Interval.

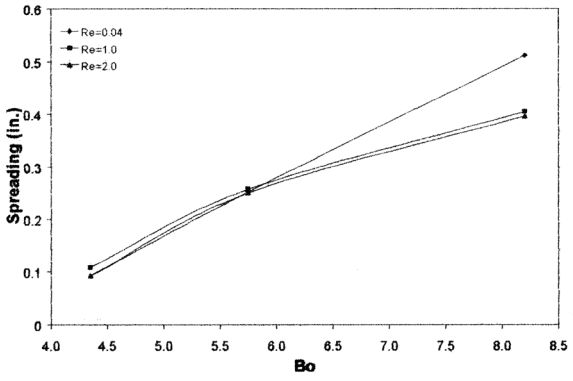

Figure 4. Spreading versus Bond Number for Each Reynolds Number at *R=2.0* inches with *Ca=0.02*.

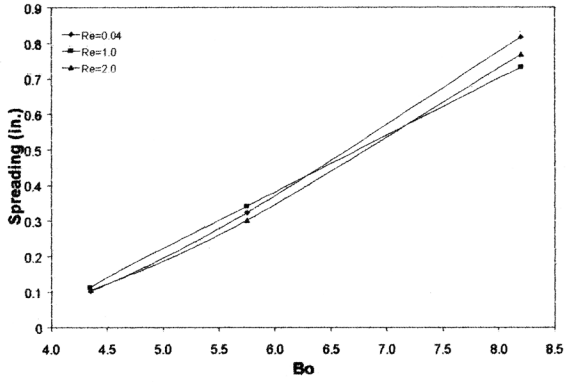

Figure 5. Spreading versus Bond Number for Each Reynolds Number at *R=4.0* inches with *Ca=0.02*.

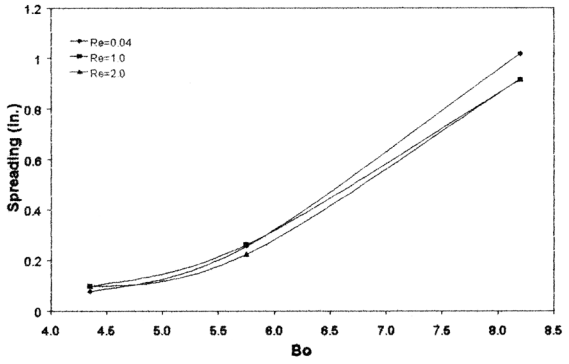

Figure 6. Spreading vs. Bond Number for Several Reynolds Numbers at *R=6.0* in with *Ca=0.02*.

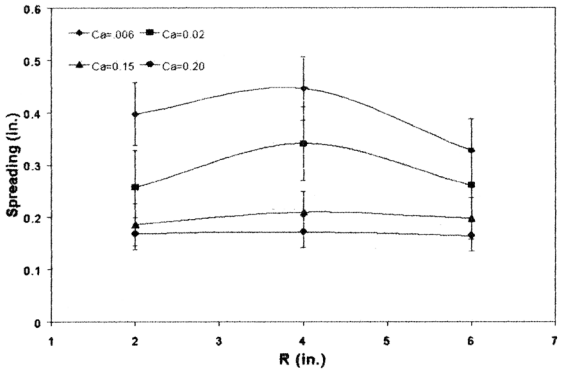

Figure 7. Spreading vs. Radius for Each Capillary Number with 95% confidence interval. Re=1.0, Bo=5.75

AN ELECTROCHEMICAL METHOD FOR MEASUREING CONVECTION AND DIFFUSION IN LIQUID METALS

Timothy J. Anderson[1], Ranga Narayanan[1], Daniel W. Crunkleton[1*], Brenda Serrano[1], and R. Pankajavalli[2]

[1] Department of Chemical Engineering, University of Florida, Gainesville, FL
[2] Thermodynamics and Kinetics Division, Materials Characterization Group, Indira Gandhi Centre for Atomic Research

In the materials industry, there are several crystal growth techniques which use liquid precursors, including the Bridgman and Czochralski techniques. In each of these methods, a semiconductor melt undergoes solidification, resulting in the formation of a crystalline phase. These techniques, however, often suffer from the disadvantage that the quality of the crystal product is adversely affected by the presence of convection which may exist in the melt. This convection is induced when an enclosure of fluid is heated from below and/or cooled from above. The temperature gradient will cause the density of the cooler fluid at the top of the container to be greater than the warmer fluid on the bottom; therefore, gravity will begin to pull the cooler fluid downward. This displaces the warmer fluid on the bottom, and the system begins to convect. This process is called buoyancy-induced convection or gravity-induced convection. Microgravity has been proposed as an environment where gravity-induced effects do not occur, and the resulting convection does not develop.

The dynamic state of fluids heated from below is determined by the Rayleigh number, a dimensionless group defined as the ratio of the buoyancy forces to the diffusion forces. There are three important values of the Rayleigh number at which important processes begin, and are denoted the first, second, and third critical Rayleigh number – Ra_{c1}, Ra_{c2}, and Ra_{c3} – and delineate the bifurcation to steady, oscillatory, and chaotic flow.

I. Proposed Solution – Sensing Convection via Electrochemical Measurements

An electrochemical method to visualize this convection has been developed which establishes initial and boundary conditions for a tracer species and subsequently monitors the dynamic response (Sears *et al.* 1992, Prasad *et al.,* 1999). The solid-state electrolyte yttria-stabIlized zirconia (YSZ) are fabricated into sensors that are attached along the periphery of the enclosure (see Figure 1). The YSZ electrolyte has the property that it selectively allows for the transport of oxygen into the liquid tin. Assuming that the flow configuration of the tin is fully developed, the now dissolved oxygen acts as a tracer specie as it follows the path of the convective flow. Other YSZ sensors, strategically placed along the side of the enclosure detect the presence of the oxygen as the flow carries the dissolved oxygen. One then obtains a sensor response over a period of time. Numerical calculations of convection are performed in this work to calibrate these sensor responses. That is, for an experiment conducted at a particular aspect ratio and Rayleigh number, *what flow configuration does one expect*? Calculations such as those

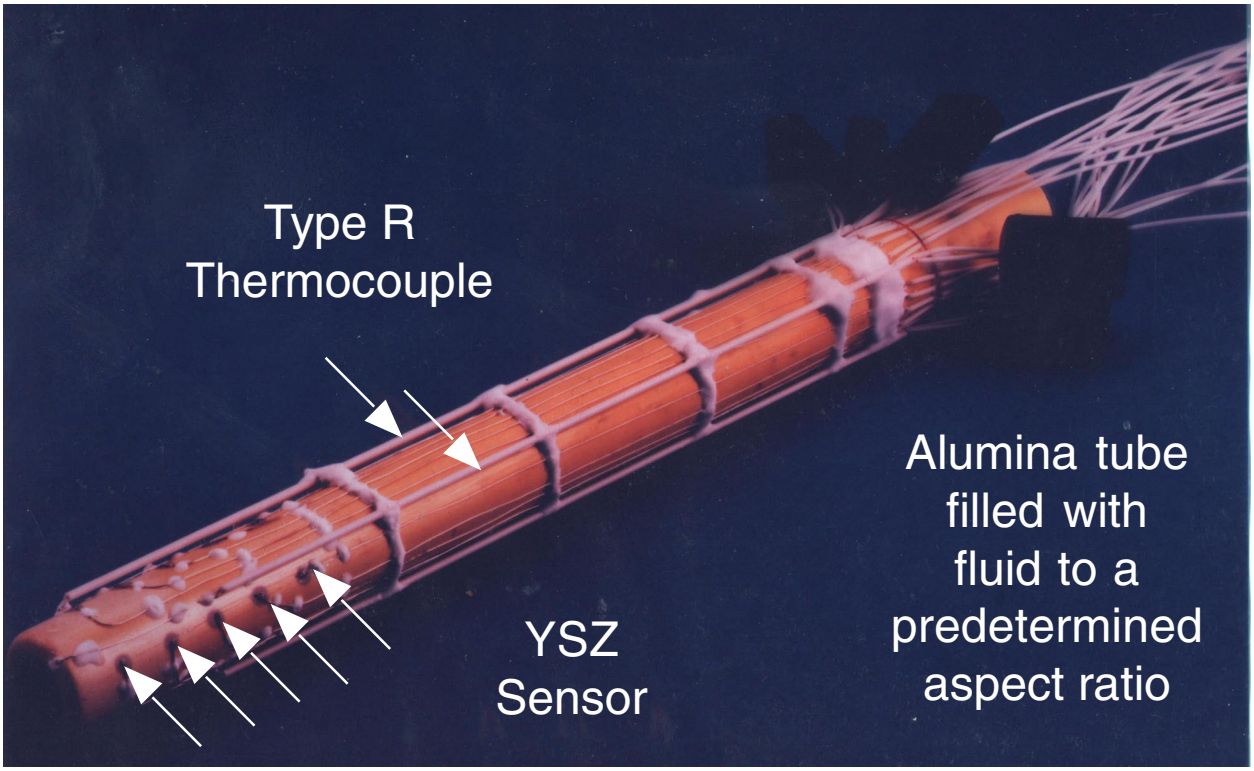

Figure 1. Prototype of Electrochemical Measurement System.

presented in this work will serve as a benchmark in translating a particular sensor response into an actual flow configuration.

There are several techniques for visualizing convective flows (Eisele *et al.* 1998); however, this electrochemical sensing technique is advantageous over existing methods for many reasons, the first of which is its non-intrusiveness (the oxygen levels are typical of those present in liquid metal processing). This electrochemical measurement system also has the advantage that it does not require the use of tracer particles which, if used in crystal growth experiments, would ruin the quality of any product. Finally, this technique is also highly adaptable to microgravity studies given power, weight, safety, and signal level requirements. The electrochemical method to visualize flow provides a fresh approach to a difficult problem that has the potential not only to enhance the understanding of the fluid dynamics of low Prandtl number fluids, but also provide a critical experimental link between computational fluid dynamics and processed material properties.

In order to quantify the convective component accurately, an accurate assessment of the diffusive effects must be undertaken. Fortunately, the electrochemical measurement technique used in this study is capable of making accurate diffusivity measurements. To do this, an isothermal fluid is arranged perpendicular to gravity and is given an initial concentration of oxygen by electrochemically titrating oxygen from a Cu/Cu_2O reference electrode. The oxygen transports from the reference electrode, and is dissolved into the studied fluid (for this study, tin and tin/lead alloys are studied). A concentration gradient is then induced by depleting oxygen from either the top or bottom of the fluid (that is, bottom-heavy or top-heavy in oxygen). The diffusivity can then be followed by measuring the EMF at the YSZ sensor at the opposite end of the fluid and analyzing the results with the large-time approximation of the one-dimensional axial diffusion equation.

II. Convection Measurements – Calculations

A computational fluid dynamics model was developed for this study, using the finite-difference method of Patankar (1980). The modeled geometry is a three-dimensional rectangle with all no-slip walls except a top, stress-free surface. The top and bottom walls are taken to be isothermal, while the others are assumed adiabatic. Rectangular geometries are used in this study because their expected flow configurations are more complex than for other co-ordinates because of the presence of corner effects, which leads to more robust sensor predictions. Liquid tin (Pr=0.008) was used as the model fluid for all simulations. The non-dimensional transport equations are

$$\nabla \bullet \vec{v} = 0 \tag{1}$$

for continuity,

$$\frac{\partial \vec{v}}{\partial t} + \vec{v}.\nabla\vec{v} = \nabla^2\vec{v} - \nabla p - \frac{Ra}{Pr}(T - T_o) \tag{2}$$

for momentum, and

$$\frac{\partial T}{\partial t} + (\vec{v}.\nabla)T = \frac{1}{Pr}\nabla^2 T \tag{3}$$

for energy, where the Boussinesq approximation has been assumed in the body force terms of the momentum balance.

III. Results

The results presented are limited to the oscillatory bifurcations of liquid tin at the second critical Rayleigh number. To determine Ra_{c2}, a calculation was performed with a Rayleigh number greater than Ra_{c1} using converged Ra_{c1} velocity profiles obtained previously (Crunkleton *et al.,* 1999) as initial guesses. If, for a particular Rayleigh number calculation, no periodic oscillations are detected, its velocity and temperature results are used as initial guesses for the next calculation with an increased Rayleigh number. This process is repeated until oscillations are detected.

Aspect ratio of 0.25

Using a mesh, oscillatory convection starts at a Rayleigh number of 250,000, which is relatively close to the first critical Rayleigh number of Ra_{c1} = 200,000. Figures 2a and 2b show the oscillatory nature of this flow for Ra = 400,000. (The Rayleigh number is somewhat higher than Ra_{c2} to amplify the oscillations, to be easier to visualize graphically).

A macroscopic visualization of the flow periodicity is given in Figure 3. The flow starts in 3(a) with one main circulation containing two small rotating cells inside this main circulation. In addition, smaller

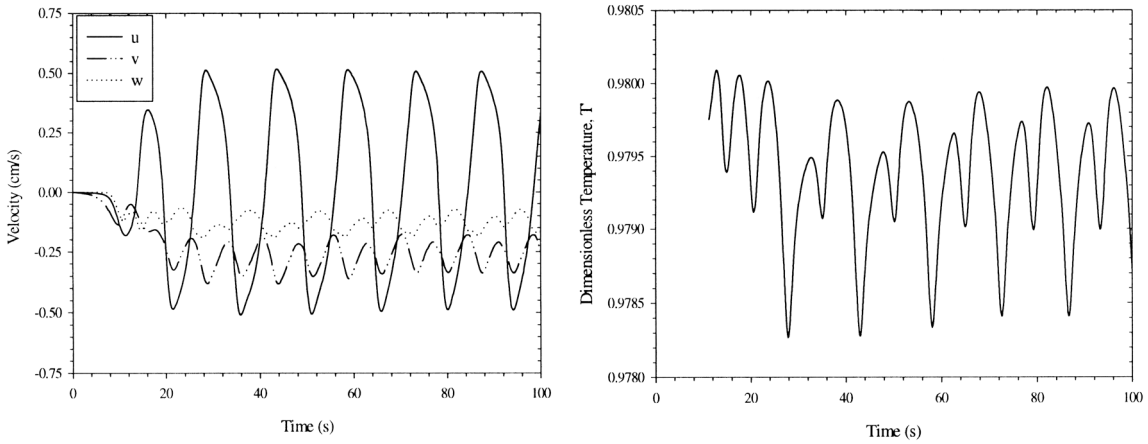

Figure 2. Oscillatory flow for Ra=400,000, γ=0.25, and Pr=0.008.

corner cells lie diagonally opposite from each other. In Figure 4(b), the two small rotating cells have grown in size and the velocity has increased. The larger diameter cell has broken down into two smaller cells, and conservation of angular momentum dictates that the velocity of the smaller cells should increase. In Figure 3(c), the center roll begins to develop in a diagonally-opposite direction to that in Figure 3(a). The above description is again repeated in the next half of the cycle.

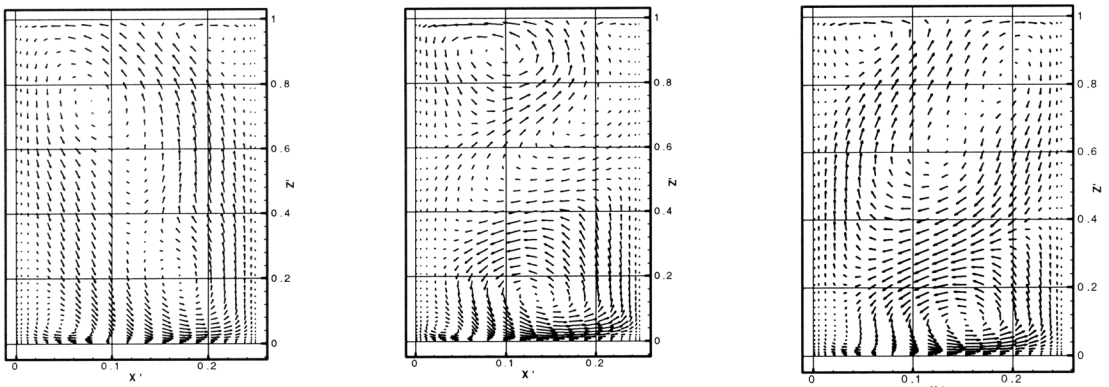

Figure 3. Macroscopic visualizations of oscillatory flow for γ=0.25.

Aspect Ratio = 1.0

Using the steady velocity profile of a single cell at a Ra_{c1} of 3550 and a mesh, the second critical Rayleigh number was determined to 83,500. The velocity components and dimensionless temperature for Ra = 85,000 are shown in Figure 4, showing definite periodic oscillations.

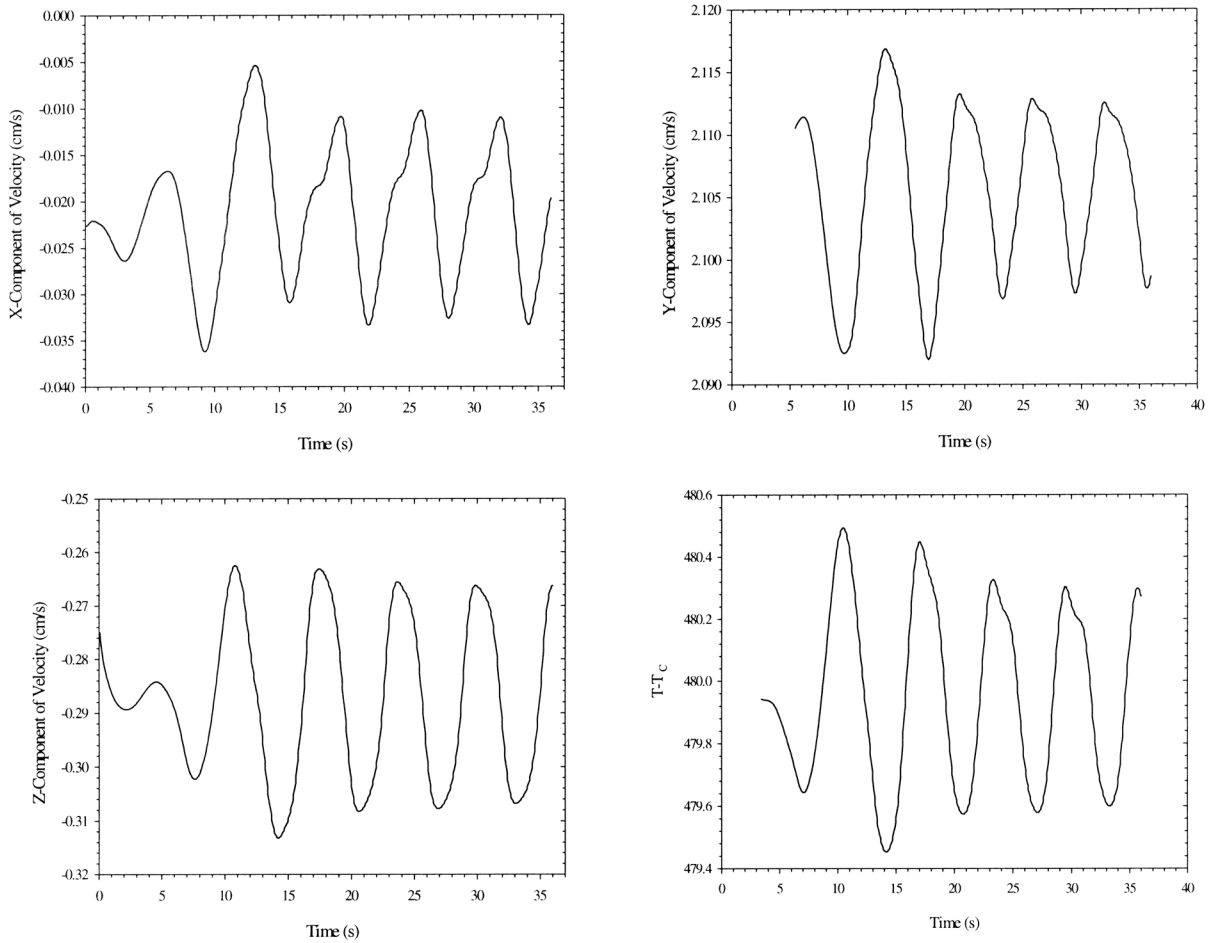

Figure 4. Oscillatory flow for Ra=85,000, γ=0.25.

Aspect Ratio = 2.0

With a 30x30x20 mesh, the calculated first critical Rayleigh number of 1900 predicts a double-celled pattern, and oscillations begin at Ra = 30,000. The oscillations that were detected, however, were not periodic, as shown in Figure 5. Even as the Rayleigh number was increased further, this same type of pattern was observed. We are currently studying this aspect ratio in more detail.

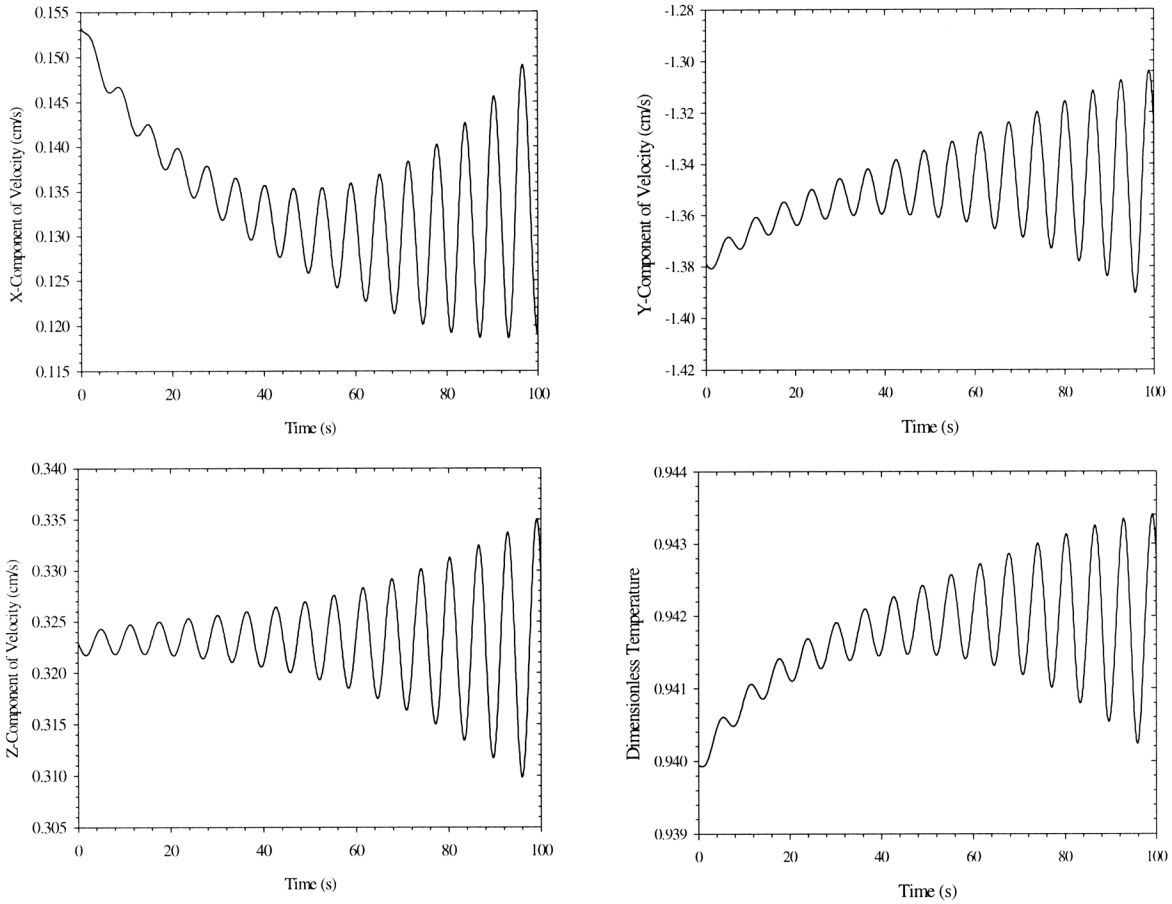

Figure 5. Oscillations for Ra=30,000, γ=2.0.

IV. Diffusivity Results

The results obtained for tin and tin/lead alloys obtained thus far are listed in Table 1 and clearly show that the measured diffusivity for the top depletion arrangement is consistently larger, indicating the presence of convection in the liquid. Currently, effort is under way to perform similar experiments of a variety of other tin-lead alloys.

Table 1. Diffusivity measurements.

X_{Sn}		D_0=A exp (-B/T) m^2/s	Temp. range (K)
1.0	(a) Bottom Depletion	1.69×10^{-7} exp(-3160/T)	756-1000
	(b) Top Depletion	3.75×10^{-7} exp(-3650/T)	758-1055
0.1	(a) Bottom Depletion	2.08×10^{-7} exp(-3460/T)	772-1076
	(b) Top Depletion	4.84×10^{-7} exp(-4000/T)	767-1028
0.9	(a) Bottom Depletion	1.97×10^{-8} exp(-2070/T)	760-959
	(b) Top Depletion	3.25×10^{-7} exp(-4370/T)	787-956

V. Conclusion

The calibration of the electrochemical measurement sensor has spurred a study of the steady-oscillatory flow transitions which occur in liquid metals and semiconductors. In this work, the results have been systematically characterized for a variety of Cartesian aspect ratios. Additionally, important details about the structure of oscillatory flows are made. Finally, the beginning of the characterization of the diffusivity of oxygen in liquid tin and tin-lead alloys have been made, with particular emphasis on the evidence of convection in these measurements.

REFERENCES

1. Crunkleton, D.W., Gupta, N., Narayanan, R., and Anderson, T. 1999 AIAA Paper 99-08440.
2. Eisele, Klaus, Zhang, Zhengji, Hirt, Felix and Ongoren, Abdullah 1998 *Chem Eng Wor* 33, 47.
3. Patankar, Suhas V. 1980 Numeric Heat Transfer and Fluid Flow, Washington, Hemisphere.
4. Prasad, S.R., Mallika, C., Anderson, T.J., and Narayanan, R. 1999 *J Crys Grow*, 198/199, 194.
5. Sears, B., Narayanan, R., Anderson, T.J., and Fripp, A.L., 1992 *J Crys Grow* 12, 404.

WETTING CHARACTERISTICS OF IMMISCIBLES

J. B. Andrews

Department of Materials and Mechanical Engineering
University of Alabama at Birmingham

INTRODUCTION

Binary immiscible alloys form two separated liquids on melting that exist over a temperature and composition range. Many desirable characteristics and applications have been proposed for these alloys (1-4). For example, some immiscible alloys show promise for use in medical applications, including use as filters for sub-micron particulates. Other alloys are expected to exhibit Type II superconductivity or high coercive magnetic field strengths. In order to obtain these desirable characteristics, it is necessary to prevent the normal segregation problems that hinder the ability to form desired microstructures in immiscible alloy systems.

The most common segregation mechanism in immiscible alloys is gravity-driven sedimentation. This difficulty usually occurs during normal ground based processing in an attempt to form a dispersed microstructure. Microgravity processing should provide a solution to this problem. However, segregation has been observed in low gravity processed immiscible alloys (5-10), as shown in Figure 1. There are obviously some critically important, but less studied, factors that influence segregation during microgravity processing. These factors include the interfacial energies between the phases (11), alloy/ampoule reactions (12), droplet migration due to gradients in surface tension brought about by temperature and compositional inhomogeneities (10), the relative volume fractions of the immiscible phases (7), and alloy/ampoule wetting characteristics (7, 12-14).

The wetting characteristics of immiscibles (WCI) project, which flew aboard NASA's fourth United States Microgravity Payload (USMP-4) mission in November 1997, was designed to provide new and critically important information on the sequence of events that lead to this massive segregation. In this investigation, transparent immiscible metal analog samples were used in order to study how the wetting behavior between the immiscible phases in hypermonotectic samples and the ampoule influence segregation. During the USMP-4 mission, the succinonitrile-glycerol (SCN-GLY) alloy system, which has been used by several researchers in past studies, was selected because the segregation process could be directly observed. This alloy system also exhibits a reasonable monotectic temperature, as shown in Figure 2. The succinonitrile-water (SCN-H_20) alloy system is also being considered as a possible system for use in future flight investigations.

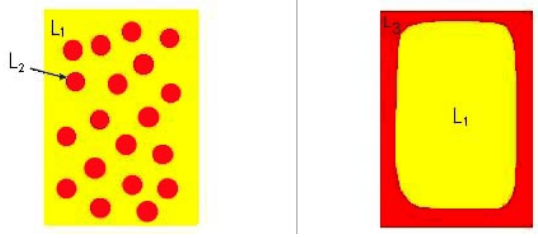

Figure 1. Early experiments carried out to form dispersed structures in immiscible alloy systems often resulted in massive segregation of the minor phase liquid phase to the container wall.

I. Background

While, there are several operative segregation mechanisms in microgravity processed immiscible systems, one of the most important of these mechanisms appears to involve the wetting characteristics between the immiscible phases and the ampoule (7, 12-14). When an immiscible (*i.e.* hypermonotectic) alloy is cooled into the miscibility gap, droplets of one of the liquid phases will form in the other. One theory postulates that if the lower volume fraction immiscible phase perfectly wets the ampoule, segregation will occur. Droplets that touch the ampoule will immediately wet the wall and spread along it. The flow produced in the adjacent liquid by this spreading action brings additional immiscible liquid droplets to the wall where the process is repeated. This sequence of events usually results in massive segregation where the low volume fraction immiscible liquid phase is found along the ampoule wall surrounding a core of the high volume fraction phase. Figure 3 schematically depicts this series process.

There is also speculation that nucleation events may be strongly affected when the minor phase perfectly wets the container wall. For perfect wetting, the surface energy of the system is actually reduced once nucleation has taken place. This results in no surface energy barrier to heterogeneous nucleation of perfectly wetting droplets on the ampoule wall. Obviously, heterogeneous nucleation would also result in the minor phase being found along the ampoule wall.

Another factor that has an influence on the segregation process is the volume fraction of the minor phase. Alloys in which the minor phase is present at a higher volume fraction may be expected to exhibit more rapid coalescence, as well as different wetting characteristics than low volume fraction alloys (12). Cahn's analysis of wetting in immiscible systems indicates perfect wetting is anticipated between one of the immiscible liquid phases and a solid surface for compositions near the center of the miscibility gap (16). The range over which this perfect wetting occurs varies with the alloy systems and with the solid surface.

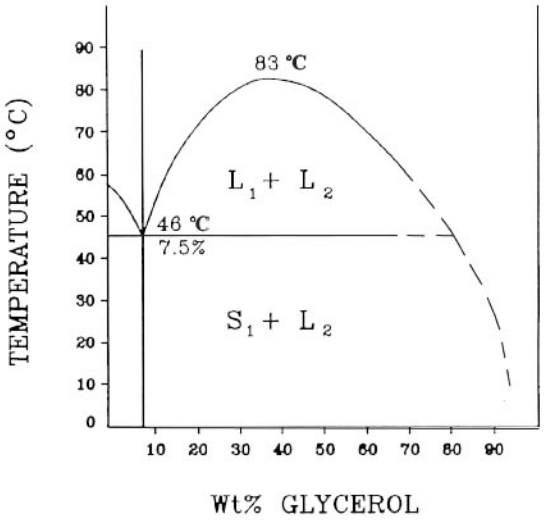

Figure 2. Partial succinonitrile-glycerol phase diagram as proposed by Kaukler (15).

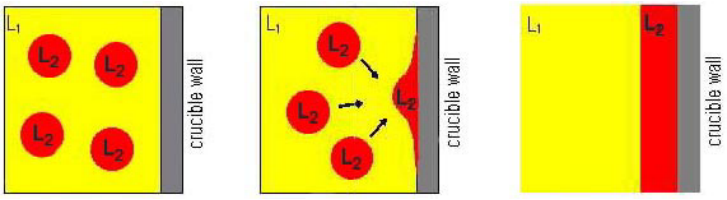

Figure 3. One possible sequence of events leading to massive segregation during microgravity solidification of immiscible alloys when the minor phase perfectly wets the container wall.

II. Experimental Approach

In this investigation, it was important that nucleation events, droplet coalescence and droplet migration all be directly observable. This requirement dictated the use of a transparent analog sample and a transparent cell assembly of a suitable aspect ratio for experimentation. Samples cells were constructed from standard 25 mm x 75 mm x 1mm microscope slides, separated by a Teflon® gasket, as shown in Figure 4. A gasket thickness of 0.13 mm was used in order to optimize optical characteristics. Fine gauge thermocouples (0.002 inches) were embedded in the gasket material on each edge of the cells to monitor nucleation temperatures and verify the thermal history during processing.

For the USMP-4 mission, twelve sample cells, with compositions varying from 15 wt% GLY to 70 wt% GLY were utilized. For processing, the sample cells containing the SCN-GLY system were heated to 90°C using a thermal chamber. The cells were held at this temperature for 15 minutes in order for homogenization to occur. Once homogenized, the cells were removed from the thermal chamber and placed on a backlit holder for observation using a microscope during cooling. The microscope was outfitted with a video camera. The camera image was displayed on a lap top computer screen within the middeck work area and was both recorded and downlinked to the ground to permit real time observation.

With the SCN-GLY system, as samples on the glycerol-rich side of the miscibility gap cool, succinonitrile-rich droplets were expected to form. For compositions near the midpoint of the miscibility gap, perfect wetting was expected to occur resulting in a succinonitrile-rich layer coating the ampoule gasket and surrounding a core of glycerol-rich liquid. For samples on the succinonitrile-rich side of the

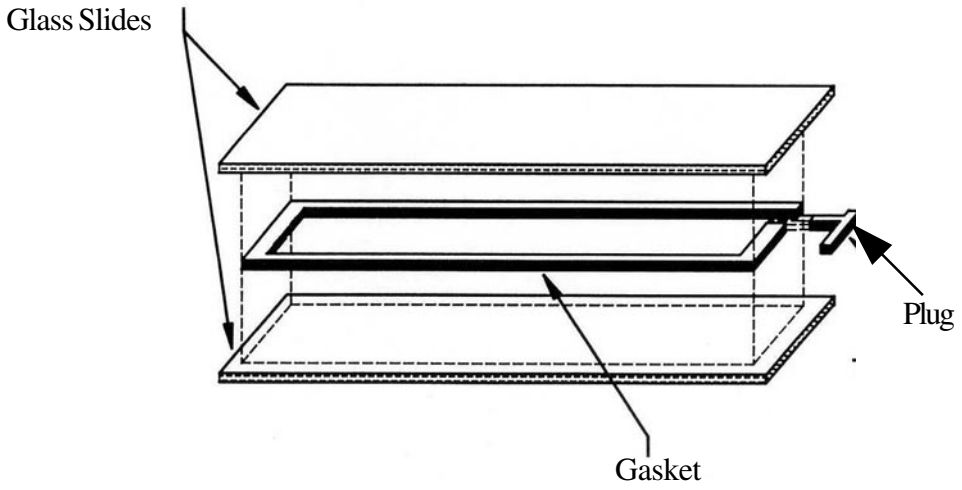

Figure 4. Sample cell assembly

miscibility gap, as the sample cools glycerol-rich droplets were expected to form. The minor glycerol-rich liquid phase should not wet the ampoule gasket. As a result, a dispersion of glycerol-rich liquid droplets in a succinonitrile-rich liquid matrix was anticipated.

III. Results from the USMP-4 Mission

In the USMP-4 investigation, twelve sample cells containing the SCN-GLY versus Teflon® combination were processed. This combination of alloy system and gasket material resulted in a narrow perfect

wetting range. Perfect wetting was observed in the 45 wt% GLY and the 50 wt% GLY, which represented only two out of the twelve samples processed. In addition, one of these two samples had partially degraded, which negatively impacted the validity of the results. Also, the fifteen minute homogenization time utilized during the flight appeared to be insufficient. This difficulty resulted in the sequence of events leading to segregation and the formation of a film of the minor immiscible phase along the gasket surface being observed during cooling. After processing and scanning around the perimeter of these samples, extensive regions of perfect wetting and segregation were found (17). Figure 5 shows still images of selected samples during processing. Figure 5(a) shows a sample with a dispersed structure, while Figure 5(b) shows one of the samples were perfect wetting occurred. Figure 5(c) shows an unanticipated result, were the glycerol-rich droplets moved away from the gasket material.

IV. Planned Improvements for the Reflight

Table 1 summarizes the difficulties encountered during the USMP-4 mission and a list of possible solutions. As mentioned earlier, the SCN-GLY system versus the Teflon® gasket combination used in the USMP-4 mission exhibited a short composition range over which perfect wetting was observed. Using an immiscible system/gasket combination with a wider perfect wetting range can significantly increase the likelihood of observing segregation events. This approach is proposed for the WCI reflight. The desired extended perfect wetting range can be accomplished by using a different gasket material (i.e. Lexan®) with the SCN-GLY system or by using a different transparent monotectic system altogether.

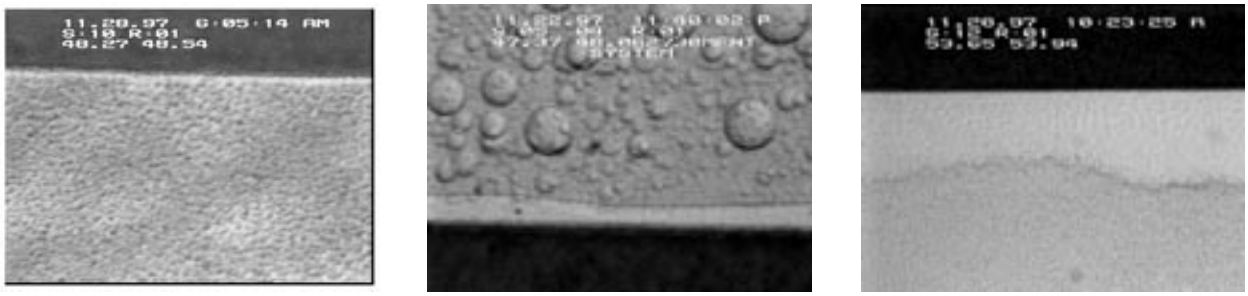

(a) (b) (c)

Figure 5. Images obtained from USMP-4 sample processing. (a) Dispersion formation observed in a SCN-GLY sample with a GLY content less than the critical. (b) Perfect wetting observed in a portion of a SCN-GLY sample with a GLY content above the critical. (c) Region adjacent to gasket surface free of glycerol-rich droplets, observed in the lowest wt% GLY sample processed.

While extensive experimentation has been carried out with the SCN-GLY alloy system, samples in this system have a shelf life at room temperature that can be as short as ten days. Degradation occurs due to polymerization of the glycerol by the succinonitrile and is highly temperature dependent. Attempts to use an inhibitor to slow the reaction have been unsuccessful to date. However, the shelf life can be extended to well over a month through storage at 4°C or below. If the SCN-GLY system is used with a new gasket material on the future reflight, then samples will either have to be processed promptly or kept cool prior to processing.

Another alternative is to use a different transparent immiscible system such as succinonitrile and water where degradation is not an issue. The larger perfect wetting range anticipated for this system over the

Table 1. Challenges identified during USMP-4 and possible solutions.

Challenges	Possible Solutions	
	Approach A	**Approach B**
The narrow perfect wetting range for SCN-GLY vs. Teflon® combination allowed investigation of wetting driven segregation processes in only two samples.	Increase perfect wetting range by using a different gasket material with the SCN-GLY system.	Change to the SCN-H_2O system to increase perfect wetting range.
Sample degradation resulted in loss of data for several sample compositions. (Cabin temperature was higher than anticipated.)	Keep samples cooled to 4ºC (or less) until needed. Shelf life at 23 ºC ~ 10 days.	Switch to a non-degrading system such as SCN-H_2O where low temperature storage is not necessary.
Segregation processes during perfect wetting occurred outside the field of view for the two pertinent samples due to incomplete homogenization.	Extend homogenization times to more than 15 minute. (Homogenization time limited by degradation.)	Can easily use longer homogenization times since not limited by degradation.

SCN-GLY system would also provide more opportunities to study segregation processes under perfect wetting conditions. Another benefit is that extended homogenization times can be utilized without fear of degradation. Special surface treatment of the glass cell surfaces may be necessary with this system to ensure that wetting occurs preferentially on the cell gasket instead of the glass cell walls.

REFERENCES

1. J. L. Reger: Interim Report, contract NAS8-28267, NASA Marshall Space Flight Center, TRW System Group, Redondo Beach, CA (1973).
2. A.J. Markworth, W. Oldfield, J. Duga, S. H. Gelles, "Investigation of Immiscible Systems and Potential Application," NASA CR-120667, 1975.
3. R. A. Parr and M. H. Johnston, "Growth Parameters for Aligned Microstructures in Directionally Solidified Aluminum-Bismuth Monotectics," Metal. Trans. 9A, 1978, 1825-1828.
4. J. Markworth, S. H. Gelles, J. J. Duga, W. Oldfield, "Immiscible Materials and Alloys," Proceedings of the 3rd Space Processing Symposium, NASA Report 74-5, June 1974.
5. S. H. Gelles and A. J. Markworth: AIAA Journal, 1978, vol 16, no. 5, 431-438.
6. T. Carlburg and H. Fredriksson: "Microgravity Studies in the Liquid-Phase Immiscible System: Aluminum-Indium," Metal. Trans., 1980, vol 11A, 1665-1676.
7. J. B. Andrews, A. C. Sandlin, P. A. Curreri, "Influence of Gravity Level and Interfacial Energies on Dispersion-Forming Tendencies in Hypermonotectic Cu-Pb-Al Alloys," Metal. Trans., 19A, 1988, 2645-2650.
8. H. C. deGroh III, H. B. Probst, "Effects of Crucible Wetting During Solidification of Immiscible Pb-Zn," NASA Technical Memorandum 101872, 1988.
9. Deruyterre, L. Froyen, "Melting and Solidification of Metallic Composites," Proceedings for the Workshop on Effect of Gravity of Solidification of Immiscible Alloys, Stockholm, ESAS, SP-219, 1984, 65-67.

10. L. Ratke, W. K. Thieringer, H. Fishchmiester, "Coarsening of Immiscible Liquid Alloys by Ostwald Ripening," Proceedings of the Norderney Symposium on Scientific Results of the German Spacelab Mission D1, 1986, 332-341.
11. P. A. Curreri, J. M. Van Alstine, D. E. Brooks, S. Bamberger, R. N. Snyder: Marshall Space Flight Center Preprint Series No. 85-0156, 1985, Marshall Space Flight Center, Huntsville, AL.
12. A.B. Cheney, J. B. Andrews, "The Evaluation of Ampoule Materials for Low-g Processing of Immiscible Alloys," Proceedings of the 6th International Symposium on Experimental Methods for Microgravity Materials Science, San Francisco, CA, Feb 28 - March 2, 1994, TMS, 191-198.
13. S. H. Gelles: NAS8-32952, Final Post Flight Report, MEA A1 Experiments, 1984, S. H. Gelles Associates, Columbus, OH.
14. Potard, Materials Processing in the Reduced Gravity Environment of Space, Elsevier Science Publishing Co., New York, NY, 1982, 543-551.
15. W. F. Kaukler: University of Alabama in Huntsville, private communication, January 1990.
16. J.W. Cahn, "Critical Point Wetting," Journal of Chemical Physics, 66, 1977, 3667-3672.
17. L.J. Little and J.B. Andrews, "Segregation in Microgravity Processed Immiscible Alloys", Proceedings of the 10th International Symposium on Experimental Methods for Microgravity Materials Science, TMS Annual Meeting, CD-ROM Publication by TMS, 1998.

COUPLED GROWTH IN HYPERMONOTECTICS

J. Barry Andrews[1] and Sam R. Coriell[2]

[1]University of Alabama at Birmingham
[2]National Institute of Standards and Technology

INTRODUCTION

The overall objective of this project is to obtain a fundamental understanding of the physics controlling solidification processes in immiscible alloy systems. The investigation involves both experimentation and the development of a model describing solidification in monotectic systems. The experimental segment was designed to first demonstrate that it is possible to obtain interface stability and steady state coupled growth in hypermonotectic alloys through microgravity processing. Microgravity results obtained to date have verified this possibility (1). Future flights will permit experimental determination of the limits of interface stability and the influence of alloy composition and growth rate on microstructure. The objectives of the modeling segment of the investigation include prediction of the limits of interface stability, modeling of convective flow due to residual acceleration, and the influence of surface tension driven flows at the solidification interface (2).

The study of solidification processes in immiscible alloy systems is hindered by the inherent convective flow that occurs on Earth and by the possibility of sedimentation of the higher density immiscible liquid phase. It has been shown that processing using a high thermal gradient and a low growth rate can lead to a stable macroscopically planar growth front even in hypermonotectic alloys (1,3). Processing under these growth conditions can avoid constitutional supercooling and prevent the formation of the minor immiscible liquid phase in advance of the solidification front. However, the solute depleted boundary layer that forms in advance of the solidification front is almost always less dense than the liquid away from the solidification front. As a result, convective instability is expected. Ground based testing has indicated that convection is a major problem in these alloy systems and leads to gross compositional variations along the sample and difficulties maintaining interface stability (4). Sustained low gravity processing conditions are necessary in order to minimize these problems and obtain solidification conditions which approach steady state.

The first phase of the coupled growth in hypermonotectics (CGH) experiment flew aboard the Life and Microgravity Spacelab (LMS) mission during the summer of 1996. Processing conditions were controlled in an attempt to force the production of an aligned fibrous phase in the microstructure of processed samples. The Advanced Gradient Heating Facility (AGHF) was used to directionally solidify the immiscible alloys. Alloys in the aluminum-indium system were studied and specialized aluminum nitride ampoules were used in order to accommodate solidification shrinkage and to control thermal end effects (5). Three alloy compositions were processed during the LMS mission in order to permit comparison

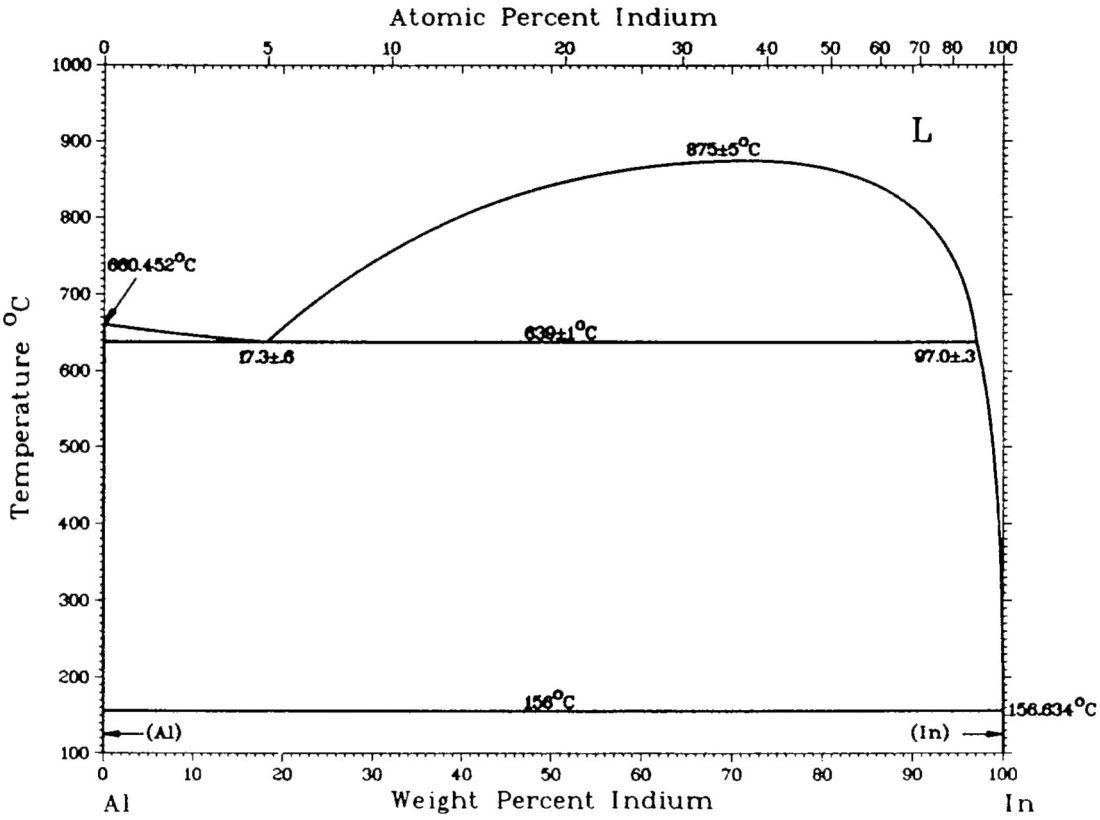

Figure 1. Phase diagram for the aluminum-indium alloy system (6).

with the model over a composition range. Two ground based control samples were subsequently processed under conditions identical to those of two of the flight samples in order to allow a direct comparison of the results.

I. Background

Two-liquid immiscibility is usually associated with monotectic alloy systems. A phase diagram for the aluminum-indium alloy system being used in this investigation is shown in Figure 1(6). The monotectic three-phase reaction occurs at a well defined temperature in a binary alloy and involves the decomposition of one liquid phase to form a solid and another liquid phase, ($L_1 \rightarrow S_1 + L_2$).

The monotectic reaction ($L_1 \rightarrow S_1 + L_2$) is quite similar to the eutectic reaction ($L \rightarrow S_1 + S_2$) that occurs in many alloy systems. In a eutectic-type system, fibrous composite structures can be formed during directional solidification as a result of the unmixing of the liquid phase to form the two product phases. In this reaction, the solute rejected during the formation of one of the product phases is consumed in the formation of the other. This "coupled growth process" is also possible in monotectic alloy systems.

It is well known that off eutectic composition alloys can be directionally solidified to produce fibrous microstructures (7,8). The physics controlling growth in monotectic systems are similar, implying off-monotectic growth should also be possible. However, there has been some controversy whether off-monotectic alloys, especially those with solute contents higher than the monotectic (*i.e.* hypermonotectic

alloys), can be directionally solidified under conditions which would lead to a stable coupled growth process and the development of a fibrous microstructure.

Interface Instability

Assuming steady state coupled growth can be maintained in an off-monotectic alloy, a solute depleted boundary layer should develop ahead of the solidification front. The composition variation with position in the liquid results in a variation in the temperature at which the miscibility gap would be entered. If the thermal gradient in the sample is insufficient to keep the local temperature above the local miscibility gap temperature, the second phase immiscible liquid can form droplets in advance of the solidification front. Using a simple constitutional supercooling analysis (9), the conditions that must be met in order to avoid this interface instability are given by the relationship

$$\frac{G_L}{V} > \frac{m_L(C_o - C_m)}{D_L} \qquad (1)$$

where G_L is the temperature gradient in the liquid, V is the solidification front velocity, m_L is the slope of the $(L_1 + L_2)$ two-phase boundary, C_O is the alloy composition, C_M is the monotectic composition, and D_L is the diffusivity of solute in the liquid.

II. Convective Instability

While the use of a high thermal gradient to growth rate ratio should make it possible to achieve steady state coupled growth during directional solidification, the solute depleted boundary layer that forms can give rise to undesirable fluid flow in the melt. In almost every known immiscible alloy system, the solute depleted boundary layer in advance of the solidification front will have a lower density than the liquid above it. This density variation can lead to convective flows which cause difficulties during solidification. In most cases the resulting convective flow can produce compositional variations that are sufficient to prevent coupled growth over a substantial portion of the sample (4,10). Analysis implies that the only way to reduce convective flows to the level required for this study is to carry out directional solidification under microgravity conditions.

III. Results and Discussion

As a first step in this investigation three alloy compositions in the aluminum-indium immiscible system were directionally solidified during the LMS mission. These samples consisted of a monotectic composition sample (17.3wt%In) and two hypermonotectic composition samples (18.5wt%In and 19.7wt%In). The Advanced Gradient Heating Facility (AGHF) was used to directionally solidify these samples at a furnace translation rate of 1.0 μm/s. Shortly after starting directional solidification of the 18.5wt%In hypermonotectic sample, all telemetry from the AGHF was lost. Since the AGHF does not have the capability to record data, there is no solidification rate or thermal gradient information available for this sample. The thermal gradients obtained in the other two samples were considerably lower than anticipated. Gradients measured from the thermocouples attached to the aluminum nitride (ALN) ampoules were as low as 67°C/cm for the flight samples which should be compared to values of 80 to 85°C/cm for samples processed in the presumably identical engineering model of the AGHF. Due at least partially to these lower thermal gradients, interface stability was not obtained in the highest composition hypermonotectic alloy (19.7wt%In).

Void Formation

Radiographic analysis revealed the presence of several voids in the flight samples and one of the ground based samples (11). A great deal of care was used in the preparation of the alloys and ampoule assemblies in order to minimize the presence of any free surfaces or voids in the samples during processing. In order to avoid free surfaces generated due to contraction of the sample during solidification, a piston and high temperature carbon spring were utilized to compensate for the volume changes. In an attempt to minimize any residual gasses which could have led to bubble formation, the alloys were vacuum induction melted. In addition, the ampoule components were all vacuum degassed at 1250°C for more than 6 hours. Finally, samples were loaded into the ampoules and sealed under a vacuum of at least 1 x 10^{-4} Torr.

An exhaustive analysis indicates these voids apparently occurred due to leakage of gas past the seal at the bottom of the ampoule (12). Each ampoule had passed helium leak testing after assembly. However, post flight testing using a more direct technique revealed measurable helium leak rates past the seals in the ampoules that contained voids. It appears that changes in the integrity of the seal occurred during subsequent handling or processing.

IV. Microstructural Differences Between Flight and Ground Samples

While the presence of voids was obviously undesirable, void-free regions of significant size were present in all samples and permitted a meaningful metallographic analysis. Analysis of the 18.5wt%In flight sample revealed a totally different variation in microstructure with position than that observed on Earth. In this sample, the first to freeze region almost immediately began to form a fibrous structure, as shown in Figure 2. This finding is consistent with that predicted for substantially reduced mixing in the liquid. As solidification progressed the microstructure remained totally fibrous with the exception of a few irregular indium particles at a location 13 mm from first to solidify. The formation of these indium particles coincided with the interface passing two voids along the edge of the sample.

At a location 26 mm from the first to freeze end of the 18.5wt%In sample, the microstructure suddenly changed from completely fibrous to dispersed. Unfortunately, data on sample temperatures, growth rates and thermal gradients were lost for this sample due to the loss of telemetry from the furnace facility. As a result, details on the processing condition variations that may have caused this change are unavailable.

Microstructural Differences Between Flight Samples

Interface stability was not obtained in the highest indium content (19.7wt%In) flight sample, resulting in a microstructure that was only partially fibrous. This finding was anticipated due to the low thermal gradients obtained. However, almost totally fibrous structures were obtained over significant lengths of both the 18.5wt%In hypermonotectic sample and the 17.3wt%In monotectic sample. This result permitted a comparison between flight samples of two different compositions to determine how the changes in volume fraction of the L_2 phase were accommodated by the microstructure.

Quantitative stereological analysis was carried out using an automated image analysis system interfaced directly to a scanning electron microscope. The system was set up to make measurements over both an entire frame, which might include grain boundaries, and in selected areas which only included the aligned circular cross-section rods within a grain. The parameters measured included the volume fraction of the

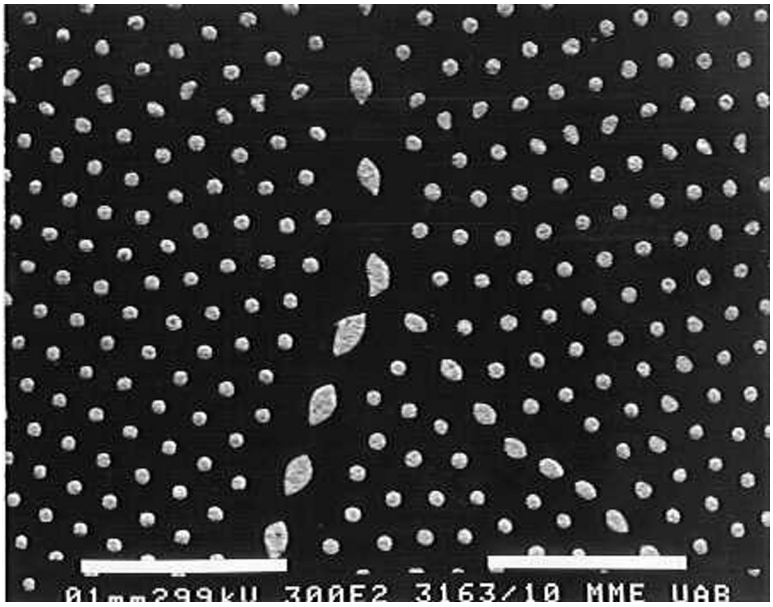

Figure 2. Scanning electron micrograph of a fibrous growth region in a directionally solidified 18.5 wt% In immiscible alloy.

rods within a grain and the overall volume fraction of the indium-rich phase in the microstructure. In addition, the image analysis system permitted automated determination of the areas of individual second phase particles. This information was used to determine the area of each of the "circular" rods within a grain and then to calculate the diameter of each rod. The results were then averaged and the 95% confidence interval determined. For the same placements, the number of "circular" rods per unit area, N_A, within a grain was determined in order to permit a comparison of changes in rod spacing. The results are tabulated in Table 1. The ranges shown represent the 95% confidence limits.

It is apparent from Table 1 that when considering only the aligned circular rod regions within grains (i.e. no lenticular rods or denuded zones at the grain boundaries) the monotectic alloy contains a rod V_V of

Table 1. Quantitative Stereological Analysis Results for Two Flight Samples.

Sample Composition (wt % In)	**V_V of rods within grains (%)**	**Diameter of rods within grains (μm)**	**N_A of rods within grains (number/mm^2)**	**V_V of rods overall (%)**
17.3	8.24 ± 0.263	8.92 ± 0.072	1224.6 ± 63	8.04 ± 0.241
18.5	9.52 ± 0.261	9.06 ± 0.103	1352.9 ± 107	9.82 ± 0.229

± values represent 95 % confidence limits.

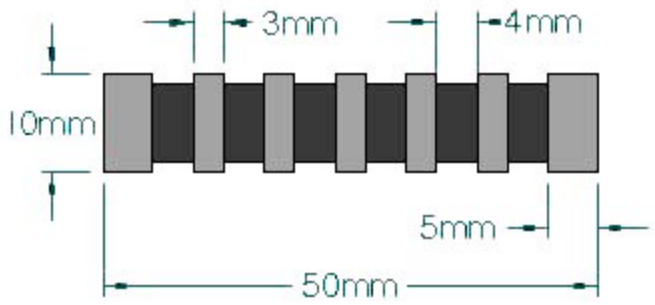

Figure 3. Proposed piston design currently under evaluation.

8.24% compared to 9.52% for the hypermonotectic alloy. This information can be taken as further verification that interface stability was obtained in the hypermonotectic alloy. (Overall volume fractions, *i.e*. not selected areas, were 8.04% vs. 9.82%).

V. Planned Improvement

Unfortunately, difficulties with void formation, loss of data telemetry, and low thermal gradients resulted in a limited extent of aligned fibrous microstructure in all of these samples. As a result, comparisons between fibrous regions were only possible for two of the flight samples and only along restricted regions within each of these samples. It is anticipated that improvements in furnace performance and ampoule design will permit the development of an aligned fibrous structure along the entire length of flight processed samples. Ampoule assembly design changes being evaluated involve modification of the piston design and possible changes in the seal material. Work is underway to identify a low melting point glass that could be used to seal the AlN ampoules. Both a low flow temperature (approximately 600°C) and a thermal expansion match with AlN are required. The use of a reactive braze is also being considered for the hermetic seal. A new piston design is under evaluation that contains multiple grooves intended to impede the movement of aluminum to the spring area due to capillary forces. (See Figure 3.) The above improvements should make it possible to obtain information over a range of solidification rates as well as over a much larger composition range.

VI. Summary

To summarize the findings to date, three immiscible aluminum-indium samples were directionally solidified during the LMS mission. Most of the samples contained voids that may have been sufficient in size to modify solidification parameters locally during processing. Compositional results obtained from the initial portion of a hypermonotectic (18.5wt%In) flight sample provide evidence that steady state growth conditions were achieved in this alloy through microgravity processing.

Microstructural analysis of the highest composition (19.7wt%In) hypermonotectic alloy revealed that interface stability was not obtained for the thermal gradient and growth rates utilized during processing. Interface stability was obtained for the initial 2.6 cm of growth in the 18.5wt%In hypermonotectic alloy. Microstructural comparisons between the monotectic alloy (17.3wt%In) and the 18.5wt%In hypermonotectic alloy confirm an increase in the volume fraction of the aligned fibrous phase. This volume fraction increase was obtained in the structure primarily by an increase in the number of rods per unit area and not by a change in rod diameter.

VII. Acknowledgments

The authors wish to thank the National Aeronautics and Space Administration for financial support of this effort through contract NAS8-99059.

REFERENCES

1. J.B. Andrews, L.J. Hayes, Y. Arikawa and S.R. Coriell, "Microgravity Solidification of Al-In Alloys", *Solidification and Gravity 2000, Proceedings of the Third International Conference*, Miskolc, Hungary, April 25 – 29, 1999, Transtec Publications, pp. 247-257, 1999.
2. S. R. Coriell, W. F. Mitchell, B.T. Murray, J.B. Andrews and Y. Arikawa, "Analysis of Monotectic Growth: Infinite Diffusion in L_2 – Phase," *J. Crystal Growth* 179, 647-657 (1997).

3. R.A. Merrick and J.B. Andrews, "Direct Observation of Solidification Processes in Immiscible Systems", *Proceedings, Experimental Methods for Microgravity Materials Science Research, 4th International Symposium*, San Diego, CA., March, 1992, pp. 7-16, 1992.
4. L.J. Hayes and J.B. Andrews, "Influence of Convection on Aligned Composite Growth in Hypermonotectic Alloys", *Proceedings of the 11th International Symposium on Experimental Methods for Microgravity Materials Science*, A CD-ROM Publication by ASM, 1999.
5. J.B. Andrews, J.S. O'Dell, A.B. Cheney,Y. Arikawa and L.J. Hayes, "Ampoule Design and Testing for Microgravity Experimentation on Coupled Growth in Hypermonotectics," *Proceedings of the 8th International Conference on Experimental Methods for Microgravity Materials Science*, a publication of the Minerals, Metals and Materials Society, R. S. Schiffman editor, 1996.
6. T.B. Massalski, *Binary Alloy Phase Diagrams,* edited by W. W. Scott, Materials Park, OH, ASM International, 1990, pp. 162.
7. F.R. Mollard and M.C. Flemings, "Growth of Composites from the Melt – Part I," *Transactions of the Metallurgical Society of AIME,* Vol. 239, 1967a, pp. 1526-1533.
8. F.R. Mollard and Flemings "Growth of Composites from the Melt – Part II," *Transactions of the Metallurgical Society of AIME,* Vol. 239, 1967b, pp.1534-15-46.
9. W. Tiller, K.A. Jackson, J.W. Rutter, and B. Chalmers, "The Redistribution of Solute Atoms During the Solidification of Metals," *Acta Metall* **1** 50-65 (1953).
10. L.J. Hayes and J.B. Andrews, "The Influence of Convection on Composition and Morphology of Directionally Solidified Hypermonotectic Alloys," *Proceedings of the 7th International Conference on Experimental Methods for Microgravity Materials Science,* a publication of the Minerals, Metals and Materials Society, R. S. Schiffman editor, 1995, pp. 87-92.
11. J.B. Andrews, L.J. Hayes, Y. Arikawa and S.R. Corriell, "Directional Solidification of Immiscible Al-In Alloys Under Microgravity Conditions," *Proceedings of the 10th International Symposium on Experimental Methods for Microgravity Materials Science,* a CD-ROM Publication by TMS, 1998.
12. J.B. Andrews, L.J. Hayes, and D. Downs, "The Source of Voids in Al-In Samples Processed during the LMS Mission", *Proceedings of the 12th International Symposium on Experimental Methods for Microgravity Materials Science*, in press.

FOAMING OF THERMOPLASTIC POLYMERS IN A DYNAMIC DECOMPRESSION AND COOLING PROCESS

KwangJin Song and Robert E. Apfel (P.I.)

Department of Mechanical Engineering
Yale University, PO Box 208286, New Haven, CT 06520-8286

ABSTRACT

Solutions of polymers in blowing liquids are decompressed into foams in a dynamic decompression and cooling (DDC) process. Adjustment of material and process conditions has allowed structure and properties of resultant foams to be varied substantially. The cellular structures of the foams are open or closed, with mean densities in the range from a low to medium level. The foamed polymers have micromorphologies of oriented fibers and fiber-networks, which tend to strengthen the materials. It is expected that in microgravity, DDC foaming will be able to produce uniform solutions of polymer/solid, resulting in foamed composites.

I. Introduction

Polymeric foams can be produced by a number of technologies (1). Among them, the expansion process is the most widely used technique wherein gas bubbles nucleate and expand either by decompression or heating of the system that contains polymers and blowing agents. Its foaming mechanism generally involves the pressure difference between the inside of the cell and the surrounding medium. In a 1932 patent (2), Munters and Tandberg first proposed a polymer foaming process that utilizes the expansion technique. The inventors produced polystyrene (PS) foams using a gaseous foaming agent. Subsequently in 1950, McIntire of the Dow Co. (3) modified this batch technique into a continuous process. Rubens *et al.*, (4) in 1962, also from the Dow Co., proposed another notable process for producing polyethylene (PE) foams, which employs 1,2-dichlorotetrafluoethane as a blowing gas. Simultaneously, in the 1960s, Blades and White of the DuPont Co. patented a different technique that employs liquids as a blowing agent (5,6). Here, homogeneous mixtures of polymer/poor solvents are decompressed through a shaping die into a closed-cellular body.

A DDC process was proposed in 1995 by Apfel that was directed at creating bulk, open-cell foams of glassy metals by using an immiscible pair of melt and blowing liquid (7). This technique in polymer foaming involves heating and mixing materials under pressure in the presence of a volatile phase. Non condensable gas super-pressurizes the mixture. Homogeneous solutions thus formed are rapidly decompressed either by opening a release valve, where foaming occurs inside a pressure vessel, or by discharging the mixtures into the atmosphere. A sudden pressure quench triggered by this procedure causes the liquid phase to be vaporized, expanding and cooling the melt by taking the latent heat of vaporization from it. We have processed semicrystalline polymers of polybutylene terephthalate (PBT) with an intrinsic viscosity of 0.66 dℓ/g, and low- and high-density

polyethylenes (LDPE, HDPE) that have different melt indices (MI, g/10 min). Resultant foams are variously characterized.

II. Morphology of DDC Foams

The DDC foaming that comprised the material inside the vessel produced both open cell foams of PBT and PE foams of a mixed cell structure having open and closed cells. The cells had sizes varying from 50 to 1000 μm in diameter (Figure 1). The mixed cell foams showed structural variations. In the skin parts, more cells were open; however, in the core parts, more cells were closed. The bubbles tended to better stabilize with decreasing MI, presumably due to increased resistance to thinning of cell walls and to retardation of melt drainage from the membranes. On the other hand, the foaming by discharging the melts out of the vessel generated closed cells that had a mean size of *ca*. 500 μm. The closed cells were quite uniform in size but slightly collapsed. SEM micrographs also revealed that the inside closed cell wall had various micromorphologies of granules, sheets, and fibers, with the wall strut that included crystalline lamellae having a thickness of a few microns.

In the DDC process, gas bubbles nucleate and grow by the non-condensable gas or the volatile solvent phase, developing stress at the cell wall of the polymer to expand the bubbles. The cell membrane will fail if this stress exceeds the modulus of the material. In general, LDPE, as

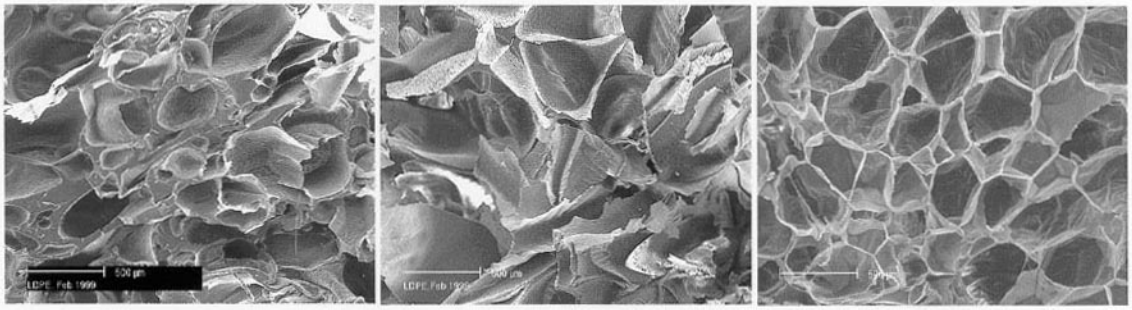

(a) LDPE with MI=2.3 (b) LDPE with MI=0.22 (c) HDPE with MI=0.5

Figure 1. SEM micrographs of the DDC foams; (a)(b): The skin parts of the LDPE foams with $\rho_f = 100$ kg/cm^3, (c) HDPE foam $\rho_f = 10$ kg/cm^3.

compared to HDPE, exhibits high degrees of strain-induced hardening due to its molecular mechanisms, which imparts to the polymer a better stability in film blowing and which should help stabilize bubbles in DDC foaming as well. The open cell structure occurring at high MI, therefore, may involve the slow hardening process associated with cooling and crystallization of the melts during foaming inside the vessel. A mixed cell structure would be a result of partial rupture of cell membranes. The formation of this structure in the DDC process could be related to nonuniform stresses over the material in a confined space. Parameters such as localized liquid/liquid phase separation and varying rates of nucleation and growth for individual bubbles could also be responsible. Bubbles nucleated in the later stage due to transient time lag or due to different mechanisms of nucleation or bubbles grown slowly due to fluctuation of the temperature may remain closed without cell failure. It seems thus that the closed cells may result from the characteristics of the foaming process that created a rapid cooling of the melt and a uniform distribution of the stress.

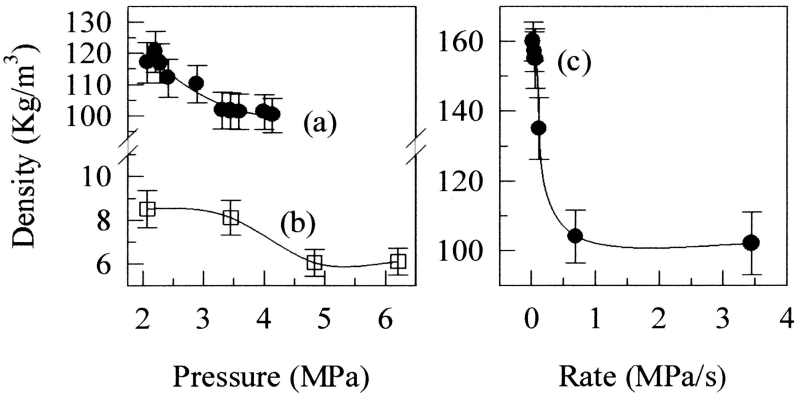

Figure 2. Mean densities (ρ_f) of the LDPE foams with MI=2.3 with process conditions; (a) Mixed cell foams at T_d = 110°C and r_d = 2.3 MPa/s, (b) Closed cell foams at T_d = 145°C, (c) Mixed cell foams at T_d = 110°C, P_d = 3.45 MPa and T_d = 110°C.

III. Mean Density of Foams

The mixed cell foams exhibited mean densities that fluctuated considerably depending on the position of the specimen. The skin and upper parts of the foams had higher densities than the core and bottom parts. This local fluctuation of the densities stems from the variations of cellular structure. At high decompression rates (r_d) above 1.5 MPa/s, the mean densities decreased with increases in the decompression pressure (P_d) and temperature (T_d), but the changes were marginal (Figure 2). At constant P_d and T_d, however, the mean foam densities increased considerably from 90 to 160 kg/m^3 with decreases in r_d. It seems that a retarded decompression suppresses the explosive evaporation of the volatile phase; the gaseous molecules may readily escape from the melt at relatively high temperatures, without causing a large degree of expansion.

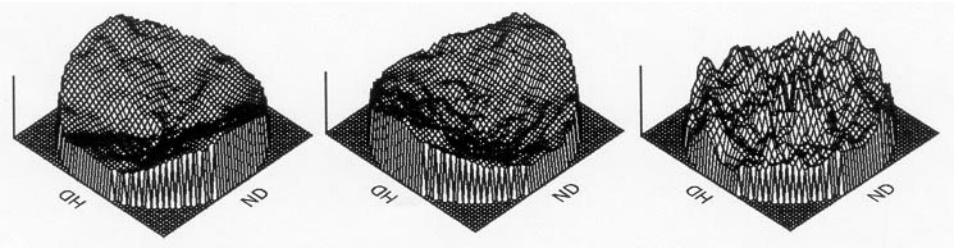

PBT (100)α Plane PBT (010)α Plane LDPE (110) Plane

Figure 3. WAXS pole figures of open cell PBT foams and closed cell HDPE foams that were produced by DDC foaming.

The closed cell foams were uniform in shape, with the low range of mean densities, below 10.0 kg/m^3, which tended to decrease with increases in P_d. As the solutions were discharged into the atmosphere, the resulting foams experienced free expansion. However, at higher P_d, a sudden expansion developed large foam cells that subsequently collapsed, yielding a tendency to increase the mean density. The cooling rate of the melt seemed not high enough to stabilize the cells as the polymer, having a poor heat conductivity, went through a rapid expansion process. The foam densities tended to increase with increases in the polymer concentration.

IV. Crystalline Structure

Because the SEM micrographs revealed oriented crystals, the DDC foams were characterized further by the wide angle X-ray scattering (WAXS) technique. In the open cell foams of PBT, the (100)α poles concentrated in the normal direction (ND) with spread in ND-HD plane while the (010)α poles focused primarily on hoop direction (HD) (Figure 3), which implies the presence of anisotropic texture in the specimen. However, though the closed cell foams of the LDPE and HDPE exhibited distinct Debye (110) and (200) rings in WAXS film photographs, distributions of their intensities were found largely isotropic along the azimuth. The (110) pole figure also held the same tendency. The pole densities varied marginally along the equator and azimuth.

Using the Wilchinsky's generalized orientation mode (8), the crystalline orientation factors ($f^{B}_{i,j}$) were computed through (9):

$$\overline{\cos^2\phi_j} = \frac{\int_0^{2\pi}\int_0^{2\pi} I_{hkl}(\phi_1,\chi_1)\cos^2\phi_1 \sin\phi_1 \, d\phi_1 d\chi_1}{\int_0^{2\pi}\int_0^{2\pi} I_{hkl}(\phi_1,\chi_1)\sin\phi_1 \, d\phi_1 d\chi_1} \quad (1)$$

$$(f^{B}_{FD,j}) = 2\overline{\cos^2\phi_{FD,j}} + \overline{\cos^2\phi_{HD,j}} - 1 \quad (2a)$$

$$(f^{B}_{HD,j}) = 2\overline{\cos^2\phi_{HD,j}} + \overline{\cos^2\phi_{FD,j}} - 1 \quad (2b)$$

where, $\overline{\cos^2\phi_j}$ is the second moments of the orientation distribution; $I_{hkl}(\phi_1,\chi_1)$ is the diffracted intensity distribution in the pole figures; $\phi_{i,j}$ is the angle between the sample direction i and the crystallographic axis j; and FD is the flow direction. As expected, the closed cell foams exhibited $(f^{B}_{i,j})$ close to zero, suggesting that the overall texture resembles isotropy. Seemingly this texture is responsible for the alignment of scattering units along the circumferential direction of the cell wall, as was observed in SEM micrographs. In contrast, the open cells of the PBT foams comprised a mild level of the chain orientation, $(f^{B}_{i,j}) \leq 0.3$, where the $(f^{B}_{FD,j})$ was higher than the $(f^{B}_{HD,j})$. The c-axis was found oriented more along the FD than the HD and the a-axis, which is normal to the plane of the phenyl ring on the chain backbone, tended to align along the ND. It appears that with DDC foaming, the PBT chains in the open cell structures tend to orient in the FD with the phenyl rings aligning roughly parallel to the foam surface. The strong FD orientation is probably due to the flow character of the evaporating solvent phase in a container.

V. Mechanical Properties

The mechanical properties of semicrystalline polymer foams are related in a complex manner to the cellular morphologies of the foam and to the properties of the polymer matrix. Included in the former are foam density, cell structure and shape, and cell size and its distributions, while the latter comprise molecular interactions, crystalline morphology and state of molecular orientation. At comparable levels of densities, foams with higher fractions and smaller size of closed cells are found to exhibit higher modulus and strength in tensile and compressive testing. Increasing density, on the other hand, strengthens foamed polymers (10).

These previous findings are consistent with the results of the DDC foams (Figure 4). HDPE foams revealed higher tensile strengths because of their high crystallinity. The tensile strengths were appreciably high which tended to increase with increasing polymer concentration. However, variations in strength-to-weight ratio were marginal. These mechanical behaviors may reflect as well the state of the chain orientation present in the foams. The tensile drawing of oriented polymers tends to bend and stretch the

covalent bonds of the molecules, resulting in a high Young's modulus and strength. In unoriented polymers, however, the deformation may increasingly involve the breakage of intermolecular forces, which imparts to the samples an inferior modulus and strength.

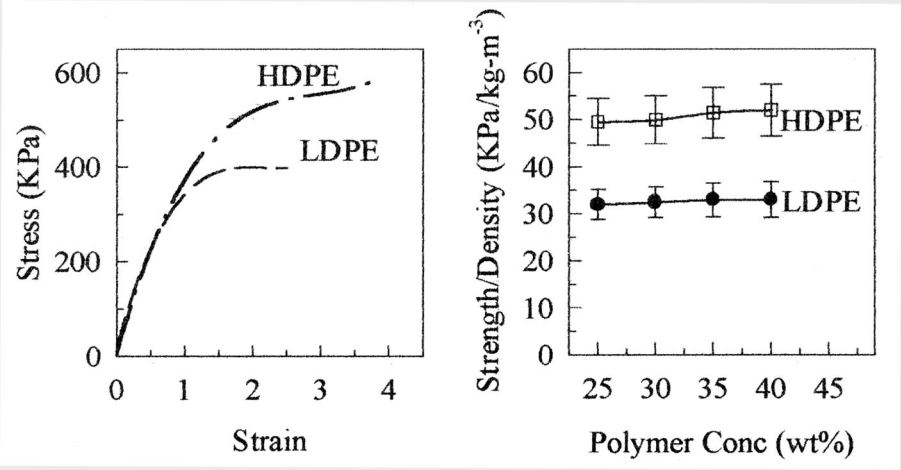

Figure 4. Tensile properties at maximum of the DDC closed cell foams along the FD.

VI. Conclusions

The DDC process has produced polymer foams of open and closed cell structures, hierarchical or uniform, with densities ranging from a low to medium level. The polymer phase contains the morphologies of oriented fibers and network-like structures, which tend to strengthen foamed products. Lightweight, DDC-foamed materials, which possess enhanced strength-to-weight ratios, will be likely fabricated in a continuous manner. However, during foaming the solutions containing species that reveal a large difference in density tend to phase segregate, greatly narrowing the parameter space of the DDC process.

The microgravity environment can aid in providing idealized conditions for the foaming. In particular, phase separation as well as layering and stratification effects are minimized so that uniform initial states can be achieved prior to decompression. Also, non-uniform heating produces convective effects which are absent in zero-g, allowing for the study of transient processes and resulting foams, which should be isotropic. These considerations are especially important when processing polymer blends and polymer/metal composites intended for high temperature applications. Therefore, DDC foaming in microgravity will serve not only the understanding of the underlying mechanisms of rapidly decompressed solid foams, but also may provide a new approach for producing structural materials to be used in space.

REFERENCES

1. Suh, K. W.; Webb, D. D. *Cellular Materials in Ency. Polym. Sci. Eng*; 2nd Eds, Wiley, NY, 1985
2. Munters, C. G.; Tandberg, J. G. U.S. Patent 2,023,204, 1935
3. McIntire, O.R. (to Dow) U.S. Patent 2,515,250, 1950
4. Rubens, L. C.; Griffin, J. D.; Urchick, D. (to Dow) U.S. Patent 3,067,147, 1962
5. Blades, H.; White, J. R. (to DuPont) U.S. Patent: 3,227,664, 1966
6. White, J. R.; Blades, H. (to DuPont) U.S. Patent: 3,542,715, 1970
7. Apfel, R. E.; U.S. Patent 5,384,203, 1995
8. Wilchinsky, Z. W. *J. Appl. Phys.*, 1960, 31, 1969
9. White, J. L.; Spruiell, J. E. *Polym. Eng. Sci.*, 1980, 20, 247
10. Meinecke, E. A.; Clark, R. C. *Mechanical Properties of Polymeric Foams*; Technomic, Westport, CT, 1973

TERRESTRIAL MEASUREMENTS OF DIFFUSIVITIES IN REFRACTORY MELTS BY PULSED MELTING OF THIN FILMS

Paul G. Sanders[1], Michael J. Aziz[1] *

[1] Division of Engineering and Applied Sciences, Harvard University, Cambridge MA 02138-2901

ABSTRACT

Laterally homogeneous pulsed melting of thin films is being investigated as a way to eliminate convection and thereby determine diffusivities in refractory melts under terrestrial conditions, providing comparison data for microgravity measurements. The silicon liquid self-diffusivity was determined by pulsed laser melting of $^{30}Si^{+}$ ion implanted silicon-on-insulator thin films. The broadening of nearly Gaussian solute concentration-depth profiles was determined *ex situ* using Secondary Ion Mass Spectrometry. Melt depth versus time and total melt duration were monitored by time-resolved lateral electrical conductance and optical reflectance measurements. One-dimensional diffusion simulations were utilized to match the final $^{30}Si^{+}$ experimental concentration spatial profile given the initial concentration profile and the temporal melt-depth profile. The silicon liquid self-diffusivity at the melting point is $(4.0 \pm 0.5) \times 10^{-4}$ cm^2/s. Calculations of buoyancy and Marangoni convection indicate that convective contamination is unlikely.

I. Introduction

Atomic transport properties of refractory melts such as Si and Ti are important from both a technological and fundamental perspective. We are studying both in the laboratory; here we focus on our results for liquid Si. The ubiquitous use of silicon in the semiconductor industry requires many processing steps, some of which involve liquid phase transport, including Czochralski and float-zone crystal growth, as well as pulsed laser-induced thin film crystallization[1,2]. More accurate knowledge of the liquid diffusivity may therefore help in process modeling and control. From a fundamental standpoint, atomistic simulations of silicon systems are common, but there is a paucity of liquid-phase experimental data, the comparison to which provides a critical test of interaction Hamiltonians and methodology. There are currently many reports of the simulated liquid self diffusivity which are compared only to experimental solute diffusivities due to the absence of an experimental value for the self diffusivity.

Liquid diffusivity is a particularly challenging property to measure accurately. Two potentially serious problems associated with liquid diffusivity measurements are convective contamination and container wall interactions[3]. The elevated melting point (T_m) and high reactivity of Si exacerbate both of these problems. Convective contamination generally occurs when there is a temperature gradient in the liquid, creating instabilities that lead to the formation of convective currents.

The likelihood of convection is increased at high temperatures and extended times. Although it is exceedingly difficult to eliminate completely convective contamination in terrestrial diffusion measurements, these effects are reduced by fine capillaries that make it difficult to establish convection currents. Although container wall interactions have been ruled out in some diffusion experiments with low T_m

* Corresponding author

materials[4], the general concern that fine capillaries can introduce problems with wall interactions is appropriate when working with reactive materials at high temperatures.

Liquid diffusivity measurements made by pulsed laser melting can minimize some of the difficulties in making accurate diffusion measurements. The thin film geometry and short melt duration make it virtually impossible to establish convection currents. The planar geometry permits accurate measurement of the sub-micron diffusion distances resulting from the short melt duration, using techniques such as Rutherford backscattering spectrometry or secondary ion mass spectrometry (SIMS). Because the melted materials are contained by a solid of the same composition, container wall interactions are minimized. Difficulties inherent in this method are the accurate measurement of the melt-depth vs. time profile and the liquid temperature. The agreement between time-resolved reflectivity measurements (TRR), SIMS concentration-depth profiles, and heat-flow simulations can minimize uncertainties in both of these quantities.

Although there have been no reports of self diffusion in liquid Si, there have been measurements of solute diffusivity in silicon and also molecular dynamics simulations of self-diffusion. The chemical similarity of silicon and germanium should lead to comparable magnitudes for silicon liquid self-diffusivity and germanium solute diffusivity in liquid Si. A Ge solute diffusivity of 2.5 x 10^{-4} cm^2/s has been determined in studies of solute partitioning[5] during rapid solidification, in which the solute liquid diffusivity is a fitting parameter in the analysis. Molecular dynamics simulations yield silicon self-diffusivities at T_m in the range of 0.6 - 2.0 x 10^{-4} cm^2/s (Table I). Simulations using the classical Stillinger-Weber potential have found a weakly activated Arrhenius-type temperature dependence of the silicon liquid self-diffusivity[11,12]. This dependence can be equally well described by a linear temperature dependence over the entire simulated temperature range (1600-1900 K).

Table I. Molecular Dynamics Simulations

Method	Si liquid self-diffusivity (10^{-4} cm^2/s)
ab initio pseudopotentials	1.9 (1800 K)[a], 2.3 (1800 K)[b]
Tight-binding	1.1 (1740 K)[c], 1.3 (1780 K)[d], 1.7 (1780 K)[e]
Stillinger-Weber	0.64 (1700 K)[f], 0.65 (1683 K)[g], 0.69 (1691 K)[h]

a. Ref.6 b. Ref. 7 c. Ref. 8 d. Ref. 9
e. Ref. 10 f. Ref. 11 g. Ref. 12 h. Ref 13

II. Experimental

The silicon-on-insulator (SOI) samples were fabricated by sequential low-pressure chemical vapor deposition (LPCVD) of both SiO_2 and Si films onto (001) Si wafers. Ion implantation of $^{30}Si^+$ at 100 keV to a dose of 4 x 10^{16} cm^2 produced a $^{30}Si^+$ peak 6 at% above the natural background of 3.1 at% at a depth of 150 nm. The samples were irradiated by a pulsed $XeCl^+$ excimer laser beam (308 nm, 25 ns FWHM; ~50 ns total duration). The specimens were melted from 1 to 5 times using a nominal fluence of 0.75 J/cm^2, which typically produced a melt duration of 155 ns and a melt depth of 180 nm. The $^{30}Si^+$ depth profiles were determined by SIMS. The $^{30}Si^+$ concentration calibration was made using the ratio of the $^{30}Si^+$:$^{28}Si^+$ ion yield.

III. Data Analysis

The top portion of the silicon film was amorphous after $^{30}Si^+$ ion implantation. The initial low-fluence shot resulted in explosive crystallization[14] mediated by a very short-lived melt, yielding a slight change in

the $^{30}Si^{+}$ concentration upon crystallization (Figure 1). This "crystallized" profile was the initial concentration profile used in all diffusion simulations. One-dimensional heat-flow calculations[15,16] using silicon thermophysical properties[17] were used to simulate the laser melt profiles. During resolidification, the TCM melt profiles agreed well with simulated melt profiles calculated for the same laser fluence. The fluences used in the melt profile calculation were selected by matching the melt durations measured by TRR. The simulated fluence was 0.01 to 0.02 J/cm^2 less than the experimental fluence, most likely resulting from variations in the sample surface reflectivity from the literature value.

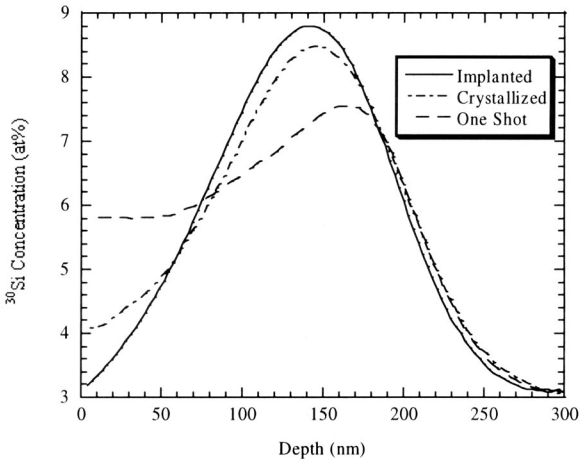

Figure 1. Concentration depth profiles of $^{30}Si^{+}$ from SIMS, showing as implanted profile and the changes after a low fluence shot (0.30 J/cm^2) for crystallization and a higher fluence shot (0.75 J/cm^2) typical of those used for the diffusion calculations. The crystallized profile was used as the initial condition for the diffusion calculations.

The simulated silicon melt depth vs. time profile and initial solute concentration-depth profile (after crystallization) were used in solving the one-dimensional diffusion equation[18] to obtain the final solute concentration profile. For each sample, the simulated fluence was varied from 0.74 to 0.76 J/cm^2 and the diffusivity was varied from 2 x 10^{-4} to 6 x 10^{-4} cm^2/s to minimize chi-squared between the final calculated diffusion profile and the final measured $^{30}Si^{+}$ profile. The slight fluence adjustment was needed to match the melt depths observed in the SIMS profiles. To account for the spatial energy variation of the laser beam, reported diffusion profiles were a Gaussian-weighted average of a suite of diffusion profiles calculated at the best-fit fluence ± 3% (the measured spatial variation of the laser beam).

IV. Results and Discussion

The average and standard error of the four measurements reported in Table II for the silicon liquid self-diffusivity at the melting point are (4.0 ± 0.3) x 10^{-4} cm^2/s. Additional uncertainties in the melt profile calculation and SIMS calibration increase the standard error to (4.0 ± 0.5) x 10^{-4} cm^2/s. In Table II, the average experimental melt duration is the average melt duration per shot determined from reflectivity, whereas the average simulated melt duration is the best-fit melt duration used in the diffusion calculations. An indication of the analysis sensitivity can be obtained from Figure 2, in which the $^{30}Si^{+}$ SIMS profile for the sample shot 2 times is plotted with diffusion simulations at D = 2, 4, and 6 x 10^{-4} cm^2/s. Clearly 4 x 10^{-4} cm^2/s is the best fit of the three.

One very important parameter in reporting the diffusivity is the temperature. Heat-flow simulations were done to determine the average liquid temperature during the course of the experiment. For small temperature ranges, the temperature dependence of the diffusivity is expected to be linear. This view is

Table II. $^{30}Si^{+}$ Liquid Self-Diffusivity Measurements

Number of Shots	Average Melt Duration (Measured) (ns)	Average Melt Duration (Simulated) (ns)	Diffusivity (cm^2/s)
1	168	160	4.3×10^{-4}
2	151	152	3.5×10^{-4}
3	152	156	4.4×10^{-4}
5	162	166	3.7×10^{-4}

supported by Stillinger-Weber calculations of the diffusivity temperature dependence[11,12]. As shown in Figure 3, the average liquid temperature is very near T_m. In fact, the simulations indicate that the time-averaged temperature ranges from T_m+3 K at the surface to T_m+12 K near the full-melt depth. Therefore, the measured diffusivity should correspond to the average melt temperature, which in this case is T_m.

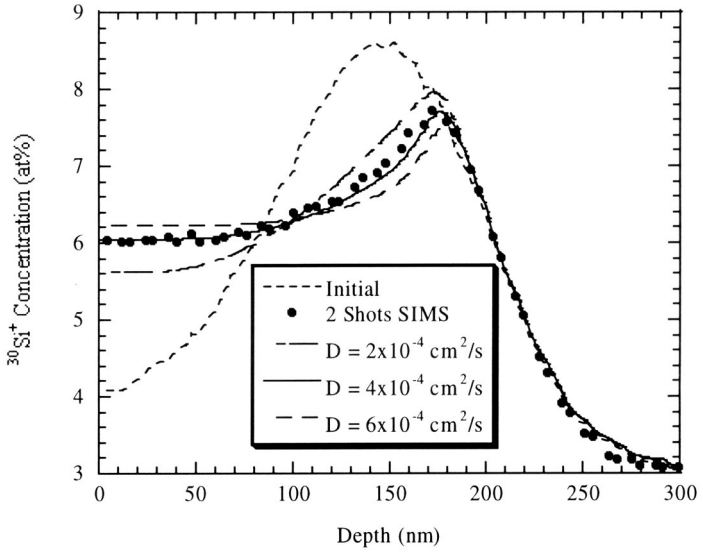

Figure 2. Comparison between experimental SIMS concentration profile and simulated diffusion profiles after 2 laser shots with diffusivities of 2, 4, and 6 x 10^{-4} cm^2/s.

With certain restrictions, it can be shown that the effective liquid diffusivity is equal to the diffusivity at T_m. A flat liquid temperature distribution in z (resulting from, e.g., a virtually infinite liquid thermal conductivity) and a linear melting and freezing velocity response ($v \propto [T - T_m]$ where T is the crystal/melt interface temperature) can be shown to yield a temporal temperature profile at any depth (see Figure 3) for which the integral of the portion of the curve above T_m is equal and opposite to that below T_m. This implies that the average liquid temperature is T_m at all depths. If the temperature dependence of the liquid diffusivity is linear, then the calculated diffusivity is a function of only the average temperature T_m. Any corrections to this model result from deviations from the above assumptions. The assumption most likely to be in error is the lack of a temperature gradient in the liquid during melt-in.

Convective contamination is always a concern in liquid diffusion measurements. Buoyancy-driven convection occurs as a result of temperature gradients within the specimen. Instabilities leading to natural convection[19] can occur if the Rayleigh number $R > 1700$. For the geometry of this experiment, $R = 6 \times 10^{-11}$. Since R has a cubic dependence on the thickness of the liquid layer, the likelihood of buoyancy-driven convection becomes significant only at melt depths > 5 mm, which is much greater than the 180 nm melt depths observed in this work.

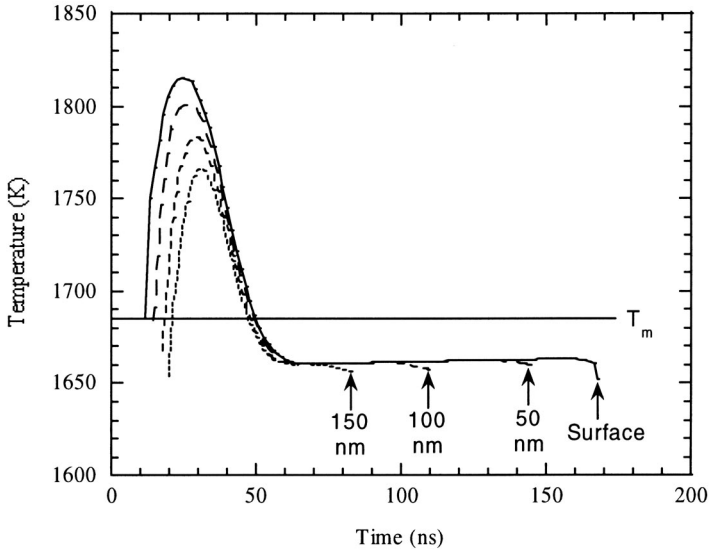

Figure 3. Liquid temperature temporal profiles at various depths determined by heat-flow calculations. The surface (solid line) melts first and freezes last, while material at 150 nm depth (dotted curve) melts later and freezes sooner. When the solidification front passes a given depth, the local temperature suddenly drops from the essentially steady-state liquid and undercooled interface value of 1660 K during solidification (see features at 60 to 170 ns).

Marangoni convection results from the temperature dependence of the surface tension and surface temperature gradients. Calculations of surface tension-driven convection using the Stokes solution to a suddenly accelerated flat plate in an infinite liquid[20] and the surface temperature variations identified in the heat-flow simulations indicate that diffusive transport is 2×10^7 times faster than transport in z due to Marangoni convection. This results primarily from the negligible overheating of the liquid but also from the aspect ratio of the specimen, as the velocity of Marangoni-induced currents in z is reduced from the surface radial velocity by the depth-to-width ratio of the melt. Buoyancy- and surface tension-driven convection currents both tend to flow in the same direction, but the probability of either contributing to mass transport in this experiment is very low.

V. Summary

The silicon liquid self-diffusivity was determined by pulsed laser melting of $^{30}Si^+$ ion implanted silicon-on-insulator thin films. One-dimensional diffusion simulations were utilized to match the final $^{30}Si^+$ experimental concentration profile given the initial concentration profile and the melt profile. The silicon liquid self-diffusivity at the melting point is $(4.0 \pm 0.5) \times 10^{-4}$ cm^2/s. Calculations of Marangoni and buoyancy driven convection indicate that convective contamination is unlikely.

This research was sponsored by NASA grant NAG8-1256. The scientific insights and programming expertise of Michael O. Thompson of Cornell University are gratefully acknowledged. The samples were prepared at the Cornell Nanofabrication Facility with the expert assistance of Michael Skvarla. Ion implantation was performed in the Surface Modification and Characterization Research Center at Oak Ridge National Laboratory. SIMS measurements were made by Thomas Mates in the Materials Department at the University of California at Santa Barbara. Howard Stone and Thomas Powers are acknowledged for valuable discussions on convection.

REFERENCES

1. R. S. Sposili and J. S. Im, Appl. Phys. A 67, 273 (1998).
2. D. Toet, M. O. Thompson, P. M. Smith, and T. W. Sigmon, Appl. Phys. Let. 74, 2170 (1999).
3. T. Iida and R. I. L. Guthrie, *The Physical Properties of Liquid Metals* (Clarendon, Oxford, England, 1993) p. 199.
4. L. B. Jalbert, F. Rosenberger, and R. M. Banish, J. Phys. Condens. Matter 10, 7113 (1998).
5. D. P. Brunco, M. O. Thompson, D. E. Hoglund, M. J. Aziz, and H.-J. Gossmann, J. Appl. Phys. 78, 1575 (1995).
6. J. R. Chelikowsky, N. Troullier, and N. Binggeli, Phys. Rev. B 49, 114 (1994).
7. I. Stich, R. Car, and M. Parrinello, Phys. Rev. B 44, 4262 (1991).
8. R. Virkkunen, K. Laasonen, and R. M. Nieminen, J. Phys. Condens. Matter 3, 7455 (1991).
9. C. Z. Wang, C. T. Chan, and K. M. Ho, Phys. Rev. B 45, 12227 (1992).
10. G. Servalli and L. Colombo, Europhys. Lett. 22, 107 (1993).
11. W. Yu, Z. Q. Wang, and D. Stroud, Phys. Rev. B 54, 13946 (1996).
12. K. Kakimoto, J. Appl. Phys. 77, 4122 (1995).
13. J. Q. Broughton and X. P. Li, Phys. Rev. B 35, 9120 (1987).
14. M. O. Thompson, G. J. Galvin, J. W. Mayer, P. S. Peercy, J. M. Poate, D. C. Jacobson, A. G. Cullis, and N. G. Chew, Phys. Rev. Lett. 52, 2360 (1984).
15. M. O. Thompson, Ph.D. thesis (Cornell University, Ithaca, New York, 1984).
16. P. Baeri and S. U. Campisano, in *Laser Annealing of Semiconductors* (Academic Press, London, 1982) p. 75.
17. M. J. Aziz, C. W. White, J. Narayan, and B. Stritzker, in *Energy Beam-Solid Interactions and Transient Thermal Processing* (Editions de Physique, Paris, 1985), p. 231.
18. Solution of one-dimensional diffusion equation with moving interface by Crank-Nicholson algorithm, M. O. Thompson (1998).
19. P. H. Roberts, "On Non-Linear Bérnard Convection," in *Non-Equilibrium Thermodynamics: Variational Techniques and Stability* (University of Chicago, Chicago, 1966) p. 126.
20. J. P. Longtin, K. Hijikata, and K. Ogawa, Int. J. Heat Mass Trans. 42, 85 (1999).

SELF-DIFFUSION IN LIQUID ELEMENTS

R. Michael Banish[1] *, Lyle B. Jalbert[1] and J. Iwan D. Alexander[2]

[1]Center for Microgravity and Materials Research
University of Alabama in Huntsville
Huntsville, AL 35899
256-890-6050; banishm@email.uah.edu
[2]Department of Mechanical and Aerospace Engineering
Case Western Reserve University
Cleveland, Ohio 44106

The final goal of this research is to establish the liquid-state, self-diffusivity temperature dependence D(T) for selected elements. This requires data sets of sufficient accuracy such that a clear statistical correlation can be drawn between these data and the (existing) theories. At the present time, the scatter in the data sets is too large to make any reliable prediction of the best fit. In order to obtain the most reliable correlations diffusivities will be determined over the majority of the elements' liquid range (up to 1400°C). We will then interpret the measured self-diffusivity data in terms of diffusion mechanisms and associated liquid structures.

With increasing insight into transport and segregation in solidification and crystal growth, reliable data for diffusivities in liquid metals and semiconductors have become essential for guidance in process development. However, at this point even self-diffusion in elemental liquids is not well understood. In particular, there is little insight into the temperature dependence of diffusivities and its correlation to the temperature-dependent liquid structure of an element. Currently, the differences between several theoretical predictions are often less than those between different sets of data for the same system. Hence, for both theoretical and technological developments, there is a clear need for diffusivity measurements of improved accuracy and precision for a large variety of elements over wide temperature ranges.

Diffusivities obtained in liquids at normal gravity are prone to be contaminated by uncontrollable convection. Simple scaling arguments illustrate the difficulty of obtaining purely diffusive transport in liquids. In a system of diffusivity 10^{-5}cm^2/sec and a typical diffusion distance of 1 cm, the characteristic diffusion velocity is of order 10^{-5} cm/s. Hence, if true diffusion is to be observed, convective flow velocities normal to the concentration gradient must be of order 10^{-7} cm/s or less. Thus, in liquids, the attainment of diffusion-dominated transport over macroscopic distances at normal gravity is obviously not a simple task. A typical criterion for claiming that convective contributions are negligible is when the logarithmic plot of concentration versus distance is linear. Our numerical modeling efforts have shown that only for extreme convective contamination (of several hundred percent) do these plots become non-linear [1,2].

* Corresponding author

We have experimentally confirmed these results using horizontally and vertically oriented ampoules. Numerical modeling efforts in our group and others has shown that in liquid metals, with their typical viscosities of 10^{-3} poise, temperature nonuniformities of a few hundredths of a degree are sufficient to generate convective contributions equal to the diffusive flux [1]. Thus, even in systems with essentially no *measurable* temperature nonuniformities, convective fluxes may be the dominant mode of transport. Liquid metal diffusion studies conducted aboard spacecraft have demonstrated the gain in precision afforded by a low-gravity environment [3-7].

Numerical modeling done as part of this project shows that convection, driven by spatial nonuniformities in temperature, as small as 0.01°C across 3mm diameter samples, can lead to measurable differences in diffusivities. Modeling of more realistic temperature nonuniformities of 0.05–0.10 °C across a 3 mm sample at 1000 °C, leads to predicted convective contaminations of 50-100% depending on the liquid's viscosity. This level of convective contamination has been seen even when no measurable temperature differences, to 0.1 °C, were present. In certain instances, buoyancy-driven convection can lead to measured diffusivities that are less than the input value [8]. Since these are self-diffusivity measurements, convective contamination due to species density differences are negligible. However, these analysis also show that conducting self-diffusion experiments in a $10^{-3}g_0$ environment is sufficient for the convective flux to be less than 1% of the diffusive. This indicates that the nominal shuttle or ISS environment is sufficient for conducting a series of benchmark self-diffusion experiments.

Based on the methodology of Codastefano, Di Russo, and Zanza [9], we have developed a technique for the *in situ* measurement of diffusivities in liquids at several temperatures with one sample. In this approach, which circumvents solidification of the diffusion sample prior to concentration profiling, the evolution of the concentration distribution of a radiotracer is followed in real time using two pairs of radiation detectors. As schematically shown in figure 1(a), we use an initially solid cylindrical diffusion sample that consists mostly of inactive material (solvent) and a short section of activated isotope, as the diffusant, located at one end. After melting of the sample and heating to a uniform measurement temperature T, the evolution of the diffusant concentration is monitored through the intensity of the radiation received through two collimators in a radiation shield. We have shown that these intensities n_1 and n_2 are proportional to the concentration C_1 and C_2, respectively [10]. The characteristic shape of the signal traces $n_1(t)$ and $n_2(t)$ associated with the spreading of the diffusant is plotted in Figure 1(b). The radiation collimation bores must be positioned at

$$z_1 = L/6,\ z_2 = 5L/6 \tag{1}$$

to satisfy the requirements of the algorithm used to evaluate the diffusivity. Here L is the sample length at the measurement temperature. The diffusivity D is then calculated from the difference of the signal traces using the relation

$$\ln[n_1(t)-n_2(t)] = A - \frac{D}{L^2}\pi^2 \cdot t \tag{2}$$

where A is a constant that depends on the concentration profile $C_0(z)$ at the beginning of the measurement. Since the $C_0(z)$ does not explicitly enter the D-evaluation, diffusivities can be consecutively determined at several temperatures during the spreading of the concentration profile in the same sample. This approach is robust because essentially any starting concentration profile is acceptable. Obviously, before the first measurement, $C_0(z)$ must have spread enough to provide a significant signal at both

detector locations. Equation (2) is based on the specific location requirement for the detectors given by equation (1) with respect to the sample length L. To use this measurement technique at several temperatures with a single sample (i.e., beyond the original setup given in [9]), an additional pair of collimation bores and detectors are required to account for the changes in L versus temperature. These additional bores/detectors are positioned such that, taking into account the thermal expansion of the sample, radiation shield and support structure, one pair satisfies equation (1) at the lowest temperature and the other pair at the highest. As a consequence, for all intermediate temperatures, there is always a collimation bore above and below the exact position required. Thus, we are able to determine the (self)-diffusivity of molten metals at three or four temperatures using a single sample. These results have been reported in a previous paper [11].

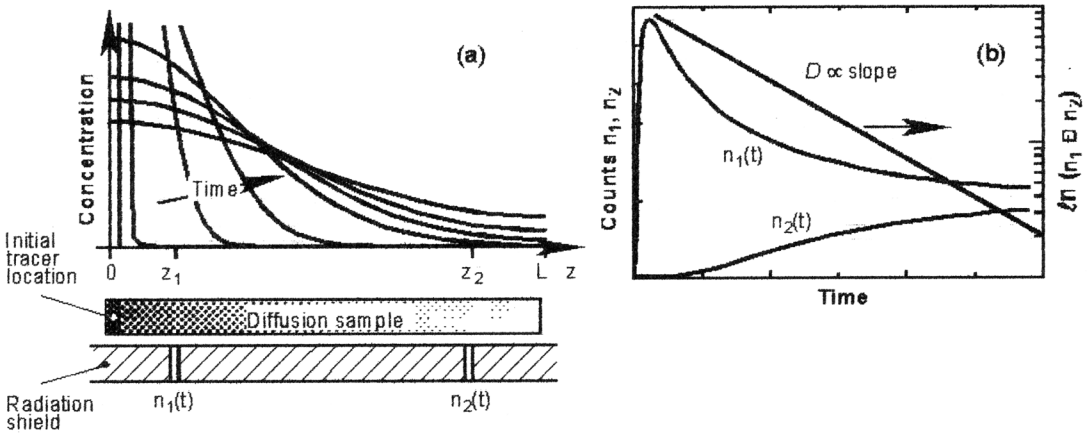

Figure 1. (a) Schematic presentation of the evolution of the concentration profile and location of the measurement positions. (b) Time traces of the signals at the two measurement locations, and corresponding presentation of the signal difference according to equation (2).

The self-diffusivity has been measured, for selected elements, both on the ground and in a low-temperature experiment performed on the Mir space station (indium only). While the diffusivities obtained at low-gravity were within the uncertainty range of our ground results, the results for the three runs are within 0.5 % of each other. This narrowing of the data range is consistent with other investigators' results, and shows the gain in precision afforded by a low-gravity environment.

The Self-Diffusion in Liquid Elements project has passed its Science Concept Review (SCR). The next review for this project is the Requirements Definition Review (RDR). Therefore, at present the ongoing activities are related to both continuing research activities and hardware design and prototype construction. These continuing research activities are:

- refinement of the choice of elements for investigation.
- optimization of measurement temperatures via statistical analysis
- numerical analysis and experimental confirmation of the effect of barriers and voids causing transport restrictions on diffusion measurements
- investigation into the use of magnetic fields to suppress convective contamination of diffusion measurements.
- numerical analysis of convective contaminations due to non-isothermal voids/bubbles.

The elements were selected for this investigation based on their "expected" D(T) behavior. Neutron, and x-ray, diffraction studies of molten elements have shown that changes, or shifts, in the liquid structure occur for many elements. Elements which show a (significantly) changing liquid structure are expected to have different temperature dependencies of their diffusivity between these regions. How "significantly" a liquid's structure

must change for a measurable difference in its diffusivity to occur is unknown. However, for elements where very little structural change is seen a single temperature dependence is expected. We have selected elements where both behaviors are predicted. The initial elements selected were aluminum, rubidium, gallium, cadmium, indium, tin, tellurium, and selenium. All of the elements selected are x-ray (gamma) photon emitters, with photon energies well within the capability of our solid-state detectors. Due to difficulties with sample cost or availability we have dropped aluminum and gallium from consideration. In their place we have added antimony, zinc, and ytterbium. The neutron diffraction data for antimony and zinc indicate changes in structure over the liquid range. There is very little diffusion data for the lanthanides.

Typically, correlating between available data and theoretical predictions are done by a curve-fitting algorithm. For some data sets a relatively high regression coefficient was obtained (>0.90). However, a more rigorous statistical approach is to calculate the "lack-of-fit" of the various theoretical predictions to the data. Using this approach, the presently available complete data sets give very poor correlation to the various theories. Optimum use of a lack-of-fit analysis for correlation to a particular model depends on a unique choice of the temperatures where the diffusivities are measured. This spacing is unique for each model prediction. Interestingly, this type of statistical analysis shows that the traditionally used equally spaced measurement locations are not the optimum for any of the theoretical predications. This statistical analysis indicates that 5 or 6 measurement temperatures are necessary for our final analysis. In order to minimize the (low-gravity) experiment time we have picked measurement locations based on two models. These temperatures were then averaged giving six values that were statistically valid for either model. In doing this, we found that these points were also valid for several other models.

If oxide layers or bubbles are present in a diffusion sample during melting, it is expected that under terrestrial conditions, they would rise to the top or the outside walls of a vertically oriented sample. Thus, a potential barrier to diffusion would be displaced to the upper end of the ampoule, where at worst it could only affect the sample length. For post-mortem techniques, such as the long capillary method, any convection induced by this displacement will lead to stirring of the sample and cause erroneous diffusivity values. However, for the real-time technique used here, this convection would be damped in a few minutes (scaling with the viscosity), and only in a highly stirred situation would the experiment be seriously compromised. Note that, given that sample temperature gradients are unavoidable, the diffusion measurements will for many liquids still be affected by buoyant convection. The potential that barriers to diffusion such as voids or oxide layers might form is, nevertheless, still present in a low-gravity environment. In fact, in a low-gravity environment, these barriers may not be displaced during the course of an experiment. Thus, the possibility that diffusive transport might be retarded or even prevented by such barriers is a concern and motivated us to analyze the consequences of partial blockages of the ampoule.

We have numerically examined, in 2-D, to what extent such deviations from 1-D transport, whether real or conceived, influence the evolution of the concentration distribution in a diffusion sample. We then evaluated the resulting non-ideal distributions in terms of apparent diffusivities D_a utilizing both the semi-infinite sample methodology and the method of Codastefano, *et al.,* used for our determinations [12]. In the semi-infinite technique the diffusion sample is assumed to be infinite in one direction, i.e., with a diffusion path of length L, the initial thickness h of the diffusant source (with uniform concentration C_0) must fulfill the condition h<<L. This condition results in the concentration profile at time *t*

$$C(z,t) = \frac{C_0}{\sqrt{\pi\, Dt}} \exp\left(\frac{-z^2}{4Dt} \right). \qquad (3)$$

Thus, a plot of ln*C* versus z^2 produces a straight line with the slope given by -1/(4*Dt*).

In the Codastefano technique, as discussed above, one monitors the solute concentrations *versus* time at the positions z = L/6 and 5L/6. The resulting time traces $C_1(t)$ and $C_2(t)$, respectively, are related to the diffusivity through a straight-line fit in the form of equation (2).

In accordance with our experiment approach, we chose a total sample length L = 30 mm, sample width w = 3 mm, and initial diffusant layer thickness h = 1 mm. Two different sets of conditions resulting in deviations from 1-D diffusive transport were assumed. (a) A planar barrier in the source-solvent interface, was extended from one wall to either y = 0.5, 0.75 or 0.95 w, plus additional cases of a 95% blockage with the connected region centered about y = 0.5 and a "pepper pot" arrangement with the repeating pattern: 0.5626 mm blocked, 0.25 mm connected, across the 3 mm cell. (b) A 1 mm square barrier on one wall, to simulate a void, was centered at x = 3 or x = 7 mm. Note that these particular positions straddle the Codastefano measurement coordinate L/6 at x = 5 mm. A y- dependent diffusivity case was also investigated, but it does not influence the results given here. We used D_0 = 10.22 x 10^{-5} cm^2/s in all simulations, which corresponds to the self-diffusivity of indium at 900 °C [23].

The numerical simulations were performed with Adaptive Research's CFD 2000 finite volume code, version 3.03. In the void and barrier cases a nonuniform grid of 62 x 30 and 61 x 40, respectively, was used. Doubling of the grid number in x- and y-direction in both the y = 3 mm void and 75% barrier cases (the cases with largest concentration gradients) resulted in insignificant changes in the concentration field. All cases were run for 10,000 seconds to obtain sufficient diffusant concentrations at the 5*L*/6 position. For comparison with pure 1-D diffusion an unobstructed, uniform-diffusivity run was performed with each grid. Diffusivities are typically deduced from the total amount of diffusant contained in cross-sectional slices of the sample. Evaluations using the semi-infinite sample methodology were based on the $C(x,t)$-profile obtained at t = 2,000 s, at which time the solute barely reaches L. The Codastefano methodology was applied to the C(L/6,t) and C(5L/6,t) traces obtained, depending on the case, between 3,000-5,000, and 10,000 s with samples taken every 10 s.

These results showed that only under ***extreme*** conditions, *i.e.*, blockages exceeding 90% and voids exceeding 40%, were measurable changes seen in the diffusivity. Even in the case of a 95% barrier, where there is strong retention of the solute behind the barrier the "error" is only 7% of the input diffusivity. However, the semi-infinite method was somewhat more sensitive than the Codastefano method. However, even in this post-mortem methodology the deviation is not that great until the barriers approach 75%. It is important to note that the effect of the barrier on the apparent diffusivity is greatly reduced once the connected region is shifted away from the wall. Thus, by using the Codastefano methodology, given any *reasonable* blockage, the measured apparent diffusivity can be assumed to be representative of only diffusive and convective contributions.

To verify the predictions of our models we conducted two experiments. Figure 2 (center) shows a cross-section of the normal diffusion sample in its ampoule and outer silica glass container typically used for the mass diffusion determination. The diffusion sample consists of two parts; a short radiotracer section (about 1 mm long) and a long benign, native abundance section (about 29 mm long). The benign section is vacuum cast in a 3 mm i.d. precision bored BN ampoule. The bottom of the ampoule is closed off using a press-fit BN plug to ensure a right circular geometry. The precast and activated ^{114m}In radiotracer section is then placed in the ampoule, and a close-fitting BN plunger is added. This plunger is held against the sample top using a low-force graphite spring, which ensures a right circular geometry. This assembly is then sealed in a silica glass cartridge (0.375" o.d.). Two separate modifica-

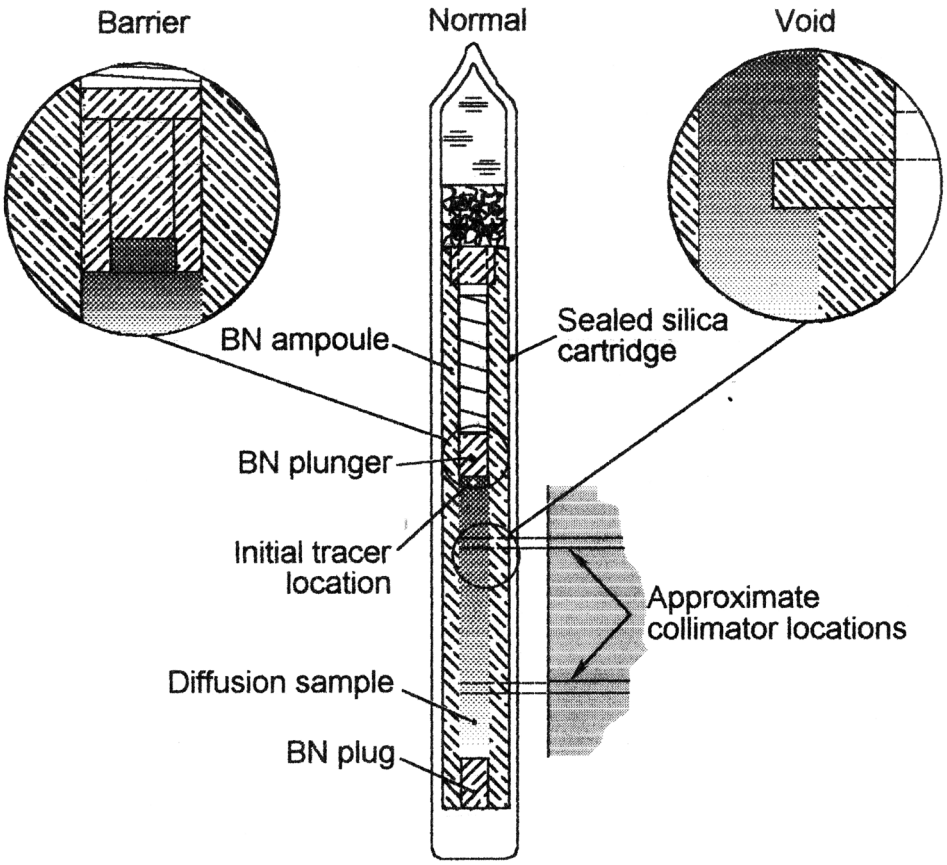

Figure 2. Diffusion sample ampoule configurations for investigating the effects of barriers and voids on the resultant diffusivity. The center cross-section shows the normal configuration. To the left and right is schematically shown the ampoule modifications used to induce a barrier (left view) or a void (right view).

tions were made to the normal configuration to induce either a barrier or void. These are also shown in Figure 2. In the first one the solute (radiotracer) area was reduced by using a 2 mm diameter source pellet (contained in a 3×2 mm diameter sleeve) diffusing into a 3 mm diameter nonradioactive host section. This modeled an effective contact area of 0.1/0.225. In the second experiment a 1 mm diameter by 1 mm long plug was inserted into the sample approximately 7 mm from the top of the sample. Thus, the cross-sectional area of the void was about 15% of the sample cross-section. Note that this plug was positioned just after the first (L/6) measurement location. Thus, it would be expected that any effect that occurs should be detected (*i.e.*, material should build up behind this location). Self-diffusion experiments conducted in modified ampoules confirmed our simulations. This ***implies*** that any measurable nonuniformity in the concentration field is not due to a disruption of the diffusion path and that the measurement methodology we employ is surprisingly insensitive to deviations from the one-dimensional transport geometry.

Magnetic fields have been widely used for suppressing convection in conducting liquids. However, the magnetic field only dampens the already present fluid motion. Thus, the field strength magnitudes necessary to suppress flows at the 10^{-6} to 10^{-7} cm/sec level are questionable. We have numerically modeled the convective damping effects at field strengths up to 3 Tesla. Only with (unrealistic) temperature nonuniformities of 0.01K were the convective flows reduced significantly below the diffusive speed. Experiments by Youdelis [13] showed that the field strengths

necessary to reduce the convective contribution to a few percent of the diffusive flux (approximately 1 T) have been shown to modify the diffusive flux itself, even in the solid state. More recent experiments by Lehmann [14] showed that at field strengths of around 1 Tesla the apparent diffusivity values no longer change. However, it is neither clear if the convective motion is totally damped nor if there is any effect on the diffusive motion itself. At this point it would be exceedingly helpful to have both sufficient low-gravity and magnetically damped terrestrial values for comparison. Thus, we have started high-fidelity numerical modeling of the effect of a magnetic field in a convectively-driven system. In addition, we are doing experiments in the superconducting magnets at Marshall Space Flight Center.

REFERENCES

1. J.I.D. Alexander, J.-F. Ramus and F. Rosenberger, Microgravity Sci. Tech. 9, 158 (1996).
2. Persson, Eriksson and Lindstrom, Convection and Other Disturbing Effects in Diffusion Experiments in Liquid Metals, *J. Physique* 41, C8-374 (1980)
3. Ukanwa, A.D., *Proceeding. III. Space Processing Sympos. Skylab Results*, Marshall Spaceflight Center, Huntsville, AL, USA, 427 (1979).
4. Reed, R.E., W. Uelhoff, and H.L. Adair, Surface-Tension-Induced Convection, NASA SP-412, Apollo-Soyuz Test Project: Summary Science Report 1, 367 (1977).
5. Smith, R. W. and Zhu, X., Diffusion in Liquid Pb-Au Binary System, *Materials Science Forum*, 215-216, 113 (1996).
6. Frohberg, G., Diffusion and Atomic Transport and Thermophysical Properties, in *Materials Science in Space*, ed. by B. Feuerbacher, H. Hamacher and R.J. Raumann (Springer, Berlin 1986), p. 93 and 425.
7. Frohberg, G., K.H. Kraatz, and H. Wever, Selfdiffusion of Sn112 and Sn124 in liquid Sn, in *Proceeding of the 5th European Symposium on Materials Science under Microgravity*, Schloss Elmau, 201 (ESA 1984).
8. J. P. Kizito, J.I.D. Alexander and R.M. Banish, submitted to J. Thermophysics.
9. P. Codastefano, A. Di Russo and V. Zanza, Rev. Sci. Instrum. 48, 1650 (1977).
10. G.A. Emslie and R.M. Banish, *accepted for* Applied Radiation and Isotopes 4 (2000).
11. L.B. Jalbert, R.M. Banish, F. Rosenberger, Phys. Rev. E 57, 1727 (1998).
12. L.B. Jalbert, F. Rosenberger and R.M. Banish, J. Phys. Condens. Matter 10, 7113 (1998).
13. Youdelis W.V., D.R. Colton and J. Cahoon, On the Theory of Alloy Solidification in a Magnetic Field, *Can. J. Physics* 42, 2238 (1964) and On the Theory of Diffusion in a Magnetic Field, *Can. J. Physics* 42, 2217 (1964)
14. T. Alboussiere, J.P. Garandet, P. Lehmann and R. Moreau, in Transfer Phenomena in Magnetohydrodynamic and Electroconducting Flows, (Kluwer Academic, Netherlands, 1999), pp 359-372.

THERMOPHYSICAL PROPERTY MEASUREMENTS of Te-BASED II-VI SEMICONDUCTOR COMPOUNDS

R. Michael Banish[1]*, Timotheee Pourpoint[2], and J. Iwan D. Alexander[3]

[1]Center for Microgravity and Materials Research
[2]Department of Mechanical Engineering
University of Alabama in Huntsville
Huntsville, AL 35899
256-890-6050; banishm@email.uah.edu
[3]Department of Mechanical and Aerospace Engineering
Case Western Reserve University
Cleveland, Ohio 44106

The goal of this research project is to measure the thermal and mass diffusivities of the pure binary tellurium based II-VI semiconductors, i.e., CdTe, ZnTe and, HgTe, and various alloys. For the mass diffusivity determinations, in addition, the diffusivity of various, electrically active impurities, will be determined. Finally, the melting point expansion of these compounds will be determined.

Buoyancy-driven convective effects often contaminate the experimental determination of transport properties such as diffusivities and conductivities. The accurate determination of transport properties requires that convective flow velocities be eliminated or significantly suppressed to a few percent of the characteristic velocity. This is generally not possible under terrestrial conditions. Solutally-driven convective contributions can be sustained by much smaller (relatively) gradients than is necessary for thermal nonuniformities only (for a discussion of this see [1] and references therein). While it can be argued that mass diffusivity measurement techniques such as nuclear magnetic resonance and inelastic neutron scattering, that probe rapid molecular motion, are insensitive to convective contributions, they are not as precise as macroscopic, averaging techniques. However, all macroscopic measurement techniques yield diffusivity data prone to be contaminated by gravity-driven convection. The use of narrow capillaries to suppress convective transport has suggested poorly understood wall effects. Magnetic fields, widely used for suppressing convection in conducting liquids, may modify the diffusive motion itself [2]. Earlier liquid (metal) diffusion studies conducted on spacecraft have demonstrated the gain in precision resulting from the drastic reduction of convection in a low-gravity environment [3-7]. However, by comparison with ground-based experiments, the most recently reported low-gravity data using a shear-cell technique appear rather inaccurate.

Thermal diffusivity measurements in melts are also prone to be contaminated by convective contributions. The use of small measuring volumes increases the likelihood that asymmetries and imperfections in the measurement apparatus itself leading to errors. The use of larger cell volumes on the other hand is prone to result in convective contamination. These problems can be especially

* Corresponding author

troublesome with II-VI semiconductors, since their thermal conductivity is smaller than that of typical container materials. Levitated drop techniques offer little relief of this problem due to the high vapor pressure of II-VI compounds. Modeling of these convective contributions is at best problematic since the assumptions for estimating or modeling these contributions depends on ground-based data already influenced by convection. Again, earlier liquid thermal conductivity/diffusivity studies conducted on spacecraft have demonstrated the gain in precision, and lower absolute values, resulting from the drastic reduction of convection in low-gravity environments [8]. Hence, there is also a need for well-defined thermal diffusivity studies under low gravity.

Our group has developed a novel molten-metal diffusivity measurement approach [8, also see paper T10]. This approach is particularly suited to the limited availability of experiment time on space flights. Diffusivities are deduced *in-situ* and in real-time from consecutive concentration profiles obtained from radioisotope emission using a multiple detector arrangement, based on the methodology of Codastefano, Di Russo, and Zanza [10]. In this approach, which circumvents solidification of the diffusion sample prior to concentration profiling, the evolution of the concentration distribution of a radiotracer is followed in real time using two pairs of radiation detectors. We use an initially solid cylindrical diffusion sample that consists mostly of inactive material (solvent) and a short section of activated isotope, as the diffusant, located at one end. After melting of the sample and heating to a uniform measurement temperature T, the evolution of the diffusant concentration is monitored through the intensity of the radiation received through two collimators in a radiation shield. We have shown that these intensities n_1 and n_2 are proportional to the concentration C_1 and C_2, respectively [10]. The radiation collimation bores must be positioned at

$$z_1 = L/6,\ z_2 = 5L/6 \tag{1}$$

to satisfy the requirements of the algorithm used to evaluate the diffusivity. Here L is the sample length at the measurement temperature. The diffusivity D is then calculated from the difference of the signal traces using the relation

$$\ln[n_1(t)-n_2(t)] = A - \frac{D}{L^2}\pi^2 \cdot t \tag{2}$$

where A is a constant that depends on the concentration profile $C_0(z)$ at the beginning of the measurement. Since the $C_0(z)$ does not explicitly enter the D-evaluation, diffusivities can be consecutively determined at several temperatures during the spreading of the concentration profile in the same sample. This approach is robust because essentially any starting concentration profile is acceptable. Obviously, before the first measurement, $C_0(z)$ must have spread enough to provide a significant signal at both detector locations. Equation (2) is based on the specific location requirement for the detectors given by equation. (1) with respect to the sample length L. To use this measurement technique at several temperatures with a single sample (i.e., beyond the original setup given in [10]), an additional pair of collimation bores and detectors are required to account for the changes in L versus temperature. These additional bores/detectors are positioned such that, taking into account the thermal expansion of the sample, radiation shield and support structure, one pair satisfies equation (1) at the lowest temperature and the other pair at the highest. As a consequence, for all intermediate temperatures, there is always a collimation bore above and below the exact position required. Thus, we are able to determine the (self)-diffusivity of molten metals at three or four temperatures using a single sample. These results have been reported in a previous paper [11].

The experimental measurement methodology we employ is surprisingly insensitive to deviations from the one-dimensional transport geometry. We have numerically [12] and analytically modeled a range of fixed and rigid blockages and voids along the transport path. The results of this modeling are that, using the above real-time methodology, that blockages of up to 90% along the transport and voids representing one-third of the cross-section have little effect on the resulting diffusivity determination. Experiments conducted in modified ampoules confirmed our simulations.

Following the idea from the algorithm for real-time mass diffusivity measurements in long, thin, cylinders we have developed a similar algorithm for the measurement of (thermal) diffusivities using a flat disk geometry. With the low thermal diffusivities of the II-VI semiconductors the ampoule wall would provide for too great of a thermal "short circuit" in a long thin cylinder geometry for accurate determinations. Therefore, we finally chose a flat disk geometry for these measurements. For our analysis we started with an infinitely long, ideally insulated, cylinder of radius a with an initial temperature distribution T(r), at t = 0;

$$T = T_0 \text{ for } 0 < r < p \bullet a \text{ and } T = 0 \text{ for } p \bullet a < r < a \tag{3}$$

where $0 < p < 1$. The evolution of the temperature versus time at a defined r is given by the expression [13]

$$T(r,t) = \frac{2}{a^2}\left\{ \int_0^a r \times f(r)dr + \sum_{n=1}^{\infty} \exp[-\kappa\alpha_n^2 t] \frac{J_0(r\alpha_n)}{J_0^2(a\alpha_n)} \int_0^a r \times f(r) J_0(\alpha_n r)dr \right\} \tag{4}$$

using a series of, geometry independent, identities and simplifications equation (4) is reduced to

$$T(r,t) = T_0 p^2 + T_0 \sum_{n=1}^{\infty} \exp\left[\frac{-\kappa\mu_n^2 t}{a^2}\right] \frac{2p}{\mu_n} \frac{J_0(r\mu_n/a)}{J_0^2(\mu_n)} J_1(\mu_n p) \tag{5}$$

where κ is the thermal diffusivity, and μ_n are the roots of the Bessel function of the first kind of order 1 (J_1). Setting p, the ratio of the heated to unheated areas, equal to μ_1/μ_2 we obtain

$$J_1(\mu_2 p) = J_1(\mu_1) = 0 \tag{6}$$

with p = 0.54. Thus, the n = 2 term of the series is set to zero. The n = 3 terms can be set to zero by choosing the temperature measurement locations r_i to be the nodes of $J_0(\mu_3 r_i/a)$. The three required values of the r_i/a's are 0.236, 0.543, and 0.851. Figure (1) shows the relation of the heated to unheated areas and the measurement locations. Note that the second measurement location is essentially at the border between the heated and unheated areas. As will be discussed below, this requirement can be relaxed considerably. Figure (2) shows the temperature time traces at the three measurement locations indicated above.

From these reductions we are left with a constant term, the n = 1 term, and higher order terms ($n \geq 4$). We now take the difference between two measurement locations, for example r_1 and r_3 to obtain

$$T(r_1,t) - T(r_3,t) = T_0 \frac{2q}{\mu_1} \frac{J_1(\mu_1 p)}{J_0^2(\mu_1)} \left(J_0\left(\frac{\mu_1 r_1}{a}\right) - J_0\left(\frac{\mu_1 r_3}{a}\right)\right) \exp\left[\frac{-\kappa\mu_1^2 t}{a^2}\right] + \Delta\,(h.o.t.(n \geq 4)) \tag{7}$$

It can be shown that the difference between the higher order term in equation. (7) are less than 1% of the n = 1 term for $\kappa t/a^2 > 0.015$, which is less than a second for our specific geometry. Neglecting these higher order terms equation (7) can then be linearized

$$\ln[T(r_1,t) - T(r_3,t)] = \ln\left[T_0 \frac{2p}{\mu_1} \frac{J_1(\mu_1 p)}{J_0^2(\mu_1)} \left(J_0\left(\mu_1 \frac{r_1}{a}\right) - J_0\left(\mu_1 \frac{r3}{a}\right)\right)\right] + \left(\frac{-\kappa\mu_1^2 t}{a^2}\right) \tag{8}$$

This then yields an expression of the form for each pair of measurement locations

$$\ln[\Delta T_{ij}] = \ln(\beta) - \left(\frac{t\mu_1^2}{a^2}\right)\kappa \tag{9}$$

where β is a constant that contains all the initial condition parameters including the initial applied temperature. Three values of the thermal diffusivity are obtained from the slopes of *ln*[ΔT] as a function of time.

Using this methodology we have numerically simulated the effects of: measurement noise, variations in the relative size of the heated region, p, for both larger and small p's, (p's as small as 0.2 have been investigated) and errors or changes in the three measurement locations. We have found that the final formulation is surprisingly robust against these modifications. When the most drastic modifications are used it takes longer for the *ln*[ΔT's] versus time to become linear. However, the time frames necessary are still practical.

We have tested this methodology measuring the thermal diffusivity of solid fine-grained graphite and boron nitride. The disks were 5 cm diameter and 0.7 cm thick. For these experiments the initial temperature profile was established by using a resistance heater compressed to one side of the sample disk. Both the correct and undersized heaters were used. Fine sheathed thermocouples were inserted into the sample at the required positions. The experiments were conducted in a vacuum chamber to minimize convective heat losses. The experimental set-up is schematically shown in Figure (3). The results for fine-grained graphite were within 10% of reported values. However, for boron nitride our results are about 40% of those reported. The experimental set-up that we employed for the graphite and boron nitride determinations does not match the starting case geometry. The starting case assumes an infinitely long cylinder heated internally. However, by choosing the disk to be relatively thin the time for heat to be conducted from one side to the other is small compared to when a temperature increase is measured at the far thermocouple. We have designed and constructed a cell for thermal diffusivity determinations in liquids. Using the undersized heater, this condition is fulfilled earlier, in fact before any increase is seen at even the innermost measurement location. We will take advantage of using a reduced heated area by being able to resistively heat the molten semiconductors through much smaller areas than originally thought.

Acknowledgments

Robert Sekerka of Carnegie Mellon University initially derived the thermal diffusivity solution. Francis Wessling of the University of Alabama in Huntsville has directed many discussions of this method and heat transfer.

REFERENCES

1. F. Rosenberger, *Fundamentals of Crystal Growth I*, Springer-Verlag, Berlin (1981).
2. Youdelis W.V., D.R. Colton and J. Cahoon, On the Theory of Alloy Solidification in a Magnetic Field, *Can. J. Physics* 42, 2238 (1964) and On the Theory of Diffusion in a Magnetic Field, *Can. J. Physics* 42, 2217 (1964)
3. Ukanwa, A.D., *Proceeding. III. Space Processing Sympos. Skylab Results*, Marshall Spaceflight Center, Huntsville, AL, USA, 427 (1979).
4. Reed, R.E., W. Uelhoff, and H.L. Adair, Surface-Tension-Induced Convection, NASA SP-412, Apollo-Soyuz Test Project: Summary Science Report 1, 367 (1977).

5. Smith, R. W. and Zhu, X., Diffusion in Liquid Pb-Au Binary System, *Materials Science Forum*, 215-216, 113 (1996).
6. Frohberg, G., Diffusion and Atomic Transport and Thermophysical Properties, in *Materials Science in Space*, ed. by B. Feuerbacher, H. Hamacher and R.J. Raumann (Springer, Berlin 1986), p. 93 and 425.
7. Frohberg, G., K.H. Kraatz, and H. Wever, Selfdiffusion of Sn112 and Sn124 in liquid Sn, in *Proceeding of the 5th European Symposium on Materials Science under Microgravity*, Schloss Elmau, 201 (ESA 1984).
8. S. Nakamura, T. Hibiya, F. Yamamoto, and T. Yokota, Int. J. of Thermophysics, 12, 783 (1991).
9. L.B. Jalbert, R.M. Banish, F. Rosenberger, Phys. Rev. E 57, 1727 (1998).
10. P. Codastefano, A. Di Russo and V. Zanza, Rev. Sci. Instrum. 48, 1650 (1977).
11. G.A. Emslie and R.M. Banish, *accepted for* Applied Radiation and Isotopes 4 (2000).
12. L.B. Jalbert, F. Rosenberger and R.M. Banish, J. Phys. Condens. Matter 10, 7113 (1998).
13. H.S. Carslaw and J.C. Jaeger, *Conduction of Heat in Solids*, Oxford University Press, New York (1959).

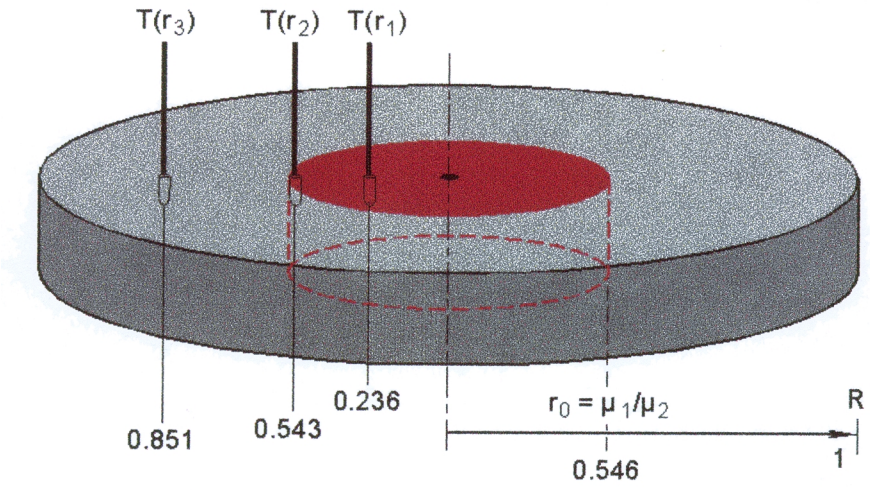

Figure 1. Isometric schematic of the heated/unheated region radii and measurement locations relative to a disk of 1 unit radius.

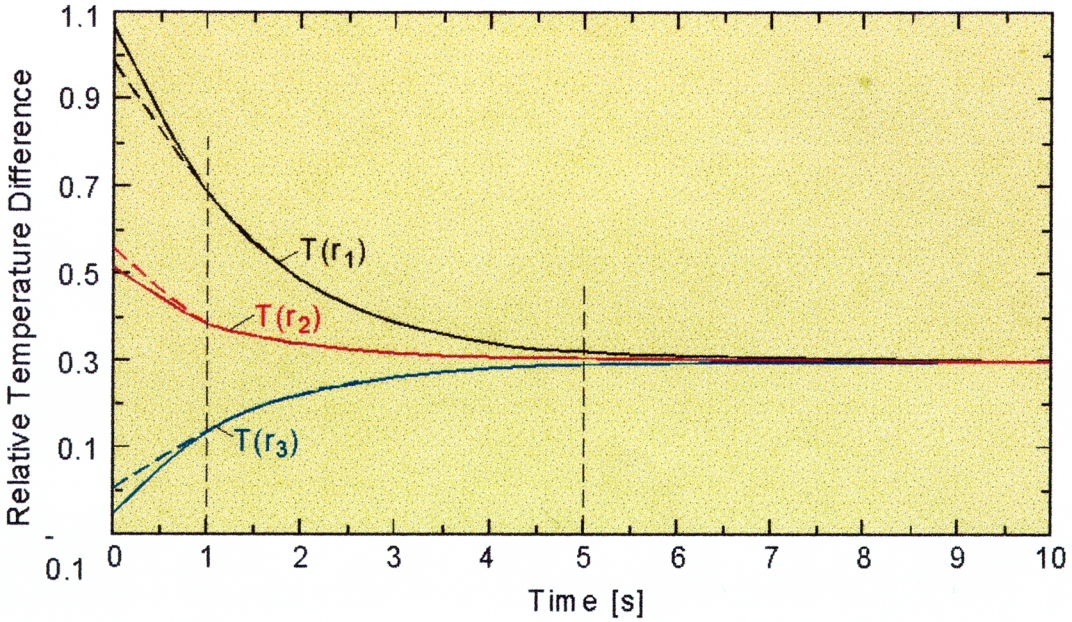

Figure 2. Temperature time-traces at the three "correct" locations. The dashed line at 1 second indicates where the temperatures coincide using the reduced and complete equations.

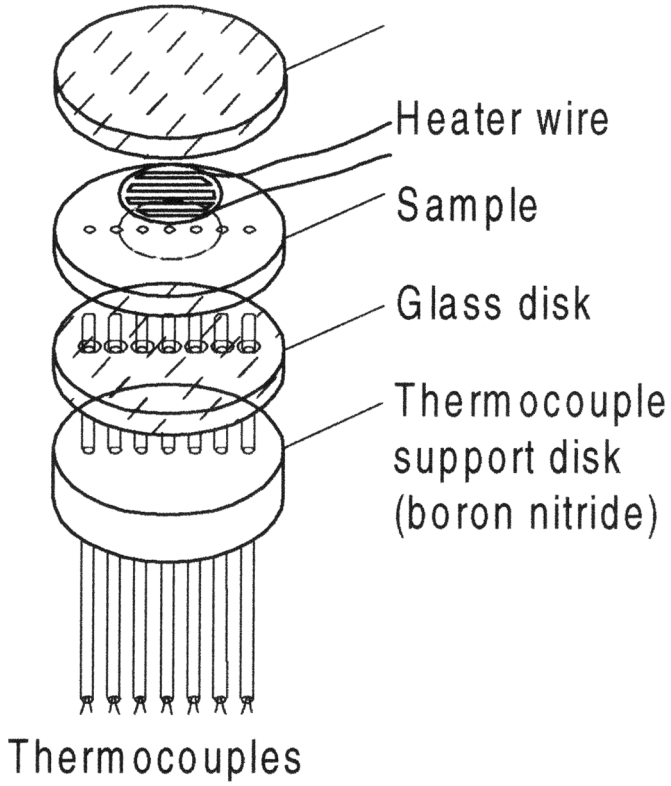

Figure 3. Schematic of experimental setup for thermal diffusivity determinations.

INVESTIGATION OF THE RELATIONSHIP BETWEEN UNDERCOOLING AND SOLIDIFICATION VELOCITY

A.A. Altgilbers, W.H. Hofmeister, and R.J. Bayuzick

Materials Science and Engineering, Vanderbilt University

INTRODUCTION

In the past few decades, several investigators have focused their efforts to correctly predict the solidification velocity as a function of undercooling for many materials. Though significant progress has been made in this area of research, there have been difficulties in unifying theoretical models with the ever-increasing volume of measured solidification velocity data.

The theory for relating the solidification velocity to undercooling developed by Boettinger, Coriel, and Trivedi[1] (the BCT theory) has been the most successful and most widely accepted theory to date. The BCT theory is based on the early work of Ivantsov[2], who approximated the growth of a single dendrite as a paraboloid of revolution. Despite the many successes of the BCT theory, the model appears to breakdown at large undercoolings.

The focus of this work is to further expand the understanding of the solidification process by measuring the solidification velocity as a function of undercooling in dilute alloys, and then using this data along with microstructural analysis to further develop the models for solidification kinetics. In order to characterize the parameters that influence the solidification process, several metallic systems are being investigated. The selected alloy systems include those systems that have a wide range of partition coefficients and differing liquid diffusion coefficients. By bracketing these parameters it is hoped that further understanding of the solidification process in alloys will be attained. The alloy systems that have been selected for this study are: Ni-Ti, Ni-Si, Ni-Sn, Ti-Ni, and Ti-Al. In addition, measurements in the Ti-Al intermetallic system, containing small additions of vanadium and niobium are of interest.

The solidification velocity is measured using a 1 MHz thermal imaging system (HSDA 96)[3] to track the solid/liquid interface as it proceeds across an electro-magnetically levitated drop. Simultaneously, the undercooling temperature is recorded using an optical pyrometer. This technique and the subsequent data analysis have been well established at Vanderbilt University. Microstructural analysis of the processed droplets is an important part of understanding the mechanisms involved in the solidification process. Optical microscopy and SEM imaging is used to characterize the dendritic growth, while microprobe analysis is employed to characterize the solute distribution after solidification.

I. Background

The BCT theory, which is commonly used to predict the solidification velocity of undercooled metals and alloys, does not correlate with the true functional dependence, particularly at high undercoolings.

The theory for solidification velocity is developed based on the development of the thermal and solutal diffusion fields that exist at a dendrite tip. The theory assumes that at low undercoolings, the effects of solute diffusion dominate the solidification velocity. At high undercoolings, the solidification velocity is predicted to be thermally controlled. The only limit placed on the magnitude of the solidification velocity is the collision limit, which states that the maximum velocity is the velocity of sound in the liquid.

Though there is disagreement between the experimental data sets for pure nickel of most of the investigators[4-11] (Figure 1), it is apparent that there is a divergence in experimental results for the solidification velocity from the BCT prediction at higher undercoolings, for nearly all of the results. The exception is the Walker[5] results, which were the original solidification velocity experiments for pure nickel. Thus, the BCT theory has been unsuccessful in predicting the divergence in exponential behavior for the solidification velocity as a function of undercooling.

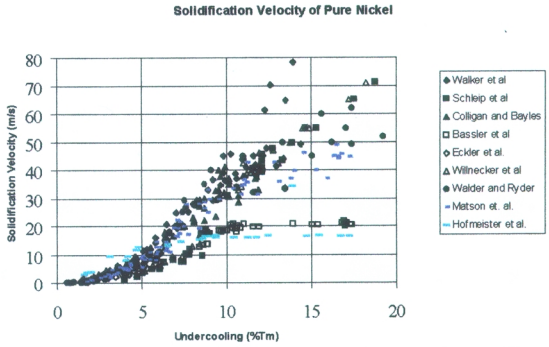

Figure 1. Cumulative plot of solidification velocity for pure nickel.

II. Experimental Procedure

The purpose of this work is to quantify the effect of low concentrations of solute on the solidification velocity. Additionally, these investigations attempt to characterize the nature of the solidification velocity plateau occurring at intermediate undercoolings and the mechanisms that cause it. Finally, this work hopes to provide a method of predicting this intermediate plateau, as well as to lay the groundwork for predicting the plateau or discontinuity in the solidification velocity at higher undercoolings.

One of the materials properties which has a large impact on the theoretical prediction of the solidification velocity is the equilibrium partition coefficient. Hence, the initial emphasis was placed on alloys with a wide range of partition coefficients. Nickel based alloys were selected because of the considerable experience by a number of investigators in the measurement of the solidification velocity of pure nickel and its alloys. The titanium-based alloys were selected because they provided an alternate engineering material of interest, solidifying a primary BCC structure.

In each alloy system, the solidification velocity is measured as a function of undercooling. The amount of undercooling is determined using an optical pyrometer, while the solidification velocity is measured using the HSDA 96. The HSDA 96 is a thermal imaging system developed at Vanderbilt University, which captures images at frame rates as high as $1x10^6$ frames/sec. It is composed of a parallel tapped 10x10 array of silicon photodiodes. The parallel tapped configuration eliminates the uncertainty introduced by the rastering techniques used in most digital imaging systems.

III. Preliminary Results

Solidification velocity data for each alloy was collected over the range of undercoolings listed in table 1. The nickel-based alloys were processed in a He-15v/oH_2 gas mixture, while the titanium-based alloys were processed in ultra-high purity He.

Table 1. A summary of solidification velocity experiments that have been conducted.

Alloy	Processing Environment	Liquidus Temperature	Minimum Undercooling	Maximum Undercooling
Ni-3a/oTi	He-15v/oH_2	1708K	99K	271K
Ni-5a/oTi	He-15v/oH_2	1693K	95K	288K
Ni-7a/oTi	He-15v/oH_2	1633K	80K	280K
Ni-1a/oSi	He-15v/oH_2	1723K	50K	290K
Ni-10a/oSi	He-15v/oH_2	1623K	105K	295K
Ni-1a/oSn	He-15v/oH_2	1723K	74K	279K
Ni-2.5a/oSn	He-15v/oH_2	1705K	103K	255K
Ni-4a/oSn	He-15v/oH_2	1683K	90K	264K
Ti-5a/oAl	UHP He	1973K	141K	273K
Ti-30a/oAl	UHP He	1933K	100K	296K
Ti-1a/oNi	UHP He	1938K	100K	249K
Ti-2a/oNi	UHP He	1923K	100K	250K
Ti-56a/oAl-4a/oV	UHP He	≈1743K	75K	319K
Ti-56a/oAl-8a/oV	UHP He	≈1743K	94K	284K

Figure 2 is a plot of the solidification velocity as a function of undercooling for the three Ni-Ti alloys that were investigated. At low undercoolings (<145K) the Ni-3a/oTi results are in agreement with the two higher concentration alloys. At higher undercoolings (>176K) the solidification velocity results for Ni-3a/oTi are consistently higher than the Ni-5a/oTi and Ni-7a/oTi results. For undercoolings ranging between 146K and 176K there is an especially noticeable difference between the Ni-3a/oTi results and the two higher concentration alloys. There appears to be a plateau in the intermediate undercooling range, as well as, the high undercooling range for Ni-3a/oTi. The two plateaus occur at 25m/s and 40m/s, respectively. The solidification velocities are similar in the two higher concentration alloys tested up to about 176K of undercooling. However, the Ni-7a/oTi solidification velocity results appear to be slightly less than the Ni-5a/oTi results at higher undercoolings (>176K). There are also two plateaus in the solidification velocity curves for the higher concentration alloys. The first plateau in the solidification

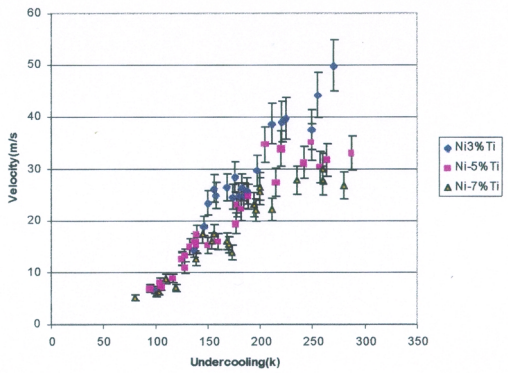

Figure 2. Cumulative plot of Ni-Ti results.

velocity occurs at ≈15m/s at lower undercoolings, while the second occurs at ≈32m/s for Ni-5a/oTi and ≈28m/s for Ni-7a/oTi at higher undercoolings. When the alloy results are compared to the experimental results for pure nickel processed under the same conditions, it is seen that the solidification velocity at undercoolings less than the initial plateau are consistent with the pure nickel results but, thereafter, solidification velocities in the alloys are less than that in pure nickel.

Two of the Ni-Sn data sets also showed a strong plateau in the solidification velocity data at high undercoolings (Figure 3). In the Ni-1a/oSn data the plateau occurs at ≈37m/s and 175K of undercooling. The plateau in the Ni-4a/oSn data occurs at ≈29m/s and 175K of undercooling. In the Ni-2.5a/oSn velocity data there is not an appreciable plateau in the solidification velocity at high undercoolings. In general, as more solute was added to this system, the solidification velocity appeared to be reduced at all undercoolings. The depression of the solidification velocity in this alloy system appears to be the most severe in the range of undercoolings between 140K and 180K. When the results from the nickel-tin alloys are compared to the results of pure nickel, it is observed that the solidification velocity in Ni-1a/oSn is approximately the same as that of pure nickel. The solidification velocity results for Ni-2.5a/oSn are less than the results for pure nickel up to approximately 200K of undercoolings. Above 200K of undercooling the results are similar. For the Ni-4a/oSn alloy, the solidification velocity of pure nickel is higher at all undercoolings measured.

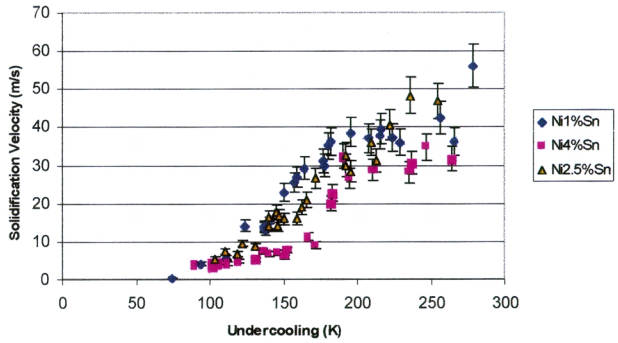

Figure 3. Cumulative plot of Ni-Sn results.

IV. Analysis and Discussion

The current hypothesis for explaining the results presented here centers on the effects of solute drag on the solidification velocity as a function of undercooling. It is believed that the solidification velocity in the alloys undergoes four distinct regimes. The first occurs when the velocity is slow enough to allow time for the solute to escape the advancing interface. In this regime the solidification velocity behaves in the same manner as the pure material. The second regime involves a departure from the solidification velocity of the pure material. This second regime occurs because the solidification velocity approaches the diffusive speed of the solute in the liquid (*i.e.* solute drag slows the advancing interface with increasing undercooling). The third regime occurs when the velocity of the solid/liquid interface becomes significantly greater than the diffusive speed of the solute (*i.e.* solute trapping occurs). The final regime, denoted by the plateau at higher solidification velocities, is still another effect of solute. In this case, however, a plateau is caused by solute drag from residual oxygen in the system. Cochrane *et al*[12] observed the effect of oxygen on the solidification velocity in pure copper, while Bassler[4] observed the effect in pure nickel. For extremely large undercoolings the solidification velocity can become high enough to overcome the effects of solute drag caused by residual oxygen. This was observed in the Ni-

Sn results. An effect of oxygen would explain the considerable disagreement between the pure nickel solidification velocity measurements between various investigations.

To show the behavior in solidification velocity described above as a function of undercoolings one can examine the Ni-5a/oTi results. Figure 4 shows a separate plot of experimental results along with the BCT calculations for pure nickel and Ni-5a/oTi. The four regimes mentioned previously are denoted on the plot. It is observed that at low undercoolings (<146K) the solidification velocity agrees with the pure nickel calculation, which corresponds to the first regime. At intermediate undercoolings (between 176K and 220K) the solidification shows agreement with the alloy calculation. Neither of the BCT calculations address the transition at intermediate undercoolings or the plateau at higher undercoolings.

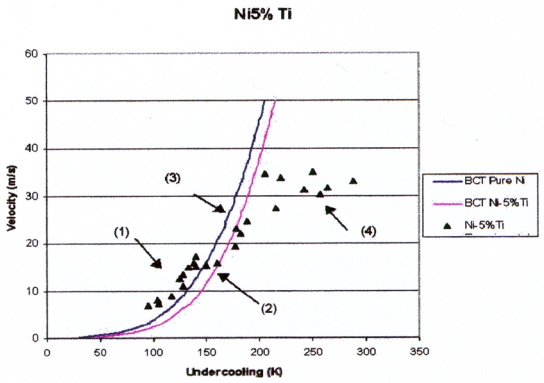

Figure 4. Ni-5a/oTi solidification velocity results plotted with the BCT calculations for pure Ni and Ni-5a/oTi.

V. Future Work

This investigation is a work-in-progress. There are a number of alloy systems that need to be studied. For alloys already processed, microstructural characterization of the droplets is needed. This includes SEM analysis and optical microscopy. In addition, microprobe analysis is needed to characterize the concentration gradients in the processed droplets. This will aid in developing a numerical model to describe the concentration gradients ahead of the solid/liquid interface.

It has been observed that the amount of stirring can effect the diffusion of solute in the liquid[13]. It is, therefore, necessary to conduct experiments in the electrostatic levitator (ESL) at the Marshall Space Flight Center. The discontinuities in solidification velocity may be different when processed in an ESL, as compared to the EML.

Finally, it is necessary to perform modeling of these particular systems and the experimental conditions regarding the effects of the thermal and solutal diffusive fields. Proper modeling could further increase the understanding of the observed relationships between undercooling and solidification velocity.

REFERENCES

1. W.J. Boettinger, S.R. Coriell and R. Trivedi, "Application of Dendrite Growth Theory to the Interpretation of Rapid Solidification Microstructures": in *Rapid Solidification Processing: Principles and Technologies, IV*, R. Mehrabian and P.A. Parrish, eds., Claitor's Publishing Division, Baton Rouge, LA, 1988, pp.13-25.

2. G.P. Ivanstov, "Temperature Field around Spherical, Cylindrical, and Needle-Shaped Crystals Growing into a Supercooled Melt," Doklady Akademii Nauk, USSR, 58, 1947, p.567.
3. B.T. Bassler, R.S. Brunner, W.H. Hofmeister and R.J. Bayuzick "Ultrahigh Speed Imaging System for the Measurement of Solidification Velocity via Direct Observation of Rapid Solidification," Rev. Sci. Instrm., 68, 4, 1997, pp. 1846-1852.
4. B.T. Bassler, "The Solidification Velocity of Undercooled Metals and Alloys" PhD Dissertation, Vanderbilt University, (1997).
5. J.L. Walker: in Principles of Solidification, B.Chambers ed. (John Wiley and Sons,Inc. New York,1984), p.114.
6. E. Schliep, R. Willnecker, D.M. Herlach and D.P. Gorler: Proceedinqs of the 6th International Conference on Rapidly Ouenched Metals, Montreal, Canada, 1987.
7. B.T. Bassler, W.H. Hofmeister, G. Carro, and R.J. Bayuzick, "The Velocity of Solidification of Highly Undercooled Nickel," Metallurgical Transactions A, vol.25A, June 1994, pp.1301-1308.
8. G.A. Colligan and B.J. Bayles "Dendritic Growth Velocity in Undercooled Nickel Melts," Acta Metallurgica, 8, 1962, pp.895-897.
9. S. Walder and P.L. Ryder,"A Simple Technique for the Measurement of Dendritic Growth Rates in Undercooled Metallic Melts and Application to Ni and Ti," Materials Science and Engineering, A203, 1995, p.197.
10. K. Eckler, D.M. Herlach, R.G. Hamerton and A.L. Greer, "Dendrite Growth Velocities in Highly Undercooled, Dilute Ni-C melts", Materials Science and Engineering, A133, 1991, p.730.
11. D.M. Matson "Imaging the Recalescence Behaviour of Undercooled Nickel," PhD Thesis, Massachusetts Institute of Technology, Cambridge, MA, 1996.
12. R.F. Cochrane, S.E. Battersby and A.M. Mullis, "Determination of the solidification in Cu and Cu-O Systems by the Melt Encasement Technique", TMS Annual Meeting, San Antonio, TX,1998.
13. R.W. Smith "Influence of G-Jitter on Liquid Diffusion-The Queld/MIM/MIR Programme," Microgravity Science and Technology, 11, 2, 1998, pp.78-83.

EQUIAXED DENDRITIC SOLIDIFICATION EXPERIMENT (EDSE)

C. Beckermann[1], A. Karma[2], I. Steinbach[3] and H. C. de Groh III[4]

[1]University of Iowa
[2]Northeastern University
[3]ACCESS e.V., Germany
[4]NASA, Glenn Research Center

OBJECTIVES

The objective of the research is to quantitatively determine and understand the fundamental mechanisms that control the microstructural evolution during equiaxed dendritic solidification. A microgravity experiment will be conducted to obtain benchmark data on the transient growth and interaction of up to four equiaxed crystals of a pure and transparent metal analog (succinonitrile, SCN) under strictly diffusion-dominated conditions. Of interest in the experiment are the transient evolution of the primary and secondary dendrite tip speeds, the dendrite morphology and solid fraction, the tip selection criterion, and the temperature field in the melt for a range of interaction "strengths" between the crystals. The experiment extends the microgravity measurements of Glicksman and co-workers isothermal dendritic growth experiment (IDGE) for steady growth of a single dendrite to a case where growth transients are introduced due to thermal interactions between neighboring dendrites – a situation closer to actual casting conditions. Corresponding Earth-based experiments will be conducted to ascertain the influence of melt convection. The experiments are supported by a variety of analytical models and numerical simulations. The data will be used to develop and test theories of transient dendritic growth and the solidification of multiple interacting equiaxed crystals in a supercooled melt.

I. Need for Microgravity

Experimental validation of present equiaxed dendritic solidification models is very limited, with only a few bulk solidification experiments conducted (on Earth) using metal alloys. There are basically four issues that have hampered the testing of such models: (i) the inability to control and quantify nucleation, (ii) the presence of uncontrolled, gravity-driven melt convection and crystal movement, (iii) the difficulty to observe growth in metallic systems, and (iv) the complications associated with coupled thermal and solutal undercoolings when using alloys. The Equiaxed Dendritic Solidification Experiment (EDSE) is designed to be simple, yet overcomes all of these limitations. In particular, gravity-driven convection can only be minimized in a microgravity environment. Due to our inability to analyze solidification microstructure evolution in the presence of this convection, it is important to first generate benchmark data for the diffusion limit.

II. Results

The research to date has concentrated on development of the science requirements for the proposed microgravity experiment; design, construction, and testing of a ground-based version of the experiment; and modeling of the growth of an assemblage of equiaxed dendritic crystals. These efforts have culminated in the passing of the Science Concept Review (SCR) in February of 1998. The research team is now preparing for the Requirements Definition Review (RDR). Some of the experimental and theoretical research has been published and is described briefly below.

III. Ground-Based Experiments

We have conducted preliminary experiments involving an assemblage of equiaxed crystals using a setup that is functionally similar to the planned EDSE. A schematic of the setup together with a photograph taken during an experiment is shown in Figure 1.

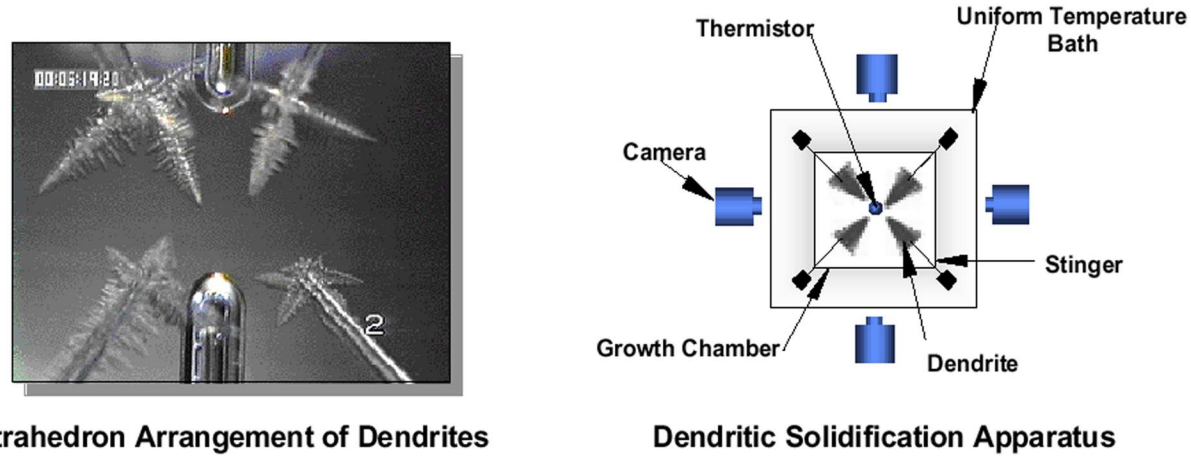

Figure1. Schematic of the equiaxed dendritic solidification apparatus and a photograph showing the tetrahedron arrangement of the dendrites.

A glass growth chamber is contained within a temperature-regulated bath. Four CCD cameras, with light sources, provide orthogonal images from four sides. The growth chamber contains pure SCN, several thermistors, and four stingers on which the dendrite growth is initiated. The tips of the stinger tubes are located at the corners of a tetrahedron with edge lengths, and hence spacing between the tips, of 10 mm. Thermoelectric coolers are mounted on the stinger ends opposite to the tips. An experiment starts by melting the SCN, then cooling the liquid to establish the desired supercooling in the growth chamber. The thermoelectric coolers are initiated and, after some time, dendrites start to emerge at the stinger tips. Although the present setup does not yet allow for a quantitative evaluation of the growth phenomena, we have performed image analysis in order to demonstrate some of the measurement techniques [1, 2]. We are presently using this setup to examine numerous issues regarding the design of the planned microgravity experiment, including dendrite initiation, imaging methods, stinger design, and others.

IV. Modeling

The proposed microgravity experiment is supported by several modeling efforts. The models are not only intended to provide the theories that will be tested using the microgravity data, but will also be used to simulate the experiment.

In one of the models, the thermal interactions between the equiaxed crystals are fully accounted for by numerically calculating the three-dimensional, transient temperature field in the supercooled melt. The shape evolution and crystallographic orientation of the crystal envelopes are calculated by linking the numerical solution with a local analytical solution for the dendrite tip speeds. A representative simulation result for a single equiaxed crystal is shown in Figure 2 [3]. This mesoscopic model was validated for the steady growth of a single crystal using IDGE data. The full model is used to establish the requirements and parameters for EDSE. Ultimately, we also plan to use the model to simulate the microgravity tests, in order to quantify the thermal field in the growth chamber.

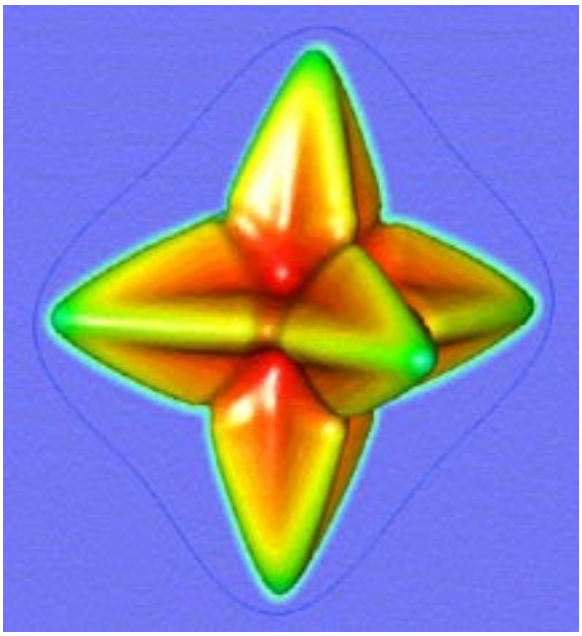

Figure 2. Mesoscopic simulation of equiaxed dendritic growth: the surface represents a confocal envelope around the dendrite arms, while the colors indicate the temperature on the envelope.

We have also performed direct numerical simulations on a microscopic scale using the phase-field model to study the growth interactions of equiaxed dendrites and the resulting transients in the dendrite tip speeds and radii. While simulations cannot yet be achieved for the conditions of the planned experiment, they do provide fundamental insight into issues such as dendrite tip operating point selection in the presence of growth interactions and transients. A major accomplishment has been the inclusion of melt convection in the phase-field model [4-6]. Figure 3 shows a representative simulation result where a uniform flow enters from the top of the domain. The selection of the velocity and shape of the dendrite tip was investigated as a function of flow rate, growth direction relative to the flow, and anisotropy strength [6].

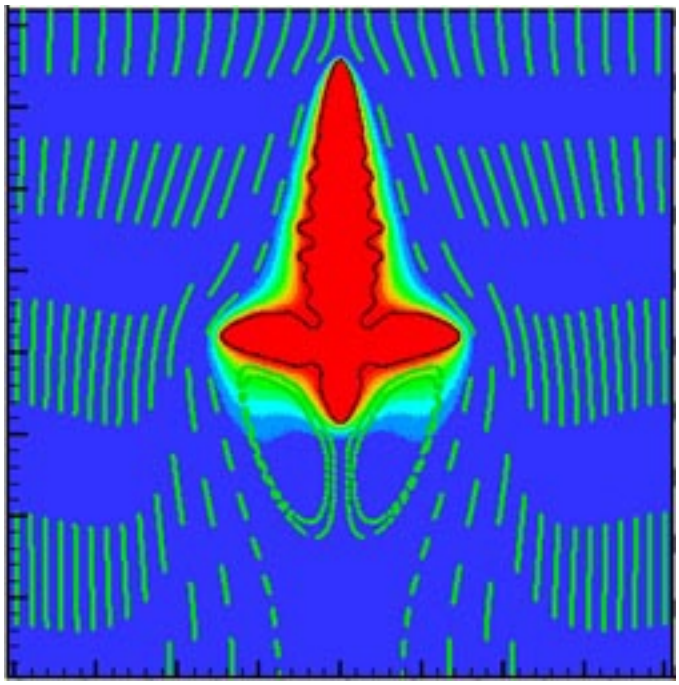

Figure 3. Two-dimensional phase-field simulation of dendritic growth with convection; the black contour line is the solid-liquid interface, the colors indicate temperature, and the light interrupted lines are streamlines (at unequal intervals).

REFERENCES

1. Li, Q., and Beckermann, C., "Evolution of Sidebranch Structure in Free Dendritic Growth," Acta Materialia, Vol. 47, 1999, pp. 2345-2356.
2. Li, Q., and Beckermann, C., "Scaling Behavior of Three-Dimensional Dendrites," Physical Review E, Vol. 57, 1998, pp. 3176-3188.
3. Steinbach, I., Beckermann, C., Kauerauf, B., Li, Q., and Guo, J., "Three-Dimensional Modeling of Equiaxed Dendritic Growth on a Mesoscopic Scale," Acta Materialia, Vol. 47, 1999, pp. 971-982.
4. Beckermann, C., Diepers, H.J., Steinbach, I., Karma, A., and Tong, X., "Modeling Melt Convection in Phase-Field Simulations of Solidification," J. Computational Physics, Vol. 154, 1999, pp. 468-496.
5. Diepers, H.J., Beckermann, C., and Steinbach, I., "Simulation of Convection and Ripening in a Binary Alloy Mush Using the Phase-Field Method," Acta Materialia, Vol. 47, 1999, pp. 3663-3678.
6. Tong, X., Beckermann, C., and Karma, A., "Velocity and Shape Selections of Dendritic Crystals in a Forced Flow," Physical Review E, Vol. 61, pp. R49-R52, 2000.

DENDRITIC ALLOY SOLIDIFICATION EXPERIMENT (DASE)

C. Beckermann[1], A. Karma[2], I. Steinbach[3] and H. C. de Groh III[4]

[1]University of Iowa
[2]Northeastern University
[3]ACCESS e.V., Germany
[4]NASA, Glenn Research Center

INTRODUCTION AND OBJECTIVES

A space experiment, and supporting ground-based research, is proposed to study the microstructural evolution in free dendritic growth from a supercooled melt of the transparent model alloy succinonitrile-acetone (SCN-ACE). The research is relevant to equiaxed solidification of metal alloy castings. The microgravity experiment will establish a benchmark for testing of equiaxed dendritic growth theories, scaling laws, and models in the presence of purely diffusive, coupled heat and solute transport, without the complicating influences of melt convection. The specific objectives are to:

- determine the selection of the dendrite tip operating state, *i.e.* the growth velocity and tip radius, for free dendritic growth of succinonitrile-acetone alloys
- determine the growth morphology and sidebranching behavior for freely grown alloy dendrites
- determine the effects of the thermal/solutal interactions in the growth of an assemblage of equiaxed alloy crystals
- determine the effects of melt convection on the free growth of alloy dendrites
- measure the surface tension anisotropy strength of succinonitrile-acetone alloys
- establish a theoretical and modeling framework for the experiments.

Microgravity experiments on equiaxed dendritic growth of alloy dendrites have not been performed in the past. The proposed experiment builds on the Isothermal Dendritic Growth Experiment (IDGE) of Glicksman and coworkers, which focused on the steady growth of a single crystal from pure supercooled melts (succinonitrile and pivalic acid). It also extends the Equiaxed Dendritic Solidification Experiment (EDSE) of the present investigators, which is concerned with the interactions and transients arising in the growth of an assemblage of equiaxed crystals (succinonitrile). However, these experiments with pure substances are not able to address the issues related to coupled heat and solute transport in growth of alloy dendrites.

I. Review of Previous Research

Chopra *et al*. [1] have conducted Earth-based experiments on free dendritic growth into a supercooled melt for the SCN-ACE system. Representative results, carefully extracted from the paper of Chopra *et al.*, for the measured dendrite tip velocity, V, and radius, R, as a function of the solute

concentration, C_0, are shown in Figure 1 (symbols) for three different supercoolings, ΔT (0.1, 0.5, and 0.9 K). At all supercoolings, the growth velocity shows a maximum at around 0.1 mol% acetone, while the radius reaches a minimum. This behavior can be explained by the competition between thermal and solutal effects. Small solute additions destabilize the tip, making it sharper (smaller radius) and thereby increasing the growth velocity. On the other hand, the solute diffuses about 100 times slower than heat, resulting in a decrease in the growth velocity at higher concentrations.

Early models of free dendritic growth into a supercooled alloy melt have been proposed by Langer [2], Lipton *et al*. (LGK) [3, 4], and Karma and Langer [5]. These models all use marginal stability theory to determine the operating point of the tip through the introduction of a stability constant σ^*. Lipton *et al*. (LKT) [6] generalized the LGK model and extended it to high growth rates. The LKT model (or LGK model in the low growth rate limit) is now the most commonly used model for dendritic growth from a supercooled alloy melt, and is reviewed in greater detail next. In 1985, Karma and Kotliar [7] developed the first microscopic solvability theory (MST) for the alloy case based on a boundary layer approximation for the thermal and solutal diffusion fields. Ben Amar and Pelce [8] generalized this theory to a fully non-local model for alloy dendrites at low supercoolings. MST is a more self-consistent solution to the dendrite problem than marginal stability theory, but gives the same results except that the parameter σ^* is a function of the interface energy anisotropy.

In the LGK/LKT model, the heat and solute diffusion field around the tip is obtained from the Ivantsov solution for a parabolic needle crystal. Then, the total supercooling ΔT (including the capillarity correction) can be related to the thermal (P_t=VR/2α) and solutal (P=VR/2D) Peclet numbers through

$$\Delta T = \left(\frac{\Delta H}{c_L}\right) Iv(P_t) + \frac{k\Delta T_0 Iv(P)}{1-(1-k)Iv(P)} + \frac{2\Gamma}{R} \qquad (1)$$

where ΔH is the latent heat of fusion, c_L is the liquid specific heat, k is the partition coefficient, ΔT_0 is the equilibrium freezing temperature range, Iv is the Ivantsov function, D is the liquid mass diffusivity, α is the liquid thermal diffusivity, and Γ is the Gibbs-Thomson coefficient. The above equation only provides the product of V and R as a function of the supercooling. A unique tip operating state (*i.e.*, tip radius) can be obtained from the following tip selection criterion for low Peclet numbers [3, 4, 6]

$$R = \frac{\Gamma/\sigma^*}{\left[2P\left(\frac{k\Delta T_0}{1-(1-k)Iv(P)}\right) + P_t\left(\frac{\Delta H/c_L}{\beta}\right)\right]} \qquad (2)$$

where σ^* is the stability or selection constant, and β is approximately unity. As used in equation (2), σ^* is *independent* of the tip speed and solute concentration [9].

Results of applying the LGK/LKT model to the experiments of Chopra *et al*. [1] are shown as solid lines in Figure 1. For these calculations, the value of σ^*=0.02 was used. It can be seen that the theory correctly predicts the measured velocity maximum at around 0.1 mol% acetone. However, there is poor quantitative agreement otherwise. The differences at vanishing solute concentration (C_0=0, pure SCN) can be attributed to buoyancy-driven thermal convection effects, which diminish as the supercooling approaches 0.9 K (lower panels). At finite solute concentrations, the

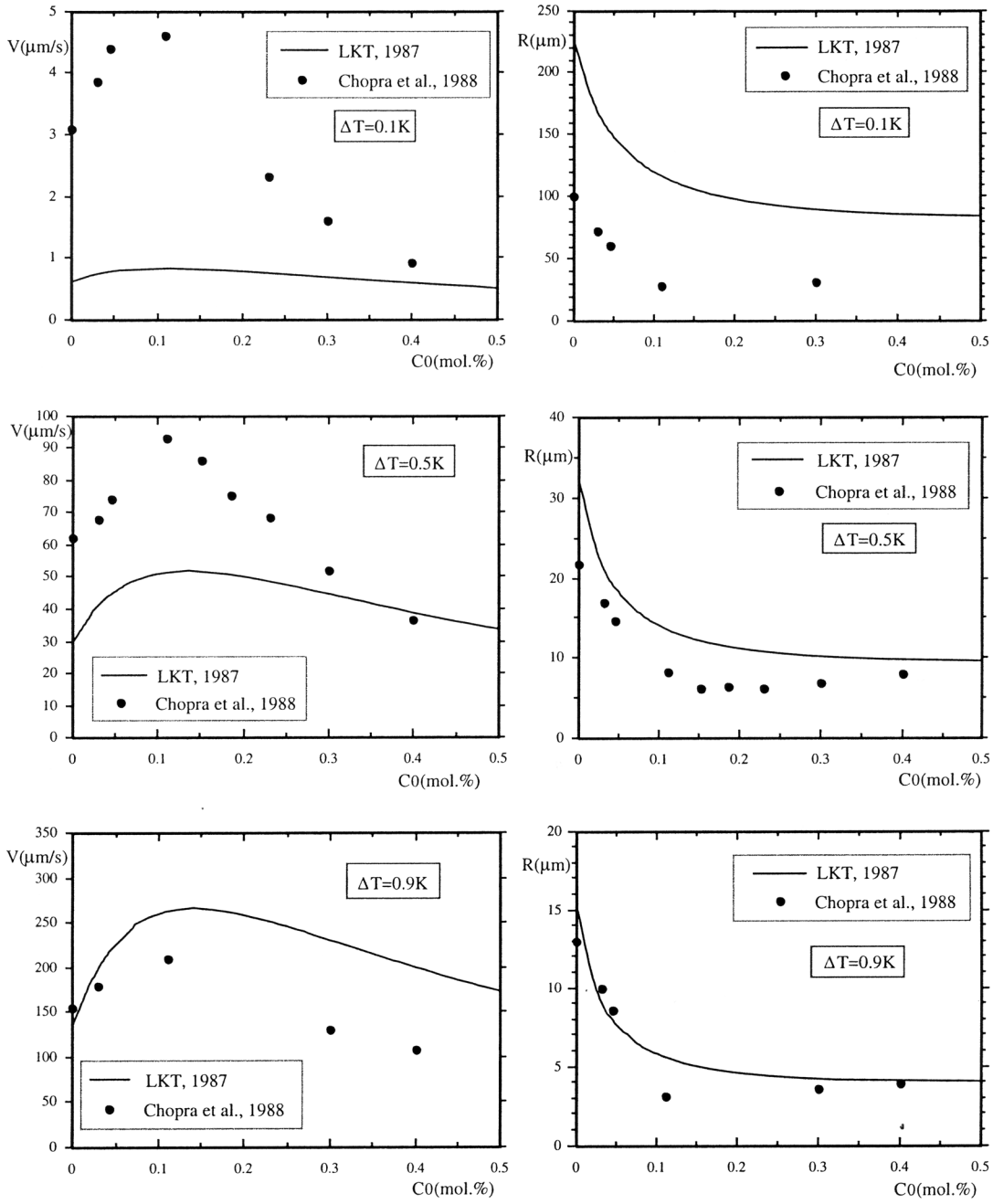

Figure 1. Comparison of LGK/LKT theory (with $\sigma^*=0.02$) with the ground-based tip velocity and radius measurements of Chopra *et al*. [1] for succinonitrile-acetone.

agreement between the Earth-based experiments and the LGK/LKT model is poor even at the higher supercooling (0.9 K) where thermal convection is not important for pure SCN. Chopra *et al*. attribute this disagreement at higher solute concentrations to the effects of buoyancy-driven solutal convection.

The issue of measuring the selection constant σ^* for succinonitrile-acetone alloys is examined in greater detail in Figure 2. To obtain this figure, we used the V and R data from Chopra *et al*. [1] and substituted them into equation (2) to determine σ^*. It can be seen that despite the presence of thermal convection, the value of $\sigma^*=0.02$ for pure SCN ($C_0=0$) is reasonably well verified for all

three supercoolings. The IDGE microgravity experiments for pure SCN have yielded a very similar value. It is interesting to note that thermal convection in the pure SCN experiments apparently does not influence significantly the selection constant, because σ* is approximately the same at all three supercoolings.

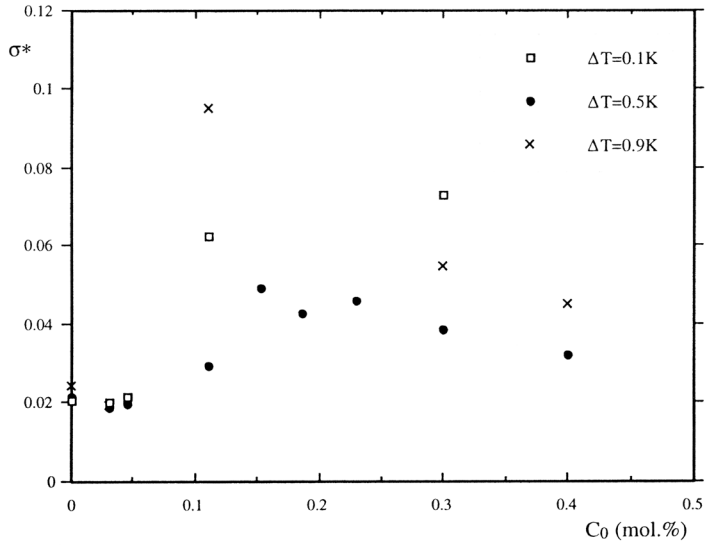

Figure 2. Selection constant σ* as a function of solute concentration obtained from the LGK/LKT selection criterion [equation (2)] using tip velocity and radius data from the ground-based experiments of Chopra *et al*. [1] for succinonitrile-acetone.

For solute concentrations beyond 0.05 mol% acetone, the measured σ* values in Figure 2 experience an abrupt rise. Furthermore, at a given concentration the σ* values for the three different supercoolings are widely scattered. It is important to realize that the measured variation of σ* with concentration is not in agreement with LGK/LKT theory, which states that σ* as defined in equation. (2) is independent of concentration (and should thus remain at 0.02). This disagreement with theory forms the main starting point for the proposed microgravity experiment, and the following additional observations can be made:

- Buoyancy-driven solutal convection could be responsible for the disagreement; however, as noted above thermal convection does not cause such significant variations in σ*. Also, the fact that at a given solute concentration the σ* value for ΔT=0.9 K is sometimes above and other times below the value for ΔT=0.1 K, while the value for ΔT=0.5 K is always below the other two values, cannot be explained by solutal convection alone.
- It is possible that the anisotropy strength of the surface tension depends on the solute concentration. Then, MST would predict a variation of σ* with concentration (even though only the surface tension anisotropy of the pure solvent enters into MST). Unfortunately, the surface tension anisotropy has not been measured as a function of concentration for succinonitrile-acetone alloys.
- The experiments of Chopra *et al.* [1] show a change in the dendrite morphology with solute concentration. The sidebranches move up toward the tip, as the concentration is increased initially and then recede backwards along the dendrite when the concentration is increased further past the point of maximum velocity. These strong variations in sidebranch activity with solute concentration could be responsible for the disagreement of the σ* measurements with theory. Also, Chopra *et al.* observed occasional tip splitting at around the maximum

velocity point, which cannot be explained by present theories. Both of the changes in the dendrite morphology with concentration are likely due to the large disparity in the thermal and solutal diffusion lengths around a growing alloy dendrite.

Current theories attribute sidebranching to the amplification of thermal noise along the sides of dendrites [10]. Moreover, it has recently been shown that the rate of amplification is very sensitive to the tip morphology, and in particular to its non-axisymmetric departure from a paraboloid of revolution as recently emphasized [10]. Therefore there is the interesting, but yet untested, possibility that the enhancement of sidebranching by a dilute impurity is due to a change of tip morphology. Accurate measurements in the absence of convection effects (*i.e.*, in microgravity) will allow us to correlate the level of sidebranching activity with the tip morphology and thus to test this hypothesis, adding in an important way to our fundamental understanding of the sidebranching mechanism in alloy systems.

II. Proposed Research

The proposed experiment will be performed using the transparent model alloy succinonitrile-acetone, which has been characterized extensively in previous Earth- and space-based experiments. Similar to IDGE and EDSE, the dendrites will be grown from stinger tips inside a temperature controlled growth chamber. First, a series of tests is planned for the steady growth of a single dendrite into an essentially infinite alloy melt. The initial thermal supercooling and the alloy concentration will be varied. Changing the alloy concentration in space will require some modification of the EDSE hardware. Optical imaging will be used to measure the dendrite tip speeds and radii, as well as microstructural parameters related to the dendrite sidebranches. Then, in a similar manner as in EDSE, experiments will be performed with multiple crystals growing from separate stingers in order to study thermal and solutal growth interactions and transients. This can be accommodated in the same growth chamber. While this represents an ambitious experimental program, it is believed that it can be accomplished in the long-duration microgravity environment available on the International Space Station. A corresponding set of Earth-based experiments will be performed to help in the design of the flight hardware and to establish benchmark data in the presence of convection effects. The surface tension anisotropy strength of succinonitrile-acetone alloys will be measured in specially designed Earth-based experiments.

Extensive theoretical analysis and numerical modeling will support the space experiment. Simulations will be performed of the free growth of alloy dendrites using the phase-field model as well as a novel mesoscopic modeling technique developed within the EDSE project. Melt convection will be modeled in some simulations in order to help understand its effect. In addition, new analytical models for the growth of single and multiple equiaxed alloy dendrites will be developed.

REFERENCES

1. Chopra, M., Glicksman, M. E., and Singh, N. B., *Metall. Trans.,* 1988, **19A**, 3087.
2. Langer, J. S., *Physicochem. Hydrodyn.*, 1980, **1**, 41.
3. Lipton, J., Glicksman, M. E., and Kurz, W., *Mater. Sci. Eng.*, 1984, **65**, 57.
4. Lipton, J., Glicksman, M. E., and Kurz, W., *Metall. Trans.,* 1987, **18A**, 345.
5. Karma, A., and Langer, J. S., *Phys. Rev.*, 1984, A**30**, 3147.
6. Lipton, J., Kurz, W., and Trivedi, R., *Acta Metall.*, 1987, **35**, 957.

7. Karma, A., and Kotliar, B. G., *Phys. Rev.*, 1985, A**31**, 3266.
8. Ben Amar, M., and Pelcé, P., *Phys. Rev.*, 1989, A**39**, 4263.
9. Trivedi, R., and Kurz, W., *International Materials Reviews*, 1994, **39**, 49.
10. Brener, E., and Temkin, D., *Phys. Rev.*, 1995, A**51**, 351.

EXPERIMENTAL AND NUMERICAL INVESTIGATION OF SOLIDIFICATION PROCESSES WITH CONVECTION

A. Benard, A.R Diaz, M.M. Koochesfahani, and J.J. McGrath

Department of Mechanical Engineering
Michigan State University
East Lansing, MI 48824

INTRODUCTION

Transport phenomena in microgravity and their influence on the microstructure of alloys during solidification have been studied by a number of researchers using either carefully crafted experiments or numerical computations. Novel experimental and numerical methods are applied in this work to study solidification processes in order to produce an improved fundamental understanding of solidification processes, including the role played by buoyancy-driven convection phenomena in determining the microstructure. A brief overview of our new program and the expected results are provided below.

The experimental work consists first of making quantitative measurements of the velocity field, and subsequently temperature field, during the solidification of an optically transparent analog of a binary metallic alloy. A novel Molecular Tagging Velocimetry (MTV) technique is used to perform the velocity field measurements. Attempts will also be made to combine MTV with Laser-Induced Fluorescence (LIF) in order to perform simultaneous temperature and velocity measurements. Such quantitative measurements during the solidification process will enhance our understanding of the diverse transport phenomena occurring during solidification and permit the refinement of the phenomenological models used in averaged transport equations. The experimental data will be compared with the results of solving the averaged governing equations.

The objectives of the numerical research are to use a fictitious domain approach to solve averaged governing equations describing the overall solidification process. The use of this method will reduce the time required to generate models by eliminating the need for cumbersome mesh generation. The method is also highly efficient for large problems. The model will be tested against the experimental data, as they become available, and improved as needed. In the following, a brief description of the numerical and experimental aspects of this work is provided.

I. Background on Solidification Processes with Convection

A significant amount of literature is now available concerning the solidification of an alloy with thermosolutal convection. It has been studied analytically using linear stability analysis (*e.g.* Worster (1997)), numerically (*e.g.* Neilson and Incropera (1991)) and experimentally (*e.g*. Prescott and Incropera (1996)**).** Complex numerical models of solidification processes have started to

emerge over the past fifteen years and experimental studies have been performed on alloy solidification to verify various aspects of the simulations, using qualitative methods mostly, or using punctual measurements. It is now possible, with the increase in computer power available, to incorporate a number of important physical aspects of alloy solidification into a numerical model and there is an ongoing interest in developing more sophisticated models.

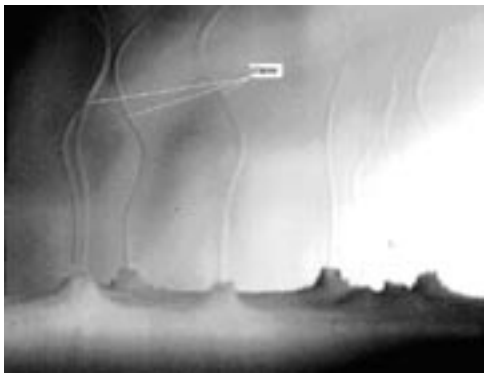

Figure 1. Observation of convective plumes emerging from the mushy zone during the solidification of an ammonium chloride solution.

There are, however, a number of issues such as nucleation, turbulence, or settling of dendrites, that must still be addressed before models can provide accurate quantitative predictions of such complicated phenomena. Software that incorporates many but not all of these features is presently available, but results from these simulations have been verified experimentally only with limited data. Typically, commercial codes are capable of 3-D simulations of solidification processes without turbulence, and kinetics effects (nucleation, growth of equiaxed dendrites) are not always included. Also, a significant meshing effort is always required to describe the geometry of the part, especially in 3-D.

To address these problems, the PIs propose to pursue a unique combined numerical and experimental work. The numerical work will be based on a numerical model and solution strategy that:

- Requires no underlying mesh for performing the computations, resulting in significant time savings during the overall modeling (this is especially important during a design phase)
- Is capable of handling complex transport phenomena for 3-D complex geometries without meshing effort
- Will be verified experimentally with *in-situ* dynamic measurements of the entire velocity and temperature fields.

The experimental work will use a new technique that:

- Allows *in-situ* dynamic measurements of whole temperature and velocity fields in samples of various sizes
- May result in simultaneous velocity and temperature measurements
- Has the potential for a scaled-down experimental setup sufficiently small to allow similar measurements in space.

II. Computational Aspects of the Proposed Work

A number of approaches have been presented in the literature to describe the relevant transport phenomena associated with solidification. Most notable are the works of Bennon and Incropera (1988), Rappaz (1989), Ni and Beckerman (1991), Ni and Incropera (1995), Beckermann *et. al.*

(1993, 1996) and Krane and Incropera *et al.* (1997a,1997b). Two- and three-dimensional simulations were performed in which continuity, momentum, mass diffusion, and the energy equations were solved to obtain a description of the solidification process.

In this work, it is proposed to implement a model based on a volume averaging procedure in order to study the characteristics of channel formation in the mushy region formed by the dendritic growth process under the influence of gravity. It will also be used to study the effect of scaling the mold size on the channel formation, and the orientation of the gravity field with respect to the chilled side. More complexity can be added to the macroscopic model in order to simulate the coarsening process in the mushy zone with time and the effects on the permeability.

The governing equations derived with the volume averaging procedure can be solved using standard methods such as finite elements or finite volume methods provided that the domain is appropriately described with an accurate mesh. This is not easy to do when the geometry is as complex as illustrated in Figure 2.

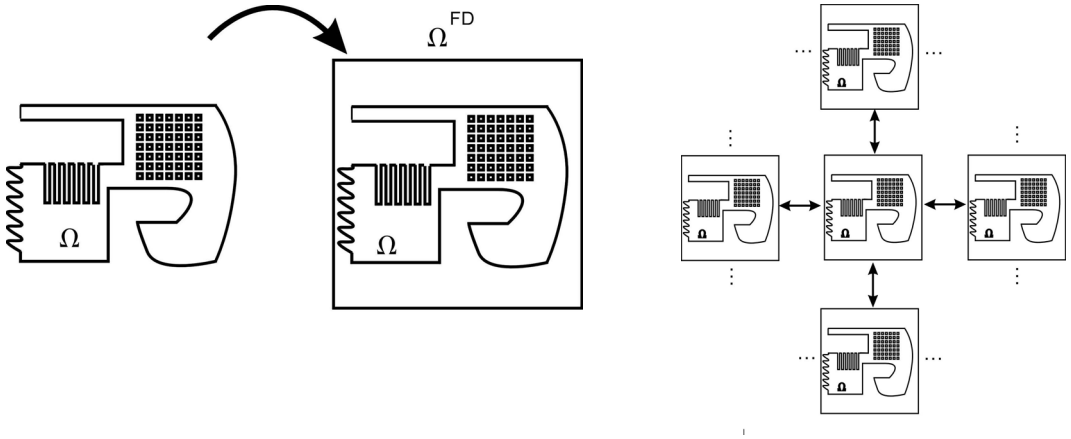

Figure 2. The fictitious domain method consists of embedding a complex geometry into a simpler auxiliary domain and using a periodic extension of the fictitious domain to allow the use of periodic functions such as wavelets.

This is where the introduction of a new set of approximations for the unknowns can help. Ideally, one would want to use functions that can be expressed without need for an underlying, structured mesh. Yet these functions must be able to *localize* values of **u,** the velocity for example, at the boundary (so that boundary conditions may be applied). Finding such functions is of course very difficult. What one can do instead is to introduce a *fictitious domain* $\mathbf{\Omega}^{FD}$ that encloses the true domain but has a much simpler geometry ($\mathbf{\Omega}^{FD}$ is in fact a square in R^2 or a cube in R^3) as illustrated in Figure 2. The goal is to solve a problem in some sense equivalent to the original problem, but defined on the much simpler domain $\mathbf{\Omega}^{FD}$. *This is the so-called fictitious domain problem*.

In the fictitious domain problem we look for the unknows, *e.g.* $\mathbf{u}^{FD}$, p^{FD}, T^{FD}, and C^{FD} defined over the whole $\mathbf{\Omega}^{FD}$, such that it is expected that they will provide a good approximation to the governing equations defined on the original problem, and that $\mathbf{u}^{FD}\big|_{\Omega} \rightarrow \mathbf{u}$ *i.e.*, that the restriction of the fictitious domain solution to converge to the solution of the original problem. Admittedly, the formulation of a successful fictitious domain approximation is delicate and there are a number of issues unresolved in the literature *e.g.* mixed boundary conditions, or the application of boundary

conditions of the third kind (other b.c.s can be accommodated). The treatment of boundary terms requires special attention for the conversion of terms such as

$$\left(\int_{\Gamma} \lambda \cdot \mathrm{v}\, d\Gamma\right)_{\substack{original \\ problem}} \rightarrow \left(\int_{\Omega} \lambda \cdot \mathrm{v}\, \|f\|\, d\Omega\right)_{\substack{fictitious \\ domain \\ problem}}$$

We recognize these difficulties but point out that there are hopeful signs that the strategy will succeed for all types of boundary conditions. Fictitious domain methods have been applied with success in a number of contexts, to solve problems in heat conduction, elasticity, heat transfer, and flow problems *e.g.* Bertrand *et al.* (1997), Diaz and DeRose (1998). Particularly relevant to this work are the results presented by Glowinski *et al,* (1998) where the integrals over the embedded domain boundaries are converted into volume integrals using measure theory and wavelet approximations

Once the problem is cast over the fictitious domain, it is easier to introduce approximations of $\mathbf{u}^{FD}$ and p^{FD} that require no structured mesh. To facilitate computations we will explore the use of $\boldsymbol{\Omega}^{FD}$ periodic functions. A particularly effective way to discretize the new fictitious domain formulation is to express dependent variables such as $\mathbf{u}^{FD}$, p^{FD}, T^{FD} and C^{FD} using wavelet bases. As wavelet functions localize behavior in both frequency and space domains, wavelet bases have a built-in mechanism to accommodate multiple scales in the geometry of the original problem, as well as in the physics of the problem.

III. Experimental Aspects of the Proposed Work

Semi-transparent analog alloys have been used for experimental studies because they permit optical access to the sample, which has proven useful for flow visualization and morphological studies. Aqueous ammonium chloride is such a system and has been used rather extensively because of its convenient freezing range and its crystallographic similarity to most metals (dendritic morphology) (Prescott and Incropera, 1996). Another advantage is that the thermophysical and transport properties are well known (*e.g.*, Beckermann and Wang, 1996) and that the system behaves in a very similar manner to metallic alloys, even though their Peclet numbers are different (convection will have a different importance with respect to molecular transport processes).

The system configurations studied include a comparison of experimental data and numerical predictions for unidirectional solidification in a bottom-chilled, and 2-D rectangular cavity configuration (Magirl and Incropera (1993)). Christenson *et al.*, (1989) compared experimental data and numerical predictions for a side-chilled, rectangular cavity configuration and they found qualitative agreement between experiments and computations. Most notably, the initial conditions were found by Christenson *et al.,* to have a very strong influence on the outcome of the computations, especially the initial concentration. The advantages offered by optical access will be further leveraged in the proposed work by applying MTV to quantify velocity fields during solidification.

A molecular complex is suitable for molecular tagging applications if its lifetime as a tracer is long enough relative to the flow convection time scale to allow sufficient displacement of the tagged regions. Since the typical velocities associated with solidification are relatively small (10 mm/s for plumes (Magirl and Incropera (1993)) a long lifetime tracer is required. Two possible tracer candidates are recently-designed supramolecular complexes (Gendrich *et al.*, (1997)) and caged fluorescein. Examples

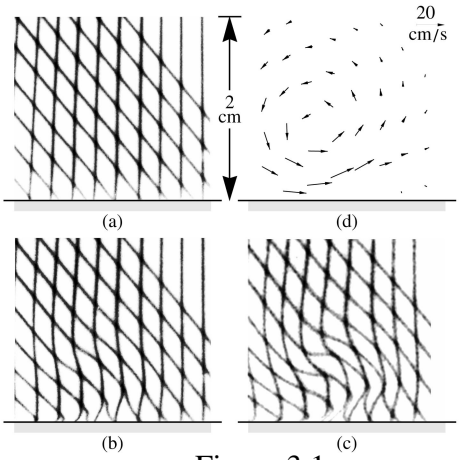

Figure 3.1

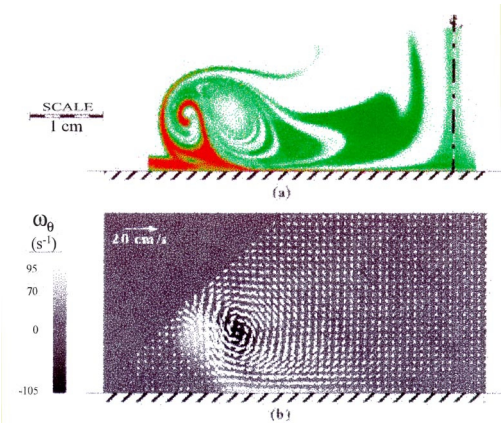

Figure 3.2

Figures 3.1 and 3.2. Example of an undistorted grid (3.1 a) and a distorted grid at two delay times (3.1 b and c) along with the velocity field deduced from these data (3.1 d); the instantaneous whole-field measurement (3.2) of two components of the velocity vector over a plane.

of velocity field measurements that can be obtained with MTV are shown in Figures 3.1 and 3.2.
We have performed a number of preliminary experiments relevant to this work. A simple version of the Magirl and Incropera (1993) bottom-chilled solidification system was constructed in our laboratory. We were able to use MTV to measure velocity in a sample of aqueous ammonium chloride, and this is shown in Figure 4 (Wirtz (1998)). This allowed determining the velocity within and around a plume located above a chimney. Notice that the 1mm plume diameter is very well captured with MTV.

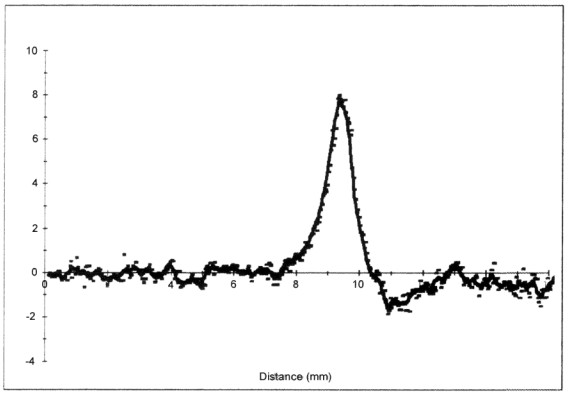

Figure 4: Velocity field measured from the displacement of the line by fluid motion 1 mm above a chimney [Wirtz *et al* (1998)].

IV. Summary of the Benefits of this Work

Some of the short-term benefits of the combined work are:

- The capability to "simultaneously" measure local temperature and velocity makes it possible to determine to what extent local thermodynamic equilibrium can be assumed at any location within the system.
- The porosity of the mushy zone is an important modeling parameter that cannot be determined easily. Detailed velocity field, including that close to the solid/liquid interface can be used in conjunction with modeling and inverse methods to infer the mushy zone porosity for defined situations of interest.

- The ability to quantify the local velocity and temperature in the immediate vicinity of crystals growing or shrinking in an equiaxed fashion would be important relative to recent modeling research (Wang *et al* (1995)).
- Detailed local velocity and temperature field measurements at the solid/liquid interface at early stages of solidification would provide important experimental details related to stability analyses.
- The development of a code that can perform rapid simulations without having to mesh complicated geometry will result in significant reductions of the design cycle.
- It will be possible to assess the validity of the codes and models by using the quantitative information obtained from the measurements at any time as initial conditions and compare the solution with measurements at a later time.
- New algorithms and computational methods will result from this work.

The long-term benefits of the proposed work are also important as it may be possible to modify existing setups on-board the experimental space station and study quantitatively a multitude of ground-based or space-based manufacturing processes. It will be possible to study a wide-range of microscale and macroscale phenomena not necessarily related to solidification.

REFERENCES

1. Beckermann, C. and Viskanta, R. Appl Mech Rev, V 46, 1-27, 1993
2. Beckermann, C. and Wang, C.Y. Metallurgical and Materials Trans. A., 27A, 2784- 2795, 1996.
3. Bennon, W.D. and Incropera, F.P. Int. J. Heat Mass Trans. 31, 2147-2160, 1988.
4· F. Bertrand, F., Tanguy, P.A., and Thibault, F. Int. J. for Num. Meth. In Fluids, 25, 719-736 (1997)
5. Christenson, M.S., Bennon, W.D. and Incropera, F.P. Int. J. Heat Mass Trans., 32, 69-79, 1989.
6. Diaz, A.R. and G.C.A. De Rose, Computational Mechanics, New Trends and Applications, E. Onate and S.R. Idelsohn (Eds), Barcelona, Spain (1998).
7. Glowinski,R, Pan, T.W. and J. Periaux. Comp. Methods Appl. Mech. Engrg. 151, 181-194, 1998.
8. Gendrich, C.P., Koochesfahani, M.M. and Nocera, D.G. Exp. in Fluids, 23 (15) 361-372, 1997.
9. Krane, M.J.M. and Incropera, F.P. Int. J. Heat Mass Transfer, 40, 3827-3835, 1997a.
10. Krane, M.J.M. and Incropera, F.P. Int. J. Heat Mass Transfer, 40, 3837-3847, 1997b.
11. Magirl, C.S. and Incropera, F.P., J. of Heat Transfer, 115, 1036-1043, 1993.
12. D.G. Neilson and F.P. Incropera, Numerical Heat Transfer,23, 1-20, 1993.
13. Ni, J. and Beckermann, C., Metall. Trans. B, 22B, 349-361, 1991.
14. Ni, J. and Incropera, F.P. Int. J. Heat Mass Transfer, 38, 1271-1284, 1995.
15. Prescott, P.J. and Incropera, F.P. Advances in Heat Transfer, 28, 231- 338, 1996.
16. Rappaz, M., Int. Mater. Rev, 34, 93-123, 1989.
17. Wang, C.Y., Ahuja, S., Beckermann, C., De Groh, H.C., Metall Mater Trans B, 26:111-119, 1995.
18. Wirtz, K., Koochesfahani,M., McGrath, J.J. and Benard, A. Proc. '98 IMECE, Anaheim,CA, 1998.
19. Worster, M. G. Ann. Rev. Fluid Mech. 29, 91-122, 1997.

KINETIC EVOLUTION OF STABLE AND METASTABLE STATES IN PROTEIN SOLUTIONS

Aleksey Lomakin, Neer Asherie and George B. Benedek

Department of Physics, Center for Materials Science and Engineering and Materials Processing Center, Massachusetts Institute of Technology, Cambridge MA 02139-4307

INTRODUCTION

The thermodynamic properties of protein solutions are important in many industrial, scientific, pharmacological and pathophysiological applications. These applications include the large scale separation of genetically engineered proteins, the production of crystals of biologically important proteins for the determination of their three-dimensional structure, the stability of highly concentrated pharmacological solutions of biological macromolecules and the inhibition of phase separation in protein condensation diseases. In all such applications the fundamental information required is the phase diagram of the macromolecule in question at various values of ionic strength, pH and temperature. Furthermore, it would be extremely valuable to be able to predict, even approximately, the location of the relevant phase boundaries. For this purpose it is highly desirable to establish the generic features of the phase diagram of protein solutions.

Phase diagrams have proven to be vitally important tools in the processing of a large variety of organic and inorganic materials, including metals, alloys, colloids and synthetic polymers. The phase behavior of protein solutions shares some general features with these systems. However, there are aspects of the phase behavior which make protein solutions unique. Proteins exhibit phenomena such as metastable liquid-liquid phase separation, aggregation, self-assembly, and gelation which are not seen in atomic and molecular systems. Our central objective is to investigate the phase behavior of protein solutions so as to effectively facilitate their materials processing.

We have been using a combination of experimentation, computer simulations and analytical theory to discover the factors which determine the location of the phase boundaries of protein and colloidal solutions. We have recently succeeded in demonstrating that, for a sufficiently short range of interaction, liquid-liquid phase separation becomes metastable with respect to crystallization. We have observed experimentally the metastability of liquid-liquid coexistence in the γ-crystallins, a family of proteins whose phase transitions are implicated in cataract formation.

Over and above this, we have discovered that the experimentally determined coexistence curves and solubility (or liquidus) lines differ significantly from those calculated using only isotropic short-range intermolecular potentials. We are able to explain the discrepancy between the experimental observations and the predictions based on isotropic interactions by including a hitherto neglected feature: the very large anisotropy in the interaction between proteins. Such anisotropy also appears to be crucial for

amorphous aggregate formation, which is of paramount importance for the practical use of proteins. We believe that our approach sheds light on the phenomenon of protein aggregation. Of course, for a complete description of protein aggregation, an understanding of the kinetic behavior of protein solutions is needed.

The formation of new phases is known to be strongly influenced by the phenomena of gravity-driven convection and sedimentation [1,2]. This is especially true for proteins, since they are large particles with slow kinetic behavior. Under microgravity conditions the effects of convection and sedimentation are greatly reduced, and thus transformations which are usually masked by the presence of gravity can be observed. Indeed, it has been recently found that glassy colloidal suspensions which did not crystallize on Earth for over a year formed crystals in microgravity conditions within a matter of days [3]. Microgravity conditions will similarly elucidate the variety of condensed phases possible in protein solutions and provide important checks on the model for the protein interactions which we investigate.

Results

We have developed an innovative Monte Carlo algorithm to analyze the liquid-liquid coexistence curves of the γ-crystallins [4]. Our Monte Carlo method uses analytic extrapolation techniques, in addition to simulation, to reconstruct the liquid-liquid coexistence curves. Our results are in perfect agreement with those obtained by more traditional Monte Carlo algorithms [5-7], but our scheme, by the economy of its design, dramatically reduces the computational time required to efficiently obtain the coexistence curves for the short ranges of interactions appropriate for protein solutions. Our Monte Carlo procedure also permits us to determine the solubility curves, since we are able to calculate the chemical potential of the liquid phase. The chemical potential of the solid phase is obtained using the Lennard-Jones Devonshire cell model [8].

Until recently, the only simulations available were those based on the assumption of isotropic interactions between the proteins. As we have stated in the introduction, in order to accurately describe the locations of the phase boundaries, the protein interactions should be modeled as both short-range *and* anisotropic ("aeolotopic"). We use a simple model in which the energy of each particle depends only on its position relative to other particles and on its own orientation, but is independent of the orientation of other particles. A protein molecule is represented by a spherical particle with a "map" of attractive regions covering a fractional area a of the surface. In our work maps consisted of s non-overlapping spots of equal area on grids formed by equidistant meridional lines intersected by lines of constant latitude. As in the isotropic square well [9], particles i and j are said to be neighbors if the distance $\mathbf{r}_{ij}$ between the centers of the two particles lies within $\sigma < \mathbf{r}_{ij} < \lambda\sigma$ (where λ is the reduced range of interaction and σ is the diameter of the hard core). A particle i is said to make a contact with its neighbor j if the vector $\mathbf{r}_{ij}$ passes through an attractive spot on protein i. The energy is defined as $-\varepsilon/2$ times the number of contacts made by the particle.

When the interactions between proteins cannot be averaged over orientations, the aeolotopic nature of these interactions becomes essential. We have argued that this happens when a particle cannot make all contacts with its neighbors (except, perhaps, in a very few special orientations) [10]. In Figure 1*a* we show the results of our simulations for the probability p_n that a particle cannot make all contacts with n randomly located neighbors for n=3 (squares) and n=5 (circles). Each point represents the results for a different map. As expected, maps with different patterns of the attractive

spots, but the same s and a, have similar probabilities. The lines are the theoretical predictions [10]. When $p_n \approx 1$, only very specific configurations of neighbors allow contacts with all neighbors and the potential is not averageable, whereas when $p_n \approx 0$, all contacts are made in numerous orientations and the aeolotopic potential is averageable. In Figure 1*b* we present the simulation results for $p_n(s,a)=0.5$ for n=3 (squares) and n=5 (circles). For maps whose s and a fall significantly above the open symbols (*i.e.* $p_n < 0.5$) the potential is averageable, below it is not. The lines are the theoretical results [10]. The solid triangle in Figure 1*b* corresponds to the parameters of the map we have used in Figure 2 (s=25, a=0.01).

The key parameter which determines whether an average potential can be used instead of an aeolotopic one is the number of neighbors n. Interactions which are averageable near the liquid-liquid critical point, where n is approximately three [4], may no longer be averageable in the crystal, where $n > 5$. Thus it is not always appropriate to use the same effective potential to describe both the liquid and solid phases.

This conclusion is borne out when we analyze the phase diagram of globular protein solutions. In Figure 2 we show as open symbols the liquidus line (squares) and coexistence curve (circles) measured for the protein γIIIb-crystallin [11,12]. We have previously shown that the isotropic square well model with a reduced range of interaction $\lambda = 1.25$ produces the correct coexistence curve (blue coexistence curve), provided that the depth of the potential has the appropriate temperature-dependence [4]. However the liquidus line predicted using the same potential in the solid (dashed red line) differs significantly from the experimental results [8]. The aeolotopic model provides a much more accurate representation of the liquidus line (blue liquidus line), and accounts in a natural way for the difference in the apparent potentials in the liquid and solid phases.

REFERENCES

1. E.H. Snell, S. Weisgerber and J.R. Helliwell, Acta Cryst. **D51**, 1099 (1995).
2. E.N. Coker, J.C. Jansens, J.A. Martens, P.A. Jacobs, F. DiRenzo, F. Fajula and A. Sacco, Micro. Meso. Mat. **23**, 119 (1998).
3. J. Zhu, M. Li, R. Rogers, M. Meyer, R.H. Ottewill, STS-73 Space Shuttle Crew, W.B. Russel and P.M. Chaikin, Nature **387**, 883 (1997).
4. A. Lomakin, N. Asherie, and G.B. Benedek, J. Chem. Phys. **104**, 1646 (1996).
5. M.H.J. Hagen and D. Frankel, J. Chem. Phys. **101**, 4093 (1994).
6. E. Lomba and N.G. Almarza, J. Chem. Phys. **100**, 8367 (1994).
7. L. Vega, E. de Miguel, L.F. Rull, G. Jackson, and I.A. McLure, J. Chem. Phys. **96**, 2296 (1992).
8. N. Asherie, A. Lomakin, and G.B. Benedek, Phys. Rev. Lett. **77**, 4832 (1996).
9. L.E. Reichl, *A Modern Course in Statistical Physics* (Univ. of Texas Press, Austin, TX, 1980).
10. A. Lomakin, N. Asherie, and G.B. Benedek, Proc. Natl. Acad. Sci USA **96**, 9465 (1999).
11. C.R. Berland, G.M. Thurston, M. Kondo, M.L. Broide, J. Pande, O.O. Ogun, and G.B.Benedek, Proc. Natl. Acad. Sci. U.S.A. **89**, 1214 (1992).
12. M.L. Broide, C.R. Berland, J. Pande, O.O. Ogun, and G.B. Benedek, Proc. Natl. Acad. Sci. U.S.A. **88**, 5660 (1991).

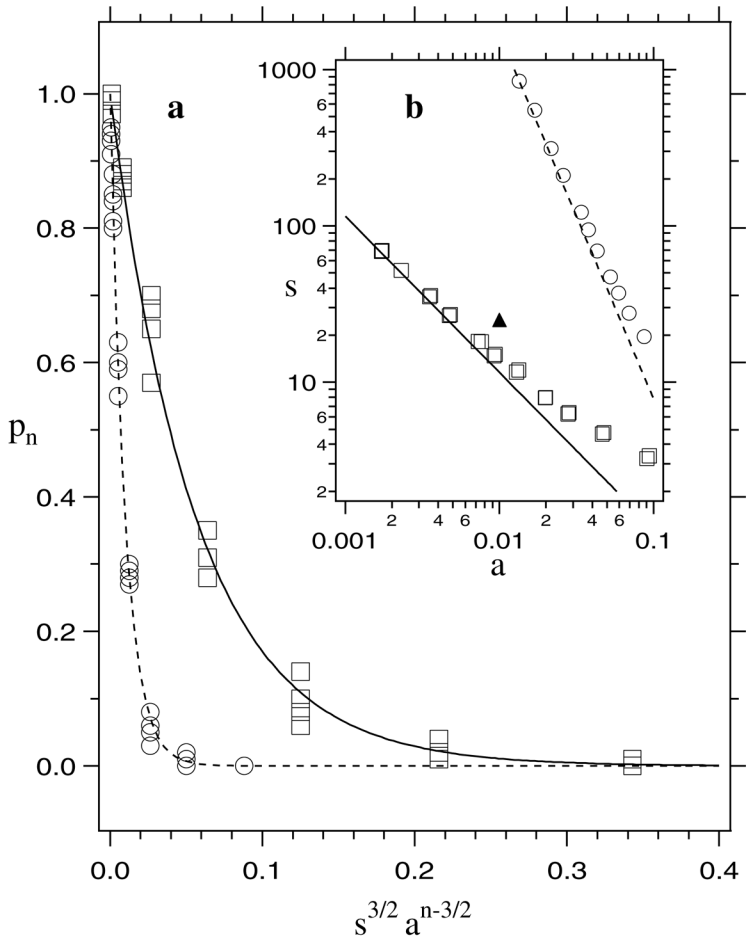

Figure 1. (*a*) The probability p_n of not making all *n* contacts. The open symbols are the simulation results for *n*=3 (squares) and *n*=5 (circles). The theoretical results for *n*=3 (solid line) and *n*=5 (dashed line) are also shown. (*b*) The boundary for averaging the potential. The open symbols are the simulation results for *n*=3 (squares) and *n*=5 (circles). The lines are the theoretical results expected for *n*=3 (solid) and *n*=5 (dashed). The solid triangle corresponds to the parameters of the aeolotopic model used in Figure 2.

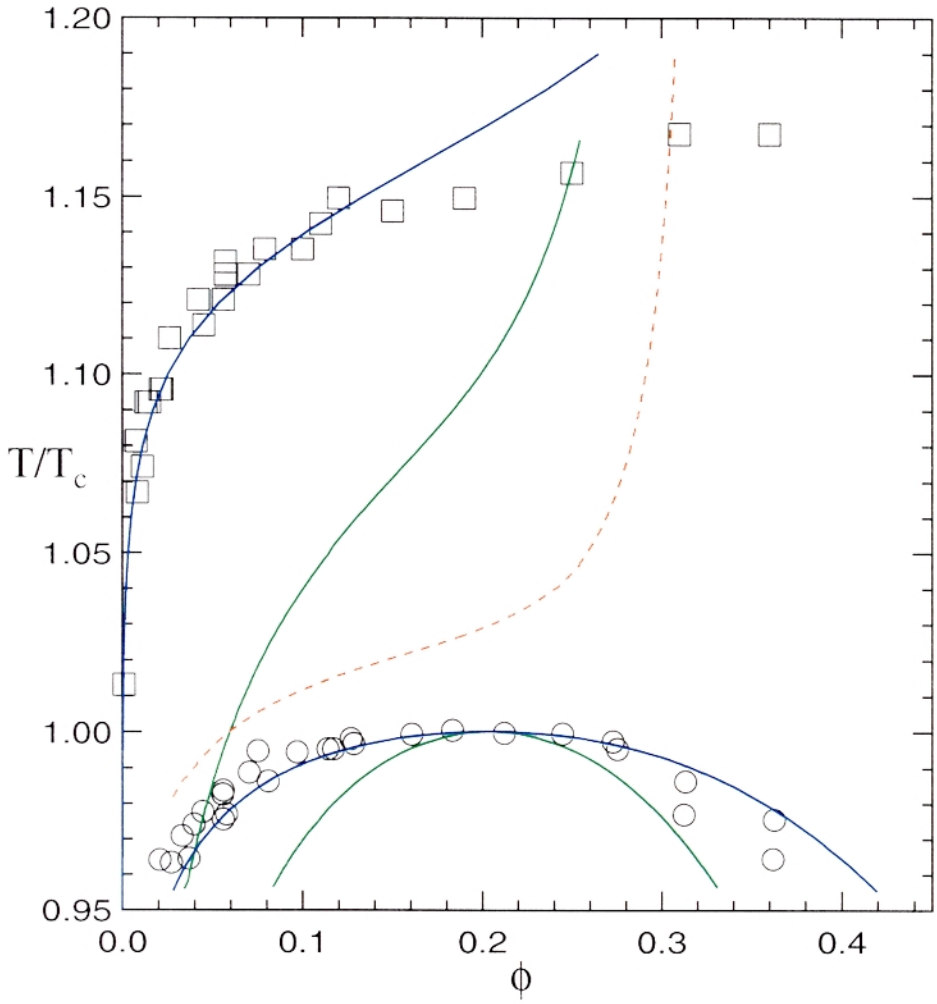

Figure. 2. The phase diagram of γIIIb-crystallin. The open symbols are the experimentally determined liquidus line (squares) and coexistence curve (circles). The green lines are the predictions for the boundaries assuming temperature-independent isotropic square well interactions. The blue lines are the predictions of the aeolotopic model.

THEORETICAL INVESTIGATIONS OF THE MECHANICAL AND ELECTRICAL PROPERTIES OF CARBON NANOTUBES

Jerry Bernholc and Christopher Roland

Department of Physics, NC State University, Raleigh, NC 27695

Carbon nanotubes are perhaps one of the more interesting of the new materials to emerge from recent scientific research. This excitement and interest derives largely from the unusual mechanical and electrical properties of nanotubes, which should allow for unique applications of interest to NASA. For example, nanotubes are predicted to be superstrong, lightweight fibers with remarkable resilience to strain. Nanotubes may therefore provide the basis for a new class of composites, as well as providing a fundamental structural component at the nanometer length scale. Turning to their electronic properties, nanotubes may be either metallic or semiconducting, and therefore have the potential of forming the basis of a future, all-carbon nanotube-based microelectronics. On our presentation, we will give a brief description of our theoretical investigations of nanotubes, with a focus on their mechanical and electrical properties. The studies were carried out with a series of complementary numerical methods covering different length and time scales, including *ab initio* and classical molecular dynamics simulations methods.

While the outstanding mechanical properties of carbon nanotubes have already been explored theoretically, there has been, until recently very little understanding of the microscopic origins of these mechanical properties. Our studies show that it is the high strength of the sp^2 bond, combined with the remarkable flexibility of the hexagonal network that plays a crucial role in these enhanced properties. Detailed classical and quantum simulations of the strain release mechanisms of nanotubes under tension show that the excess strain is released by the formation of a (5-7-7-5) defect via the rotation of a carbon-carbon bond about its center [1]. Such a defect is formed spontaneously under tensions of 5 %, or more and marks the onset of further transformations, either via plastic transformation (separation of dislocation cores) or brittle (crack formation and extension). Because of the anisotropic nature of the graphene sheet comprising the nanotubes, the specific response of the nanotube depends on the helicity of the nanotube - i.e., the way in which the graphene sheet is rolled. We have therefore calculated a map of the different response of the nanotubes towards strain [2], shown in Figure 1. Roughly speaking, ductile behavior is associated with armchair (n,n) nanotube, while brittle behavior is characteristic of (n,0) zigzag tubes.

To the best of our knowledge, this is the first such classification of the material properties of a such a material.

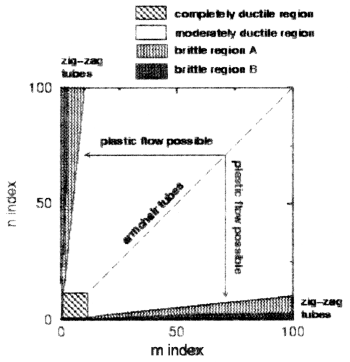

Figure 1. Ductile-brittle domain map for carbon nanotubes with diameters up to 13 nm. Different shaded areas correspond to different possible behaviors, as discussed in detail in Reference [2].

Furthermore, we have also investigated the mechanical properties of nanotubes in the presence of ad-atoms and ad-dimers [3]. Most interesting, in the presence of ad-dimers a new set of defects form which consist of rotated hexagons separated from the rest of the nanotube via (5-7) pairs, as shown in Figure 2. Under tensions of 5-10 %, it is favorable for the number of hexagons in these extended defects to increase ultimately forming a small tube segment having a different helicity thereby allowing for the natural formation of different electronic heterojunctions. Our studies indicate that the formation of such structures is most favorable for zigzag tubes. Thus, ad-dimers induce plastic behavior on tubes that are otherwise brittle in a controlled manner, as shown in Figure 3.

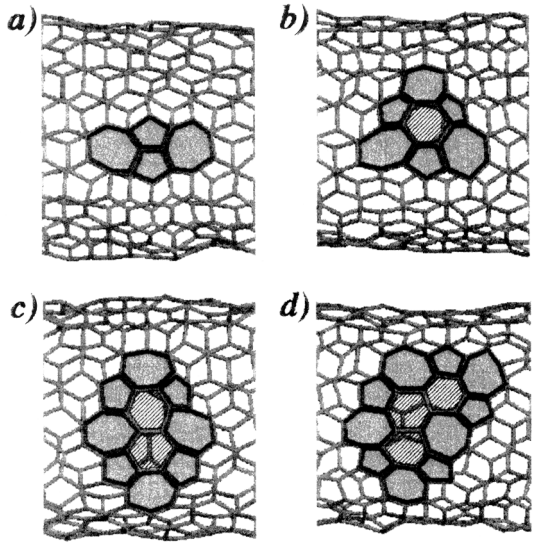

Figure 2. Sample configurations showing the time evolution of a carbon ad-dimer on a (10,10) nanotube under 3% strain: (a) (7-5-5-7) defect forms after 4 ps; (b) bond rotation leads to defect with one rotated hexagon at 346 ps; (c) two hexagons at 421 ps; and (d) three hexagons at 2.35 ns.

Since identification of the different defect structures will mostly be via scanning tunneling microscopy (STM), we have simulated images of these native defects on carbon nanotubes using a standard tight-binding model [4]. For the most part, the simulated STM images show a strong correlation with the underlying atomic structure. The images are for most part unique, and are dominated by "rings" that are associated with the pentagons inside the defect. We have also simulated STM images of different electronic heterojunctions, such as quantum dots and MIMs of

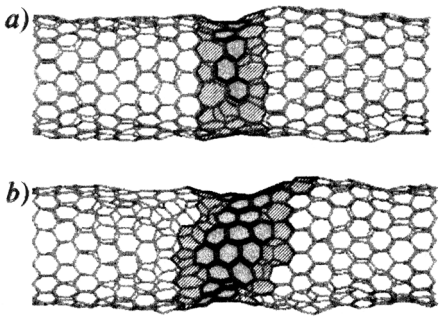

Figure 3. Time evolution of a (17,0) nanotube with an ad-dimer under 7.5% strain at 3000 K, illustrating the spontaneous winding of the defect around the tube: (a) the initial configuration consisting of a single turn, and (b) the final configuration corresponding to about three turns after 1 ns.

various sizes. These images are for the most part dominated by the (5-7) pairs at the edges of the defects: the sandwiched tube only becomes apparent when the structures are sufficiently elongated. An example of such an STM picture is shown in Figure 4.

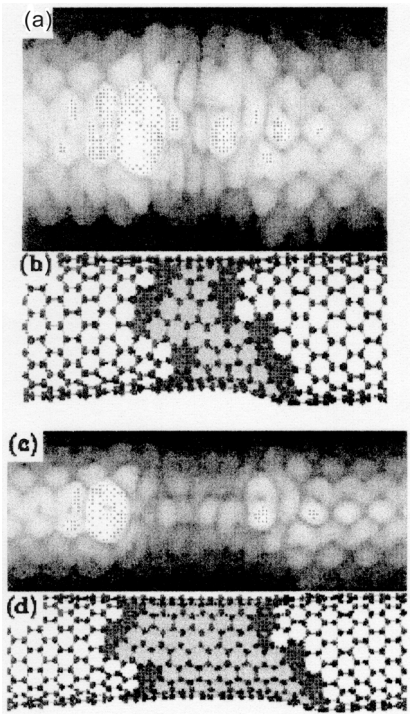

Figure 4. STM images of (17,0)/(8,8)/(17,0) carbon nanotube heterojunction: (a) and (b) show the STM image and the corresponding atomic geometry; (c) and (d) the same for the heterojunction with the (8,8) section artificially enlarged. For more details, see Reference [4].

Turning to the electronic properties of carbon nanotubes, it has already been noted that nanotubes have the potential of forming a microelectronics. Progress has been rapid, and some prototypical devices have already been explored with nanomanipulators. In order to investigate the conductance of nanotubes, one of the key components needed to calculate I-V curves at the nanometer length scale, we have combined standard tight-binding formalism and an orbital-based *ab initio* approach [5] with a Green's function based formalism and used the Landauer formula to calculate conductances [6].

Initially, our studies have focused on the strain-induced defects discussed previously [1-4], both on pristine tubes and in the presence of ad-dimers. We find that the effects of the defects on the conductance is relatively modest, so that it is unlikely that one can associate a specific conductance signature with any given defect. As expected, defects usually decrease the conductances because of enhanced backscattering effects. Many of the defects also lead to significant "dips" in the conductance, either slightly above or below the Fermi level. These effects are due to defect-induced localized states, which show up as peaks in the local density of states, and as the rings associated with the STM images already mentioned. Concerning transport through the different electronic heterojunctions, there was no DC transport through the specific structures examined, without significantly shifting the bias voltages, despite the significant number of states that are induced within the gaps [4]. We have also examined much more distorted geometries such as bent carbon nanotubes [7]. Bent armchair nanotubes keep their metallic character for most practical purposes, even though there is an opening of a small symmetry-related pseudogap for small diameter tubes. Metallic chiral nanotubes undergo a bending-induced metal-semiconductor transition that manifests itself in the occurrence of effective barriers for transmission, while bent zig-zag tubes were always found to be semiconducting for the diameters considered. Topological defects were always found to increase the resistance of the metallic nanotubes to an extent that is strongly dependent on their density per unit length. Finally, open-ended nanotubes that are put in close proximity with each other were found to rebond and form conducting electrical contacts [7]. These results provide a clear interpretation of some recent experimental findings, and suggest avenues for their uses as devices.

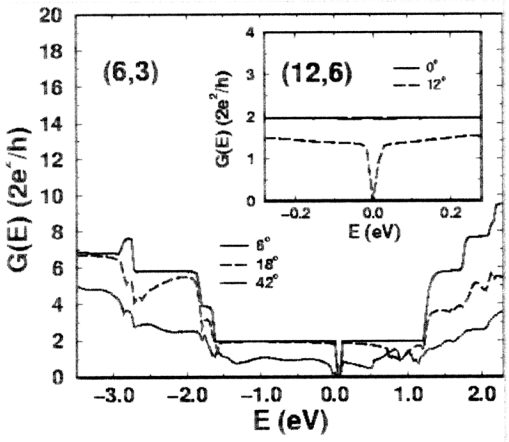

Figure 5. Conductance of a bent (6,3) chiral nanotube. Different curves correspond to different bending angles: 6°, 24°, and 42° as shown in the legend. Inset: conductance of a bent (12,6) chiral nanotube for 0°, 12° angle. The Fermi energy is taken as reference. For more details, see Reference [7].

In addition to the DC conductances of carbon nanotubes, we have also studied their dynamic conductances, *i.e.*, the conductance in the presence of AC fields [8]. The AC response of the nanotubes is, of course, complicated, because the time-dependent fields can take the system out of equilibrium. Under AC conditions, electrodynamics shows that displacement currents are induced, which can substantially alter the transport properties of the system. It is absolutely crucial to include the effects of these displacement fields for two fundamental reasons. First, they are needed to ensure conservation of the total current; second, quantum transport must be gauge invariant, which implies that physics depends only on voltage differences. Another important phenomena associated with the AC response of a conductor is that of photon-assisted tunneling: in the presence of a time-varying potential, electrons can absorb photons and thereby inelastically tunnel through other

levels. To investigate AC response of nanotubes, we have used the nonequilibrium Green's function formalism combined with simple tight-binding models. Specifically, the AC response of tubes of different helicities, both with and without defects, and an electronic heterojunction were investigated. Because of the induced displacement currents, the dynamic conductance of the nanotubes differs significantly from the DC conductance displaying both capacitive and inductive responses. The important role of photon-assisted transport through the nanotubes is revealed, and its implications for experiments discussed.

Finally, we have examined spin-coherent quantum transport through a carbon-nanotube based magnetic tunnel junction device, as shown in Figure 6 [9]. This project is based on a recent experiment [Tsukagoshi, Alphenaar and Ago, Nature 401, 572 (1999)], in which nanotubes were contacted to ferromagnetic Co leads. The data showed that the nanotubes have a very long spin-coherence length which was estimated to be about 130 nm. Nanotubes may therefore be ideal candidates for achieving molecular scale magnetoelectronics in which both the charge and spin-degrees of freedom are used in the operation of a functional device. In order to understand these devices, we first studied the behavior of finite-sized nanotubes coupled to metallic jellium leads. The observed behavior is strikingly different from the previous results in that transport is now dominated by length-dependent resonant tunneling, as shown by the sharp conductance peaks of Figure 6. Physically, this resonance behavior may be attributed to scattering at the contacts between the nanotubes and the leads. When the nanotube is contacted by ferromagnetic leads, we find clear evidence of length-dependent spin valve effect of up to 20%. This is shown in Figure 7, which displays the resistance as a function of the magnetization angle of the second lead: when the two magnetizations are parallel, then the resistance is low; when the magnetization is antiparallel, the resistance is high. These results are in complete agreement with the experiments and point to the possibility of forming nanotube based spin-valve transistors at the nanometer length scale, as already achieved in conventional multilayer technology.

In summary, we have examined both the mechanical and electronic properties of carbon nanotubes. The mechanical behavior is dominated by the formation of a (5-7-7-5) defect, which forms spontaneously when the strain is 5 % or more. This defect governs the initial response of the nanotube,

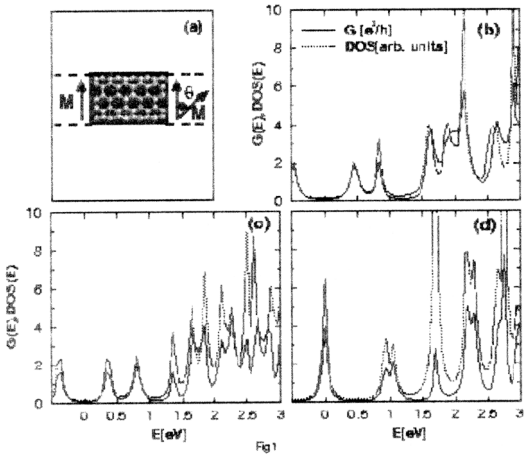

Figure 6. (a) Schematic plot of the nanotube magnetic tunnel junction with ferromagnetic electrodes whose moments point in different directions. (b)-(d) Conductances (solid line) and local density of states (dashed line) for (5,5) nanotubes as a function of electron energy. Here, (b) is for length N=5; (c) N=6; and (c) N=7. For more information about the length-dependence of the nanotubes, see Reference [9].

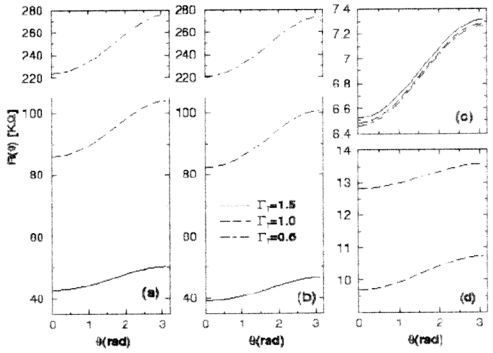

Figure 7. Conductance of (5,5) nanotube device for different coupling parameters and tube lengths, as a function of magnetization angle, as shown in Figure 6a. Results are: (a) for N=5; (b) N=6; and (c) N=7 devices. Note the clear length-dependence of the spin valve effect. Here (d) shows similar results for defective (10,10) nanotubes: lower curve – a (7-5-5-7) defect; upper curve – a (5-7-7-5) defect. See Reference [9] for more information.

and because of the anisotropy of the graphene sheet, determines the brittle versus ductile behavior of the nanotubes. In the presence of strain and addimers, a new set of extended defects form that ultimately can be used to form different electronic heterojunctions on the (n,0) zigzag tubes. To aid in the identification of these defects, we have simulated their STM signatures, which shows their experimental identification should in principle be straightforward. Turning to the electronic properties of nanotubes and their devices, we have investigated their conductances with a Green's function based formalism. Transport properties of defective and bent nanotubes were studied, along with the AC response of nanotubes. Finally, we have also invested the properties of nanotubes that are contacted to ferromagnetic leads. Such devices display a clear spin-valve behavior, which should allow for the formation of interesting spin-based devices.

REFERENCES

1. M. Buongiorno Nardelli, B.I. Yakobsen, and J. Bernholc, "Mechanisms of strain relief in carbon nanotubes", Phys. Rev. B 57, R4277 (1998).
2. M. Buongiorno Nardelli, B.I. Yakobsen, and J. Bernholc, "Brittle and ductile behavior in carbon nanotubes", Phys. Rev. Lett. 81, 4656 (1998).
3. D. Orlikowski, M. Buongiorno Nardelli, J. Bernholc and C. Roland, "Ad-dimers on strained carbon nanotubes: A new route for quantum dot formation?", Phys. Rev. Lett. 83, 4132 (1999).
4. D. Orlikowski, M. Buongiorno Nardelli, J. Bernholc and C. Roland, "Theoretical STM signatures and transport properties of native defects in carbon nanotubes", Phys. Rev. B 61, 14194 (2000).
5. J.-L. Fattebert and J. Bernholc, "Towards grid-based O(N) DFT methods: optimized non-orthogonal orbitals with multigrid acceleration", Phys. Rev. B, in press 2000.
6. M. Buongiorno Nardelli, "A general approach to electronic transport in extended systems: application to carbon nanotubes", Phys. Rev. B 60, 7828 (1999).
7. M. Buongiorno Nardelli and J. Bernholc, "Mechanical deformation and coherent transport in carbon nanotubes", Phys. Rev. B 60, R16338 (1999).
8. C. Roland, M. Buongiorno Nardelli, J. Wang and H. Guo, "Dynamic conductance of carbon nanotubes", Phys. Rev. Lett. 84, 2921 (2000).
9. H. Mehrez, J. Taylor, H. Guo, J. Wang and C. Roland, "Carbon nanotube based magnetic tunnel junctions", Phys. Rev. Lett. 84, 2682 (2000).

DISPERSION MICROSTRUCTURE AND RHEOLOGY IN CERAMICS PROCESSING

J. F. Brady

Division of Chemistry and Chemical Engineering, 210-41
California Institute of Technology
Pasadena, CA 91125 USA
Phone: 626-395-4183
Fax: 626-568-8743
email: jfbrady@caltech.edu

Ceramics provide a potentially very useful class of materials owing to their physical properties; they are light, hard, resistant to abrasion, chemically inert, stable at high temperatures, and excellent thermal and electrical insulators [1]. Further, by casting from a liquid suspension and subsequently sintering, many complex parts and shapes can be fabricated [2]. Although the resultant properties of ceramics can be outstanding, they often suffer from extreme brittleness. This brittleness is caused by the propagation of cracks, which is in turn due to microstructural defects. These defects may be caused by a number of different factors, such as particle agglomeration, migration or segregation prior to sintering, or due to inhomogeneous volume change upon sintering. If a ceramic's microstructure can be controlled and rendered homogeneous prior to (and after) sintering optimal material properties may be realized in an economic way.

Typically, high-performance ceramics are produced using monodisperse submicron-sized particulate suspensions from which the ceramics are cast. By controlling the size and processing a dense uniform microstructure may be formed prior to sintering. This route has met with limited success even though the maximum volume fraction of ceramic particulates that can be achieved prior to sintering is 0.74. The limited success may stem from the fact that a perfect crystal of mono-sized particles has slip planes that yield easily, and from the fact that there is still a large amount of void space that must be eliminated upon sintering.

An alternate approach is to use a mixture of particle sizes [3,4]. It is well know that solids fractions of 90% can be obtained with a bidisperse suspension of spherical particles. And even greater loadings are possible with tridisperse systems. Crystalline slip planes can be eliminated with a mixture of particle sizes. In addition to achieving high solids fractions, and therefore reducing potential sintering inhomogeneities, a mixture of two different types of particles can also impart desirable properties in a 'composite' ceramic. For example, zirconia in alumina has been used to arrest crack propagation owing to the transformation toughening of zirconia under stress [5]. Of critical importance for processing is the fact that particles that differ in size or composition are subject to gravitational phase separation. Hence, processing in a gravity-reduced environment offers substantial benefits.

For bi- or poly-disperse suspensions to be successful, the microstructure must be controlled during processing. It has been observed experimentally that for the same total volume fraction, a mixture of two particle sizes leads to a reduction in the suspension viscosity, with obvious advantages for ease of processing [6-14] . Although there are several heuristic models to explain this viscosity reduction phenomena, there is no fundamental explanation and very little theoretical work has been done. Furthermore, the viscosity reduction is only one factor. Of much greater importance is the microstructure formed during processing, for this determines the ultimate success or failure of the ceramic. As an example of the importance flow has on microstructure, figure 1 shows the flow-induced ordering that can occur in bidisperse Brownian suspensions. To date there have been no experimental studies of microstructure formation during flow of bidisperse suspensions and the results of this study open up the intriguing possibility that one can form highly ordered states by processing. The results in Figure 1, do not include hydrodynamic interactions between particles and it is an open question whether the order will be destroyed upon the inclusion of hydrodynamics.

Figure 2 shows results for the zero shear viscosity of a bidisperse suspension of Brownian hard-spheres at a total volume fraction of 0.45 determined by Brownian Dynamics. The size ratio is 2 to 1. The figure shows the variation in the viscosity as a function of the fraction of small particles, X_s, compared with the experimental results of Shikata, *et al* [15]. The comparison is quite encouraging and shows that the simulations are capable of quantitative predictions.

Future work will be to extend the simulations to a greater range of volume fractions and size ratios. Over what range does the ordering persist? Can one see evidence of phase separation by depletion forces? And how is this influenced by flow? Also, the simulation results are for Brownian particles that do not interact hydrodynamically. For the shear thinning behavior shown here, it is known that hydrodynamic interactions have only a quantitative, and not qualitative, effect on the results. Does this carry over to mixtures as recent experiments suggest? At high shear rates, however, hydrodynamically interacting hard-spheres show shear thickening due to the formation of lubricationally bound clusters of particles. Will these clusters be disrupted by the addition of small particles that can get into the lubrication gaps between the large particles and break the connectivity and thereby prevent shear thickening? To answer this question, we will need to improve the speed of the simulation of hydrodynamically interacting particles and work is in progress in developing a fast O(N ln N) Accelerated Stokesian Dynamics simulation capability. Figure 3 shows that we have a method that scales linearly with the number of particles. This method is currently being extended to bidisperse suspensions.

REFERENCES

1. National Research Council 1989 *Materials Science and Engineering for the 1990s*, National Academy Press.
2. Somiya, S. 1989 *Advanced Technical Ceramics*, Academic Press.
3. Reed, J.S. 1988 in *Ceramic Transactions, Ceramic Powder Science II*, The American Ceramic Society, p.601.
4. Brook, R.J., Tuan, W.H. and Xue, L.A. 1988 in *Ceramic Transactions, Ceramic Powder Science II*, The American Ceramic Society, p.811.
5. Hannink, R.H.J. and Swain, M.V. 1994 *Ann. Rev. Mater. Sci.* **24**, 359.
6. Ferris, K.J. 1968 *Trans. Soc. Rheol.* **12**, 281.

7. Chong, J.S., Christiansen, E.B. and Baer, A.D. 1971 *J. Appl. Polym. Sci.* **15**, 2007.
8. Rodriguez, B.E., Kaler, E.W. and Wolfe, M.S. 1992 *Langmuir* **8**, 3282.
9. Hoffman, R. 1992 *J. Rheol.* **36**, 947.
10. Shapiro, A.P. and Probstein, R.F. 1992 *Phys. Rev. Lett.* **68**, 1422.
11. Chang, C. and Powell, R.L. 1993 *J. Fluid Mech.* **253**, 1.
12. Chang, C. and Powell, R.L. 1994 *J. Rheol.* **38**, 85.
13. Woutersen, A.T.J.M. and de Kruif, C.G. 1993 *J. Rheol.* **37**, 681.
14. Wagner, N. J. and Woutersen, A.T.J.M. 1994 *J. Fluid Mech.* **278**, 267.
15. Shikata, T., Niwa, H and Morishima, Y. 1998, *J. Rheol* **42**, 765.

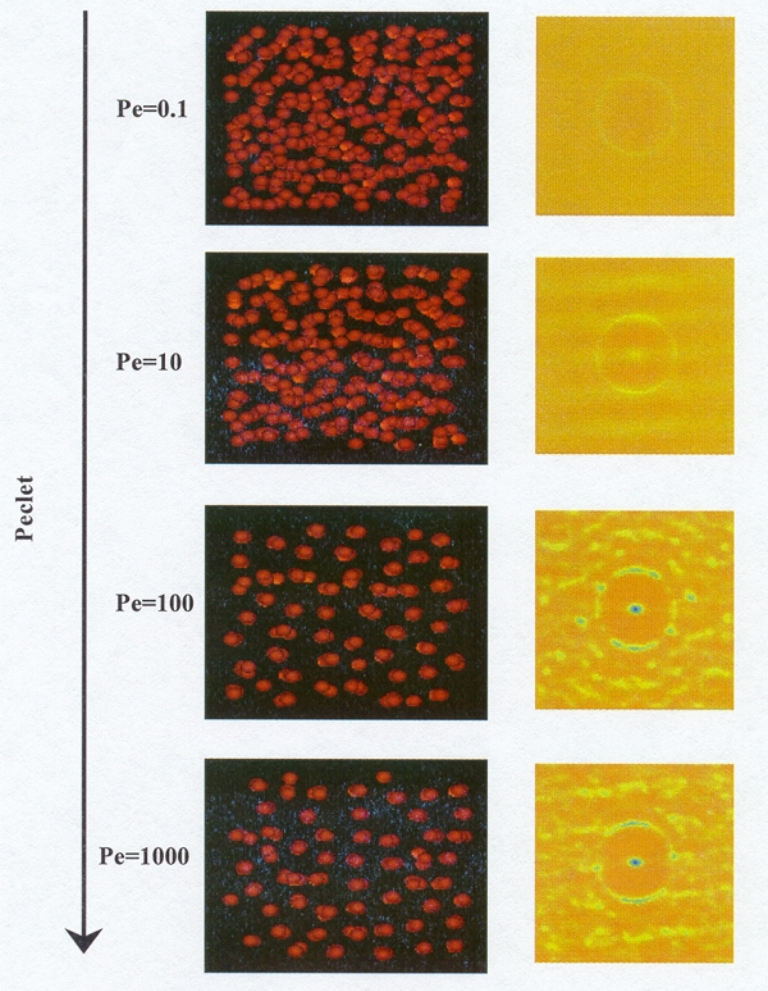

Figure 1. 3-D location plots and 2-D density plots of the large particles in a bidisperse suspension of Brownian hard spheres without hydrodynamic interactions at a total volume fraction of 0.45 for different Peclet numbers (dimensionless ratio of shear to Brownian forces). The size ratio is 2:1 and 75% of the particles are large. The plots display the view looking down the velocity gradient-vorticity plane – the flow is coming out of the page. On the density plots, green color denotes the maximum likelihood of locating a (large) particle at that position while orange designates the lowest probability. As the flow strength is increased the large particles order into flowing strings, which are arranged in an hexagonal pattern. The small particles are located between the strings but are not ordered.

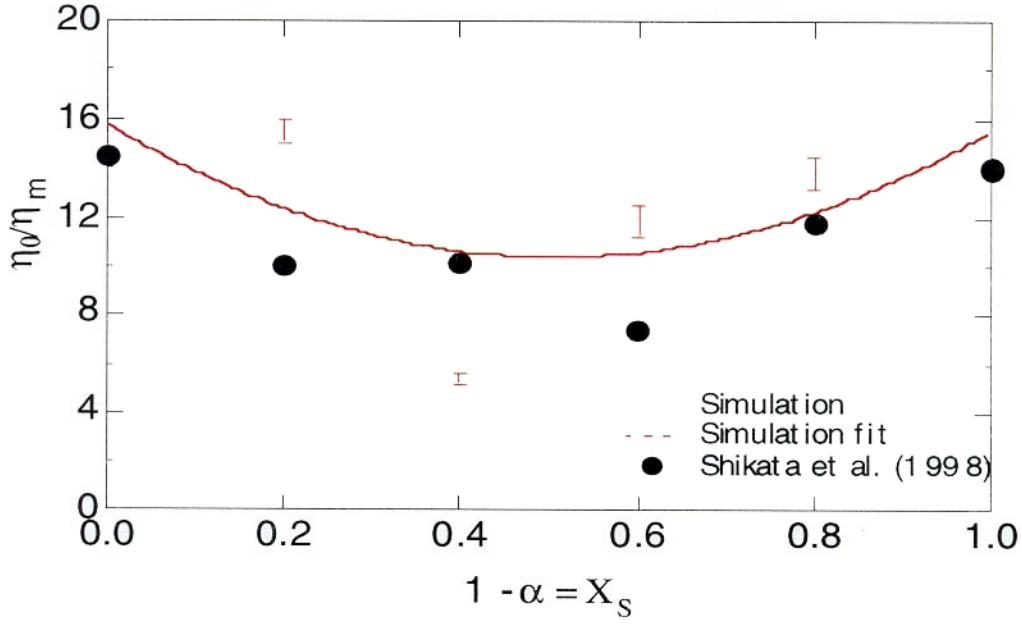

Figure 2. Plot of the dependence of reduced zero-shear viscosity on X_s, the ratio of solids volume fraction occupied by small particles to the total solids volume. The simulation data (bars) are displayed along with a polynomial fit, and the experimental results of Shikata *et al* (1998).

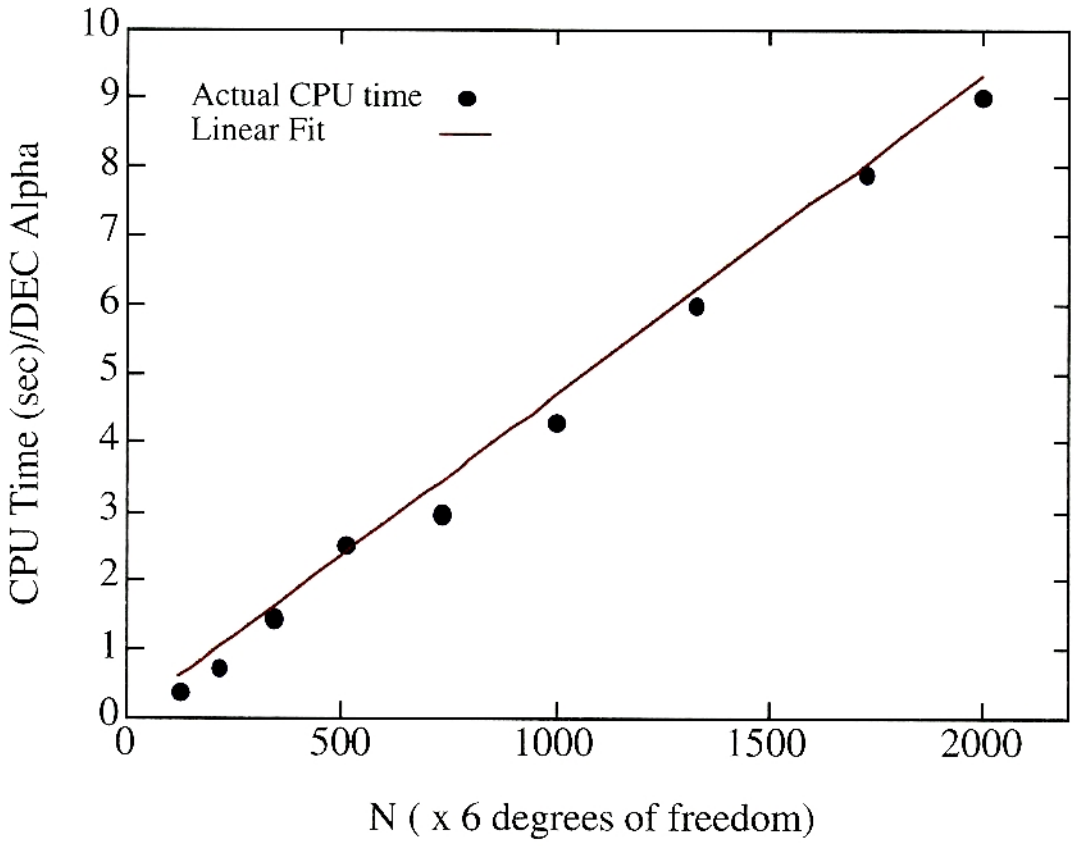

Figure 3. Plot of the CPU time vs. the number of particles in the simulation for the new version of Stokesian Dynamics – Accelerated Stokesian Dynamics (ASD). In ASD full hydrodynamic interactions are included with the same accuracy as conventional SD.

COMBUSTION SYNTHESIS OF MATERIALS IN MICROGRAVITY

Kenneth Brezinsky

Department of Chemical Engineering, M/C 110
University of Illinois at Chicago
810 South Clinton Street; Chicago, IL 60607
(312) 996-9430
Kenbrez@uic.edu

Transition metal nitrides have become increasingly attractive for their distinctive thermodynamic, mechanical, electrical, magnetic and superconducting characteristics; the high degree of melting temperature, hardness, electrical resistivity and magnetic susceptibility are comparable to the corresponding transition metals. In particular, nitrides of the group IV metals in the periodic table, including titanium, represent higher melting temperatures and chemical stability than those of the transition metals in other groups, mainly due to the unique bonding structure between the solid metal and nonmetal components. Accordingly, a detailed experimental study of the self-propagating high-temperature synthesis (SHS) of titanium nitride was conducted to improve the conversion yield and illustrate the mechanism of formation of this representative transition metal nitride. Further investigations are currently under way to apply and build upon the same techniques used for the synthesis of titanium nitride in the SHS of other transition metal nitrides, such as molybdenum nitride and niobium nitride, as well as several carbides produced in solid-solid SHS.

The conditions of the titanium nitride investigation were atmospheric pressure, room temperature and normal-gravity in a fluidized bed of gaseous nitrogen (99.995%) and solid, spherical titanium particles of approximately 50 microns in diameter. Several parameters, such as the strength of the random motion of the fluidized particles, particle size, thermodynamic properties of the fluid and thermodynamic properties of the circulating particles were proven to cause considerable variance in the ignition characteristics of the fluidized bed. For the fluidized bed combustion system, a homogenous dispersion of the titanium particles in the freeboard was necessary. A nitrogen-purged, dual-syringe particle injection system was devised to aid in creating the desired particle distribution and facilitate ignition, Figure 1. The titanium particles were successfully ignited to attain a high conversion yield at the atmospheric pressure condition. This is in contrast to previous investigations in which high-pressure conditions were utilized to aid in ignition and increase the conversion yield.

From this atmospheric system, a maximum conversion yield for the combustion synthesis of titanium nitride of approximately 60% was obtained at a feed rate to the freeboard of 27.0 g/min, Figure 2. The yield decreases from its maximum with both a decrease and increase in feeding rates. The highest conversion yield was ascribed to increased nitrogen accessibility to the precursor particle surface by increasing the interstitial distances between particles in the fluidization to an optimal distance under these conditions.

Analysis of the product composition was performed both qualitatively and quantitatively utilizing several techniques including scanning electron microscopy (SEM), energy dispersion spectroscopy (EDS) and X-ray diffraction. Using the Debye-Shearer method of X-ray diffraction, the product was confirmed to be within 5% of stoichiometric titanium nitride. The X-ray diffraction results also indicated that some of the product nitride contained high concentrations of pure titanium metal, while other product spheres were pure titanium nitride, as indicated by a few intense diffracted rays at the proper Bragg's angle for pure titanium. This was confirmed through analysis of a cross sectional slice of the product nitride. In analyzing a size distributed series of product, two unique morphologies were obtained. Smaller diameter product particles were indeed pure nitride, indicating close to 100% conversion. As particle diameter increased, a residual titanium core appeared that increased in size with a corresponding increase in product particle diameter. This observation of a titanium core was further confirmed by both visual and analytical techniques. Under a high power light microscope, a silvery metallic inner core appeared to be surrounded by a porous gold shell. EDS confirmed the presence of a titanium nitride outer shell and a pure titanium inner core.

The fluidized bed combustion apparatus was applied to the examination of the synthesis of several other transition metal nitrides including niobium nitride and molybdenum nitride. Similar results for each of these nitrides were obtained. No data was confirmed for the yield of these systems due to added ignition sources, such as titanium and sodium azide. There is no published literature on the combustion synthesis of these materials under atmospheric conditions.

Similar trends in morphology for the niobium and molybdenum nitrides to those for titanium nitride were found and confirmed. Size distributions were analyzed and trends also similar to those in the titanium nitride investigation were seen, although the thickness of the nitride shell layer was not as large. This finding indicates that the conversion yields of these transition metal nitrides were probably lower than those of titanium nitride.

Solid-solid combustion synthesis investigations have also been conducted with the fluidized bed apparatus and are currently being continued.

REFERENCES

1. Synthesis of Titanium Nitride," Twenty-eighth Proceedings of the Combustion Institute, 2000 (Accepted).
2. Lee, K.O., Cohen, J.J. and Brezinsky, K.: "Self-Propagating High-Temperature Synthesis of Titanium Nitride," AIAA, 37th AIAA Aerospace Sciences Meeting and Exhibit, Paper No. AIAA 99-0697, Reno, Nevada, Jan. 11-14, 1999.
3. Lee, K.O., Cohen, J.J. and Brezinsky, K.: "Combustion Synthesis of Titanium Nitride under Fluidization," 1998 NASA Microgravity Materials Science Conference, Huntsville, AL, July 14-16, 1998.
4. Lee, K.O., Cohen, J.J. and Brezinsky, K.: "Fluidized Bed Combustion Synthesis of Titanium Nitride," Work-in-Progress Poster (#W2G09), Twenty-seventh Symposium (Int'l) on Combustion, The Combustion Institute, Boulder, Colorado, Aug. 2-7, 1998.
5. Cohen, J.J., Lee, K.O. and Brezinsky, K.: "Combustion Synthesis of Nitride," The Joint Meeting of the United States Section of the Combustion Institute, Washington, D.C., Mar. 14-17, 1999.

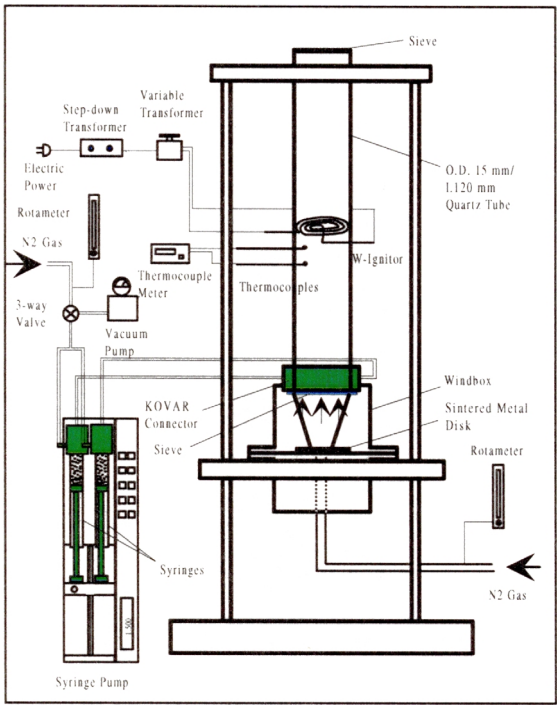

Figure 1. A nitrogen-purged, dual particle injection system.

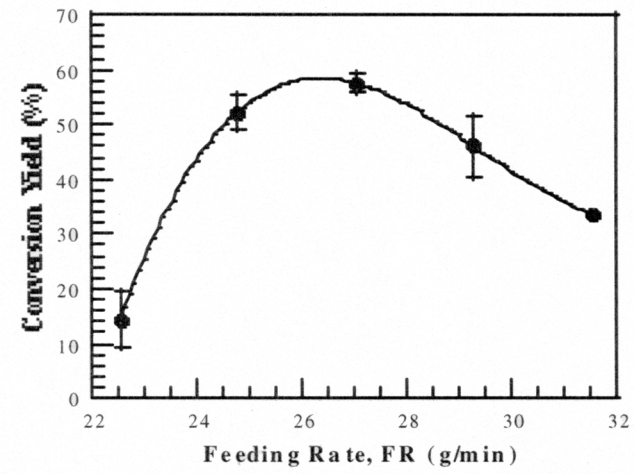

Figure 2. Maximum conversion yield for the combustion synthesis of titanium nitride obtained at a feed rate to the freeboard of 27.0 g/min.

STUDY OF DEVELOPMENT OF POLYMER STRUCTURE IN MICROGRAVITY USING ELLIPSOMETRY

Georgi Georgiev, David Berns and Peggy Cebe

Tufts University
Department of Physics and Astronomy
Science and Technology Center
Medford, MA 02155

Crystalline or liquid crystalline polymers processed from solution or from the quiescent melt exhibit optical birefringence as a result of formation of superstructures, such as spherulites, axialites, dendrites or liquid crystalline phases. In other types of processing, stresses imposed on the polymer during processing result in anisotropic alignment of the polymer chains, leading again to birefringence. The first objective of this investigation is to provide a method for real-time, *in-situ* characterization of optical anisotropy which can develop in polymeric materials processed or treated in the microgravity environment. Our method of choice for optical characterization is a variation of ellipsometry based on Stokes analysis [1,2]. We use ellipsometry to measure the retardation and azimuthal angle of optically anisotropic polymeric materials in real-time, during processing or treatment. In addition, the embodiment of the method provides two-dimensional, i.e., spatially resolved, information about the optical parameters across the field of view. Unlike conventional reflection ellipsometry with coherent light sources, our method uses transmission of monochromatic, incoherent, light for image analysis. High speed detection allows image collection at video rates. A second objective of the work is to apply this novel instrument to ground-based studies of the development of structure in polymeric, and liquid crystalline polymeric (LCP), materials. We aim to provide fundamental information about the formation of optically anisotropic structure, including measurement of phase transformation kinetics and development of textures.

The construction of the instrument has now been completed. As shown in Figure 1, the instrument consists of the following components: (1) monochromatic, incoherent light source; (2) heat absorber; (3) interference filter; (4) mirror; (5) fixed-orientation linear polarizer; (6,7) precision universal compensator comprising two voltage-controlled liquid crystal variable phase retarders; (8) sample mounting stage with manual translation and rotation; (9) long working distance objective lens; (10) left circular analyzer; (11,12) CCD camera; and, (14) computer for data collection and analysis of images with frame grabber card and software. For high temperature work, a Mettler hot stage (8) and its controller (13) are used.

The variable phase retarders and the camera have been interfaced to the computer. Computer programs have been written to vary the voltage, hence the phase, of the retarders systematically, so the polarization state of the incident light passes through four well-defined states of ellipticity. Intensity is collected and analyzed at every pixel in the camera's CCD array. Computer programs have been written for intensity collection and analysis. A set of four equations, based in Stokes analysis [1], is solved simultaneously and the result gives the sample retardation, δ (where $\delta = (2\pi/\lambda)\, d\Delta n$, and λ is the incident light wavelength, d is the thickness of the sample, and Δn is the sample birefringence) and the

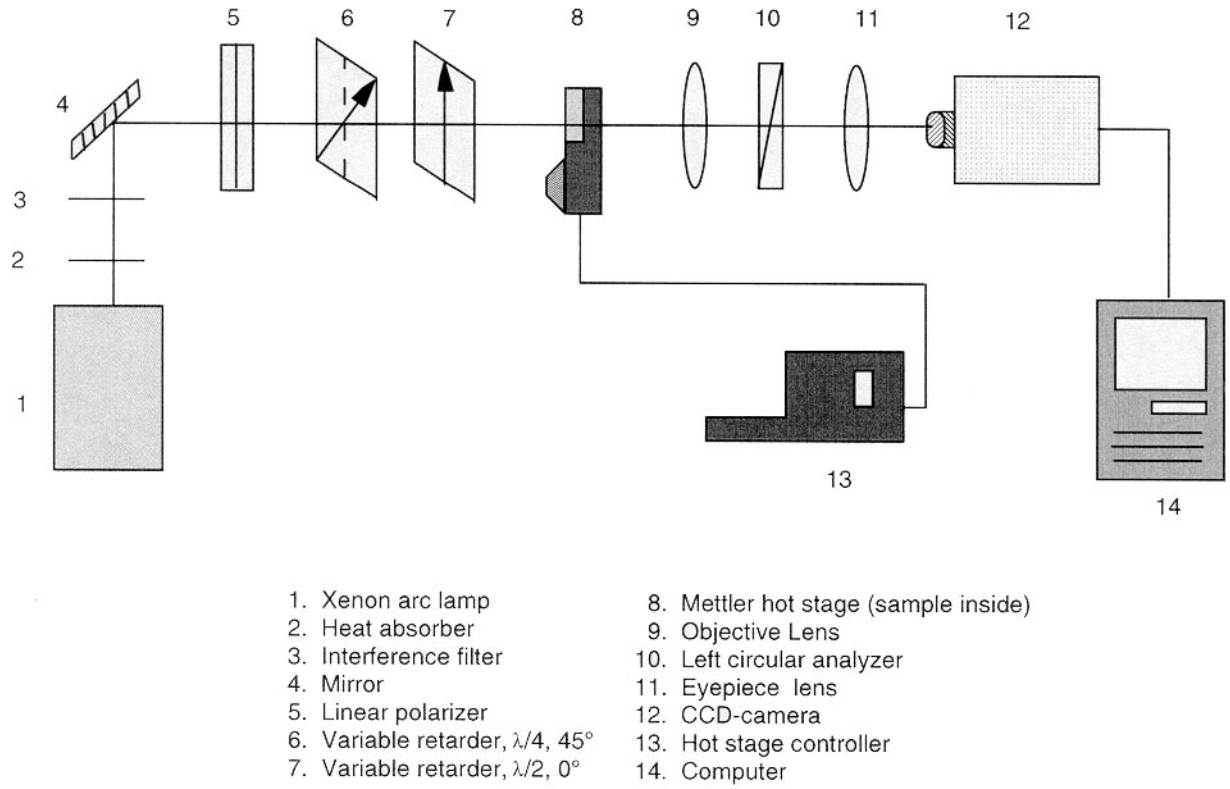

Figure 1. Experimental set-up for the Spatially Resolved Transmission Ellipsometer.

azimuthal angle, ϕ. The retardation is obviously known only to within factors of 2π. The azimuthal angle relates the position of the sample's uniaxial optic axis to the laboratory reference state of initial linear polarization.

For test measurements, a cell comprising a uniaxial liquid crystal (LC) display was studied [3]. Two Indium-Tin-Oxide (ITO) coated glass slides were coated with a polymer alignment layer by spin casting. The conducting but transparent ITO allows a voltage to be applied across the cell without deteriorating the transmitted optical signal. The cell gap was established by using microrod spacers in a UV curable epoxy. Nematic liquid crystals filled the cell by capillary action. An alternating sinusoidal voltage was supplied to the cell by a frequency generator, at oscillation frequency of 1kHz. The oscillatory voltage is used in preference to dc in order to avoid degradation of the electric field caused by mobile ionic impurities which tend to plate out at the electrodes. Initially, with no voltage applied to the test cell, the optic axis of the nematic liquid crystals lies nearly perpendicular to the travel direction of the incident radiation (perpendicular to the surface normal of the LC cell). As voltage is applied, the optic axis rotates as the individual liquid crystal molecules behave as dipoles in the applied field. With increasing applied voltage, the optic axis becomes aligned more nearly parallel to the travel direction of the incident radiation (parallel to the surface normal of the LC cell).

As shown in Figure 2, with our instrument, we track the orientation of the uniaxial optic axis, and the sample retardation, as voltage increases from 0 to10.0 volts in steps of 0.1 volt. The retardation of the test cell cycles through 10π radians over this range of applied voltages. The retardation is resolved to 0.02π radians, or ~11nm for light of wavelength 550nm. In this test cell, the thickness does not vary as a function of voltage. Therefore, the measured retardation can be assigned solely to the variation in Δn. As the extraordinary axis aligns through its 90° rotation (from perpendicular to parallel to the cell's

surface normal), the LC cell behaves as a variable retarder, providing retardation from 0 to 10 π radians. Here, with knowledge of the initial state of zero birefringence at zero voltage, we are able to calibrate the retardation changes exactly.

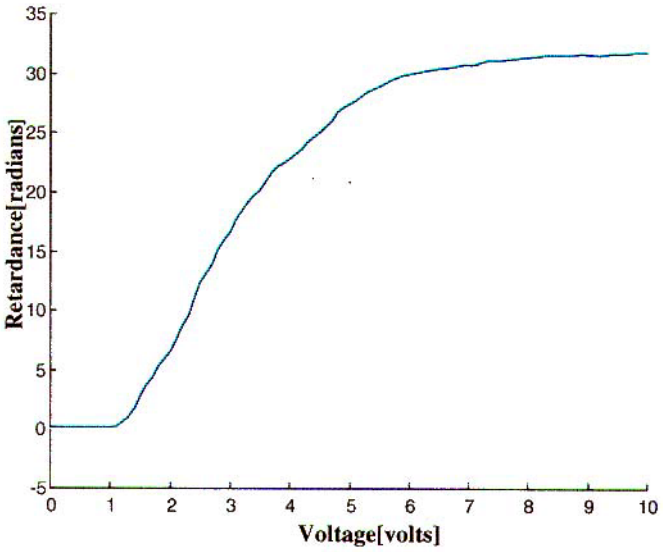

Figure 2. Retardance versus voltage calibration curve for the Liquid Crystal cell. The retardance changes over a range of 10 π radians as applied voltage changes from 0 to 10 volts (at a frequency of 1kHz).

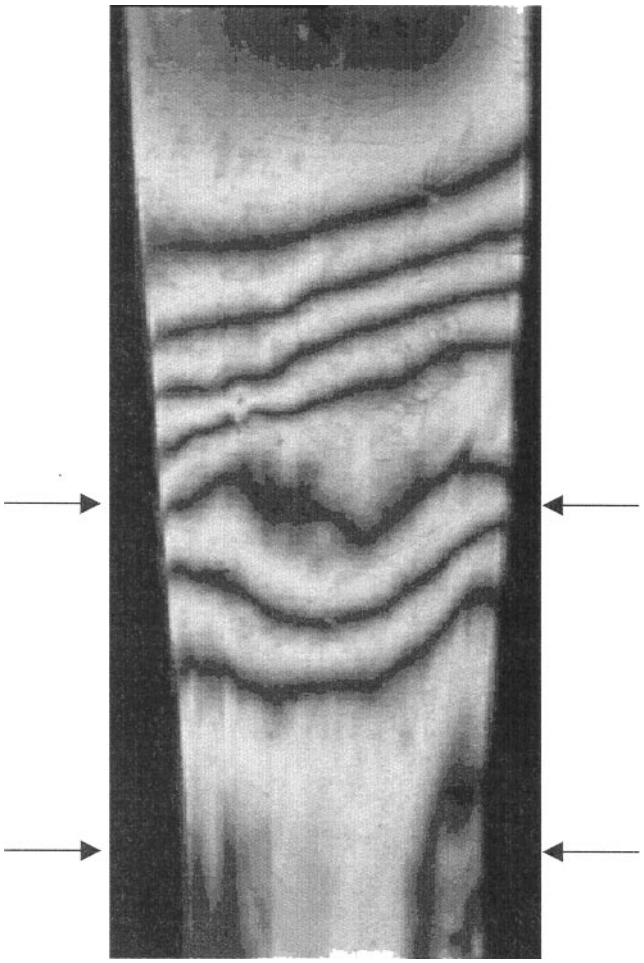

Figure 3. Area of the sample near the advancing neck of drawn sample of metalocene polyethylene. The orientation of the polarizer and the analyzer is +/- 45° to the vertical and the direction of the applied drawing stress is vertical. The arrows indicate an area for which the retardance is mapped in Figure 4.

Next, we demonstrate the measurement of retardation in a drawn sample of polyethylene film. Thick films were made by compression molding pellets of metallocene polyethylene (m-PE) at 200°C between Kapton™-covered ferrotype plates [4]. The m-PE pellets were Exceed 350D60, from EXXON. The melt flow index was 1.0 g/10min., and the material had M_n=43,390 and M_w=112,600 [5]. Films were cut into thin strips and subjected to zone-drawing at elevated temperatures following the zone-drawing technique of Kunugi's group [6]. The sample studied here was drawn at 30°C, with a dead weight of 500g producing a drawing stress of 3.3MPa. Fiduciary marks on the sample allowed the draw ratio (final length/initial length) to be calculated at 1.4. When examined between crossed polarizers, as shown in Figure 3, the sample exhibited a very irregular pattern of birefringence in the portion of the film near the advancing neck. The direction of the applied drawing stress is vertical in the Figure, and the polarizer and analyzer are oriented at +/- 45° to the vertical.

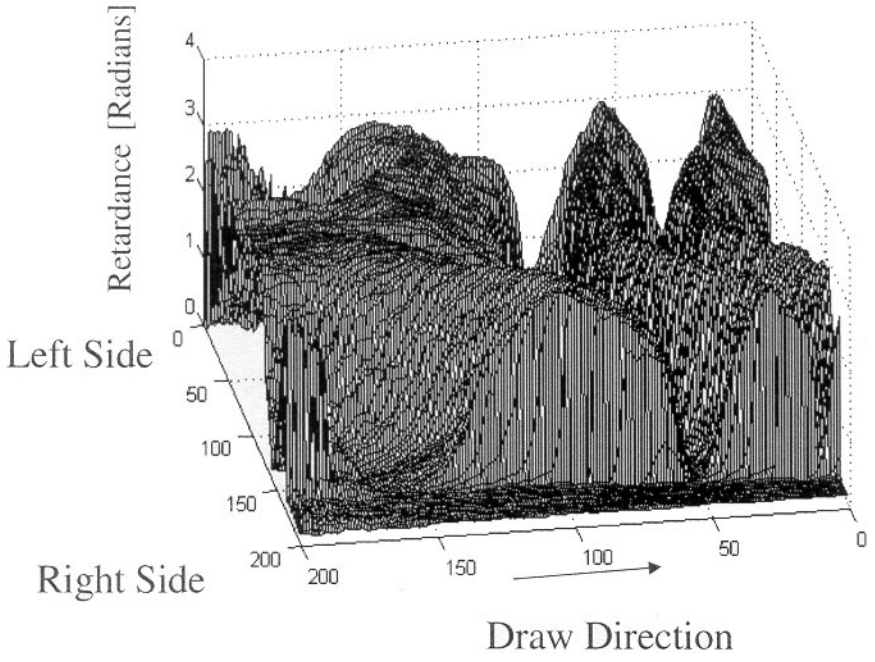

Figure 4. Three-dimensional retardance map of drawn sample's section shown in the area between the arrows on Figure 3.

Between the undrawn material at the top of the Figure, and the fully drawn material at the bottom, there is a zone of high birefringence indicated by alternating light and dark stripes across the sample. As seen from the Figure, the width of the sample (and the thickness, which cannot be seen directly) is decreasing from top to bottom. Polymer chains of m-PE are becoming oriented along the draw direction under the applied stress. The combined effects of thickness decrease and chain orientation result in the observed birefringence.

Figure 4 shows the three-dimensional retardance map of the same sample shown in Figure 3. The 3-D view is slightly from above the plane, and corresponds to looking from right to left in Figure 3, with the vertical draw direction indicated. Cyclic variation of retardance is observed. In actual fact, the retardation is steadily increasing. The value of retardation, δ, is known only to within factors of 2π radians and this results in the cyclic variation seen in Figure 4. Knowledge of the initial (undrawn) and final (drawn) birefringence would be needed to resolve the retardance, in cases such as the present one in which extremely large values of retardance are seen.

While the initial study, including instrument construction, is a ground-based investigation, we anticipate that the instrument will be readily prototyped for operation in the microgravity setting. The instrument contains no moving parts and is therefore very robust. The instrument offers several unique advantages over other forms of ellipsometry: it operates in transmission mode; thin films or bulk samples can be investigated; two-dimensional, spatially resolved images are obtained; the optical anisotropy is quantified in terms of retardation and azimuthal angle; temporal resolution of these properties at video rates is possible. Polymer processing from melts or from solution, including crystallization kinetics or polymerization kinetics will be able to be monitored with this instrument. Furthermore, the ground based studies will lead to a fundamental understanding of the formation of optical anisotropy during processing in the gravity environment, with extension to the microgravity environment. This instrument would also be useful in studies of other types of macromolecules such as biological proteins.

REFERENCES

1. M. Born, and E.Wolf. *Principles of Optics : Electromagnetic Theory of Propagation,* Interference and Diffraction of Light, 1999.
2. R. Oldenbourg and G. Mei. *J. Microscopy*, 180(2), 140 (1995).
3. Dr. Lawrence J. Friedman, (Raytheon) provided the LC test cell and independent retardation calibration curve.
4. D. Berns, E. Oyebode, P. Cebe. *Proceedings of the American Chemical Society, Division of Polymeric Materials: Science and Engineering*, 82, 66 (2000).
5. Dr. R. Bamberger, EXXON Corp., private communication, 1997.
6. T. Kunugi, S. Oomori, S. Mikami. *Polymer*, 29(5), 814(1988).

THREE-DIMENSIONAL VELOCITY FIELD CHARACTERIZATION IN A BRIDGMAN APPARATUS: TECHNIQUE DEVELOPMENT AND ANALYSIS

James S. Slepicka, Yi Ge, and Soyoung Stephen Cha

University of Illinois at Chicago

INTRODUCTION

The three-dimensional (3-D) motion of melts is an unavoidable intrinsic problem that arises in crystal growth. It may be the most important physical property, which needs to be accurately characterized for optimization of the processing. The velocity fields are induced even in microgravity space experiments owing to residual gravity and g-jitters. The induced convection can affect the solidification phenomena in various detrimental manners, which causes solute concentration redistribution including end-to-end macro-segregation and radial segregation as well as undesirable temperature variations in a melt. Crystal growth poses challenging experimental restrictions in flow diagnostics, inhibiting the application of conventional planar and point probes. At the current state of both ground- and space-based experiments, appropriate optical diagnostic techniques are thus very necessary to identify the convective velocity effects on crystal growth. The experimental velocity characterization is also vital to the validation and improvement of numerical modeling capability. The goal of this investigation was to develop two unique experimental techniques for measuring 3-D velocity fields closer to a practical state appropriate for microgravity experiments and to apply them to real experimental measurements including a Bridgman crystal growth configuration. The Bridgman configuration is one of the most important basic arrangements and its velocity measurement is of great technological importance. Eventually, application of these techniques can be extended to other space-based experiments through technology perfection and hardware miniaturization, not only for crystal growth but also for other allied areas.

In the proposed research, two major efforts were pursued for detecting 3-D three-component velocity fields: that is, development of stereoscopic imaging velocimetry (SIV) [1,2] based on dual CCD sensor observation and holographic diffraction image velocimetry (HDIV) [3,4] based on double-reference-beam holographic recording. For these techniques, the velocity is detected by observing the motion of fine marker particles, which are dispersed in the fluid and follow the flow streams. The strengths of these two techniques include greater experimental freedom in illuminating and observing convective flow fields. The volumetric illumination for capturing 3-D fields can be arbitrary in direction and cross-sectional shape. The observation direction also does not impose restriction. These two techniques are complementary in nature. SIV is advantageous in system simplicity for building compact hardware and in software efficiency for continual near-real-time monitoring. It, however, exhibits weaknesses of low detection resolution of CCD sensors, causing limitations in spatial resolution, detection area, and dynamic range. The HDIV approach releases these limitations. It is effective for obtaining good spatial resolution

and wide dynamic range from a single observation direction. However, the velocity extraction is rather involved and allows only slow post-processing. Its setup is also complex and its development is less mature than SIV. It is believed that these complementary techniques together can eventually cover a broad range of space experiment requirements including complex or transient phenomena.

I. Description of the Methods and Experimental Results

For SIV, images of individual particles or equivalently data points are not completely recoverable. The data loss mostly occurs during the processes of centroid identification of overlapping particles and particle tracking of crisscrossing tracks. The loss becomes more prominent as the particle density increases. In order to maximize the data recovery and to enhance the measurement accuracy, artificial neural networks were implemented in these processings. Since the previous 1998 NASA Microgravity Materials Science Conference [5], new algorithms have been developed to make the technique more widely applicable. These include new methods for robust camera calibration as well as for tracking of small particle images based on the Hopfield neural networks in global optimization. For tracking, stochastic networks have also been investigated by adding time-decreasing white Gaussian noise based on the independent Wiener processes. The Hopfield networks may take a number of iterations to be able to arrive at a stable state. The networks use essentially a gradient-descent method for the minimization of error energy, and such methods do not usually reach a global minimum. In an effect to achieve enhanced global optimization, stochastic neural networks (diffusion machine) were applied by adding white Gaussian noise based on the independent Wiener process [6,7]. Our two tracking algorithms based on both the Hopfield neural networks and stochastic neural networks were tested with the synthetically generated data of a known flow field. The results were then compared with the output, which was obtained from the original tracks of the known flow field. To study the effects of particle density in the tested flow, the particle population was increased gradually. Table 1 shows the results of particle tracking. The success rates for tracking were 100%, 99.0%, and 98.3% with 200, 400 and 600 particles, respectively, in the field. The successful recovery rates were very high for both methods but the stochastic neural networks performed better. To investigate and test the performance in a more realistic manner, laminar water jets emerging from a circular and square tubes as well as the flow inside the tubes were measured. The tip velocity profiles were in good agreement with the analytical predictions. Figure 1 is the plot of the tip velocity of the circular tube.

The HDIV technique was tested with a breadboard setup for various situations and operational modes for fundamental investigations to characterize important experimental parameters as well as to identify some remedial solutions in addition to those previously reported [5]. 3-D flow measurement and testing was continued with the flow field generated by a falling ball in a vertical test section. A double-pulsed laser was employed to holographically record the horizontally illuminated volume field. An example of the additional velocity field analyzed at a typical section is shown in Figure 2. More accurate methods for out-of-plane component velocity extraction, as compared with the previous developed image correlation approach [3], have been investigated based on two approaches: that is, statistical correlation of image intensity deviations through maximum likelihood estimation and optical Young's fringe analysis [4]. For the correlation approach, the intensity variances of the diffraction images of individual particles were compared. The computer simulation and actual experiments produced comparable results. Figure 3 shows a typical plot of standard deviation (SD) of image intensities. The location where the maximum SD matches is the displaced field position. The approach appears to warrant further investigation to provide the measurement accuracy better than the previous value of $0.2d^2/\lambda$ where d and λ are the image element size and laser wavelength, respec-

tively. The Young's fringe approach utilizes phase-shifted fringe spacing in the Fourier transform domain. It is still in refinement process.

The experimental investigations that have been conducted to measure 3-D flow phenomena with SIV and HDIV techniques allowed performance assessment under realistic environments since the characteristics of these flows have been well understood. Currently, directional solidification under a Bridgman configuration is being experimented with a transparent metal analog as depicted in Figure 4. In the future, all the results from the experiments will be compared with computational modeling and other important parameters will also be extracted.

II. Conclusion

Our theoretical, numerical, and experimental investigations have proven SIV and HDIV to be viable candidates for reliable measurement of 3-D flow velocities for material processing in space or on ground. The strengths of these techniques include greater experimental freedom in volumetric field illumination and observation, both of which impose no restriction in direction and cross-sectional shape unlike conventional particle image velocimetry and holographic techniques. For SIV, the results have demonstrated significant advantages in using the neural networks. For HDIV, no specific particle focusing is required and seeding of higher particle concentration is possible during recording unlike other two-dimensional techniques. The results have demonstrated good agreement between the experimental and analytical velocity profiles. With current activities focused on further improving the processing efficiency and overall accuracy and automation, it is believed that these techniques can become important flow diagnostic tools to meet the increasing demands for measuring flow velocity and particle size in crystal growth and material processing.

REFERENCES

1. Y. Ge and S. S. Cha, AIAA Journal, 38, 487 (2000).
2. Y. Ge and S. S. Cha, in SPIE Proc. on Materials Research in Low Gravity II, 3792, 274, (1999).
3. J. S. Slepicka and S. S. Cha, AIAA J., 35, 1201 (1997).
4. J. S. Slepicka, J. Li and S. S. Cha, in VSJ Proc. on Optical Technology and Image Processing in Fluid, Thermal, and Combustion Flow, Paper AB121 (1998).
5. J. S. Slepicka, Y. Ge, and S. S. Cha, NASA Microgravity Materials Science Conference, Pub. NASA/CP-1999-209092, Huntsville, AL, (1998).
6. E. Wong, Algorithmica, 6, 467 (1991).
7. J. Biro, Z. koronkai, T. Tron, in IEEE Proc. on International Conference on Neural Networks, 1, 513 (1996).

Table 1. Successful recovery rates of the tracking methods based on neural networks.

Number of particles	Hopfield Neural Networks			Stochastic Neural Networks		
	Correct tracks	**Incorrect tracks**	**Successful recovery rate**	**Correct tracks**	**Incorrect tracks**	**Successful recovery rate**
200	**200**	**0**	**100%**	**200**	**0**	**100%**
300	**299**	**0**	**99.7%**	**298**	**0**	**99.3%**
400	**394**	**6**	**98.5%**	**396**	**1**	**99%**
500	**493**	**6**	**98.6%**	**495**	**4**	**99%**
600	**586**	**14**	**97.7%**	**590**	**5**	**98.3%**

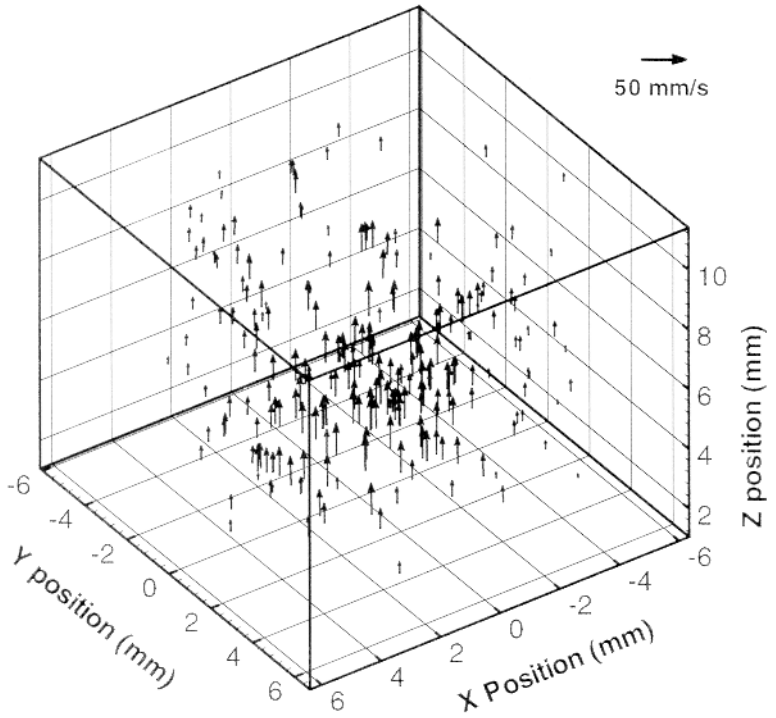

Figure 1 .Three-dimensional velocity field obtained with SIV.

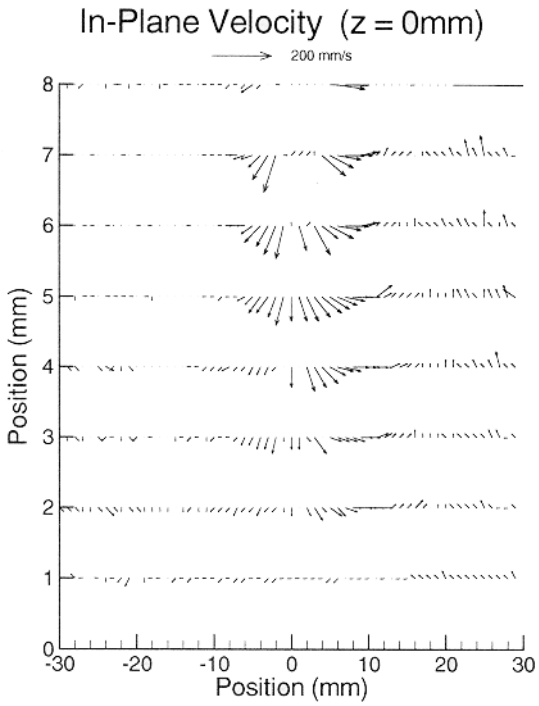

Figure 2. Typical plot of in-plane velocity components for the 3-D flow around a sphere at the center.

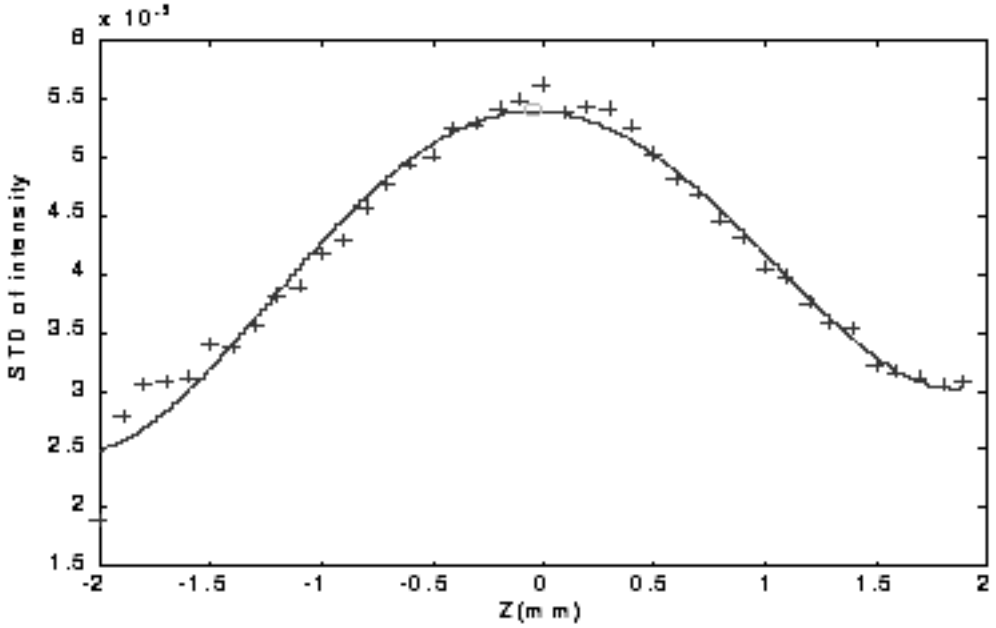

Figure 3. Plot of standard deviations of image intensities.

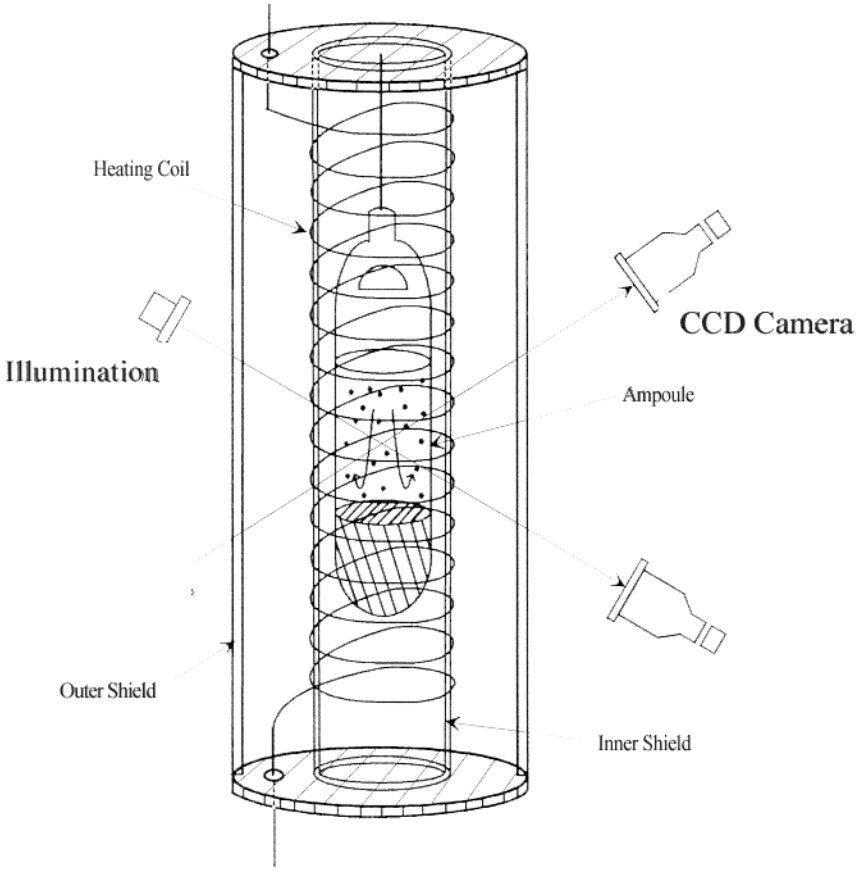

Figure 4. Setup for velocity measurement of directional solidification in a Bridgman configuration.

DIFFERENTIAL PHASE-SHIFTING INTERFEROMETRY STUDIES OF THE ONSET OF MORPHOLOGICAL INSTABILITY OF STEPPED INTERFACES GROWING FROM SOLUTION

N. A. Booth[1], P. Vekilov[1], A.A. Chernov[2]*

[1]Center for Microgravity and Materials Research, UAH, AL 35899
[2]Universities Space Research Association, 4950 Corporate Drive, Suite 100, Huntsville, AL 35806

INTRODUCTION

The general objective of this work is to obtain fundamental insight into the onset and development of morphological instability on stepped crystal interfaces. This problem is part of the general studies of the onset of pattern formation and other self-organizational phenomena in a variety of systems. This phenomenon has added importance as it essentially determines the structure and perfection of the grown crystals. Despite extensive observations and discussions of step bunches, neither their origin, nor their development have thus far been experimentally addressed in a quantitative manner.

I. Basic Concepts

In contrast to rough surfaces that loose stability by forming cellular structures, stepped interfaces loose stability by forming step bunches (see refs 1-5 for summary). To summarize the basic morphological stability concepts consider an ideal vicinal face *i.e.,* a surface deviating from a singular crystallographic orientation by a small angle (Figure 1a) [6-10]. Such a surface is built of elementary steps separated by singular terraces of uniform width. During growth, the steps move in the same direction at a velocity *v*. The growing vicinal face is called morphologically stable if it remains microscopically flat, *i.e.*, the steps remain essentially equidistant. The face is said to be unstable if occasional ripples, *i.e.*, step bunches (Figure 1b) develop. The critical wavelength for stability loss is defined as the threshold discriminating between increase and decrease of the perturbation amplitude in time. For a given initial set of unperturbed slope *p*, normal average growth rate *V* and shear liquid flow rate *S*, the stability condition determines the critical perturbation wavelength, $2\pi/k_x$ (k_x is the perturbation wavenumber, Figure 1b).

The risers of step bunches are built of elementary steps separated by smooth singular terraces of a noticeably smaller width than the terraces between bunches and elementary steps. Thus, the competition between the elementary steps for solute supply via diffusion is more severe within bunches. This leads to the bunch phase velocity (v_x in Figure1) being lower than for widely separated elementary steps. Because of both the lower propagation rate and shorter terrace exposures, bunches trap impurities in amounts different from those trapped by widely separated elementary steps. This leads to internal impurity rich striations propagating through the crystal as it grows [11-12]. Step bunching may also lead

* Corresponding author. Email: Alex.Chernov@msfc.nasa.gov

to the trapping of macroscopic inclusions by the growing crystal. Both striations and inclusions are generally detrimental to the perfection of a given crystal and hence impact on its usefulness *e.g.*, its ability to diffract to high order.

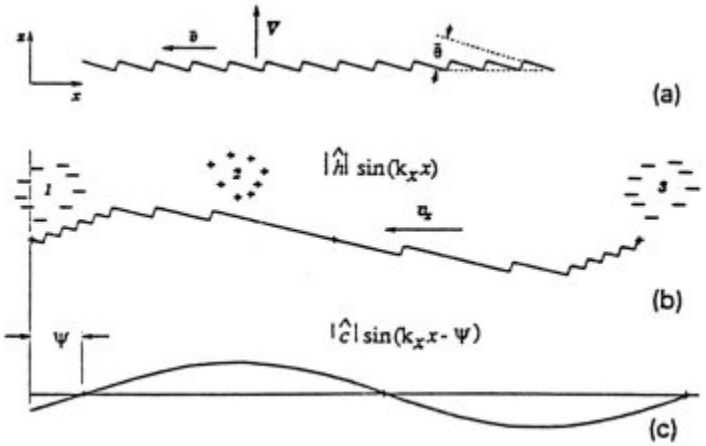

Figure 1. Profile of the (a) unperturbed and (b) periodically perturbed vicinal surface growing at a rate V in the z direction. Asymmetry of the step orientation and thus step motion to the left (at a velocity of v) on the unperturbed face gives rise to a variation in the step density on the perturbed surface. The clouds of "+" and "-" symbolize regions of enriched or depleted solute, respectively, resulting from the variation in step density. The phase shift ψ of the concentration perturbation relative to the interface perturbation is shown in (c) and is responsible for stabilization or destabilization; v_x is the tangential velocity of the step bunches.

Of particular interest is the effect of the direction of solution flow over a surface. Predictions from linear stability theory indicate that a solution flowing above a vicinal face of a crystal can either enhance or prevent the development of step bunches, depending on the direction of the steady shear flow in relation to the direction of step motion; this has also been observed in experiments. Phenomenologically this flow induced stabilization and destabilization is a result of broken symmetry of a vicinal face. The mechanism for this is currently understood as follows: Occasional step bunches caused by various kinds of fluctuations induce decreases in the concentration (and/or temperature rise) in the solution about these bunches. In Figure 1 a simple periodic perturbation (Figure 1b) of an initially flat vicinal surface (Figure 1a) is shown together with the corresponding concentration profile. The less supersaturated clouds (Figure 1b) of the solution are dragged by the flow either up or down the step flow stream, depending on the flow direction. If dragged upstream, the depleted solution comes first to a valley on the perturbed surface and thus causes stabilization. If dragged downstream destabilization is enhanced.

An oscillating flow field will change the concentration above the surface. A quasi-static approximation to the effect of an oscillating flow on the stability of vicinal face has been discussed by Potapenko [13]. A number of crystal growth experiments have demonstrated that alternating fluid flow, *i.e.* solution mixing, essentially diminishes the creation of macrosteps and thus improves crystal homogeneity, eliminating *e.g.* inclusions trapped by these macrosteps. However, step bunches and macrosteps still exist on the crystal surface and the controlled elementary step flow has not yet been achieved. Therefore the question remains how the alternating fluid flow above the growing crystal face influences its stability with respect to step bunching.

II. Experimental Technique

The experimental setup for these studies centers around a phase shifting Michelson interferometer with the growing crystal face being used as one of the two reflecting surfaces. A schematic diagram of our experimental setup is shown in Figure. 2. The crystallization subsystem consists of a thermostated solution circulator, connecting tubing and a crystallization cell. Temperature in the solution circulator is kept constant within 0.02°C by the attached controller linked to a temperature sensor and resistance heater inserted directly in the solution. The solution is circulated through the crystallization cell by the centrifugal pump that allows both flow rate and direction variations. The optical subsystem differs from the classical Michelson interferometry setups by its use of a phase shifter placed between the beam splitter and reference mirror. Phase differences introduced in the reference beam allow the collection of a series of interference images of an object with controlled shifts of the interference fringes. By the use of a suitable algorithm each series of images can be processed to restore the phase of the interference signal and from it evaluate the morphology of the surface. The method of processing the images is described in the Data Analysis section below. The video subsystem consists of a digital camera (Megapixel, 12 bit) capable of collecting 60 images a second interfaced via frame grabbers to a computer.

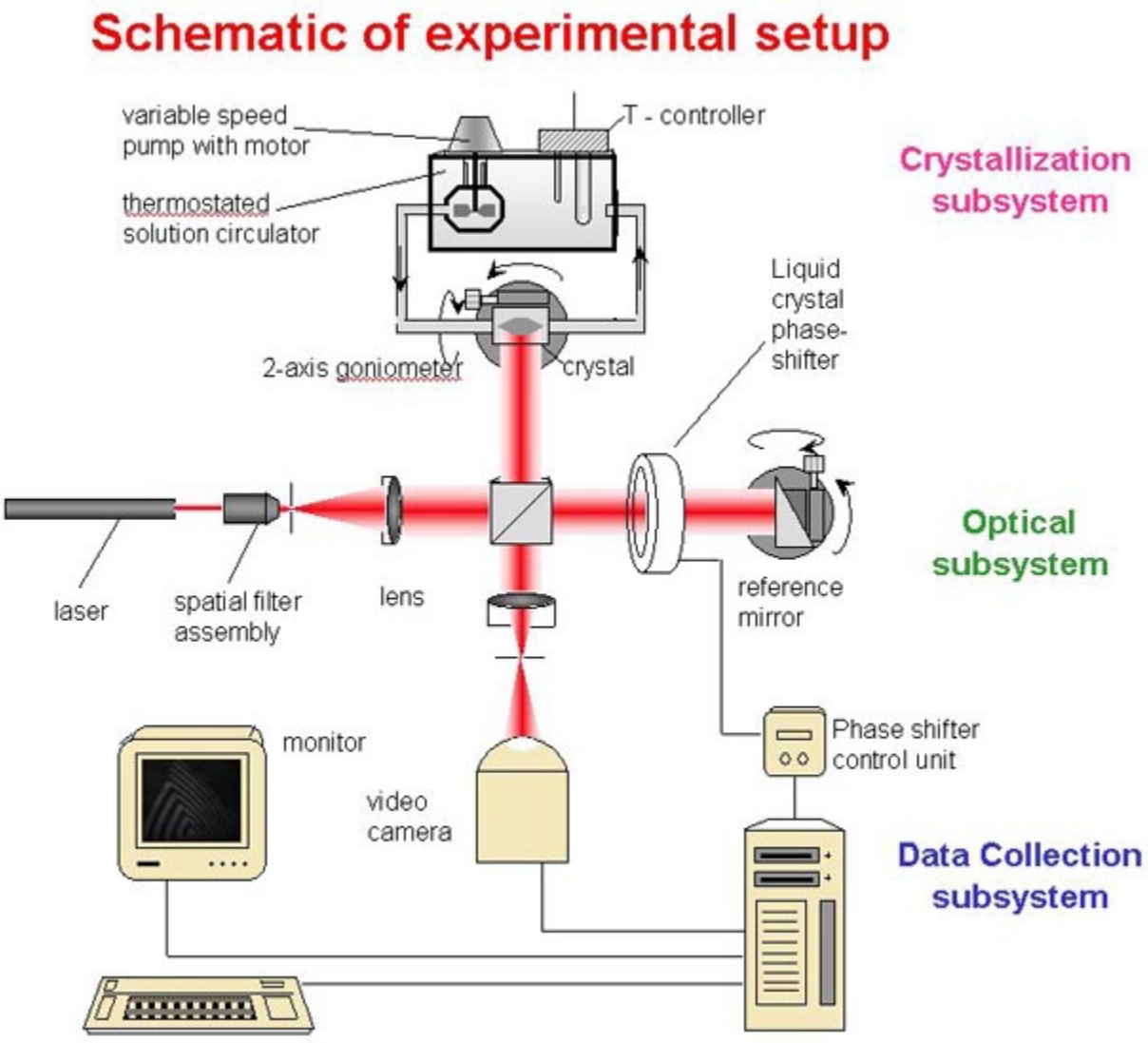

Figure 2. Schematic diagram of the experimental and data collection equipment.

The time to collect a set of phase-shifted images can be estimated as follows. We choose to use a 5-image scheme with a phase difference of π/2 between images, the fifth being identical to the first. The time required for the phase shifter to acquire a p/2 phase change and for the camera to capture an image is around 30 milliseconds, hence the time to collect the 5-image sequence is ~0.15 seconds. A step moving at around 1μm/s passes a distance of 0.15μm for this time. This size is comparable to the size on the crystal surface corresponding to one pixel. Therefore we have the potential to be able to resolve groups of steps consisting of two or three elementary units.

III. Data Analysis

The processing of the series of phase-shifted images is illustrated in Figure 3. Phase shifting interferometry is based on the fact that the phase at a pixel in an interferometric image is proportional to the relative height of the surface area imaged by this pixel. Thus the surface features are averaged over the area corresponding to the pixel, *i.e.* the lateral resolution is determined by the magnification and the pixel size. In the 5-image algorithm that we choose the phase, Φ, and the relative height, *h*, at each pixel are calculated from the five intensities according to the formula shown in Figure 3. In this formula, λ is the wavelength of the laser, *n* is the refractive index of the solution, I_i are the pixel intensities of the i^{th} image, i=1,2,3,4,5. Since the arctangent function takes values in the range (-π/2, π/2) the initial relative surface height profile displayed in Figure 3a breaks at height corresponding to the limits of this range. An algorithm is used to connect the segments and provide a continuous profile as in Figure 3b. The profile in Figure 3c was obtained by subtracting the average slope from the trace in Figure 3b. This shows clearly the variations in local slope across the surface. By repeating this process for every line of data that constitutes the image one can produce a grey scale map of the surface as shown in Figure 4. For the case of the test results from a flat mirror we are able to see the surface roughness of the reflective surface. When applied to a growing crystal face we hope to be able to clearly resolve and trace the progress of macrosteps across it.

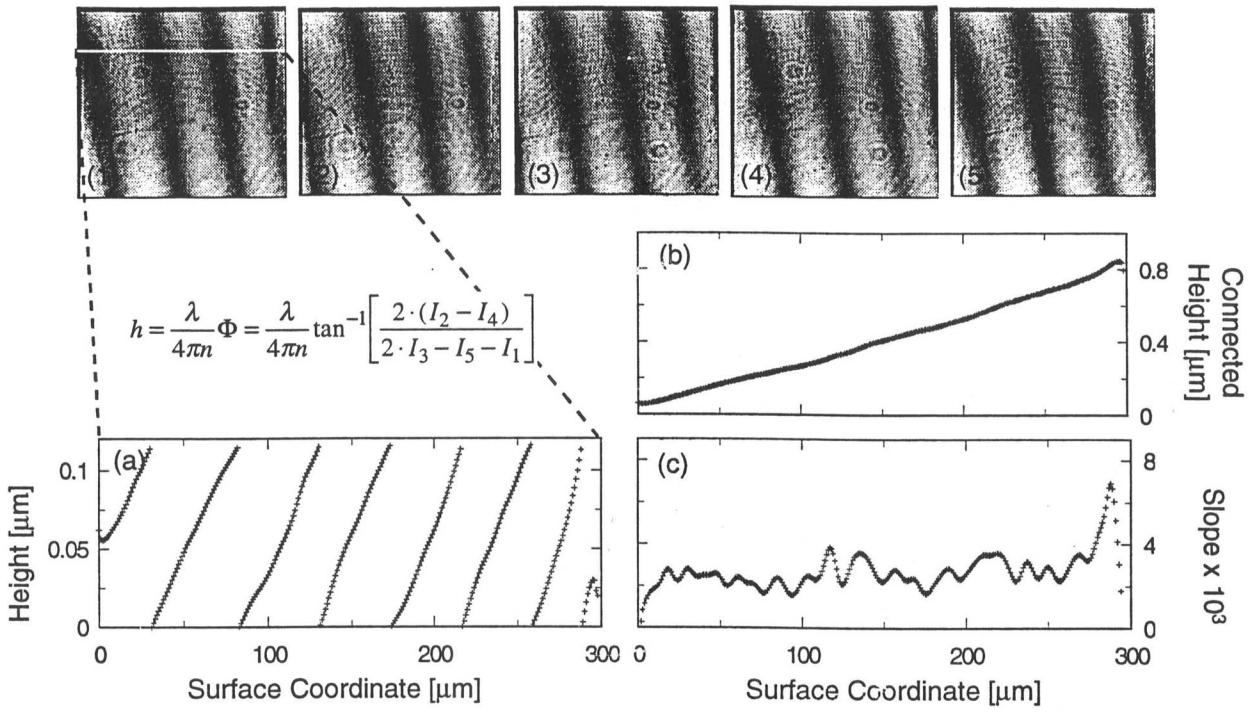

Figure 3. Illustration of the processing of the 5 phase shifted images to obtain surface morphology of a test object (glass mirror).

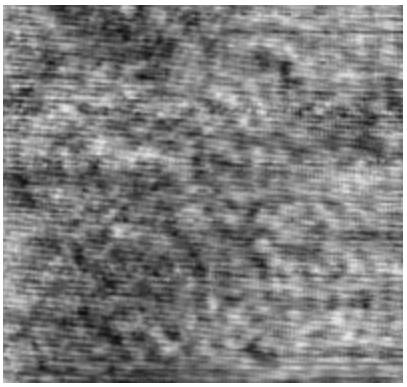

Figure 4. This illustrates a surface plot obtained by repeating the process outlined in Figure 2 over the entire surface. The plot shows the surface roughness of the mirror test surface with an estimated vertical resolution of around 30 angstroms. The image represents a 3 mm x 3 mm square in real space on the surface of the mirror.

IV. Experimental Results

After performing extensive tests we are satisfied that all the experimental subsystems are functioning as intended and we are able to collect repeatable results. Therefore we have commenced studies using a growing potassium dihydrogen phosphate (KDP, formula KH_2PO_4) crystal, images from the first experimental run are shown in Figure 5. The analysis of these results is ongoing.

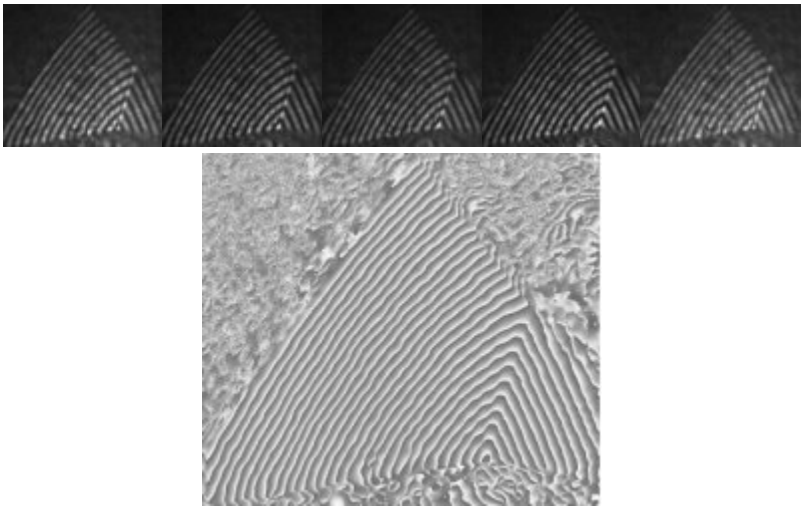

(a)

(b)

Figure 5. (a) Shows the five individual interferograms from a (101) face of a KDP crystal. The result of the 5-image algorithm is shown in (b). Each image represents a 3 mm x 3 mm square in real space.

In cooperation with Drs. B. T. Murray, S. R. Coriell and G. B. McFadden theoretical analysis of an alternating solution flow on the vicinal faces stability has been performed. It was found that the solution flowing over a face parallel to it and alternatively in and counter the direction of the step motion, decreases both the stabilizing and the destabilizing effect of the steady state flow. This alternative flow influences the steady state flow effect when the amplitude of solution oscillations at the distance that the concentration wave induced by the vicinal stepped surface perturbation penetrates is comparable to the perturbation wavelength. This condition provides the criterion for the efficient flow oscillation frequency.

V. Conclusions

We have constructed an experimental setup capable of observing *in-situ* crystal growth. While still in the preliminary stages of operation we are confident that the potential outlined in Experimental Tech-

niques and Data Analysis. The results of theoretical work have suggested that flow oscillations are important when stability is determined mainly by anisotropy of interface kinetics rather than by surface energy.

REFERENCES

1. S. R. Coriell and G. B. McFadden, Morphological Stability, Handbook of Crystal Growth, ed. D. T. J. Hurle, North Holland, Amsterdam, 1993, Vol. 1C, p785
2. M. C. Flemmings, Solidification Processing (McGraw Hill, NY, 1974)
3. S. H. Davis, Effects of Flow on Morphological Stability, ibid, p.860
4. M. E. Glicksman and S. P. March, The Dendrite, Handbook of Crystal Growth, Ed. D. T. J. Hurle, Vol. 1C (North Holland, Elsevier, 1993), P1075
5. J. Krug and H. Spon, Solids Far From Equilibrium, Ed. C. Godreche (Cambridge University Press, Cambridge, 1992), p479
6. A. A. Chernov, J. Cryst. Growth, 118 (1992) 333
7. A. A. Chernov, S. R. Coriell and B. T. Murray, J. Cryst. Growth, 132 (1993) 405
8. S. R. Coreill, B. T. Murray and A. A. Chernov, J. Cryst. Growth, 141 (1994) 219
9. A. A. Chernov, S. R. Coriell and B. T. Murray, J. Cryst. Growth, 149 (1995) 120
10. S. R. Coriell, B. T. Murray, A. A. Chernov and G. B. McFadden, J. Cryst. Growth, 169 (1996) 773
11. T. Nishinaga, K. Pak and S. Uchiyama, J. Cryst. Growth, 43 (1978) 85
12. H. J. Scheel, Appl. Phys. Lett., 37 (1980) 70
13. S. Yu. Potapenko, J. Cryst. Growth 186 (1998) 446

FORCES DURING MANUFACTURE AND ASSEMBLY OF MICROSCALE DISCRETE ELECTRONIC COMPONENTS

Michael J. Cima

Ceramics Processing Research Laboratory
Department of Materials Science and Engineering
Massachusetts Institute of Technology

The proposed research in hybrid assembly will focus on electronic/optical component surface mount challenges for the next century. Discrete components are rapidly decreasing in dimension. Some components are becoming so small that the assembly processes used to mount them must account for static electric charge, van der Waals forces acting through surfaces, other adhesion forces, and, in the not too distant future, Brownian dynamics. Optical system assembly will present the same challenges with the added requirement of ultra precision placement. The dimensions and masses of these components place them at the boundary between ballistic entities (subject to gravity), electrostatic bodies (subject to static surface charge forces), and colloidal bodies (subject to surface and Brownian forces). The assembly processes are also subject to static charge in dielectric media such as air.

The research program will demonstrate controlled electrostatic and electrophoretic forces and the use of radiation pressure for the assembly of small components. Printed areas of electrostatic charge or patterned electrode areas with applied potential will be used to attract charged components to a target. The electric field between the part and target will provide the force necessary to accurately direct the component to its correct position for final placement. The radiation pressure provided by the focused laser beam will be used to direct the component as it moves through air or a liquid medium toward the electrode. The final orientation of the component at the target area will be determined by the shape of the target area on the substrate. This latter feature is a "lock and key" type mechanism like that used with fluidic self-assembly processes.

Both dry and wet assembly methods will be explored. These methods are referred to as electrostatic/shape assembly and electrophoretic/shape assembly, respectively. Electrostatic/shape assembly uses electric charge in much the same way as modern xerographic applications which attract charged toner particles towards charged areas on a photoconductor to create an image. The static charge that can be generated on a free surface in air limits the total charge that can be applied to a component. This limitation occurs because of dielectric breakdown of air (or the ambient gas used in the experiment). An electrical ground plane opposite the charged surface allows image charges to balance the surface charge, so that the electric field is contained almost entirely within the dielectric. Thus the surface charge density that may be applied to a target area on a thin, electrically grounded dielectric substrate, is limited by the dielectric strength of the substrate, allowing a much higher surface charge to be deposited.

Some initial experiments in which a grounded silica substrate is charged with a corona discharge device show that a surface charge of approximately 200 $\mu C/m^2$ may be deposited. The decay time of this charge appears to be on the order of hours. The ability to create patterned areas of surface charge on a silica substrate has also been investigated. The silica surface was coated with a thin layer of gold, leaving a 4 mm square area exposed. The surface was uniformly charged with a corona discharge device. The conductive area was then grounded briefly to allow the charge to dissipate, while the uncoated silica region was expected to retain its charge. The approximate charge measured on the uncoated square was 40 $\mu C/m^2$. The field created by the charged target area must be sufficient to overcome friction should the part land outside of the target area. Calculations show that friction will be difficult to overcome for parts less than 10 microns in size. Thus, electrophoretic positioning in an electrolyte will be used for particles in the 0.5 to 10 micron range.

The in-plane Brownian motion of micron scale silica particles on a silica surface in water have been observed. Illumination with a diffuse laser beam allowed the motion of the particles to be tracked *in situ*. Particle motion was recorded using a video system and was later analyzed using image processing techniques. The diffusion of particles on the surface was observed in the absence of any applied electric field or radiation pressure. This technique was used to investigate the motion of particles during assembly onto a lithographically patterned substrate for a photonic bandgap application. These results were compared with the electrophoretic mobility of particles subject to an in-plane field applied between patterned gold electrodes. The effect of field strength on mobility was considered for several different electrode geometries. Additional experiments will focus on the use of the field to manipulate the particles and cause them to assemble in a desired pattern.

Basic measurements and demonstrations of electrostatic/shape assembly and electrophoretic/shape assembly are compromised because of gravitational forces on either the part or the media in which the part is immersed. Gravitational forces are on the order of the coloumbic and van der Waals forces acting on the particle in an air or fluid medium. Thus, part trajectories are influenced by gravity. The friction between the part and the surface on which it rests will also be affected by the gravitational component normal to the substrate. Electrostatic/shape assembly requires that the charged part be moved sufficiently close to the target area so that it can experience the field necessary to move it toward the target. This capture distance is limited by gravity since it is the other dominant body force. Electrophoretic/shape assembly is limited by convective flows in the media. Microscale particles are observed to exhibit mixed Brownian and ballistic behavior. Additional movement is also observed since the media is never really quiescent in a terrestrial experiment. Small thermal gradients are inevitable in the illuminated stage of a microscope and can considerably compromise the interpretation of the experiments. Microgravity conditions are therefore necessary to isolate and fully characterize the forces involved during assembly.

DYNAMIC REDUCTION OF MULTICOMPONENT, TRANSITION-METAL-CATION-BEARING CERAMIC MELTS AND THEIR INTERNAL CRYSTALLINE NUCLEATION

Rebecca L.A. Everman and Reid F. Cooper[1]

Department of Materials Science and Engineering
University of Wisconsin–Madison
1509 University Avenue
Madison, WI 53706–1595 USA

ABSTRACT

Melts that contain multiple cations can be forced to undergo a dynamic reduction reaction, given appropriate control of the activity of oxygen of the process environment. In the case where a transition metal oxide component is a constituent of the melt, such that the melt becomes a small-polaron-type semiconductor, the reaction dynamic can produce a uniform distribution of metal—either as fine crystals or as fine, discrete droplets, depending on the temperature—within the melt. (The metal that is produced is the one having the smallest, *i.e.*, least negative, ΔG^o of oxidation.) These metal precipitates, which should prove distinctly resistant to coarsening, can subsequently serve as substrates for the heterogeneous nucleation of crystalline oxides during cooling of the reacted liquid.

For a p-type oxide melt, the kinetics of the reduction reaction involves (1) the ablation of O^{2-} from the surface (via acceptance of electron holes—$2h^{\bullet}$—from the melt; *i.e.*, $O^{2-} + 2h^{\bullet} = \frac{1}{2}O_{2(g)}$ at the free surface), (2) the diffusion of cations from the free surface inward, charge-compensated by a counterflux of $h^{\bullet}$ and (3) reaction at an internal front in which metal is produced by the acceptance of electrons (*i.e.*, the creation of $h^{\bullet}$) from the component transition-metal cation(s). The dynamic is seen as a "mirror image" of that for the internal oxidation of alloys.

We have pursued experiments on dynamic reduction of a synthetic Fe^{2+}-bearing magnesium aluminosilicate melt. Experimental conditions included temperatures ~1400°C and an oxygen activity of 10^{-13}, controlled dynamically by flowing $CO:CO_2$. The experiments are designed to precipitate crystalline iron from the melt. The reaction morphology seen includes the formation of distinctly faceted Fe crystals on the free surface, at a scale ~5μm, and internal precipitates of iron at a scale of ~10–40 nm. In addition, the precipitation of Fe affects the polymerization (molecular structure) of the remaining aluminosilicate melt and, with it, physical properties such as the viscosity.

The research has both engineering and scientific application. From an engineering perspective, there exists at present no successful way to create a fine-grained, dense refractory oxide ceramic (*e.g.*, α-Al_2O_3) via solidification of an inviscid (*i.e.*, non-glass-forming) melt. Distribution of internal heterogeneities—specifically colloidal metal—in the melt allows extrapolation of glass-ceramic processing ideas

Corresponding author: cooper@engr.wisc.edu; (608) 262-1133

to inviscid melt systems. These process requirements involve containerless processing in that (1) one must control carefully the oxygen activity at the surface of the melt and (2) containers offer potent (competitive) sites for heterogeneous crystalline nucleation; microgravity is necessary both (1) for quiescence during the reduction reaction (convection in the melt must be avoided to control the reaction morphology) and (2) to avoid buoyancy-driven separation of metal and inviscid ceramic phases.

I. Introduction and Theoretical Background

Because of the difficulty of gaining a very-high density of internal sites for crystalline nucleation, it is all but impossible to create dense, fine-grained polycrystalline ceramics by solidification. The one exception are glass-ceramic materials [1], in which viscous, glass-forming ("strong") melts are doped to promote stable or metastable liquid-phase immiscibility on a 1–10 nm scale; post-"casting" thermal treatment results in highly uniform, internal nucleation and a final grain size that can be as fine as 100 nm (arising from ~10^{15} nuclei/cm^3). Because of the liquid viscosity requirement, though, glass-ceramic materials are limited primarily to silicates. Fusion-cast refractory oxides, *e.g.*, Al_2O_3, MgO, $MgAl_2O_4$, etc., are not amenable to such processing because the liquids are far too inviscid. The engineering goal of this research to identify and develop such a process; our approach has emphasized dynamic redox reactions that cause internal structural change in the melt.

An internal chemical reaction mechanism that is rate-limited by bulk diffusion should inherently result in an even distribution of product phase that could serve as nucleation sites. Because melt structure is a function of cation valence and is an important factor in its nucleation behavior, redox reactions are useful for understanding internal reactions and subsequent nucleation within the melt. Our group has studied oxidation of Fe-bearing magnesium aluminosilicate (Fe–MAS) melts and glasses, demonstrating an internal reaction where fine-scale ferrite phases form internally, uniformly [*e.g.*, 2, 3]; in the case of melts an "isothermal undercooling" is developed through shifts in the phase diagram as a function of the activity of oxygen. The oxidation experiments have a drawback, however, of the coarsening (ripening) of the precipitated ferrite phase. This disadvantage can perhaps be eliminated in a reduction reaction, i.e., where a metal colloid is formed internally, due to the activation barrier of the required valence changes (*i.e.*, from metal to ion and back) required for chemical diffusion through the ionic melt "matrix." The physics of dynamic reduction can perhaps be exploited to produce a finely dispersed metallic second phase that is resistant to coarsening and serves, thus, as heterogeneous nucleation sites for crystallization of the residual—though majority—ionic melt.

We have pursued the reduction studies again concentrating on iron-bearing aluminosilicate melts. The material studied was selected for two purposes: (1) the temperature capabilities of experimental apparatus available and (2) the broader application to microgravity science of the experiments. With respect to the latter, the study of dynamic reduction not only has implications for the materials community but also the planetary science/astrophysics community. These implications lie in the fact that the structures formed in these reduction experiments in silicate melts resemble structures observed in primitive chondrules in meteorites [e.g., 4]. Thus, an understanding of the dynamics involved in the reduction of these experimental silicate compositions provide insight into the thermodynamic conditions and kinetic constraints of processes in the protosolar nebula—microgravity science, indeed!

Internal Reduction and its Application to the Amorphous State

Schmalzried [5, 6] summarized the characteristics of both internal oxidation and reduction reactions in crystalline metallic and oxide alloys (solid solutions). The typical reaction morphology has both an

internal reaction front and a reaction occurring at the surface with a region of chemical diffusion between the two. The thermodynamic and kinetic requirements for a reaction to occur internally (as opposed to solely free-surface reactions) include: (1) that one species should be more noble than the other (*e.g.*, $|\Delta G^\circ_{AO}| << |\Delta G^\circ_{BO}|$), (2) that the transport coefficient for cations be greater than that for any oxygen species (*e.g.*, $c_{o2}\text{-}D_{o2}\text{-} << c_{M2+}D_{M2+}$), and (3) that the semiconductor condition be satisfied (*e.g.*, for a p-type material, $c_{h\bullet}\, D_{h\bullet} >> c_{M2+}D_{M2+}$, where $h^\bullet$ are electron holes). As for the third criterion, rapidly mobile electronic defects serve to decouple the motion of ions in the melt by providing local charge neutrality [cf. 3].

An Fe–MAS composition was chosen to initiate this study of internal reduction in melts. This composition fulfills all of the requirements stated above: (1) the iron in this glass is much more noble than any of the other cations, that is, $|\Delta G^\circ_{FeO}| << |\Delta G^\circ_{MgO}|$; (2) the divalent (network-modifying) cations are more mobile than either anionic or molecular/atomic oxygen; (3) the semiconductor condition is satisfied. The fulfillment of these last two criteria is demonstrated in the oxidation experiments on the same composition [3].

A dynamics model of the proposed internal reduction reaction is shown in Figure 1. The internal reaction (at interface ξ'') produces metallic iron and electron holes while, at the free surface (interface ξ'), ionic oxygen transforms to molecular oxygen via consumption of $h^\bullet$. In between ξ'' and ξ', $h^\bullet$ diffuse towards the surface, charge-balanced by a counterflux of divalent cations (predominately Mg^{2+}). The increase of cation concentration internally forces internal reduction. The extraction of Fe at ξ'' makes the silicate "matrix" nominally iron-free (*i.e.*, ionic Fe in the silicate melt exists at a concentration level associated with point defects in crystalline solids); as such, interdiffusion of Mg^{2+} and Fe^{2+} beyond ξ'' (*i.e.*, at greater depth) becomes critical in supplying Fe^{2+} to the metal-producing reaction at ξ''.

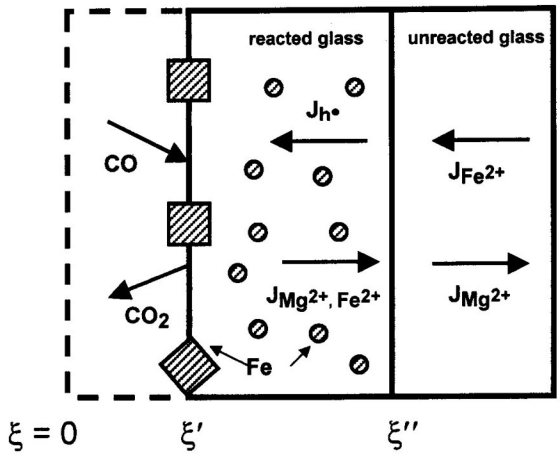

Figure 1. Schematic of the dynamic reduction process operating in a melt exposed to a highly reducing atmosphere: fine metal precipitates are produced at an internal front, ξ''.

The dynamics overall involve two reactions and two steps of chemical diffusion. Studies of oxidation behavior (the mirror-image, kinetically, of the reduction reaction) have demonstrated parabolic kinetics, proving that it is the chemical diffusion of the divalent, network-modifying cations that is rate limiting. In crystalline oxide solutions *(e.g.*, $[Mg_x,Fe_{1-x}]O$ with the rocksalt structure) the dynamic is accomplished by the coupled diffusion of cation vacancies and $h^\bullet$ [5]. In the amorphous state it is difficult to articulate a point-defect thermodynamics; nevertheless, the phenomenology of these dynamic redox reactions opens the way to approach such a description [*e.g.*, 2].

This report outlines our experimental effort to discern the validity of this model for reduction and internal formation of colloidal metal and, further, its impact on control of internal nucleation of the residual ionic melt.

II. Experimental Approach

The Fe–MAS material was prepared so that its nominal MAS composition lies along the cordierite-enstatite-liquid divariant but with a ~20 mol% substitution of Fe^{2+} for Mg^{2+}; as prepared, the composition is (mol%; X-ray fluorescence analysis) 59.3 SiO_2; 9.1 Al_2O_3; 26.0 MgO; 4.7 FeO; 0.8 Fe_2O_3. The initial melt was prepared from the fusion of mixed oxide powders of "AR" grade or higher; the melt was rapidly quenched to a homogeneous glass.

The reduction experiments were conducted in a vertical tube furnace by suspending a ~2 mm cube cut from the glass and wrapped in an iron (99.99% metals basis) wire cage. At temperature, the melt was held in the wire cage by surface tension. The samples were reacted at temperatures ranging from 1380 ≥ T(°C) ≥ 1290. The temperature was monitored by a type C (W/W–26at% Re) thermocouple no more than 1 cm away from the sample; T variation in an experiment was ±2°C. The partial pressure of oxygen (p_{O2}) in the furnace was controlled by a flowing gas mixture of CO_2 and CO mixed at a ratio of 1:240; the gas reaction creates an equilibrium p_{O2} some 10^3 lower than the quartz-iron-fayalite ("QIF" [7]) buffer, specifically the p_{O2} ranged from 10^{-14} atm at 1290°C to 10^{-13} atm at 1380°C. The p_{O2} was monitored actively by a Y_2O_3-stabilized ZrO_2 oxygen sensor located inside the furnace tube at the same level as the sample.

The sample cage was suspended between two molybdenum wires by a tungsten filament. When the reaction time was over, the sample was dropped out of the hot zone of the furnace by applying a voltage across the Mo wires and burning the W filament. This approach produced nearly instantaneous quenching of a specimen. The resulting samples were stored in a desiccator to slow any further reaction with the ambient air.

III. Experimental Results

The reacted melt droplets were viewed using light and electron microscopies. The exterior of the droplets, seen in Figure 2 in a secondary electron image (scanning electron microscopy), display a

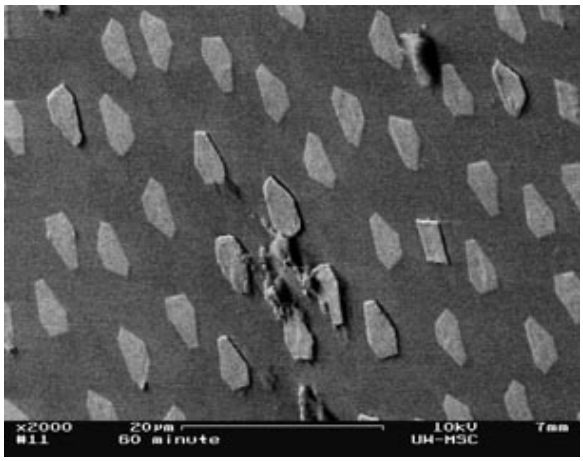

Figure 2. Secondary electron image of the free surface of a quenched Fe-MAS droplet processed at T = 1380°C and $p_{O2} \approx 10^{-13}$atm for 1 h. Faceted iron crystals, most with (111) exposed, are evident. These coarsen via vapor-phase transport of Fe.

uniform distribution of faceted crystals over the surface. The facets correspond to a cubic symmetry with (001) and (111) faces intersecting the surface of the droplet. These surface crystals demonstrate coarsening as a function of time at temperature. Wavelength dispersive X-ray spectroscopy (electron microprobe) was used to verify the composition of the crystals: they are predominately iron but demonstrate, too, an increasing degree of oxidation on the surface corresponding to the age of the sample at the time of its analysis.

When the droplets are sectioned and imaged in transmitted light, the reacted zone is clearly visible with a distinct color change from dark brown to nearly clear or light blue-green as shown in Figure 3. This color change delineates clearly the location of the internal reaction front, ξ''. The four large, opaque spots are pieces of the iron wire cage. The internal reaction front appears to be indented near the pieces of wire; the distance between the internal reaction front and the iron wire is roughly equivalent to the distance between the free surface and the internal reaction front, *i.e.*, as measured as far away from the wires as possible).

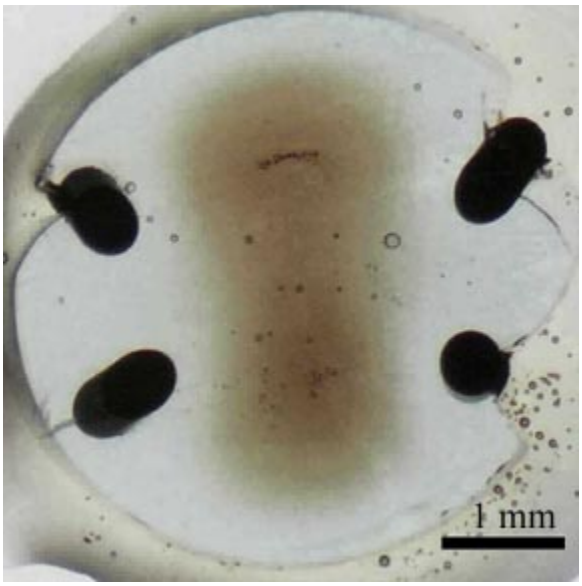

Figure 3. Transmitted light micrograph of a sectioned droplet processed at 1380°C, p_{O2} ~10^{-13}atm for ½ h. The darker brown color in the center is the original color of the glass; the change from nominally clear to brown occurs at ξ'' (cf. Figure 1). Within the clear area are found the fine precipitates of Fe (Figure 4). The four large black spots are remnants of the iron wire cage used to suspend the droplets.

Transmission electron microscopy revealed non-faceted particles (approaching spherical) having diameters in the range 10-40 nm (Figure 4). These were too small to be probed uniquely by x-ray spectroscopy (*i.e.*, one cannot isolate the particles in the electron beam). Nevertheless, the scattering contrast used to create the image confirms the particles as (at least) iron-rich. One sees, too, that these particles have begun to cluster and sinter together.

IV. Discussion/Commentary

Clearly the results of the experiment are in agreement with the ideas presented in the Introduction as well as the schematic model presented as Figure 1: the reduction reaction proceeds internally and finely divided metallic precipitates result. The spatial scale of the reaction (Figure 3) is consistent with its being rate-limited by chemical diffusion of the network-modifying cations, though we are still engaged in a quantitative analysis of the kinetics.

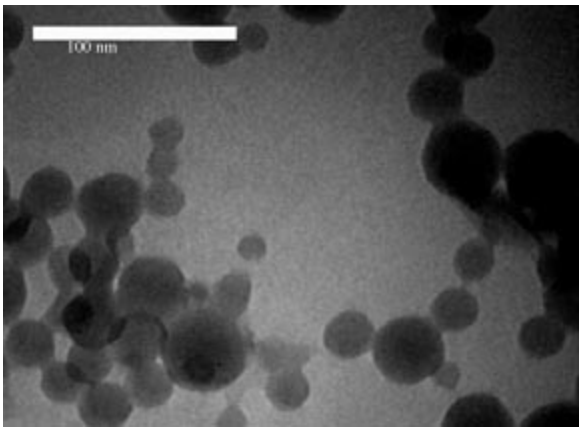

Figure 4. A zero-loss (scattering contrast), transmission electron microscopy image of a (1380°C; p_{O2} ~10^{-13}atm; 1 h) droplet between ξ′ and ξ″. The dark phase is (at least) iron-rich; consistent with the optical properties of the processed glass (cf. Figure 3), these precipitates are probably Fe metal. The size distribution is uniform throughout the reacted region; coarsening as seen on the free surface is not encountered. The clustering is curious and is a point of current study.

Following the cation-diffusion idea, the reactions at ξ′ and ξ″ (Figure 1) can be articulated in a structural context that reveals something of the chemical diffusion response. Specifically, we employ the notation of Hess [8], which scrutinizes the bonding environment of the O^{2-} in the melt. Thus, at the free surface ξ′:

$$2SiOMg_{0.5} + \overleftarrow{6SiOFe_{0.33}} = MgO + 2SiOSi + 4SiOFe_{0.5} + {}^{1}/_{2}O_{2}(g) \quad , \qquad (1)$$
$$= \overrightarrow{2SiOMg_{0.5}} + 4SiOFe_{0.5} + SiOSi + {}^{1}/_{2}O_{2}(g)$$

and, at ξ″:

$$\overrightarrow{2SiOMg_{0.5}} + 6SiOFe_{0.5} = Fe^{\circ} + \overleftarrow{6SiOFe_{0.33}} + 2SiOMg_{0.5} \qquad (2)$$

Here, for example, $2SiOM_{0.5}$ (M ≡ Mg, Fe) is a network-modifying divalent cation, $3SiOFe_{0.33}$ is a network-modifying Fe^{3+} (≡ $h^{\bullet}$) [cf. 3]. All mass and charge balances apply to these reactions. What one sees is a depolymerization (*i.e.*, an increase in modifying-cation/oxygen ratio) at the free surface and a repolymerization at the reduction front, ξ″. Thus the arrows shown in Equations. (1) and (2) indicate the mobile species between ξ′ and ξ″. As one can calculate the concentrations of these species using solution models [cf. 9], a "point-defect" perspective for diffusion-accomplished reactions in the amorphous state is clearly suggested. Such theoretical developments, as well as an analysis of the usefulness of the fine metal precipitates in heterogeneous nucleation of the ionic melt are subjects of our continuing research.

REFERENCES

1. G.H. Beall, *Ann. Rev. Mater. Sci.*, 22, 91-119 (1992).
2. R.F. Cooper *et al.*, *Science*, 274, 1173-1176 (1996).
3. G.B. Cook and R.F. Cooper, *Am. Mineral.*, 85, 397-406 (2000).
4. E.A. King, in: *Chondrules and their Origins*, E.A. King, ed., Lunar and Planet. Inst., Houston, TX, pp. 180-187 (1983).
5. H. Schmalzried, *Ber. Bunsenges. Phys. Chem.,* 87, 551-558 (1983).
6. H. Schmalzried, *Ber. Bunsenges. Phys. Chem.,* 88, 1186-1191 (1984).
7. J. Myers and H.P. Eugster, *Contrib. Mineral. Petrol.*, 82, 75-90 (1983).
8. P.C. Hess, in: *Physics of Magmatic Processes*, R. B. Hargraves, ed., Princeton Univ., Princeton, NJ, pp. 3-48 (1980).
9. P.C. Hess, *Rev. Mineral.*, 32, 145-189 (1995).

SEDIMENTATION AND MACROSEGREGATION IN QUIESCENT MELTING AND LIQUID PHASE SINTERING

T.H. Courtney, Y. Du, and S.Z. Lu

Department of Materials Science and Engineering, Michigan Technological University

ABSTRACT

There are several existing explanations for the cause for the solid-phase sedimentation often observed during liquid phase sintering (LPS). An alternative cause - macrosegregation during melting and long-range liquid concentration gradients accompanying this segregation - is offered here. Macrosegregation during LPS (or melting) can arise if the densities of the alloy components differ. For example, in melting if the higher-melting component is not present in amounts sufficient to develop an interconnected structure, this component can sink (assuming it is more dense than the liquid) to the crucible bottom. This produces a liquid head consisting of (to a first approximation) the pure lower-melting component. The segregation takes considerable time to eliminate as it exists over a macroscopic distance (the initial particle-settling distance). Similar considerations apply to LPS. Elimination of macrosegregation proceeds in stages. Following initial settling, the liquid in the liquid-plus-solid zone formed by the settling attains its equilibrium composition. Elimination of the long-range liquid concentration gradient takes place subsequently. The tendencies for macrosegregation and the structural evolution in melted/sintered materials can be summarized in a melting map which has axes of alloy and alloy liquidus compositions. Estimated times for the various melting stages can be placed on such a map. The scenario described here is supported by experimental studies of LPS in Pb-Sn alloys.

I. Introduction

Metallurgists usually think in terms of "solidification" when considering liquid/solid transformations. We are less often concerned with what "goes on" during melting. There is reason. Commercial melting operations usually involve turbulent liquid flow which produces a melt uniform in composition prior to its being cast. As a consequence, the structure and properties of the casting/ingot are dictated by the solidification process.

Melting need not involve turbulent flow. Such quiescent melting is common to many laboratory operations; for example, if a resistance furnace is used for the heating, turbulent flow can be avoided. Quiescent melting can result in macrosegregation due to the effects of gravity. When the temperature exceeds the melting temperature of the lower melting component, the unmelted solid may either sink (or float) to the crucible end prior to dissolving in the liquid. If such settling occurs (there are situations where it does not), macrosegregation results.[1] Such macrosegregation can also occur during LPS. Later, we present experimental results demonstrating this.

II. Some Thought Experiments

We begin with a thought experiment. Consider a binary isomorphous system (Figure 1) in which A melts at a lower temperature than B. The density of solid B as greater than that of liquid A. Take a cylinder of A and place it within a crucible; place a like cylinder of B above it. The relative amounts of A and B are chosen so that equilibrium corresponds to a fully liquid state. Heat the container to a temperature above A's melting temperature but below that of B. On doing this, the solid cylinder of B sinks to the crucible bottom, and a head of liquid A lies above it. Melting in this case requires long-range diffusion. The "melting time" is on the order of the square of the solid length divided by D_L, the liquid diffusion coefficient. This scenario is so simple that it is obvious. However, much the same thing can happen in conventional quiescent melting operations.

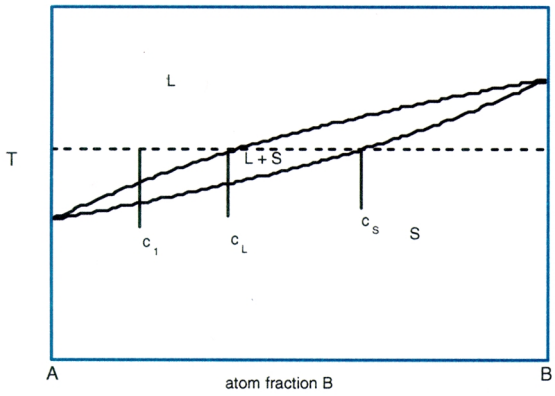

Figure 1. Binary isomorphous system used to discuss macrosegregation in melting and LPS.

We now consider this kind of melting and extend the description to LPS; only details differ between the processes. We describe a melting scenario, presenting at each stage of the process the anticipated structure, and provide approximate times for the several melting stages.[2]

We consider compositions in atom fractions and take the elemental atomic volumes as equal. They are not, but the assumption reduces the complexity of the description while maintaining focus on the physics of the process. The corrections required due to the differing elemental atomic volumes are straightforward [2]. We prepare a macroscopically homogeneous mixture of A and B in the form of granules, pellets, or powders and heat the mixture above A's melting temperature but below B's.[3] We first consider alloy compositions c_1 (cf. Figure 1) less than the liquidus (c_L.) At equilibrium this material is a homogeneous liquid of composition c_1. Thus, this is a melting operation. When A melts, the B particles may sink to the container bottom. Whether this happens depends on the initial B volume fraction. If it exceeds a critical value (V_{cs}) the amount of B present is sufficient to establish an interconnected solid. Then initial settling does not occur. We treat V_{cs} as a system-dependent parameter with a value lying between *ca*. 0.2 to 0.6 [3-5].

If the B volume fraction is less than V_{cs}, the B particles settle at a velocity on the order of the Stokes velocity [2,3]. Settling continues until the solid-phase volume fraction reaches V_{cs} near the container bottom. If this settling is rapid enough (it usually is), B does not dissolve in A during the settling. Thus, the resultant structure (Figure 2a) consists of a pure A liquid head situated above a "mushy zone" of pure solid B immersed in pure liquid A.

The B particles in the mushy zone then dissolve in the liquid there until the liquid mushy-zone composition reaches c_L. The time for this is on the order of r^2/D_L, where r is the solid-particle radius. The mushy zone may persist following this stage if the average B concentration there remains above c_L. The particle solution causes a recession of the mushy zone since the solid particle volume fraction is reduced by the solution whereas the stipulation of a critical V_{cs} remains. Thus, following this second melting stage the sample consists of a liquid head of pure A (existing over the initial settling distance), a second liquid zone having composition c_L (caused by the recession of the mushy zone), and a mushy zone of length less than the initial one. This mushy zone now contains pure solid B and liquid of composition c_L (Figure 2b).

Two other processes follow. First, the solid in the mushy zone incorporates A as it attempts to reach the solidus composition. The time for this is about r^2/D_s (D_S = a solid-state diffusion coefficient). D_s values are often about 10^{-4} D_L so this homogenization takes place relatively late in the process. However, solid-state homogenization does not alter our "story." While incorporation of A into the solid increases the mushy-zone solid volume fraction, V_{cs} is a minimum volume fraction, and the mushy zone can incorporate a solid volume fraction greater than V_{cs}. Thus, during solid-state homogenization the interface between the liquid and the mushy zone remains fixed even as the solid volume fraction in the mushy zone increases. Finally, solid-state homogenization is pertinent to liquid-phase sintered structures. For alloys that melt ($c_1 < c_L$), the solid usually completely dissolves before appreciable solid-state diffusion occurs.

The second later process is final melting (if $c_1 < c_L$). It is achieved by long-range diffusion of A from the liquid head to the mushy zone (and reverse diffusion of B). This leads to further solid dissolving in the mushy zone. Equilibrium is reached when a liquid of uniform composition c_1 is attained (Figure 2c(i)). This equilibration time is on the order of the square of the original liquid head length divided by D_L. This time is usually orders of magnitude greater than the time to produce a uniform liquid composition in the mushy zone.

There are two differences in treating LPS ($c_1 > c_L$). First, the equilibrium structure now contains a mushy zone (Figure 2.c(ii)). And, since a solid phase is present at equilibrium, equilibrium is not reached until the solid composition is adjusted to c_S.

III. The Zone Sizes and Melting Maps

In [2] we showed that initial settling (*i.e.*, $x_o/L > 0$; Fig. 2a) occurs only if $c_1 < V_{cs}$. This was done by an atom balance. Additional atomic balances can be used to determine the relative extents of the different zones illustrated in Figure 2 [2]. The results are summarized in Table 1. They apply to a system in which the elemental atomic volumes are the same. However, as noted previously, conversion to a situation where this is not the case is straightforward.

The relationships among the different liquid zone lengths and c_1, c_L, and V_{cs} are linear. They can be represented in a "melting map" which has axes of c_1 and c_L and is constructed for a specific value of V_{cs}. A map for $V_{cs} = 0.6$ is shown in Figure 3a . One way of viewing such a map is to divide it into two regions; one for melting ($c_L > c_1$) and one for LPS ($c_L < c_1$).

Three subregions - **xy1**, **x11**, and **011** - are shown in the "melting" area of Figure 3a. The designations correspond to the values of x/L at the completion of each of the three melting stages. Thus,

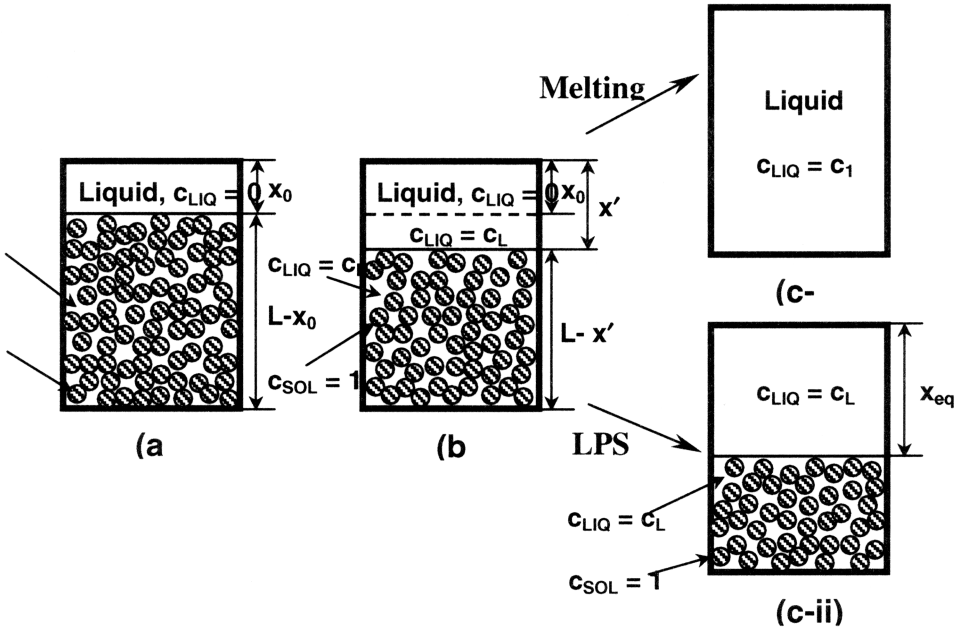

Figure 2. Schematics of structural development in melting and LPS when gravity instigated macrosegregation occurs. Details of the processes are described in the text.

the last 1 in the sequence signifies that the final state is fully liquid. An **x** as the first letter in the sequence (as opposed to a 0) means that initial particle settling occurs. Thus, the boundary between **xy1** (and **x11**) and **011** is established at $c_1 = V_{cs}$.

When $x_o/L > 0$, the structure following initial settling consists of a liquid head (pure A) and a mushy zone (pure solid B plus pure liquid A). Subsequently B dissolves in the mushy zone and the structure in a sample designated **xy1** now consists of a zone of pure liquid A (occupying the fractional distance **x** at the sample top), a liquid region of composition c_L over the fractional distance **y-x**, and a mushy zone containing pure B immersed in liquid of composition c_L. Following solution of B for a sample designated **x11**, the sample is completely liquid. However, two liquid regions exist; one is pure A (near the sample top) and the other (near the sample bottom) has composition c_L. Thus, compositional equilibrium in alloys denoted **x11** and **xy1** requires long-range liquid diffusion.

Only **011** compositions undergo "normal" melting. In them, dissolution of solid B takes place uniformly over the sample length and, at its completion (the first **1** in the designation), the liquid is of uniform composition c_L. Such alloys require no long-range liquid diffusion to homogenize them. Heating a mixture of A and B above B's melting temperature does not necessarily prevent macrosegregation. That is, for compositions prone to settling, B particles can do so during the time spent in increasing the temperature from the melting temperature of A to that of B, a heating rate on the order of several hundred K/s may be needed to melt B before it settles to the crucible bottom [2].

There are also three subregions - **xyz**, **0xx**, and **000** - in the LPS regime of Figure 3a. Initial settling occurs for **xyz** compositions. These alloys the mushy zone recedes during dissolution of solid B. Thus, these alloys develop long-range liquid concentration gradients. When these are eliminated, the liquid has translated to a fractional position **z**. Alloys noted **0xx** do not undergo initial settling. However, during solution of B in the liquid, a fully liquid zone forms. But this zone

Table 1. Structural evolution during melting and liquid phase sintering.

	Melting	Liquid Phase Sintering
x_0/L	$1 - (c_1/V_{cs})$	$1 - (c_1/V_{cs})$
x'/L	$\{(1-V_{cs})c_L + (x_0/L)V_{cs}\}/V_{cs(}(1-c_L)$	$\{(1-V_{cs})c_L + (x_0/L)V_{cs} - c_L)\}/V_{cs(}(1-c_L)$
x_{eq}/L	1	$\{(1-V_{cs})c_L + V_{cs} - c_L)\}/V_{cs(}(1-c_L)$

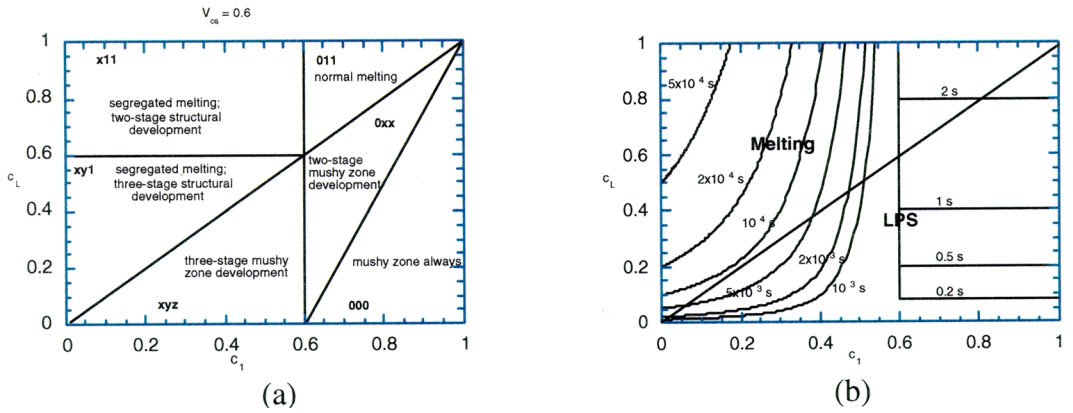

Figure 3. (a) A melting map illustrating the evolution of structure during melting/LPS. ($V_{cs} = 0.6$ for the situation here). (b) Liquid compositional equilibration times superimposed on the melting map.

has composition c_L and, therefore, liquid compositional uniformity is reached at the end of the B solution stage (hence the double x). The situation does not differ much for **000** compositions. Here, however, the overall B content is high enough so that a mushy zone occupies the whole of the sample length throughout LPS. During the B solution stage, though, the average solid content in the mushy zone is reduced.

Figure 3a can also be viewed as defining whether or not long-range liquid concentration gradients develop during melting/LPS. Compositions not displaying initial settling do not develop such gradients, and vice-versa. The differences in the liquid compositional equilibration times for the situations are striking. The times for each of the melting stages are known approximately [2]. This permits liquid compositional equilibration times to be displayed on a melting map, as is done in Figure 3b for a system for which $V_{cs} = 0.6$. The times shown were determined as follows. If $c_1 > V_{cs}$ there is no initial settling; liquid compositional equilibrium is attained following solution of B in the mushy zone and the times shown on the map are the B solution time (on the order of $(r^2/D_L)c_L$; system parameters used in calculating times are given in [2]). These times are short (although they are typically longer than initial particle settling times). As a consequence, liquid compositional uniformity in LPS and melting is attained quickly when $c^1 > V_{cs}$. For alloys displaying initial settling and, therefore, long-range liquid concentration gradients, the time required to eliminate these is about $x_o^2 c_L/D_L$. Chemical equilibrium during LPS also requires the solid to have the composition c_S. The time to achieve this is about $(r^2/D_S)(1-c_S)$. This time is considerably longer than the B solution time. The solid-state homogenization time could be estimated were D_s known, and this time could also be displayed in Figure 3b. However, it is probably just as convenient to add the solid-state homogenization time to the times displayed in Figure 3b.

The ideas put forth here are fairly simple. But that does not mean they are readily absorbed at first reading. In [2] we have included a table that might help in this regard. It summarizes equilibration

times for melting/LPS and structural evolution during processing. The various times associated with the several processes are also provided.

IV. Some Experimental Results

We have conducted a number of experiments employing two model systems (Pb-Sn and Ni-W). The results suggest the above scenario is followed. A paper is currently being written that provides details [6]. Here we use one Pb-Sn alloy composition as an illustrative example. The Pb-Sn system is a simple eutectic (eutectic composition of 71.9 at. % Sn). Before proceeding, though, some comments on how melting and liquid-phase sintering differ in a eutectic and in a binary isomorphous system are in order.

Consider melting of a eutectic alloy. The original solid consists of equiaxed α and β grains, and the phase compositions are equilibrated at a temperature slightly below the eutectic. The alloy is now heated above the eutectic. The reaction is

$$\alpha + \beta \rightarrow L$$

Melting takes place at the interface between the two solid phases. The liquid interfacial compositions are the equilibrium ones. That is, one composition is hypo- and the other hypereutectic; however, the average liquid composition is the eutectic. As melting proceeds, the steric hindrance provided by the solid phases to their sinking/floating is removed. Then α particles sink to the container bottom (α is the denser phase) and β particles float to its top. Eventually a skeletal solid forms at both locations. At the end of this stage we anticipate that the mushy zones contain solid particles imbedded in a liquid of eutectic composition. The liquid between the zones also has this composition. Liquid compositional equilibrium is then established in the mushy zones; *i.e.*, the liquids there attain the respective equilibrium liquidi. This is accompanied by solid phase dissolution in the zones and concurrent sedimentation. A long-range concentration gradient across the liquid zone is simultaneously established. Nearer the container top the liquid has composition $c_{L\beta}$; nearer the bottom it has composition $c_{L\alpha}$. As the long-range composition gradient is reduced, additional solid dissolves in both mushy zones and the zones further recede. Melting is complete when the mushy zones disappear. However, a long-range concentration gradient may persist even after the structure is fully liquid. Clearly, the stages of melting of a eutectic parallel those of melting of a binary isomorphous alloy.

A hypereutectic Pb-78 at. % Sn alloy heat-treated at 186^{o} C (3^{o} C above the eutectic), is used to illustrate. Starting materials were prepared by melting the elements and shaking the alloy vigorously prior to solidification. The alloy was then swaged. Prior to heat-treating, the structure consisted of equiaxed α and β grains.

Optical micrographs of this alloy after heating for 1 hr and 40 min are shown in Figures 4a-e. A schematic of the macrostructure is also shown in Figure 4. Five zones can be distinguished. A Sn-rich mushy zone is found near the sample top. Below this is a zone containing β dendrites (Figures 4b and c); thus, at the heat-treatment temperature this zone was a hypereutectic liquid. A region of almost fully eutectic structure (bottom of Figure 4c) separates this region from one in which primary α dendrites are present (Figure 4d). Thus, the liquid in this zone was hypoeutectic. Finally, at the sample bottom a Pb-rich mushy zone is observed (Figure 4e). When the heat-treatment time is extended to 6 hr and 40 min, macrosegregation persists but to a lesser degree (Figure 5a-c). For example, a Pb-rich mushy zone is no longer present, and the region containing α dendrites is

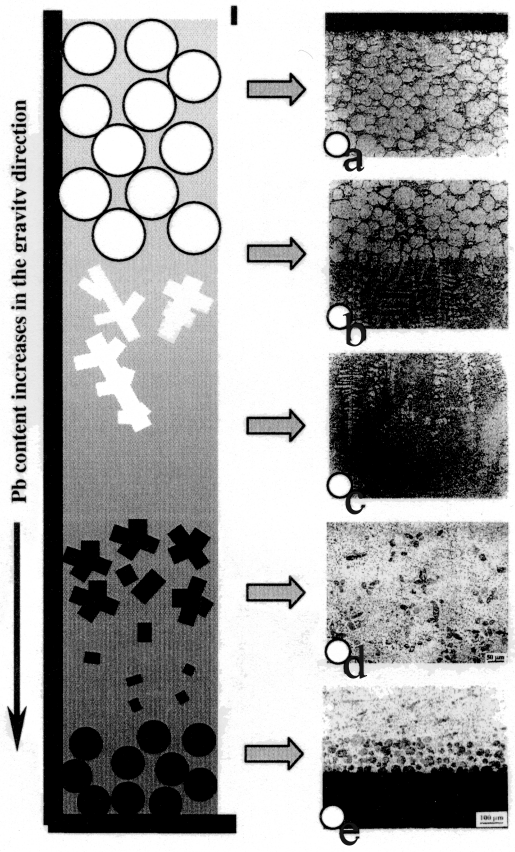

Figure 4. Microstructures [(a)-(e)] and schematic macrostructure (left) of the 78 at. % Sn alloy heat-treated for 1 hr and 40 min at 186° C. The sequence (a) to (e) is from sample top to bottom and clearly indicates that macrosegregation is present in the sample.

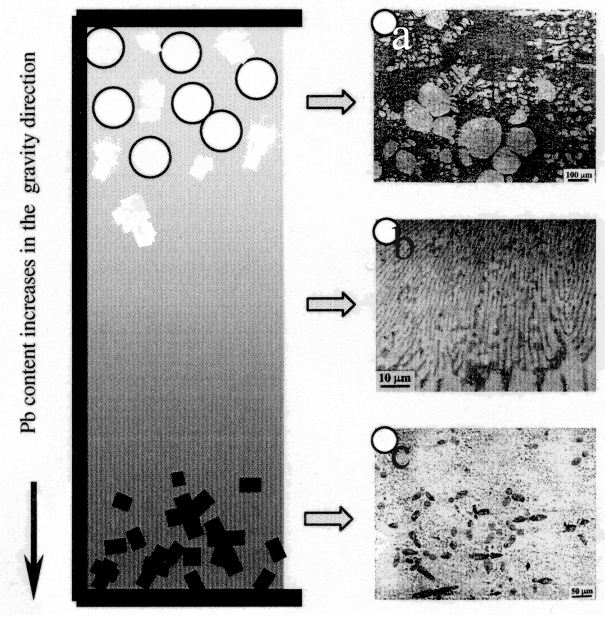

Figure 5. Microstructures [(a)-(c)] and schematic macrostructure (left) of the 78 at. % Sn alloy heat-treated for 6 hr and 40 min at 186° C. The sequence (a) to (c) is from sample top to bottom. Macrosegregation is reduced compared to what is displayed in Figure 4.

reduced. Likewise, the Sn-rich mushy zone is less pronounced. Similar macrosegregation has been observed in a series of hypo- and hypereutectic Pb-Sn compositions. All respond similarly to a LPS treatment. Results of this work are being readied for publication.

V. Summary and Conclusions

When two-phase solids are melted or liquid-phase sintered, long-range liquid concentration gradients can develop as a result of particle settling. The settling can lead to further particle sedimentation that comes about as the liquid composition becomes uniform. We have shown, by concept and examples, how initial settling can lead to particle sedimentation. On this basis, "true" sedimentation cannot be studied prior to elimination of the long-range liquid concentration gradient. "Melting maps," which illustrate the proclivities of a given alloy composition for sedimentation, are convenient guides to the phenomenon. Times for compositional equilibrium can be approximately calculated and superimposed on such maps.

VI. End Notes

[1] - This is the "melting" equivalent of dendrite settling that can give rise to macrosegregation during solidification [1].
[2] - We realize there is overlap between/among the stages. However, it is not only convenient to consider the stages sequential but, in many instances, the durations of the stages differ considerably thereby justifying considering them sequential.
[3] - The situation of heating above B's melting temperature is a "limiting" case, discussed later.

REFERENCES

1. D. A. Porter and K. E. Easterling, "Phase Transformations in Metals and Alloys," 2nd ed., Chapman-Hall, London, 1992, pp. 237-238.
2. T. H. Courtney, Y. Du, and S. Z. Lu, submitted for publication.
3. A. N. Niemi and T. H. Courtney, Acta Metall., 1983, vol. 31, pp. 1393-1401.
4. S. C. Hardy and P. W. Voorhees, Metall. Trans. A, 1988, vol. 19A, pp. 2713-2721.
5. S. C. Yang and R. M. German, Metall. Trans. A, 1991, vol. 22A, pp. 786-791.

INTEGRATION OF THE QMSFRG DATABASE INTO THE HZETRN CODE

F.A. Cucinotta[1*], M.R. Shavers[2], R.K. Tripathi[3], and J.W. Wilson[3]

[1]NASA, Johnson Space Center
[2]Loma Linda University
[3]NASA, Langley Research Center

Accurate nuclear interaction data bases are needed for describing the transport of space radiation in matter including space craft structures, atmospheres, and tissues. Transport models support the identification and development of new material concepts for human and electronic part protection. Quantum effects are manifested in nuclear reactions in several ways including interference effects between terms in the multiple scattering series, the many-body nuclear wave functions (for *e.g.* the roles of shell structure and Fermi momentum) and nuclear clustering. The quantum multiple scattering fragmentation model (QMSFRG) is a comprehensive model for generating nuclear interaction databases for galactic cosmic ray (GCR) transport. Other nuclear databases including the NUCFRG model and Monte-Carlo simulation codes such as FLUKA, LAHET, HETC, and GEANT ignore quantum effects. These codes fail to describe many important features of nuclear reactions and are thus inaccurate for the evaluation of materials for radiation protection. Previously we have shown that quantum effects are manifested through constructive interference in forward production spectra, the effects of Fermi momentum on production spectra, cluster nuclei knockout, and the nuclear response function. Quantum effects are especially important for heavy ions with mass numbers less than 20 that dominate radiation transport in human tissues and for the materials that are expected to be superior in space radiation protection.

We describe the integration of the QMSFRG model into the HZETRN transport code. Integration milestones include proper treatment of odd-even charge-mass effects in nuclear fragmentation and the momentum distribution of nucleon production from GCR primary heavy ions. We have also modified the two-body amplitudes in the model to include nuclear medium effects. In order to include a comprehensive description of the GCR isotopic composition in materials, we have described the isotopic composition of the GCR by extending the 59-isotope version of HZETRN to an 120-isotope version. The isotopic composition of most primary GCR elements (including H, He, C, N, O, Ne, Mg, Si, Ar, Ca, Cr, and Fe) are included in the extended model. We discuss results for the high-energy neutron composition inside materials, and the charge and mass distribution for benchmark GCR problems.

* The full report for this project was not included due to image complications. Please contact Dr. Cucinotta for more information on this project.

ADAPTIVE-GRID METHODS FOR PHASE FIELD MODELS OF MICROSTRUCTURE DEVELOPMENT

Jonathan A. Dantzig[1] and Nigel Goldenfeld[2]

[1]Department of Mechanical and Industrial Engineering
[2]Department of Physics
University of Illinois at Urbana-Champaign

Modeling solidification microstructures has become an area of intense study in recent years. The properties of large scale cast products, ranging from automobile engine blocks to aircraft components and other industrial applications, are strongly dependent on the physics that occur at the mesoscopic and microscopic length scales during solidification. The predominant morphology found in solidification microstructures is the dendrite, a tree-like pattern of solid around which solidification proceeds. The microscopic properties of cast products are determined by the length scales of these dendrites, and their associated segregation profiles. For this reason understanding the mechanisms for pattern selection in dendritic growth has attracted a great deal of interest from the experimental and theoretical communities.

In particular, a great deal of research has been undertaken to understand such issues as dendrite morphology, shape and growth speed. Experiments on dendrite evolution in pure materials by Glicksman and coworkers on succinonitrile (SCN), and more recently pivalic acid (PVA), as well as other transparent analogs of metals, have provided tests of theories for dendritic growth, and have stimulated considerable theoretical progress [5, 7]. These experiments have clearly demonstrated that in certain parameter ranges the physics of the dendrite tip can be characterized by a steady value for the dendrite tip velocity, radius of curvature and shape. Away from the tip, the time-dependent dendrite exhibits a characteristic sidebranching as it propagates, which is not yet well understood. These experiments are performed by observing individual dendrites growing into an undercooled melt. The experiments are characterized by the dimensionless undercooling. Most experiments are performed at low undercooling.

The geometric complexity of dendritic microstructures has greatly hampered further theoretical progress. Several numerical calculations of evolving dendrite shapes have been attempted. The goal of these calculations is to test the theory by comparing computed dendrite shapes and scaling laws with experimental observations. The solution of the dendrite growth problem has been made more tractable with the introduction of the phase field model [8]. The phase field model avoids the problem of front tracking by introducing an auxiliary continuous order parameter that couples to the evolution of the thermal or solutal field. The phase field interpolates between the solid and liquid phases, attaining two different constant values in either phase, with a rapid transition region in the vicinity of the solidification front.

The price to be paid for the convenience of using the continuous order parameter is the introduction of a new length scale W which represents a boundary layer over which the order parameter changes sign. This distance is referred to as the interface width. One requirement of the phase field model is to recover the Stefan limit in a manner that is independent of the interface width as W approaches some appropriate limit.

While expanding the horizon of solidification modeling, phase field modeling has still been limited to small systems sizes. The main problem is the requirement that the interface region must be resolved to order of the capillary length, within a domain whose size is set by diffusion. For small dimensionless undercooling, the ratio of the system dimension to this minimal grid spacing can be greater than 100,000. Our research has focused on extending the computationally tractable regime for phase field models to low undercooling. What is needed to go beyond the high undercooling limit is an effective adaptive technique which dynamically coarsens the grid spacing away from the front.

We have developed a new, computationally efficient adaptive-grid algorithm for solving a class of phase field models suitable for the study of phase-boundary evolution. We study two-dimensional dendritic solidification modeled using two coupled fields, one for the order parameter and the other for the thermal or solute field. Our algorithm effectively combines and implements ideas of adaptive-mesh refinement in the context of dynamic data structures, allowing us to enlarge the window of large-scale solidification modeling.

This new approach has allowed us to explore numerous new problems in solidification. Space does not permit a complete description of all of the work which we have done since the last report in this series. Instead, we highlight work which we did in collaboration with Prof. Glicksman and Dr. Koss of Rensselaer Polytechnic Institute to examine some of their experimental observations. The following report was derived from our paper on this subject in Physical Review Letters. [13]

We explore dendritic growth dynamics at low undercooling, using the full diffusion equation dynamics. We find that the time-dependent evolution of 2-D dendrite profiles is self-affine in time, generalizing the results of Ref. [1] for the case of growth with a non-constant flux. Underlying this scaling behavior is a power law dependence on time of the dendrite tip position and maximum dendrite width. We find that scaling of these quantities displays a cross-over from a growth regime different from that of Hele-Shaw flow, to one characterized by steady-state tip growth. Meanwhile, comparison of our low undercooling simulations with microscopic solvability theory gives good agreement for the value of the so-called stability parameter. We also examine scaling in 3-D dendrite data on pivalic acid obtained from NASA's fourth United States Microgravity Payload (USMP-4) Isothermal Dendritic Growth Experiment (IDGE), also finding self-affine scaling in the global time-dependent PVA dendrite profiles.

The simulated dendrites are modeled using the phase-field model employed in [6]. Temperature T is rescaled to $U = c_{\mathrm{P}}(T - T_M)/L$, where c_P is the specific heat at constant pressure, L is the latent heat of fusion and T_M is the melting temperature. The order parameter is defined by ϕ with $\phi = 1$ in the solid, and $\phi = -1$ in the liquid, and the interface defined by $\phi = 0$. In what follows time is rescaled by the time scale τ_0 characterizing atomic movement in the interface, and length by the length scale W_0 characterizing the width of the liquid–solid interface. The model is given by

$$\frac{\partial U}{dt} = D\nabla^2 U + \frac{1}{2}\frac{\partial \phi}{\partial t}$$

$$A^2(\vec{n})\ \frac{\partial \phi}{dt} = \nabla \cdot (A^2(\vec{n})\nabla\phi) + (\phi - \lambda U(1-\phi^2))(1-\phi^2) \tag{1}$$

$$+\ \frac{\partial}{\partial x}\left(|\nabla\phi|^2 A(\vec{n})\frac{\partial A(\vec{n})}{\partial \phi_{,x}}\right) + \frac{\partial}{\partial y}\left(|\nabla\phi|^2 A(\vec{n})\frac{\partial A(\vec{n})}{\partial \phi_{,y}}\right),$$

where $D = \alpha\tau_o/W^2_o$, α is the thermal diffusivity, and λ controls the coupling of U and ϕ. Anisotropy has been introduced in Equation (1) by defining the width of the interface to be $W(\vec{n}) = W_o A(\vec{n})$ and the characteristic time by $\tau(\vec{n}) = \tau_o A^2(\vec{n})$ [6], where $A(\vec{n}) \in [0,1]$, and $A(\vec{n}) = (1\text{-}3\varepsilon)\left[1+\frac{4\varepsilon}{1-3\varepsilon}\frac{(\phi_{,x})^4+(\phi_{,y})^4}{|\nabla\phi|^4}\right]$. The vector $\vec{n} = (\phi_{,x}\hat{x} + \phi_{,y}\hat{y})/(\phi^2_{,x} + \phi^2_{,y})^{1/2}$ is the normal to the contours of ϕ, and $\phi_{,x}$ and $\phi_{,y}$ represent partial derivatives with respect to x and y. The constant ε parameterizes the deviation of $W(\vec{n})$ from W_o. We expect the results to be similar for other definitions of anisotropy [4]. The parameters of Equation (1) are related to the appropriate Stefan problem using the relationships given in [6]. In particular, W, τ, λ and D may be chosen to simulate an arbitrary, anisotropic capillary length $d(\vec{n})$, and interface attachment coefficient $\beta(\vec{n})$, which we chose here as β=0, a limit appropriate for SCN and PVA.

Table 1: Parameters for simulated dendrites. The time t*=255622.4

Δ	ε	Δx_{min}	Δt	D	d_0	L_x	L_y
0.25	0.05	0.78	0.048	13	0.043	12800	6400
0.1(A)	0.05	0.78	0.08	13	0.043	102400	51200
0.1(B)	0.05	1.56	0.08	30	0.01846	102400	51200
0.05($t < t^*$)	0.025	1.56	0.03	40	0.01385	102400	51200
0.05($t > t^*$)	0.025	0.78	0.03	40	0.01385	102400	51200

Simulated dendrites were computed by solving Equation (1) using the adaptive-grid method of Reference [11, 12]. Simulated dendrites were grown in a 2-D quarter-infinite space using zero-flux boundary conditions along the sides of the system. Growth was initiated by a small quarter disk of radius R_0 centered at the origin. The preferred growth directions are along the x and y axes, making these the directions of growth of dendrite branches. The order parameter is initially set to its equilibrium value $\phi_0(\vec{x}) = -\tanh((|\vec{x}| - R_0)/\sqrt{2})$ along the interface. The initial temperature decays exponentially from $U = 0$ at the interface to its far-field, undercooled value $-\Delta$ as $\vec{x} \to \infty$. Simulation data presented in this paper were obtained for three undercoolings: $\Delta = 0.25$ and 0.1 and 0.05. Details of these data are presented in Table 1. The two data sets for $\Delta = 0.1$ correspond to different minimum grid spacings Δx_{min} [11, 12]. Seed radii used in our simulations were R_0= 8.5, 15, 30, 30 for $\Delta = 0.25$, 0.1(A), 0.1 (B), 0.05, respectively. In all cases R_0 is smaller than the thermal diffusion length by a factor of 20 or greater.

The results of our low undercooling simulations are also contrasted here with new experimental data obtained from PVA dendrites. These experiments were performed by four of the authors (LaCombe, Lupulescu, Koss and Glicksman) during NASA's USMP-4 Isothermal Dendritic Growth Experiment (IDGE). This experiment is described in detail elsewhere [7]. The IDGE experiment is designed to study dendrites grown under microgravity conditions, where transport in this particular process is considered to be conduction-limited. The crystals are grown in an undercooled melt, controlled to within 0.001K. Growth is monitored thermometrically, while images are obtained from two perpendicular directions using video and still cameras (electronic and film).

Experimental results presented here were compared with four independent data subsets for dendrites grown at undercoolings of 0.58K, 0.63K, and 0.47K. We present the results from experiments corresponding to $\Delta = 0.052$. These data were captured at times $t_1 = 42.48$, $t_2 = 62.73$, and $t_3 = 82.98$ seconds after the dendrite was detected. The anisotropy for PVA was estimated at $\varepsilon_{pva} = 0.025$ [10].

We found the individual primary arms of our simulated dendrites to be self-affine, beyond some transient time, at all undercoolings examined. Figure 1 shows the (Δ-dependent) scaling profile for 2-D dendrites grown at $\Delta = 0.05$ and $\Delta = 0.25$, respectively. The global scaling profile is obtained by scaling the x-direction by $(x- x_b)/X_{max}$, where $X_{max}(t)$ is the distance from the tip $x_{tip}(t)$ to the base $x_b(t)$ of the dendrite arm, and the y-direction by $y/Y_{max}(t)$, the maximum half-width of the lateral dimension of the primary dendrite arm. The tip and transverse directions were found to scale as $X_{max} \sim t^{\beta}$ and $Y_{max} \sim t^{\gamma}$, where for $\Delta = 0.05$, 0.1*A*, 0.1*B* and 0.25, β= 0.0.73, 0.73, 0.78, 0.97, and $\gamma = 0.43$, 0.43, 0.45, and 0.55, respectively. For the $\Delta = 0.25$ data, which at late times contained sidebranching induced by lattice-noise, we define $Y_{max}(t)$ using the *mean* interface position, obtained by smoothing the data. This definition of the sidebranch envelope gives different results than using the maximum of the sidebranch envelope [3,9].

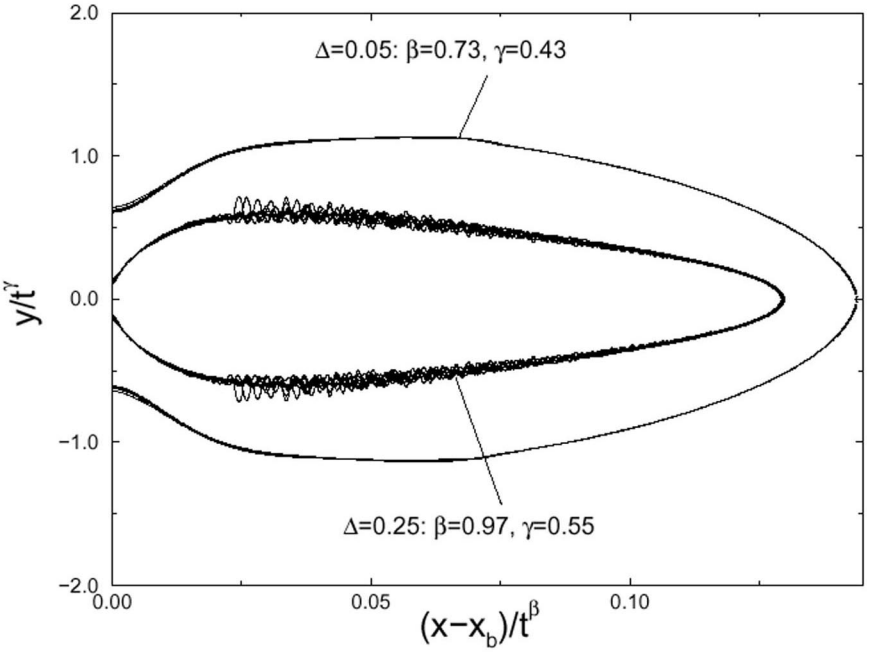

Figure 1. Comparison of scaled dendrite profiles for $\Delta = 0.05$ and $\Delta = 0.25$. For $\Delta = 0.25$, nine times are plotted, spaced between $28643 < t < 66083$. For $\Delta = 0.05$, there are six times in the range $222022 < t < 279622$.

At low undercooling, long-lived transient interactions between neighboring primary dendrite arms causes their velocity and tip radius to deviate (within simulation time scales) from their steady-state values predicted by solvability theory [11]. However, we do find that the *stability parameter* $\sigma^* = 2d_oD/V R^2$, where V and R are the time-dependent velocity and tip radius, agrees well with the value predicted by solvability theory. Figure 2 shows σ^* vs. time from our simulations at $\Delta = 0.25$, 0.1 and 0.05. Error bars were estimated using ΔV, the fluctuations in velocity, and ΔR, deviations in radius of curvature. The radius was obtained by fitting to a second order polynomial near the tip. Deviations in the fit gave an estimate for ΔR. Data for $\Delta = 0.1$ set B, omitted for clarity, converge

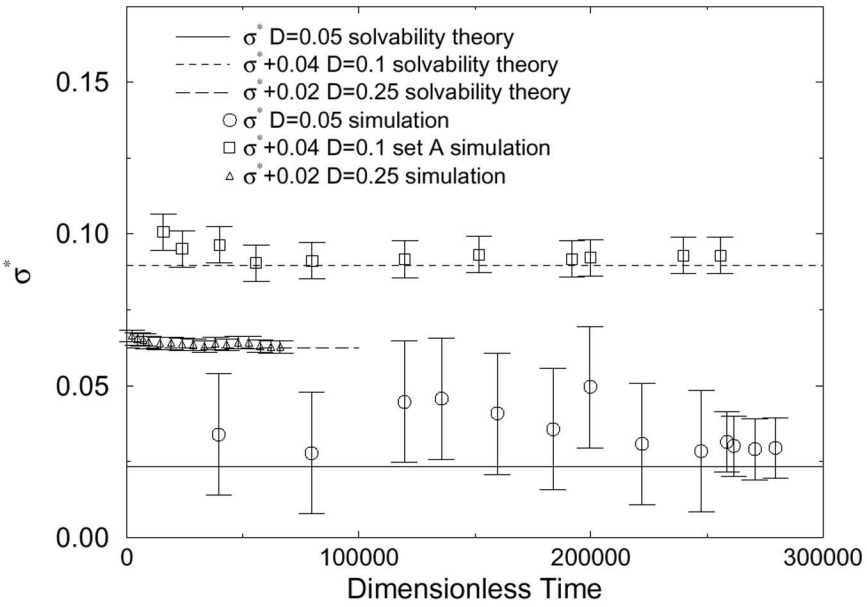

Figure 2. Simulation data of σ^* vs. time for $\Delta = 0.25, 0.1$ (set A) and 0.05. For clarity, the $\Delta = 0.1$ and 0.25 data have been shifted along the y-axis by 0.04 and 0.02, respectively.

to approximately the same σ^* as the $\Delta = 0.1$ set A data, but display somewhat larger fluctuations around the mean, due to the larger grid spacing used.

The time-dependent behavior of the tip position and lateral growth rate of our 2-D dendrites are characterized by the scaling of $X_{\max}(t)$ and $Y_{\max}(t)$. Figure 3 shows $X_{\max}$ and $Y_{\max}$ scaled onto respective crossover functions of the form

$$X_{\max}(t)/L_D = \frac{t}{\tau_D} F_X(t/\tau_D), \tag{2}$$

and

$$Y_{\max}(t)/L_D = \left(\frac{t}{\tau_D}\right)^{1/2} F_Y(t/\tau_D), \tag{3}$$

The parameters L_D and τ_D are effective diffusion length and time scales characterizing the intermediate regime, and are fit to give collapse of the $X_{\max}$ and $Y_{\max}$ data. The data for $F_X(z)$ show a crossover scaling from fit to approximately $F_X(z) \sim z^{-0.25}$ at early times to $F_X(z) \sim z^{-0.03}$ in the steady-state regime. The cross-over in $F_Y(z)$ is given by $F_Y(z) \sim z^{-0.07}$ at small z to $F_Y(z) \sim z^{0.05}$ at large arguments of $F_Y(z)$. Exponent errors were approximately ±0.02, except for the $\Delta = 0.25$ data at late time, where they were ±0.05. These asymptotic limits are demonstrated by the leveling off of $F_X(\chi)$ and $F_Y(\chi)$ as $\chi = t/\tau_D$ becomes large.

We note that our scaling of the data is different from that of Almgren, *et al.* [2], who scaled their dendrite shapes on the tip position measured from the origin, rather than the root. We do this because our method produces better data collapse over the *entire* dendrite arm. However, this approach necessarily results in different numerical values for the exponents.

Self-affine time-dependent scaling was also found in the mean dendrite profiles of the new 3-D IDGE PVA data. Figure 4 shows the scaled PVA data for $t = t_1, t_2, t_3$. For comparison these data are superimposed on our 2-D simulation data for $\Delta = 0.05$, $\varepsilon = 0.025$. There is a slight asymmetry in the PVA data, likely due to interactions with other dendrite arms. For this reason, we scaled with

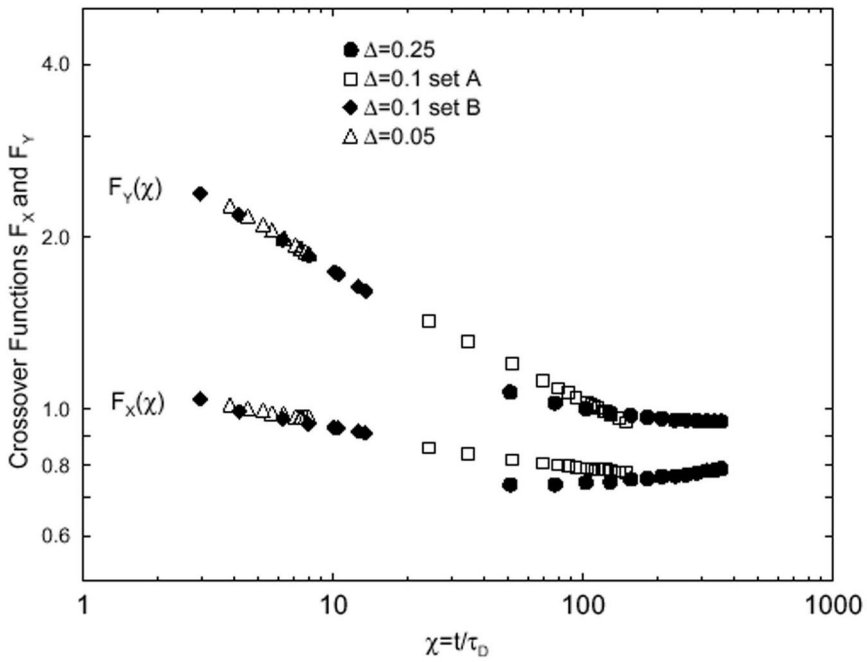

Figure 3. Crossover scaling functions describing lateral width of simulated dendrite arm Y_{max} and tip-to-base distance X_{max} , for $\Delta = 0.25,0.1$ (sets A and B) and 0.05.

respect to the top side the dendrite profile. Similar scaling was observed in all four IDGE data sets. The experimental and simulated profiles show clear differences near the tip, as one would expect. Curiously, however, the profile shapes are in good agreement away from the tip. Similar results were also found in our $\Delta = 0.1$ data. The reason for this is illustrated in Figure 4, which shows that the difference in 2-D dendrite profiles is small away from the tip.

As plausible explanation for the apparent agreement between our low undercooling 2-D simulations and our 3-D experimental data, we note that away from the tip, the diffusion field is more cylindrically symmetric than at the tip because the local diffusion length is larger. Thus diffusion of heat away from the interface is better approximated by the 2-D diffusion equation. We hope to examine this idea critically, as well as to accurately determine the experimental scaling behavior in future publications.

We thank Wouter-Jan Rappel for the code to obtain solvability results, Terry Chay for useful discussions. We also thank Julie Frei, and Douglas Corrigan for assistance in obtaining the PVA dendrite profiles. This has been supported by the NASA Microgravity Research Program, under Grants NAG8-1249, and NAS3-25368.

REFERENCES

1. R. Almgren. *J. Comp. Phys.*, 106:337, 1993.
2. R. Almgren, W. S. Dai, and V. Hakim. *Phys. Rev. Lett.*, 71:3461, 1993.
3. U. Bisang and J. H. Bilgram. *Phys. Rev. Lett.*, 75:3898, 1995.
4. G. Caginalp. *IMA J. Math.*, 39:51, 1987.
5. M. E. Glicksman. *Materials Science and Engineering*, 65:45, 1984.
6. A. Karma and W.-J. Rappel. *Phys. Rev. E*, 53:3017, 1995.

7. M.B. Koss, M.E. Glicksman, A.O. Lupulescu, L.A. Tennenhouse, J.C. LaCombe, D.C. Corrigan, J.E. Frei, and D.C. Malarik. In *36th Aerospace Sciences Meeting*. AIAA-98-0809.
8. J.S. Langer. *Rev. Mod. Phys.*, 52:1, 1980.
9. Q. Li and C. Beckermann. *Phys. Rev. E*, 57:3176, 1997.
10. M. Muschol, D. Liu, and H. Z. Cummins. *Phys. Rev. A*, 46:1038, 1992.
11. N. Provatas, J. Dantzig, and N. Goldenfeld. *Phys. Rev. Lett.*, 80:3308, 1998.
12. N. Provatas, J. Dantzig, and N. Goldenfeld. *J. Comp. Phys.*, 148:1, 1999.
13. N. Provatas, N. Goldenfeld, J. A. Dantzig, J. C. LaCombe, A. Lupulescu, M. B. Koss, M. E. Glicksman, and R. Almgren. Crossover scaling in dendritic growth evolution at low under cooling. *Physical Review Letters*, 82(22):4496–4499, 1999.

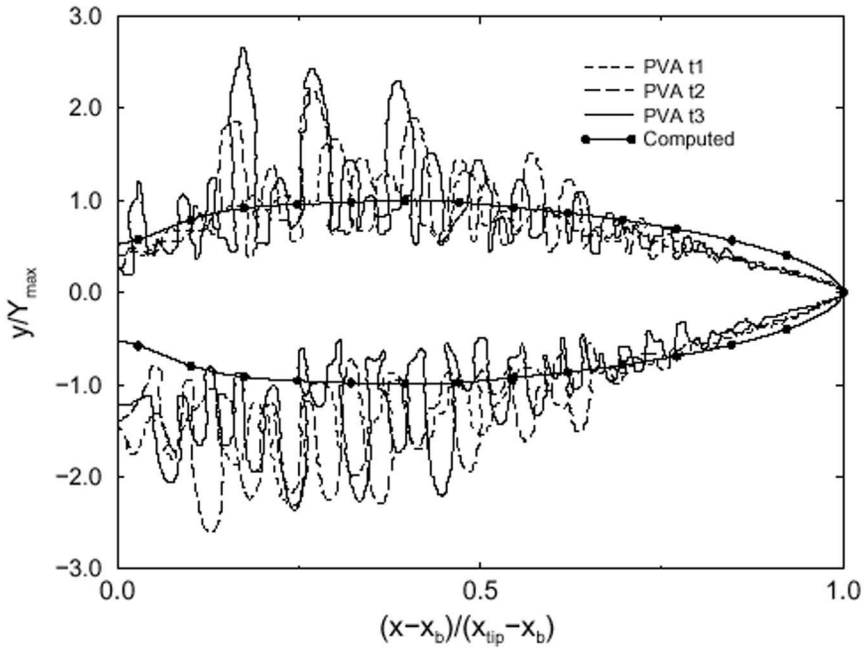

Figure 4. Scaled USMP-4 PVA dendrites grown at $\Delta = 0.052$. 2-D simulation data is superimposed for $\Delta = 0.05, \in = 0.025$. Comparison of 2-D and 3-D data made merely to illustrate self-affinity in both 2-D and 3-D dendrites.

PHASE FIELD MODELING OF MICROSTRUCTURE DEVELOPMENT IN MICROGRAVITY

Jonathan A. Dantzig[1] and Nigel Goldenfeld[2]

[1]Department of Mechanical and Industrial Engineering
[2]Department of Physics
University of Illinois at Urbana-Champaign

This newly funded project seeks to extend our NASA-sponsored project on modeling of dendritic microstructures to facilitate collaboration between our research group and those of other NASA investigators. In our ongoing program, we have applied advanced computational techniques to study microstructural evolution in dendritic solidification, for both pure isolated dendrites and directionally solidified alloys. This work has enabled us to compute dendritic microstructures using both realistic material parameters and experimentally relevant processing conditions, thus allowing for the first time direct comparison of phase field computations with laboratory observations.

This work has been well received by the materials science and physics communities, and has led to several opportunities for collaboration with scientists working on experimental investigations of pattern selection and segregation in solidification. While we have been able to pursue these collaborations to a limited extent, with some important findings, this project focuses specifically on those collaborations.

We have two target collaborations: with Prof. Glicksman's group working on the Isothermal Dendritic Growth Experiment (IDGE), and with Prof. Poirier's group studying directional solidification in Pb-Sb alloys. These two space experiments match well with our two thrusts in modeling, one for pure materials, as in the IDGE, and the other directional solidification. Such collaboration will benefit all of the research groups involved, and will provide for rapid dissemination of the results of our work where it will have significant impact.

KINETICS OF NUCLEATION AND CRYSTAL GROWTH IN GLASS FORMING MELTS IN MICROGRAVITY (NASA GRANT: NAG8-1465)

Delbert E. Day and Chandra S. Ray

Ceramic Engineering Department and Graduate Center for Materials Research
University of Missouri-Rolla, Rolla, MO 65409
(573) 341 - 4354 (tel), (573) 341 - 2071 (fax), day@umr.edu/csray@umr.edu

INTRODUCTION

This flight definition project has the specific objective of investigating the kinetics of nucleation and crystal growth in high temperature inorganic oxide, glass forming melts in microgravity. It is related to one[1] of our previous NASA projects that was concerned with glass formation for high temperature containerless melts in microgravity. The previous work culminated in two experiments[2,3] which were conducted aboard the space shuttle in 1983 and 1985 and which consisted of melting (at 1500° C) and cooling levitated 6 to 8 mm diameter spherical samples in a Single Axis Acoustic Levitator (SAAL) furnace.

Compared to other types of materials, there have been relatively few experiments, 6 to 8, conducted on inorganic glasses in space. These experiments[2-11] have been concerned with mass transport (alkali diffusion), containerless melting, critical cooling rate for glass formation, chemical homogeneity, fiber pulling, and crystallization of glass forming melts. One of the most important and consistent findings in all of these experiments has been that the glasses prepared in microgravity are more resistant to crystallization (better glass former) and more chemically homogeneous than equivalent glasses made on Earth (1g). The chemical composition of the melt appears relatively unimportant since the same general results have been reported for oxide, fluoride and chalcogenide melts. These results for space-processed glasses have important implications, since glasses with a higher resistance to crystallization or higher chemical homogeneity than those attainable on Earth can significantly advance applications in areas such as fiber optics communications, high power laser glasses, and other photonic devices where glasses are the key functional materials.

The classical theories for nucleation and crystal growth for a glass or melt do not contain any parameter that is directly dependent upon the g-value, so it is not readily apparent why glasses prepared in microgravity should be more resistant to crystallization than equivalent glasses prepared on Earth. Similarly, the gravity-driven convection in a fluid melt is believed to be the primary force field that is responsible for melt homogenization on Earth. Thus, it is not obvious why a glass prepared in space, where gravity-driven convection is ideally absent, would be more chemically homogeneous than a glass identically prepared on Earth. The primary objective of the present research is to obtain experimental data for the nucleation rate and crystal growth rate for a well characterized silicate melt (lithium disilicate) processed entirely in space (low gravity) and

compare these rates with the nucleation and crystal growth rates for a similar glass prepared identically on Earth (1g). The nucleation and crystal growth rates for a melt prepared in space have never been measured directly, but such data are expected to explain (at least partially) these puzzling, but extremely interesting results that have great scientific and practical relevance to the development, manufacturing, and use of inorganic glasses, glass-ceramics, the new bulk metallic glasses (BMG), and other solids derived from a melt.

I. Experiment

The present paper describes our overall plan for measuring, for the first time, the nucleation rate (I) and the crystal growth rate (U), each at three different temperatures, for a $Li_2O.2SiO_2$ (LS_2) glass prepared in space, see Tables 1 and 2. The glasses prepared in space will be made by remelting a glass prepared on Earth. A glass cylinder contained in a doubly sealed platinum cylinder (2.5 cm long and 1.0 cm in diameter) will be melted at 1400° C for 3 h and quenched to glass at an appropriate cooling rate. After melting and cooling, the encapsulated glass samples will be given a nucleation heat treatment at either 440, 455, or 470° C for 1 to 5 h and a crystal growth heat treatment at 590, 610, or 630° C for 10 to 30 min. The samples heat treated in space will be analyzed on Earth to determine I and U which will be compared with the I and U values for glasses melted and heat treated (for nucleation and crystal growth) identically on Earth.

Table 1. Experimental plans for measuring nucleation rate (I) for a LS_2 glass in space (samples are doubly sealed in platinum capsules).

Sample Type	Melting in Space Temp./Time	Nucleation				Crystal Development Temp./Time
			Time, Hour			
		Temp. °C	1	3	5	
A	1400 °C/3h	440	✓	✓	✓	600 °C/20 min
		455	✓	✓	✓	
		470	✓	✓	✓	
A	None (Melted on Earth)	440	✓	✓	✓	
		455	✓	✓	✓	
		470	✓	✓	✓	
A,B	1400 °C/3h	None (A-N, B-N)				None

Table 2. Experimental plans for measuring crystal growth rate (U) for a LS_2 glass in space (samples are doubly sealed in platinum capsules).

Sample Type	Melting in Space Temp./Time	Nucleation Temp./Time	Crystal Growth			
				Time, Min		
			Temp. °C	10	20	30
A	1400 °C/3h	455 °C/30 min	590	✓	✓	✓
			610	✓	✓	✓
			630	✓	✓	✓
A	None (Melted on Earth)	455 °C/30 min	590	✓	✓	✓
			610	✓	✓	✓
			630	✓	✓	✓
A,B	1400 °C/3h		None (A-N, B-N)			

A, Glass premelted on Earth.

B, Glass premelted on Earth with a colored spot.

A-N, B-N: Melted in space, but no nucleation or crystal growth heat treatment in space.

The traditional method[12, 13] , which requires measuring the number or size of crystals by optical microscopy on polished sections of the heat treated samples, will generally be used to determine I and U. A newly developed alternative method[14] which uses differential thermal analysis (DTA) and which has several advantages (faster, smaller amount of samples, less complexity for sample processing) over the traditional method will also be used for measuring I and U. As shown in Figures 1 and 2, the values of I or U for a LS_2 glass determined by the present DTA method are in excellent agreement with the I and U values determined by the more time consuming, traditional method.

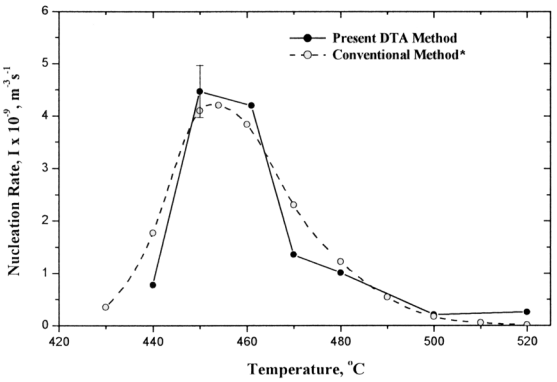

Figure 1. Nucleation rate (I) for $Li_2O.2SiO_2$ glass as a function of temperature.

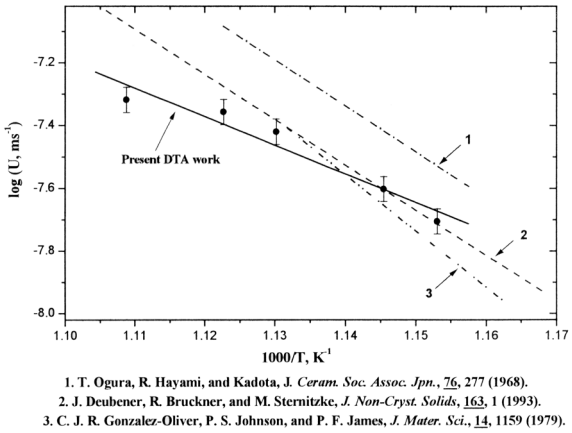

1. T. Ogura, R. Hayami, and Kadota, J. *Ceram. Soc. Assoc. Jpn.*, 76, 277 (1968).
2. J. Deubener, R. Bruckner, and M. Sternitzke, *J. Non-Cryst. Solids*, 163, 1 (1993).
3. C. J. R. Gonzalez-Oliver, P. S. Johnson, and P. F. James, *J. Mater. Sci.*, 14, 1159 (1979).

Figure 2. Crystal growth rate (U) for $Li_2O.2Sio_2$ glass as a function of temperture.

Some of the glass samples melted in space in platinum capsules will be returned to Earth in their as-quenched condition (i.e., without any heat treatment for nucleation and crystal growth in space) for structural evaluation, measuring specific properties, and determining the concentration of quenched-in nuclei (N_q) in these glasses (samples in the bottom row of Tables 1 and 2). A comparison of N_q in the space and Earth melted glasses will provide qualitative information on the degree of chemical homogeneity in these glasses. A glass containing a colored (blue) spot on its surface (sample B in Tables 1 and 2) will also be remelted in space for assessing the extent of fluid flow in high temperature melts in microgravity. Any movement of the blue spot in the melt will leave a blue trail in the melt.

II. Hypothesis

The reason why space glasses appear to be more resistant to crystallization than identical glasses prepared on Earth is not known at this time, but "shear thinning" is suspected to be a likely reason. "Shear

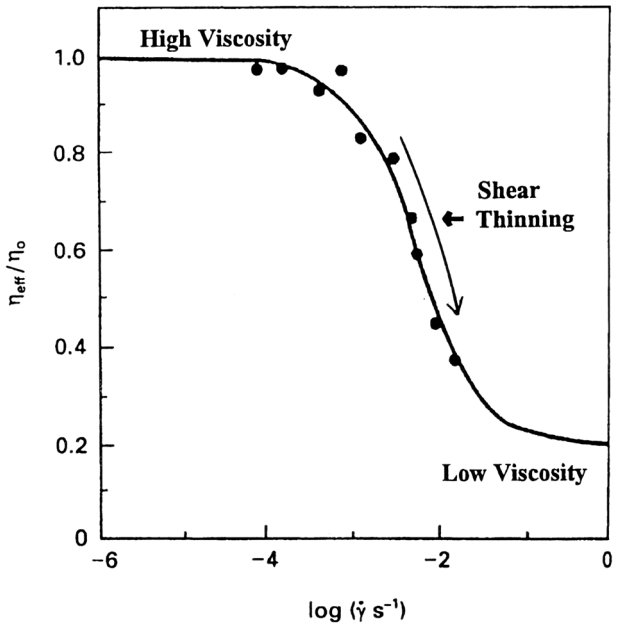

Figure 3. Change in the effective viscosity (η_{eff} with shear rate $\dot{\gamma}$ for a $Li_2O.2SiO_2$ glass at 483°C ($\eta_{\cap}$ ~ 2.24 x 10^{10} Pa.s). From reference 18.

thinning" is the reduction in viscosity, which occurs with increasing shear rate in non-Newtonian liquids at a constant temperature as shown in Figure 3. Such a reduction in viscosity with increasing shear rate has been reported for several commercial glasses[15-17], including the lithium disilicate (LS_2) composition[18,19] that will be used in our space experiments. The reported[17,18] decrease in viscosity with increasing shear rate for a LS_2 glass is shown in Figure 3. Our hypothesis is that the gravity-driven convective flow that is normally present to some degree in a melt on Earth will be much smaller or ideally absent in the same melt in space. Thus, the nearly stagnant melt in space should experience a smaller (or negligible) shear rate and, consequently, have a higher viscosity (less shear thinning) than a melt on Earth at the same temperature as schematically shown in Figure 4. A higher viscosity for the space glass would be expected to make it more resistant to crystallization because of the smaller nucleation and crystal growth rates, see Figure 4.

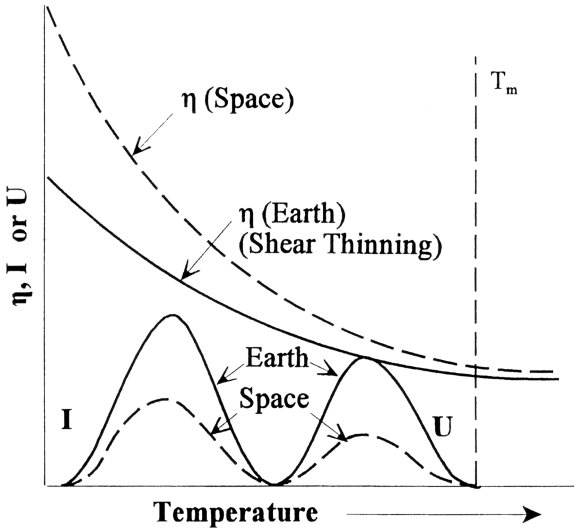

Figure 4. Schematic representation of the anticipated viscosity (η), nucleation rate (I), and crystal growth rate (U) for a melt in space and for the identical melt on Earth based on "shearing thinning."

Computer modeling for the rates of fluid flow and shear across a LS_2 melt of the same shape and size (cylindrical, 2.5 cm long and 1.0 cm in diameter) as those proposed for the flight experiments were performed in collaboration with Drs. N. Ramachandran of USRA and E. Ethridge of MSFC, NASA. The results show that the shear rate scales linearly with the gravity level for a constant temperature gradient across the melt and increases with increasing temperature gradient, see Figure 5. This means that the shear rate for a glass prepared in space ($< 10^{-4}$ g) will be at least four orders of magnitude less than that in the same glass prepared at 1g. Data for glasses such as LS_2 indicate that a reduction of four orders of magnitude in the shear rate for the space glass could cause the viscosity to increase from 2 to 10 times. Such an increase in viscosity could decrease the crystallization tendency (or increase the glass forming tendency) by factors from 16 to 10,000 compared to an identical glass prepared on Earth.

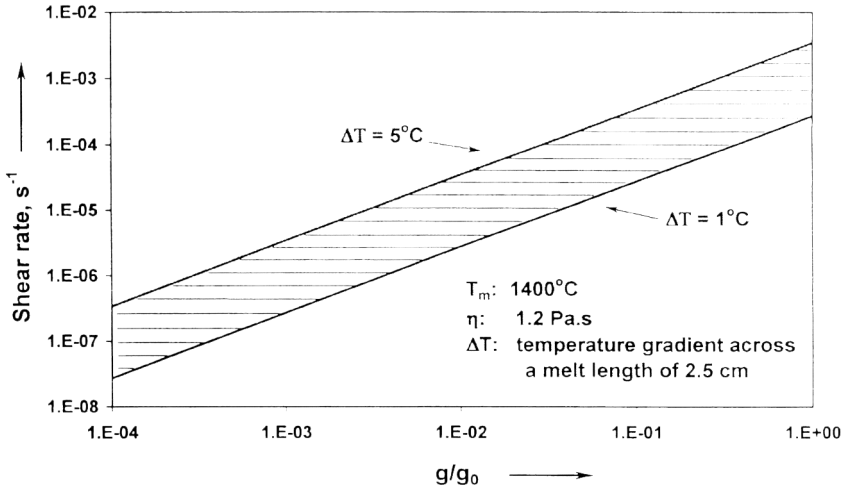

Figure 5. Calculated shear rate for a $Li_2O.2SiO_2$ melt as a function of gravity.

III. Comments

If the values for I and U for the LS_2 glass prepared in microgravity are indeed found to be smaller than the glass made on Earth, then our understanding of the fundamental processes for nucleation and crystal growth in glasses will be greatly improved. The classical equations for I and U will have to be modified to account for differences in gravity through the viscosity term in these equations. This enhanced understanding of the fundamental mechanisms for glass formation, nucleation, and crystallization could lead to improvements in present-day glass processing technology on Earth, thereby, improving our ability to produce glasses of higher quality and improved properties.

REFERENCES

1. Day, D. E., *Containerless Processing of Glass Forming Melts in Space*, NASA Contract *NAS8-34758*, February 1982 – December 1988.
2. Ray, C. S. and Day, D. E., *NASA Technical Memorandum #4069*, vol. 2, pp. 537-556 (1988).
3. Ray, C. S. and Day, D. E., *Proc. Mater. Res. Symp.*, 87, 239 (1987).
4. Barta, C., Stourac, L., Triska, A., Kocka, J. and Zavetova, M., *J. Non-Cryst. Solids*, 35 & 36, 1239 (1980).
5. Barta, C., Trnka, J., Triska, A. and Frumar, M., *Adv. Space Res.*, 1, 121 (1981).
6. Petrovskii, G. T., Ryumin, V. V. and Semeshkin, I. V., *Steklo i Keramika*, 1, 5 (1983).
7. Braetsch, V. and Frischat, G. H., *Naturwissen-Schaffen*, 73, 368 (1986).

8. Frischat, G. H., *J. Non-Cryst. Solids*, 183, 92 (1995).
9. Varma, S., Prasad, S. E., Murley, I., Wheat, T. A. and Abe, K., *Proc. Spacebound*, 91, 248 (1991); *ibid*, 92, 109 (1992).
10. Tucker, D. S., Workman, G. L. and Smith, G. A., *J. Mater. Res.*, 12, 2223 (1997).
11. Tucker, D. S., Scripa, R. N., Wang, B and Rigsbee, J. M., *Proc. 18th Int. Cong. On Glass*, 5-10 July 1998, San Francisco.
12. James, P. F., *Phys. Chem. Glasses*, 15, 95 (1974).
13. Narayan, K. L., Kelton, K. F. and Ray, C. S., *J. Non-Cryst. Solids*, 195, 148 (1996).
14. Ray, C. S., Fang, X., and Day, D. E., *J. Am. Ceram. Soc.*, 83, 865 (2000).
15. Li, J. H. and Uhlmann, D. R., *J. Non-Cryst. Solids*, 3, 127 (1970).
16. Simmons, J. H., Mohr, R. K. and Montrose, C. J., *J. Appl. Phys.*, 53, 4075 (1982).
17. Jacobs, J. M., *M S Thesis*, Alfred University, Alfred, NY, (1999).
18. Deubener, J. and Bruckner, R., *J. Non-Cryst. Solids*, 209, 96 (1997).
19. Gutzow, I., Durschang, B. and Russel, C., *J. Mater. Sci.*, 32, 5389 (1997); *ibid*, 32, 5405 (1997).

RECOVERY OF MINERALS IN MARTIAN SOILS VIA SUPERCRITICAL FLUID EXTRACTION

Kenneth A. Debelak* and John A. Roth

Department of Chemical Engineering
Vanderbilt University
Nashville, TN 37235

We are investigating the use of supercritical fluids to extract mineral and/or carbonaceous material from Martian surface soils and its igneous crust. Two candidate supercritical fluids are carbon dioxide and water. The Martian atmosphere is composed mostly of carbon dioxide (~95.3%) and could therefore provide an *in-situ* source of carbon dioxide. Water, although present in the Martian atmosphere at only ~ 0.03%, is also a candidate supercritical solvent. Previous work done with supercritical fluids has focused primarily on their solvating properties with organic compounds. Interestingly, the first work reported by Hannay and Hogarth (1) at a meeting of the Royal Society of London in 1879 observed that increasing or decreasing the pressure caused several inorganic salts *e.g.*, cobalt chloride, potassium iodide, and potassium bromide, to dissolve or precipitate in supercritical ethanol. In high-pressure boilers, silica, present in most boiler feed waters, is dissolved in supercritical steam and transported as dissolved silica to the turbine blades. As the pressure is reduced the silica precipitates onto the turbine blades eventually requiring the shutdown of the generator. In supercritical water oxidation processes for waste treatment, dissolved salts present a similar problem. Figure 1 shows the solubility of silicon dioxide (SiO_2) in supercritical water (2) The solubility curve has a shape characteristic of supercritical systems. At a high pressure (greater than 1750 atmospheres) increasing the temperature results in an increase in solubility of silica, while at low pressures, less than 400 atm., the solubility decreases as temperature increases. There are only a few studies in the literature where supercritical fluids are used in extractive metallurgy. Bolt (3) modified the Mond process in which supercritical carbon monoxide was used to produce nickel carbonyl ($Ni(CO)_4$). Tolley and Tester (4) studied the solubility of titanium tetrachloride ($TiCl_4$) in supercritical CO_2. They reported complete miscibility of $TiCl_4$ with supercritical CO_2 (infinite solubility). At 1500 psig, $TiCl_4$ and CO_2 form a single liquid phase below 50 °C. Tolley *et al.* (5) also reported on the solubility and thermodynamics of tin tetrachloride in supercritical CO_2. Some of their data for $TiCl_4$ are shown in Figure 2. Three criteria have been suggested to predict which materials are suitable for supercritical extraction (6):

1. Hydrocarbons or lipophilic compounds of low molecular weight and polarity are easily extracted with supercritical CO_2.
2. Compounds with polar groups are not easily extracted with supercritical CO_2.
3. Separation of mixtures is facilitated if components differing mass, vapor pressure, or polarity.

Materials which meet these criteria of supercritical fluid extraction are volatile metal chlorides such as germanium and titanium tetrachloride, and metal carbonyls such as $Ni(CO_4)$ and cobalt carbonyl. We propose to capitalize on the increased solubility and transport properties of minerals, salts and/or organic material in either supercritical carbon dioxide to recover these materials for use on Mars. We

will perform experiments to determine the solubilities and the recoverability of minerals and salts in supercritical carbon dioxide. Although ample solubility data exist for organic compounds, virtually no data exists for inorganic compounds. In addition, the criteria stated above have been developed for organic compounds. Criteria for predicting solubility of inorganic compounds is non-existent.

The solvating strength of a supercritical fluid is directly related to the density, which can be varied and controlled by regulating pressure, temperature, or both. Supercritical fluids have densities and solvating properties similar to liquid solvents, but have extremely rapid diffusion characteristics, and viscosities closer to those of gases (7). We plan to take advantage of these solvating properties to extract mineral and/or carbonaceous material from Martian surface soils and its igneous crust We will vary the temperature and pressure to determine the maximum solubility in supercritical CO_2. The experimental setup will use a flow-through system as shown in Figure 3. Materials to be extracted are contained in the extraction vessel. Supercritical CO_2 or supercritical water will flow through the extractor continuously removing the materials. The effluent stream will be monitored for the materials. The effluent stream will be sent to a separator where the temperature and pressure will be reduced to separate the materials from the CO_2 or water fluid. The CO_2 or water stream can then be reused. The minerals will then be recovered for further processing.

The Viking Lander missions have provided *in-situ* data for elemental analysis of the composition of Martian soils. The elemental analysis was performed by X-ray fluorescence spectroscopy. However all mineralogical information must be inferred based on the constraints placed by the concentrations of elements and other observations. The chemical analysis of the Martian soil by XRF has been reported in several publications (8-11). The Viking XRF experiments were limited in that they could not detect elements of atomic number less than 12. Therefore, the elements C, N, and Na which are important in mineral formation could not be detected. Table 1 shows the elemental concentration of the Martian soil determined by the Viking X-Ray Fluorescence, reported as oxides of the elements detected (8).

The solubility of a material in a supercritical fluid or in a mixture containing a supercritical component is essential for evaluating the viability of a minerals recovery process. Predictive procedures continue to improve, but require physical properties of both the solute and solvent along with an equation of state.

Table 1. Average Weight % Composition of Sediments Determined by the Viking Lander X-Ray Fluorescence Spectrometers (7)

	Viking Lander I	Viking Lander II
SiO_2	44	43
TiO_2	0.62	0.54
Al_2O_3	7.3	7
Fe_2O_3	17.5	17.3
MgO	6	6
CaO	5.7	5.7
K_2O	<0.5	<0.5
SO_3	6.7	7.9
Cl	0.8	0.4
Other	2	2
Total	91	90

The cubic equations of state, Redlich-Kwong or Peng-Robinson, which include parameters, which describe the temperature dependence of the attractive terms, have proven most useful. However, the interaction parameters have been determined mostly from experimental data, and only after proper use of mixing rules and the assignment of the interaction parameters. Carleson, *et al,* (14) have recently developed a group contribution method to predict interaction parameters in the absence of experimental data. However, even modified cubic equations of state are poor predictors. We will use either the Redlich-Kwong or the Peng-Robinson equation of state along with van der Waals type mixing rules to correlate the solubilities of the minerals. Brennecke and Eckert (15) reviewed the various equations of state and concluded that the Peng-Robinson may be as good as more complicated equations. The constants a and b in the Peng-Robinson equation are determined from critical constants and acentric factors for the pure compounds. In mixtures, the constants are determined using Van der Waals mixing rules.

The mixture parameters a and b are related to the pure component terms a_i and b_i by

$$a_{\text{mixture}} = \sum_{i=1}^{n} \sum_{j=1}^{n} x_i x_j a_{ij} \quad (1)$$

$$a_{ij} = (1-k_{ij})(a_i a_j)^{1/2}, \; i \neq j \quad (2)$$

$$b_{\text{mixture}} = \sum_{i-1}^{n} x_i b_i \quad (3)$$

$$a_{ii} = a_i \quad (4)$$

x_i are mole fractions, a_i are pure component constants, and k_{ij} is the interaction parameter. The fugacity coefficient can be related by

$$RT\ln\phi_i = -\int_{\infty}^{V}\left[\left(\frac{\partial P}{\partial N_i}\right)_{T,V,N_{ij}} - \frac{RT}{V}\right]dV - RT\ln Z \quad (5)$$

$$\ln\phi_i = \frac{b_i}{b}(Z-1) - \ln(Z-B) + \frac{A}{2^{1.5}B}\left[2\frac{\sum_{j-1}^{n} x_j a_{ij}}{a_m} - \frac{b_i}{b_m}\right]\ln\left[\frac{Z - B(1-2^{0.5})}{Z + B(1+2^{0.5})}\right] \quad (6)$$

N_i is the moles of component i and Z is the compressibility. The Peng-Robinson equation of state relates pressure and volume to Z, and by using the mixing rules, the fugacity coefficient is determined in equations 5 and 6. The relation between A and B and the compressibility is given by

$$Z^3 - (1 - B)Z^2 + (A - 3B^2 - 2B)Z - (AB^2_B - B^3) = 0 \quad (7)$$

$$A = \frac{AP}{R^2T^2} \qquad B = \frac{bP}{R^2T^2} \quad (8)$$

Terrestrial extractive metallurgy has made use of the solvating power of water to recover different types of minerals. The availability and solvating power of water has made it the ubiquitous solvent of choice. On Mars carbon dioxide is the ubiquitous material. Water is available but not near as abundant. We are proposing to determine if supercritical carbon dioxide can be used to extract mineral matter from Martian soils. It is available in abundance. We will investigate the feasibility of the initial process or processes used to separate minerals for further processing. It may be possible to recover water, oxygen, and carbon from oxides, carbonates, and bound water using supercritical extraction and/or additional processing. The solubility of the mineral matter from Martian soils could also be the basis for an analyti-

cal instrument to be included on a future Mars probe. Currently available from several manufacturers are supercritical chromatographs. A system suitable for inclusion on a future Mars probe could be designed to solubilize and concentrate minerals for further analysis or even return to Earth.

REFERENCES

1. Hannay, J.B. and J. Hogarth, "On the solubility of Solids in Gases," Proc. R. Soc. London, V. 29, 1879, pp324-326.
2. Kennedy, R.G., "A portion of the system silica-water," Econ. Geol., 45:269, 1950
3. Boldt, J.R., The Winning of Nickel, Van Nostrand, 1967, pp374-31.
4. Tolley, W.K. and L.S. Tester, "Supercritical CO_2 Solubility of $TiCl_4$", U.S. Dept. of Int. Rep. Invest.,Bur. Mines, 1989, RI 9216.
5. Tolley, W.K.;Giles, N.F. ; Oscarson, J.L. ; Rowley, R.L. ; ; Izatt, R.M. "Thermodynamic Properties of Mixing for $SnCl_4$ Dissolved in Supercritical CO_2, A Combined Experimental and Molecular Dynamics Study." Fluid Phase Equilibria v 73 n 3 May 1 1992 p267-284
6. Stahl, E. and K.W., "Dense Gas Extraction on a Laboratory Scale: A Survey of Recent Results," Fluid and Phase Equilibria, B. 10, 1983, pp269-278.
7. McHugh, M.A. and V.J. Krukonis, "Supercritical Fluid Extraction, Principles and Practice," Butterworth, Boston, 1986.
8. Clark, B.C., A.K. Baird, R.J. Weldon, D.M. Tsuaki, L.Schnabel, and M.P. Candelaria, Chemical Composition of Martian Fines," J.Geophys. Res. 87:10059-10067, 1982.
9. Clark, B.C. et al. "Inorganic Analysis of Martian Surface Samples at Viking Landing Sites" Science, 194:1283:1288, 1976
10. Clark, B,C. et al. "The Viking X-ray Fluoresence Experiment: Analytical Methods and Early Results", J. J.Geophys. Res. 82:4577-4594, 1977
11. Stroker, C.R., et al. "The Physical and Chemical Properties and Resource Potential of Martian Surface Soils," Resources of Near-Earth Space, Eds. J.S. Lewis, M.S. Mathews, and M.L. Guerrieri. Univ. of Arizona Press, pp659-708, 1993
12. Allen, C.C., et al. NASA Johnson Space Flight Center, Houston, TX
13. http://mars.jpl.nasa.gov/apxs_oxides.htm
14. Carlson, T. E., S. Chandra, C. Wai, L. Wai, S.S. Huang, "Group Contribution Method for Estimating Solubility of Selected Hydrocarbons Solutes in Supercritical Carbon Dioxide," Supercritical Fluid Engineering Science, Ed. E. Kiran and J.F. Brennecke, ACS Symposium Series 514, 1993, CH. 24.
15. Brennecke, J.F. and C.A. Eckert, AICHE J. 1989, 35(9), 1409
16. NASA Research Announcement, Dec. 16, 1998, "Microgravity Materials Science: Research and Flighty Experiment Opportunities", NRA-96-HEDS-02, NASA, Washington, D.C.

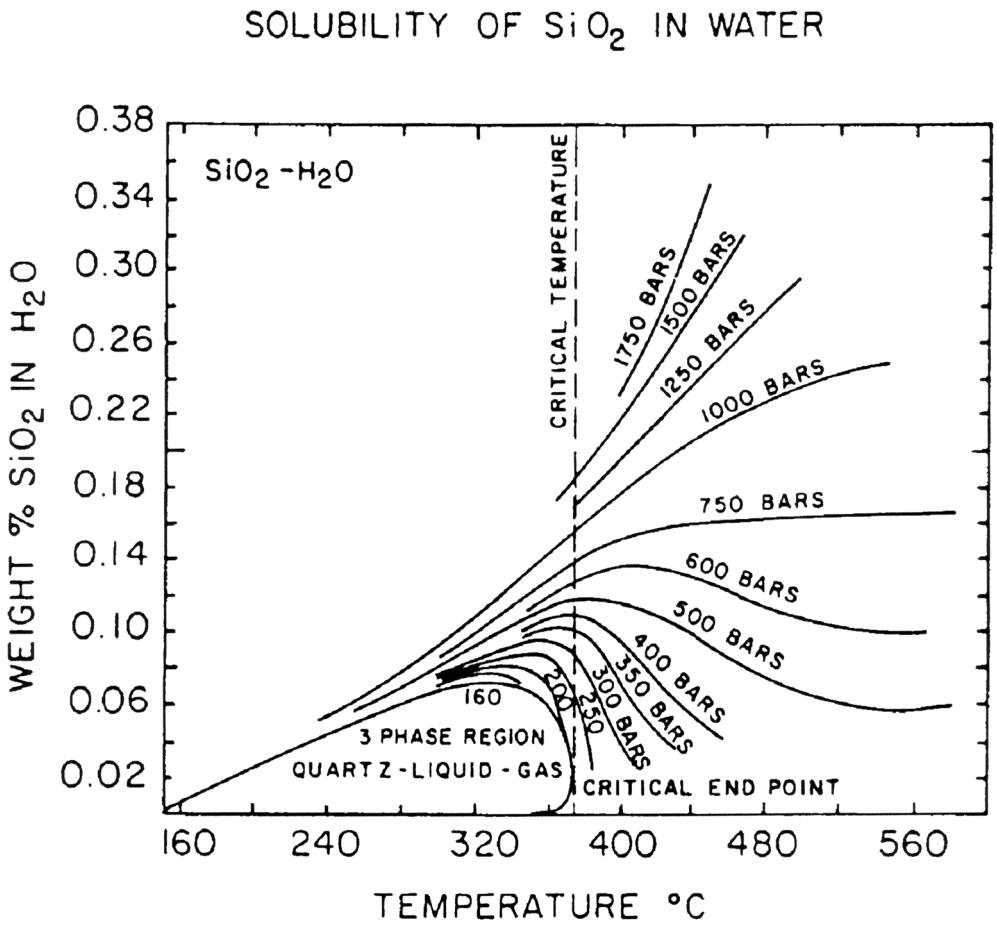

Figure 1. Solubility behavior of solid silica in supercritical water (Kennedy, 1950).

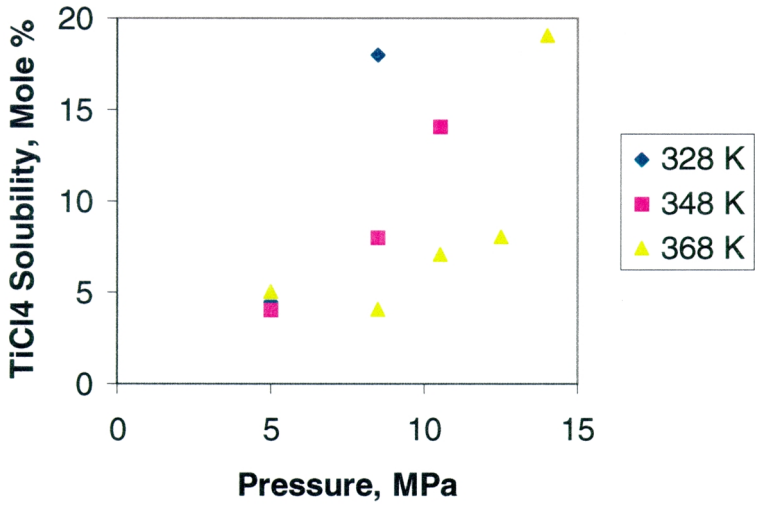

Figure 2. $TiCl_4$ solubility in CO_2.

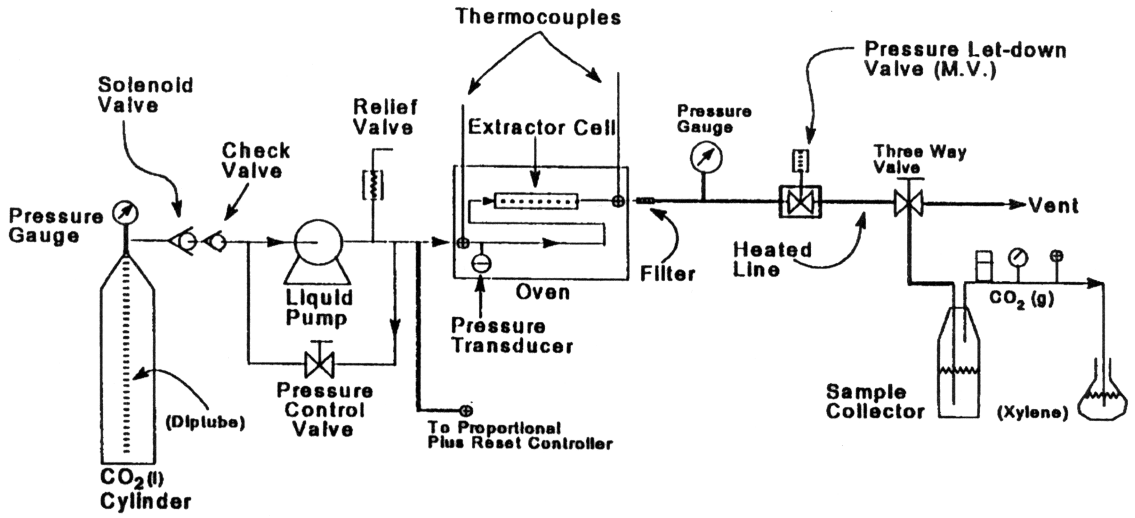

Figure 3. Schematic diagram of the experimental setup.

FIRST PRINCIPLES CALCULATIONS OF MOLTEN II-VI COMPOUNDS AND THEIR SOLIDIFICATION BEHAVIOR

J.J. Derby * and J.R. Chelikowsky

Department of Chemical Engineering and Materials Science, University of Minnesota

The goal of the ground-based research proposed here is to employ first-principles atomistic simulations to obtain a more fundamental understanding of the physical behavior of molten binary and ternary alloys of the group II elements cadmium (Cd), mercury (Hg), and zinc (Zn), and group VI elements tellurium (Te) and selenium (Se). Specifically, we will employ atomistic simulations with fully quantum mechanical forces. This procedure allows a parameter-free description of the liquid state and has been applied to liquid silicon, germanium and gallium arsenide; the resulting descriptions are in good agreement with existing experimental data. Other than our previous studies of liquid CdTe, no comparable simulations have been performed for II-VI semiconductors.

These materials are employed in a variety of technologically important electronic and electro-optical devices; however, the growth of high-quality, single-crystal substrates of these compounds has typically proven to be extremely difficult under terrestrial conditions. As such, they present ideal model systems to probe using microgravity techniques. Indeed, many ongoing, NASA-funded space-flight and ground-based experiments are studying several technologically significant and scientifically interesting II-VI semiconducting alloys. For example, complicated segregation behavior in ternary II-VI systems is being studied by groups at NASA Marshall Space Flight Center, and recent growth experiments of CdZnTe in a microgravity environment aboard the First United States Microgravity Laboratory resulted in material which was far superior in structural perfection compared to Earth-grown material under similar conditions. We seek to obtain a more fundamental understanding of the properties of these molten liquids so that the physical mechanisms acting during crystal growth can be elucidated. An additional significant outcome of this work will be the theoretical prediction of valuable physical properties, such as diffusivities, which are not currently known and are very difficult to measure accurately via experiments. Such predictions will be extremely useful for use in macroscopic process models and for comparison with NASA-funded experimental property measurements of II-VI compounds.

We anticipate that this work will provide a more fundamental understanding of molten II-VI semiconductor alloys and their behavior during crystal growth. This knowledge will significantly complement ongoing NASA-funded research on the growth of these compounds, specifically by identifying unambiguously the factors responsible for II-VI growth under microgravity and ground-based growth conditions. In addition, the proposed research will be carried out in collaboration with ongoing modeling of macroscopic transport in melt growth systems, both under micro-gravity and terrestrial conditions, by the Derby research group at the University of Minnesota. The unraveling of the mechanistic couplings between atomistic events and macroscopic

* Corresponding author

transport in crystal growth systems poses intellectual challenges comparable to the "Grand Challenge" supercomputer problems of the pure physical sciences and is perhaps even more compelling due to the tremendous economic value associated with the manufacturing of advanced crystalline materials. This contention is bolstered by a recent DOE/NSF study which has identified computational materials research as an activity which can strongly enhance U.S. industry's competitive edge. Ultimately, our goal is the ability to link crystal properties and device performance with growth conditions and the macroscopic factors which influence them.

THEORETICAL ANALYSIS OF 3-D, TRANSIENT CONVECTION AND SEGREGATION IN MICROGRAVITY BRIDGMAN CRYSTAL GROWTH

J.J. Derby* and A. Yeckel

Department of Chemical Engineering and Materials Science
University of Minnesota

Key to the advancement of crystal growth processing is a better understanding of the dominant influence of buoyancy-driven convection on segregation and morphological stability during crystal growth on Earth. Since these effects in turn play a critical role in establishing the structure and properties of grown materials, considerable interest has developed for their study by use of the microgravity environment provided by space flight. However, space flight experiments are still subject to accelerations that rapidly vary in magnitude and direction, and such variations complicate experiments by the introduction of significant transient and three-dimensional effects. We are developing rigorous process models that account for such three-dimensional, transient phenomena during melt crystal growth under microgravity conditions.

There has long been interest in employing the microgravity environment of space to process advanced materials. Growing crystals in space has the alluring potential to reduce convective flow velocities to the point where diffusion-controlled growth is possible, thus promoting the growth of higher quality crystals and enabling the detailed study of segregation phenomena. Early space experiments confirmed that microgravity processing could significantly reduce the level of melt convection. Uniform doping was not achieved, however, indicating that convection was not completely damped in the melt. Recent experiments conducted on the first United States Microgravity Laboratory also indicated that convection was not totally damped. Clearly, reducing the magnitude of the gravitation force alone was not sufficient to achieve diffusion-controlled growth in these experiments. Other effects can also complicate the microgravity environment, especially those associated with time-dependent changes in the direction and magnitude of the gravity vector (g-jitter). These effects induce flow in the melt that is three-dimensional and time-dependent.

Previous attempts to model the effects of g-jitter have relied on an assumption of 2-D, axisymmetric behavior that greatly simplifies analysis. This work will directly address the limitations of such models. The rigorous simulation of three-dimensional, transient effects will allow, for the first time, quantitative analyses of segregation phenomena in microgravity systems. This capability will be extremely important for the unambiguous interpretation of flight experiments, and, perhaps more importantly, will provide a tool to design the conditions needed in future flight experiments to best study the effects of microgravity on segregation theory. We will report on progress made in several areas.

While the pseudo-binary assumption has frequently been applied to study segregation in ternary systems, the behavior of multicomponent diffusion in a truly ternary system is considerably more complicated. We present initial results on the the application of the Stefan-Maxwell equations to describe

* Corresponding author

multicomponent mass transfer and segregation during growth of a ternary alloy. This nonlinear, transient problem is solved using a two-dimensional finite element method which rigorously accounts for heat transfer, mass transfer, fluid mechanics, and the position of the solid-liquid interface. We present results to demonstrate how coupling between components can lead to retrograde concentration profiles in the diffusion layer, where, in stark contrast to the simple Fickian diffusion predicted by pseudo-binary models, a component diffuses against its activity gradient. Such behavior may have significant consequences in setting compositional profiles during the growth of II-VI alloys.

Buoyancy-driven melt convection dominates mass transport in many crystal growth systems, thereby having a critical effect on solute segregation. Since segregation in turn plays a key role in determining the properties of grown materials, there is widespread interest in the application of various methods to modify or suppress convection. We present detailed theoretical analyses of several such methods applied to vertical Bridgman crystal growth. These include processing in the microgravity environment provided by space flight, application of a magnetic field, and steady crucible rotation, all of which tend to reduce buoyancy-driven convection. Also considered is accelerated crucible rotation, which has the opposite effect of the other methods: it tends to promote melt mixing by enhancing convective transport. Our analyses show that buoyancy-driven convection persists in dominating mass transport in all cases considered. Indeed, in some cases segregation is worsened by use of these methods. Furthermore, all of these methods can induce significant transient and three-dimensional effects, which greatly complicate the analysis of these systems.

Finally, our fully 3-D modelling approach will be discussed. We provide an overview of finite-element models employed to simulate melt and solution crystal growth, emphasizing the challenges of modeling three-dimensional, transient phenomena and interfacial effects with moving boundaries.

ATOMISTIC SIMULATIONS OF CADMIUM TELLURIDE: TOWARD UNDERSTANDING THE BENEFITS OF MICROGRAVITY CRYSTAL GROWTH

J.J. Derby * and J.R. Chelikowsky

Department of Chemical Engineering and Materials Science, University of Minnesota

Progress in crystal growth on Earth or in space will depend on a more fundamental understanding of the important coupling between atomistic-scale processes which control the properties of grown crystalline material and the macroscopic transport conditions imposed by the growth system. Our long-term goal is to understand the mechanisms which influence crystal quality through the hierarchy of length and time scales relevant to these atomistic-scale and macro-scale processes. The immediate goal of the research summarized here is to employ atomistic simulation to understand better the melt growth of cadmium telluride (CdTe) and its alloy cadmium zinc telluride (CdZnTe). These materials are employed in a variety of technologically important electronic and electro-optical devices; however, the growth of high-quality, large-area single crystal substrate has proven to be extremely difficult under terrestrial conditions. We seek to obtain a more fundamental understanding of the properties of cadmium telluride so that the physical mechanisms responsible for growth can be elucidated. A secondary objective of our work is the prediction of high-temperature thermophysical properties of liquid and solid CdTe.

The primary thrust of this work will be to clarify the role of microgravity in interpreting the growth of CdTe and its alloys; however, this work promises to support future microgravity research in other substantial ways. Atomistic simulations will provide predictions of the high-temperature thermophysical properties. Accurate high-temperature properties are needed for reliable materials processing models, but such data are extremely difficult to obtain from experimental measurements (many of which have been undertaken in microgravity environments). The prediction of these properties using atomistic simulation clearly complements ongoing and future microgravity process modeling and experimental property measurement efforts. Another likely benefit from this work is that a more complete understanding of the structure of molten CdTe and alloys will aid the development of seeding procedures for melt growth. For Earth-based processes, reliable seeding techniques have not yet been developed for these materials, yet such procedures have been identified as one of the most needed process improvement to increase yields. Undoubtedly, as further microgravity experiments on the melt growth of CdZnTe are performed, seeded growth experiments will be desired and the knowledge obtained from atomistic simulations will be invaluable.

We have successfully employed *ab initio* pseudopotentials to compute the electronic structure of solid and liquid CdTe. Subsequent work focused on performing first principles molecular dynamics simulations on the liquid state using interatomic forces between atoms to calculate the atomic trajectories and integrate the equations of motions to simulate the liquid. The liquid was modeled by considering a 64 atom unit cell with periodic boundary conditions; the atoms were randomly placed in this cell and initially heated to a very high temperature. After cooling the system to a temperature slightly above the melting temperature, we analyzed the resulting liquid.

* Corresponding author

We have determined the pair correlation function, the self-diffusion of the Cd and Te atoms, and have performed an analysis of the liquid structure. We compared the theoretical results for the pair correlation function to experimental x-ray and neutron work. Our initial comparisons are quite encouraging; the predicted and experimental distributions are quite similar. Likewise, our computed diffusion coefficients are consistent with experiments.

Of particular interest is the theoretical confirmation that CdTe is a molten semiconductor. All semiconductors of IV row, such as silicon, and III-V materials, such as gallium arsenide, assume metallic behavior when melted. This is in contrast to some II-VI semiconductors such as CdTe which retain their semiconducting behavior in both the liquid and the solid state. In order to understand this difference, we have performed *ab initio* molecular dynamics simulations of liquid GaAs and CdTe. Using the Kubo-Greenwood formalism, we predict the conductivity of both liquids and confirm the differences observed experimentally. We relate the conductivity differences between II-VI and III-V semiconductors to strong structural differences occurring within the melt. These melt structures may also be responsible for the difficulty in growing single-crystalline CdTe from the melt.

REAL-TIME OPTICAL MONITORING OF FLOW KINETICS AND GAS PHASE REACTIONS UNDER HIGH-PRESSURE OMCVD CONDITIONS

N. Dietz *, S. McCall and K.J. Bachmann

Department Materials Science & Engineering,
North Carolina State University, Raleigh, NC 27695

ABSTRACT

This contribution addresses the real-time optical characterization of gas flow and gas phase reactions as they play a crucial role for chemical vapor phase depositions utilizing elevated and high pressure chemical vapor deposition (HPCVD) conditions. The objectives of these experiments are to validate on the basis of results on real-time optical diagnostics process models simulation codes, and provide input parameter sets needed for analysis and control of chemical vapor deposition at elevated pressures. Access to microgravity is required to retain high pressure conditions of laminar flow, which is essential for successful acquisition and interpretation of the optical data. In this contribution, we describe the design and construction of the HPCVD system, which include access ports for various optical methods of real-time process monitoring and to analyze the initial stages of heteroepitaxy and steady-state growth in the different pressure ranges. To analyze the onset of turbulence, provisions are made for implementation of experimental methods for *in-situ* characterization of the nature of flow. This knowledge will be the basis for the design definition of experiments under microgravity, where gas flow conditions, gas phase and surface chemistry, might be analyzed by remote controlled real-time diagnostics tools, developed in this research project.

I. Introduction

In this paper we describe our process in work on the real-time optical monitoring of high-pressure chemical vapor deposition, building on previous research presented elsewhere[1,2]. The objective is to study the kinetics of nucleation and coalescence of heteroepitaxial thin films, which is an important step of chemical vapor deposition since it defines the perfection of the heteroepitaxial film both in terms of extended defect formation and chemical integrity of the interface. It also defines the film quality during the later stages of film growth. Present growth efforts focus on low pressure processing to minimize the influence of flow dynamics on process uniformity and favors for III-V compounds organometallic chemical vapor deposition (OMCVD). However, the extension to above atmospheric pressures is necessary for retaining stoichiometric single phase surface composition for materials that are characterized by large thermal decomposition pressures at optimum processing temperatures. For example, $Ga_xIn_{1-x}N$ heterostructures have been identified as an important basis for manufacturing of optoelectronic and microelectronic devices, such as, light sources, detectors and high power microwave devices for which large potential markets can be identified. Due to the high thermal decomposition pressure of InN, these devices are at present limited to gallium-rich compositions. High nitrogen pressure has been demonstrated to suppress thermal decomposition of InN, but has not been applied yet in chemical

*Corresponding author: ndietz@unity.ncsu.edu

vapor deposition or etching experiments. Because of the difficulty with maintaining stochiometry at elevated temperature, current knowledge regarding thermodynamic data for InN, *e.g.*, its melting point, temperature-dependent heat capacity, heat and entropy of formation are known with far less accuracy than for InP, InAs and InSb. Gaining access to these data will require the development of new real-time optical diagnostics, capable of obtaining sufficient accurate data on flow conditions, gas phase reactions as well as on the surface reaction kinetic to support modeling and simulations of thin film growth under laminar and/or turbulent flow conditions at sup-atmospheric pressure. The present focus is on the heteroepitaxial growth of group III-nitrides/phosphides.

II. Properties of Group III Nitrides and Methods of Heteroepitaxy

Group III nitride films have been grown on a variety of compound substrates by several vapor growth methods, such as, halide transport[3] plasma-assisted OMCVD[3] and gas source molecular beam epitaxy of GaN on 6H-SiC on (11.0) and (00.1) misoriented by 4° off the singular surface toward [11][4,5], and conventional OMCVD on AlN coated sapphire using ammonia as nitrogen source[6,7]. A two-step OMCVD process[8,9], growing first a buffer layer at low temperature (1073 K) followed by high temperature (1273K) GaN growth, allows suppression of three-dimensional growth. A trade-off is made in this method between promoting continuous film growth and preserving surface stoichiometry, favoring growth at relatively high pressure[10].

The p - T - x relations in the indium - nitrogen system are not known at present, but studies of the nitrogen pressure needed to prevent thermal decomposition of bulk InN according to

$$\mathrm{InN(s)} \rightarrow \mathrm{In(1)} + \frac{1}{2}\mathrm{N_2(g)} \tag{1}$$

results in the $p - T^{-1}$ relation shown in Figure 1[11]. We note that since reversibility has not been shown by McChesney *et al*., the interpretation of the linear relation between p and T according to the equation

$$p(N_2) \rightarrow p_0 \exp\left[-\frac{\Delta H_r}{R}\left(\frac{1}{T} - \frac{1}{T_0}\right)\right] \tag{2}$$

obtained by integration of van t'Hoff's reaction isobar is not reliable. However, for the purpose of our study this is not important since it suffices to know that in the range $p_{N2} \bullet 10^2$ atm at substrate temperature • 900 K surface decomposition of InN will be effectively suppressed. In view of the higher melting temperature of InN (~1200°C) as compared to InP (1062°C) this appears to be a minimum requirement for the growth of high quality epitaxial InN heterostructures. Most low pressure OMCVD studies of InN employ substrate temperatures of ~ 773K, which in the case of ALE has been extended to 823K, where difficulties with loss of indium from the surface and formation of indium droplets in the epilayer becomes severe [12].

The problem of turbulence in high pressure vapor deposition of thin film heterostructures for large Reynolds number flows is an impediment to the successful processing of advanced materials for microelectronics and optoelectronics applications, such as InN and its solid solutions, which are characterized by thermal decomposition pressures exceeding atmospheric pressure at their optimum processing temperature. Control of defect formation mandates operating temperatures in excess of 600°C, and requires a nitrogen pressure of • 100 atm to avoid surface decomposition. In order to address the problem of materials processing at super-atmospheric pressure by high pressure organometallic chemical vapor deposition (HPOMCVD) additional insights can be provided by real-time process monitoring using optical real-time diagnostics.

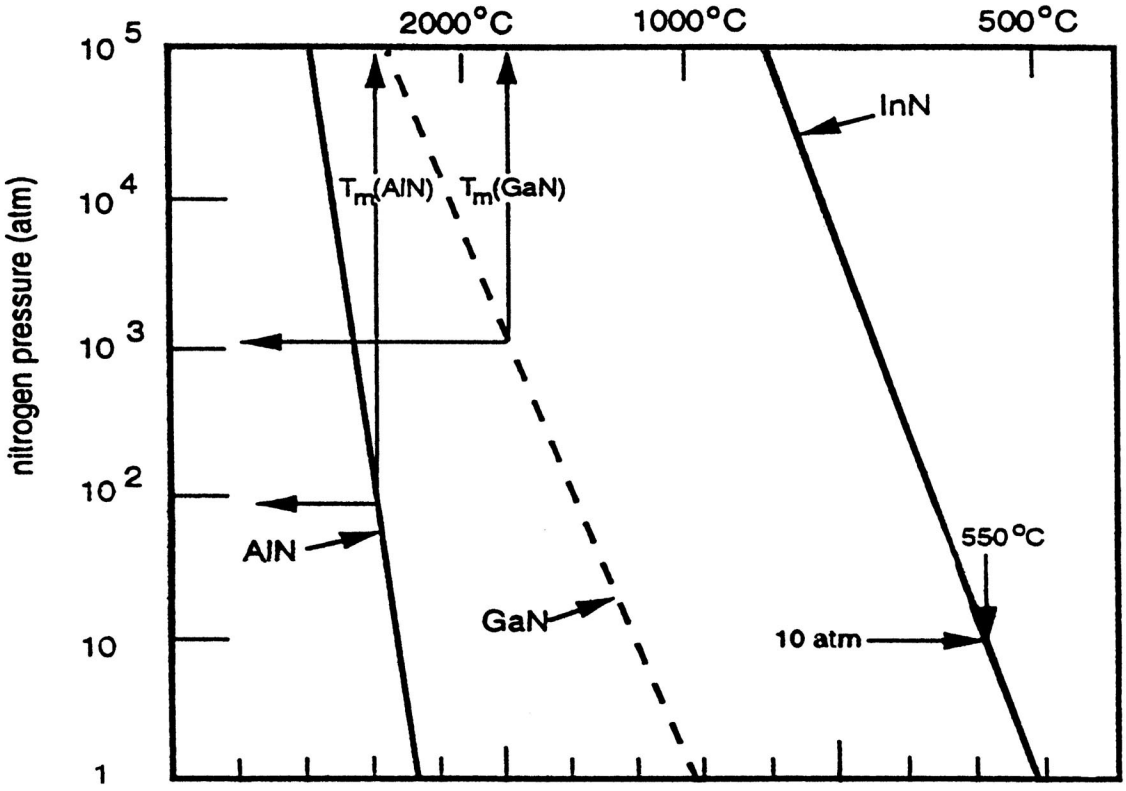

Figure 1. Thermal decomposition pressure vs. reciprocal temperature for AlN, GaN and InN. After McChesney *et al.*[11].

III. Reactor Design and Implementation

The reactor design is aimed at analyzing gas phase and surface kinetic reactions parameter during HPCVD gas flow and film growth under normal and reduced gravity conditions. As depicted in Figure 2, the design employs machined inner walls grading in and out of the entrance and exit ports such that the flow channel formed does not change in cross section from entrance to the exit. The substrate blocks are incorporated symmetrically in the upper and lower channel walls. Thus the bifurcation of nutrient fluxes to the top and bottom channel walls is symmetric to the center-line. Thus well behaved flow and deposition can be expected to prevail at $< 10^{-4}$ g gravity in the targeted pressure range. A fully machined and assembled half-part of this reactor system is shown in Figure 3. Two of these inner parts together form the inner shell of the HPCVD reactor, which will be inserted in a 6-inch diameter pressure confinement shell that withstands pressures up to 100 atm.

Figure 4 shows schematically a cross-sectional cut along the optical probe axis and perpendicular to the flow axis - of the inner reactor system, where the two half-parts are put together and the optical sapphire rods are attached. Because of the symmetry of the lay-out of the top and bottom channel walls with regard to the channel center line and a coupled control of substrate heating, we expect under conditions of laminar flow equivalent nucleation and overgrowth kinetics on both substrate surfaces. Both inner half parts are identical with exemption of the angle of incidence for principal angle reflectance spectroscopy (PARS), which have been chosen 28 deg and 30 deg for the upper and lower part, respectively. As schematically depicted in Figure 5a, PARS utilizes p-polarized light impinging the substrate-ambient interface near the principal angle φ_P. The angle of total reflection, φ_T, is approximately 5 deg above φ_P.

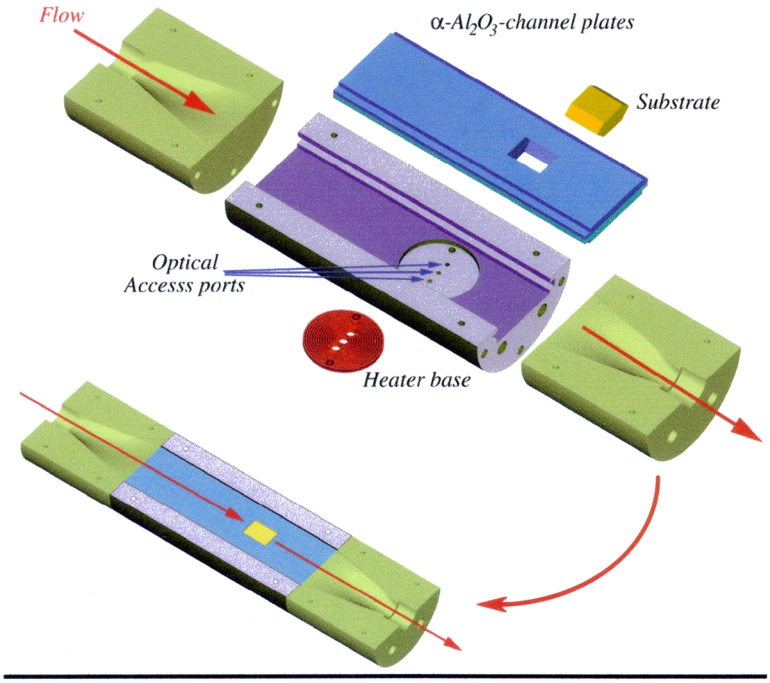

Figure 2. Schematic perspective outline of the inner HPCVD reactor. The design provides optical access ports for real-time gas-phase and surface diagnostics.

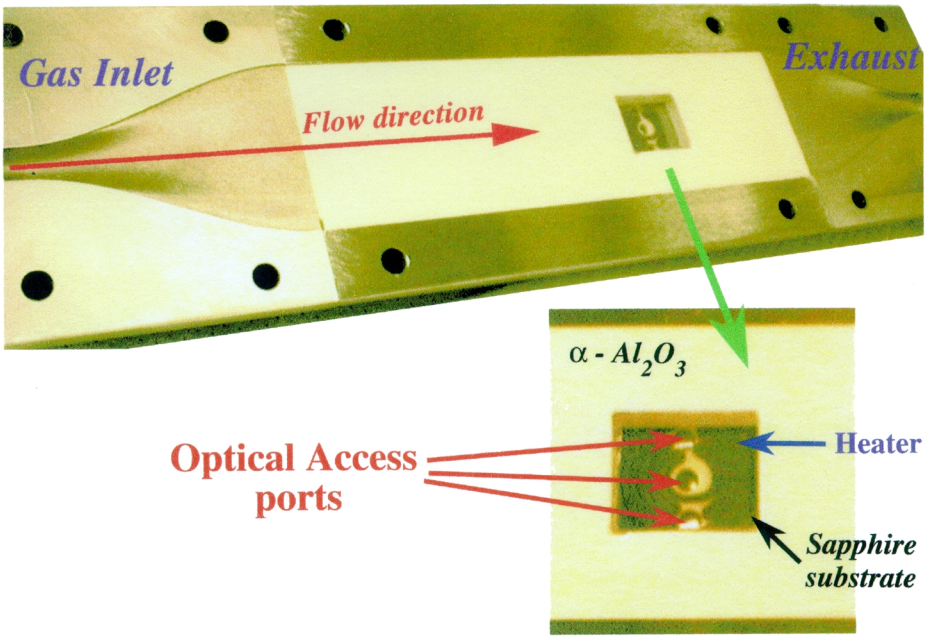

Figure 3. Perspective view of one of the machined and assembled inner half-parts of the HPCVD reactor. The transparent sapphire substrate allows a view on the heater element as well as to the optical ports entering from the back.

The wavelength dependency of the principal angle is shown in Figure 5b with a calculated shift of more than 2 deg in the wavelength range of 200 nm and 1700 nm. The temperature shift is in the order of 0.2 deg between room temperature (RT) and 1000°C. Utilizing these two angles of incidence, two independent but complementary measurements can be performed at the same time. The entrance- and exit ports for PARS, together with the normal incidence access port, will be also used Raman spectroscopy.

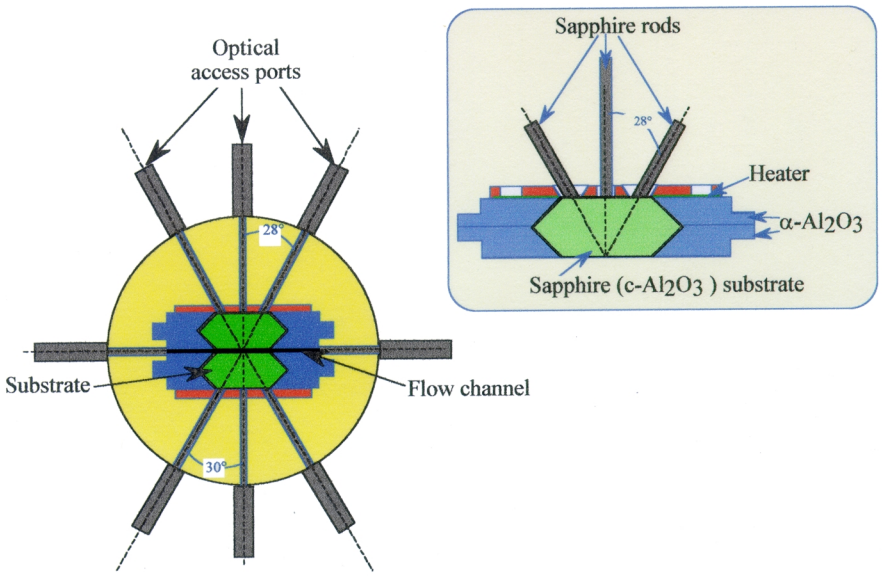

Figure 4. Schematic cross-sectional view of the inner HPCVD reactor. Optical access to the growth surface is provided by optical rods through the back-side of the substrate for PARS, Raman and normal-incidence reflectance.

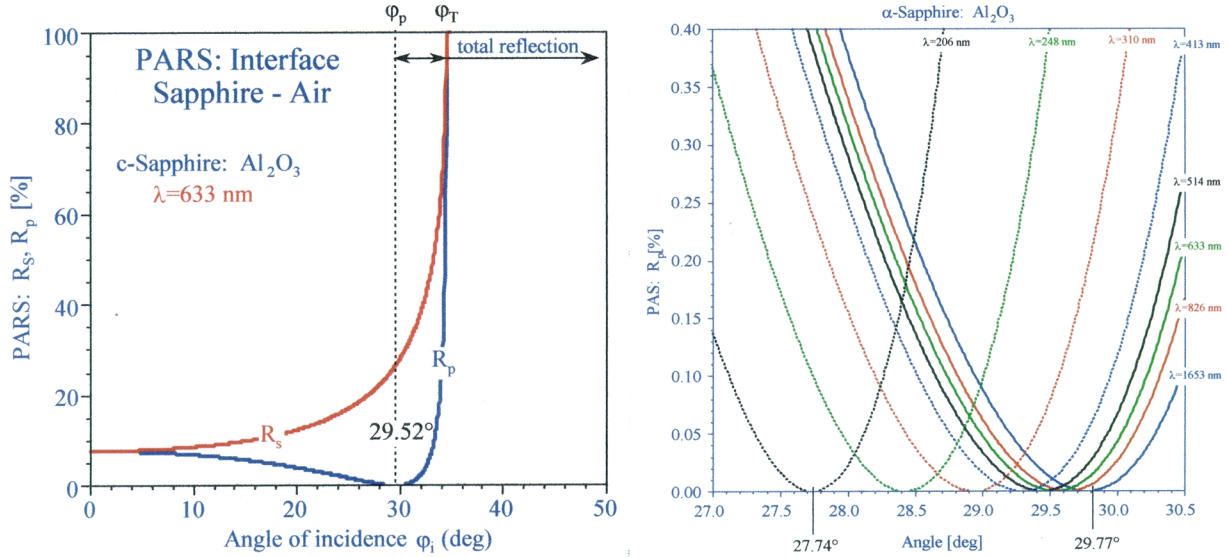

Figure 5. a. Angle dependency of reflectance for p- and s- polarized light at the interface sapphire ambient. Depicted are the characteristic angles: principal angle φ_P and total reflection angle φ_T.
b. Wavelength dependency of the p-polarized reflectance component and shift in the principal angle φ_P in the wavelength range of 200 nm and 1700 nm, calculated for the sapphire ambient interface.

For flow visualization, analysis of flow dynamic, as well as for studies of gas phase reactions, optical access ports are integrated perpendicular to the flow axis. Rayleigh scattering[13] has been utilized widely in detecting turbulent flow (see refs.[14,15] for recent reviews). Operation at high frequency ν is desirable since the Rayleigh scattered intensity $I_R(\nu)$ is proportional to the fourth power of ν. Limits in the useful range of ν are imposed by effects on gas phase chemical kinetics, so that tradeoffs between sensitivity and control of chemical mechanisms must be made. Etalons have been used to advantage in analyses of flow dynamics based on quantitative analyses of contributions of molecular motion to the line shape for Rayleigh-Brillouin scattering[16,17] and for achieving high resolution in Raman line shape analysis. At low pressure and high temperature, where thermal motion is described by the Maxwell-Boltzmann

distribution, a Gaussian line shape is observed for the Doppler-shifted intensity. However, at high pressure, the Gaussian line shape is altered by superposition of Lorentzian components associated with collective motions, such as, thermal diffusion and Brillouin scattering from acoustic waves[14]. Because of the relatively small solid angle for collection of incoherently scattered radiation it may be necessary to add absorption spectroscopy at specific energies in resonance with vibrational-rotational signatures for the most important molecular fragments diffusing toward the surface of the growing film. Simultaneous monitoring of Raman scattering, absorption spectroscopy, Rayleigh-Brillouin scattering, and PARS, provides information on temporal and spatial temperature fluctuations, variations in flow velocity components, and variations of concentrations of specific constituents in the vapor phase. In conjunction with the results of process simulations these experimental data provide all necessary experimental input needed for flow simulation and process control.

IV. Acknowledgments

We would like to acknowledge support of this work by NASA cooperative Agreement NCC8-95, NASA grant NAG8-1686, and DOD MURI Grant F-49620-95-1-0447.

REFERENCES

1. K.J. Bachmann, S. McCall, S. LeSure, N. Sukidi and F. Wang, J. Jpn. Soc. Microgravity Appl. Vol. 15 p. 436 (1998).
2. K.J. Bachmann, B.H. Cardelino, C.E. Moore, C.A. Cardelino, N. Sukidi and S. McCall, Mat. Soc. Symp. Proc. Vol. 569, p. 59 (1999).
3. S-W Choi, G Lucowsky and K.J. Bachmann, MRS Symp. Proc. Vol. 204, p.195 (1991).
4. Z. Sitar, M.J. Paisley, B. Yan, J. Ruan, W.J. Choyke and R. F. Davis, J. Vac. Sci. Technol. B8, p. 316 (1990).
5. J.M. Van Hove, G.J. Cosimini, E. Nelson, A.M. Wowchak and P.P. Chow, J. Crystal Growth 150, p.908 (1995).
6. H. Amano, M. Kito, K. Hiramatsu and I. Akasaki, Jpn. J. Appl. Phys. 28, L2112, (1989).
7. I. Akasaki, H. Amano, H. Murakami, M. Sassa, H. Kato and K. Manabe, J. Crystal Growth 128, p. 379 (1993).
8. I. Akasaki, H. Amano, Y. Koide, K. Hiramatsu and N. Sawaki, J. Crystal Growth 98, p. 209 (1989).
9. S. Nakamura, Jpn. J. Appl. Phys. 30, L1705 (1991).
10. T. Sasaki, J. Crystal Growth 129, p. 81 (1993).
11. Conf. Proc. 1997 Int. Conf. on Indium Phosphide and Related Materials, Hyannis, MA, Institute of Electrical and ElectronicsEngineers, Inc., Danvers, MA, 1997, p. 233
12. Conf. Proc. 1997 Int. Conf. on Indium Phosphide and Related Materials, Hyannis, MA, Institute of Electrical and ElectronicsEngineers, Inc., Danvers, MA, 1997, p. 633
13. A.T. Young, Phys. Today 35 (1982) 42.
14. R.B. Miles and W.R. Lempert, Annu. Rev. Fluid Mech. 29, p. 285 (1997).
15. J.P Bonnet, D. Gressilon and J.P. Taran, Annu. Rev. Fluid. Mech. 30, p. 231 (1998).
16. G. Tenti, C.D. Boley, and R.C. Desai, Can. J. Phys. 52, p. 285 (1974).
17. J.A. Lock, R.G. Seasholtz and W.T. John, Appl. Optics 31, p. 2839 (1992).

HIGH TEMPERATURE PHASES AND PHASE EQUILIBRIA IN REACTIVE MOLTEN METAL–BASED SYSTEMS

E.L. Dreizin

New Jersey Institute of Technology

INTRODUCTION

Recently, the high-temperature portions of metal-gas phase diagrams (specifically, Al-O, Mg-O, Cu-O, Zr-O-N, Ti-O-N, B-C, and B-O) have been used to interpret previously poorly understood metal combustion processes such as explosions of burning metal particles and brightness jumps observed in burning metal particle streaks [1-7]. It was recognized that phase transitions occurring in molten metal-gas systems could be the causes of these dramatic changes in the metal combustion scenario. The composition and phase changes in these analyzed particles correlated with the observed combustion behavior. However, most of these phase transitions are not well characterized, and the basis on which they are proposed is the elemental analysis of partially burned and rapidly quenched metal particles. This new research is aimed at exploring and characterizing some of these phase changes and, more generally, at addressing high-temperature phase equilibria in reactive, molten, metal-based systems.

Below, specific hypotheses in need of experimental test will be discussed for two particular systems of interest in this program.

A. Zirconium-Oxygen-Nitrogen System

Experiments in which zirconium particles burned in air [6] indicated that both oxygen and nitrogen are dissolved in pure molten zirconium. The particles which burn in the 2400-2700 K temperature range (higher than the Zr melting point of 2125 K), were quenched by impinging onto aluminum foil. This method gives a rapid cooling rate (~10^5 K/s) and minimal particle deformation. The internal composition history of burning Zr was determined by analyzing many identically produced and ignited particles that were quenched after different combustion times. The quenched particles were fairly uniform in morphology and composition indicating that the rapid cooling rate suppressed phase separation and, essentially, froze the composition of the burning liquid particle. The particle composition history indicates that the rate of nitrogen dissolution was initially higher than that of oxygen. The decrease in the dissolved nitrogen concentration indicates a solubility limit for nitrogen in the molten Zr-O-N system which has not been reported in the literature. At a temperature close to 2340 K, the eutectic transition in the binary Zr-O system, the burning particles exploded with a popping sound indicative of gas release. After explosion, stoichiometric ZrO_2 is found in the fragmented combustion products. Based on the experimental observations summarized above, the following scenario was hypothesized: both oxygen and nitrogen dissolve in molten zirconium and produce a liquid solution in which the solubility limits for oxygen and nitrogen are different. At a temperature close to the eutectic in the binary Zr-O system (2340 K), a non-variant

phase transition occurs in the Zr-O-N system producing a solid zirconium-oxygen solution, nitrogen gas and zirconium oxide:

$$ZrO_xN_y^{liquid} \xrightarrow{2340K} \alpha\ Zr^{solid\_solution} + ZrO_2^{solid} + N_2^{gas}$$

B. Boron-Oxygen-Carbon System

A recent study of ignition and combustion of electrically heated boron filaments [8] showed that they burned in two distinct stages, consistent with earlier boron particle combustion studies [9, 10]. The onset of stage one combustion always occurred in the same narrow temperature range of 1770±70 K. It is known that two phase transitions, amorphous to ß and *α* to ß, rhombohedral boron structures occur in pure solid boron in the same temperature range. Surprisingly, analyses of the filaments quenched at the instant they reached 1770 K showed (Figure 1) spherical voids indicative of the production of both liquid and gaseous phases even though the boron melting point of 2350 K has not been reached. The compositions measured in the cross-sections included boron, oxygen, and carbon (present in the original boron as an impurity). It is thus hypothesized that the presence of oxygen and carbon affects the phase transitions occurring in pure boron and results in the production of new liquid and gaseous phases. In addition, significant amounts of dissolved oxygen were detected in the interiors of partially burned and quenched boron filaments. These findings are interpreted as indicating that oxygen dissolution occurs in heterogeneous boron combustion in oxygen. They also suggest that the oxygen solubility limit was reached and exceeded so that a phase transition accompanied by the gas (*e.g.*, BO_2 and/or BO) release occurred and produced large voids.

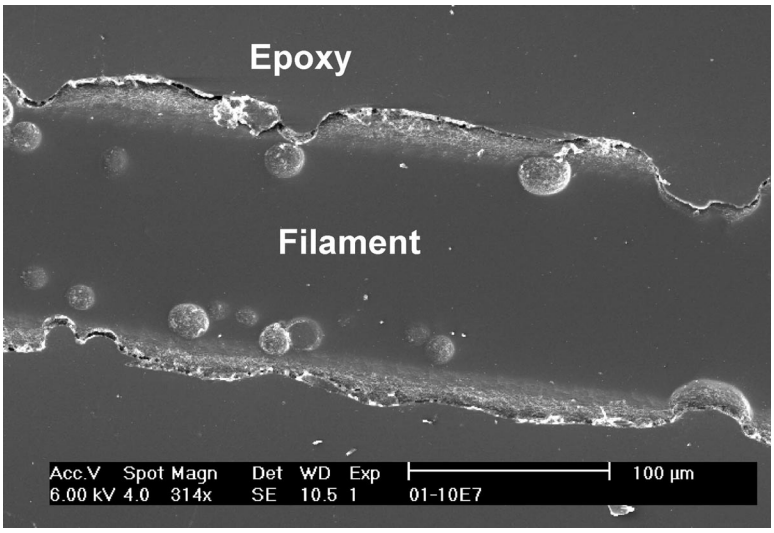

Figure 1. SEM image of the cross-section of a boron filament heated in air and quenched at the moment of stage one combustion onset (when heated to 1770K) [8]. Spherical voids visible within the filament cross-section indicate production of both liquid and gaseous phases at temperatures below the boron melting point.

In both of the above examples, the (currently unknown) phase equilibria occurring in molten metal based systems were hypothesized to interpret combustion phenomena. A literature search has shown a lack of information on phase equilibria for these two and for many other systems all of which:

a) consist of components with vastly different melting points and
b) have a high chemical reactivity at elevated temperatures.

Examples include Al/Al_2O_3, Mg/MgO, $Zr/ZrO_2/ZrN$, $Ti/Ti_2O_3/TiN$, B/B_2O_3, B_4C/B_2O_3, etc. One reason for the lack of data on high temperature phase equilibria in such systems is that experimentally complicated containerless methods are needed for material processing since these materials will react with essentially any container material at high temperatures. Moreover, a phase segregation will inevitably occur even if a containerless experiment is carried out in normal gravity in which two materials having different melting points and densities are heated and melted (*i.e.*, a lower melting point phase would drip off or accumulate at the bottom of the more refractory phase). Such a phase segregation does not allow one to experimentally characterize the phase equilibria of interest. These are the important factors showing that the microgravity environment is uniquely suitable for an adequate experimental study.

I. Research Objective and Value

The general research objective is to experimentally characterize the high-temperature phase compositions and phase equilibria in molten metal-based binary and ternary systems. Boron-carbon-oxygen and zirconium-oxygen-nitrogen systems have been chosen as the first two systems addressed in this project. This selection is based on the applications that we are most familiar with (*i.e.*, high-energy density materials) and also on the materials science literature that we are aware of that describes materials currently being actively investigated for other applications.

The results of this research are expected to be compiled and presented as phase diagram cross-sections (at selected temperatures) for the materials explored. This information will be valuable for both fundamental understanding of the nature of these materials and also for their practical use in many areas. New high-energy density metal-based materials will be developed that will consist of metastable metal-oxygen (*e.g.*, Zr-O, B-O, Al-O, etc.) solutions. In such materials, fuel and oxidizer will be premixed on the atomic level to provide a fast combustion rate and a significantly enhanced performance of propellants, explosives, and incendiaries. The performance enhancement will be achieved by exploiting phase transitions occurring in the liquid, high-temperature, igniting or burning metal-gas systems. Thus, reliable information on the phase equilibria and transitions occurring in such systems will lead directly to better performance control of the presently available metallized energetic materials and to the design of new, more effective compositions. Similar information on the high-temperature phase equilibria becomes vital for many rapidly developing technological areas. New ionic conductors based on zirconium oxynitrides and doped zirconium oxides are being developed for use in oxygen sensors and fuel cells [11, 12]. These devices are often employed at elevated temperatures at which the stability of the known oxynitride phases is not well known. The high-temperature equilibria addressed in this research will provide information needed to assess their phase stability, predict the stable and metastable phases that can be formed, critically evaluate and modify the material synthesis and processing techniques. Knowledge of the high-temperature phase equilibria for the boron-oxygen and boron-carbon-oxygen systems is essential for development and fabrication of many new semiconductors, glasses, and ultra-hard materials (*e.g.*, [13, 14, 15]).

II. General Approach

Containerless microgravity experiments will be conducted in which solid components (*e.g.*, powders) premixed at room temperature will be heated in a controlled pressure inert gas or vacuum environment, kept at a high temperature for a period of time, and rapidly quenched. The initial

components will include pure metals, solid metal–gas solution phases (*e.g.*, αZr produced by the annealing of a pure metal in an oxygen and/or nitrogen environment), carbon and metal carbides, oxides, and nitrides. Xenon lamp will be used to heat the sample pellets. The gas environment is expected to be inert because the focus of this research is at the condensed phase equilibria. However, the experimental design will be modified (*i.e.*, a reactive gas component such as oxygen or nitrogen will be added) should the need to address phase equilibria with gas phase species, *e.g.*, BO_2 will be identified in our experiments. The rate of the sample heating, the maximum temperature, and the time at the maximum temperature will be the parameters varied independently in the microgravity experiments. A rapid quenching technique, splat quenching, will be employed to achieve a fast cooling rate. Phases produced at the high temperatures will be analyzed using both real time observation of the sample behavior, optical temperature measurements, and, most importantly, detailed analyses of the quenched samples. Quenched samples will be subjected to various annealing cycles to address the stability of the detected phases at different temperatures.

III. Relevant Research

Equilibria in metal-based systems at elevated temperatures are being actively explored (see for example reference books [16, 17], an article [18], and current microgravity research [19-24]. However, equilibria existing in the molten metal-based binary and ternary systems are not well known and research efforts in that direction are very limited. The phase equilibria existing in liquid phases are important for many material processing and, especially, welding and joining technologies. Also, many examples exist of high temperature melts that can be rapidly quenched to produce metastable phases with unique properties beneficial for practical applications. Familiar examples are metal glasses and nanocrystalline materials [25].

The current microgravity materials science projects address various aspects of the phase equilibria in high-temperature condensed systems, such as microstructure evolution in two-phase systems [19, 20], non-equilibrium structure and glass formation in oxide melts and semiconductors [21, 22, 23]. These studies focus more on the structure formation in the crystallized materials rather than on the phase equilibria existing in the molten systems. In some projects, phase separation in immiscible alloys is addressed [19, 20] and phase diagrams for liquid metal-metal and oxide-oxide systems are being investigated [21, 22]. In this program, a different class of molten systems is addressed, namely metal-based systems that contain chemically active components with greatly different melting temperatures. Reliable thermodynamic information describing such systems is crucial for understanding of fundamental metal combustion mechanisms and for designing new metal-based high energy density materials. Research has also been active in the area of zirconium-oxygen-nitrogen compounds as prospective ionic conductors for fuel cells and oxygen sensors [11, 12]. Gas sensing elements are also being developed based on boron oxide [14]. Their processing, stability, and joining all involve high temperatures and it is important to know which phases could form in a particular temperature range.

Binary Zr-O and Zr-N phase diagrams are known fairly well [16, 17], however, information is scarce on phase equilibria in the ternary Zr-O-N system. While both zirconium oxide and nitride are refractory (melting points are 2983 and 3233 K, respectively), zirconium melts at a lower temperature, 2128 K, which makes the compounds containing Zr metal as a precursor much more difficult to study than the pseudo-binary ZrO_2-ZrN compounds used more often. It is known that ZrN can be oxidized to ZrO_2 in an oxygen environment [26], however, the solubility limit of nitrogen in zirconium-oxygen liquid solutions is not known. It will be determined in this program.

The boron-oxygen binary phase diagram is essentially unexplored, largely due to the difficulties in handling molten boria. Boria melts at 723 K, a temperature much lower than the melting point of boron, 2350 K [27]. Molten boria is extremely reactive and thus experiments are often contaminated by the container materials. In addition, in normal gravity experiments, molten boria cannot be maintained uniformly mixed with refractory boron and forms a drop or a pool at the bottom of the sample. This great difference in the boron and boria melting points makes the normal gravity containerless experiments (*e.g.*, electro- and aero-acoustic levitation) unsuitable for this system. The boron-carbon phase diagram and solid phases have been explored for several decades [16, 28, 29]. A number of boron-rich compounds, such as $B_{12}C$, B_9C, B_8C, $B_{15}C_2$, $B_{13}C_2$ are described [28, 29]. It has also been shown that oxygen can readily substitute for some of the carbon atoms in a crystalline lattice, forming, for example, a $B_8C_{1-x}O_x$ phase. However, equilibrium compositions existing in the liquid phase are not well known. Some of the specific features of the B-C-O systems expected to be investigated in this project are effects of oxygen and carbon on the phase transitions occurring in pure boron, namely amorphous to ß and ß to α rhombohedral phases known to occur in the range of 1623 - 1923 K. In our recent research addressing the mechanism of boron filament ignition, an intriguing correlation between the distribution of carbon impurity and oxygen was observed [8]. A phase transition from ß to a boron seemed to be affected by both carbon and oxygen presence. Also, spherical voids indicative of a gas release in a liquid phase were observed in samples pre-heated in air to ~ 1770 K (a temperature much lower than the pure boron melting point) and quenched.

REFERENCES

1. Price, E.W., in *Fundamentals of Solid Propellant Combustion* (K.K.Kuo and M. Summerfield, Eds.), AIAA, New York, 1984, pp. 479-514
2. Nelson, L.S., *Nature*, p. 741, August 14, 1965
3. Nelson, L.S., Rosner, D.E., Kurzius, S.C., and Levine, H.S., Twelfth Symposium (International) on Combustion The Combustion Institute, Pittsburgh, PA, pp. 59-70 (1968)
4. Dreizin, E.L, Suslov, A.V., and Trunov, M.A., *Combust Sci. Techn*., 89, 22 (1993)
5. Dreizin, E.L., *Progress in Energy and Combustion Science*, 26 (1):57-78 (2000)
6. Molodetsky, I.E., Law, C.K., and Dreizin, E.L., *Twenty-Sixth Symposium (Int'l) on Combustion,* The Combustion Institute, Pittsburgh, 1997, pp. 1919-1927
7. Molodetsky, E.P.Vicenzi, Dreizin, E.L., and C.K. Law *Combust. Flame*,112:522-532 (1998)
8. Dreizin, E.L., Keil, D.G., Felder, W., and Vicenzi, E.P., *Combust. Flame* 119:272-290, (1999)
9. Li, S.C., and Williams, F.A., *23rd Int. Symp. on Combustion*, p. 1147-1154 (1990)
10. King, M.K., in *Combustion of Boron-Based Solid Propellants and Solid Fuels*, CRC Press, Boca Raton, pp. 1-80 (1993)
11. Chiacchi, F.T., Crane, K.M., Badwal, S.P.S., *Solid State Ionics* 73:49 (1994)
12. Kartha, S., and Grimes, P., *Physics Today* 11:54 (1994)
13. Zehringer, R., Künzli, H., Oelhafen, P., and Hollenstein, C., Journal of Nuclear Materials 176 &177:370374 (1990)
14. Kervalishvili, P.J., Oganezov, K.A., Tabutsidze, M.L., and Andriasova, I.A., *J. Mater. Res.* 7:1822-1828 (1991)
15. Belyansky, M., and Trenary, M. *Surface Science Spectra* 3: 147-150 (1995)
16. Massalski, T.B., Okamoto, H., Subramanian, P.R., and Kacprzak, L. (Eds) *Binary Alloy Phase Diagrams*. ASM Publ., Materials Park, OH, 1990
17. Levinskiy, Y.V., *P-T-X Binary Phase Diagrams of Metal Systems*, Moscow, Metallurgia, (1990) (In Russian)

18. Okamoto, H., and Massalski, T.B., *Journal of Phase Equilibria*, 15:500 (1994)
19. Li, D., Robinson, M.B., Rathz T.J., and Williams, G. Liquidus temperatures and solidification behavior in the copper-niobium system. *Acta Materialia*, 46, 3859 (1998)
20. Li, D., Robinson, M.B., Rathz, T.J., and Williams, G. Direct determination of the metastable liquid miscibility gap in undercooled Cu-Co alloys. *Mater. Letters*, 36, 152 (1998)
21. Lin, I.-C., Navrotsky, A., Weber, J.K.R., and Nordine, P.C. Thermodynamics of glass formation and metastable solidification of molten Y3Al5O12. *J. Non-Cryst. Solids*, in press (1998)
22. Weber, J.K.R. Behavior of molten oxides under containerless conditions. Eur. J. Solid State Inorg. Chem., 34, 847-859 (1997)
23. Jackson, K.A., Beatty, K.M., and Minke, M.V. Monte Carlo simulation of non-equilibrium segregation during crystal growth. *J. Non-Crystalline Solids*, 219, 100-109 (1997)
24. Wilcox, W.R., Regel, L.L., and Smith, R.W. ''Use of microgravity to control the microstructure of eutectics.'' *Proceedings of the NASA Microgravity Materials Science Conference*, Huntsville, Alabama (1998)
25. Cahn, R.W., and Haasen, P., *Physical Metallurgy*. North Holland Physics Publishing, Amsterdam, Oxford, New York, Tokyo (1983)
26. Blumenthal, W.B. and Roach, J.D. in *Kirk-Otmer Encyclopedia of Chemical Technology*, V. 22 (H.F. Mark, J.J. McKetta, D.F. Otmer, and A. Standen, Eds.) Interscience Publishers, NY, p. 624 (1970).
27. Chase, M.W., Davies, C.A., Downey, J.R., Frurip, D.J., McDonald, R.A., and Syverud, A.N., JANAF Thermochemical Tables, *Journal of Physical and Chemical Reference Data*, Vol. 14, Suppl. 1, pp. 175-179 (1985)
28. Türkes, P.R.H., Swartz, E.T., and Pohl, R.O., *AIP Conference Proceedings 140, Boron-Rich Solids*. Albuquerque, NM, 1985, (Lerner R.G, Series Editor), pp. 346-352
29. Schwetz, K., A., and Karduck, P., *AIP Conference Proceedings 231, Boron-Rich Solids*. Albuquerque, NM, 1990, (Emin, D., Aselage, T.L., Switendick, A.C., Morosin, E.B., and Beckel, C.L., Editors), pp. 405-413

REACTIONS AND SURFACE TRANSFORMATIONS OF A BIOACTIVE MATERIAL IN A SIMULATED MICROGRAVITY ENVIRONMENT: AN EXPERIMENTAL AND NUMERICAL STUDY

P. Ducheyne, S. Radin, P.S. Ayyaswamy, H. Gao

Center for Bioactive Materials and Tissue Engineering
School of Engineering and Applied Sciences, University of Pennsylvania

Simulated microgravity (μg) conditions of NASA designed Rotating Wall Bioreactor Vessels (RWVs) have been found favorable for the growth of *in vitro* 3-D bone-like tissue [1]. Such 3-D tissue growth could have wide clinical applications. The 3-D bone growth in RWVs is facilitated by the use of microcarriers which provide structural support [1-3]. Microcarrier materials which promote cellular function (bioactive materials) not only provide structural support but also enhance 3-D bone tissue formation. Based on extensive physico-chemical and biochemical analyses [4, 5], bioactive glass (BG) has been demonstrated to be an attractive candidate for use as bioactive microcarrier material. BG surface reactions are closely related to its stimulatory effect on bone cell function [4]. Since the nature of BG reactions under the simulated μg conditions of RWVs is unknown, the objective of this study is to analyze the BG behavior in the RWV environment using experimental and numerical methods.

BG behavior upon immersion in the RWV environment was tested and compared with that at static conditions at normal gravity. The most reactive among bioactive glasses BG 45S5 [6] (W, %: 45.0 % SiO_2, 24.5 % CaO, 24.5 % Na_2O and 6.0 % P_2O_5, MO-Sci Co., Rolla, MO) was used for the study. A High Aspect Ratio Vessel (HARV-50 ml, Synthecon, Houston, TX) which rotates around a horizontal axis was used to simulate the μg-environment. Based on our previous numerical analysis [7], a rotational speed of 10 rpm, and size of granules in the range 40-70 μm were employed to maintain simulated μg-conditions (~ 0.01 g) for the BG granules loaded in the HARV. The following physiological solutions (pH 7.4 at 37^0C) were used for the immersion experiments: tris(hydroxylmethyl)aminomethane buffered solution (T), this solution complemented with electrolytes typical for plasma (TE), this last solution with serum (TES). The duration of immersion in T was set at 1, 3, 6, and 24 hours. The immersion time was also extended to 48 hours in TE and TES. Post-immersion, the material surfaces were analyzed using Fourier Transform Infrared (FTIR) spectroscopy. Changes in the solution composition were determined using atomic absorption spectroscopy (AAS) and colorimetry.

Changes in the concentrations of Ca-, P- and Si-ions as a function of immersion time in T, TE and TES are shown in Figures 1, 2, and 3 respectively. The time-dependent changes in the ion-concentrations indicate that at both static and HARV conditions, BG reactions in solutions include initial leaching of all ions, followed by P-uptake and a slow down in the Si- and Ca-release. The data suggest a two-stage process, an initial BG dissolution followed by the formation of Ca-P phases. Although the sequence of the reactions was similar under both testing conditions, the kinetics of the BG reactions were remarkably enhanced in the HARV environment for all solutions tested. As shown in Table 1, in the ion- and

serum-free T, the rates of the initial Si-, Ca- and P- release in the HARV were 2.5, 3.2 and 6 times greater than those under static conditions. The release rates were also enhanced in the presence of electrolytes and serum (TE and TES). This enhancement in the initial ion-release in the HARV dramatically affected the subsequent reactions. In fact, as a result of the increased Si-release, saturation with dissolved silica was reached in the HARV while the solution remained undersaturated at static conditions within the time frame of the experiment. Moreover, as shown in Table 2, the enhanced release of Ca- and P-ions in HARV led to a 10-fold increase in the [Ca]x[P] ionic product (indicative of solution saturation with Ca-P phases). This increase resulted in faster and greater P-uptake during the subsequent stage of precipitation. Actually, the 10-fold increase in the ionic product in the HARV led to a 10-fold increase in the total amount of P-uptake (Table 2). The increased amount of P-uptake indicates an increase in the amount of Ca-P precipitation at the BG surface. Thus, the data suggests a direct relationship between the enhanced initial Ca- and P-release from BG in the HARV and the enhanced formation of the Ca-P layer at the BG surface. FTIR analysis confirmed that the amount of the Ca-P phases at the BG surface was greater in the HARV than under static conditions.

Table 1. Initial rates of Si-, Ca- and P-release from BG immersed using HARV and static conditions.

Ion	Release rate, μg/mg h^{-}					
	T		TE		TES	
	HARV	static	HARV	static	HARV	static
Si	50.0	20.0	50.0	25.0	50.0	10.0
Ca	80.0	25.0	55.0	14.0	60.0	14.0
P	12.0	2.0	7.0	0.7	nd	nd

Note: * release rates are normalized by weight of immersed BG
* nd: not determined

Table 2. [Ca]x[P] ionic product resulting from Ca- and P- release and the total amount of subsequent P-uptake in T under HARV and static conditions.

Reaction product	HARV	static
[Ca]x[P], mM	1.04	0.11
P-uptake, mM	0.35	0.03

Note: P-uptake was determined as a difference between the [P]max and [P]min within 24 hours of immersion

Numerical models were developed to simulate the mass transport of chemical species to and from the BG surface under static and HARV conditions. It was determined that under static conditions, diffusion is the mass transfer mechanism, while under simulated μg-conditions of the HARV, mass transfer involved both diffusion and convection. As shown in Figure 4, the numerical results for time-dependent changes in the ion concentrations showed an excellent agreement with the experimental data at both static and HARV conditions. The numerical study suggests that the lack of sedimentation and the dual mechanism of the mass transport – diffusion and convection – are at the basis of the enhanced BG reactions and surface transformations under the simulated μg-conditions of the NASA-designed rotating wall vessel bioreactors.

REFERENCES

1. L. E. Freed and G. Vunjak-Novakovic, Cultivation of cell-polymer constructs in simulated microgravity, Biotech.Bioeng, 46: 306, 1995.
2. P. J. Duke, E. L. Daane and D. Montufar-Solis, Studies of chondrogenesis in rotating systems, J. Cell. Biochem. 51:274, 1993
3. Q. Qiu, P. Ducheyne, H. Gao, and P. Ayyaswamy, Formation and differentiation of three-dimentional rat marrow cell culture on microcarriers in a rotating-wall vessel, J.Tissue Eng., 4:19-34, 1998
4. P. Ducheyne, ch. 9 in: "Hip surgery: New materials and developments," eds. L. Sedel & M. Cabanela, Martin Dunitz, London, 1998.
5. S. Radin, P. Ducheyne, B. Rothman, A. Conti, The effect of in vitro modeling conditions on the surface reactions of bioactive glass, J. Biomed Mat. Res., 37: 363-75, 1997
6. L.L. Hench, Bioceramics: from concept to clinic, J.Am.Cera.Soc., 74: 1487-510, 1997
7. H. Gao, P. S. Ayyaswamy, and P. Ducheyne, Dynamics of a microcarrier particle in the simulated microgravity environment of a rotating-wall vessel, Microgravity Sci. Technol., X/3, 154-165, 1997.

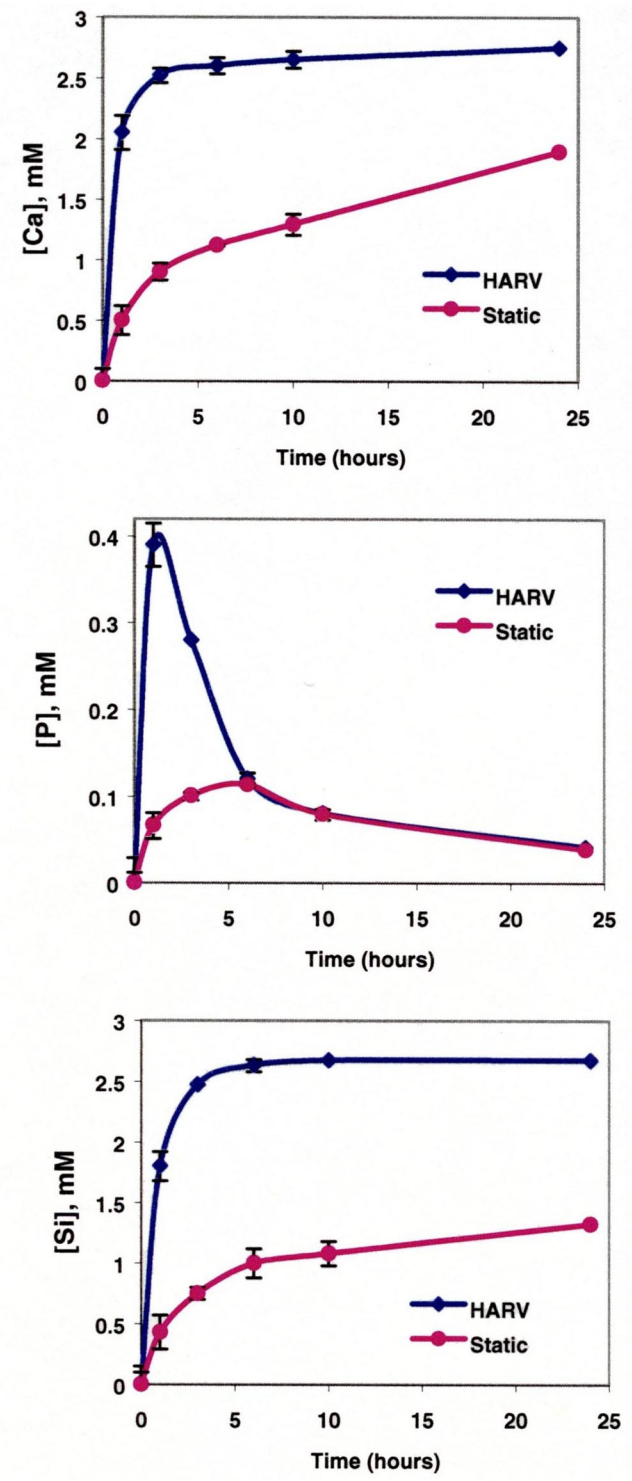

Figure 1. Changes in the [Ca], [P] and [Si] as a function of immersion time in ion- and serum free T solution under the HARV and static conditions.

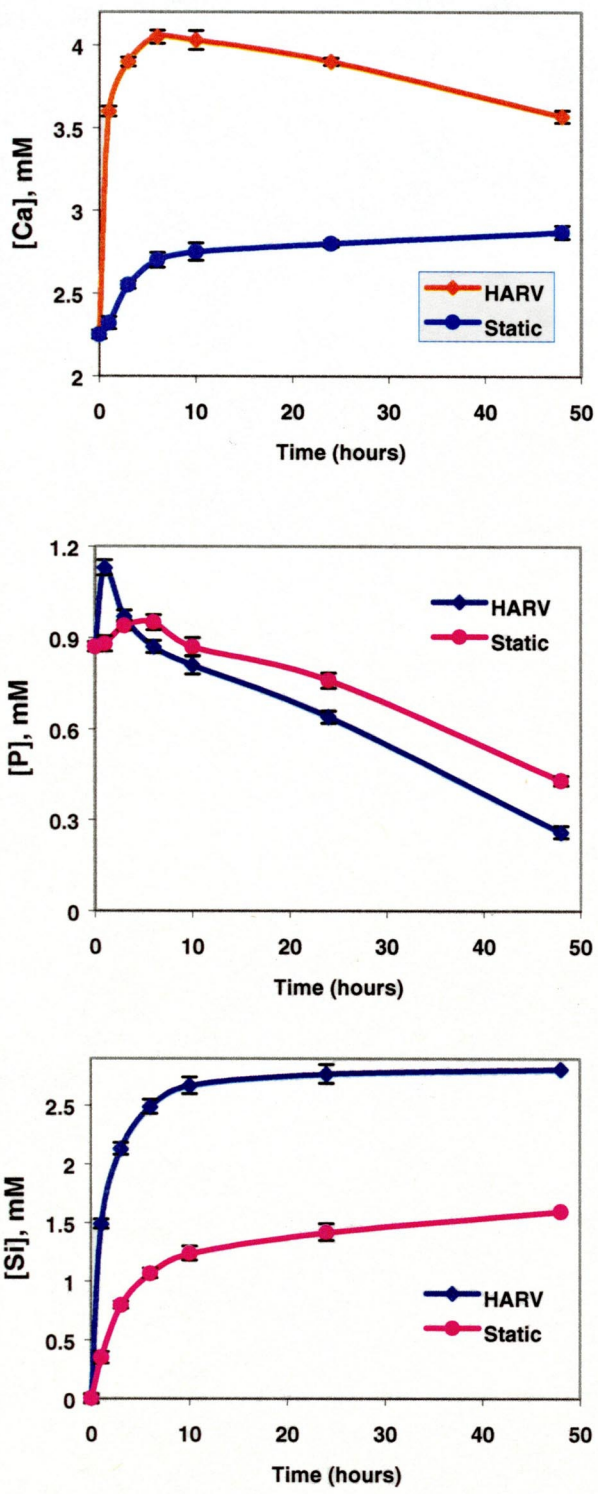

Figure 2. Changes in the [Ca], [P] and [Si] as a function of immersion time in serum-containing TES under the HARV and static conditions.

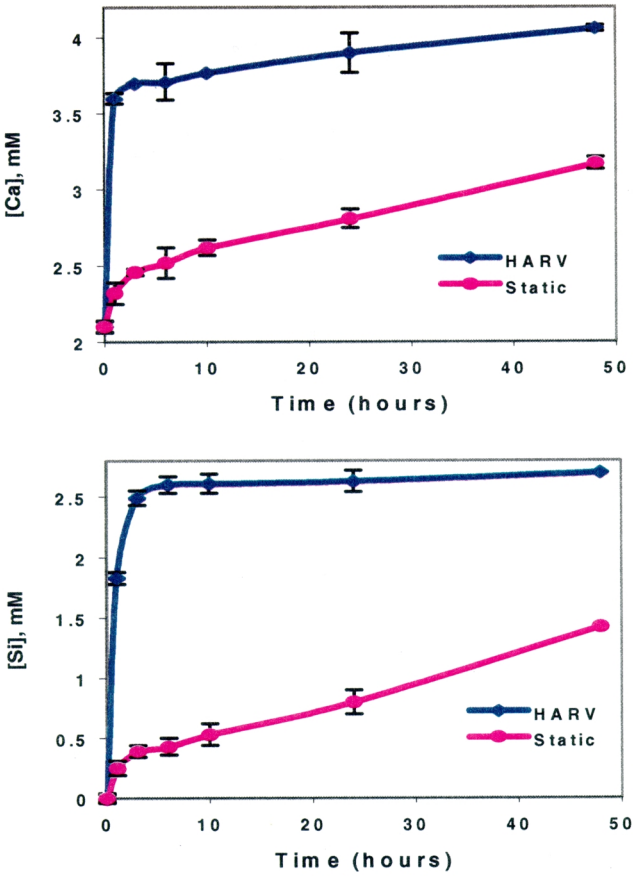

Figure 3. Changes in [Ca] and [Si] concentrations as a function of immersion time in electrolyte- and serum-containing TES under the HARV and static conditions.

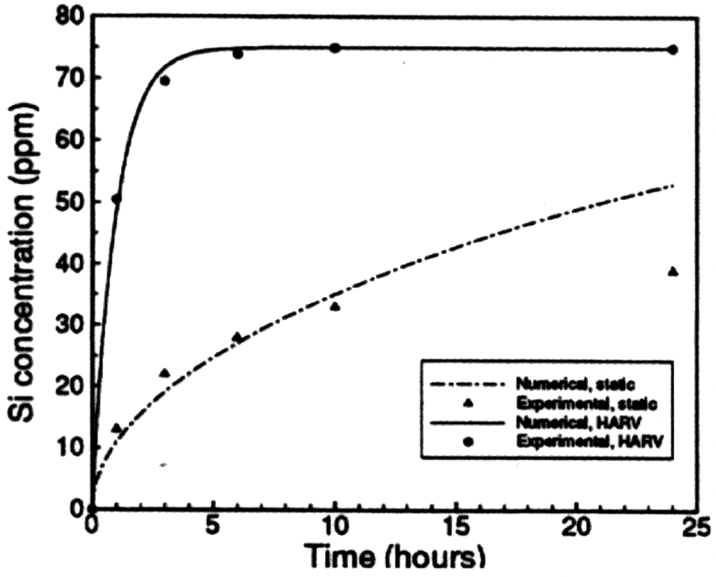

Figure 4. Numerical and experimental data for time-dependent Si-release in T solution under the HARV and static conditions.

COMBINED SYNCHROTRON WHITE BEAM X-RAY TOPOGRAPHY AND HIGH RESOLUTION TRIPLE AXIS X-RAY DIFFRACTION CHARACTERIZATION AND ANALYSIS OF CRYSTALS GROWN IN MICROGRAVITY AND GROUND-BASED ENVIRONMENTS

M. Dudley[1] (P.I.) and R.J. Matyi[2] (Co-I.)

[1]Dept. of Materials Science & Engineering,
SUNY at Stony Brook, Stony Brook NY 11794-2275
(516)-632-8500; FAX (516)-632-8052; e-mail: mdudley@ccmail.sunysb.edu
[2]Dept. of Materials Science & Engineering,
University of Wisconsin-Madison, 1500 Engineering Drive, Madison WI 53706
(608)-263-1716; FAX (608)-262-8353; e-mail: matyi@engr.wisc.edu

I. Research Objectives and Relevance to Microgravity

The objective of the research proposed here is to carry out detailed studies of defect and general distortion distributions in crystals grown in both microgravity and ground based environments (*e.g.* using modified Bridgman, Vapor Transport or Traveling Heater Method techniques) using a combination of synchrotron white beam X-ray topography (SWBXT)[1] and high resolution triple crystal X-ray diffractometry (HRTXD).[2] This unique combination of techniques is expected to reveal detailed differences between crystals grown in these two different environments and to enable meaningful assessment to be made of the influence of a microgravity environment on various aspects of the quality of crystals grown therein. SWBXT and HRTXD are complementary analytical techniques which are most sensitive and useful at contrasting ends of the "scale" of defect densities in crystals. By applying both techniques to the same crystals, it will be possible to provide detailed and quantitative assessments of the defect structure from regions that range from highly perfect (where SWBXT is expected to be the superior characterization tool) to highly imperfect (where HRTXD should be the superior method). This unified and continuous view of the defect structure should lead to valuable insights into the effect of growth conditions on the defect generation process. This research program draws upon the extensive experience that has been gained at the State University of New York - Stony Brook and University of Wisconsin - Madison in the analysis of defects in semiconductors using advanced methods of X-ray diffraction. Prof. Michael Dudley of SUNY - Stony Brook has worked closely with the crystal growth community at NASA's Marshall Space Flight Center (MSFC) in applying methods of SWBXT to numerous semiconductor crystals grown both on Earth and in microgravity. His counterpart, Prof. Richard Matyi of UW - Madison, has been actively engaged in demonstrating the capabilities of HRTXD to a variety of semiconductor materials. By combining these complementary techniques it should be possible to obtain a deeper understanding of the process of defect generation than would be possible with either technique alone, or perhaps by any structural probe.

The significance of the research described here is that it will directly determine the influence of a microgravity environment on the detailed defect and distortion distribution in crystals produced in flight

experiments, and will enable direct comparison to be drawn with crystals produced in ground based experiments. Confirmation has already been obtained that effects resulting from the limited flight times available for microgravity crystal growth experiments can exert control over the microstructure of the crystals grown, potentially detracting from the intended assessment of the influence of the magnitude of the gravity vector on these processes. Determination of the influence of cooling rate on the defect microstructure of crystals is crucial for selection of experimental conditions under which the effects of the gravity vector on crystal growth quality can be usefully investigated. Once such selection has been optimized, differences in microstructure observed in microgravity grown crystals may be safely attributed to the influence of the gravity vector and not to artifacts related to compressed growth schedules.

II. Significant Results to Date and Future Plans

To date, cooperative studies have been carried out on the following materials: flight and ground based CdZnTe (4% Zn), grown by Dr. D. Larson at Stony Brook, ground-based CdTe grown by Dr. W. Palosz at Marshall Space Flight Center (MSFC); ground-based ZnSe, grown by Dr. C.-H. Su at MSFC, ground-based $Hg_{1-x}Cd_xTe$, grown, in the presence and absence of a rotating magnetic field, by Dr. D.C. Gillies at MSFC; and ground-based and flight-based $Hg_{1-x}Cd_xTe$ grown by Dr. D. Gillies (USMP2). Selected results from flight-based $Hg_{1-x}Cd_xTe$, and ground based CdTe are discussed here. Results from other materials have been discussed in previous reports.[3-9]

For the case of the $Hg_{1-x}Cd_xTe$ flight samples, wafers cut parallel and perpendicular to the growth axis were examined. An example is shown in figures 1 and 2. SWBXT showed that this flight sample consisted of three grains, one of which is twinned. Figure 1 shows a reflection topograph, recorded from the largest of these grains, in which there is no orientation contrast between the matrix and twinned regions.

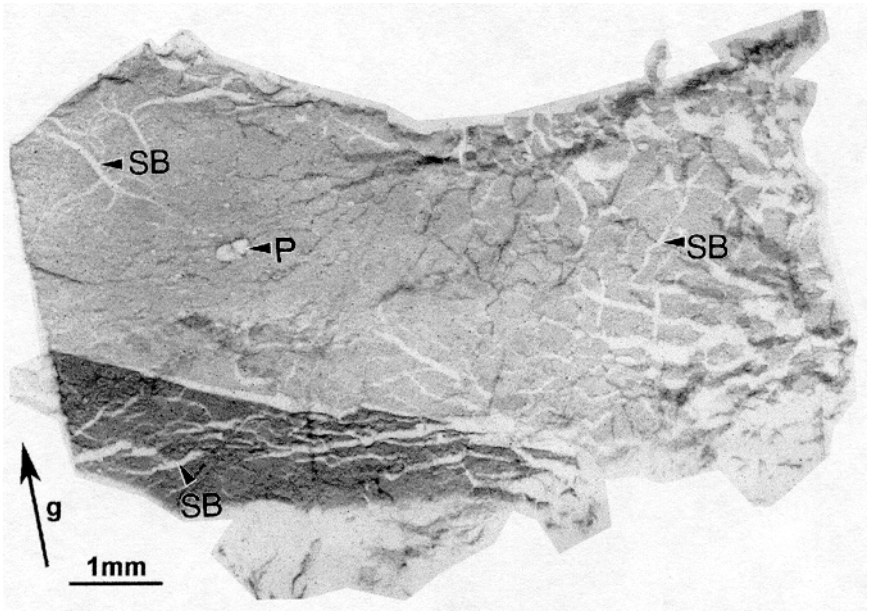

Figure 1. **MCT 27Q 106-11S** Reflection topograph: Grain 1 (Matrix + Twin). SB is subgrain boudary, P is precipitate.

Figure 2 shows the matrix region only. Both the matrix and twinned regions are composed of fairly large subgrains (200-1000 μm) separated by misorientations ranging from 5-70 arc seconds. Interior of the

subgrains appears to be of fairly good crystalline quality. Circular regions of white contrast are observed in some regions. These could be inclusions of Te. Extremely high crystal quality was revealed in the early stages of growth, with very low dislocation densities (of the order of $10^4 cm^{-2}$ in regions) and small angle boundary densities being evident. Such quality is unprecedented in ground-based crystals. HRTXD is currently being carried out on these crystals.

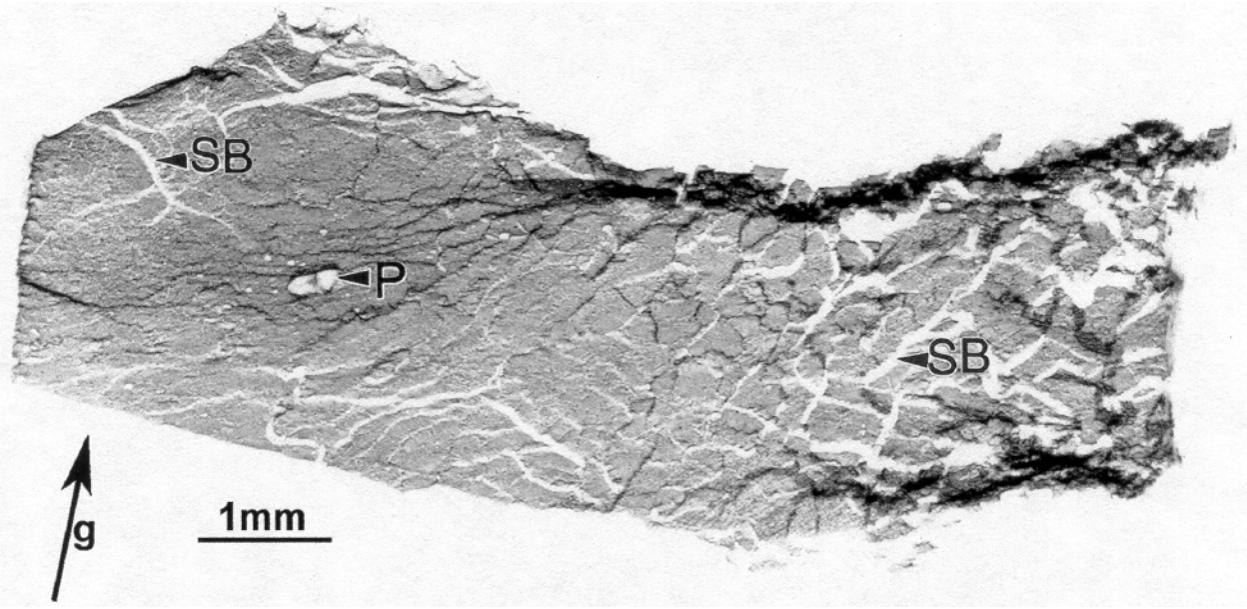

Figure 2. **MCT 27Q 106-11S** Reflection topograph: Grain 1 (Matrix)

For the case of the CdTe grown by Dr. W. Palosz of MSFC, the goal of the project was to investigate the effect of post-growth cool-down conditions on the crystallographic quality of the crystals. The crystals were grown by "contactless" Physical Vapor Transport using the Low Supersaturation Nucleation technique. The growth ampoule contained a small amount of excess tellurium and hydrogen. The crystals grew on a silica glass pedestal without contact with the side walls of the ampoule. In one case the crystal was allowed to get in contact with the wall later into the growth process. The source temperature was about 930°C, the undercooling up to 10-15°C, the growth rate a few mm per day. After growth the ampoules were cooled down at different rates, from very fast to very slow. For those crystals where wall contact was avoided, those which were subjected to the fastest cooling rates exhibited the highest defect densities, as expected. Polygonized dislocations structures comprising numerous small angle boundaries were observed, as shown in Figure 3.

Similarly the samples subjected to the slowest cooling rates exhibited the lowest defect densities, as shown in the high magnification topograph presented as figure 4, where individual dislocations can be clearly resolved. For those crystals where wall contact was not avoided, higher defect densities and severe lattice distortion were observed. This work serves as an excellent demonstration of the influence of the post-growth cooling environment on the defect structures of crystals. It also underlines the significance of the role of wall contact on determining the overall final crystal quality. HRTXD is currently being carried out on these crystals.

In future work, a complete description will be sought of the type and distribution of all defects present in the crystals to be examined. Crystals will initially be examined in boule and then wafer form using both SWBXT and HRTXD in order to reveal the overall distribution of defects and distortion in the crystals and to relate this distribution to growth conditions.

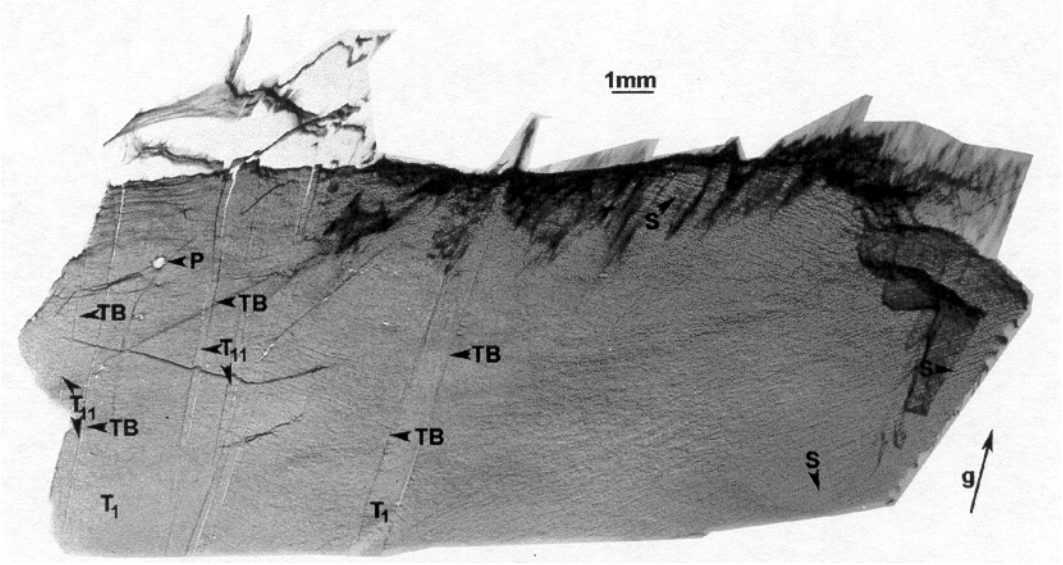

Figure 3. Reflection topograph recorded from a CdTe sample where the ampoule was removed from the furnace and allowed to cool in air. TB is twin boundary, S is subgrain boundary.

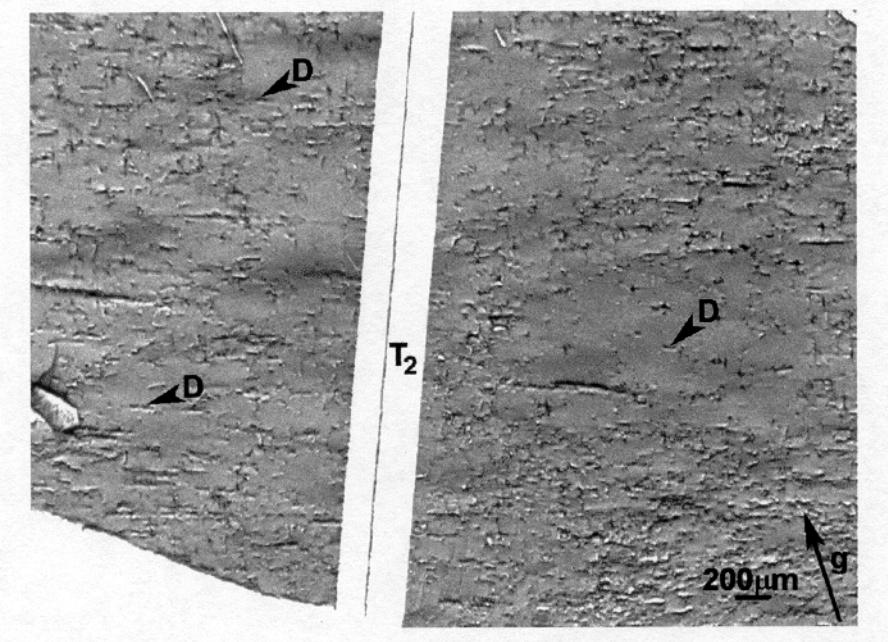

Figure 4. Reflection topograph recorded from a CdTe sample cooled at a constant rate of 10°C per hour. D is individual dislocation.

REFERENCES

1. M. Dudley, in "Applications of Synchrotron Radiation Techniques to Materials Science", D.L. Perry, R. Stockbauer, N. Shinn, K. D'Amico, and L. Terminello (Eds.) Mat. Res.Soc. Symp. Proc., 307, 213-224, (1993).
2. J. Su, H. Chung, Y. Guo, M. Dudley, H.M. Volz, C. Salles, and R.J. Matyi, Advances in X-ray Analysis, 41, 148-154, 1999.
3. H. Chung, B. Raghothamachar, J. Wu, M. Dudley, D.J. Larson, Jr., and D.C. Gillies, in "Defect and Impurity-Engineered Semiconductors and Devices", S. Ahok, J. Chevallier, I. Akasaki, N.M. Johnson, and B.L. Sopori (Eds.), Mat. Res. Soc. Symp. Proc., 378, 41-46, (1995).

4. H. Chung, B. Raghothamachar, M. Dudley, D.J. Larson, Jr., in "Space Processing of Materials", SPIE Proceedings Vol. 2809, 45-56, (1996).
5. H. Chung, B. Raghothamachar, W. Zhou, M. Dudley, D.C. Gillies in "Applications of Synchrotron Radiation to Materials Science", L. Terminello, S. Mini, D. L. Perry, and H. Ade (Eds.), Mat. Res. Soc. Symp. Proc., 437, 107-112, (1996).
6. W. Palosz, D. Gillies, K. Grasza, H. Chung, B. Raghothamachar and M. Dudley J. Crystal Growth, 182, 37-52, (1997).
7. B. Raghothamachar, H. Chung, M. Dudley, D.J. Larson, Jr., J. Electronic Materials, 27, 556-563, (1998).
8. M. Dudley, D.J. Larson Jr., H. Chung, and B. Raghothamachar, in Proceedings of 31st COSPAR Scientific Assembly, Birmingham, UK, July 14-21, 1996, Advances in Space Research, 22, 1179-1188, (1998).
9. J. Su, H. Chung, Y. Guo, M. Dudley, H.M. Volz, C. Salles, and R.J. Matyi, Advances in X-ray Analysis, 41, 148-154, 1999.

FUNDAMENTAL STUDIES OF CRYSTAL GROWTH OF MICROPOROUS MATERIALS

Prabir K. Dutta

Department of Chemistry
The Ohio State University

INTRODUCTION

Microporous materials include a large group of solids of varying chemical composition as well as porosity. These materials are characterized by channels and cavities of molecular dimensions. The framework structure is made up of interconnecting T-O-T' bonds, where T and T' can be Si, Al, P, Ga, Fe, Co, Zn, B and a host of other elements. Materials with Si-O-Al bonding in the framework are called zeolites and are extensively used in many applications. Ion-exchange properties of these materials are exploited in the consumer and environmental industries. Chemical and petroleum industries use zeolites as catalysts in hydrocarbon transformations. Synthesis of new microporous frameworks has led to the development of new technologies, and thus considerable effort worldwide is expended in their discovery. Microporous materials are typically made under hydrothermal conditions. Influence of nature of starting reactants, structure directing agents, pH, temperature, aging all have profound influence on the synthesis process. This is primarily because the most interesting open frameworks are not necessarily the stable structures in the reaction medium. Thus, the discovery of new frameworks is often tied to finding the right composition and synthesis conditions that allow for kinetic stabilization of the structure. This complexity of the synthesis process and limited understanding of it has made it difficult to develop directed synthesis of microporous materials and most advances in this field have been made by trial and error. The basic issues in crystal growth of these materials include:

- Nature of the nucleation process
- Molecular structure and assembly of nuclei
- Growth of nuclei into crystals
- Morphology control
- Transformation of frameworks into other structures.

The NASA-funded research described in this paper focuses on all the above issues and has been described in several publications. [1-6] Below we present the highlights of our program, especially with the focus on possible experiments in microgravity.

I. Results and Discussion

A. Reverse Micelle Based Synthesis

Our primary focus in developing this area of research has been to investigate if we can take advantage of the considerably lower rates of sedimentation in microgravity.

Synthesis Process

Conventional synthesis of microporous materials usually involves mixing together reactants in an aqueous medium and results in immediate formation of an amorphous precipitate, often referred to as the gel. Crystal growth proceeds from the gel. Several experiments have been reported using such procedures under microgravity conditions. Because of the presence of the gel, it is difficult to analyze the reaction process. Our approach has been to develop a new method of microporous materials synthesis that avoids the formation of the gel and makes the system more amenable to analysis during crystal growth. The microporous materials that we focus on are zincophosphates, and we refer to them as ZnPO. Reverse micelles have been demonstrated over several decades to be a unique reaction medium for synthesis of nanoparticles of a wide class of materials. We were the first to report that microporous materials can also be synthesized under the appropriate conditions from reverse micellar reactants. The metastable nature of microporous materials requires a well-controlled compositional environment for synthesis and the particular reverse micelle needs to be chosen carefully. Thus, the open-pore framework zincophosphate X (ZnPO-X) with a faujasite structure could not be synthesized with AOT reverse micelles, because the high levels of Na^+ in the water pool thwarted the nucleation of ZnPO-X and promoted the formation of a more condensed structure zincophosphate sodalite (ZnPO-S). Figure 1 compares these two frameworks. Understanding the reasons for failure of AOT reverse micelles in growing ZnPO-X led to the examination of cationic reverse micelles, especially the two-tailed surfactant dimethyldioctylammonium chloride (DODMAC), and its use resulted in the successful synthesis of ZnPO-X.

Crystallization Pathways

We have examined the nucleation and crystal growth process of ZnPO-X and ZnPO-S from reverse micelles in detail. The important step in formation of crystal nuclei involves exchange processes between reverse micelles, as depicted in Figure 2. If reactant composition is chosen such that only a small fraction of the micelles have the right supersaturation to form nuclei, then these nuclei can commence crystal growth using up the non-nucleated reverse micelles. After the crystals reach a certain size, they begin to settle via gravity, avoiding further growth in size. This process of crystal nucleation, growth and settling process can continue for days. On the other hand, if the reactant composition is such that supersaturation is exceeded in a large fraction of the micelles, then rapid precipitation of an amorphous solid can occur, resembling the conventional synthesis. This control over crystallization pathways by minor changes in the reactant composition is unique to the reverse micellar medium.

Sedimentation Control

The observation that crystal growth ceases on settling led us to examine ways to keep crystals suspended in the reaction medium. We have used rotation cells, which by gentle centrifugal forces can counteract gravity. Both ZnPO-S from AOT detergent system as well as ZnPO-X using DODMAC were examined. Unfortunately, aggregation of crystallites occurred, leading us to the conclusion that although the crystals could be suspended for longer periods of time in rotating cells, the experimental results were not meaningful.

Another approach we have developed for controlling crystal size is via a seeding process. We had observed that the yields of the ZnPO-X produced by the reverse micellar reaction were in the range of 15-20%, indicating that a significant fraction of zinc and phosphate species were still present in the organic medium. We rationalized the reason for the low yields on the basis of the micellar exchange process discussed earlier (Figure 2). As crystal growth occurs from nucleated reverse

micelles, the composition of the non-nucleated reverse micelles also change with time via collisional exchange, and eventually more of these have the right composition to form nuclei. However, this leads to a decrease in non-nucleated reverse micelles that are the source for nutrients available for growth. Eventually the reverse micelles with nuclei have no source of remaining nutrients and the crystal growth stops. However, this solution with nuclei acts as an excellent seed system for growth of new crystals if provided with a source of reverse micelles as nutrients. The seed solution was added to a reverse micelle system that provided a source of nutrients, in narrow columns of varying lengths. Three such experiments were performed with columns of height of 0.71, 1.78 and 2.62 meters. Products were collected from the bottom of the column after one day for the two shorter columns and after two days for the longer column. From the SEM images shown in Figure 3, we observed an average size of 3, 6 and 15 μm with increasing column height, respectively. The size of the crystals was increased by controlling the time they spend in the medium, which depended on the length of the column.

B. Morphological Control and Crystal Dissolution Pathways

A second emphasis of our research program has been to develop experiments that take advantage of the decrease in buoyancy-driven convection in microgravity. This has focused on developing synthetic strategies to modify morphology and examine crystal transformation of different frameworks. Morphological control of microporous crystalline materials via synthetic routes is important for several reasons. For instance, it provides information about parameters that control nucleation and crystal growth, thereby illuminating aspects of the synthesis mechanism. Also, control of morphology is important for targeting various applications. We have shown that by altering composition, the morphology ZnPO-X could be changed. Previously reported synthesis of ZnPO-X at 4°C led to the formation of crystals with the characteristic octahedral morphology of faujasitic structures. Sizes of these crystals are in the <10 μm range. We found that by increasing the $TMAOH/H_3PO_4$ and Zn^{2+}/Na^+ ratios, the morphology was drastically altered to produce large hexagonal platelet type crystals with diameters around 100 μm. Figure 4 demonstrates the morphological change. Based on electron microscopy data, we concluded that the presence of twin planes was leading to crystals with the platelet-like morphology.

The possibility of synthesizing reasonably large flat crystals of ZnPO-X has made it feasible to do detailed Raman microprobe spectroscopic experiments. In particular, we have focused on microprobe Raman spectroscopy and examined how dissolution of ZnPO-X crystals occurs as a function of different monovalent cations in the medium. The vibrational information obtained from Raman spectroscopy made it possible to analyze the structural changes at the molecular level. In the presence of H^+, at a pH of 3, the vibrational bands due to ZnPO-X disappeared completely in 12 minutes. These were replaced by Raman bands of hopeite, $Zn_3(PO_4)_2$, a condensed form of zincophosphate. Electron microscopic experiments showed that the ZnPO-X was gradually getting covered with a film of hopeite. If, instead of H^+, Li^+, or Cs^+ were used, then the ZnPO-X gradually converted to framework structures of LiA(BW) and $CsZnPO_4$, respectively. How H^+, Li^+ and Cs^+ destabilize in the ZnPO-X structure was also manifested in the vibrational band of tetramethylammonium (TMA) ions trapped in the sodalite cages of ZnPO-X. Upon exchange with H^+, Li^+, and Cs^+, prior to collapse of the ZnPO-X and loss of TMA from the Raman spectra, there is a significant broadening of the TMA band at 765 cm^{-1}. The bandwidth changes from ~ 6 cm^{-1} for Na^+ to 11,12 and 16 cm^{-1} for H^+, Cs^+ and Li^+, respectively. Our interpretation is that, upon ion exchange with these cations, there is a distortion of the ZnPO-X framework, which makes the framework more susceptible to hydrolysis.

Influence of Framework Topology on Crystal Dissolution

Our primary interest is a fundamental understanding of the molecular assembly of microporous materials. Can that goal be attained by examining crystal dissolution? We believe that to be the case for several reasons. First, the most interesting microporous frameworks are metastable structures and evolve to more condensed topologies with time. Second, clues regarding the complexity of the dissolution fragments of different frameworks provide information about the stability of the building units.

In addition to Raman spectroscopy, we are developing several other techniques using to study the crystal dissolution process. The UV-Visible spectroscopic technique involves use a pH sensitive dye. The dissolution of sodalite and ZnPO-X at low pH and the deposition of hopeite changes the Zn/P ratio, thus releasing the phosphate ions in solution which increases the pH of solution close to the surface. We have monitored this pH change with a colorimetric dye. Figure 5 shows the change in UV-visible spectra around a dissolving ZnPO-S crytal with time. We are planning to extend this study to use fluorescence microprobe techniques for better spatially sensitive measurements. These studies are providing us useful data for developing mathematical models of the crystal dissolution process. Influence of buoyancy-driven convection on the dissolution process is expected to be different for frameworks of different topologies.

C. Proposed experiments in Microgravity

There are two aspects of microgravity that we want to exploit. These include lack of sedimentation and absence of buoyancy driven convection. As we have demonstrated, under particular conditions of reverse micelle composition, crystal growth occurs in a layer-by-lay fashion. Avoiding sedimentation in these systems will lead to the growth of larger crystals. Light scattering will be used to follow the growth of crystals in microgravity. Seeding experiments to grow larger crystals is also possible, something that has not been accomplished in conventional synthesis.

The second aspect of the microgravity experiments will focus on microprobe Raman studies and absorption/fluorescence microscopy based on pH sensitive dyes. By comparing results in 1g and microgravity, we will discover if different surface intermediates are present during dissolution of different frameworks.

REFERENCES

1. Crystal Growth of Faujasitic Microporous Zincophosphate Crystals Using Reverse Micelles as Reactants. Ramsharan Singh and Prabir K. Dutta, *Langmuir* 2000, *16,* 4148-4153.
2. Synthesis of microporous faujasitic-like zincophosphates from reverse micelles, Mario J. Castagnola and Prabir K. Dutta, *Microporous and Mesoporous Materials* 2000*, 34,* 61-65.
3. Crystal growth of zincophosphates from conventional media and reverse micelles: mechanistic implications. Mario J. Castagnola and Prabir K. Dutta, *Microporous Mesoporous Mater.* 1998, *20*, 149-159.
4. Reverse Micelle Based Growth of Zincophosphate Sodalite: Examination of Crystal Growth. K. S. N Reddy, L. M. Salvati, Prabir K. Dutta, Phillip B. Abel, Kwang I. Suh and Rafat R.Ansari, *J. Phys. Chem.* 1996, *100,* 9870-9880.
5. Controlled growth of microporous crystals nucleated in reverse micelles.Prabir K. Dutta, Michael Jakupca, K. Satya Narayana Reddy and Louis Salvati, *Nature (London)* 1995, *374,*44-6.
6. Synthesis of Platelet-Like Faujasitic Zincophophate X Crystals, M. J. Castagnola, P. K. Dutta, Proceedings of the 12th International Zeolite Conference, Materials Research Society, **1999**, 1627-1632.

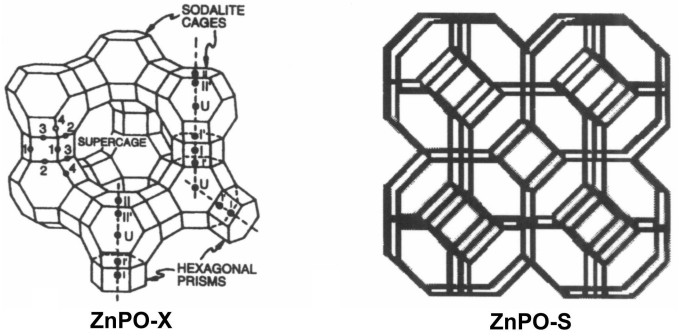

Figure 1. Microporous frameworks of interest to this study.

Figure 2. Exchange processes in reverse micelles.

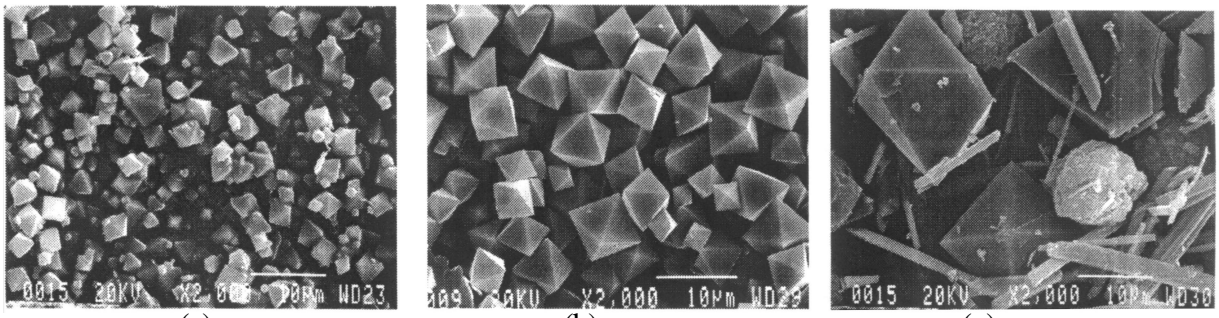
(a) (b) (c)

Figure 3. The scanning electron micrograph of ZnPO-X crystals obtained via the reverse micelle experiment from columns of various length, (a) after 1 day from a height of 0.71 meter reaction mixture, (b) after 1 day from a height of 1.78 meter reaction mixture and (c) after 2 days from a height of 2.62 meter reaction mixture.

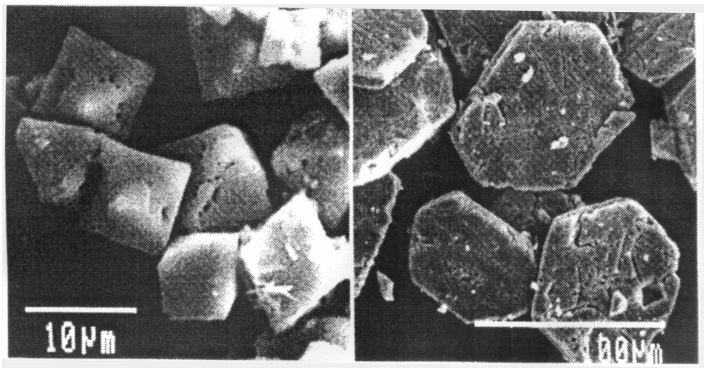

Figure 4. Scanning electron micrograph of ZnPO-X dissolving crystals obtained via control of composition.

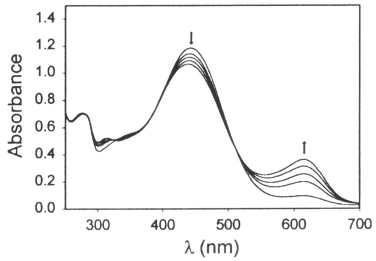

Figure 5. pH change around a ZnPO-S crystal with time as measured by the spectrum of dye.

NUCLEATION AND POLYMERIZATION EXPERIMENTS IN THE VAPOR PHASE

M. Rusyniak, Y.B. Pithawalla and M.S. El-Shall*

Department of Chemistry
Virginia Commonwealth University
Richmond, VA 23284-2006
Phone: (804) 828-3518; Fax: (804) 828-8599
E-Mail: selshall@hsc.vcu.edu

INTRODUCTION

This research project is focused on two interrelated processes that can be affected by microgravity: 1) Vapor-to-liquid homogeneous and ion-induced nucleation, and 2) Polymerization and nanoparticles' formation from the gas phase. In the nucleation research we focus on three important areas. The first is the effect of carrier gas pressure on the rate of homogeneous nucleation from the vapor phase. The second and third areas involve studies of oscillatory and ion-induced nucleation, respectively. In the polymerization studies, we provide evidence for the initiation of gas phase polymerization of isoprene and propene using direct and coupled charge transfer mechanisms from the benzene radical cation.

I. Vapor Phase Nucleation Studies

Nucleation is one of the most ubiquitous and important phenomena in science and technology [1]. The nucleus for homogeneous nucleation remains one of the most elusive entities known in chemical physics, and has never been observed directly [1]. Only the consequences of its presence, *e.g.,* droplet formation, precipitation, etc. are observed. The typical measurements of vapor to liquid nucleation rates involve light scattering from liquid droplets that fall, under the influence of gravity, from the supersaturated vapors. The development of the thermal diffusion cloud chamber (DCC) has provided the foundation for significant advances in the study of the nucleation phenomenon from a supersaturated vapor [2,3]. The DCC is a reliable tool for the production of supersaturated vapors, and is applicable to a wide variety of nucleation studies including homogeneous, photo- induced and ion-induced nucleation studies. Detailed description of the DCC and its principles of operation are given elsewhere [2,3].

One of the important current issues in nucleation research is whether the observed effect of a carrier gas is due to convection and instability in the operating conditions of DCC under 1-g or if it actually represents a real contribution to the nucleation process. There is no other way to answer this question except by complete elimination of the convection and other instability conditions by carrying out the nucleation experiments in microgravity. Recent measurements of critical supersaturations for the vapor phase homogeneous nucleation of several substances using the DCC technique exhibit a dependence on the pressure of the carrier gas used in the experiments [2,3]. Since pressure effects on homogeneous nucleation have most commonly been observed in DCC experiments, it is possible that these effects are mainly related to the nature of the experimental technique. One of the major limitations of the current nucleation experiments is the coupling between nucleation and growth. The nuclei, which typically have

radii on the order of nanometers, are transient and once formed continue to grow. Nucleation experiments rely on light scattering from macroscopic droplets to detect the nucleation events. This permits the detection of particles no less than a few microns in diameter. Since the droplet must grow several orders of magnitude prior to detection, it is necessary to consider the possible roles of the droplet growth and motion on the experimental results. We have presented a model of the droplet growth and motion in a DCC to explain the pressure dependent results. The model demonstrates that at higher carrier gas pressures the growth of the droplets is retarded and the optical scattering signal from the particles is reduced. It is concluded that the observed effect may not result from a pressure dependence of the nucleation rate, but from a pressure dependence of the droplet growth and motion. If it is possible to increase the time required for the droplet to travel to the bottom surface of the chamber then it may be possible to study the role of the carrier gas pressure in the absence of the limiting factors affecting the droplet growth and motion. The primary forces that act to accelerate the droplet in the DCC are the gravitational force, the thermophoretic force and the drag force. Thermophoretic force acts in the direction of decreasing temperature, which is upward since the temperature decreases linearly from the bottom to the top of the chamber. The drag force always acts in a direction opposite to the velocity of the droplet. So the primary force responsible for the acceleration of the droplets toward the bottom surface of the chamber is the gravitational force.

Using the model presented in Reference 2, the effects of reduced gravity on the growth and motion of droplets were investigated. The results of model calculations for the growth and motion of droplets under several different gravitational forces are shown in Figure 1. When the acceleration of gravity is reduced to 10^{-3} g, the lifetime of the droplets in the chamber increases drastically to nearly 3 seconds. This allows enough time for the droplets to grow to greater than 30 microns in radius. At a gravity force of 10^{-6} g, the droplet grows to greater than 0.5 mm and survives in the chamber for more than five seconds. Because of the low pressure of these simulations the droplets are removed to the upper surface of the chamber by the thermophoretic force. However, at higher pressures (> 1 atm) this force will be negligible. This suggests that a long duration, high quality microgravity environment may be ideal for the study of the pressure effects of the carrier gas on the nucleation kinetics and the growth and motion of droplets.

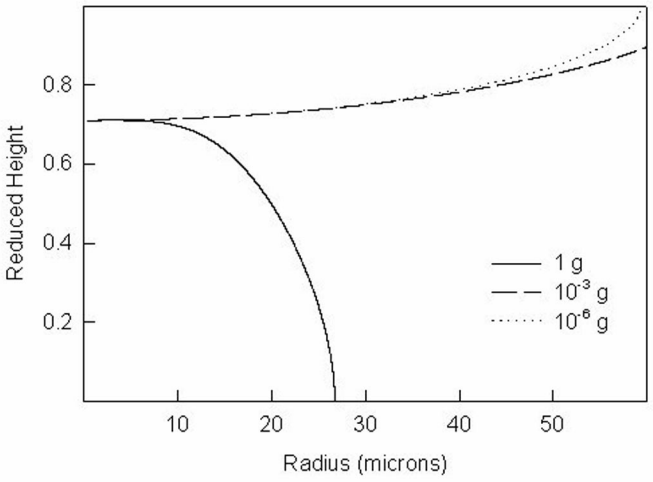

Figure 1. Model simulation of the growth and motion of 1-propanol droplets for different gravity fields in the diffusion cloud chamber at T (bottom plate) =303 K, T (top plate) = 258 K and a total pressure of 100 kPa.

At relatively high supersaturation, corresponding to high rates of nucleation, nonlinear effects can result in the breakdown of the steady state condition usually assumed in the use of the DCC for nucleation

studies. The system undergoes a transition from steady state behavior to stable oscillatory behavior [4]. In this project, we use the DCC to study the oscillatory nucleation in supersaturated vapors of dodecane, hexadecane and octadecane, and correlate the frequency of oscillation with properties of the condensing vapor. Figure 2 displays the scattered light intensity versus time along with the Fourier transform power spectra for the studied higher alkanes at the experimental conditions corresponding to the oscillatory regime in the DCC. It is clear that the fundamental frequency of the oscillatory nucleation decreases from dodecane to hexadecane to octadecane. This is also the order of increasing molecular weight, normal boiling point, critical temperature and the enthalpy of vaporization among the three alkanes.

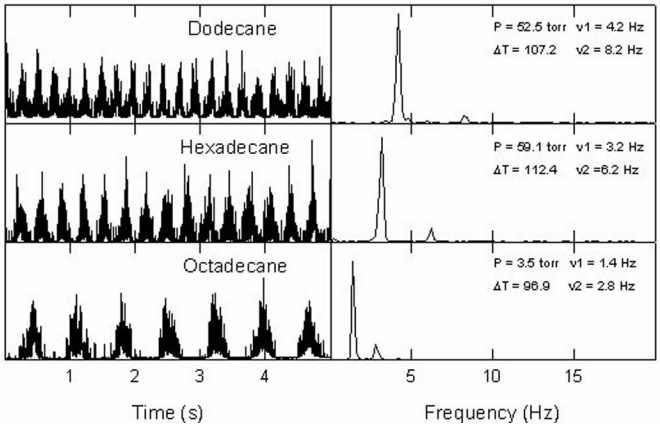

Figure 2. Oscillatory nucleation of dodecane, hexadecane and octadecane.

The nucleated droplets regulate their own formation by depleting, through condensation, the concentration of the monomer species until a sufficient number of droplets are removed to allow the monomer concentration to build up again. The nonlinear effects in nucleation and growth are general manifestation of the inhibitory feedback control. We are currently developing a model to explain the oscillatory nucleation and predict the frequency of oscillation.

We are also studying the phenomenon of ion-induced nucleation that is of great importance not only as a subject for basic scientific inquiries of complex phenomena in chemical physics but also for many atmospheric and environmental implications. Recently, we have demonstrated the first application of Resonance Enhanced Multiphoton Ionization (REMPI) to selectively generate molecular ions within a supersaturated host vapor and study their nucleating behavior [5-9]. Our approach is based on the selective ionization by REMPI of a chromophore molecule present at a dilute concentration within a supersaturated host vapor. The experiment uses a DCC to produce a steady-state supersaturated vapor. Selected ions generated within the supersaturated vapor, cluster with the vapor molecules forming condensation nuclei which rapidly grow within the supersaturated vapor to macroscopic liquid droplets that can be detected by light scattering. The method has tremendous amplification and detection capabilities and is expected to provide a valuable and new analytical tool for the identification of trace components in the vapor phase. We have presented the application of the REMPI nucleation technique for the measurements of the mobility of solvated and precritical cluster ions in supersaturated vapors under well-defined nucleation conditions [9]. The results verify the trend predicted by Thomson's model of increasing the size of the solvated cluster ion by increasing the vapor supersaturation. With this method, it is now possible to compare the mobility of precritical clusters containing positive or negative ions. This will provide the critical data necessary in order to resolve the long-standing question regarding the effect of the charge sign on the rate of ion-induced nucleation.

II. Gas Phase Polymerization Studies

Despite the fact that solutions and bulk liquids are the preferred medium for many industrial and laboratory polymerization processes, our fundamental understanding of the polymerization reactions in solution remains limited. Under normal circumstances, polymerization is conducted in condensed systems (monomer liquid or solution) in which multiple reactions (initiation, propagation, chain transfer, termination, etc.) are occurring simultaneously. Information regarding the exact nature of each mechanistic step and understanding of elementary events occurring in the course of polymerization remain largely unavailable. In solution the problem is further complicated by reactions within the solvent. In the gas phase, it is possible to observe the direct formation, in real time, of product polymeric radicals, cations or anions of a chosen size. In contrast, in the liquid phase, one is usually forced to infer what has happened by the qualitative and quantitative analysis of the products. From a practical point of view, gas phase polymerization can lead to the synthesis of defect-free, uniform thin polymeric films of controlled morphology and tailored compositions with excellent electrical and optical properties for many technological applications such as protective coatings and electrical insulators. For example, the polymeric species could be deposited from the gas phase in a size-selected manner on metal or semiconductor surfaces.

Unfortunately, the achievement of true homogeneous gas phase polymerization for the synthesis of high molecular weight polymers is very difficult, and has not really been accomplished successfully in the past. The main problem is the extreme involatility of the large polymers, rendering it impossible to keep them in the gas phase. The application of microgravity to the study of gas phase polymerization is expected to result in a better control of the process and may also lead to important technological advances.

The ion chemistry of the olefins and diolefins plays an important role in the gas phase polymerization process [10-14]. These monomers can be induced to oligomerize and/or polymerize through bimolecular ion-molecule reactions in the gas phase [10-14]. In this project, we study the laser-initiated, gas phase oligomerization of isoprene and propene. The initiation reactions involve a direct or a concerted charge transfer process from the benzene radical cation ($C_6H_6^{+\bullet}$) generated by multiphoton ionization. In order to establish the mechanistic features of the initiation process, selective ionization of the aromatic component is necessary to avoid direct ionization of the olefin monomer. For this reason, we use Resonant-Two- Photon-Ionization coupled with High Pressure Mass Spectrometry (R2PI-HPMS) where the mode of ionization is selective for the aromatic component [15]. In these experiments, no direct photoionization of isoprene was observed in the absence of C_6H_6 in the reaction mixture. Figure 3 displays the R2PI mass spectrum obtained for a mixture of benzene and isoprene in N_2 carrier gas at a source pressure of 0.042 torr.

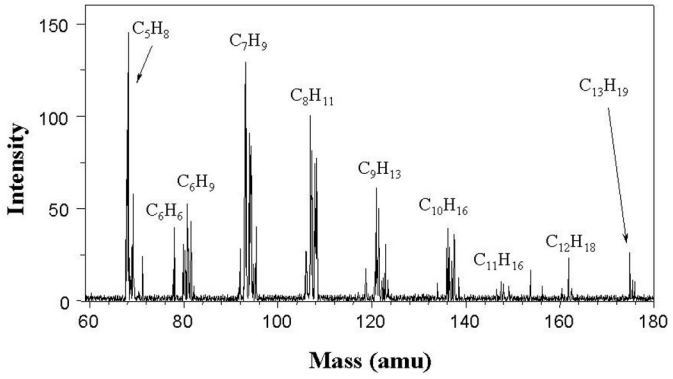

Figure 3. Mass spectrum obtained in a benzene/isoprene/ N_2 mixture.

Since the ionization potential, IP(isoprene) < IP(benzene), direct charge transfer from benzene $^{+\bullet}$ to isoprene takes place according to Reaction 1.

$$C_6H_6^{+\bullet} + C_5H_8 \rightarrow C_5H_8^{+\bullet} + C_6H_6 \qquad (1)$$

Following the generation of $C_5H_8^{+\bullet}$, it undergoes a series of well known addition and elimination reactions with neutral isoprene which produce the ion sequences C_xH_y with x =6-13 and y>x.[3] By increasing the concentration of isoprene in the reaction cell, ions corresponding to isoprene oligomers $(C_5H_8)_n^{+\bullet}$ up to n=4 could be observed.

In the benzene (C_6H_6) /propene (C_3H_6) system, the aromatic initiator (C_6H_6) has an IP between the reactant's monomer (C_3H_6) and its covalent dimer (C_6H_{12}), *i.e.*; IP(C_3H_6) > IP(C_6H_6) > IP(C_6H_{12}). Therefore, direct charge transfer from $C_6H_6^{+\bullet}$ to C_3H_6 is not observed due to the large endothermicity of 0.48 eV and only the adduct $C_6H_6^{+\bullet}(C_3H_6)$ is formed. However, coupled reactions of charge transfer with covalent condensation involving the $C_6H_6^{+\bullet}$ ion and two C_3H_6 molecules are observed according to the overall process:

$$C_6H_6^{+\bullet} + 2\,C_3H_6 \rightarrow C_6H_{12}^{+\bullet} + C_6H_6 \qquad (2)$$

This reaction represents an initiation mechanism for the gas phase polymerization of propene since it results in the formation of the dimer radical cation ($C_6H_{12}^{+\bullet}$), which can sequentially add several propene molecules. At higher concentrations of propene, the reaction products are the propene oligomers $(C_3H_6)^{+\bullet}_n$ with n = 2-7 and the adduct series $C_6H_6^{+\bullet}(C_3H_6)_m$ with m≤6. Figure 4 displays the time profiles corresponding to the sequential generation of the $(C_3H_6)^{+\bullet}_n$ series with n up to 5 (denoted as P_2, P_3, P_4 and P_5, and B for benzene).

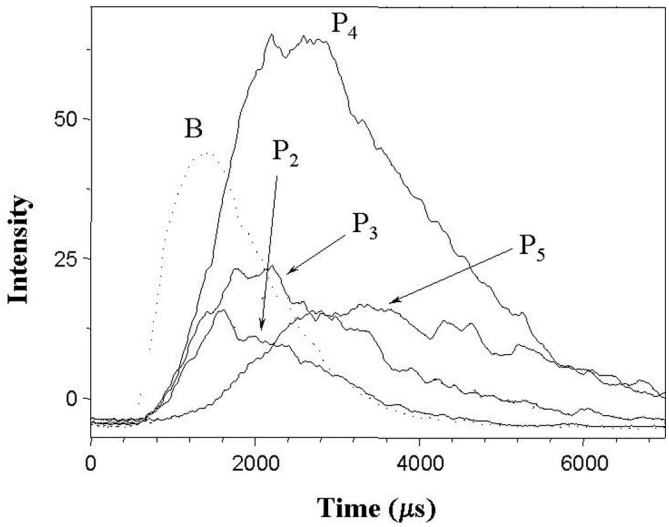

Figure 4. Time profiles for the generation of the gas phase propene oligomers.

The significance of the coupled charge transfer/covalent condensation reactions is that the overall process leads exclusively to the formation of condensation products $(C_3H_6)^{+\bullet}_n$ and avoids other competitive channels in the ion-molecule reactions of propene. For example, the reactions of $C_3H_6^{+\bullet}$ with neutral C_3H_6 involve several channels starting with the formation of the $C_3H_7^+$, $C_4H_7^+$ and $C_4H_8^{+\bullet}$ ions and their association products.

III. Implications for Gas Phase Polymerization in Microgravity

Gas phase polymerization can be initiated by photon irradiation or electron beam ionization of the monomer vapor. Another initiation method may involve plasma polymerization. The size of the product polymer particles is limited in normal gravity by gravitational settling. Polymerization can be terminated by recombination, or by the injection of inhibitors. In the microgravity experiments, polymerization will be initiated by irradiation by a high-pressure Hg / Xe UV lamp, or by electron irradiation using an electron gun based on a hot filament, or by plasma ionization using RF-field between two electrodes. The growth of the particles will be monitored by scattering of a test laser beam introduced perpendicular to the photoinitiating UV light or by a CCD camera. The product particles will be collected and the particle size distribution will be analyzed microscopically.

IV. Summary and Conclusions

The growth of nuclei in supersaturated vapors under microgravity conditions is expected to provide a more accurate and reliable picture of the growth process that can now be used to test the validity of different nucleation theories.

The study of gas phase polymerization is an important intellectual and technological frontier, which promises unique results not only for a fundamental understanding of polymerization reactions, but also for the development of new materials with unique properties. In the past it has been almost impossible to study gas phase chain polymerization because the involatile product molecules condensed out of the gas phase. The application of microgravity to the study of gas phase polymerization is expected to result in a better control of the process and may also lead to important technological advances.

The current research also involves the synthesis semiconductor, metallic and intermetallic nanoparticles. Recent experiments on the growth of the nanoparticles into treelike aggregates in the gas phase will be presented and some unique properties of the FeAl and TiAl intermetallic nanoparticles will be discussed.

REFERENCES

1. Abraham, F. F. "Homogeneous Nucleation Theory", Academic Press, New York, (1974).
2. Kane, D. B.; Fisenko, S. P.; Rusyniak, M.; El-Shall, M. S. J. Chem. Phys. 111, 8496 (1999).
3. Kane, D.; El-Shall, M. S. J. Chem. Phys. 105, 7617 (1996).
4. Brito, J.; Heist, R. H. Chem. Eng. Commun. 15, 133 (1982).
5. Kane, D.; Daly, G. M.; El-Shall, M. S. J. Phys. Chem. 99, 7867 (1995).
6. Kane, D.; El-Shall, M. S. Chem. Phys. Letters 259, 482 (1996).
7. Kane, D.; Fisenko, S.; El-Shall, M. S. Chem. Phys. Letters 277, 6, 12 (1997).
8. Kane, D. "Application of Resonance Enhanced Multiphoton Ionization to the Study of Ion Nucleation in Supersaturated Vapors", Ph.D. dissertation, Virginia Commonwealth University, Richmond, VA, 1997.
9. Kane, D. B.; Rusyniak, M.; Fisenko, S. P.; El-Shall, M. S. J. Phys. Chem. 104, xxx (2000).
10. Pithawalla, Y. B.; Gao, J.; El-Shall, M. S. Polymer Preprints 41, 1074 (2000).
11. Pithawalla, Y. B.; El-Shall, M. S. in *"Solvent-Free Polymerizations and Processes",* Long, T. E and Hunt, M. O. Eds, ACS Symposium series 713, 232 (1998).
12. Meot-Ner, M.; Sieck, L. W.; El-Shall, M. S.; Daly, G. M. J. Am. Chem. Soc. 117, 7737 (1995).
13. Pithawalla, Y. B.; Gao, J.; Yu, Z.; El-Shall, M. S. Macromolecules 29, 8558 (1996).
14. Meot-Ner, M.; Pithawalla, Y. B.; Gao, J.; Yu, Z.; El-Shall, M. S. J. Am. Chem. Soc. 119, 8332. (1997).
15. Daly, G. M.; Meot-Ner, M.; Pithawalla, Y. B.; El-Shall, M. S. J. Chem. Phys. 104, 7965 (1996).

MECHANISMS FOR THE CRYSTALLIZATION OF ZBLAN

Edwin C. Ethridge and Dennis S. Tucker

NASA/MSFC, Huntsville, AL 35812

The heavy metal fluoride glasses represent a class of reasonably good glass forming compositions with very unique infrared optical properties that have been of interest to researchers for 20 years[1]. The most extensively studied glass with the most potential for practical applications is ZBLAN which contains the fluorides of zirconium, barium, lanthanum, aluminum, and sodium. It has a broad transmission range (0.3-6 um), low index of refraction (~1.43), low dispersion, low Raleigh scattering, ultra-low thermal dispersion, and potential ultra-low signal attenuation[2]. Potential applications include fiber amplifiers, fiber optic gyroscopes, delivery systems for laser cutting, drilling and surgery, radiation resistant data links, nonlinear optical systems, and ultra-low-loss repeater-less transcontinental and transoceanic optical fiber. Potential markets for these materials are in the tens of billions of dollars per year[3].

Optical fiber from this system possess excellent transmission characteristics in the IR, but the glass is somewhat susceptible to nucleation and crystallization. The theoretical intrinsic loss coefficient for ZBLAN at 2 microns is 0.001 dB/Km. Extrinsic losses, however, cause significant attenuation. The lowest loss coefficient measured is 0.7 dB/Km. This compares with the loss coefficient for fiber optic grade fused silica glass of 0.2 dB/Km. The extrinsic losses in ZBLAN have been attributed to 1) impurities which might be lowered by containerless processing and 2) to scattering from micro-crystallites that form during glass preform production or during fiber drawing.

A number of experiments have been performed with glass forming materials in space that provide evidence of enhanced glass formation for glasses prepared in space. These experiments have been of two types, crystallization studies and diffusion studies. In general, the glasses have been shown to have much more homogeneous compositional distribution[4] than terrestrial samples and the glasses have been shown to be more resistant to crystallization[5,6]. Two groups have even reported that the crystallization of ZBLAN is reduced by processing in low-g. This investigation will examine the effects of vibration and shear on the crystallization of ZBLAN. This will be accomplished by comparing quiescent experiments with those under controlled vibration and to compare 1-g experiments with those in low-g and 2-g KC 135 aircraft experiments.

It is known that flow in undercooled polymer melts initiates crystallization[7]. It is also known that extrusion processing of glass-ceramic glass-forming melts catalyses the nucleation and growth of crystals[8]. Relatively high growth and nucleation rates have been reported in lithium di-silicate melts extruded at 540^0C where steady state nucleation and growth are practically zero for non-stressed samples[9]. Even though under most conditions glasses exhibit Newtonian viscous flow, non-Newtonian viscous flow is known at high strain rates in highly viscous melts[10,11]. A number of glass forming liquids have been shown to exhibit shear thinning with an order of magnitude lowering of the viscosity. This is attributed to structural rearrangements in the liquid, and in particular to the orientation of anisometric, chain like flow

units[12]. In phosphate melts, evidence of anisotropic behavior in sheared glass melts is indicated at viscosities less than 10^6 poise, being attributed to the "orientation of the phosphate tetrahedra chains"[13]. Shear thinning in lower viscosity liquids is indicated by molecular dynamics studies of a simple Lenard-Jones liquid consisting of spherical hard spheres. A tendency of the molecules to order themselves into layers parallel to the flow was indicated. The "stresses enhance the fluidity and create a liquid which has directionality"[14] .

If shear thinning does occur, one can predict the effect on crystallization[9]. Viscosity is the only directly measurable kinetic parameter used in crystal nucleation and growth equations. In the classical treatment of crystallization[15] the nucleation rate, I, and crystal growth rate, U, are both inversely proportional to viscosity, η, with the viscosity term appearing in the pre-exponential factor.

$$I = (k_n/\eta) \exp[-b\alpha^3\beta T_m/T(1-T_r)^2]$$

$$U = (k'_n/\eta) [1-\exp(-\beta(T_m-T/T)]$$

Where T_m is the melting temperature, T is the absolute temperature, and T_r is the reduced temperature. The kinetic constants k_n and k'_n, shape factor, b, and dimensionless parameters related to the liquid-crystal interfacial tension, α, and entropy of fusion, β, are described elsewhere[15].

The fraction of glass crystallized, X, with time at a given temperature[16] is a function of the rate of nucleation, the third power of the growth rate, and the fourth power of time.

$$X = \pi/3(IU^3t^4)$$

Under conditions of shear thinning, the effective viscosity decreases with increasing shear rate so that the viscosity can be expressed as a function of shear rate.

$$\eta = \eta(\varepsilon)$$

The crystallization parameters such as the nucleation rate will also be a function of shear rate.

$$I(\varepsilon) = (k_n/\eta(\varepsilon))\exp[-b\alpha^3\beta T_m/T(1-T_r)^2]$$

Low g-processing is known to greatly reduce convection, which reduces shear in the liquid. This would reduce any shear thinning in the liquid subsequently increasing the viscosity of the liquid, thereby reducing nucleation and growth rates. For an increase in viscosity by a factor of 2, the nucleation and growth rates each are reduced by half, but the fraction crystallized is reduced by a factor of 16. Since shear in liquid occurs as a result of fluid flow and fluid flow is greatly reduced in low gravity, we have crystallization equations which are affected by gravitational effects.

I. Experimental Method

We will utilize a rapid thermal analyzer method developed by the PI[17] to examine the crystallization of ZBLAN. The system involves the suspension of a sample on a thermocouple which is rapidly heated by a radiant source. Because of the low thermal mass of the system, it is suitable for collection of thermal data during rapid heating and cooling. It was utilized for studies of the heterogeneous nucleation of reluctant glass formers[18]. Data will be collected for a range of heating and cooling rates. Time-tem-

perature-crystallization diagrams can be determined from the quenching data from which critical glass cooling rates can be determined.

Initial experiments will be processed under quiescent conditions. Once the system is characterized and materials properties are determined, experiments will be repeated under conditions of controlled frequency and amplitude of oscillation to determine the sensitivity of crystallization to the level of shear in the liquid. Once small amplitude oscillation methods are fully established, experiments will be performed on the KC-135 under low-g and 2-g for comparison with 1-g experiments

The viscosity of ZBLAN is fairly well characterized over the entire temperature range with data from around the melting temperature, around the glass transition temperature, and some measurements in the intermediate range. We would also like to determine if it is possible to observe shear thinning in ZBLAN melts at low shear rates.

II. Value of Experimental Research

By performing the experiments and meeting the objectives, we will gain valuable insights for the understanding of the mechanisms of crystallization and glass formation in low gravity. The establishment of a new mechanism for enhanced glass formation would stimulate more interest from the glass research discipline.

REFERENCES

1. M.G. Drexhage, C.T. Moynihan, and M. Robinson, editors (1987) Halide Glasses II, Materials Science Forum V19-20, Proceed. of the 4th Inter. Symp. On Halide Glass.
2. S. Varma, S.E. Prasad, A. Ahmad, T.A. Wheat, and K. Abe (1992), Proc. Spacebound '92, Canadian Space Agency, Ottawa.
3. Business Communications Co. (1997) "Fiber Optics and Fiber Optics Materials," Business Communications Co., Norwalk, CT, GB-073N, February 1997.
4. G.H. Frischat (1995), J. Non-Cry. Solids 183:92-99.
5. C.S. Ray and D.E. Day (1987) Proceedings of the Materials Research Society Symposia on Materials Processing in the Reduced Gravity Environment of Space, R.H. Doremus and P.C. Nordine, Eds., 87:239.
6. C. Barta, L Stourac, A. Triska, J Kocka, and M Zavetova, (1980), J. Non-Cry. Solids 35&36: 1239-1244.
7. A.J. Pennings, J.M.A. van der Mark, and H.C. Booji (1970) Kolloid. Z.u.Z.f.Polymere 236:99.
8. Gutzow, I., B. Durschang, and C. Russel (1997), J. Mater. Sci. 32:5389-5403.
9. Gutzow, I., C. Russel, and B. Durschang (1997), J. Mater. Sci. 32:5405-5411.
10. J.H. Li and D.R. Uhlmann (1970), J.Non-Cry Solids 3:127-147
11. J.H. Simmons, R.K Mohr, and C.J. Monrose (1982), J. Appl. Phys. 53:4075-4080.
12. R. Wasche and R. Bruckner, (1986), Phys. Chem. Glass. 27:87-94.
13. A.Habeck and R. Bruckner (1993), J. Non-Cry. Solids. 162:225-236.
14. D.M. Heyes, J.J. Kim, C.J. Monrose, and T.A. Litovitz (1980), J. Chem. Phys.73:3987-3996.
15. D Turnbull, Contemp Phys. 10:473(1969).
16. D.R. Uhlmann, J. Non-Cry. Solids 7:337(1972).
17. E.C. Ethridge and P.A. Curreri, (1988), Rev. Sci. Instru. 59:184-186.
18. E.C. Ethridge, P.A. Curreri, and D. Pline, (1987), J. Am. Ceramic Soc. 70:553-556.

EXPLOITING THE TEMPERATURE DEPENDENCE OF MAGNETIC SUSCEPTIBILITY TO CONTROL CONVECTION IN FUNDAMENTAL STUDIES OF SOLIDIFICATION PHENOMENA

C. Seybert[1], J.W. Evans[1 *], F. Leslie[2], W.K. Jones Jr.[3]

[1]University of California, Berkeley
[2]NASA, Marshall Space Flight Center
[3]Motorola, Adv. Prod. Tech. Center

It is well known that convection is a dominant mass transport mechanism when materials are solidified on Earth's surface. This convection is caused by gradients in density (and therefore gravitational force) that are brought about by gradients in temperature, composition or both. Diffusion of solute is therefore dwarfed by convection and the study of fundamental parameters, such as dendrite tip shape and growth velocity in the absence of convection is nearly impossible. Significant experimental work has therefore been carried out in orbiting laboratories with the intent of minimizing convection by minimizing gravity. One of the best known experiments of this kind is the Isothermal Dendritic Growth Experiment (IDGE), supported by NASA. Naturally such experiments are costly and one objective of the present investigation is to develop an experimental method whereby convection can be halted, in solidification and other experiments, on the Earth's surface. A second objective is to use the method to minimize convection resulting from the residual accelerations suffered by experiments in microgravity.

The method to be used to minimize convection relies on the dependence of the magnetic susceptibility of a fluid on temperature or composition (whichever is driving convection). All materials experience a force when placed in a magnetic field gradient. The direction and magnitude of that force depend on the magnetic susceptibility of the material. Consequently the force will vary if the susceptibility varies with temperature or composition. With a magnetic field gradient in the right direction (typically upward) and of the right magnitude, this variation in the magnetic force can be made to exactly cancel the variation in the gravitational force.

Figure 1 is a cartoon illustrating this principle (and the geometry of the experiment described below. A fluid between a cold wall and a hot wall is experiencing a downward gravitational force and an upward magnetic body force. The former force (per unit volume) diminishes towards the hot wall where the fluid is less dense. In the absence of other forces, this would bring about the usual natural convection (flow down the cold wall, from left to right across the bottom, up the hot wall and back across the top). The buoyancy that brings about this flow is represented by the differences in the arrows representing the gravitational force, *i.e.* the upward pointing arrow near the hot wall. If the susceptibility of the fluid is temperature dependent (*e.g.* a paramagnetic liquid) then there is a difference between the magnetic body force in the vicinities of the hot and cold wall. This is labeled a "magnetic buoyancy" in the cartoon. If the magnetic field gradient is adjusted to the right value then this magnetic buoyancy exactly counters the normal buoyancy.

* Corresponding author

The total body force acting on the fluid is

$$\frac{\chi}{2\mu_0}\nabla(B^2)-\rho g$$

where χ is the susceptibility, B the magnetic flux density, ρ the density, g the gravitational acceleration and μ_0 the permeability of free space. At a critical magnetic field gradient given by

$$\nabla(B^2)_C=2\mu_0 g\left(\frac{d\rho/dT}{d\chi/dT}\right)$$

the body force becomes independent of temperature (T).

To demonstrate the principle, a solution of $MnCl_2$ in water has been used. First the variation of the susceptibility of this paramagnetic solution with temperature and concentration was measured. Then a "cell," containing this solution and 50 mm long by 15 mm high by 155 mm wide, was placed in a superconducting magnet at Marshall Space Flight Center. The magnetic field was measured at various positions within the bore of the magnet using a Hall effect probe. In this way, a position was found where the magnetic field gradient was predominantly upward; the magnitude of the gradient could then be adjusted by adjusting the current of the magnet. The ends of the cell consisted of machined copper blocks maintained at controlled temperatures by circulating water from constant temperature baths. The walls of the cell were of rectangular section glass tubing so that the cell contents could be seen. Velocities arising from thermal gradients within the cell were measured by particle image velocimetry (PIV). Particles used for this purpose were silver-coated hollow glass spheres of 11 micrometers mean diameter and nearly the same density as the solution. A central vertical plane of the cell was illuminated by a laser beam passing through a cylindrical lens. Digital images of the particles were captured on a CCD camera and fed to a computer so that frame-to-frame movements of particles traveling with the fluid were captured. These images were employed to compute velocity maps using commercial PIV software.

In a typical experiment the cold end of the cell was maintained at 10^0C and the warm end at 30^0C. Results are seen in Figure 2 where (in accordance with expectations arising from the second equation above) the velocity has been plotted versus the square of the current through the superconducting magnet). With no current in the magnet, *i.e.* with only natural convection allowed to occur, the fluid was observed to circulate with a maximum measured speed of 1.15 mm/s. It was visually apparent that this circulation was diminished as the current was increased. At currents of approximately 20A the flow was halted, to within the precision of the PIV measurements. At yet higher currents the convection was reversed with the hotter solution sinking and the cooler solution rising. At 40A this reversed convection had a maximum measured speed of 1.37 mm/s.

The measurements of susceptibility and density allow an estimate of the field gradient necessary to halt convection in the experiment. That estimate was $7.8T^2$/m and the convection was observed to halt in the magnet at a current giving $7.2T^2$/m from the magnetic field measurements. Calculations of the flow have been carried out using the computational fluid dynamics software FLUENT® and show good agreement with the measurements.

A more limited number of measurements has been carried out with the manganese chloride solution in the process of solidifying. The cold end of the cell was maintained at -10^0C while the other end was at

0^0C. In this case too it was possible to find a current at which the field produced by the magnet was able to virtually halt convection. The work is part of a continuing investigation now entering the third of its four years with support from NASA.

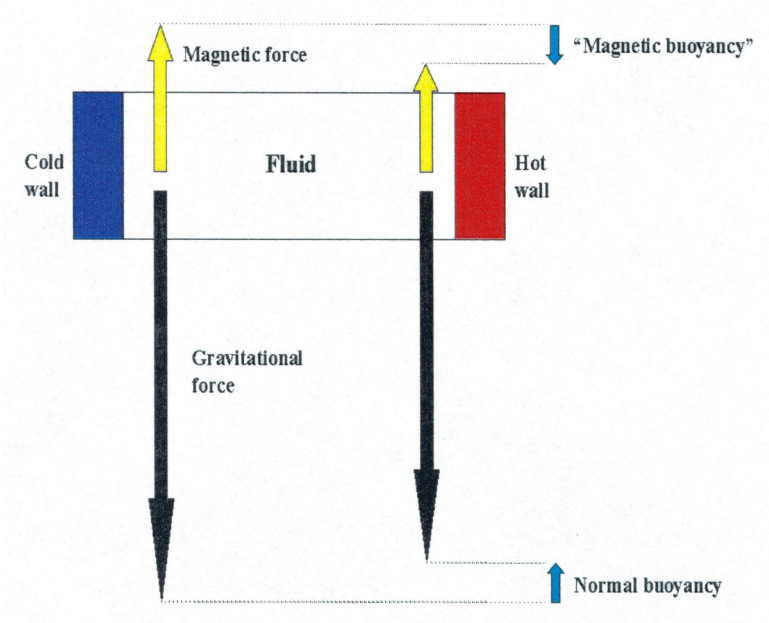

Figure 1. Illustration demonstrating the halting of natural convection by countering normal buoyancy with a "magnetic buoyancy".

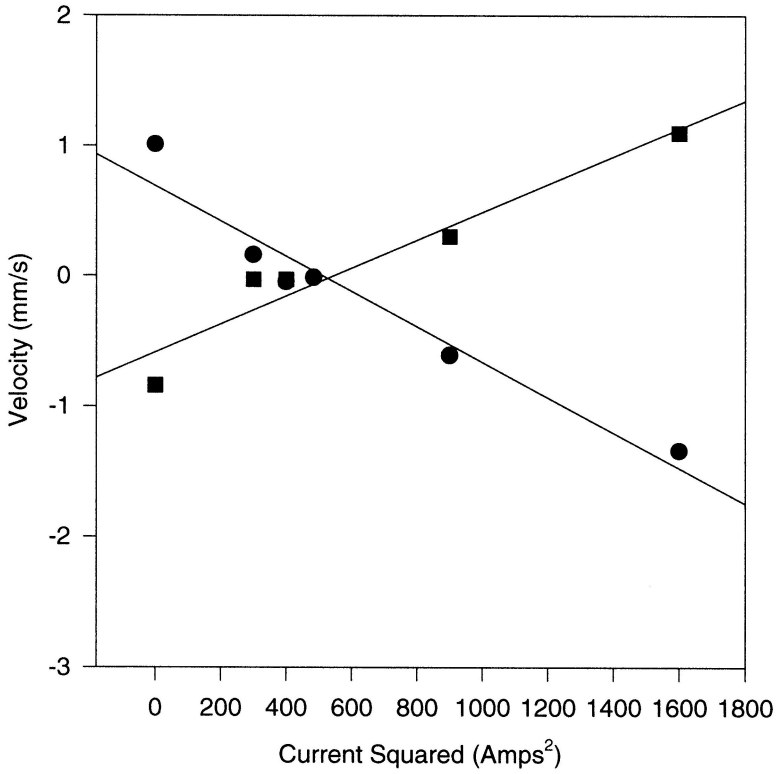

Figure 2. Velocity of the fluid at two different points in the cell were measured and plotted at different currents in the magnet. As can be seen in the graph, the flow was halted at approximately 20 Amps, corresponding to 7.2 T^2/m.

INVESTIGATION OF VIBRATIONAL CONTROL OF CONVECTIVE FLOWS OF THE BRIDGMAN CRYSTAL GROWTH TECHNIQUE

Alexandre I. Fedoseyev

Center for Microgravity and Materials Research
University of Alabama in Huntsville

INTRODUCTION

The character of natural buoyant convection in rigidly contained inhomogeneous fluids can be drastically altered by vibration of the container. For certain experiments and operating conditions, vibrations are expected to have a significant influence on heat and mass transfer on board the International Space Station (ISS). Furthermore, it appears that g-jitter vibrations will exist on ISS over a wide range of frequencies [1]. In general, vibrational flows are very complex and are governed by many parameters. This complexity makes it almost impossible to correctly predict vibrational effects empirically. Thus, a careful theoretical approach combined with numerical modeling is essential. Available flight experiment data clearly show that, once initiated by "g-jitter", the effects of convective flows can persist for long times even when the g-jitter disturbance (and consequent flow) were short-lived [2-7].

In many terrestrial crystal growth situations, convective transport of heat and constituent components is dominated by buoyancy driven convection. Control of convective transport continues to be an important aspect of crystal growth research. Several groups are actively pursuing control of convection using static and rotating magnetic fields. Magnetic fields cannot be used for flow control in melts and solutions that are poor conductors. Flow suppression through vibration or vibro-convective mixing may offer an attractive alternative in such cases.

Recent work has shown that the character of natural buoyant convection in non-uniformly heated, rigidly contained inhomogeneous fluids can be drastically altered by vibration of the container. A review and relevant theoretical and experimental research can be found in publications [1-13]. Thus, vibrational induced flow can potentially be used to influence and even control transport in some crystal growth situations. A practical quantitative understanding of vibrational convection as a control parameter in crystal growth situations is currently not available. The objective of the work is to assess the feasibility of the use of vibration to suppress, or control, convection in order to achieve transport control during crystal growth.

Buoyancy driven vibro-convective motion occurs when oscillatory displacement of a container wall induces the acceleration of a container wall relative to the inner fluid. The vibration may be viewed as a time-dependent modulation of steady gravity. In a closed container the fluid will move as a rigid body with a container. If, however, the fluid density is nonuniform, fluid motion may ensue. The magnitude of this motion, of course, depends on the orientation of the vibrational direction with respect to the local density gradients. Note that, similar to Rayleigh-Benard configura-

tions, there may be a "critical" threshold for the coupled vibrational frequency and amplitude, to cause convection. Interestingly, it should be noted that in case of a constant density fluid subject to spatially nonuniform vibration, fluid motion can also occur (for example, angular vibration [11]).

To properly investigate influence of translational, circularly polarized and rotational (angular) vibration necessitates the use of the full 3-D equations governing the transport of heat, mass and momentum. Selected examples of our ongoing work on this topic are outlined below.

We consider a purely thermovibrational convection in a differentially heated cylindrical cavity with no consideration of solidification. The fluid is taken to be Newtonian and the Boussinesq approximation is assumed to hold. The calculations were performed for identification and characterization of thermovibrational flow and are part of an ongoing project involving flow visualization model experiments being conducted by Feigelson [10].

I. Mathematical Model for Translational and Polarized Vibration

Translational vibration corresponds to a linear displacement such as, for example, $\boldsymbol{u}=\boldsymbol{d}\cos\omega t$, where $\boldsymbol{d}$ is a real vector giving the displacement magnitude and ω is the frequency. In this case the ampoule is displaced back and forth upon the same line. Polarized vibrations are characterized by a displacement $\boldsymbol{u}=Re\{\boldsymbol{d}e^{i\omega t}\}$ where $\boldsymbol{d}=\boldsymbol{d}_1 - i\boldsymbol{d}_2$ (see Figure 1(a,b)). Here the instantaneous vibration direction rotates in the polarization plane defined by the real vectors $\boldsymbol{d}_1$ and $\boldsymbol{d}_2$. A sketch showing both translational and circular polarized vibrations is presented in Figure 1. In a reference frame fixed to a vibrating ampoule, the momentum equation is

$$\frac{\partial v}{\partial t} + (\boldsymbol{v}\cdot\nabla)\,\boldsymbol{v} = -\nabla p + Pr\nabla^2\boldsymbol{v} + Ra_T Pr\,(\Theta + \alpha C)\boldsymbol{k} + Ra^*_T Pr\,(\Theta + \alpha C)\,\boldsymbol{f}\,(\Omega, t), \qquad (1)$$

where length, time and velocity are scaled by R_0, R_0^2/κ and κ/R_0. Here R_0 is the ampoule radius and κ is the thermal diffusivity. The nondimensional concentration and temperature, are given by Θ, and C, respectively. The function $\boldsymbol{f}(\Omega, t)$ is the acceleration of the vibrating ampoule and $\Omega=\omega R_0^2/\kappa$ is a dimensionless frequency. The continuity and heat-mass transfer equations complete the problem formulation. The Prandtl, Schmidt, thermal and vibrational Rayleigh numbers and the buoyancy ratio are given by

$$Pr = \frac{\nu}{\kappa},\ Sc = \frac{\nu}{D},\ Ra_T = \frac{\beta\Delta T g R^3}{\nu\kappa},\ \alpha = \frac{\beta_c c_\infty}{\beta\Delta T},\ Ra^*_T = \frac{d\omega^2\beta\Delta T R^3}{\nu\kappa}. \qquad (2)$$

Here β and β_C are the thermal and solutal expansion coefficients and ΔT, c_∞, g, d, ω, $\boldsymbol{k}$, ν, D are the characteristic longitudinal temperature difference, reference concentration in the melt, gravitational acceleration, vibrational displacement amplitude and frequency, direction of gravity, kinematic viscosity and solute diffusivity, respectively. The dimensionless number Ra^*_T is the vibrational Rayleigh number and $Ra^*_S = \alpha Ra^*_T$. Equation (2) is solved together with the equations governing heat and species transfer and the continuity equation.

II. Rotational Vibration

The equations of motion for angular vibrations take on a more complicated form (see Figure 1c). A container of length L is subjected to an angular displacement $\theta(t)$ in the x_1^*-x_3^* plane. Here the coordinates $\boldsymbol{x}^*$ are referred to a fixed laboratory frame of reference. The position vector to the mass center of the cylinder is parallel to the side of the cylinder and is given by $\boldsymbol{q}^* = R_0[-\sin\theta\ \mathbf{i}_1^* + \cos\theta\ \mathbf{i}_3^*]$ where

R_0 is the distance from the origin **0*** to the mass center of the cylinder and $\theta(t) = \varepsilon \sin\Omega_0 t$. In a frame of reference moving with the container, the equations of motion have the form

$$\rho \frac{D\boldsymbol{v}}{Dt} = \text{div}\, \boldsymbol{T} - \rho \boldsymbol{k} (\sin\theta \boldsymbol{i}_1 + \cos\theta \boldsymbol{i}_3) + \rho[2\tilde{\Omega}\boldsymbol{v} - \tilde{\Omega}^2\boldsymbol{x} + \dot{\tilde{\Omega}}\boldsymbol{x} + \varepsilon^2\Omega^2{}_0 R_0 \cos\Omega_0 t \boldsymbol{i}_1] \quad (3)$$

where D/Dt denotes the material derivative, v is the velocity of the fluid relative to the moving reference frame, ρ is the density of the fluid, $\tilde{\boldsymbol{\Omega}}$ is the rate of rotation tensor for the moving frame with respect to the fixed frame of reference, $\dot{\tilde{\boldsymbol{\Omega}}}$ is its time derivative and $\boldsymbol{T}$ is the Newtonian stress tensor for the fluid. The dimensionless equations governing the transport of momentum, mass and heat in the cylinder are obtained after using L, L^2/κ, κ/L, and $\Delta T = T_H - T_C$ to scale, respectively, length, time, velocity and temperature. The governing dimensionless parameters are the dimensionless frequency $\Omega = \Omega_0 L^2/\kappa$, the dimensionless container radius, $\vartheta = R_0/L$, the Prandtl, Pr, and the Rayleigh, Ra, vibrational Rayleigh Ra_Ω, and Ekman, E, numbers. The latter are given by

$$Pr = \frac{\nu}{\kappa}, \; Ra = \frac{\beta \Delta T g L^3}{\kappa \nu}, \; Ra_\Omega = \frac{\beta \Delta T \Omega_0{}^2 L^4}{\kappa \nu}, \; E = \frac{\nu}{\Omega_0 L^2}, \quad (4)$$

where β, ν, g and κ are the coefficient of thermal expansion, kinematic viscosity, gravitational acceleration and thermal diffusivity, respectively. This system of equations differ from the usual equations in the absence of rotation in that additional terms are present; the Coriolis term which is proportional to $\varepsilon Pr/E$, and the centrifugal term which is proportional to $\varepsilon^2 \vartheta Ra_\Omega Pr$ and varies with linearly with position in the ampoule. The importance of the latter term depends on the dimensions of the amplitude of the angular vibration, ε, and the ratio ϑ. The rocking motion of the angular vibration under consideration means that centrifugal terms give rise to a periodic forcing that fluctuates about the mean value at twice the period of the angular vibration.

Since the above system of equations has not been well studied, a conservative approach was adopted for the study of angular vibrations and we confine our investigation to a parametric study of flow regimes and transitions for thermo-vibrational situations in the absence of solidification.

III. Solution Method

The equations are solved in primitive variable form using a Finite Element Method code FEMINA/3-D developed by the PI [14]. The continuity equation and momentum equations are considered simultaneously at each time step. This eliminates many problems related to boundary conditions and places only slight limitations on the time step size for transient problems. The regularization for the incompressibility condition makes the solution procedure more efficient, and allows the same order finite element approximation for both the velocity and pressure [15]. This approach makes it possible to solve large 3-D time-dependent problems (up to 300,000 unknowns) on a SGI O2 workstation with reasonable computation times.

We implemented the above 3-D models of convective buoyancy-driven melt flow in differentially heated cylindrical containers using the FEMINA/3D code. This code was carefully tested on benchmarked experimental and numerical data for a variety of 2-D/3-D viscous and thermo-convective flow problems and flows under magnetic field [15,16,19].

For rotational vibrations the Ekman number can be of the order 10^{-4} to 10^{-5} for frequencies on the order of 1Hz. This results in large coefficients, Pr/E, for the Coriolis terms in the governing equations and causes difficulties in the numerical solution. To resolve this we implemented a high accuracy solution

method using preconditioning by high order incomplete decomposition (accuracy up to 10^{-9}). The computation times reduced by one to two orders of magnitude and the memory size by a factor of 8 for 3-D flows compared to currently available commercial codes (*e.g.,* CFD2000). A typical solution time for a transient problem is about two hours on a SGI O2.

IV. Results and Discussion

We verified the validity of the Boussinesq model for semiconductor and oxide melts under microgravity conditions. This topic has been discussed recently by Perera, Sekerka [17], Pukhnachev [18] and Gershuni, Lyubimov [11]. If the nondimensional criteria, proposed by Pukhnachev, $Pu = gL^3\nu^{-1}\kappa^{-1}$ is less than 1, then the Boussinesq model for thermal convection may not be valid. Our estimates show that the Boussinesq model is quite adequate for a differentially heated closed ampoule and the range of parameters and material properties under investigation. The values of Pu are of the order 10^4 to 10^5 for semiconductor and oxide melts for $g/g_0 = 10^{-5}$ to 10^{-4}, clearly well above 1.

A parametric study of translational and rotational vibrations under typical microgravity and terrestrial conditions for typical semiconductor melts was performed. A snapshot of a typical flow pattern for translational vibration is presented in Fig. 2(a). Even in the total absence of gravity the vibrations have resulted in detectable flows. For the cases examined, the temperature distribution remains almost unperturbed (due to the low Pr and weak flow strength).

The angle between the direction of vibration and the ampoule has been studied for translational vibrations in the presence of an axial temperature gradient. At high frequencies and when the angle is zero, no influence of the vibration on the flow was observed, even when vibrational the Raleigh number is very high. The maximum observed effect corresponds to an angle of 90 degrees. Here transport is significantly enhanced.

Typical flow patterns for rotational vibrations flow regimes are presented in Figure 2(b). Maximal velocity values are observed at the end of the ampoule that is farthest from the rotation origin.

The influence of vibrations on heat and mass transfer becomes significant for oxide melts due to their low thermal diffusivity ($Pr \sim 10$). These flow patterns are shown in Figure 3(a) for the case of circular polarized vibration. Initially (at time $t = 0$), the species concentration was $c=1$ at the lower quarter of the cylinder and $c = 0$ elsewhere. The evolution of the species concentration (process of mixing) and velocity (minimal and maximal values of V_z) is shown in Figure 3(b,c). Complete mixing occurs in about ten seconds. The heat transfer (local Nusselt number at the top and the bottom) is also enhanced by about an order of magnitude. If the frequency of vibration is high, of the order of 100Hz (for fixed Ra_Ω), then the changes in heat and mass transfer due to vibrations become less significant. This corresponds to earlier experimental observations [7, 8].

Our results show that both translational, circular polarized and angular vibration can cause average melt flow for a range of parameters typical of practical semiconductor growth. For a given vibration amplitude and frequency, circular polarized and rotational (angular) vibrations result in more intensive melt flows than translational ones.

The influence of forced vibration on g-jitter induced flows using the Space Acceleration Measurement System microacceleration data from the Second United Microgravity Laborotory (USML-2) mission was also investigated [13]. Motivated by the predictions of the averaged equation theory presented in Ref. [11], translational vibration was applied parallel to the ampoule axis (and thus, the temperature gradient) in an

attempt to damp unwanted irregular time-dependent flow caused by g-jitter. While the flow variation with time becomes more regular, we did not succeed in completely suppressing the g-jitter flow. We found that the use of the same amplitude vibration in the direction orthogonal to the ampoule axis is more effective. This induces intensive thermal vibration flows and flow disturbances due to g-jitter become practically insignificant.

V. Summary

The influence of translational, circularly polarized and rotational (angular) vibration in analysis in a model Bridgman melt growth configuration was investigated. The nature of the flows produced by the types of vibration under consideration necessitated the use of the full 3-D equations governing the transport of heat, mass and momentum. The governing equations were solved numerically. Flow patterns for translational, circular polarized and rotational (angular) vibrations and g-jitter microaccelerations were analyzed. For translational vibration, thermovibrational flow is strongly dependent on the angle between the vibration direction and temperature gradient. Circular polarized and rotational vibrations result in more intensive melt flows than translational ones. The simultaneous action of vibrations and magnetic field [19] is currently being studied.

REFERENCES

1. Don Hurle (Ed.), Proc. of the Physical Sciences Working Group Workshop on g-sensitivity of planned experimentation on ISS, *Microgravity Sci. Technol.,* 11, 2/3 (1998).
2. J.I.D. Alexander, J-P. Garandet, J.J. Favier, A. Lizee, *J. Cryst. Growth*, 178 (1997) 657-661.
3. J.D. Trollinger, M. Rottenkolber and F. Elandalouss, *Meas. Sci. Technol* , 8 (1997) 1573.
4. J.D. Trollinger, R. Ranel and R.B. Lai, *Appl. Opt.* 35, (1996) 681-689.
5. R. Naumann, AIAA 99-1028, Proc. 37th AIAA Meeting, Reno, 11-17 Jan. 1999.
6. Y-C. Lu, J.-J. Shiau, R.S. Feigelson and R.K. Route, *J. Cryst. Growth*, 102 (1990) 807.
7. R.C. DeMattei and R.S. Feigelson, *J. Cryst. Growth*, 128 (1993) 1062-1068.
8. W-S. Liu, J. F. Wolf, D. F. Elwell, R. S. Feigelson, *J. Cryst. Growth,* 82 (1987) 589-597.
9. E.V. Zharikov, L.V. Prihodko, N.R. Storozhev, *J. Cryst. Growth,* 99 (1990) 910-914.
10. R. Feigelson and E. Zharikov, *NASA/CP 1999-209092,* 1999.
11. G. Gershuni, D. Lyubimov, *Thermal Vibrational Convection*, Wiley, N.Y., 1997
12. A. Lizee, J.I.D. Alexander, *Phys. Rev., E* 56 (1997) 4152.
13. A.I. Fedoseyev, J.I.D. Alexander, *J. Cryst. Growth,* 211 (2000), 34-42.
14. V.I. Polezhaev, A. I. Fedoseyev at al. Mathematical Modeling of Convective Heat and Mass Transfer on the Basis of Navier-Stokes Equations, Nauka, Moscow, 1987.
15. A.I. Fedoseyev, CFD Journal, No. 1, 9 (2000), to appear.
16. A.I. Fedoseyev, E.J. Kansa, C. Marin, M.P. Volz, A.G. Ostrogorsky, AIAA-2000-0859.
17. P.S. Perera and R.F. Sekerka, *Physics of Fluids*, 9 (1997) 376-391
18. V. Pukhnachev, Microconvection in a vertical layer, *Fluid Dynamics*, 5 (1994) 76-84.
19. A.I. Fedoseyev, J.I.D. Alexander, AIAA-2000-0698, Proc. 38th AIAA Meeting, Reno, 2000.

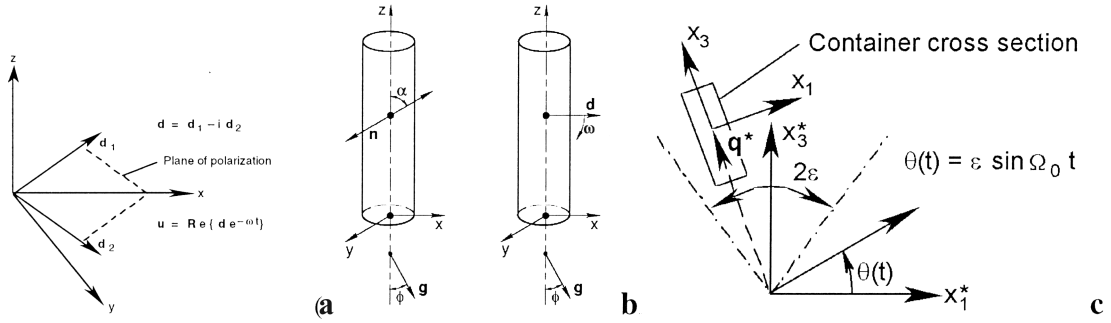

Figure 1. Translational vibration (a), d_1 or $d_2 = 0$; polarized vibration (b), $d_1, d_2 \neq 0$; φ is the angle between gravity vector and the ampoule axis, α is the angle between the vibration direction and the ampoule axis; (c) rotational (angular) vibration. The container is rotated at an angle $\theta(t)$ about a center of rotation at $\boldsymbol{x}^* = 0$. The vector $\boldsymbol{q}^*$ connects the center of rotation to the mass center of the container.

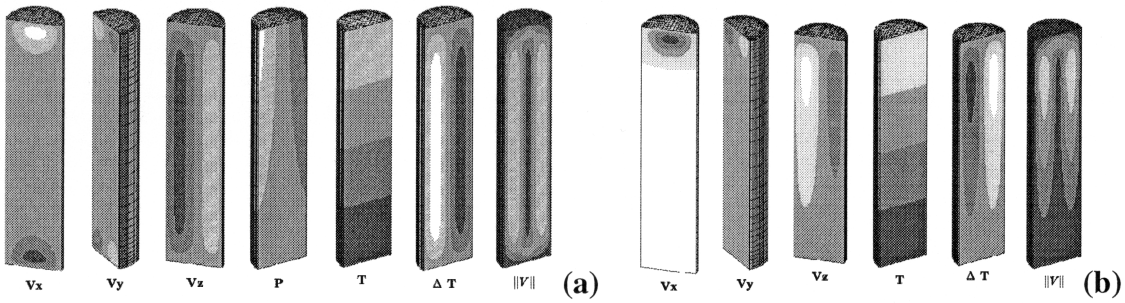

Figure 2. (a) Instantaneous 3D flow patterns for a lateral translational vibration at **0g**, $Ra = 0$, $Ra_T = 7.25 \cdot 10^4$, $Pr = 0.01$, $\omega = 100 Hz$. The velocity components are V_x, V_y, V_z, P is the pressure, T is the temperature, ΔT is the temperature disturbance and $|V|$ - velocity magnitude. The grayscale range corresponds to maximum values (white) of the velocity, temperature and pressure variables to their minimum values (black). Vibrations are applied along the horizontal (x-direction); (b) 3-D melt flow patterns for angular vibration at zero-g, $Ra = 0$, $Ra_\Omega = 4.6 \cdot 10^5$, $Pr = 0.01$, $\omega = 100\ Hz$.

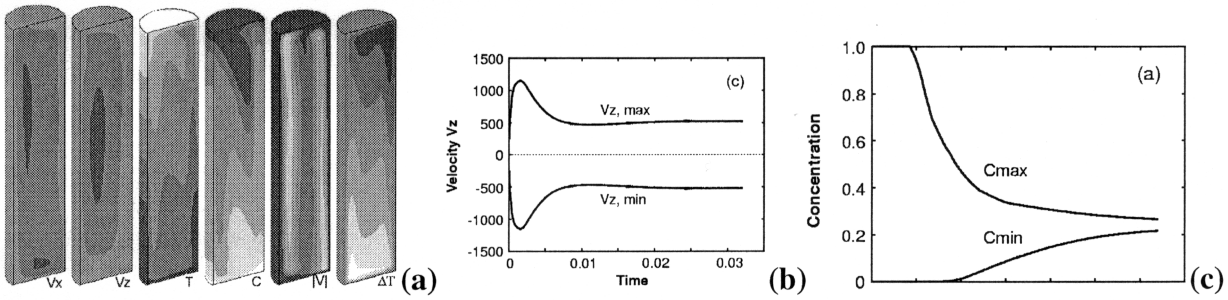

Figure 3. (a) 3-D flow patterns for circularly polarized vibration, $Ra = 7.25 \cdot 10^3$, $Ra = 7.4 \cdot 10^6$, $Pr = 15$, $\omega = 10 Hz$, C is the concentration; (b) Temporal evolution of velocity extrema Vz, and (c) species concentration C.

INVESTIGATION OF THE CRYSTAL GROWTH OF DIELECTRIC MATERIALS BY THE BRIDGMAN TECHNIQUE USING VIBRATIONAL CONTROL

R.S. Feigelson[1] and E.V. Zharikov[2]

[1]Stanford University, Stanford, California
[2]General Physics Institute, Moscow, Russia

INTRODUCTION

The principal goal of this ground-based program is to investigate the influence of low frequency vibrations on the fluid flow and quality of dielectric oxide crystals grown by the vertical Bridgman method. This experimental program, a collaborative effort between Stanford University and the General Physics Institute of the Russian Academy of Sciences in Moscow, includes a strong emphasis on both physical modeling and the growth of some technologically important materials. The program involves a study of vibro-convective buoyancy-driven flows in cylindrical configurations with the expectation of being able to use vibrational flows to control buoyancy driven fluid transport to off-set the effect of "g-jitter" during microgravity Bridgman crystal growth. This program together with theoretical and numerical investigations of vibrational control will lead to a new parametric control variable which can be used to either suppress or control convection, and thereby heat and mass transport during Bridgman crystal growth. It is expected to be effective in either a terrestrial or space environment.

The following primary objectives of the research have been accomplished.

1) The most appropriate methods for introducing vibrations into the melts have been determined. In this research, forced convection can be introduced into the melt by a number of techniques involving either external or internal forces. Research being carried out at the General Physics Institute has focused on introducing forced convection internally, and work being done at Stanford University has focused on externally induced convection.

2) The vibration induced flows have been correlated with interface shape and position, growth rate, crystal perfection, and dopant distribution in $NaNO_3$ growth systems.

3) The effects of low frequency vibrations on fluid flow in Bridgman type crystal growth processes have been studied. Flows were examined in both non-crystallizing water/glycerin mixtures and the low melting temperature $NaNO_3$ system.

I. Internal Vibrations

At the General Physics Institute, an axially vibrating disk suspended in the melt is used as the source of internal vibrations. Crystal growth was conducted in quartz ampoules (d=13 mm) in a transparent multizone quartz furnace. The system provided visual observation of both an interface and flows in a

melt. The furnace heaters, translation mechanisms and vibrator were controlled using a personal computer and CAMAC crate. This setup allowed for setting a necessary temperature profile to be main-

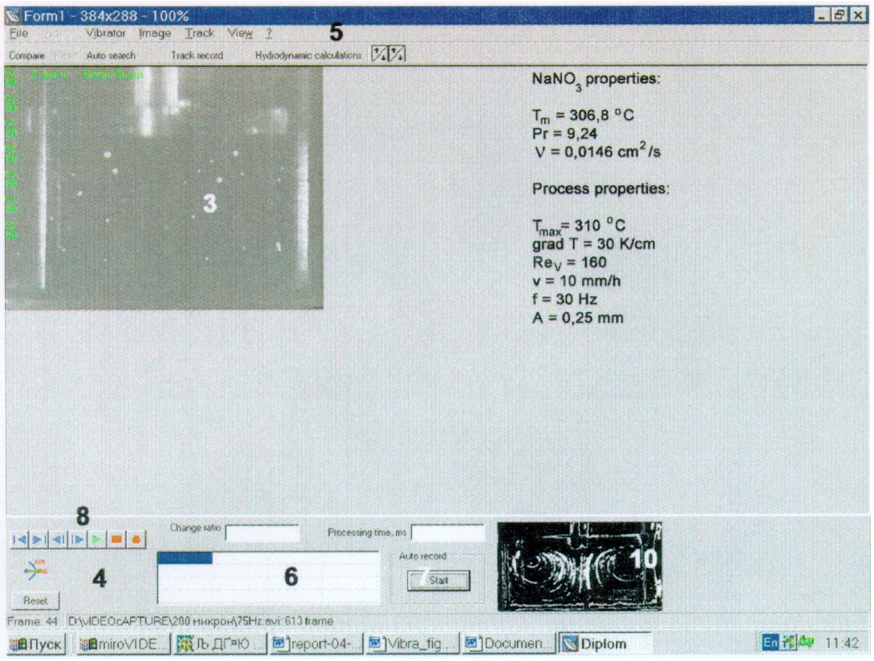

Figure 1. User interface of the program for melt structure visualization

tained within an accuracy 0.3 K. Translations were conducted by two step-servo motors working in the speed range from 0 up to 34 mm/h. The electromagnetic transducer controlled by PC sound card generated the low-frequency (LF) oscillations. The oscillating body was a quartz disk (d = 11 mm) submerged into the melt and located above the interface. An analog videocamcorder was used for observation of melt flows and interface shape. The signal from the camcorder was transferred to the PC. If necessary, videocapture and digitization was used for the most characteristic moments of the growth process. To visualize the flows, the tracers made from aluminum particles by the size 20-40 microns were added into the melt.

Special software was designed and used for processing the video images. Figure 1 shows the user interface of the program. A sequence of video frames (real-time AVI-format movie playing in area 3 on Figure 1) were captured and digitized. Then the frames were placed one over another to form a map of the flows (area 10 on Figure1). The combined image was filtered to remove steady objects like the heating spiral, splotches, non-moving particles, etc. The map demonstrates the stop image of the flows similar to the streaks seen in a long exposure photograph. Then the flow velocities in different parts of the melt were calculated producing a dynamic image of the flows. Using the data obtained and physical properties of the melt, the hydrodynamic properties of the melt were calculated.

The solid-liquid interface curvature for the $NaNO_3$ growth system was measured as a function of vibrational parameters. (Figure 2) Under constant vibrational frequency, two dependences of interface curvature vs. frequency amplitude could be observed. At first an amplitude increase results in a weak increase of interface convexity. Further amplitude increase results in an extreme change of the interface curvature and it becomes strongly concave. For every frequency, an amplitude exists at which the interface is flat. An amplitude which corresponds to the flat interface at 50 Hz was used with a growth rate of 10 mm/h and proceeded to grow the same quality of single crystals as for non-vibration controlled growth at 2 mm/h. Crystal quality was determined through measurements of light scattering and dislocation densities.

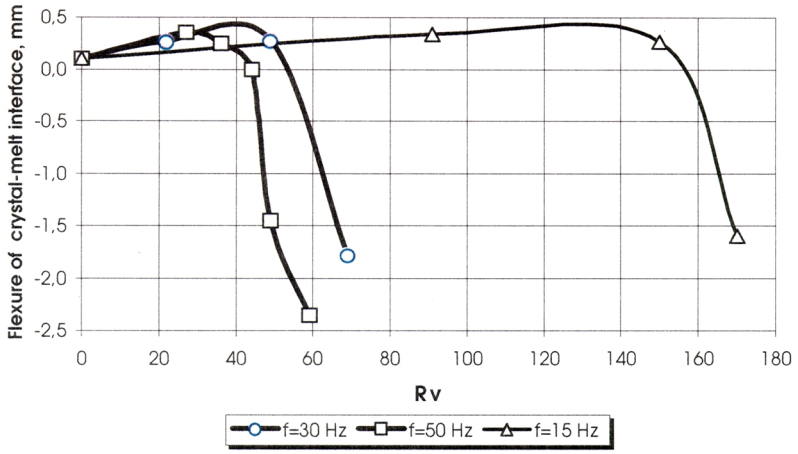

Figure 2. Curvature of crystal-melt interface vs. vibrational Reynolds coefficient

Another part of the $NaNO_3$ study dealt with doped crystals and the effect of fluid flow on segregation coefficients. Silver ions in the form of $AgNO_3$ were used as the dopant and were measured using electron microprobe analysis (Camebax, France). The Ag concentration profiles for different growth conditions can be found in Figure 3 (radial profile) and 4 (axial profile). It should be noted that in this set of experimental conditions the non-vibrating crystal was grown at 2 mm/h because single crystals would not grow at higher rate without vibrations.

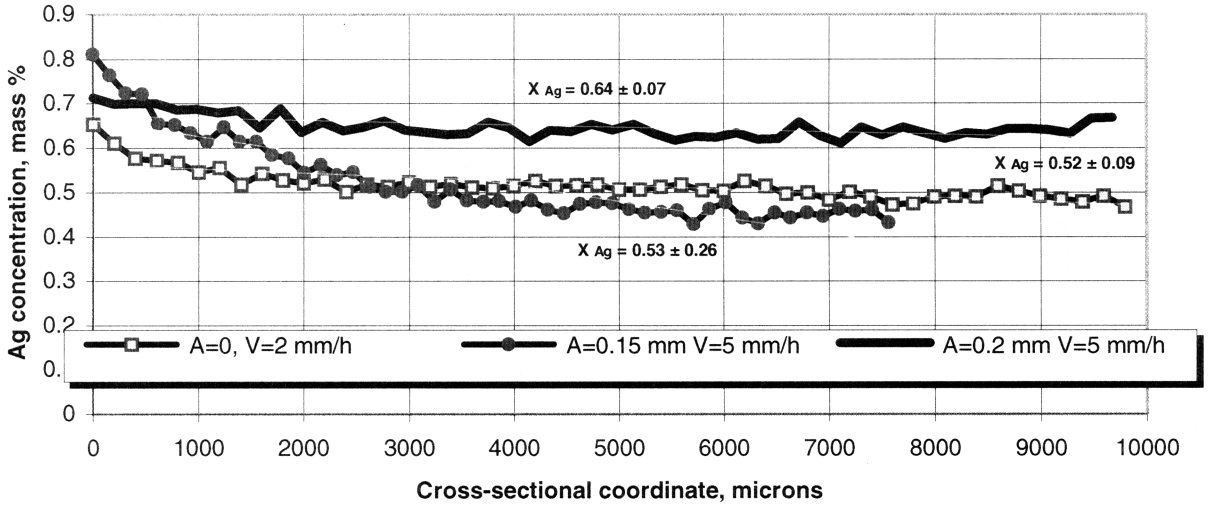

Figure 3. Radial Ag profile of doped $NaNO_3$ crystals

The "vibrational" crystal grown with a flat interface (A = 0.2 mm) shows a Ag deviation from the average value of ~11 rel% in the radial profile (Figure 3). The traditionally grown crystal (no vibrations) shows a deviation of ~17rel%, and the worst results (~49rel%) were seen for the "vibrational" crystal with a convex interface (0.15 mm). The sharp drop in dopant concentrations along the axial direction (Figure 4) for the "vibrational" crystals corresponds to the position where vibrations were initiated.

The effective distribution coefficient of Ag dopant came nearer to the equilibrium value with increasing vibrational amplitude and decreasing interface curvature. For "non-vibrating" crystal, $K^{Ag}_{eff} = 0.88$, while for the crystal grown at F=50 Hz, A=0.2mm (flat interface), $K^{Ag}_{eff} = 0.78$. The equilibrium distribution coefficient ($K^{Ag}_{eq.}$) is equal to 0.76 according to T-x diagram of quasibinary system $NaNO_3$ - $AgNO_3$.

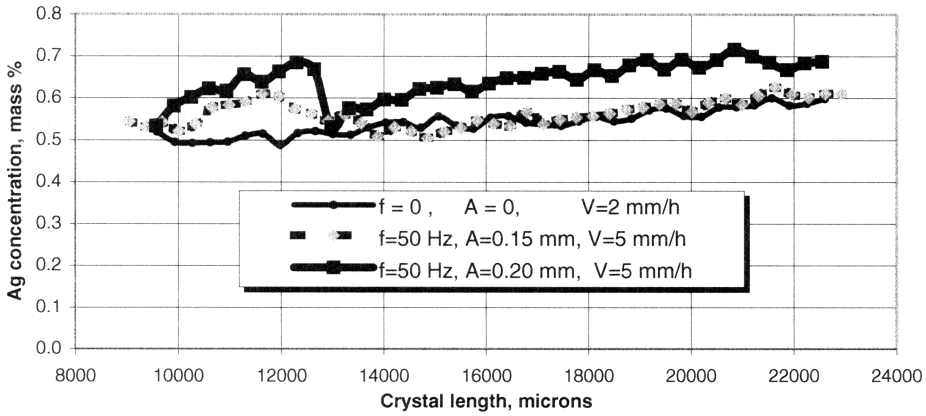

Figure 4. Axial Ag profile of doped $NaNO_3$ crystals

II. External Vibrations

The externally induced forced convection being studied at Stanford is applied through a technique called Coupled Vibrational Stirring or CVS. CVS is a mixing technique which uses orthogonally coupled transverse vibrations to move the crucible around an axis other than that of the crucible. This motion forms a surface wave in the melt which drives fluid flow. Flow has been observed to spiral slowly down the crucible wall and move up the center in a tight vortex.

The Stanford group has focused mainly on studying flow visualization and mixing behavior of the non-crystallizing water/glycerin system. The data obtained through such experiments will be used to determine the optimal operating conditions for actual crystal growth systems.

The first set of experiments conducted using the non-crystallizing system involved measurements including the mixing time and wave height as a function of the ampoule diameter, aspect ratio, viscosity of the fluid, and frequency of vibration. Flows were characterized by using either dyes injected at the bottom of the crucible, neutrally buoyant particles mixed into solution, or a combination of the two. Typical operating parameters of the flow modeling were: frequencies in the range of 0-10 Hz, amplitudes in the range of 0.7-2.0 mm, viscosities of 1, 5, 10, 15, and 20 cp, ampoule diameters of 1.6, 2.2, 3.2, 4.4, and 5.7 cm, and aspect ratios between 1-5.

The generation of a surface wave was found to be the driving force for all fluid flow in this system. Fluid flow was easily observed at frequencies as low as 1 Hz in systems with a free surface. In several experiments the surface wave was surpressed by using a piston-like clamp. The elimination of the surface wave caused no fluid motion to be observed regardless of vibrational frequency or amplitude. However, if a small air bubble was present under the clamped surface fluid flow was observed. In a free surface system, a typical surface wave would measure 1 cm from the surface's rest position if a 4.4 cm diameter ampoule for a 1cp solution at a frequency of 4 Hz and a vibrational amplitude of 1.5 mm.

Particle velocities were measured using streak photography. The length of a streak on an exposure produced by a moving particle coupled with the shutter time of the camera were used to estimate the velocities. As an example of data obtained, a 3.2 cm diameter ampoule filled to an aspect ratio of 3 with a 1 cp solution had an estimated particle velocity of 6.2 cm/s when the vibrations were set to a 5.8 Hz frequency and a 1.5 mm amplitude.

A couple of important issues uncovered during this series of experiments included the collapse of the driving wave above certain resonance frequencies, and the possibility that the induced flows would not circulate through the entire melt if the parameters were not adjusted properly.

The surface wave was found to collapse with increasing frequency in the large diameter ampoules (3.2, 4.4, and 5.7 cm). The frequency at which the wave vanished depended not only on the ampoule diameter, but on the previous history of the fluid. If a frequency was placed on a fluid that was initially at rest (dead start) then the wave would collapse at a much lower frequency than that of a fluid in which the frequency was slowly ramped up. A typical result can be seen in figure 5.

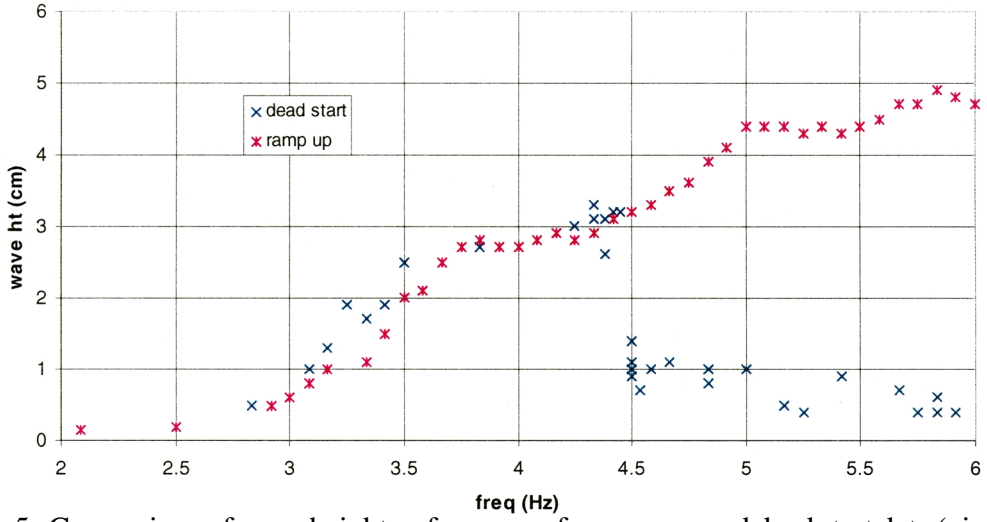

Figure 5. Comparison of wave height vs frequency for ramp up and dead start data (visc=1cp, dia=6.98cm, ht=12.6cm, amp=0.15cm, AR=1.80)

The depth of fluid motion below the driving surface wave becomes an important factor in determining what frequency of vibration should be set for the real growth systems. If the flows do not reach the growth interface, then the vibrational mixing will be ineffective. The depth of motion was measured by observing the motion of neutrally buoyant particles and was found to be strongly dependent on frequency and viscosity. (Figure 6)

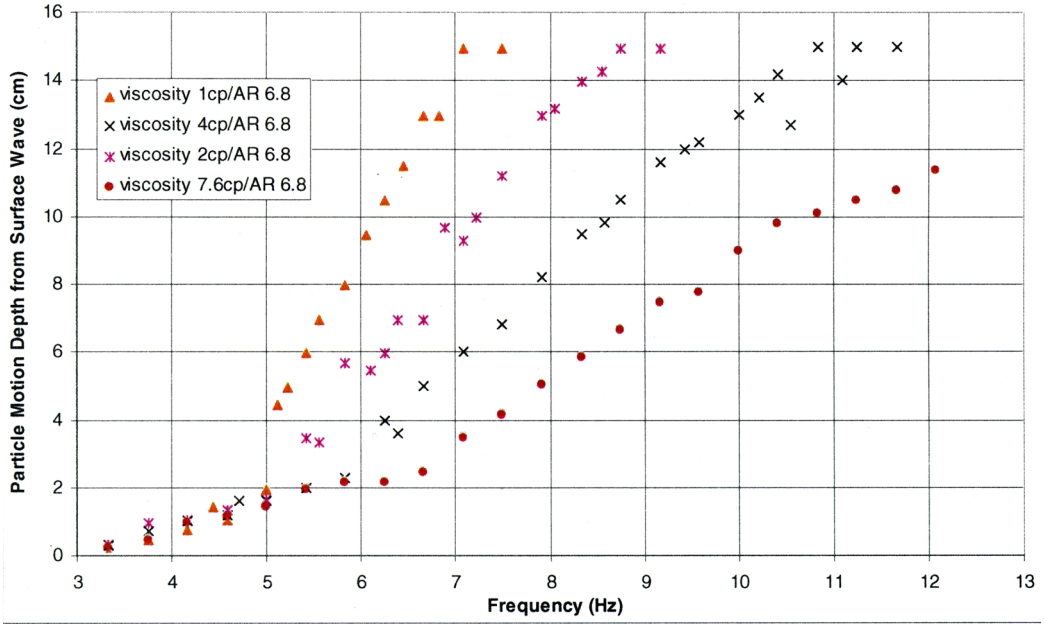

Figure 6. Motion depth versus frequency of vibration (dia=2.2cm, amp=0.15cm)

III. Summary

The growth of $NaNO_3$ crystals under the influence of internal vibrations has been performed in Bridgman systems. Interface shape and curvature was measured along with flows in the melts using videocapture techniques. Doping experiments were performed with $AgNO_3$. As a result of the doping experiment, it was determined that variation of the vibration parameters can control the effective distribution coefficient and control the concentration distribution along the crystal.

Flows generated in the CVS system have been studied using water glycerin solutions. Wave height, mixing time, particle velocities, etc. were measured as a function of ampoule diameter, vibrational amplitude and frequency, fluid viscosity, and aspect ratio.

A low temperature growth furnace incorporating CVS has been designed, fabricated, and tested. Several $NaNO_3$ crystals of the same quality of the GPI group have been grown. Experiments to parallel the particle velocity and dopant experiments carried out in Moscow will be performed in the near future with this external vibration growth system.

THE ROLE OF CONVECTION AND GROWTH COMPETITION IN PHASE SELECTION IN MICROGRAVITY: CONTROLLED CONVECTION IN THE CONTAINERLESS PROCESSING OF STEEL ALLOYS

D.M. Matson[1]*, W. Löser[2], J.R. Rogers[3], and M.C. Flemings[1]

[1] Department of Materials Science and Engineering, Massachusetts Institute of Technology
[2] Institute of Solid State and Materials Research, Dresden Germany
[3] NASA Marshall Space Flight Center

ABSTRACT

Containerless processing using electromagnetic levitation (EML) is a powerful technique in the investigation of reactive molten metal systems. On ground, the power required to overcome the weight of the sample is sufficient to cause significant heating and induce substantial melt convection. In microgravity, the heating and positioning fields may be decoupled and the field strength may be varied to achieve the desired level of convection within the limits set by the geometry of the levitation coil and the sample size.

From high-speed digital images of the double recalescence behavior of Fe-Cr-Ni alloys in ground-based testing and in reduced-gravity aboard the NASA KC-135 parabolic aircraft, we have shown that phase selection can be predicted based on a growth competition model. An important parameter in this model is the delay time between primary nucleation and subsequent nucleation of the stable solid within the liquid/metastable solid array. This delay time is a strong function of composition and a weak function of the undercooling of the melt below the metastable liquidus. From the results obtained during the first Microgravity Sciences Laboratory (MSL-1) mission, we also know that convection may significantly influence the delay time, especially at low undercoolings. Currently, it is unclear what mechanism controls the formation of a heterogeneous site that allows nucleation of the austenitic phase on the pre-existing ferrite skeleton. By examining the behavior of the delay time under different convective conditions, we hypothesize that we can differentiate between several of these mechanisms to gain an understanding of how to control microstructural evolution. We will anchor these predictions by examining samples quenched at different times following primary recalescence in microgravity.

A second important parameter in the growth competition model is the identification of the growth rate of the stable phase into the semi-solid array that formed during primary recalescence. Current dendritic growth theory is inadequate in predicting solidification behavior under these conditions as metallographic analyses show that stable phase growth proceeds along the interface between the metastable solid and residual liquid. Since growth velocity is independent of the initial undercooling relative to the metastable liquidus, we hypothesize that purely thermal effects can be separated from other important growth model parameters by careful selection of the liquid composition in a ternary system.

I. Background

Ground-based research on levitation melted samples and on rapidly solidified atomized droplets has shown the strong influence of processing conditions on the selection between bcc-ferrite (delta) and the fcc-austenite (gamma) in Fe-Ni and Fe-Cr-Ni alloys. Early work on metastable formation in Fe-Ni alloys was accomplished by investigation of the solidification behavior of fine powders including the work of Cech [1], Kelly and VanderSande [2], and Thoma and Perepezko [3]. The metastable phase formation was identified using a metallographic technique. With the addition of chromium, the ternary alloy must be investigated using a containerless technique to limit the potential for contamination of the melt through interaction with crucible walls [4].

During double recalescence, the temperature of the sample rises during ferrite growth followed by a second thermal rise as the austenite grows into the liquid-solid mixture that formed during primary recalescence. In separate investigations, Koseki and Flemings [4], Loser [5], Moir [6] and Volkmann [7-9] found that in order to obtain double recalescence events, a composition specific critical undercooling must be achieved. When velocity was plotted as a function of undercooling, this critical undercooling also corresponds to a point where a sudden decrease in the array growth velocity is observed. The value of the critical undercooling was seen to be depressed significantly below the extension of the metastable solidus in the equilibrium phase diagram. This phenomenon was attributed to a nucleation controlled phase selection mechanism [6-9] best described using the Diffuse Interface Theory (DIT) [10] with an optimized nuclei composition.

Experimental evidence contrary to these results was obtained using a high-speed digital imaging technique. The enhanced spatial resolution of the technique allows for analysis of small (less than 180 microns square) discrete surface elements across the entire visual surface of the droplet instead of an average signal obtained over a wide target region (4 mm diameter)[11]. Images taken at acquisition speeds of up to 40,500 frames per second both in ground-based testing [12] and using a pyrometry technique in microgravity [13-15] showed that the occurrence of the double recalescence phenomena extends to temperatures slightly above the metastable extension of the solidus of the ferrite equilibrium phase diagram. A mosaic of images taken during growth from a trigger is shown in Figure 1(a) and a series taken from spontaneous heterogeneous nucleation from a site on the surface of the levitated melt in Figure 1(b). Both image series were obtained in ground-based experiments.

Using a containerless processing quench technique, Koseki [16] showed metallographic evidence indicating that growth of the austenitic phase proceeds around the existing metastable ferrite dendritic array and along the solid-liquid interface which formed during primary recalescence. Investigators from MIT found that in ground-based EML experiments three possible secondary nucleation initiation site categories exist. The nucleation of the second phase occurs either at the same site as primary nucleation, located at some unrelated point within the semi-solid, or along the edges of the growing metastable array [13]. The delay time between recalescence events is a weak function of undercooling, as shown in Figure 2, and appears to be significantly longer in microgravity experiments conducted as part of the MLS-1 mission.

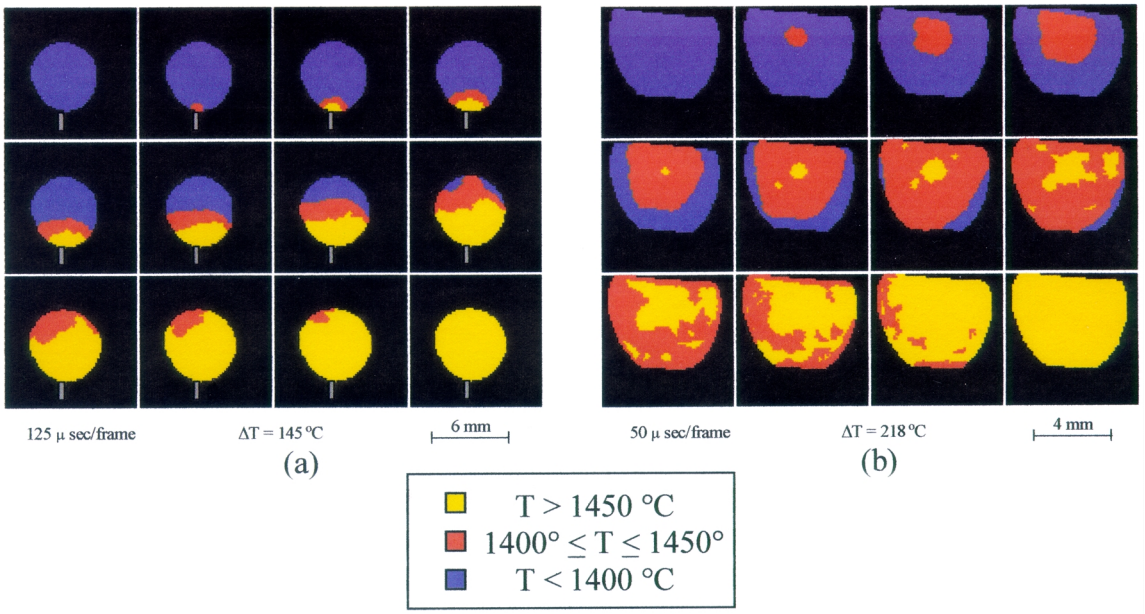

Figure 1. A series of digital images of double recalescence in Fe-12Cr-16Ni (wt%)
(a) Growth from a nucleation stimulation trigger for velocity measurement.
(b) Spontaneous primary nucleation with subsequent multiple secondary nucleation.

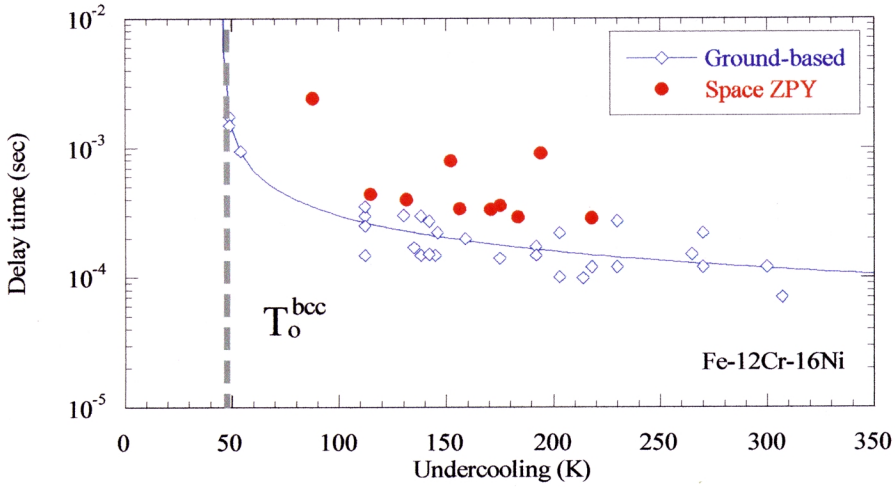

Figure 2. Delay time as a function of undercooling for Fe-12Cr-16Ni alloy

The growth rate as a function of phase and undercooling is shown in Figure 3 for a Fe-12wt%Cr-16 wt% Ni alloy[15]. Note that the metastable phase grows at a lower rate than the stable phase at all temperatures where simultaneous growth occurs and that the stable phase growth rate is independent of the primary phase undercooling. This occurs because the temperature is relatively constant following primary solidification and subsequent growth must always occur into an array at the same temperature (and thus the undercooling and the driving force are constant and a strong function of alloy composition).

If the results of previous investigators are re-interpreted in light of the growth competition model [13], the existence of an apparent depression of the critical undercooling may instead represent an indirect measurement of the critical velocity. This velocity is defined as the crossing point where the growth rate of the metastable phase into the liquid equals the rate of growth of the stable phase into the semi-solid under conditions of competitive growth [15]. This hypothesis must be checked by comparison to direct

measurements obtained using a video analysis technique. A comparison between direct and indirect measurement techniques is shown in Figure 4 where the growth rate of the stable phase into the array is plotted as a function of a measure of the thermal driving force, $\Delta T_o = T_o^{fcc} - T_o^{bcc}$, the difference in critical temperatures. Many other investigations into verification of experimental and theoretical approaches to quantifying the influence of convection on dendritic growth and microstructural development have recently been published [17-20] and have application to our proposed microgravity experiments.

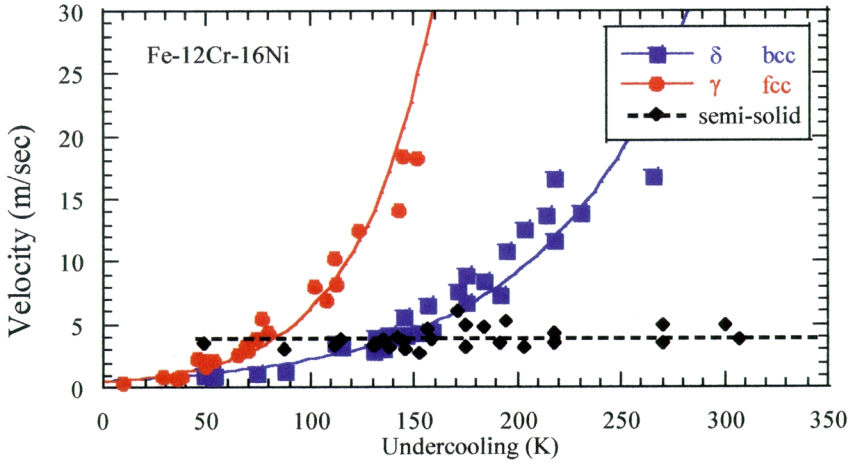

Figure 3. Growth rate as a function of phase and undercooling as measured in ground-based electromagnetic levitation testing.

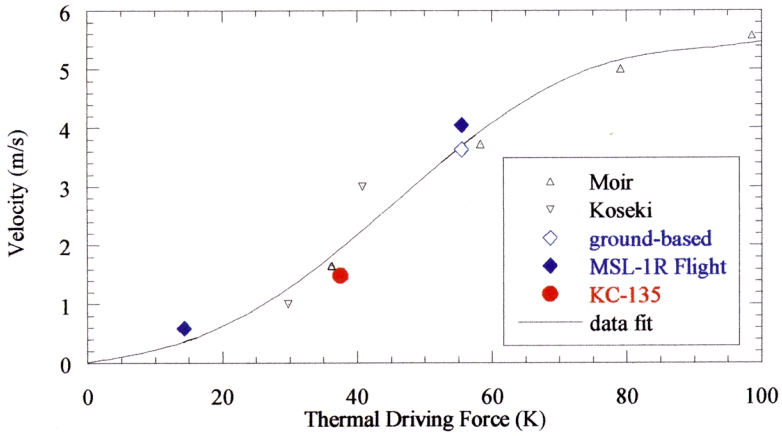

Figure 4. Growth rate of stable phase into the metastable liquid-solid array formed during primary recalescence as a function of the difference between critical temperatures $\Delta T = T^{fcc} - T_o^{bcc}$; Circles represent direct measurements using a video technique, other symbols represent an indirect extrapolation from the data on critical undercoolings measured by other investigators.

II. Controlled Convection in Microgravity

In order to investigate the role of convection on the mechanism for stable phase nucleation within the metastable array, the flow condition must be known and constant. As part of the MSL-1 mission, Hyers and Trapaga [21] developed a method to quantify magnetically driven flows by evaluating the magnetic forces along the surface of the droplet and then using a commercial finite element fluid dynamics program to predict flow conditions as a function of coil geometry. In ground-based testing, an electromagnetically levitated 7-millimeter diameter droplet with no rotation or translation is predicted to develop a maximum steady-state flow on the order of 50 cm/sec at the equilibrium melting temperature. Since heating and levitation are accomplished with the same coil, we cannot decrease the field strength without catastrophically terminating the test.

Maximum fluid flows within the droplet may be reduced to a lower limit on the order of 5 cm/sec using the TEMPUS facility in microgravity at a nominal positioning control setting of 4 volts as shown in Figure 5 [22]. Below this limit, sample stability within the coils is potentially compromised. If it is desirable to increase the recirculation flows within the droplet, both the quadrupole positioning coil and the dipole heating coil may be independently adjusted to provide the desired increase in convection.

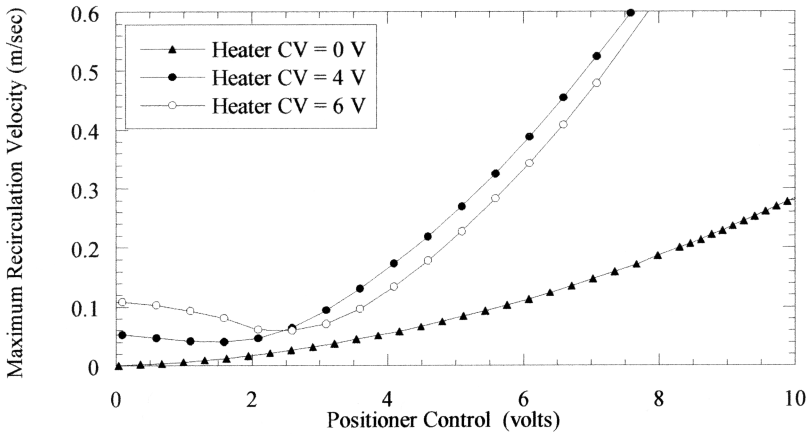

Figure 5. Convection conditions achievable in a 7mm droplet of molten steel using the TEMPUS STS-94 coil system [22] (Hyers, 1999)

The calculation of the flow conditions within the droplet can only be accomplished for quiescent conditions and thus the high-quality microgravity environment available in Spacelab or the International Space Station (ISS) is required so that we can select and control convection within the sample. Since we are interested in nucleation phenomena which show an appreciable change in behavior within the range $5 < v < 50$ cm/sec, we can use TEMPUS to investigate the flow conditions between these two extremes. By careful selection of operating parameters and sample size, we will be able to control the cooling rate and the Reynolds number independently and decoupled each from the recirculation velocity. It is also desirable to conduct experiments where no electromagnetically induced flows exist. These experiments are currently under preliminary investigation using the NASA/MSFC Electrostatic Levitator (ESL).

Thus, the purpose of this program is to develop a better understanding of how nucleation and growth of the austenitic phase affect phase selection in ternary steel alloys following formation of a primary metastable dendritic array. Two major objectives will be addressed. We will :

(1) investigate the mechanism for stable phase nucleation by defining how convection influences the delay time in microgravity over a broad range of fluid flow conditions;

(2) examine the relationship between alloy composition and the growth rate of the stable phase within the metastable array following primary recalescence.

The value of this research is that the results have application to welding operations in microgravity and the design of industrial spray forming and strip casting operations for a commercially important class of structural materials. In addition, this research addresses fundamental issues relating to rapid solidification behavior, metastable phase selection and analysis of the processes governing microstructural evolution.

REFERENCES

1. R.E. Cech, Trans. AIME, 206, 1956, p. 585
2. T.F. Kelly and J.B. VanderSande, Int. J. Rapid Solidification, 3, 1987, p. 51

3. D.J. Thoma and J.H. Perepezko, Met. Trans., 23A, 1992, p. 1347
4. T. Koseki and M.C. Flemings, Met. Trans., 26A, 1995, p. 2991
5. W. Löser, T. Volkmann, and D.M. Herlach, Mater. Sci. Engr., A178, 1994, p. 163
6. S. Moir and D.M. Herlach, Acta Metall., 45(7), 1997, p. 2827
7. T. Volkmann, W. Löser, and D.M. Herlach, Int. J. Thermo., 17(5), 1996, p. 1217
8. T. Volkmann, W. Löser, and D.M. Herlach, Met. Trans., 28A, 1997, p. 453
9. T. Volkmann, W. Löser, and D.M. Herlach, Met. Trans., 28A, 1997, p. 461
10. L. Granasy, J. Non-Cryst. Solids, v. 162, 1993, p. 301
11. D.M. Matson, in Solidification 1998, S.P. Marsh et al, eds., TMS Warrendale PA, 1998, p. 233
12. D.M. Matson, A. Shokuhfar, J.W. Lum, and M.C. Flemings, in Solidification Science and Processing, I. Ohnaka and D.M. Stefanescu, eds.,TMS Warrendale PA, 1996, pp. 19-26
13. M. C. Flemings and D. M. Matson, in NASA/CP 1998-208868, M. B. Robinson, ed., NASA-MSFC AL, 1998, p. 281
14. D. M. Matson, Wolfgang Löser, and M. C. Flemings, in Solidification 1999, W. H. Hofmeister, J. R. Rogers, N. B. Singh, S. P. Marsh, and P. W. Voorhees, eds., TMS Warrendale PA, 1999, p. 99
15. D. M. Matson, in Materials in Space – Science, Technology, and Exploration, A. F. Hepp, J. M. Prahl, T. G. Keith, S. G. Bailey, and J. R. Fowler, eds., TMS Warrendale PA, 1999, p. 227
16. T. Koseki and M.C. Flemings, Met. Trans., 27A, 1996, p. 3226
17. Y. Miyata and T. Umemura, Mat. Sci. Forum, 215-216, 1996, 209
18. M.D Dupouy, D. Camel, and J.J. Favier, J. of Crystal Growth, 154, 1995, 370
19. P. Bouissou, B. Perrin, and P. Tabeling, Phys. Rev. A, 40, 1989, 509
20. R.F. Sekerka, S.R. Coriell, and G.B. McFadden, J. of Crystal Growth, 154, 1995, 370
21. G. Trapaga, D. M. Matson, R. W. Hyers, and M. C. Flemings, in Proceedings of the Julian Szekely Memorial Symposium on Materials Processing, H. Y. Sohn, J. W. Evans, and D. Apelian, eds., TMS Warrendale PA, 1997, p. 453
22. R.W. Hyers, personal communication, 1999

THERMAL STABILITY AND CONDUCTIVITY PROPERTIES OF MONOMERIC AND POLYMERIC OXANORBORNENES

Miroslaw Trznadel, Jason T. Manka, Piotr Kaszynski, and Andrienne C. Friedli *

Department of Chemistry, Middle Tennessee State University
Murfreesboro, Tennessee 37132
afriedli@mtsu.edu

INTRODUCTION

The goal of our research is to develop a new class of anionic polymer electrolytes for use in organic solid state batteries. The resulting devices are expected to be lightweight and non-toxic with applications in energy storage and power supply for the human exploration and development of space, as well as for communications devices on Earth. Critical characteristics for successful ion-conducting materials are high cation mobility, electrochemical / chemical stability, and high charge density. Here we report progress toward organic solid state electrolyte systems which are designed to satisfy these requirements.

The key feature of our electrolyte design is the identity of the charged groups, which affect the mobility of counterions. We have selected the diffuse spherical *closo*-boron clusters, $B_{10}H_{10}^{2-}$ and $B_{12}H_{12}^{2-}$, which contain boron and hydrogen, and the monocarbaborate cluster, $CB_{11}H_{12}^{1-}$. These clusters carry delocalized charges and may be derivatized or be covalently attached into a polymeric structure. The spherical electrostatic field generated by the clusters can stabilize nearby positive charges, potentially promoting high mobility of cations (especially Li^+) in polymer solutions. Another important structural feature of materials appropriate for polyelectrolytes appears to be flexibility and a high oxygen-to-carbon atom ratio.[1] In compliance with this empirical requirement, we have incorporated oligoethylene glycol chains, which promote conductivity of ions, into all of our polymers. To simplify polymer purification and processing, the polymers or copolymers should be soluble, have a reproducible distribution of molecular weights, and the polymerization conditions should be tolerant of charged groups. Given these restrictions, we chose to begin our investigation with polymers formed by ring opening metathesis polymerization (ROMP) of 7-oxabicyclo[2.2.1]-hept-2-ene derivatives (oxanorbornenes) such as **1a**. ROMP may be carried out in either aqueous or organic solutions, and results in low polydispersity, stable polymers with semi-rigid backbone structures.[2] Established ROMP methodology (Scheme 1) to form **poly(1a)** and derivatives, as well as emerging understanding of the resulting polymer microstructure, make this backbone structure ideal for our purposes. Appropriate derivatives of **poly(1)** have the potential to be soluble, non-toxic, stable polymers with a variety of charged groups, and are expected to be good candidates for battery materials.

Two approaches to boron-containing solid-state electrolytes were pursued using the general strategy described above. A *polymer electrolyte* design relies on the doping of lithium salts of boron clusters into homopolymer **poly(1b)**. The *polyelectrolyte* design incorporates boron clusters into the **poly(1c)** polymer through covalent bonding.

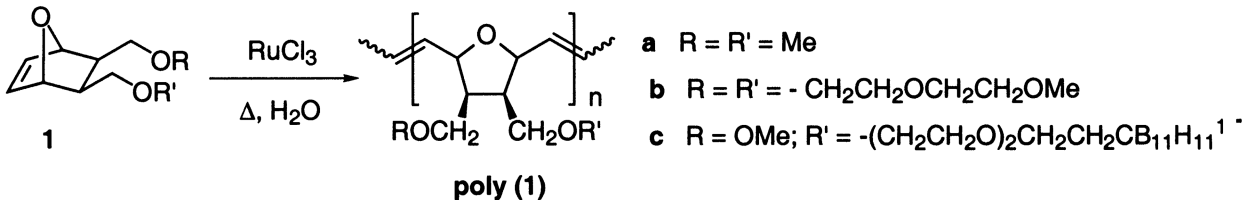

Scheme 1. ROMP synthesis of poly(1) and several derivatives of interest.

I. Monomer Synthesis and Properties

Scheme 2 summarizes the synthesis of monomers used in the study. To access the symmetrical diether **1b**, classical Diels-Alder adduct **2** was reduced to **3**, then reacted under Williamson ether synthesis conditions with $MeOCH_2CH_2OCH_2CH_2OTs$. Also beginning with **3**, literature procedures[3] were used to obtain **4**, and subsequently, unsymmetrical ether **5**.[4] Treatment of **5** with NaI in acetone, followed by $Li_2CB_{11}H_{11}$ resulted in the carbaundecaborate derivative (**1c**). Both the symmetrical and unsymmetrical ether syntheses were complicated by incomplete formation of diethers, even under conditions of elevated temperature, and thus required difficult separations. Of the monomers studied, only **1b** and **3** were found to be significantly soluble in water. These and most other monomers are hygroscopic, and some contained water or THF even after rigorous purification.

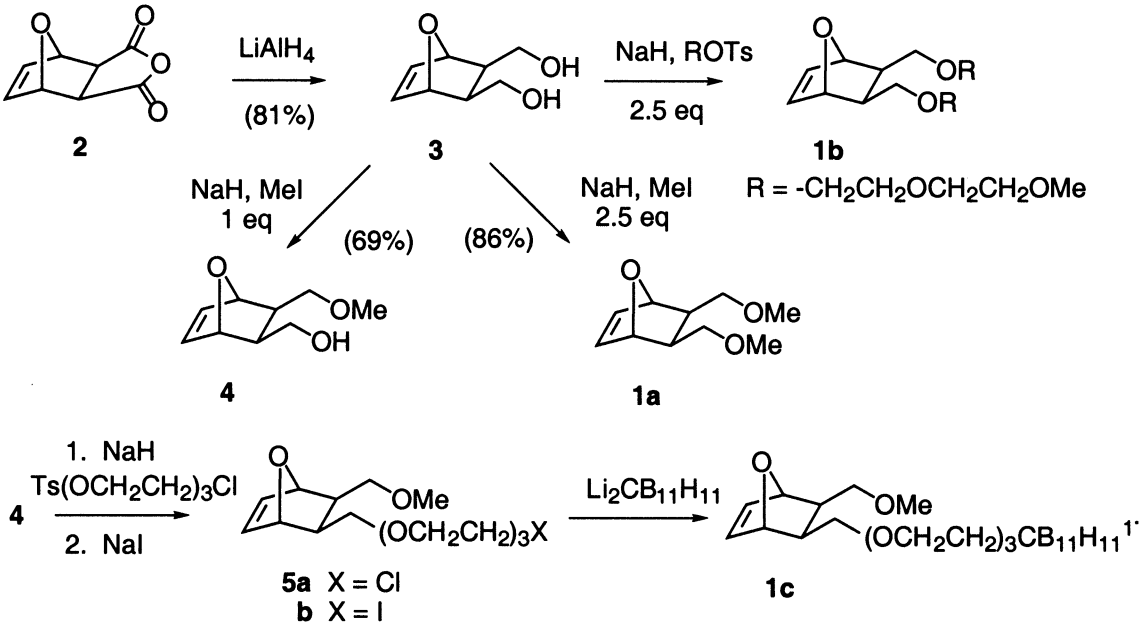

Scheme 2. Synthesis of neutral and charged monomers.

En route to the monomers described in Scheme 1, four 5,6-disubstituted-7-oxabicyclo[2.2.1]hept-2-enes were synthesized on a large (³0.1 mol) scale. In order to assess the thermal stability of the monomers for purification by distillation, the retro Diels-Alder (rDA) decomposition of selected derivatives (Scheme 3) was studied experimentally and computationally.[5]

Thermal gravimetric analysis of **1a** and **2-4** demonstrated rapid and complete weight losses at onset temperatures ranging from 147 °C to 217 °C (Figure 1). The kinetics of the rDA of **1a** were measured using integration of selected ^1H NMR peaks belonging to the starting material and one product. The first order rate constants were $k = 1.91\text{-}14.2 \times 10^{-5}\ s^{-1}$ when measured at four temperatures between

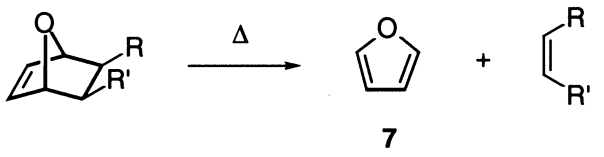

7

2 R, R' = -COOCO-
1a R = R' = CH_2OMe
6 R, R' = -CH_2OCH_2-
11 R = R' = CH_2CH_2

8 R, R' = -COOCO-
9 R = R' = CH_2OMe
10 R, R' = -CH_2OCH_2-
12 R, R' = H

Scheme 3. Reagents and products of the retro Diels-Alder reaction of **1a, 2, 6**, and **11**.

124 and 150 °C (Figure 2). These were used to calculate the Arrhenius activation parameters E_a (34.5 ± 0.5 kcal/mol) and ln A (1.77 ± 0.03) x 10^4).

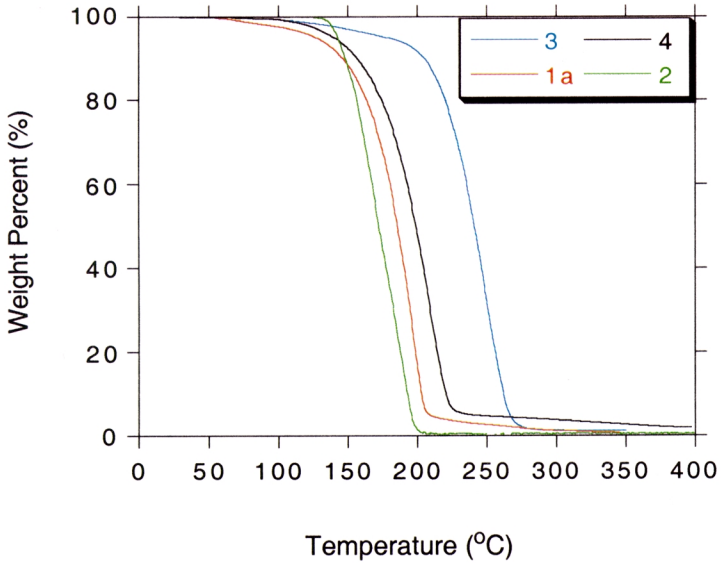

Figure 1. Thermal Gravimetric Analysis of **1a** and **2-4**.

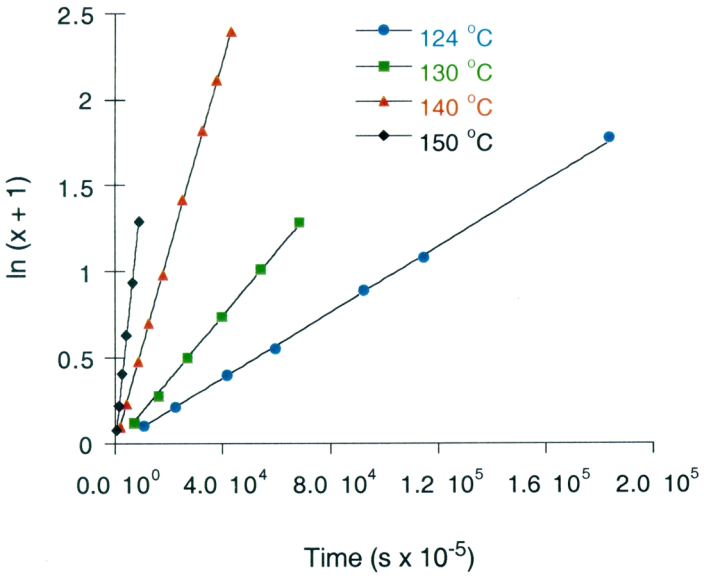

Figure 2. Kinetic data for decomposition of **1a** at four temperatures.

Modeling of the activation parameters found for 1a with density functional theory (DFT) calculations for similar compounds gave close quantitative correlations for $\Delta H^{\ddagger}$, $\Delta G^{\ddagger}$, and $\Delta S^{\ddagger}$ as shown in Table 1.

Table 1. Experimental and Calculated (B3LYP/6-31G*) Thermochemical Parameters for the Retro Diels-Alder Reaction.[a]

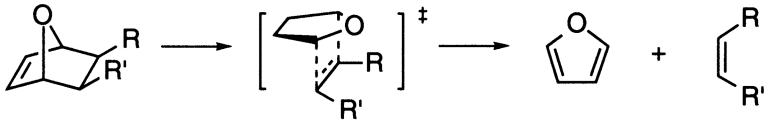

Compound	R, R'	Reaction overall			Activation parameters		
		ΔH	ΔS	ΔG	$\Delta H^{\ddagger}$	$\Delta S^{\ddagger}$	$\Delta G^{\ddagger}$
2-exo	-COOCO-	+3.44	+45.9	-10.2	22.4 (25.0)[b]	2.95 (0.17)[b]	21.6
6-anti	$-CH_2OCH_2-$	+3.07	+48.2	-11.3	31.8 (34.5)[c]	4.11 (5.0)[c]	30.5
11	H	+5.3 (-15.2)[d]	+43.5 (36.7)[d]	-7.6 (-6.7)[d]	31.2	3.1	30.3

[a] ΔG and ΔH are in units of kcal/mol; ΔS is in units of eu. The temperature for the gas-phase calculated values is 298 K. Experimental data are in parentheses. [b] Reference 6. [c] Diether **1a**. [d] Data quoted in Vogel, P.; Cossy, J.; Plumet, J.; Arjona, O. *Tetrahedron* 1999, *55*, 13521-13642.

The observed activation energy was significantly larger (by 9.5 kcal/mol) than that previously measured[6] and calculated[7] for **2**. This energy difference, illustrated in Figure 3, is attributed to the lower LUMO energy of maleic anhydride (**8**) as compared to **10**. All the reactions examined were entropy driven.

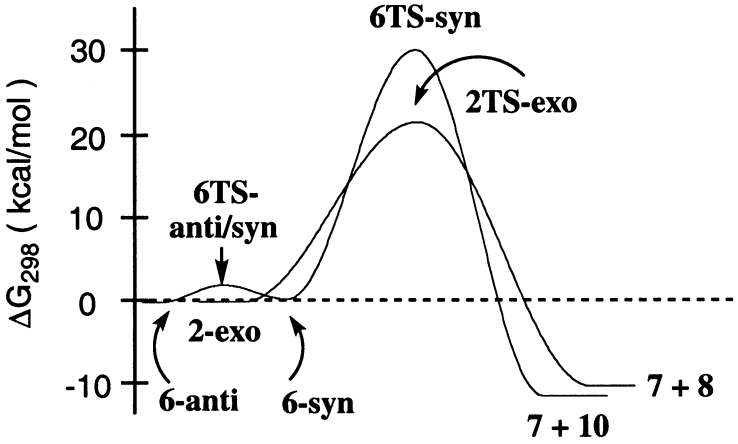

Figure 3. B3LYP/6-31G* Gibbs free energy change calculated for the retro Diels-Alder reaction coordinate for **2** and **6**.

II. Polymer Synthesis and Properties

Homopolymerizations (of **1a, 1b, 1c**, and other monomers) and copolymerizations (of **1a** or **1b** with charged monomers or other neutral monomers) were carried out in deoxygenated water solutions containing $RuCl_3$ catalyst (Scheme 1). The resulting polymers had soluble fractions, and poorly soluble fractions with a tendency to swell in polar organic solvents. **Poly(1b)** is unusual in that it is soluble in common organic solvents of medium and high polarity, facilitating the casting of films from THF solutions. The adhesive and mechanical properties of these films appear to be favorable for device applications and will be studied in the future.

Monomers such as **1a** that were sparingly soluble in water produced a significant amount of poorly soluble polymer of higher molecular weight (M_n = 2.6-37 x 10^5) and narrower polydispersity[5] than water-soluble **1b**. Polymer thermal properties included T_d onsets between 264 °C and 467 °C. Among the high molecular weight polymers and copolymers of **poly(1a)**, a polymer with a high T_g (192 °C), another with a T_m (195 °C), and one with a T_c (34 °C) were observed. Extraction of **poly(1b)** with organic solvents resulted in three broad polymeric fractions. Each was rubbery, but had no discernible phase transitions in the range of 30 °C to 300 °C. For polymers mixed with hygroscopic lithium salts, Differential Scanning Calorimetry showed an endotherm at ~150 °C, but this disappeared when the samples were dried in a vacuum oven.

III. Conductivity Measurements

Preliminary measurements using the four-point probe technique on 10-40 μm films of **poly(1b)** as solid solutions with alkali metal salts of boron clusters ($LiClO_4$, $Li_2B_{12}H_{12}$, $Li_2B_{10}H_{10}$, $Na_2B_{10}H_{10}$, $Na_2B_{12}H_{12}$) resulted in increases in conductivity when compared to pure polymer. Conductivity in **poly(1b)** increased up to two orders of magnitude for the salts tested when polymer and salt were combined in the ratio of one equivalent of Li for every 8 oxygens within the polymer. However, neither the expected[8] linear dependence of conductivity on temperature, nor a clear dependence on concentration were observed for **poly(1a), poly(1b)** or poly(ethylene oxide) mixtures with salts.

IV. Conclusions and Future Work

The second phase of research has begun with the measurement of film conductivities of **poly(1b)** mixed with lithium salts of boron clusters. The increases in conductivity for solid solutions of boron clusters in **poly(1)** are smaller than expected and are not directly comparable to literature measurements. Future work will include impedance measurements on solid solutions of **poly(1b)** over broad frequency and temperature ranges for a variety of concentrations of salts. These results will be compared to measurements on **poly(1c)** and poly(ethylene oxide) with standard lithium salts such as $LiClO_4$ for reference.

V. Acknowledgments

Financial support for the early development of cationic and neutral polyelectrolytes was provided by the Petroleum Research Fund (PRF #30202-GB7) and Middle Tennessee State University.

REFERENCES

1. Gray, F. *Solid Polymer Electrolytes*; VCH: New York, 1991.
2. Novak, B. M. Ph.D. Dissertation, California Institute of Technology, 1989; Novak, B. M.;Grubbs, R. H. *J. Am. Chem. Soc.* 1988, *110*, 7542-7543; *ibid*.pp. 960-961.
3. Lu, S.-Y.; Armass, J. M.; Majid, N.; Glennon, D.; Byerley, A.; Heatley, F.; Quayle, P.; Booth, C.; Yeates, S. G.; Padget, J. C. *Macromol. Chem. Phys.* 1994, *195*, 1273-1288.
4. Zheng, M. D.A. Dissertation, Middle Tennessee State University, 1997.
5. Manka, J. T.; Douglass, A. D.; Kaszynski, P.; Friedli, A. C., *J. Org. Chem.,* accepted.
6. Dewar, M. J. S.; Pierini, A. B. *J. Am. Chem. Soc.* 1984, *106*, 203-208.
7. Calvo-Losada, S.; Suárez, D. *J. Am. Chem. Soc.* 2000, *122*, 390-391.
8. Meyer, W. H. *Adv. Mater.* 1998, *10*, 439-448.

GRAVITATIONAL EFFECTS ON DISTORTION IN SINTERING

Randall M. German and Ronald G. Iacocca

Center for Innovative Sintered Products
P/M Lab, 147 Research West
The Pennsylvania State University
University Park, PA 16802-6809

ABSTRACT

Liquid phase sintering (LPS) is used to fabricate high-performance, net-shape structures from powders. The powders are shaped into an oversized structure that densifies to a target size. When a liquid forms during sintering, it generates a capillary stress that combines with rapid atomic motion to densify the structure. Models for LPS treat the pores between the powders as permeable balloons in the microstructure that progressively fill by atomic diffusion. Density differences between the solid, liquid, and pore phases result in phase separation resulting in different compositions and properties between the component top and bottom. Along with phase separation, gravity also causes shape distortion, which denies the benefit of net-shape processing. To avoid these problems, industry restricts the use of LPS to compositions with high solid contents. Consequently, the property ranges attainable via LPS are constrained by gravitational effects. If these problems could be solved, then many useful materials and devices would be fabricated net-shape by LPS. Examples opportunities are seen in high thermal conductivity heat sinks for computers, tougher cutting tools for machining, high precision automotive transmission gears, and more corrosion and wear resistant molds for plastic shaping.

I. Background

Among the liquid phase sintering compositions, tungsten heavy alloys are recognized as the model system. These are typically W-Ni-Cu or W-Ni-Fe alloys. For our studies, these heavy alloys are beneficial because of the large density difference between liquid and solid phases that exacerbates gravity effects in small samples. On Earth, tungsten heavy alloys sinter to full density in about 30 min after liquid formation, but the amount of liquid cannot exceed roughly 25 vol.% to avoid distortion and solid-liquid separation. At lower liquid contents, the solid skeleton reduces distortion, but densification becomes difficult because of this same rigidity. Thus, because of gravity effects, LPS is only successful over a limited range of compositions.

Microgravity LPS evidences very different behavior, with incomplete densification and more distortion. The lack of pore buoyancy and a lower solid skeleton rigidity (no gravity-induced grain contacts) allows for pore coarsening, giving less densification and lower dimensional precision. It is this pore stability that is a critical difference between 1g and μg LPS conditions. Theory fails to predict a gravity effect. Thus, an improved understanding of gravity-porosity

effects on microstructure and macrostructure are needed as related to densification and distortion. Accordingly, experiments are planned for a range of compositions and initial pore structures. These experiments will use powder compacts with intentional variations in pore size, porosity, solid content, dihedral angle, and isothermal hold time, allowing observation on microstructure evolution, strength, viscosity, density, and distortion. From the experiments we will extract the gravity-porosity relations with respect to microstructure, rheology, densification, and distortion.

II. Research Concepts

Findings from this research will quantify the gravity-porosity effects on system rheology during liquid phase sintering, and will isolate the role of grain contacts and pores on densification and distortion. These data will enable creation of models to predict composition, microstructure, or processing effects on performance (density) and precision. A rheological response model has been constructed for the gravity effect in solid-liquid-pore structures. It requires experimental data to answer questions on key interactions. The time dependence of distortion and densification depend on component strength and viscosity, which are determined by the microstructure evolution. These parameters will be determined using axial video imaging and captured in samples retrieved after selected sintering times in parallel microgravity and ground-based experiments. In turn the knowledge from these studies will expand the range of compositions and devices that can be produced by this cost-effective, net-shaping technology.

To achieve the objectives, microgravity sintering is required with composition changes to adjust the solid:liquid ratio (via changing the initial tungsten content from 60 to 97 wt.% W). Matrix composition changes (Ni-Fe, Ni-Cu, or Cu-Ni alloys) will be used to vary the dihedral angle and solid solubility in the liquid. Variations in porosity and pore size will be induced by use of a fugitive polymer added to the powder in compaction and extracted in a hydrogen-vacuum presintering treatment. The high strength after presintering will ensure survival of launch and handling. Porosity levels of 30 or 70% (range possible by compaction) and pore sizes of 7 or 60 μm (smaller and larger than 12-15 μm solid grains) will be created by changing the amount and size of the added polymer. Test compacts will be cylinders about 12 mm in diameter and 12 mm in height. They will be heated at a target of 10°C/min and initially cooled at 3°C/min. One sample will be visualized using remote imaging, while the other samples will be obscured, but will undergo the same thermal cycle. Isothermal sintering holds from 1 min to 120 min will be performed at 1050, 1300, 1400, or 1500°C under vacuum in both ground and microgravity conditions.

Sintering runs will be performed in both gravity conditions. Acceleration records are desired during the microgravity cycles. Video imaging will provide close time resolution on sintering events, allowing clarification of factors such as the location of first melt formation, densification kinetics, distortion onset, pore closure, and distortion kinetics. Post-sintering analysis will focus on density, dimensions, weight, pore size distribution, and microstructure, including gradients in the sintered compacts.

Findings from this research will be used to improve modeling of LPS by including gravity-porosity effects with attention to two roles from gravity. One is related to grain structure connectivity as it impacts on system rigidity (strength and viscosity). The second is related to porosity effects on viscosity during sintering. A time dependent rheological model for densification and

distortion has been formulated that includes gravity effects in the contiguity and connectivity (solid-solid connections in the microstructure) and solid-liquid-pore interactions. This model lacks verification, yet provides an important conceptual base for analyzing the results.

Already, new insight on densification and distortion is possible using newly developed *in situ* video imaging. The results to date using 1g experiments show densification and distortion are sequential events. Distortion is inhibited until the structure has nearly densified. Consequently, shape loss occurs after most of the pores are filled with liquid. One implication for improved dimensional control is to under-sinter the component, giving up on performance.

Microgravity and ground-based measurements on 88 wt.% W heavy alloys both showed distortion increases over time. When extrapolated to zero time, there is still substantial distortion associated with liquid formation. The time dependent distortion has been modeled using viscous flow concepts, but with guesses on the viscosity and strength. When sintered under μg conditions, high liquid content alloys exhibit distortion, usually more than observed on Earth. This distortion is large in the first minute, but continues during sintering. Experimental results show near zero strength during densification that allows weak surface tractions to induce distortion. Based on observations with an alloy of 88 wt.% W, the strength is estimated from the distortion profiles as approximately 0.4 kPa. Thus, a new rheological model is emerging that treats strength evolution and viscosity as time-dependent events that link to the microstructure. In turn, porosity affects both parameters and since pores are subjected to buoyancy effects on Earth, microgravity experiments are needed to isolate pore structure effects on densification and distortion, with fundamental links to the strength and viscosity.

Confirmation of the strength loss on liquid formation is evident by the distortion of samples previously liquid phase sintered to full density. Upon reheating in μg the compact reshaped toward a sphere from its original cylinder shape. The sintered structure consisted of solid-solid bonds, yet grain boundary penetration by newly formed liquid resulted in a loss of strength. Earth-based experiments with a variety of alloys correlated grain connectivity after sintering with shape retention. Distortion depends on the microstructure weakness during liquid penetration of grain boundaries in low dihedral angle and high liquid content compositions. If solid skeletal bond growth is slow when compared with densification, then distortion occurs as the pores close. Neck growth rates are near 0.5 μm/s [60]. Bond growth forms a rigid structure, but often after distortion. Alternatively, if solid bond growth is fast when compared with densification, then shape retention is expected with slower densification. Several experiments have been used to define the microgravity conditions and the critical experiments needed with respect to alloy composition, sintering time, and peak temperature, allowing calculation of strength, connectivity, and contiguity roles with respect to distortion. So far the finite element based rheological model has proven accurate for the 1g cases, but the role of porosity and pore size is missing in the treatment of μg LPS.

REFERENCES

1. R. M. German, Y. Liu and A. Griffo, "Gravitational Effects on Grain Coarsening During Liquid Phase Sintering," *Metallurgical and Materials Transactions*, 1997, vol. 28A, pp. 215-221.
2. A. Upadhyaya and R. M. German, "Control of Distortion during Liquid Phase Sintering," *Plansee Proceedings*, vol. 2, Fourteenth International Plansee Seminar, Plansee AG, Reutte, Austria, 1997, pp. 68-85.

3. R. G. Iacocca, P. Downs, and R. M. German, "Three Dimensional Microstructures of Sintered Materials," *Advances in Powder Metallurgy and Particulate Materials - 1997*, Metal Powder Industries Federation, Princeton, NJ, 1997, pp. 16.13-16.21.
4. R. Ganesan, A. Griffo, and R. M. German, "Finite Element Modeling of Distortion during Liquid Phase Sintering," *Metallurgical and Materials Transactions*, 1998, vol. 29A, pp. 659-664.
5. A. Upadhyaya and R. M. German, "Densification and Dilation of Sintered W-Cu Alloys," *International Journal of Powder Metallurgy*, 1998, vol. 34, no. 2, pp. 43-55.
6. R. M. German, "New Powder Shaping Concepts and Their Applications in Refractory Metals and Hard Materials," *Tungsten Refractory Metals and Alloys*, A. Bose and R. J. Dowding (eds.), Metal Powder Industries Federation, Princeton, NJ, 1998, pp. 1-9.
7. J. L. Johnson, A. Upadhyaya, and R. M. German, "Microstructural Effects on Distortion and Solid-Liquid Segregation during Liquid Phase Sintering under Microgravity Conditions," *Metallurgical and Materials Transactions*, 1998, vol. 29B, pp. 857-866.
8. A. Upadhyaya and R. M. German, "Shape Distortion in Liquid-Phase-Sintered Tungsten Heavy Alloys," *Metallurgical and Materials Transactions*, 1998, vol. 29A, pp. 2631-2638.
9. R. M. German and E. A. Olevsky, "Grain Growth Dependence on the Solid-Liquid Ratio in Liquid Phase Sintering," *Proceedings 1998 Powder Metallurgy World Congress*, vol. 2, European Powder Metallurgy Association, Shrewsbury, UK, 1998, pp. 357-362.
10. A. Upadhyaya and R. M. German, "Effect of Gravity on Microstructure and Macrostructure of Tungsten Heavy Alloys," *Advances in Powder Metallurgy and Particulate Materials - 1998*, vol. 1, Metal Powder Industries Federation, Princeton, NJ, 1998, pp. 3.11-3.17.
11. R. M. German and E. A. Olevsky, "Microstructure Coarsening During Liquid Phase Sintering," *Advances in Powder Metallurgy and Particulate Materials - 1998*, vol. 3, Metal Powder Industries Federation, Princeton, NJ, 1998, pp. 23.3-12.17.
12. A. Upadhyaya, A. Lal, K. Sivaraman, R. M. German, "In Situ Imaging of High Temperature Sintering," *Advances in Powder Metallurgy and Particulate Materials - 1998*, vol. 3, Metal Powder Industries Federation, Princeton, NJ, 1998, pp. 12.75-12.84.
13. E. A. Olevsky and R. M. German, "Gravity-Induced Dimensional Nonuniformity Under Sintering," *Advances in Powder Metallurgy and Particulate Materials - 1998*, vol. 3, Metal Powder Industries Federation, Princeton, NJ, 1998, pp. 12.85-12.93.
14. J. Liu, A. Lal, and R. M. German, "Shape Distortion Induced by Gravity in Solid Phase Sintering," *Advances in Powder Metallurgy and Particulate Materials - 1998*, vol. 3, Metal Powder Industries Federation, Princeton, NJ, 1998, pp. 12.95-12.102.
15. Y. Liu, R. M. German, R. G. Iacocca, "Microstructure Quantification Procedures in Sintered Materials," *Advances in Powder Metallurgy and Particulate Materials - 1998*, vol. 3, Metal Powder Industries Federation, Princeton, NJ, 1998, pp. 13.3-13.17.
16. A. Lal, J. Liu, G. A. Shoales, and R. M. German, "Component Shape Retention in Supersolidus Liquid Phase Sintering of Prealloyed Powders," *Advances in Powder Metallurgy and Particulate Materials - 1998*, Metal Powder Industries Federation, Princeton, NJ, pp. 12.33-12.43.
17. A. Upadhyaya and R. M. German, "Role of Microstructure on Compact Shape Retention during Liquid Phase Sintering," *Powder Injection Molding Technology*, R. M. German, H. Wiesner, and R.G. Cornwall (eds.), Innovative Material Solution, State College, PA, 1998, pp. 241-258.
18. R. M. German and E. A. Olevsky, "Modeling Grain Growth Dependence on the Liquid Content in Liquid Phase Sintered Materials," *Metallurgical and Materials Transactions*, 1998, vol. 29A, pp. 3057-3067.
19. Y. Liu, R. M. German, and R. G. Iacocca, "Microstructure Quantification Procedures in Liquid-Phase Sintered Materials," *Acta Materialia*, 1999, vol. 47, pp. 915-926.

20. A. Upadhyaya, R. G. Iacocca, and R. M. German, "Gravitational Effects on Compact Shaping and Microstructure during Liquid-Phase Sintering," *Journal of Metals*, 1999, vol. 51, no. 4, pp. 37-40.
21. J. Liu and R. M. German, "Distance or Spacing Parameters in Agglomerated Monosized Spherical Particulate Systems," *Particle and Particulate Systems*, 1999, vol. 16, pp. 35-38.
22. J. Liu, Y. Liu, A. Lal, and R. M. German, "Shape Distortion Induced by Gravity in the Initial Stage of Solid Phase Sintering," *Scripta Materialia*, 1999, vol. 40, pp. 1221-1227.
23. A. Upadhyaya, B. Ozkal, and R. M. German, "Application of Interference Layering for Metallography of Sintered Alloys," *P/M Science and Technology Briefs*, 1999, vol. 1, no. 2, pp. 17-21.
24. J. Liu, A. Upadhyaya, and R. M. German, "Application of Percolation Theory in Predicting Shape Distortion During Liquid-Phase Sintering," *Metallurgical and Materials Transactions*, 1999, vol. 30A, pp. 2209-2220.
25. A. Tewari, A. M Gokhale, and R. M. German, "Effect of Gravity on Three-Dimensional Coordination Number Distribution in Liquid Phase Sintered Microstructures," *Acta Materialia*, 1999, vol. 47, pp. 3721-3734.
26. J. Liu and R. M. German, "Densification and Shape Distortion in Liquid Phase Sintering," *Metallurgical and Materials Transactions*, 1999, vol. 30A, pp. 3211-3217.
27. X. Xu, A Upadhyaya, R. M. German, R. G. German, "The Effect of Porosity on Distortion of Liquid Phase Sintered Tungsten Heavy Alloys," *International Journal of Refractory Metals and Hard Materials*, 1999, vol. 17, pp. 369-379.
28. E. A. Olevsky and R. M. German, "Gravity-Induced Dimensional Nonuniformity Under Sintering Taking into Consideration Grain Segregation ," *Advances in Powder Metallurgy and Particulate Materials - 1999*, vol. 1, Metal Powder Industries Federation, Princeton, NJ, 1999, pp. 3.107-3.114.
29. R. M. German, "Strength Loss and Distortion in Liquid Phase Sintering," *Advances in Powder Metallurgy and Particulate Materials - 1999*, vol. 1, Metal Powder Industries Federation, Princeton, NJ, 1999, pp. 3.139-3.151.
30. X. Xu, A. Upadhyaya, R. M. German, and R. G. Iacocca, "Porosity Effect on Distortion and Microstructural Evolution in Liquid Phase Sintering," *Advances in Powder Metallurgy and Particulate Materials - 1999*, vol. 1, Metal Powder Industries Federation, Princeton, NJ, 1999, pp. 3.153-3.162.
31. Y. Liu, J. Liu, and R. M. German, "Gravity as a Source of Inhomogeneities in Liquid Phase Sintering," *Advances in Powder Metallurgy and Particulate Materials - 1999*, vol. 1, Metal Powder Industries Federation, Princeton, NJ, 1999, pp. 3.177-3.188.
32. Y. Liu and R. M. German, "A Computer Imaging Technique to Observe Three Dimensional Microstructure in Opaque Sintered Materials," *Advances in Powder Metallurgy and Particulate Materials - 1999*, vol. 3, Metal Powder Industries Federation, Princeton, NJ, 1999, pp. 11.61-11.75.
33. J. Liu, A. Lal, and R. M. German, "Densification and Shape Retention in Supersolidus Liquid Phase Sintering," *Acta Materialia*, 1999, vol. 47, pp. 4615-4626.
34. A. Lal, T. J. Weaver, and R. M. German, "Direct Observation of P/M Parts During Sintering," *Advances in Powder Metallurgy and Particulate Materials - 1999*, vol. 1, Metal Powder Industries Federation, Princeton, NJ, 1999, pp. 3.73-3.80.
35. E. A. Olevsky and R. M. German, "Effect of Gravity on Dimensional Change During Sintering - I. Shrinkage Anisotropy," *Acta Materialia*, 2000, vol. 48, pp. 1153-1166.
36. E. A. Olevsky, R. M. German, and A. Upadhyaya, "Effect of Gravity on Dimensional Change During Sintering - II. Shape Distortion," *Acta Materialia*, 2000, vol. 48, pp. 1167-1180.

USE OF COMPUTED TOMOGRAPHY FOR CHARACTERIZING MATERIALS GROWN TERRESTRIALLY AND IN MICROGRAVITY

Donald C. Gillies[1]* and H.P. Engel[2]

[1] NASA, Marshall Space Flight Center
[2]Wyle Labs, Kennedy Space Center

The purpose behind this work is to provide NASA Principal Investigators (PIs) rapid information, non-destructively, about their samples. This information will be in the form of density values throughout the samples, especially within slices 1 mm high. With correct interpretation and good calibration, these values will enable the PI to obtain macro chemical compositional analysis for his/her samples. Alternatively, the technique will provide information about the porosity level and its distribution within the sample. Experience gained with a NASA Microgravity Research Division-sponsored Advanced Technology Development (ATD) project on this topic has brought the technique to a level of maturity at which it has become a viable characterization tool for many of the Materials Science PIs, but with equipment that could never be supported within their own facilities. The existing computed tomography (CT) facility at NASA's Kennedy Space Center (KSC) is ideally situated to furnish information rapidly and conveniently to PIs, particularly immediately before and after flight missions.

CT scanning is based on the ability to process millions of attenuation values resulting from the interaction of a high energy photon beam with a sample. By changing the direction of the incident beam, the algorithms can furnish the values for linear absorption coefficients in two dimensional space within the slice being irradiated. CT arrangements, including the one at KSC, typically use banks of many detectors, and both translate and rotate the sample. The technique has several important implications for use by the MRD PIs. First, the system is capable of examining several square feet of sample within the narrow height selected. This means that many samples, and of very different types, can be examined simultaneously. Secondly, as the absorption values can be obtained in two dimensions, it becomes possible to obtain values while the samples are still encased. During the ATD project, satisfactory results were obtained for metallic samples while they were still within their protective Sample Ampoule Cartridge Assemblies (SACAs). Thus the technique is capable of measuring density within not only a fused silica ampoule, but also while within the encasing inconel cartridge. With the exception of edge effects, the work is quantitative. The CT system at KSC is being used with a cobalt-60 source, as compared with the normal x-ray sources employed. To our knowledge this feature is unique world wide, and has the advantage of producing a monochromatic beam with no preferential absorption as happens with the x-ray generated beams. So-called beam hardening effects are thus eliminated. Experience has shown that continuous operation of the CT system with translation of 1mm between analytical slices can analyze fully a 72 mm length of sample within 24 hours. Complete data reduction and interpretation may take longer, but the information afforded is available very quickly, and before the PI's samples leave KSC. The implications of this in the Space Station era are tremendous. With the need for transport of many samples to and from ISS, rapid analysis is essential to provide the required information to the PI for any succeeding campaign on ISS. If it is necessary for the samples to be returned to the PI's facility prior to reliable scientific information being obtained, there are obvious

* Corresponding Author

implications to the planning of the experiments. CT will enable the PI to have an early assessment of the quality of all of the samples, and with the analysis being done at KSC as soon samples are released from the shuttle, there is the possibility of rapidly obtaining important scientific data.

The proposed work here will be predominantly a service to current and future PIs and as such "will lead to the definition or enhance the understanding of existing or potential flight experiments in material science." The ATD project referred to above was only funded for one year, and at less than a five-man month effort, and there is a pressing need for further interpretive work on several fields. First, there is a need to determine the optimal technique for interpreting the histograms and statistics of the CT data. This is particularly true for compounds, be they solid solutions or two phase mixtures. In conjunction with this is the need for more standards, of high purity and particularly of metallographically well characterized structures. Examination of existing PI samples will be important preparation for the future ISS campaigns. Secondly, there is a need to establish and implement the instrument requirements for improving both spatial and statistical resolution. Since the installation of the KSC CT instrument, there have been many improvements in CT technology particularly in detector efficiency, size and resolution. The specifications are now being sought for the procurement of the next generation of CT instrument at KSC; it is essential that MRD has an input into these specifications. Finally, it should be noted that this project has implications to inject technology into the private sector. The ability to examine a product rapidly and non-destructively has obvious implications for industrial usage.

FOLLOW-ON RESEARCH ACTIVITIES FOR THE RENSSELAER ISOTHERMAL DENDRITIC GROWTH EXPERIMENT (RIDGE)

J.C. LaCombe *, M.B. Koss, A.O. Lupulescu, J.E. Frei, C. Giummarra, and M.E. Glicksman

Rensselaer Polytechnic Institute

The RIDGE effort continues the aegis of the earlier, NASA-sponsored, Isothermal Dendritic Growth Experiment (IDGE) series of experiments through the continued analysis of microgravity data acquired during these earlier space flights. The preliminary observations presented here demonstrate that there are significant differences between SCN and the more anisotropic PVA dendrites. The side branch structure becomes amplified only further behind the tip, and the interface shape is generally wider (*i.e.* more hyperbolic than parabolic) in PVA than in SCN. These characteristics are seen to affect the process of heat transport. Additionally, the dendrites grown during the fourth United States Microgravity Payload (USMP-4) exhibit time-dependent growth characteristics and may not always have reached steady-state growth during the experiment.

I. Introduction and Background

The RIDGE effort furthers the basic objectives of the earlier, NASA-sponsored, Isothermal Dendritic Growth Experiment (IDGE) series of space flight experiments through the continued analysis of microgravity data acquired during these earlier experiments. The IDGE consisted of 180 experiments on dendritic growth in succinonitrile (SCN), flown in 1994 and 1996 on the USMP-2 and USMP-3 shuttle missions, respectively, and 116 experiments on pivalic acid (PVA), flown aboard USMP-4 in late 1997. The use of the microgravity environment permitted the acquisition of data that was largely free of the complicated influences on the heat transfer process that acceleration-driven natural convection creates. Discoveries were made during each space flight concerning the dendritic growth behavior of these pure model substances. The USMP-4, pivalic acid data set, still requires considerable amounts of analysis, and serves as a focal point of the RIDGE efforts.

The importance of the RIDGE studies is based in the fact that dendritic solidification is of considerable engineering interest. This interest is due to the role that dendrites play in forming many microstructures and the related material properties of these processed materials [1]. Additionally, dendritic growth serves as a model problem in the fields of pattern formation, non-equilibrium physics, and computational condensed matter and material physics.

Most theories of dendrite crystal formation consist of two components [2, 3]. The first of these concerns the transport of heat and solute from the solid-liquid interface into the melt. The second component involves the physics of interfacial stability, which when combined with transport theory, results in a full solution describing steady-state dendritic growth. Until recently, neither of these two aspects of the theory could be tested critically because of the effects of gravity-induced convection, which modifies the transport processes, and alters the growth kinetics. The Isothermal Dendritic Growth Experiment

* Corresponding author

(IDGE) addressed this lack of data over the past decade by conducting measurements of dendritic growth in low-Earth orbit, aboard three USMP shuttle missions.

As mentioned above, the USMP-2 and USMP-3 missions involved tests of the model material succinonitrile (SCN), whereas the USMP-4 mission used the material pivalic acid (PVA). Both of these materials are transparent organic materials that act as models of engineering materials in that they solidify dendritically and possess molecular fcc (PVA) and bcc (SCN) crystal structures. Additional important factors leading to their use was their low melting temperatures and optical transparency. A comprehensive description of the IDGE experiment setup and methodology, as well as the results of the USMP-2 flight, can be found in [4].

The present study (RIDGE) continues where the IDGE left off, with additional analysis of the microgravity-derived experimental data produced during the earlier space flights. The data presented here were produced using two data sources. The first of these is from 35mm film, which produces images of high spatial precision, but low temporal frequency. The second data source is electronic video, recorded at 30 frames per second, but at lower spatial resolution. The film data is particularly well suited for analysis of the steady-state characteristics of the growth process. The video data is more suited for analysis of some transient, or time-dependent features of the growth process. Presented here are three key preliminary results obtained so far.

II. Transient Characteristics of Dendritic Growth in PVA

Analysis Technique

The data consists of tip positions over time, shown in Figure 1. Dendrite tip locations were obtained from electronic images, using a sub-pixel interpolation scheme to enhance the spatial resolution beyond the raw measurement precision of ~22 microns (one pixel). After image processing, dendrite tip-position measurement precision is improved to ~2 microns (~ 1/10 pixel).

Results and Discussion

A representative microgravity growth cycle is shown in Figure 1 [5]. It represents approximately 100 seconds of tip-displacement data (as a function of time) from a typical growth. The initial transient behavior is thought to be indicative of the dendrite developing its own diffusion field, as it evolves from its initial nucleus. Later in the growth, the dendrite appears to be growing at nearly a constant rate, but closer inspection reveals that there is still a systematic deviation from steady-state growth [6], with a persisting, although decreasing, acceleration. The cause of the transient aspects of this process is not yet well understood. The persisting acceleration may simply be a continuation of the initial transient, or may be produced by the measured dendrite's growth away from competing crystals, which are more proximate early in the growth, while the dendrite is of comparable size to the initial nucleus.

The data later in the growth suggest that some long-range thermal influences might contribute to the slowly diminishing acceleration. It is possible that these dendrites were all grown within a "sufficiently small" growth chamber. This configuration has been shown by Pines, Chait, and Zlatkowski [7] to potentially cause a growing dendrite to accelerate as it approaches a wall at a fixed supercooled temperature. However, all the growths presented here have small thermal lengths compared to the distance between the dendrite tip and the chamber wall. Taking these considerations into account it is our

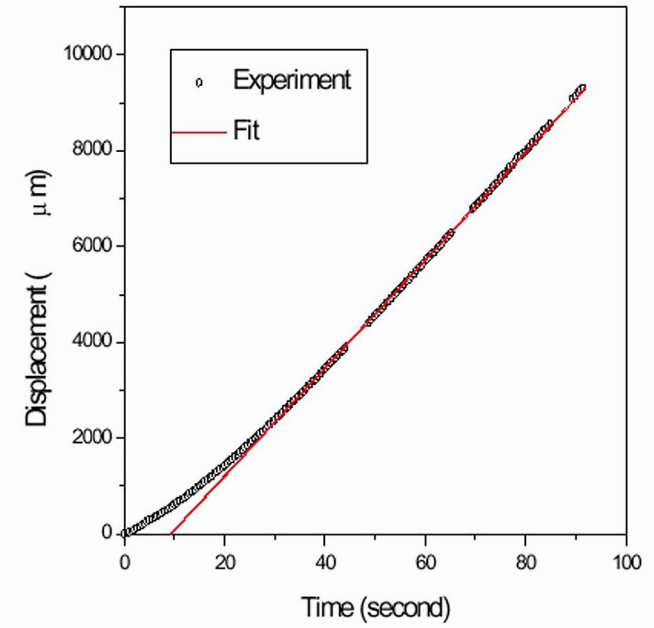

Figure 1. Tip displacement vs. time for a dendrite grown at 0.58 K supercooling. The linear regression was performed using data from the more steady-state portion of the growth (after~30 sec.)

present belief that this second-stage transient effect is also fundamental to isolated dendritic growth. Since dendrites are not truly parabolic bodies of revolution [8, 9], there is no compelling phenomenological reason that dendrites should grow strictly at a constant rate. A more complete analysis will be performed to explore this hypothesis further.

III. PVA Side-Branch Measurements

Analysis Technique

The 35 mm IDGE negatives were analyzed using a microscope-vernier system. The position and amplitude of the side-branches were measured with respect to the centerline of the dendrite with the origin at the dendrite tip (Figure 2). The first detectable side-branch is identified as the closest measurable branch to the tip. This point also defines the beginning of the uniformly spaced side branch region. Beyond this is the coarsening region, which begins with the first side-branch with an amplitude smaller than its tip-side neighbor. The distance between side-branches was measured tip-to-tip parallel to the axial centerline. All measurements were corrected for magnification and stereographic projection.

Results and Discussion

The measurements presented here included only dendrites with isolated tips and which were orientated in such a way as to allow accurate measurement of the side-branches, *i.e.*, with the side-branches normal to the imaging plane. Brief summaries of the preliminary findings using this data are shown below.

Within the range of standard deviation, the normalized distance to the first detectable side-branch shows little variation with supercooling (Figure 3). This distance can be represented as

$$D_o = C_o R \qquad \text{Equation (1)}$$

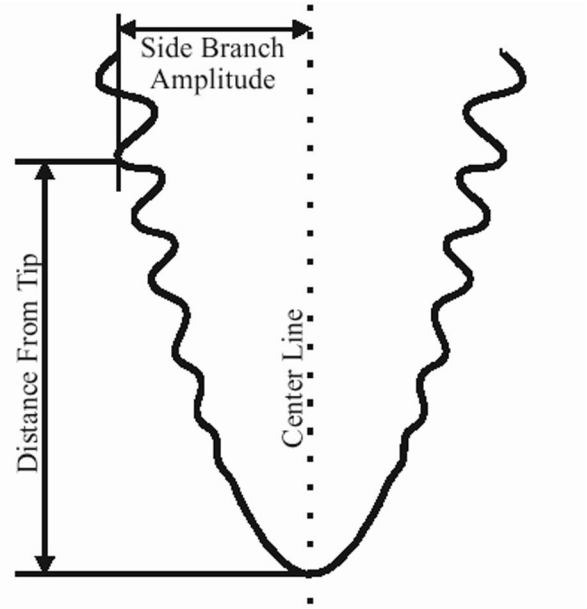

Figure 2. Side branch measurements. The origin was fixed at the tip of the dendrite.

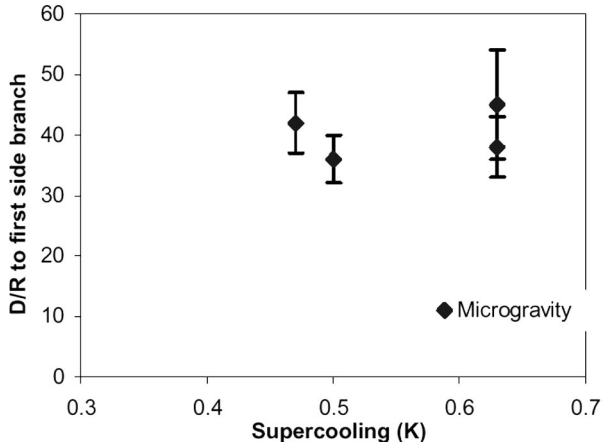

Figure 3. Distance to the first detectable side-branch scaled by the tip radius for various supercoolings.

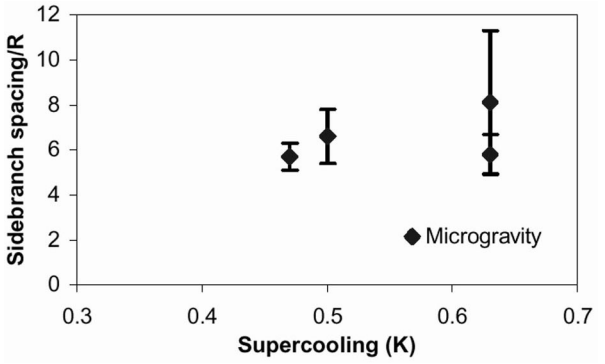

Figure 4. Average normalized side-branch spacing within a region extending 70 radii behind the tip.

where D_o is the distance to the first detectable side branch, R is the measured dendrite tip radius and C_o is the scaling constant. The preliminary data in Figure 3 indicates a scaling constant value of $C_{o(g=0)} = 41.0 \pm 4.6$ relating the position of the first detectable side-branch and the applied supercooling.

Within ~76 radii of the tip, where the side-branch spacing is uniform and unaffected by the coarsening process, there is no detectable variation of the normalized side-branch spacing with supercooling (Figure 4). The side branch spacing can be represented as

$$\lambda_u = C_u R \,, \qquad \text{Equation (2)}$$

where λ_u is the side-branch spacing within the uniform region, and C_u is the scaling constant, with a preliminary measured value of $C_{u(g=0)} = 6.6 \pm 1.1$ (g=0 indicates it was measured in low-Earth orbit).

To characterize the shape of the side-branch envelope, the position of the side-branch tips (distance from the tip) constituted the *x* coordinate, and the *y* coordinate was taken from the amplitude of the branches. These data were linearly regressed in the form,

$$x/R = \alpha(y/R)^{\beta} \,. \qquad \text{Equation (3)}$$

It is difficult at this stage of the analysis to determine if (and how) α and β scale with supercooling. If the α and β values are independent of supercooling, the preliminary regressed values of the fitting constants to Equation 3 are $\alpha_{(g=0)} = 2.81 \pm 1.04$ and $\beta_{(g=0)} = 1.21 \pm 0.16$.

Comparison with SCN

Previous work has been undertaken on the side-branch characteristics of succinonitrile under microgravity and terrestrial conditions [10]. For comparison, the preliminary results for PVA and the earlier reported SCN results (both obtained under microgravity conditions) are provided below in Table 1. Comparison of these data indicates that measurable differences clearly exist between PVA and SCN dendrite side-branching characteristics.

Table 1. Comparison of Side-branch Scaling Constants.

	$C_{o(g=0)}$	$\lambda_{u(g=0)}$	$\alpha_{(g=0)}$	$\beta_{(g=0)}$
Pivalic Acid	41.0±4.6	6.6±1.1	2.81±1.04	1.21±0.16
Succinonitrile	11.8±1.7	2.98±0.32	1.81±0.13	1.174±0.071

IV. Steady-State Growth Behavior

Analysis Technique

A test of steady-state theory requires simultaneous measurements of both the dendritic growth rate, *V*, and the radius of curvature at the tip of the dendrite, *R*. These measurements were obtained from the USMP-4 pivalic acid dendrites by using the 35 mm IDGE negatives described above with electronic image-capturing equipment as well as custom image-processing software [11].

Péclet Number Measurements

A zero-parameter test of the transport theory is provided by examination of the dependence of the Péclet number on the applied supercooling. The Péclet number, $Pe=VR/2\alpha$, is shown in Figure 5 as a function of the dimensionless supercooling, $\Delta = \Delta T/(L/c_p)$, where ΔT is the dimensional supercooling, *L* is the heat of fusion, and c_p is the specific heat.

Figure 5 includes the experimental data points as well as transport theory predictions for a range of interface shapes [12]. The paraboloidal interface shape (the Ivantsov model), is plotted as the solid blue line, and is clearly not in agreement with the pivalic acid experimental measurements. The other theory lines represent a range of varying interface shapes extending from the paraboloid, through a set of wider hyperboloids. The parameter Q is used along with the radius of curvature at the tip, R, to describe the hyperboloid, ($Q = 0$ is a paraboloid). As Q becomes more negative, the hyperboloid becomes wider. The average value of Q measured thus far for PVA is $Q = -0.0045 \pm 0.001$ (about 20 % of the available data has been examined). If the shape of pivalic acid dendrites behave similarly to succinonitrile dendrites, this value of Q is not expected be a strong function of either the supercooling or the convective environment [9]. When compared with the experimental data, it appears that the appropriate theory line for the observed interface shape agrees reasonably well with the experimentally measured Péclet numbers, particularly at the higher supercoolings.

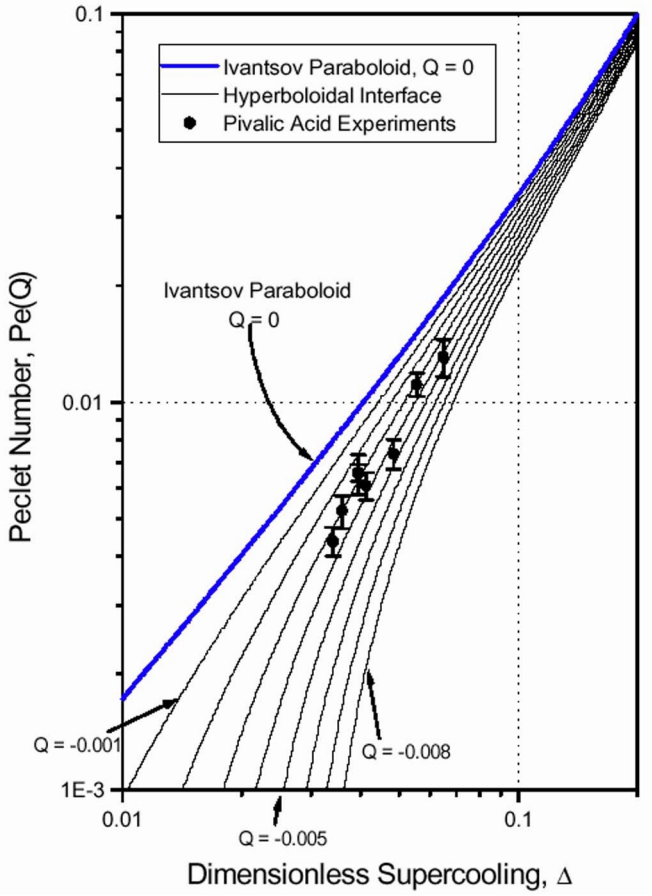

Figure 5. Péclet number as a function of supercooling. Experimental data are plotted as the solid black points.

V. Summary

Characterization of both the steady state and transient aspects of dendritic growth in succinonitrile and pivalic acid continues. These preliminary observations demonstrate that there are significant differences between SCN and the more anisotropic PVA dendrites. The side branch structure becomes amplified further behind the tip, and the interface shape is generally wider in PVA than in SCN. These characteristics affect the transport process, and additional work is under way to produce evidence that the selection process is also affected. Additionally, the dendrites grown during USMP-4 may not always have reached steady-state growth during the experiment.

VI. Acknowledgements

This work will be supported by the microgravity program at the NASA MSFC. Additional support since the conclusion of IDGE was provided by the Jon Todd Horton Chair in Metallurgical Engineering at Rensselaer Polytechnic Institute.

REFERENCES

1. Condensed Matter and Materials Physics: Basic Research for Tomorrow's Technology, 1999, National Academy Press: Washington, DC.
2. J.S. Langer, Rev. Mod. Phys., 52, 1, 1, (1980).
3. P. Pelcé, ed. *Dynamics of Curved Fronts,* 1988, Academic Press, Inc.: New York. 514.
4. M.B. Koss, L.A. Tennenhouse, J.C. LaCombe, M.E. Glicksman, and Winsa E.A., Metall. And Materials Trans. A, vol. 30A, 3177, (1999).
5. J.E. Frei, et al., AIAA 36th Aerospace Sciences Meeting and Exhibit: Reno, AIAA-2000-0941 (2000).
6. J.C. LaCombe, M.B. Koss, M.E. Glicksman, Phys. Rev. Lett. 83,2997-3000 (1999).
7. V. Pines, A. Chait, and M. Zlatkowski, J. Cryst. Growth 167, 383-386 (1996).
8. S.C. Huang and M.E. Glicksman, Acta Metall. 29, 701-715 (1981).
9. J.C. LaCombe, M.B. Koss, V.E. Fradkov, and M.E. Glicksman, Phys. Rev E. 52, 2778-2786 (1995).
10. D.P. Corrigan, M.B. Koss, J.C. LaCombe, K.D. de Jager, L.A. Tennenhouse and M.E. Glicksman, Phys. Rev. E 60, (1999)
11. A.O. Lupulescu, J.C. LaCombe, J.E. Frei, M.E. Glicksman, and M.B. Koss, EMMMS Proceedings, 2000 TMS Annual Meeting. (ASM, in press) (2000).
12. J.C. LaCombe, M.B. Koss, D.P. Corrigan, A.O. Lupulescu, L.A. Tennenhouse, and M.E. Glicksman, J. Cryst. Growth 206, 331 (1999).

THE ISOTHERMAL DENDRITIC GROWTH EXPERIMENT (IDGE)

M.E. Glicksman[1] , M.B. Koss[1] *, J.C. LaCombe[1], A.O. Lupulescu[1], J.E. Frei[1], C. Guimarra[1], and D.C. Malarik[2]

[1]Materials Science and Engineering Department, Rensselaer Polytechnic Institute
[2]Microgravity Science Division, NASA Glenn Research Center

Dendritic solidification is one of the simplest examples of pattern formation where a structureless melt evolves into a ramified crystalline microstructure; it is a common mode of solidification in many materials, but especially so in metals and alloys. There is considerable engineering interest in dendrites because of the role dendrites play in the determination of microstructure, and thereby in influencing the physical properties of cast metals and alloys. Dendritic solidification provides important examples of non-equilibrium physics, pattern formation dynamics, and models for computational condensed matter and material physics.

Current theories of dendritic growth generally couple diffusion effects in the melt with the physics introduced by the interface. Unfortunately, in terrestrial based experiments, convective effects in the melt alter the growth process in such a manner as to prevent definitive analysis of convective, diffusive or interfacial effects. Thus, the effective elimination of convection in the melt by operating experiments on orbit were required to produce high-fidelity data needed for achieving further progress. This simple fact comprised the scientific justification for the IDGE.

I. The Isothermal Dendritic Growth Experiment (IDGE)

The IDGE consisted of a series of three related, NASA-supported, microgravity experiments, all of which were flown aboard the space shuttle Columbia. These experimental microgravity missions were designed and operated to grow and record dendritic solidification events in a well-characterized test system in the virtual absence of any gravity-induced convective heat transfer. The scientific output from these microgravity experiments comprises a wealth of benchmark-quality dendritic growth data for critically testing solidification scaling laws [1]. The verification of these scaling laws constituted the primary scientific goal of the IDGE.

The three successful flights of IDGE resulted in a considerable body of “primary science.” This science, based on hundreds of experiments conducted in space, entailed delineating the steady-state features of dendrites grown under diffusion-limited conditions. In addition to completing the primary science tasks, however, a large collection of still-images and video data of dendrites taken on orbit has been compiled.

The first flight of the IDGE, launched on STS-62, took place in March, 1994, as a component experiment of the second United States Microgravity Payload (USMP-2). The second IDGE flight was launched on STS-75, in February/March, 1996, on USMP-3. Both of these flights used ultra-pure

* Corresponding author

(5-9's plus) succinonitrile (SCN) as the dendritic test material. SCN is an organic plastic crystal that forms dendrites similar to those of the body centered cubic (BCC) metals. SCN provides a nearly ideal physical model for dendrites in ferrous metals. The third and final IDGE flight (USMP-4) was launched on STS-87, in November of 1997. The last flight employed a different test material, viz., pivalic acid (PVA) — a face centered cubic (FCC) organic plastic crystal that solidifies analogous to many non-ferrous metals. PVA, like SCN, has convenient properties for conducting precision experiments. However, unlike SCN, PVA exhibits a large anisotropy of its solid–melt interfacial energy, which is believed to be the key physical parameter in the subtle selection process of dendritic operating states.

The accomplishments of the IDGE series are summarized briefly herein, particularly in reference to an analysis of Ivantsov's thermal diffusion model [2]. Despite its simplicity, and the fact that more elaborate models for dendritic growth exist, the Ivantsov model, when compared against an appropriate data set, provides critical insights to dendritic phenomena. Ivantsov's analysis identified the key diffusion phenomenon needed in any predictive model of dendritic growth. In the simpler case of a pure material, the Ivantsov model provides an excellent framework to examine the extent to which thermal diffusion limits dendritic growth. Additionally, Ivantsov's model provides a starting point — or basis solution — to begin to include other physical effects, such as interfacial stability, which when combined with the transport of latent heat or solute results in dendritic pattern formation.

II. USMP-2 Results on SCN

The main conclusions drawn by comparing the on–orbit IDGE data with terrestrial dendritic growth data obtained using the same apparatus and techniques, are: 1) Convective effects under terrestrial conditions cause growth speed increases up to a factor of 2 at the lower supercoolings ($\Delta T<0.5$ K). 2) Convection effects remain discernible under terrestrial conditions up to supercoolings as high as 1.7K — far higher than previously thought. 3) In the supercooling range above about 0.47K, microgravity data remain virtually free of convective or chamber-wall effects, and may be used reliably for examining diffusion-limited dendritic growth theories. 4) The diffusion solution to the dendrite problem, combined with a unique scaling constant, σ^*, does not provide consistent prediction of the growth velocity and dendritic tip radii. 5) Péclet numbers calculated from Ivantsov's solution are close to but deviate systematically from the IDGE microgravity data (Figure 1). 6) The scaling parameter, σ^*, is not a "universal" constant. Finally, 7) the measurements of σ^* from the terrestrial and microgravity data are in good agreement with each other, despite a difference of over six orders-of-magnitude in the quasi-static acceleration environments of low-Earth orbit and terrestrial conditions (Figure 2) [1].

More recently, Corrigan *et. al.,* used these data to measure side branch characteristics, from which they concluded that in both microgravity and terrestrial gravity, independent of supercooling, the side branch spacing is approximately 3R, the distance to the first significant side-branch is approximately 12R, whereas the overall dendritic envelope of a downward growing dendrite is greater under terrestrial condition then under microgravity conditions [3].

In order to examine how the dendrite tip and its trailing side–branch structure affect the energy transport process, LaCombe *et. al.,* [4] applied the method of moving heat sources, a Green's function approach like that of Schaefer [5], to the problem of dendritic growth. The superposition of latent heat sources is accomplished mathematically by integration, starting at the tip and extending to interfacial

areas aft of it. When computed in this manner it is unnecessary to integrate an infinite distance behind the tip. Instead, heat sources located far from the tip provide contributions to the tip's temperature that become vanishingly small.

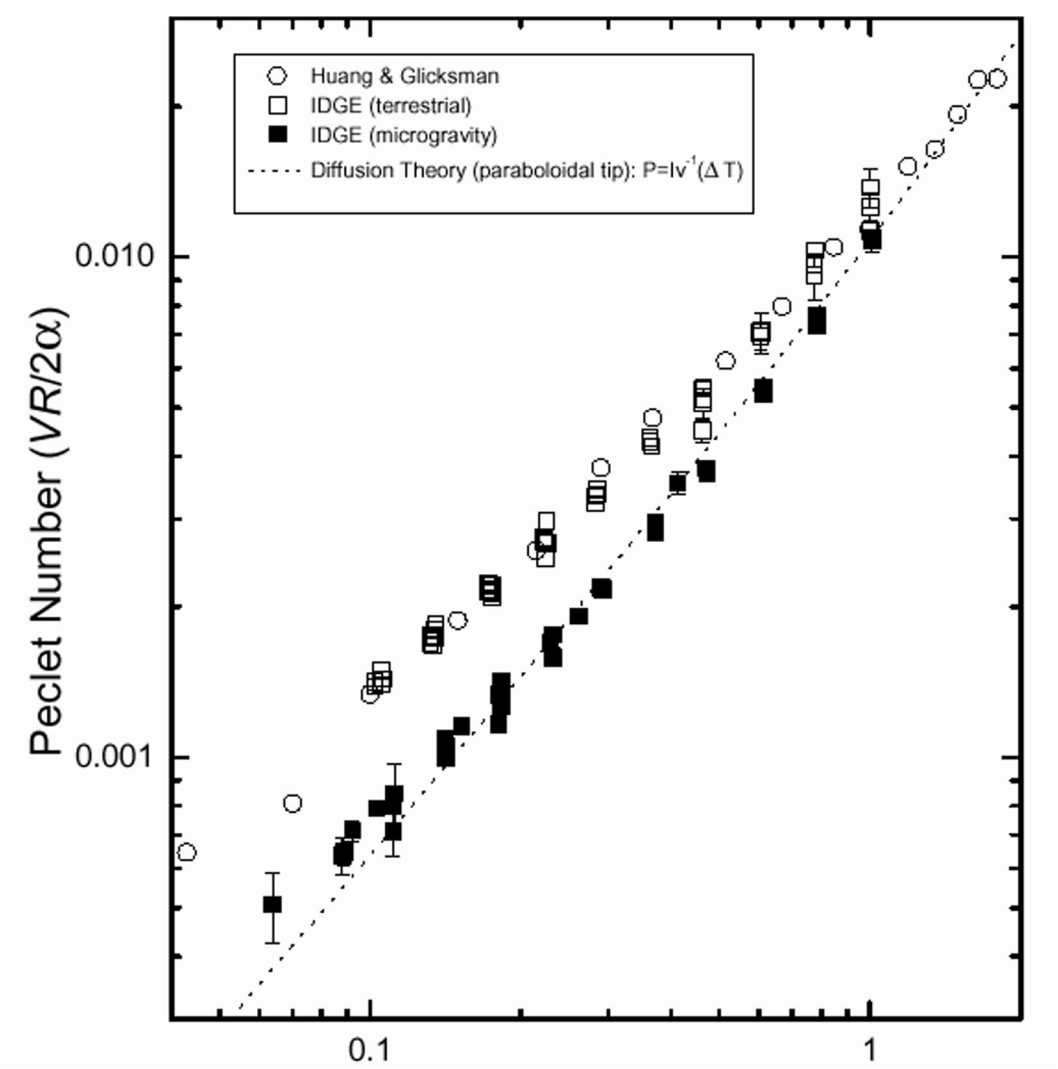

Figure 1. Péclet number versus supercooling. The Péclet number is a zero parameter test of the Ivantsov model as there are no adjustable parameters. The data are in approximate agreement with theory. At the lower supercoolings chamber effects become important, whereas at the higher supercooling, sidebranching is important.

The Green's function model was applied to the range of Péclet numbers and supercoolings in the IDGE. Using the upper end of the experimental Péclet range *(*P~0.01) the integration range was limited to the region that is not dominated by the side branching (*i.e.* from the tip back to about 12R from the tip). We find that, at most, about 75% of the tip temperature is accounted for via heat sources within 12R of the tip. This suggests that at least 25% of the tip's temperature derives from sources well within the side-branch region of the dendrite- a non-steady region not described by any simple function. For the lower Péclet numbers produced in the IDGE experiments *(*P~0.001), the side-branch region may contribute as much as ca. 60% of the tip temperature.

This observation adds support to Schaefer's original finding that under steady-state conditions interfacial regions remote from the tip contribute to the field surrounding the tip [4]. Other analysis indicates that

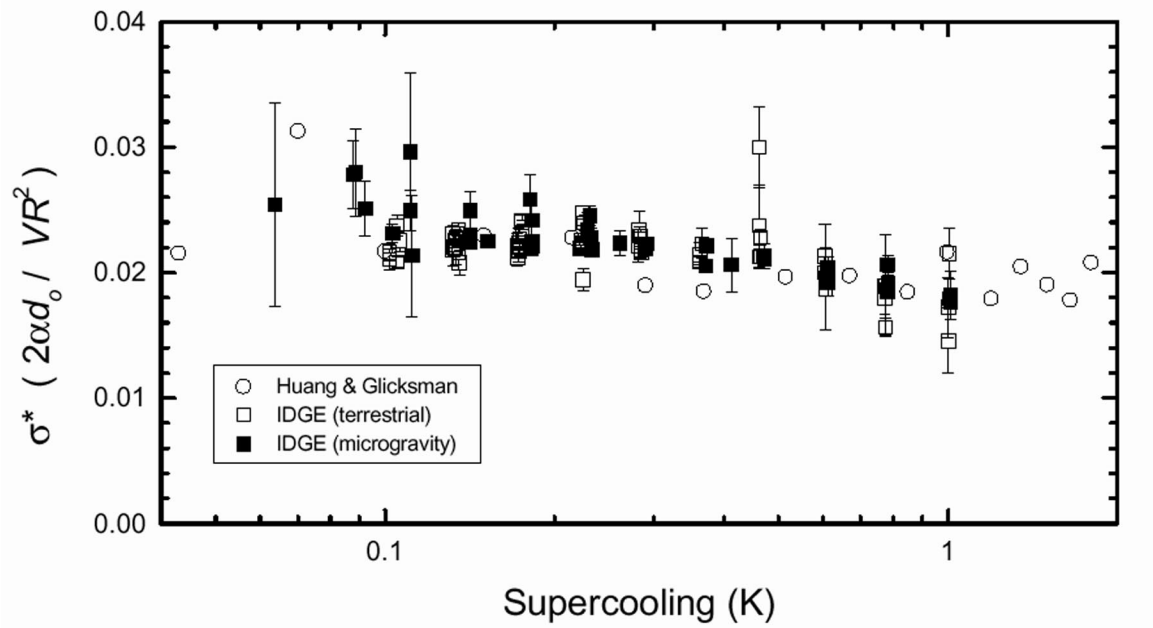

Figure 2: The scaling rule versus supercooling. In spite of the large uncertainties in some of the measurements, the scaling parameter does not appear to be a constant over the full supercooling range of these experiments. The scaling parameter data from both microgravity and terrestrial experiments are indistinguishable from each other here, but measurements from USMP-3 showed statistically significant differences.

shape-corrections near the tip itself, based on reasonable estimates of the three dimensional shape, do not significantly affect the Péclet number-supercooling curve unless side branching is taken into consideration [3]. Additionally, as there is believed to be a stochastic aspect to the side branch structure, it follows that the scatter in the IDGE might be explained by random variations in the side branch structure, and the corresponding influence that this region has on heat flow at the tip. The importance of these non-steady state features to the evolution of the dendrite, suggests the necessity of an experiment such as the TDSE that will help to further characterize and define the extent to which these issues impact the growth process.

III. USMP-3 Results on SCN

The second IDGE flight, launched on USMP-3/STS-75, supported almost all the conclusions cited above. Specifically, with sufficient repeated observations [6], it now appears that the terrestrial values of ó * are statistically distinguishable from their value in microgravity. The second IDGE flight also clarified issues at lower supercoolings as to the role of residual convection, wall proximity, or other factors, by showing definitively that certain features of the growth data are not due to convection [5,7]. It appears that quasi- steady accelerations up to at least 50 μg_o can be treated as essentially zero g_o. It was also argued as to what extent the effects at low supercoolings are due to wall–proximity effects. Finally, in addition to re–addressing topics included in the first IDGE flight, the second flight also yielded sufficient data to extract a three–dimensional reconstruction of the dendritic tip shape [8,9].

IV. USMP-4 Results on PVA

The data and analysis based on images received using telemetry from space obtained from the final flight of the IDGE are at a preliminary stage. Dendritic growth speed in PVA as a function of the supercooling may be compared to terrestrially measured PVA data, and to microgravity data scaled from prior SCN

data. The results of these preliminary analyses indicate that PVA data are in good overall agreement with the SCN data. This implies that dendritic growth in PVA, like SCN, is a diffusion limited process. Little, if any, interfacial kinetic hindrances appear to be present.

Preliminary data assessing the nature of boundary–layer interactions in PVA shows that the velocity levels off at its maximum steady–state value when the nearest neighbor distance (tip-to-tip) exceeds twice the thermal diffusion distance, $2l_d$. Here $l_d = \alpha/V$ (α is the thermal diffusivity and V is the tip speed). When the nearest neighbor spacing falls below $2l_d$, thermal boundary layers overlap and interact, causing the dendrite speed to fall. This particular phenomenon of neighbor interactions has never been observed before, because convective free conditions are required to ensure that dendritic growth is limited by thermal diffusion.

Currently, velocity and side–branching measurements are being extracted from flight videos and 35mm film. These video sequences provide 30 frames per second images recorded at 256 gray- levels- albeit at a much lower spatial resolution than recorded on the 35 mm still film. Efforts have centered on using new software analysis tools developed by the Transient Dendritic Solidification Experiment (TDSE) for video data extraction, and a corresponding examination of ground-based video data. Results thus far indicate that there are several interesting transient aspects evident in the dendrite tip-displacement versus time data. The first observation is that although PVA dendrites initially appear to grow at a constant rate, they actually do not. This is evidenced by the observation that the residuals from a straight line regressed through nearly linear displacement data have a small but persistent transient. This observation could not be obtained at the small data rates obtained with 35 mm film. Lastly, by performing a spectral analysis on these residuals, we find not only that they are not random, but that the tip region oscillates with a fundamental frequency and harmonics consistent with the side branch spacing.

V. Future Activities

Despite the fact that the IDGE project has officially concluded in September 1999, new discoveries and ideas continue to emerge and develop from the large microgravity IDGE database. In the future, additional details of these evolving developments may be found from the NASA-sponsored Follow On Activities of the Rensselaer IDGE project, a.k.a., RIDGE.

VI. Acknowledgements

The requirements for designing, building, testing, and operating a complex, highly interactive scientific microgravity experiment in low-Earth orbit are beyond the skills and resources of any one individual or organization. An infrastructure and diverse teams of dedicated professionals are required. Over the last ten years the following individuals contributed significantly to the design, construction and operation of this experiment, which enabled the acquisition of the results contained herein. We thank all at Rensselaer Polytechnic Institute, Troy, NY who helped with these projects. In addition, we thank all those at or associated with NASA's Glenn (formerly Lewis) Research Center, Cleveland, OH who helped with this project. Special thanks are due for the continued understanding, interest, and financial support provided by the National Aeronautics and Space Administration, Life and Microgravity Sciences and Application Division, (Code U), Washington, DC, under Contract NAS3-25368, with liaison provided by Microgravity Science Division (formerly the Space Experiments Division), NASA Glenn Research Center, Cleveland, OH. The successful operation of the experiment would not have been possible without the efforts of the USMP Mission Scientist and the associated Mission Management

teams at the Marshall Space Flight Center. Thanks also goes to those who oversaw POCC training and simulations, and the POCC cadre who coordinated and implemented the project's space flight operations. Finally, we also extend our deepest thanks to the crews of STS-62, 75, and 87, and the support groups at all the NASA research centers involved with the space shuttle's activities.

REFERENCES

1. M.B. Koss, J.C. LaCombe, L.A. Tennenhouse, M.E. Glicksman, and E.A. Winsa, Metallurgical and Materials Transactions A, 30A, (2000), p. 3177
2. P. Pelcé, ed. Dynamics of Curved Fronts. 1988, Academic Press, Inc.: New York. 514.
3. D.P. Corrigan, M.B. Koss, J.C. LaCombe, L.A. Tennenhouse, K.D. de jager, and M.E.Glicksman, Phys. Rev. E, 60, (1999), p. 7217
4. J.C. LaCombe, M.B. Koss, D.C. Corrigan, A.O. Lupulescu, L.A. Tennenhouse, and M.E. Glicksman, J. Crystal Growth, 206, (1999) p. 331
5. R.J. Schaefer, J. Crystal Growth, 43, (1978), p. 17
6. Rensselaer Polytechnic Institute, Troy, NY, unpublished research, (1998)
7. L.A. Tennenhouse, M.B. Koss, J.C. LaCombe, and M.E. Glicksman, J. Crystal Growth, 174, (1997), p. 82
8. J.C. LaCombe, M.B. Koss, V.E. Fradkov, and M.E. Glicksman, Phys. Rev. E, 52, (1995), p. 2278
9. J.C. LaCombe, Ph.D. Thesis, Rensselaer Polytechnic Institute, Troy, NY (1998)

EVOLUTION OF LOCAL MICROSTRUCTURES: SPATIAL INSTABILITIES OF COARSENING CLUSTERS

Martin E. Glicksman[1], Donald O. Frazier[2], Jan R. Rogers[2], William K. Witherow[2], J. Patton Downey[2]

[1]Materials Science & Engineering Dept., Rensselaer Polytechnic Institute, Troy, NY.
[2]NASA Marshall Space Flight Center, Microgravity Department, Huntsville, AL.

INTRODUCTION

This work examines the diffusional growth of discrete phase particles dispersed within a matrix. Engineering materials are often microstructurally heterogeneous, and the details of the microstructure determine how well that material performs in a given application. Critical to the development of designing multiphase microstructures with long–term stability is the process of Ostwald ripening. Ripening, or phase coarsening, is diffusion–limited and arises in *polydisperse* multiphase materials. Growth and dissolution occur because fluxes of solute, driven by chemical potential gradients at the interfaces of the dispersed phase material, depend on particle size. Competitive kinetics of these processes dictates that larger particles grow at the expense of smaller ones, overall leading to an increase of the average particle size. The classical treatment of phase coarsening was done by Todes, Lifshitz, and Slyozov, (TLS)[1,2] in the limit of zero volume fraction, V_V=0 of the dispersed phase. Since the publication of TLS theory, there have been numerous investigations, many of which sought to describe the kinetic scaling behavior over a range of volume fractions. Some studies in the literature report that the relative increase in coarsening rate at low (but not zero) volume fractions compared to that predicted by TLS is proportional to $V_v^{1/2}$, whereas others suggest $V_v^{1/3}$. This issue has been addressed recently by simulation studies at low volume fractions in three dimensions by members of the Rensselaer/MSFC team.[3-5]

I. Background and Objectives

Our studies of ripening behavior using large–scale numerical simulations suggest that although there are different circumstances which can lead to either scaling law, the most important length scale at low volume fractions is a diffusional screening length. This screening length places limits on the extent and applicability of a mean-field description, and can result in local divergences from mean-field behavior. The numerical simulations we employed exploit the use of a recently developed "snapshot" technique[6], and identify the nature of the coarsening dynamics at various volume fractions. Preliminary results of numerical and experimental investigations, focused on the growth of finite particle clusters, provide important insight into the nature of the transition between the two scaling regimes. The companion microgravity experiment centers on the growth within finite particle clusters, and follows the temporal dynamics driving microstructural evolution, using holography.

This research effort will extend our preliminary discoveries and develop a critical microgravity experiment to observe these phenomena in a suitably quiescent environment. Work accomplished to date

shows that the critical cross–over between the two scaling regimes ($V_v^{1/2}$ versus $V_v^{1/3}$) is a function of both the volume fraction, which, intuitively, affects this screening length, and the cluster size, n, where n is the number of particles comprising the cluster. Specifically, the cross–over occurs at a critical volume fraction for which $V_V \approx 1/(3n^2)$. One also expects that the volume fraction itself fluctuates from region-to-region, because the local size and distribution of particles vary. Thus, spatial variances should arise in the local kinetics. One of the scientific objectives of this work is to identify the nature of these microstructural fluctuations. This added level of understanding will be of importance in the development of more predictive models for microstructural evolution in heterogeneous materials.

II. Theory

The continuity equation assumes neither nucleation nor coalescence:

$$\frac{\partial F}{\partial t} + \frac{\partial}{\partial R}[v(R)\cdot F] = 0$$

Our approach in this work will seek to obtain $v(R)$, the time rate of change of the radius, R, of a particle, in a given cluster. $F(R,t)$ is the size distribution function. Source/sink strength (volume flux), B_i^{TLS}, is the diffusion analog of electrostatic charge,

$$B_i^{TLS} = [1 - \frac{R_i}{R^*}]$$

R^* is the critical radius given by, $R^* = \lambda/\varphi_\infty$

φ_∞ is the background matrix potential, assumed uniform throughout the matrix phase;

λ is a capillary length defined by

$$\lambda = 2\frac{\gamma\Omega}{k_B T}$$

where γ is interfacial energy, Ω is molar volume, k_B is Boltzmann's constant, and T is the absolute temperature.

Since the zero volume fraction restriction in TLS results in the total neglect of direct interactions among particles, a more realistic approach which introduces the influence of volume fraction on coarsening kinetics was that employed by Marqusee and Ross.[7]

Their approach applies spatially coarse-grained background diffusion potential:

$$\nabla^2\varphi = -4\pi\sigma$$

where σ, a source/sink density in the matrix space, introduces a coarse-grained local background potential, $\varphi(\mathbf{r})$, due to droplets surrounding a coarsening droplet centered at point r in the matrix,

$$\varphi(\mathbf{r}) = \sum_i \frac{\lambda B_i}{|r - r_i|}\exp(-\kappa\cdot|r - r_i|) + \varphi_\infty.$$

The volume flux, B_i, becomes

$$B_i = \left(1 - \frac{R_i\varphi_\infty}{\lambda}\right)(1 + \kappa R_i) = B_i^{TLS}(1 + \kappa R_i)$$

where $\kappa = [4\pi N_v \langle R\rangle]^{1/2}$ represents the natural cut-off distance for direct multiparticle interactions via the diffusion field, beyond which the particles are isolated from each other by the intervening two-phase medium. N_v is the number of particles per unit volume, and $\langle R\rangle$ is the average droplet radius in the cluster.

For droplet clusters comprising finite coarsening systems, one may define physically distinct coarse-grained length scales; among them are: (1) the diffusion screening radius, $\Lambda_D \equiv \kappa^{-1}$; (2) the average droplet radius in the cluster, $\Lambda_R \approx \langle R \rangle$; (therefore, $\Lambda_D = [4\pi N_v \langle R \rangle]^{-1/2}$) For large Λ_D (sparse particle density), the screened potential approaches unscreened potential. (3) The spatial extent of the total coarsening system, Λ_{tot}, as defined for a "spherical cluster" by $\Lambda_{tot} = \left(\frac{4\pi}{3}\right)^{-1/3}\left(\frac{n}{N_v}\right)^{1/3}$; where n is the total number of particles remaining at a given time. When $\Lambda_D \geq \Lambda_{tot}$ diffusion screening is not operative as a factor.

We can now relate the time-rate of change of radius, $v(R_i) = \frac{2\lambda D c_0 \Omega}{R_i^2} B_i$, where D is the diffusion coefficient and c_0 is the equilibrium solubility of the droplet phase, and B_i is now representative of the volume flux of a droplet in a finite coarsening cluster. The experimental parameters for determining the time-rate of change of each droplet within a given cluster are accessible through physicochemical measurement and holography.

III. Experiment

Experimental objectives are:

- Measure $v(R_i)$ of each cluster droplet in holography cell(s).
- Determine, in mixed-dimensional system (3-*D* droplets undergoing 2-*D* diffusion), the existence of spatial instabilities in microstructural homogeneity due to some undefined "screening length."
- In a fully 3-*D* system in microgravity, verify TLS coarsening rate deviation dependence on local volume fractions for global volume fractions less than 1%. The volume fraction for a *finite* coarsening cluster is defined as,

$$V_v = \frac{\sum_{i=1}^{n} \pi R^3_i}{\Lambda^3_{tot}} .$$

The experimental approach is comprised of ground-based work to extend prior mixed-dimensional studies, and a flight experiment to study finite coarsening kinetics in three dimensions.

A. Ground-based experiment

The ground-based experimental study of diffusional coarsening has proceeded in a well-characterized liquid-liquid two-phase system. Ideally, the experiment is performed at an isopycnic point to maximize exclusion of gravity-induced system disturbances, such as convection flow. This allows observations for the long times required to investigate coarsening. A holographic technique has been instrumental in prior work, and will continue to be the primary method to study both the influence of local environmental conditions on individual droplet size histories and measurement of global averages. Prior ground-based coarsening work focused on two-dimensional diffusion of three-dimensional droplets attached to a glass surface (mixed-dimensional case).[4,5] Mixed dimensional work permits long-term ripening studies in 1-*g*, because the dispersed phase remains attached to the test cell wall.

Holographic techniques allow measurement of the locations and sizes of individual precipitates. This technique has proven adequate for the mixed-dimensional case. Its modification for the three-dimensional case is under development. Automated numerical image analysis of the holographic images is of

practical important for experiments involving measurements of a large number of droplets. The investigators have also performed preliminary development in this area. The software to accomplish the data extraction will significantly accelerate the normally tedious job of quantitatively analyzing holograms involving thousands of droplets, where each droplet is to be identified, located, and measured, and allow thorough analysis of the entire population.

B. Flight Experiment

A fully three-dimensional coarsening study requires long-duration quality microgravity to prevent phase separation via Stokes settling. In this instance, there is no wall attachment to prevent sedimentation, so a microgravity environment is an imperative. During ground-based coarsening of a 3-D dispersed droplet phase, the dispersion would normally become rapidly depleted of larger ripening droplets. Ideal operation near the isopycnic temperature minimizes sedimentation of large droplets, but small temperature fluctuations ($\pm$ 0.001K) cause the droplets to move to the extent that their positions are not stable for the long times required for these studies. The relative position of the droplets would also vary significantly in time. It would not be possible to explore local microstructural effects from diffusion because sedimentation effects would alter the droplet population more rapidly. This and other factors, such as distortion of the diffusion field and buoyancy-driven convection obscure the basic kinetics. These factors impose a clear imperative for microgravity investigation of three-dimensional coarsening kinetics, and observation of evolution of microstructure under quiescent conditions.

Preparation for microgravity studies have proceeded by assessing three approaches for droplet dispersion:

1. Jet break-up in microgravity to control the distribution of droplets in each cluster.
2. Site saturation method [Nucleation of Crystals from Solution (NCS)[8]] for forming droplet clusters by quench.
3. Normal quench: A cell, filled with selected homogeneous parent phase, is quenched below the consolute temperature to the isopycnic temperature in the two-phase region. Ground based testing with rotation of the two-phase isopycnic system compensates for small density differences between the phases, minimizing sedimentation during coarsening.

All three approaches have been tested, with the quench being the method of choice. For approaches 1 and 2, aside from difficulties in implementation, it is difficult to establish precisely that the two phases are the desired equilibrium phases, because they must, of necessity, be stored separately prior to mixing. Without knowledge of the precise solvated concentration, the discrete phase volume fraction would be nearly impossible to determine accurately. For method 3, implementation is easier, insofar as the initial concentration will be as precise as it normally is during laboratory experimentation, and the two phases will be in equilibrium with each other even if temperatures are slightly different from that desired. Additionally, the "quench" approach allows for repeating the experiment using the same test cell simply by heating above the consolate temperature, mixing and quenching again. Methods 1 and 2 are "one shot" experiments, which is not desirable for the space flight experiment.

The rotating quench cell (RQC) design is based on the work of Roberts, et. al., to optimize the parameters for a rotating mixed-phase reactor [9]. The RQC is designed for droplets to maintain suspension by rotating the RQC. Although the RQC rotates at the appropriate rotational speed, suspended droplets remain influenced by viscous drag and tend to rotate with the fluid phase. A balance of their gravitational and centrifugal forces with viscous drag determines their motion relative to the rotating fluid. At high

rotation rates, droplets with densities greater than the matrix fluid phase will tend to move toward the cell walls. On the other hand, high rotation rates cause droplets with densities less than the matrix phase to tend to drift toward the cell longitudinal axis.

Regardless of the side of the phase diagram miscibility-gap on which the experiment is performed, the majority phase—not the droplet phase—must preferentially wet the inside cell wall surfaces. If the droplet phase preferentially wets, nucleated droplets will wet and spread over the cell surface, distorting observable droplet volume fractions, introducing unknown concentration gradients at the cell surfaces, and possibly compromising imaging processing.

Furthermore, diffusion fields associated with droplets near container walls differ from diffusion fields of droplets situated well within in the bulk. One must be concerned with perturbations to the three-dimensional diffusion field due to wall effects. The distance at which such perturbations to the three-dimensional diffusion field can occur is a function of the average droplet size within a cluster of a given volume fraction. Therefore, for a fully three-dimensional experiment, a significant droplet population should reside near the central axis of the RQC, and outside of a diffusional screening distance, $\lambda=(4\pi\bar{R}N/V_V)^{-1/2}$, due to the container walls. Our ability to operate above or below the isopycnic point on either side of the miscibility-gap will allow flexibility in locating an adequate representation of droplets near the RQC primary axis.

Finally, holographic imaging is the optical tool selected for observing these phenomena. Figure 1 shows a hologram during three-dimensional coarsening of succinonitrile-water in a RQC. Figure 2 is a sequence of holograms during the mixed-dimensional coarsening of succinonitrile-water. Figure 3 represents an automated composite from digitized images of holograms using intensity distribution constraints. Clearly, holography provides more data than does conventional optical imaging techniques. A reconstructed hologram is amenable to various optical characterization techniques, *e.g.*, *in situ* microscopy, and interferometry. In particular, automated numerical image analysis of holographic images is important for experiments such as ELMS that involve measurement of large numbers of particles. An important aspect of the experimental study will include determining the extent of modifications required allowing incorporation of holography within the operating envelope of the millikelvin thermostat (MITH) hardware.

REFERENCES

1. O.M. Todes, J. Phys. Chem (Sov) 20, 629 (1946).
2. I.M. Lifshitz and V.V. Slyozov, J. Phys. Chem. Solids 19, 35 (1961)
3. V.E. Fradkov, M.E. Glicksman, S.P. Marsh, Phys. Rev. E. 53(3), 3925 (1996).
4. J.R. Rogers, J.P. Downey, W.K. Witherow, B.R. Facemire, D.O. Frazier, V.E. Fradkov, S.S. Mani, and M.E. Glicksman, J. Electronic Mat. 23(10), 999 (1994).
5. V.E. Fradkov, S.S. Mani, M.E. Glicksman, J.R. Rogers, J.P. Downey, W.K. Witherow, B.R. Facemire, and D.O. Frazier, J. Electronic Mat. 23(10), 1007 (1994).
6. H. Mandyam, M.E. Glicksman, J. Helsing,.S.P. Marsh, Phys. Rev. E. 58(2), 2119 (1998).
7. J.A. Marqusee and J. Ross, J. Chem. Phys. 80, 536 (1984).
8. R.L. Kroes, D.A. Reiss, S.L. Lehoczky, "Nucleation of Crystals from Solution in Microgravity", Joint Launch + One Year Science Review of USML-1 and USMP-1 with the Microgravity Measurement Group, NASA Conference Publication 3272, Vol II, 663 (1994).
9. G.O. Roberts, D.M. Kornfeld, and W.W. Fowlis, J. Fluid Mech. 229, 555 (1991).

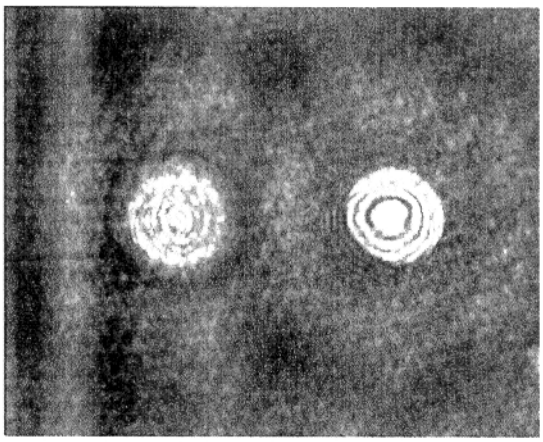

Right particle on test cell wall and in focus.

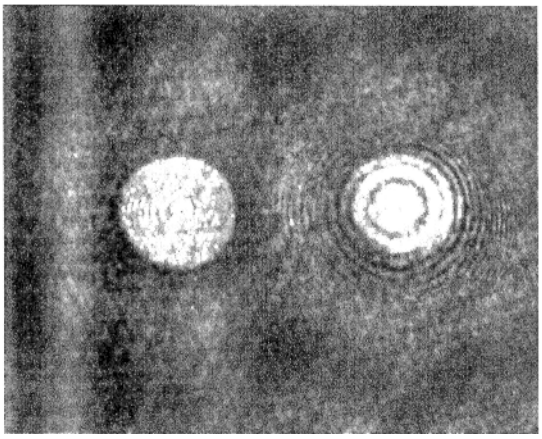

Left particle in volume of test cell and in focus.

Figure 1. Hologram during three-dimensional coarsening of succinonitrile-water solution in a rotating quench cell.

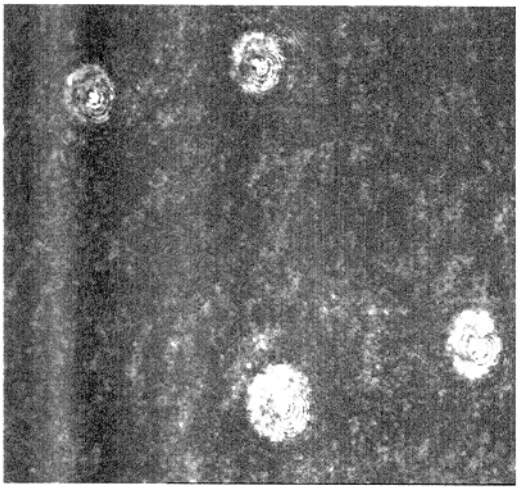

Hologram 100

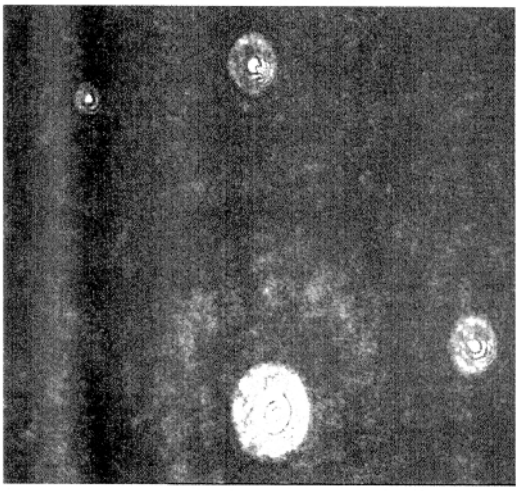

Hologram 129

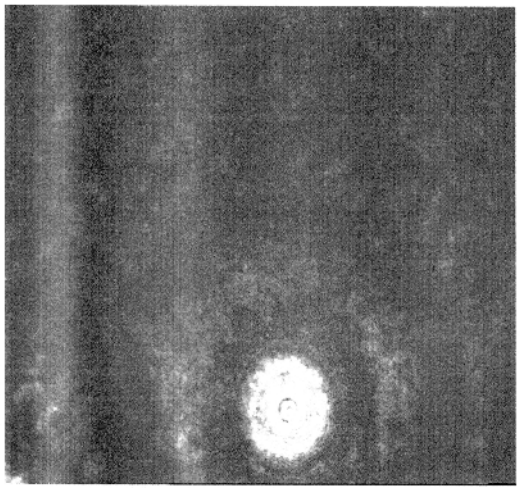

Hologram 151

Figure 2. Holograms of mixed-dimensional coarsening of succinonitrile-water system in pyrex cells: discrete phase is succinonitrile rich.

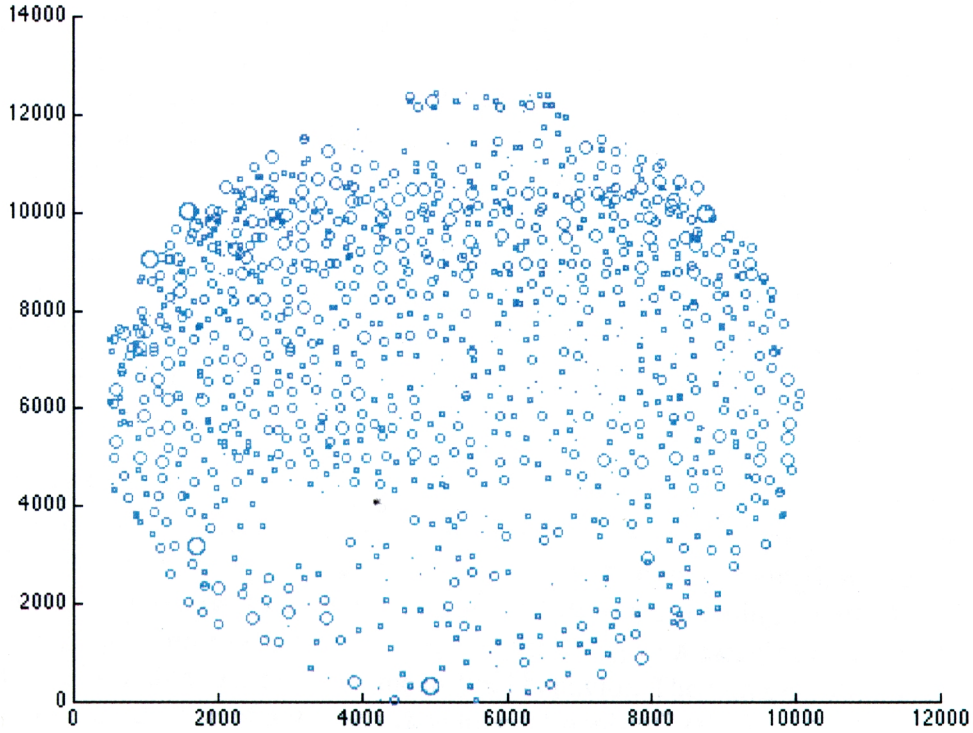

Figure 3. Automated composite of droplet spatial location and size distribution from magnified and digitized images of holograms using intensity distribution constraints.

EFFECT OF GRAVITY ON THE EVOLUTION OF SPATIAL ARRANGEMENT OF FEATURES IN MICROSTRUCTURES: A QUANTITATIVE APPROACH

A.M. Gokhale and A. Tewari

School of Materials Science and Engineering
Georgia Institute of Technology, Atlanta, GA-30332

INTRODUCTION

A microstructure is a collection of volumes, internal-surfaces, lines, and points. Depending on its dimensionality, each microstructural feature has associated with it, size, shape, volume, surface area, curvature, *etc*., and location. The distribution of relative locations of microstructural features is manifested in the spatial patterns, correlations, clustering, short and long range interactions, microstructural gradients, segregation, etc. The spatial arrangement of features in microstructure also governs particle packing, connectivity, distribution of inter-particle contacts, etc. Evolution of spatial arrangement of microstructural features is an aspect of microstructure development that may be significantly affected by gravity, particularly, when liquid phases are present during the evolution processes. For example, gravity may affect distribution of coordination numbers of grains/particles, agglomeration tendencies, spatial correlations among particles sizes, etc. The objectives of this research have been to develop Stereology and image analyses based techniques for quantitative characterization of spatial arrangement of features in three-dimensional microstructure, and apply these techniques to quantify the effect of gravity of evolution of microstructure during liquid phase sintering (LPS). The Principal Investigator (PI) and his graduate students have successfully developed a combination of efficient montage serial sectioning and digital image processing techniques that permits reconstruction of *large volume* of three-dimensional microstructure observed at *high resolution,* from a stack of large area high resolution montage serial sections [1]. Combination of methodology to reconstruct such a large volume of three-dimensional microstructure that provides sufficiently large number of features and minimize the edge effects, and unbiased statistical sampling using *disector* probe [2], yield a practical and efficient procedure for reliable estimation of some important descriptors of the spatial arrangement of grains/particles in three-dimensional microstructure. These techniques have been applied to quantify the effect of gravity the evolution of spatial arrangement of tungsten grains in the liquid phase sintered specimens of W-Fe-Ni alloys. The measurements have been performed on ground-based as well as microgravity environment (first Microgravity Science Laboratory/MSL-1 and second International microgravity Laboratory/IML-2 missions) processed specimens provided by Professor R.M. German. The evolution of bivariate coordination number distribution [3,4], first, second, and third nearest neighbor distance, and true grain size distributions [4] of tungsten grains have been characterized. It is observed that in both ground-based as well as microgravity-processed specimens the tungsten grains form almost completely connected network. Therefore, absence of gravity does not lead to a liquid phase sintered microstructure consisting of discrete and separate tungsten grains uniformly distributed in the Fe-Ni alloy matrix. The quantitative microstructural data have revealed interesting trends concerning the effect of gravity on evolution

coordination number distribution and nearest neighbor distributions of the tungsten grains in these liquid phase sintered microstructures. The digital images of three-dimensional microstructures are presented in the next section. The quantitative microstructural data and observations are discussed in the subsequent sections.

I. Reconstruction of Three-Dimensional Microstructure From Serial Sections

Figure1 depicts the surface rendered three-dimensional microstructure of the tungsten grains in the specimens liquid phase sintered for 1 minute in microgravity environment. Figure-2 shows some connected chains of tungsten grains. The details of three-dimensional microstructural reconstruction are reported elsewhere [1,4]. Examination of large volumes of 3-D microstructures in all specimens revealed that in ground based as well as microgravity processed specimens, the tungsten grains are almost completely connected, and both the grains and the matrix are co-continuous.

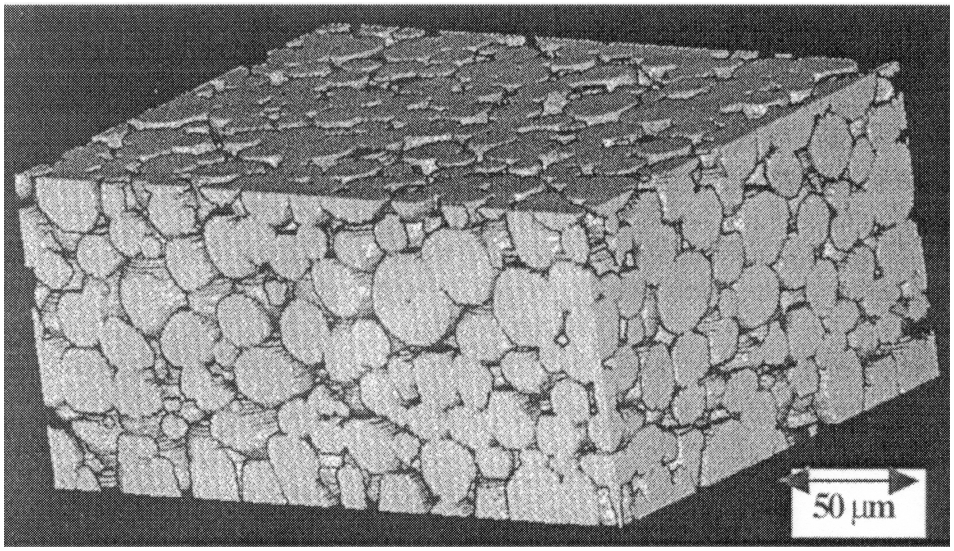

Figure1. Surface rendered three-dimensional microstructure of tungsten grains in a 83wt% W-Ni-Fe alloy specimen liquid phase sintered for 1 minute at 1507 C.

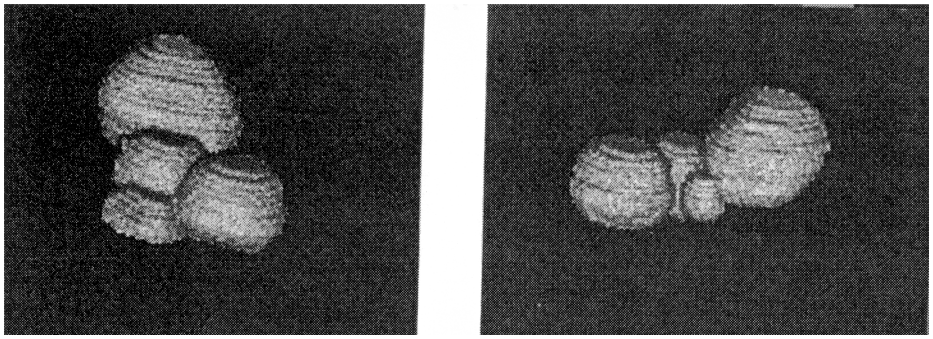

Figure 2. Surface rendering of clusters of tungsten grains extracted from 3-D-reconstruction.

II. Evolution of Coordination Number Distribution

The coordination number of a grain is the number of other grains that are in direct contact with it. In general, a distribution of coordination numbers exists in powder-processed microstructures. The coordination number is sensitive to the size of the grain, and therefore a bivariate coordination number distribution is of interest. The bivariate coordination number distribution evolves during the liquid phase sintering

process, and it is affected by gravity. The coordination number distribution is an important descriptor of short range spatial arrangement of grains in liquid phase sintered microstructures, and it affects the connectivity of the grains. The mean coordination number (often referred as just coordination number or connectivity in LPS literature) is the average value of the coordination number distribution in three-dimensional microstructure. In this research program, the three-dimensional bivariate coordination number distributions have been experimentally measured from the three-dimensional microstructural images reconstructed from 90 montage serial sections. Figure 3 depicts the bivariate coordination number distribution of tungsten grains in one of the specimens.

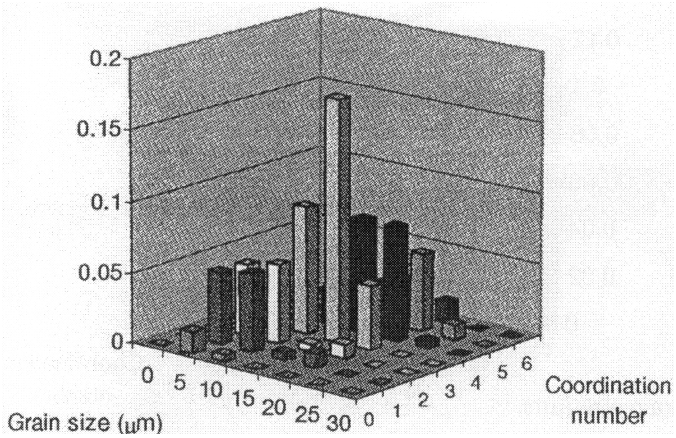

Figure 3. Bivariate distribution of three-dimensional coordination numbers of tungsten grains in a 83wt%W-Ni-Fe alloy specimen liquid phase sintered in microgravity environment for 1 minute at 1507 degree centigrade.

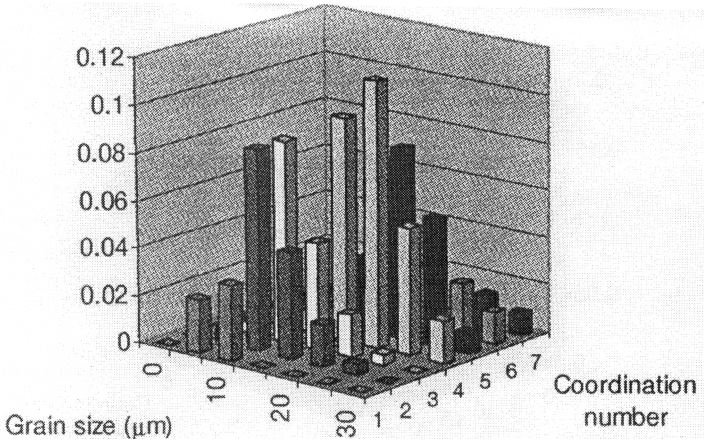

Figure 4. Bivariate three-dimensional coordination number distribution of tungsten grains in a 83wt%W-Ni-Fe alloy specimen liquid phase sintered in normal gravity for 1 minute at 1507 degree centigrade.

It is observed that for a given coordination number there is always one size class with the highest probability of forming that number of grain contacts. As the coordination number increases, the size class with highest probability also increases. Therefore, there is a strong correlation between the grain size and coordination number. To quantify this correlation, from the bivariate frequency functions, one can compute average size of the grains D_c having a specific fixed coordination number, C. Figure 5 shows plots of D_c vs. C for the four data sets. Observe that, the average size D_c having C number of contacts increases **monotonically** with the number of contacts.

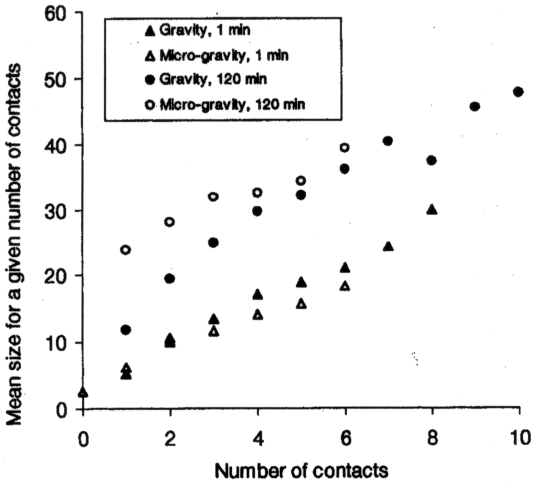

Figure 5. Mean size of grains having the given coordination number versus the coordination number for four specimens of 83wt% W-Ni-Fe alloy liquid phase sintered at 1507 C.

To extract simple expression for the quantitative correlation between D_c and C, normalize both the variables: divide D_c by the experimentally measured three-dimensional global average grain size A , and divide C by the mean coordination number C_0. The normalized plot of $[D_c / A]^2$ vs. $[C/C_0]$ for four specimens of 83wt%W0Ni-Fe alloy are shown in Figure-6.

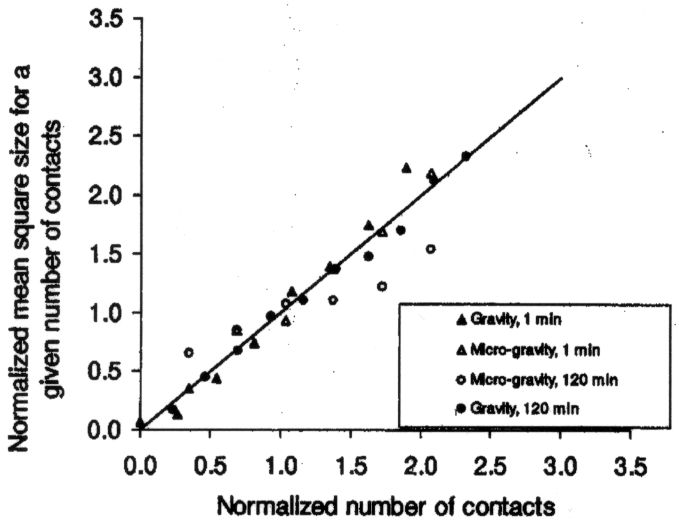

Figure 6. Normalized plot of $[D_c / A]^2$ vs. $[C/C_0]$ for four specimens of 83wt% W-Ni-Fe alloy liquid phase sintered at 1507 C.

Observe that, (i) the plot is linear, indicating that $[D_c / A]^2$ varies linearly with $[C/C_0]$, and (ii) the data points for all the specimens fall on a single straight line, whose slope is one and intercept is zero. Note that these four data sets represent specimens whose global average grain size differs by more than a factor of two (1 min and 120 min specimens), volume fraction of tungsten grains varies from 0.59 to 0.74 (due to gravitational settling effects), mean coordination number varies from 2.9 to 4.3, and they represent specimens processed in normal gravity and microgravity. Despite these differences in the processing parameters, average size, amount of W grains, and mean coordination number, a single relationship describes the correlation between grain size and coordination number. This correlation can be expressed as follows.

$$[D_c / A]^2 = C/C_0$$

The surface area of the grains is directly proportional to the square of their size. Therefore, the equation implies that in a microstructure, although individual grains of different sizes may have the same coordination number, on the average, grains with larger surface area are likely to have a higher coordination number, and average surface area of the grains having a given coordination number increases linearly with the coordination number.

Table 1. Mean three-dimensional coordination number of tungsten grains in 83wt% -Ni-Fe alloy specimens liquid phase sintered at 1507 C. The values pertain to the regions at the specimen bottom.

Property	Specimen	Normal gravity	Normal gravity	Microgravity	Microgravity
		1 minute	120 minute	1 minute	120 minute
Mean coordination number	83 wt% W- Ni – Fe alloy	3.7	4.3	2.9	2.9

Table I gives the mean coordination numbers of tungsten grains in the specimens of liquid phase sintered 83wt%W-Ni-Fe. Note that, (i) the mean coordination number of tungsten grains in the microgravity environment is significantly lower than that for the specimens processed in normal gravity, at both low and high sintering times, and (ii) the mean coordination of the tungsten grains for the specimens processed in microgravity appears to be insensitive to the sintering time. The higher mean coordination number for gravity sintered specimens may be partly due to gravitational settling leading to more dense packing of the grains. There have been many observations, which show that if the density difference between the solid grains and the liquid is high, the resulting coordination number is also high [6]. This difference in the coordination number can be attributed to the pressure exerted by the solid grains on each other. For the specimens processed in normal gravity, this phenomenon also results in a systematic increase in the coordination number along the gravity direction.

III. Evolution of Nearest Neighbor Distributions

Figure 7 shows normalized distribution of the frequency function of first nearest neighbor distances; the nearest neighbor distances are divided by their corresponding mean values. Observe that the data points for the four specimens fall on the same curve. Similar trends are observed for the frequency function of the normalized second nearest neighbor distances as well. These data suggest that evolution of the first and second nearest neighbor distances of tungsten grains in this alloy is simply a scale factor change. The effect of sintering times as well as gravity appears to reside only in the mean values.

Similar trends are observed for normalized grain size distributions of the ground based specimens, but the normalized grain size distributions in the microgravity-processed specimens does not appear to be time invariant. The evolution of mean grain volumes also shows some interesting trends: mean grain volume in 83wt%W-Ni-Fe alloy specimen liquid phase sintered for one minute in normal gravity is about two times larger than that of the corresponding microgravity processed specimen, however in the specimens sintered for 120 minutes there is only 12% difference in the mean grain volumes of the corresponding specimens. These differences could be due to gravitational effects on grain coalescence [Niemi *et al.*, 1981] as well as on grain coarsening [Liu, Heany, and German, 1997]. Experimental

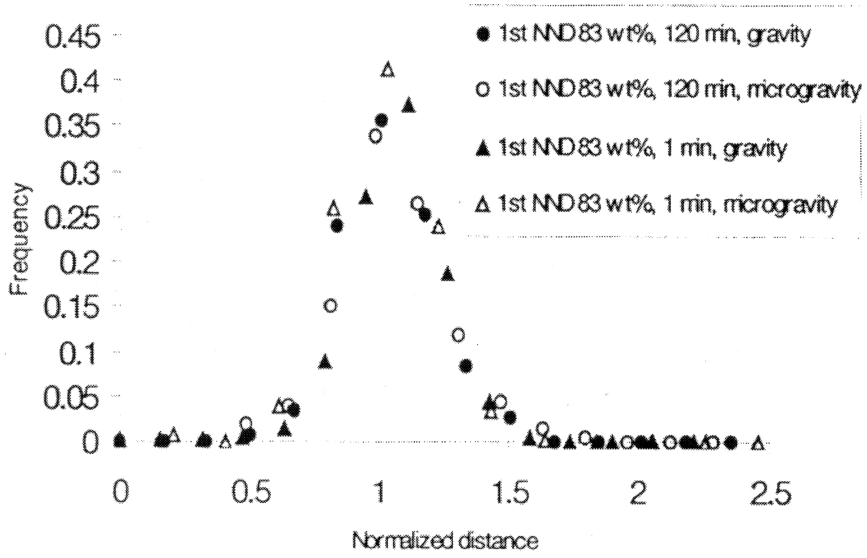

Figure 7. Normalized frequency distributions of the first nearest neighbor distances of tungsten grains in 83wt%W-Ni-Fe alloy liquid phase sintered at 1507 C.

data on more specimens that cover a wider range of sintering times, volume fractions, and dihedral angles is necessary to completely understand these evolution processes.

REFERENCES

1. A. Tewari and A.M. Gokhale: "Application of Three-Dimensional Digital Image Processing for Re construction of Microstructural Volume From Serial Sections", Materials Characterization, Vol. 44, pp. 259-269, 2000.
2. H.J.G. Gundersen, H.J.G.: "Stereology of Arbitrary Particles: A Review of Unbiased Number Estimators", Journal of Microscopy, Vol. 143, PP. 3-45, 1986.
3. A. Tewari, A.M. Gokhale, and R.M. German: "Effect of Gravity on Three-Dimensional Coordination number Distribution in Liquid Phase Sintered Microstructures", Acta Materialia. Vol. 47, PP. 3721-3734, 1999.
4. Asim Tewari, Ph.D. disseretation, Georgia Institute of Technology, Atlanta, GA, 1999.
5. A.N. Niemi, L.E. Baxa, J.K. Lee, and T.H. Courtney, Modern Developments in Powder Metallurgy, Metals Powder Industries Federation, Princeton, NJ. Vol. 2, PP. 483-495, 1981.
6. Y. Liu, D.F. Heaney, and R.M. German, Acta Metall. Mater, Vol. 43, PP. 1587-1593, 1995.

INFLUENCE OF SOLUTOCAPILLARY CONVECTION ON MACROVOID DEFECT FORMATION IN POLYMERIC MEMBRANES

M.R. Pekny[1], J. Zartman[2], A.R. Greenberg[2,*], P. Todd[3], and W.B. Krantz[4]

[1]Intel Corporation, Santa Clara, CA 95054-3202
[2]University of Colorado, Boulder, CO 80309-0427
[3]Space Hardware Optimization Technology, Inc., Greenville, IN 47124
[4]University of Cincinnati, Cincinnati, OH 45221-0171

Introduction

Macrovoids (MVs) are large (10–50 μm) pores often found in polymeric membranes prepared via phase-inversion techniques. They are generally considered undesirable, as they adversely affect the permeability properties and performance of polymeric membranes for microfiltration, ultrafiltration, and reverse osmosis. However, MVs can be useful in certain thin-film applications in which vapor transmission is necessary, or for use as reservoirs for enzymes or liquid membrane material. If more could be learned about the nature and causes of MV formation, it might be possible to devise techniques to control and/or prevent MV formation that are more effective than those currently employed.

Two hypotheses for the MV growth mechanism have been advanced. Reuvers [1] proposed that once initiated, MV growth can be attributed to diffusion of (primarily) solvent to the MV nuclei. Because this mechanism does not involve gross movement of the MV, the presence or absence of body forces such as buoyancy should not significantly affect MV growth. Moreover, Reuvers asserts that interfacial processes (such as solutocapillary convection (SC)) do not affect MV formation. If this is the correct mechanism, addition of a surfactant to the membrane casting solution should not affect MV morphology. Although originally formulated for MVs observed in wet-cast membranes (*i.e.*, where phase inversion is caused by contacting the polymer solution with a nonsolvent bath), the logic used by Reuvers applies to dry-cast membranes as well (*i.e.*, where phase inversion is caused by evaporation of a volatile solvent from a polymer/solvent/ nonsolvent solution). On the other hand, Shojaie *et al*. [2] proposed that solutocapillary convection induced by a steep surface-tension gradient along the MV/bulk solution interface enhances mass transfer to the growing MV. This interfacial convection exerts a force that pulls the growing MV downward into the casting solution [3]. Both buoyancy and viscous drag hinder MV growth by inhibiting this motion. Thus, removing the buoyancy force by casting in microgravity should augment MV growth according to this hypothesis. Moreover, Berg and Acrivos [4] have shown that surfactants stabilize liquid/liquid interfaces against solutocapillary flow through a phenomenon known as surface elasticity. If solutocapillary convection is indeed the main driving force for MV growth, addition of a surfactant additive to the casting solution should markedly retard MV growth.

*corresponding author

Whereas neither surface tension nor gravity has a significant effect on MV growth according to the first hypothesis, buoyancy forces should be important if the second hypothesis is correct. The overall goal of this research is to test these two hypotheses in order to improve our understanding of the MV growth process in solvent-cast polymeric membranes. Studying MV growth in low-g conditions is pivotal to our ability to discriminate between these two hypotheses.

I. Materials and Methods

In order to investigate the effects of buoyancy on MV growth, a set of membrane-casting experiments was conducted on the NASA KC-135 aircraft [5]. These experiments used casting solutions of cellulose acetate (CA)/acetone/water and were designed to study the effect of casting thickness (75 or 150 μm), gravity (0-g or 1-g), composition (pure water and aqueous solutions of 300 ppm Triton X-100 (J.T. Baker Co.) or 300 ppm Fluorad FC-170C (3M) surfactant), and solvent/nonsolvent (S/NS) ratio (2:1, 2.33:1, or 2.75:1 by weight). The concentration of polymer (Eastman 398-10 with an average MW of 40,000 and acetyl content of 39.8%) was held constant at 10 wt%.

A separate set of ground-based experiments was performed in order to determine the effects of surfactants on macrovoid penetration depth (MVPD). Membranes were cast with a single initial thickness (1.02 mm) from solutions with a single composition (10 wt% CA, 28 wt% nonsolvent, and 62 wt% acetone). The only variable in these experiments was the nonsolvent used (water or water with 300 ppm Triton X-100).

Modeling studies have shown that subtle changes in gas-phase mass-transfer dynamics can have profound effects on the morphology of dry-cast membranes [2]. Therefore, we used a membrane casting apparatus (MCA) identical to that described by Konagurthu *et al*. [3] in all KC-135 experiments. Because gas-phase mass-transfer is driven by diffusion in this apparatus, it is not affected by the presence or lack of gravity. In contrast, the gas-phase mass-transfer dynamics associated with membranes dry-cast via traditional techniques would be significantly altered in a low-gravity environment. A more traditional apparatus, identical to the one described by Shojaie *et al*. [2], was used in the penetration-depth (PD) experiments.

Quantitative evaluation of the final membrane morphology was obtained from scanning electron micrographs (SEM) [5, 6]. Computer-based analysis of these micrographs was performed to measure the following properties: Linear MV number density ($\overline{N}_{MV}$), MV area fraction (X_{MV}), MV size ratio (MVSR) and MV penetration depth (MVPD), where

$$\overline{N}_{MV} = \text{Number of MVs / Length of cross section},$$

$$X_{MV} = \text{Area occupied by MVs / Area of cross section},$$

$$\text{MVSR} = (\text{Final membrane thickness} \times X_{MV}) / \overline{N}_{MV},$$

$$\text{MVPD} = \text{Distance from membrane top surface to MV bottom surface.}$$

The significance of the observed differences in these properties was evaluated using standard statistical techniques.

Ground-based videomicroscopy (VM) experiments were also conducted to study MV growth during the dry casting of CA/acetone/nonsolvent solutions [5]. Solid TiO_2 particles (Degussa Aerosil P25, average primary particle size = 21 nm) were added to the casting solution to act as tracer particles for flow visualization. Experiments were performed with a casting solution composition of 10 wt% CA, 30 wt% nonsolvent, 60 wt% acetone, and 450 ppm TiO_2. The nonsolvent utilized was either water or water with 300 ppm Triton X-100 surfactant.

All microscopy experiments were performed on a Nikon EFD-3 optical microscope. Images were recorded with a JVC-TK1270 CCD camera and ported to a computer (Apple Power Macintosh G3) for storage and analysis (NIH Scion Image 1.62a image analysis software). In several of the experiments, a dark-field filter was used to enhance the contrast between MVs, tracer particles, and the surrounding casting solution. An infrared filter was used to avoid heating of the casting solution. The casting solution was injected between two horizontal glass plates with a spacing of ~800 μm. Phase separation and MV growth were caused by evaporation of acetone from the open end of the parallel glass plates. The VM permitted observing the advance of the demixing front, the initiation and growth of MVs, and the flow field via the use of tracer particles.

II. Results and Discussion

No MVs were observed in any of the membranes cast with an initial thickness of 75 μm. This is consistent with experiments performed by Paulsen *et al.* [7] and demonstrates that MVs are never present in membranes cast below a certain minimum initial thickness. In addition, none of the membranes cast with a S/NS ratio of 2.75:1 contained MVs. Moreover, the final thickness of membranes cast with an initial thickness of 150 μm often varied considerably. Therefore, the following discussion of the casting results only applies to membranes with a final thickness of 20-40 μm cast from solutions with a S/NS ratio of 2:1 or 2.33:1. Overall, in almost all cases the MVs penetrate to the bottom surface of the membranes. Qualitative comparison of SEM images reveals that MVs are generally larger in membranes with an S/NS ratio of 2:1 than in otherwise equivalent membranes with a S/NS ratio of 2.33:1. In addition, qualitative analysis of SEM images of membranes cast from surfactant-free solutions with a S/NS ratio of 2:1 (Figure 1) suggests that MV growth is augmented in 0-g relative to 1-g. Indeed, statistical analysis reveals that $\overline{N}_{MV}$, X_{MV}, and MVSR are all significantly higher in membranes cast from surfactant-free solutions with a S/NS ratio of 2:1 in zero-g than in otherwise equivalent membranes cast in 1-g. These results provide important evidence that solutocapillary convection does occur at the MV/solution interface and tends to augment MV growth, at least for the particular conditions used in these experiments.

In contrast, we found that buoyancy has no statistically significant effect on $\overline{N}_{MV}$ in membranes cast from solutions containing surfactants and/or solutions with an S/NS ratio of 2.33:1. Moreover, although X_{MV} was not measured for these membranes, qualitative analysis of SEM images did not indicate any obvious, consistent differences in MV size or structure between these particular membranes. Thus, buoyancy has no significant effect on MV growth in membranes cast from solutions with an S/NS ratio of 2.33:1 and/or solutions containing surfactants. However, this observation does not necessarily imply that the solutocapillary hypothesis is invalid. Because buoyancy should have no major effect on MV growth in the absence of solutocapillary convection, it is not surprising that buoyancy had no effect on MV growth in surfactant-containing membranes, as surfactants inhibit solutocapillary convection via surface elasticity. Moreover, it is not surprising that buoyancy had no significant effect on membranes cast from solutions with a S/NS ratio of

2.33:1 since *both* buoyancy (force proportional to MV radius cubed) and viscous drag (force proportional to MV radius to the first power) inhibit growth via solutocapillary convection. It is quite possible that the buoyancy force was insignificant relative to the drag force on the small MVs typical of membranes cast from solutions with an S/NS ratio of 2.33:1. Calculations performed by Pekny [5] support this claim.

The effect of surfactant solutes on MV morphology is illustrated in Figure 2. MVs are typically larger in surfactant-free membranes cast from solutions with a S/NS ratio of 2.33:1 than in equivalent surfactant-containing membranes in both 0- and 1-g. Moreover, surfactant-containing membranes cast from solutions with a S/NS ratio of 2.33:1 were the only membranes for which MVPD < final membrane thickness. These observations are consistent with the solutocapillary hypothesis but not the diffusive hypothesis. However, no such trends are evident in membranes cast from solutions with a S/NS ratio of 2:1. This is possibly due to the relatively fast demixing kinetics observed in such solutions [5]; demixing occurs so rapidly that surfactant solutes do not have sufficient time to diffuse to the MV/solution interface and inhibit solutocapillary convection. However, we also found that $\overline{N}_{MV}$ is significantly higher in surfactant-containing membranes cast in 1-g from solutions with a S/NS ratio of 2:1 than in otherwise equivalent surfactant-free membranes. The reason for this trend is not clear.

Perhaps the most direct way to verify that solutocapillary convection occurs is to investigate the effects of buoyancy and surfactants on MVPD. Unfortunately, this requires casting relatively thick membranes to ensure that MVs do not penetrate the entire membrane thickness. It was not possible to cast sufficiently thick membranes that completely phase separate and solidify during the short duration of 0-g available on the KC-135 (20-30 sec). However, a separate set of ground-based experiments was performed in order to determine the effects of surfactants on MVPD. The results of these experiments are summarized in Table 1. Representative morphologies of the PD membranes are shown in Figure 3. As expected, MVPD, as well as $\overline{N}_{MV}$, X_{MV}, and MVSR are all higher in surfactant-free membranes than in membranes containing Triton X-100 surfactant, indicating that solutocapillary convection tends to augment MV growth in these membranes. However, the small sample sizes used in these experiments did not enable a statistically significant difference to be established. If these trends can be verified, such results would provide additional support for the SC hypothesis.

Table 1. MV Parameters of Penetration Depth-Experiment Membranes

Surfactant	Final Thickness (μm)	$\overline{N}_{MV}$	X_{MV}	MVSR	MVPD
None	280±23	12±9	7±5	1950±750	80±13
Triton	280±30	4±5	2±1	1100±390	61±18

Flow visualization experiments can provide information that is quite useful in assessing the characteristics of MV growth. Prior to the onset of demixing, considerable cellular motion of tracer particles near the casting solution (CS)/gas (G) interface was observed. The tracer particles moved in a more-or-less circular pattern at relatively high velocities (~50 μm/sec). Although it is difficult to measure the size of these convection cells because they were larger than the field of view of the

microscope, we estimate that they are ~1-2 mm in diameter. These convection cells quickly dissipated when the solution at the CS/G interface began to demix (after approximately one minute). The volume of the demixed region increased with time as the demixing front advanced further into the casting solution. After the convection cells dissipated, the tracer particle motion slowed considerably to ~3-4 μm/sec. Although the results indicated that the fluid velocity normal to the plane of the demixing front was faster near the MV boundary than in the bulk solution, the differences were not statistically significant. Moreover, rapid circulatory motion was observed within the MVs. Interestingly, the particles appeared to penetrate into the MVs, thereby suggesting some type of convection into the MVs. The MV growth in these experiments was undoubtedly influenced by solutocapillary convection at the MV interface.

It is worth noting that very little particle motion could be seen after the onset of demixing if the casting fluid was observed in real-time. This is due to the relatively slow mass-transfer associated with dry casting in this flow-visualization macrovoid (VFMV) apparatus. It was necessary to play back videos of demixing and MV formation 15-20 times faster than real time in order to observe the fluid motion. From these videos it became apparent that MV growth occurs in these VFMV experiments in three distinct phases: (1) fast initial growth; (2) an intermediate period of slow growth; and (3) subsequent collapse. However, it is quite possible that the latter two phases of MV growth might not occur in conventional membrane casting owing to the limited time available for demixing.

III. Acknowledgement

The authors gratefully acknowledge support of this research by the NASA Microgravity Research Division (NAG8-1475), 3M Corporation, Bioserve Space Technologies and the NSF I/U CRC Center for Membrane Applied Science and Technology (MAST) at the University of Colorado (CU), and the CU Graduate School (Dean's Small Grant Award).

REFERENCES

1. Reuvers, A.J. Ph.D. Dissertation. University of Twente. 1987.
2. Shojaie, S.S., W.B. Krantz and A.R. Greenberg, *J. Mem. Sci.* 1994, 94, 255. (Parts I and II)
3. Konagurthu, S., W.B. Krantz, and P. Todd, *Proc. of Euromembrane '95*.
4. Berg, J.C. and A. Acrivos, *Chem. Eng. Sci.* 1965, 20, 737.
5. Pekny, M.R., MS Thesis. University of Colorado-Boulder. 1999.
6. Pekny, M.R., J. Zartman, A.R. Greenberg, W.B. Krantz, and P. Todd, *ACS Polymer Preprints* 2000, 41, 1060.
7. Paulsen, F.G.; Shojaie, S.S.; Krantz, W.B. *J. Mem. Sci.* 1994, *91*, 265.

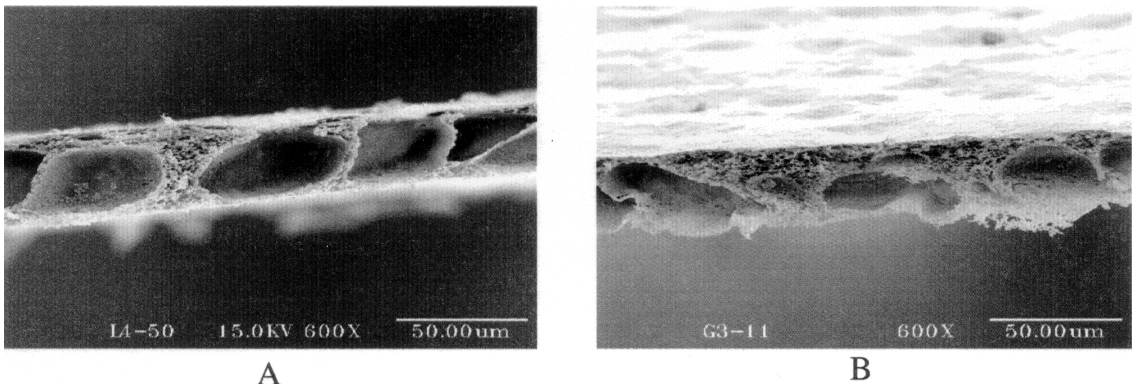

Figure 1. SEM micrographs of membranes cast with an initial thickness of 150 µm from solutions with pure water NS and an S/NS ratio of 2:1. *A* was cast in 0-g, and *B* was cast in 1-g.

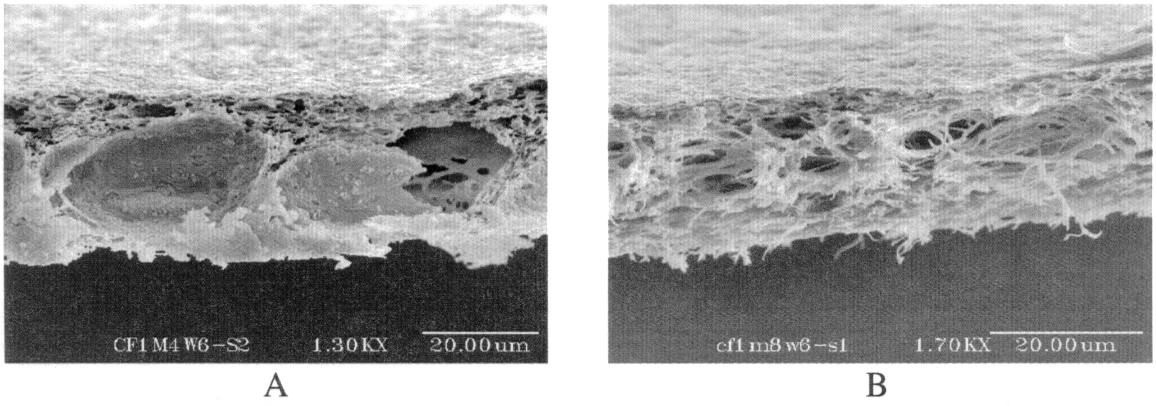

Figure 2. SEM micrographs of membranes cast in 1-g with an initial thickness of 150 µm from solutions with an S/NS ratio of 2.33:1. *A* was cast with pure water NS, and *B* was cast with water containing 300-ppm Fluorad FC-170C surfactant.

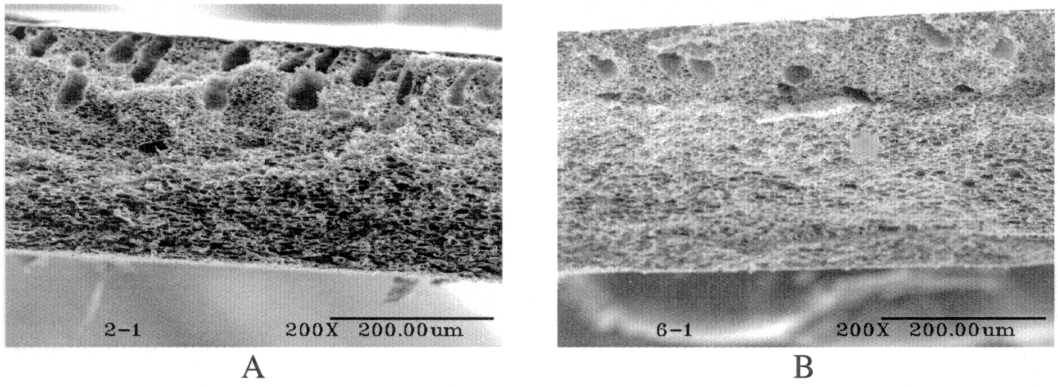

Figure 3. SEM micrographs of membranes cast in 1-g with an initial thickness of 1.02 mm from solutions containing 10% CA, 28% NS and 62% acetone (S/NS=2.21:1). *A* was cast with pure water NS, and *B* was cast with water containing 300-ppm Triton X-100 surfactant.

UTILIZING CONTROLLED VIBRATIONS IN A MICROGRAVITY ENVIRONMENT TO UNDERSTAND AND PROMOTE MICROSTRUCTURAL HOMOGENEITY DURING FLOATING-ZONE CRYSTAL GROWTH

A.V. Anilkumar[1], J. Bhowmick[1], and R.N. Grugel[2]

[1]Vanderbilt University, Box 1743-B, Nashville, TN- 37235
[2]NASA Marshall Space Flight Center MS-SD47, Huntsville, AL-35812

ABSTRACT

Our previous experiments with $NaNO_3$ float-zones revealed that steady thermocapillary flow can be balanced/offset by the controlled surface streaming flow induced by end-wall vibration. In the current experiments we are examining the effects of streaming flow on steadying/stabilizing nonsteady thermocapillary flow in such zones. To this effect we have set up a controlled $NaNO_3$ half-zone experiment, where the processing parameters, like zone dimensions and temperature gradients, can be easily varied to generate nonsteady thermocapillary flows. In the present paper we present preliminary results of our investigations into stabilizing such flows by employing end-wall vibration.

I. Introduction

The float-zone technique for unidirectional semiconductor crystal growth is an established self-contained materials processing technique. Its advantages are that it precludes introduction of impurities from the crucible walls, and it minimizes crystal defects attributed to expansion/ contraction stresses at the solidification-crucible interface. The typical procedure in float-zoning involves feeding a polycrystalline rod at the top into the melt zone, where it is melted in a non-contact fashion by a ring heater, and is withdrawn at the bottom as a single crystal. Normally a dopant is added to the feed rod to produce a crystal with desired properties.

The float-zone technique has attracted a lot of attention in the Space-based materials processing context. However, here, one needs to be worried about gravity-independent thermocapillary convection, arising from variations in the surface tension at the melt/vapor interface, which can cause non-uniform dopant distribution and crystal striations[1], which are detrimental to crystal quality.

In order to minimize/eliminate the detrimental effects of thermocapillary convection, we have examined the role of end-wall vibration in offsetting thermocapillary flow[2]. Our novel experiments have revealed that end-wall vibration generates a surface streaming flow that can be used to offset thermocapillary flow. We have demonstrated the beneficial effects of surface streaming flow in half-zones of silicone oil, and Sodium Nitrate[2, 3]. Also, our preliminary float-zone solidification experiments with Sodium Nitrate-Barium Nitrate eutectic alloy have pointed out the favorable changes in microstructure brought about by vibration-induced streaming flow[3, 4]. In addition,

we have initiated a parallel theoretical effort to understand the fluid dynamics of vibration-induced streaming and the balancing of thermocapillary flows[5].

As advancement on our experimental efforts, we are concentrating on balancing/steadying nonsteady thermocapillary flows in sodium nitrate half-zones. In a model apparatus, where one end of a sodium nitrate crystal is heated to generate a liquid bridge (half-zone), we see that the thermal field is readily oscillatory. The oscillations of the thermal field are at a frequency of around 1 Hz (varying with zone dimensions etc.). These temperature oscillations are a manifestation of the hydrothermal wave instability of the steady thermocapillary flow. Tracer particles can be seen traversing the flow field in a zigzag fashion, following the onset of this instability. In the context of float-zone processing, it has been established that oscillatory thermocapillary flows cause dopant striations in crystals and undermine their quality[1]. The oscillatory thermocapillary flow field exhibits many pure and mixed instability modes[6], which can be both axisymmetric and non-axisymmetric. In our preliminary experiments. We have examined the effects of vibration-induced surface streaming flow on an axisymmetric nonsteady thermocapillary flow field. Here, we have been able to null the thermal oscillations and sustain both a steady and a quiescent flow field.

II. Experimental Results

The schematic of the experimental apparatus is shown as an inset in the figure 1. The polycrystalline rod of $NaNO_3$ is positioned vertically, and a cylindrical liquid bridge of molten $NaNO_3$ is established by controlled heating at the top. The basis of thermal control is the control of the heater temperature to utmost precision by employing a feedback proportional integral derivative (PID) control loop, using a thermocouple embedded in the heater rod. The zone thermalization time is about two hours, after which the flow balancing experiments are initiated. Depending on the zone heating conditions, the zone takes on different aspect ratios. The onset of oscillatory thermocapillary flow is monitored by a fine-wire thermocouple inserted into the zone. Figure 1, shows the results in a 8 mm diameter $NaNO_3$ zone. Initially, the thermal oscillations have a peak-peak amplitude of 12K, at a frequency of around 0.5 Hz. (with a carrier wave riding on them a frequency of ~ 0.04 Hz.). Visual observation of the particle trajectories in the cross section of the zone confirms that the oscillatory flow field is axisymmetric (n = 2 mode[6]). On vibrating the bottom end-wall at a frequency of 1000 Hz. with an amplitude of ~10 μm (rms), the thermal field becomes quiescent as the thermal oscillations are damped out. On stopping the vibration, the thermal field becomes oscillatory again. It can also be noticed that the mean temperature, as measured by the thermocouple, drops on initiating the vibration. This is probably due to thermal redistribution in the zone, and the added heat loss from the zone surface due to vibration. However, when the mean temperature of the field is restored to its original level, by raising the temperature at the heater end, the thermal balance can still be sustained by vibration.

III. Future Work

The present results confirm that end-wall vibration does stabilize the oscillatory thermocapillary field. We are in the process of systematically investigating the balancing effects for the whole range of nonsteady thermocapillary flow fields, including both axisymmetric and non-axisymmetric. The next logical step in these efforts is to examine the effects of end-wall vibration during float-zone processing under nonsteady thermocapillary conditions. To facilitate this, we have built a float-zone apparatus with a very precise control of the processing temperature and environment. Among other approaches, we intend to process the crystal under imposed oscillatory

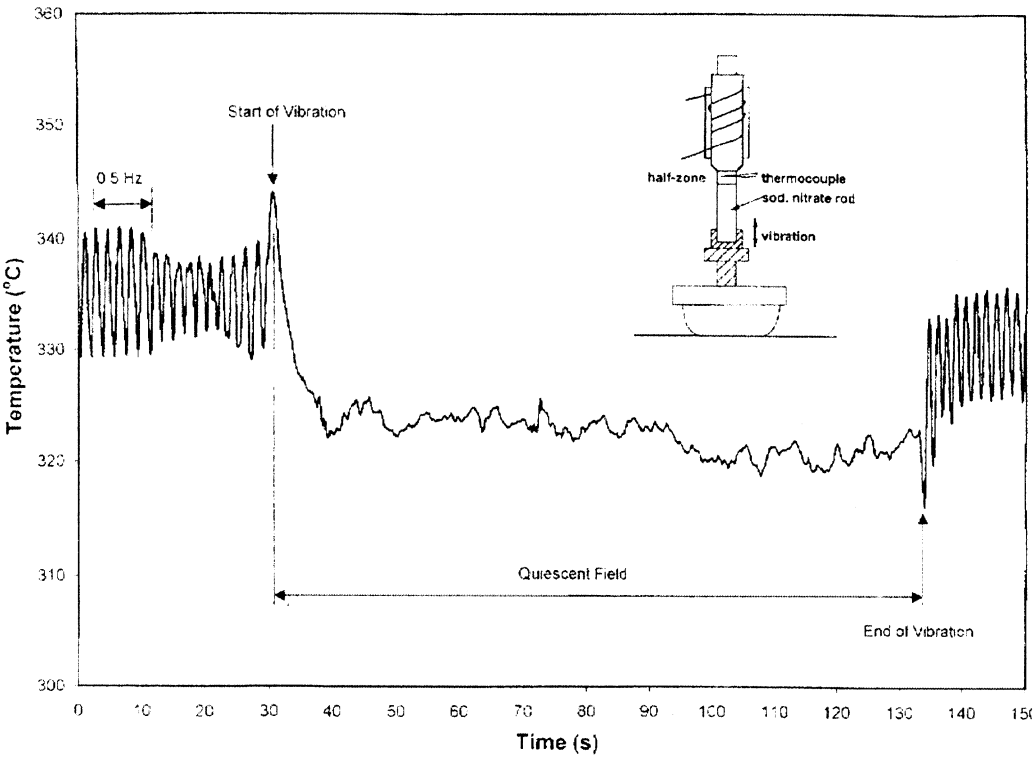

Figure 1. Effect of end-wall vibration on nonsteady thermocapillary flow.

thermal conditions, by varying the melt temperature in a periodic way. We will examine the processed crystal (both morphology and microstructure), when processed both upwards and downwards. We will then vibrate the zone, to examine the effects of end-wall vibration on crystal quality. While the ultimate objective of our experiments will be to work with semiconductor materials, at this intermediate level we are interested in demonstrating certain cause-effect relationships with the analogue materials like Sodium Nitrate, and Sodium Nitrate-Barium Nitrate eutectics.

IV. Acknowledgements

Appreciation is expressed to NASA, Grant # NAG8-1230, and the Universities Space Research Association.

REFERENCES

1. M. Jurisch and W. Loser, ' Analysis of periodic non-rotational W striations in Mo single crystal due to nonsteady thermocapillary convection', J. Cryst. Growth **102**, 214 (1990).
2. A.V. Anilkumar, R.N. Grugel, X.F. Shen, C.P. Lee, and T.G. Wang, 'Control of thermocapillary convection in a liquid bridge by vibration', J. Appl. Phys. **73**, 4165 (1993).
3. R.N. Grugel, X.F. Shen, A.V. Anilkumar, and T.G. Wang, 'The influence of vibration on microstructural uniformity during floating-zone crystal growth', J. Cryst. Growth 142, 209 (1994).
4. X.F. Shen, A.V. Anilkumar, R.N. Grugel, and T.G. Wang, 'Utilizing vibration to promote microstructural homogeneity during floating-zone crystal growth processing', J. Cryst. Growth 165, 438 (1996).
5. C.P. Lee, A.V. Anilkumar, and T.G. Wang, 'Streaming generated in a liquid bridge due to nonlinear oscillations driven by the vibration of an end wall', Phys. Fluids 8, 3234 (1996).
6. F. Preisser, D. Schwabe, and A. Scharmann, 'Steady and oscillatory thermocapillary convection in liquid columns with free cylindrical surface', J. Fluid Mech. 126, 545 (1983).

SOLIDIFICATION PROCESSING OF IMMISCIBLE LIQUIDS IN THE PRESENCE OF APPLIED ULTRASONIC ENERGY

R.N. Grugel[1], A.I. Fedoseyev[2], and S. Kim[3]

[1]Marshall Space Flight Center, MS-SD47, Huntsville, AL 35812
[2]University of Alabama in Huntsville, Center for Microgravity and Materials Research, Huntsville, AL 35895
[3]Hoseo University, Department of Materials Science and Engineering, Chung-Nam, Korea

Uniform microstructural distribution during solidification of immiscible liquids (*e.g.*, oil and water; aluminum and lead) on Earth is hampered by inherent density differences between the phases. Microgravity processing minimizes settling but segregation still occurs due to gravity independent wetting and coalescence phenomena. Experiments with the transparent organic, metal analogue, succinonitrile-glycerol system were conducted in conjunction with applied ultrasonic energy. The processing parameters associated with this technique have been evaluated in view of optimizing dispersion uniformity. Characterization of the experimental results in terms of a modeling effort will also be presented.

INTER- DIFFUSION IN THE PRESENCE OF FREE CONVECTION

P. K. Gupta and Z. Hu

Dept. of Materials Science and Engineering
The Ohio State University Columbus, OH 43210

ABSTRACT

Compositional changes during isothermal interdiffusion generally cause density variations in a diffusing system. Such compositionally-induced density variations give rise to free convection in ground based experiments and interfere with the analysis of composition profiles for determining interdiffusion coefficients. One method to eliminate the effect of free convection during interdiffusion is to carry out experiments in zero-gravity conditions. Another way is to examine the influence of convection and correct for this effect when analyzing for diffusion coefficients in ground based experiments. This paper describes experimental results on interdiffusion in PbO-SiO2 melts under conditions both stable and unstable with respect to free convection.

I. Introduction

Interdiffusion describes the evolution of compositional inhomogeneities in systems containing more than one component. Since most material systems of technological importance contain at least two components and since interdiffusion is the rate controlling step in the kinetics of most processing operations involving compositional changes (such as crystal growth, dissolution, and chemical reactions), establishment of accurate values of interdiffusion coefficients and of their variations with respect to temperature and composition is of much interest.

Frequently, interdiffusion coefficients are determined by measuring the composition profile by a suitable analytical probe following the diffusive evolution of a planar sharp boundary between two homogeneous solutions of different compositions. When the time of diffusion is short enough so that the end compositions (away from the sharp boundary) are not influenced, the method is referred to as the 'infinite couple method'. For diffusion in an infinite couple configuration, the composition profiles after different diffusion times can be superimposed on each other when plotted against a reduced variable $x/\sqrt{t}$ where x is the distance from the location of the original sharp boundary (called the Matano interface) and t is the time of diffusion. The location of the Matano interface can be determined using a simple procedure from the measured composition profile [1]. The values of the interdiffusion coefficient as a function of composition can be determined from the measured composition profile of an infinite couple using the Matano analysis [2]. Sauer and Freise [3] have extended the Matano analysis to systems exhibiting changes in volume upon mixing. While the infinite couple method works well for solid systems, the measurements in liquids (such as liquid metals, electrolyte solutions, slags, and magmas) and in supercooled liquid systems (such as glasses) are complicated in ground-based experiments because of i) the presence of free convection during interdiffusion caused by compositionally-induced density variations and ii) the pres-

ence of the gravitational drift (i.e., bias caused by gravitational driving force on the random motions of different components present in the system). It is the gravitational drift that is responsible for a non-uniform composition profile in equilibrium with the denser component segregating towards the bottom. To determine interdiffusion coefficients in liquids, there are two possible approaches. One is to design experiments in which the effect of free convection is eliminated or reduced. The other is to take into account the presence of free convection and gravitational drift in the analysis of infinite couple composition profiles. Most of the effort to date has followed the first approach. In ground-based experiments, a simple way to reduce free convection is to align the composition (and consequently the density) gradient along the direction of gravity. A stable (convection-free) configuration results when density decreases monotonically upwards at all points at all times (we shall refer to this as the '*normal*' configuration) [4]. In the normal configuration, convection is eliminated in those binary systems where the density varies monotonically with composition. In binary systems where the density varies non-monotonically with composition as well as in multicomponent systems [5], convection during interdiffusion cannot be ruled out. When density increases in the upward direction (the '*inverted*' configuration), convective instabilities can develop provided that the magnitude of the solutal Rayleigh number (Ra) [6] is larger than a critical value:

$$Ra = g \beta L^4 (dc/dz) / (\nu D) \qquad (1)$$

Here g is the acceleration due to gravity, β the solutal expansion coefficient [$= 1/\rho_o (d\rho/dc)$], $\rho$the mass density, c the composition, ν the kinematic viscosity ($= \eta/\rho$ where η is the shear viscosity), D the interdiffusion coefficient, z the vertical distance (measured positive in the upward direction), and L is a characteristic length. For a circular tube, L is equal to the radius, r, of the tube. It is customary, following equation (1), to use thin capillary tubes [7] to reduce convection. However, Frischat [8] has shown that new problems arise due to prominent capillary effects in thin tubes. Furthermore, use of capillaries does not eliminate the need to account for the gravitational drift. It is desirable, therefore, to develop the second approach of exploring analytical schemes of correcting for the presence of free convection and gravitational drift in ground based experiments. This forms the motivation of our research program.

II. Relevance to Microgravity

Determination of interdiffusion coefficients in liquid systems using isothermal composition profiles from ground based diffusion experiments is difficult due to the presence of free convection caused by compositionally-induced density variations and due to the gravitational drift. The compositionally-induced density variations are intrinsic to interdiffusion and cannot be eliminated. In principle, only the experiments in zero-gravity environment, where both convection and gravitational drift are eliminated, can yield the true values of the interdiffusion coefficients. Zero gravity experiments are also needed to validate any procedure developed to correct for free convection and gravitational drift in ground based experiments.

III. Experiments and Results

Our approach is to develop an analytical procedure for correcting for the presence of free convection and of gravitational drift when analyzing composition profiles in ground-based interdiffusion experiments. The validity of this procedure will be established in future by performing experiments in a zero-gravity environment which will provide the accurate values of the diffusion coefficients. We plan to develop such a correction procedure for the infinite couple configuration in binary systems with the diffusion direction both parallel and anti-parallel to the direction of gravity. To characterize the effect of convec-

tion on interdiffusion, we are studying experimentally composition profiles in infinite couples in both the normal configurations (with density increasing downward in the direction of gravity) where convection is not expected to be present as well as in the inverted configurations (with density increasing upwards) where convective instabilities may develop. In addition, we haven chosen to work with an oxide glass system. This is because diffusion profiles can be easily preserved by quenching the diffusion couple to room temperature where subsequent measurements can be performed at a convenient time. Simple liquids are not suitable for this purpose since the diffusion profiles change rapidly at room temperature making it difficult to study them. A second reason for choosing oxide glass is that the viscosity of oxide glasses can be varied over a wide range by a suitable choice of temperature. Lastly, oxide glasses being transparent allow for a visual examination of flow fields. In particular, we have chosen the PbO-SiO_2 glass system because it exhibits a large single phase composition range in which good glass can be formed easily, has a large monotonic increase in density with composition (thus the convection effects should be enhanced), the composition profiles can be measured accurately by techniques such as the electron microprobe, and many of the relevant properties have been measured as a function of composition in this system (see Table I).

PbO-SiO_2 glasses of three different compositions (40, 50, and 60 mole% PbO) were melted. Most of our experiments to date have used the 40% and 50 % compositions. Table I lists some relevant properties of these two compositions. Disks of 7 mm diameter and 3 to 4 mm height were core-drilled from bubble free regions of the cast glass. These disks were polished to make both sides planar and parallel. Infinite couples were made by placing disks of different compositions inside flat bottom platinum cups (7 mm ID and 10 mm height). The assembly was preheated for half hour at a temperature of 300C to remove any entrapped air. Diffusion experiments were performed at two temperatures (750C and 850C) in both normal and inverted orientations for two different times (30 and 90 minutes). After quenching to room temperature, the platinum crucibles were sectioned along the axis and the resulting sections were polished for examination by optical microscopy as well for chemical analysis by a Phillips XL30 scanning electron microscope. Calibration standards were used to convert intensities into mole fractions. Examples of our results are shown in figures 1 to 3 which show composition profiles (in terms of mole percent PbO) versus distance from their respective Matano interfaces. Figure 1 compares two profiles on the same sample showing typical reproducibility in our experiments. Figure 2 shows profiles of the normal configuration samples at 750C for different diffusion times. Figure 3 compares profiles of normal and inverted configurations at 750C and 30 minutes.

IV. Discussion

Figure 4 shows the composition profiles of Figure 2 plotted as function of the reduced variable $x/\sqrt{t}$. The profiles of these normal couples superimpose well on each other indicating that interdiffusion is the dominant process and that the effect of gravitational drift is negligible. These profiles were analyzed for interdiffusion coefficients using the Sauer and Freise procedure [3] taking into account the variation of the molar volume with composition. For this purpose, the molar volume was determined as a function of composition at 750 C. Using these molar volume data, interdiffusion coefficients were calculated as a function of composition. Figure 5 shows the results. As expected, our values are somewhat less than the values at 850 C reported by Schmalzried [10]. We have also performed experiments at 850 C and these data are being analyzed presently. The value of the Rayleigh number (equation 1) at 750 C is extremely large ($\approx 2.5 \times 10^8$) for the inverted sample implying that this configuration is unstable [9]. The results in figure 3 show that there is little effect of convection at 750 C since the profiles of normal and inverted couples are in good agreement. Furthermore, there was no evidence of convection from either

optical or SEM examination of these samples. The probable reason for the absence of any observable convection in these samples at 750C in spite of the large Rayleigh number is that the kinetics of convection are extremely slow for this system. The Rayleigh number for the inverted sample at 850 C is also large ($\approx 5x10^7$). A preliminary back scattered image of the inverted sample at 850C and 30 minutes shows clear evidence of convection in this sample. The experiments at 850 C are in the process of being analyzed.

V. Conclusions

This work is still in progress and the complete results are not available at this time. However, we observe the following trends:

a) The effect of gravitational drift appears to be negligible in this system at 750 C.
b) Convection in inverted samples appears to be insignificant at 750C even though the Rayleigh number is large (greater than the critical value).
c) Convection is definitely present in inverted samples at 850C.
d) The values of the interdiffusion coefficient as a function of composition found in this work are in reasonable agreement with the published work.

REFERENCES

1. F. J. J. Van Loo, Acta Metallurgia, 18, 1107 (1970).
2. P. Shewmon, "Diffusion in Solids", TMS (1989).
3. F. Sauer and V. Freise, Z. Elektrochem, 66, 353 (1962).
4. R. P. Wendt, J. Phys Chem, 66, 1740 (1962).
5. J. S. Turner, Ann Rev Fluid Mech, 17, 11 (1985).
6. R. A. Wooding, Proc. Royal Soc. (London) Series A, 252, 120 (1959).
7. J. D. Verhoeven, Trans. Met. Soc. AIME, 242, 1937 (1968).
8. M. Meier and G. H. Frischat, Phys. and Chem. of Glasses, 34, 71 (1993).
9. E. L. Cussler, "Diffusion: Mass Transfer in Fluid Systems" Cambridge (1997).
10. H. Schmalzried, Y. Tanaka, and B. Langanke, Z. Physikalische Chemie, 128S, 205 (1981)

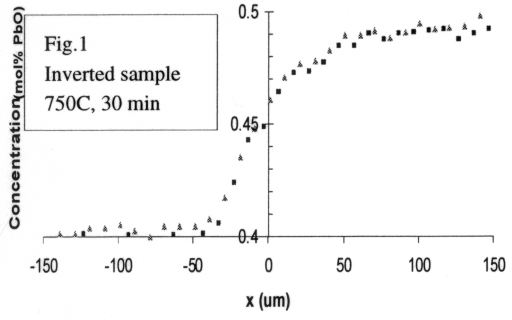

Figure 1. An example of the reproducibility of composition profiles in our experiments.

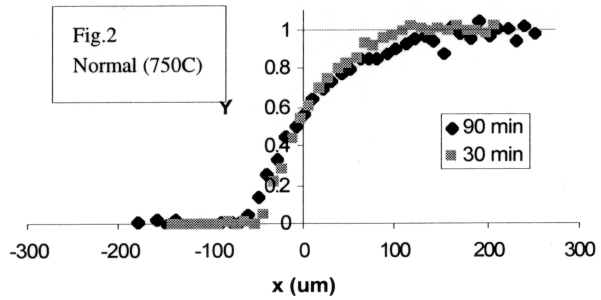

Figure 2. Comparison of normalized composition profiles at 750C of normal couples for diffusion times of 30 and 90 minutes.

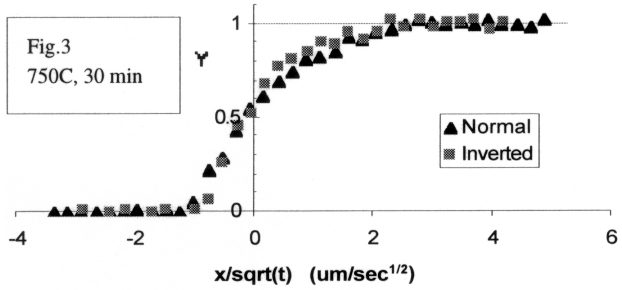

Figure 3. Comparison of the normalized composition profiles at 750C of normal and inverted couples both for diffusion times of 30 minutes.

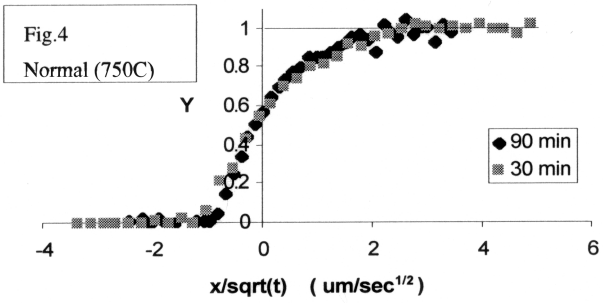

Figure 4. Composition profiles of figure 2 replotted against the reduced variable $x/\sqrt{t}$.

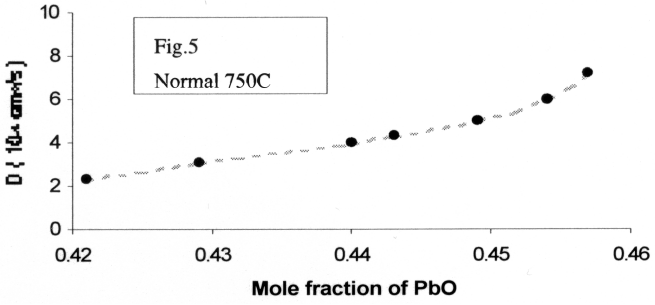

Figure 5. The interdiffusion coefficient values shown as a function of the mole fraction of PbO at 750 C.

Table 1. Properties of PbO-SiO_2 glasses.

		40mol% PbO	50mol% PbO
$\rho^{750°C}$ (g/cm^3)	[*]	5.24	5.69
T_g (K)	[*]	720	683
$\beta^{750°C}$		0.83	0.76
$v^{750°C}$(cm^2/s)		1206.1	61.5
$D^{750°C}$(cm^2/s)	[*]	10^{-9}	$5*10^{-9}$
$v^{850°C}$(cm^2/s)		87.9	6.9
$D^{850°C}$(cm^2/s)	[10]	10^{-8}	$2*10^{-8}$

[*]: Bansal, N.P., and Doremus, R.H., "Handbook of Glass Properties", Academic Press, (1986).

Appendix A: Author Index

Main Menu

M

N

O

P

R

S

T

U

V

W

Y

Z

AADSF	Advanced Automated Directional Solidification Furnace
AAL	Aero-Acoustic Levitation
AAS	Atomic Absorption Spectroscopy
ACCESS	Advanced Cosmic Ray Composition Experiment
ACRT	Accelerated Crucible Rotation Technique
AGHF	Advanced Gradient Heating Facility
AHP	Axial Heat Processing
ALICE	Heavy ion experiment being built for the Large Hadron Collider (LHC) project at CERN, Geneva, Switzerland
ALN	Aluminum Nitride
AOTF	Acousto-Optic Tunable Filter
AP	Ammonium persulfate
ASD	Accelerated Stokesian Dynamics
ATD	Advanced Technology Development
ATLAS	Atmospheric Laboratory for Applications and Science
BCC	Body Centered Cubit
BEI	Backscatter Electron Images
BG	Bioactive Glass
BMG	Bulk Metallic Glasses
BODIPY	A fluorescein derivative
BRYNTRN	Radiation transport code
BUU	Boltzmann-Uehling-Uhlenbeck
CA	Cellular Automata
CAM	CO_2 Acquisition Membrane
CCD	Charge-Coupled Device
CDC	Container-Less Directional Solidification
CERN	European Laboratory for Particle Physics (Geneva, Switzerland)
CFD	Computational Fluid Dynamics
CFX	Commercial Flow Code
CGB	Crystal Growth with a Baffle
CGH	Coupled Growth in Hypermonotectics
CMDS	Center for Materials Development in Space (at the University of Alabama in Huntsville, AL)
CMMR	Center for Microgravity Materials Research (at the University of Alabama in Huntsville, AL)
CNES	Centre National d'Etudes Spatiales (France)
CNES	Centre Nationale d'Études Spatiales ("National Center for Space Studies," French Space Agency)
CRI	Containerless Research Incorporated
CSLM	Coarsening in Solid-Liquid Mixtures
CSM	Colorado School of Mines
CT	Computed Tomography
CTE	Coefficient of Thermal Expansion
CVS	Coupled Vibrational Stirring
DCC	Diffusion Cloud Chamber

Main Menu

DCVA	N,N-dimethyl-p-(2,2-dicyanovinyl) aniline
DDC	Dynamic Decompression and Cooling
DECLIC	Dispositif pour l'Etude de la Croissance et des Liquides Critiques (DECLIC) (Facility for the Study of the Growth and the Fluids near Critical Point)
DIT	Diffusion Interface Theory
DLS	Dynamic Light Scattering
DLVO	Derjaguin, Landau, Verwey, Overbeek
DMSO	High temperature solvent
DNS	Direct Numerical Simulations
DODMAC	Dimethyldioctylammonium chloride
DOE	Department of Energy
DPIMS	Diffusion Processes in Molten Semiconductors
DSC	Differential Scanning Calorimetry
DTA	Differential Thermal Analysis
EBW	Electron-Beam Welding
ED	Electron Diffraction
EDG	Electro Dynamic Gradient
EDGE	Equiaxed Dendritic Solidification Experiment
EDS	Energy Dispersion Spectroscopy
EDS	Energy Dispersive X-ray Spectroscopy
EIS	Electrochemical Impedance Spectroscopy
EIT	Effective Interfacial Tension
EITIC	Effective Interfacial Tension Induced Convection
EKTAPRO	A Kodak camera
ELMS	Evolution of Local Microstructures
ELT	Electrodynamic Levitator Trap
EML	Electromagnetic Levitator
EPD	Etch Pit Density
EPMA	Electron Probe Micro-Analyzer
ESL	Electrostatic Levitation/Levitator
EXPRESS	(Expedite the Processing of Experiments to Space Station)
FCC	Face Centered Cubit
FDLB	Finite Difference Lattice Boltzmann
Fe-MAS	Fe-bearing Magnesium Aluminosulphate
FLUENT	Computational fluid dynamics software
FLUKA	A Monte-Carlo simulation code for radiation transport
FTIR	Fourier Transform Infrared Spectrometry
FZ	Float/floating Zone
GCR	Galactic Cosmic Ray
GDMS	Glow Discharge Mass Spectroscopy
GEANT	A Monte-Carlo simulation code for radiation transport
GF-AA	Graphite Furnace- Atomic Absorption Spectroscopy
GFL	Gas Film Levitation
GOSAMR	Gelation of Sols; Applied Microgravity Research
GTAW	Gas-Tungsten Arc Welding
GUI	Graphical User Interface
HAD	High-density Amorphous

HARV	High Aspect Ratio Vessel
HBT	High Performance Transistors
HD	Hoop Direction
HDDA	hexane diol diacrylate
HDIV	Holographic Diffraction Image Velocimetry
HDPE	High-Density Polyethylenes
HECT	High Energy Transport Code
HEDS	Human Exploration and Development of Space
HEMA	hydroxyethyl methancrylate
HETC	A Monte-Carlo simulation code for radiation transport
HPCVD	High Pressure Chemical Vapor Deposition
HPMS	High Pressure Mass Spectrometry
HRTXD	High Resolution Triple Crystal X-ray Diffractometry/Diffraction
HTESL	High Temperature Electrostatic Levitator
HTSC	High Temperature Superconductor
HZETRN	Radiation transport code
ICP-AES	Inductively Coupled Plasma-Atomic Emission Spectroscopy
ICP-MS	Inductively Coupled Plasma-Mass Spectrometry
IDGE	Isothermal Dendritic Growth Experiment
IML	International Microgravity Laboratory
INFN	Instituto Nazionale di Fisica Nucleare (Italian National Nuclear Physics funding agency)
IR	Infra Red
ISCP	*In-Situ* Consumables Production
ISPP	*In-Situ* Propellent Production
ISRU	*In-Situ* Resource Utilization
ISS	International Space Station
ITO	Indium-Tin-Oxide
JPL	Jet Propulsion Laboratory (Pasadena, CA, managed by the California Institute of Technology)
JSC	NASA Johnson Space Center (Houston, TX)
KC-135	A NASA aircraft that performs parabolic maneuvers to produce short durations (20 seconds) of reduced gravity (0.01 g) environment.
KDP	Potassium Dihydrogen Phosphate
KSC	NASA Kennedy Space Center (Cape Canaveral, FL)
LAHET	A Monte-Carlo simulation code for radiation transport
LaRC	NASA Langley Research Center (Hampton, VA)
LB	Langmuir-Blodgett
LB	Lattice Boltzmann
LBNL	Lawrence Berkeley National Laboratory
LBW	Laser Beam Welding
LC	Liquid Crystal
LCP	Liquid Crystalline Polymeric
LDA	Low-density Amorphous
LDPE	Low-Density Polyethylenes
LED	Light Emitting Diode
LEO	Low Earth Orbit

LET	Linear Energy Transfer
LF	Low Frequency
LIF	Laser-Induced Fluorescence
LM	Lockheed Martin
LMS	Life and Microgravity Spacelab
LPS	Liquid Phase Sintering
MCA	Membrane Casting Apparatus
MCA	Multi-Channel Analyzer
MD	Molecular Dynamics
MDO	Multidisciplinary Optimization
MEPHISTO	Matérial pour l'Étude des Phenomènes Intéressants de la Solidification sur Terre et en Orbite ("Apparatus for the Study of Interesting Phenomena of Solidification on Earth and in Orbit")
MeV	One million electron volts
MGB	Materials Science Glovebox
MI	Melt Indices
MIT	Massachusetts Institute of Technology
MITH	Millikelvin Thermostat
MNR	Nuclear Magnetic Resonance
MOCVD	Metal Organic Chemical Vapor Deposition
MOR	Modulus of Rupture
MRD	Microgravity Research Division
MSAD	Microgravity Science and Applications Department
MSFC	NASA Marshall Space Flight Center (Huntsville, AL)
MSL	Microgravity Sciences Laboratory
MSL-1R	Materials Sciences Laboratory (R represents the reflight)
MST	Microscopic Solvability Theory
MST	Minimum Spanning Tree
MTF	Membrane Test Facility
MTF	Moderate Temperature Facility
MTV	Molecular Tagging Velocimetry
MV	Macrovoids
MVPD	Macrovoid Penetration Depth
NAA	Neutron Activation Analysis
NCS	Nucleation of Crystals from Solution
NCSL	Nanocrystal Superlattices
ND	Normal Direction
NIST	National Institute of Standards and Technology
NLO	Nonlinear Optical
NMR	Nuclear Magnetic Resonance
NRA	NASA Research Announcement
NSF	National Science Foundation
NUCFRG	A radiation transport code
OB	Oberbeck-Boussinesq
OMCVD	Organometallic Chemical Vapor Deposition
OO	Object Oriented
ORBITEC	Orbital Technologies Corporation

OSD	Office of the Secretary of Defense
PAW	Physics Analysis Workstation
PB	Polybutadiene
PBT	Polybutylene terephthalate
PC	Personal Computer
PD	Penetration Depth
PDLC	Polymer Dispersed Liquid Crystals
PDM	Power Distribution Module
PE	Polyethylene
PEE	Polyethylethylene
PEO	Polyethylene Oxide
PEP	Particle Engulfment and Pushing
PI	Principal Investigator
PID	Proportional Integral Derivative
PIPS	Polymerization Induced Phase Separation
PIV	Particle Image Velocimetry
PL	Photoluminescence
PMMA	polymethylmethacrylate
POCC	Payload Operations Control Center (NASA MSFC)
Pr	Prandtl Number
PS	polystyrene
PVA	Pivalic Acid
PVT	Physical Vapor Transport
QMSFRG	Quantum Multiple Scattering Fragmentation Model, a radiation transport code
QMST	Quantum Multiple Scattering Theories
R2PI	Resonant-Two-Photon-Ionization
RDF	Radial Distribution Function
RDR	Requirements Definition Review
RE	Rare Earth
Re	Reynolds Number
REMPI	Resonance Enhanced Multiphoton Ionization
RIDGE	Rensellaer Isothermal Dendritic Growth Experiment
RMF	Rotating Magnetic Field
ROMP	Ring Opening Metathesis Polymerization
ROOT	An object-oriented physics analysis infrastructure
RQC	Rotating Quench Cell
RWV	Rotating Wall Bioreactor Vessel
SAMS	Space Acceleration Measurement System
SAXS	Small-Angle X-ray Scattering
Sc	Schmidt Number
SCN	Succinonitrile
SCN-ACE	Succinonitrile-acetone
SCN-E	Succinonitrile-ethanol
SCN-GLY	Succinonitrile-glycerol
SCN-W	Succinonitrile-water
SCR	Science Concepts Review
SD	Standard Deviations

SD	Stokesian Dynamics
SEM	Scanning Electron Microscopy
SEP	Société Européene de Propulsion
Sh	Sherwood Number
SHG	Second Harmonig Generation
SHIVA	Spaceflight Holography Investigation in a Virtual Apparatus
SHS	Self-propagating High-temperature Synthesis
SIMS	Secondary Ion Mass Spectrometry
SIPS	Solvent Induced Phase Separation
SIV	Stereoscopic Imaging Velocimetry
SLI	Solid-liquid Interface
SOPC	Stearoyl, Oleoyl Phosphatidylcholine
SPE	Solar Particle Event
STM	Scanning Tunneling Microscopcy
STS	Space Transportation System (Shuttle/external tank/solid rocket booster system, also a Shuttle mission designation)
SUBSA	Solidification Using the Baffle in Sealed Ampoules
SWBXT	Synchrotron White Beam X-ray Topography
TDSE	Transient Dendritic Solidification Experiment
TEM	Transmission Electron Microscopy
TEM	Tunneling Electron Microscope
TEMC	Thermoelectromagnetic Convection
TEMPUS	Tiegelfreies Elektromagnetisches Prozessieren Unter Schwerelosigkeit (German Electromagnetic Containerless Processing Facility)
TEOS	Tetraethylorthosilicate
TEPC	Tissue Equivalent Proportional Counter
THM	Traveling Heater Method
TIPS	Thermally Induced Phase Separation
TLS	Two Level System
TMF	Traveling Magnetic Field
TRL	Technology Readiness Level
TRR	Time-Resolved Relativity
TSL Theory	Classical Theory of Phase Coarsening by Todes, Lifshitz, and Slyozov
TTT	Time-Temperature-Transformation
UAH	University of Alabama in Huntsville
UF	Utilization Flight
USAXS	Ultra-Small Angle X-ray Scattering
USML	United States Microgravity Laboratory
USMP	United States Microgravity Payload
UV	Ultra Violet
UW	University of Wisconsin
VB	Vertical Bridgman
VFMV	Flow-Visualized Microvoid
WAXS	Wide Angle X-Ray Scattering
WCI	Wetting Characteristics of Immiscibles
XCAP	Image analysis software
XRD	X-ray Diffraction

XRF	X-ray Fluorescence
YAG	Yttria Aluminum Garnet
YSV	Yttria Stabilized Zirconia
YSZ	Yttria-stabilized zirconia
ZBLAN	A glass which contains the fluorides of zirconium, barium, lanthanum, aluminum, and sodium

Prof. Reza Abbaschian
University of Florida
Department of Materials Science and Engineering
P.O. Box 116400
132 Rhines Hall
Gainesville, FL 32611-2066
T 352-846-3300; F 352-392-7219
rabba@mse.ufl.edu

Dr. M. Abid
University of Southern California
Department of Aerospace and Mechanical Engineering
Los Angeles, CA 90089-1453

Prof. James H. Adair
Pennsylvania State University
Materials Science and Engineering
217 Materials Research Laboratory
University Park, PA 16802
T 814-863-6047; F 814-863-9704
JAdair@mrl.psu.edu

Dr. J. D. Adam
Northrop Grumman Corporation
Science and Technology Center
ESSS MS-3D14, ATL
1212 Winterson Road
Linthicum, MD 21090
F 410-765-7652

Prof. Rigoberto Castillo Advincula
University of Alabama, Birmingham
Department of Chemistry
CHEM Building, Room 201
901 14th Street South
Birmingham, AL 35294-1240
T 205-934-8286; F 205-934-2543
gobet@uab.edu

Dr. N. I. Agladze
Cornell University
Laboratory of Atomic and Solid State Physics
517 Clark Hall
Ithaca, NY 14853-2501
F 607-255-6428

Mr. William Ainsworth
University of Southern Mississippi
Department of Chemistry and Biochemistry
P. O. Box 5043
Hattiesburg, MS 39406-5053
F 601-266-6045

Prof. Ali Reza Alemozafar
Stanford University
Laboratory for Advanced Materials
McCullough Building
476 Lomita Mall
Stanford, CA 94305-4045

Prof. Iwan Alexander
Case Western Reserve University
Department of Mechanical and Aerospace Engineering
416 Glennan Building
10900 Euclid Avenue
Cleveland, OH 44106
T 216-368-6045; F 216-368-6445
ida2@po.cwru.edu

Dr. Andreas Alexandrou
Worcester Polytechnic Institute
Mechanical Engineering Department
100 Institute Road
Worcester, MA 01609-2280
T 508-831-5147; F 508-831-5680
andalexa@wpi.wpi.edu

Prof. Jens Alkemper
Northwestern University
Department of Materials Science and Engineering
2225 North Campus Drive
Evanston, IL 60208-3108
T 847-491-5943; F 847-491-7820
j-alkemper@nwu.edu

Prof. M. Cengiz Altan
University of Oklahoma
School of Aerospace and Mechanical Engineering
865 Asp Avenue, Room 212
Norman, OK 73019
T 405-325-1737; F 405-325-1088
altan@ou.edu

Mr. Alex Altgilbers
Vanderbilt University
5527 Kenadall Drive
Nashville, TN 37209
T 615-322-2756; F 615-343-8645
asa@vuse.vanderbilt.edu

Prof. D. M. Anderson
George Mason University
Department of Mathematical Sciences
Fairfax, CA 27599

Prof. Timothy J. Anderson
University of Florida
Department of Chemical Engineering
P.O. Box 116005
Gainesville, FL 32611
T 352-392-0881; F 352-392-9513
tim@nersp.nerdc.ufl.edu

Prof. J. Barry Andrews
University of Alabama, Birmingham
Department of Materials and
Mechanical Engineering, BEC 254
1150 10th Avenue Southwest
Birmingham, AL 35294
T 205-934-8452; F 205-934-8485
bandrews@Engr.uab.edu

Prof. A. V. Anilkumar
Vanderbilt University
1743 Station B
Nashville, TN 37235
T 615-343-7293; F 615-343-8730
nil@vuse.vanderbilt.edu

Prof. Robert E. Apfel
Yale University
Department of Mechanical Engineering
Room M-1
9 Hillhouse Avenue
P.O. Box 208286
New Haven, CT 06520-8286
T 203-432-4346; F 203-432-7654
robert.apfel@yale.edu

Dr. Neer Asherie
Massachusetts Institute of Technology
Department of Physics
Center for Materials Science and Engineering
Material Processing Center
77 Massachusetts Avenue
Cambridge, MA 02139

Dr. Michael R. Ayers
Lawrence Berkeley National Laboratory
1 Cyclotron Road
MS 70-110A
Berkeley, CA 94720
T 510-486-4292; F 510-486-7303
mrayers@inreach.com

Prof. Portonovo S. Ayyaswamy
University of Pennsylvania
Department of Mechanical Engineering and
Applied Mechanics
Philadelphia, PA 19104-6315
T 215-898-8362; F 215-573-6334
ayya@eniac.seas.upenn.edu

Prof. Michael J. Aziz
Harvard University
Division of Engineering and Applied Sciences
29 Oxford Street
Cambridge, MA 02138-2901
T 617-495-9884; F 617-495-9837
maziz@harvard.edu

Prof. Klaus J. Bachmann
North Carolina State University
Department of Materials Science and Engineering
Research Bldg.-1, Room 219
Box 7919, Centennial Campus
100 Capability Drive
Raleigh, NC 27695-7919
T 919-513-1926; F 919-515-3419
k_bachmann@ncsu.edu

Prof. Renal Backov
University of Florida
Department of Chemistry
P.O. Box 117200
Gainesville, FL 32611-7200
F 352-392-3255

Prof. F. F. Badavi
Christopher Newport University
1 University Place
Newport News, VA 23606

Dr. Gautam D. Badhwar
NASA JSC
Solar System Division
Mail Code SN
2101 NASA Road One
Houston, TX 77058-3696
T 281-483-5065; F 281-483-5276
gautam.d.badhwar1@jsc.nasa.gov

Dr. S. Baker
University of Massachusetts
Polymer Science and Engineering Department
Amhurst, MA 01003-4530

Prof. R. Michael Banish
University of Alabama, Huntsville
CMMR, VBRH, D-11
301 Sparkman Drive
Huntsville, AL 35899
T 256-824-6969; F 256-824-6944
banishm@email.uah.edu

Prof. Frank S. Bates
University of Minnesota
Department of Chemical Engineering and
Materials Science
Amundson Hall
421 Washington Avenue, S.E.
Minneapolis, MN 55455-0132

Prof. R. H. Baughman
New Jersey Institute of Technology
University Heights
Newark, NJ 07102-1982

Prof. Robert J. Bayuzick
Vanderbilt University
Department of Chemical Engineering
303A Olim Hall
Nashville, TN 37235
T 615-322-7047; F 615-343-8645
bayuzick@vuse.vanderbilt.edu

Prof. Christoph Beckermann
University of Iowa
Department of Mechanical Engineering
2412 SC Engineering Building
Iowa City, IA 52242-1527
T 319-335-5681; F 319-335-5669
becker@Engr.uiowa.edu

Mr. Giulio Bellizia
University of Illinois, Chicago
2828 North Pine Grove, Apt. 317
Chicago, IL 60657
T 312-413-7601; F 312-413-0447

Prof. Andre Benard
Michigan State University
Department of Mechanical Engineering
2555 Engineering Building
East Lansing, MI 48824
T 517-432-1522; F 517-353-1750
benard@egr.msu.edu

Prof. George B. Benedek
Massachusetts Institute of Technology
Department of Physics
Room 13-2005
77 Massachusetts Avenue
Cambridge, MA 02139-4307
T 617-253-4828; F 617-225-2585
gbb@mit.edu

Dr. K. W. Benz
Kristallographisches Inst.
Der Universitat
Hebelstrasse 25 D-7800
Freiberg, Germany

Prof. H. Bermudez
University of Pennsylvania
120 Hayden Hall
3320 Smith Walk
Philadelphia, PA 19104

Prof. Jerry Bernholc
North Carolina State University
Department of Physics
Box 8202
Raleigh, NC 27695-8202
T 919-515-3126; F 919-515-7331
bernholc@ncsu.edu

Dr. David Berns
Tufts University
Department of Physics and Astronomy
Science and Technology Center, Room 208
4 Colby Street
Medford, MA 02155
F 617-627-3744

Dr. J. Bhowmick
Vanderbilt University
1743 Station B
Nashville, TN 37235
F 615-343-8730

Dr. Konstantinos Boboridis
National Institute of Standards and Technology
100 Bureau Drive
MS 8555
Gaithersburg, MD 20899-8555

Dr. William J. Boettinger
National Institute of Standards and Technology
Metallurgy Division
Materials Science and Engineering Lab.
Bldg. 223, Room A153
Gaithersburg, MD 20899
T 301-975-6160; F 301-975-4553
wboettinger@nist.gov

Prof. G. Bonilla
University of Massachusetts, Amherst
Department of Chemical Engineering
Goessmann Laboratory
Amherst, MA 01003

Prof. Nicholas Booth
University of Alabama in Huntsville
CMMR, VBRH, D-29
Huntsville, AL 35899
T 256-824-6019; F 256-824-6499
boothn@email.uah.edu

Prof. Christopher Bowman
University of Colorado, Boulder
Department of Chemical Engineering
Campus Box 424
Boulder, CO 80309-0424
T 303-492-3247; F 303-492-4341
bowmanc@colorado.edu

Prof. John F. Brady
California Institute of Technology
Division of Chemistry and Chemical Engineering
210-41
Pasadena, CA 91125
T 626-395-4183; F 626-568-8743
jfbrady@caltech.edu

Prof. A. Brannan
University of Minnesota
Department of Chemical Engineering and Materials Science
Amundson Hall
421 Washington Avenue S.E.
Minneapolis, MN 55455-0132

Prof. Robert F. Brebrick
Marquette University
Department of Mechanical and Industrial Engineering
P.O. Box 1881
Milwaukee, WI 53201-1881
robert.brebrick@marquette.edu

Prof. Kenneth Brezinsky
University of Illinois, Chicago
Department of Chemical Engineering
810 South Clinton Street
Chicago, IL 60607-7000
kenbrez@uic.edu

Prof. M. E. Brown
Kansas State University
Department of Chemistry
311 CHEM-BIOCHEM
Manhattan, KS 66506
mpeterso@ksu.edu

Dr. R. Brun
CERN
EP/AIP
Bat. 12 1-013
CH-1221 Geneva 23, Switzerland
F 41 22 767 9480

Prof. Arnold Burger
Fisk University
Center for Photonic Materials and Devices
Department of Physics
1000 17th Avenue N
Nashville, TN 37208-3051
T 615-329-8516; F 615-329-8634
aburger@dubois.fisk.edu

Dr. Craig Burkhard
Clarkson University
International Center for Gravity, Materials Science and Applications
Box 5814
Potsdam, NY 13699-5814
F 315-268-3833

Dr. Federico Carminati
CERN
EP/AIP, Bat. 12 1-013
CH-1221 Geneva 23, Switzerland
T 41 22 767 4959; F 41 22 767 9480
frederico.carminati@cern.ch

Dr. William E. Carswell
University of Alabama in Huntsville
Mail Code SD47
Marshall Space Flight Center
MSFC, AL 35812
T 256-544-0829; F 256-544-8762
bill.carswell@msfc.nasa.gov

Dr. Adrian V. Catalina
Universities Space Research Assoc.
Mail Code SD47
Marshall Space Flight Center
MSFC, AL 35812
T 256-544-1326; F 256-544-2559
adrian.catalina@msfc.nasa.gov

Prof. Peggy Cebe
Tufts University
Department of Physics and Astronomy
Science and Technology Center, Room 208
4 Colby Street
Medford, MA 02155
T 617-627-3365; F 617-627-3744
peggy@cebe.phy.tufts.edu

Prof. Soyoung Stephen Cha
University of Illinois, Chicago
Department of Mechanical Engineering
M/C 251, 2039 ERF
842 West Taylor Street
Chicago, IL 60607-7022
T 312-996-9612; F 312-413-0447
sscha@uic.edu

Dr. Arnon Chait
NASA GRC
Mail Stop 105-1
21000 Brookpark Road
Cleveland, OH 44135
T 216-433-3558; F 216-433-5033
arnon.chait@grc.nasa.gov

Mr. Yuri Chekanov
University of Southern Mississippi
Department of Chemistry and Biochemistry
P. O. Box 5043
Hattiesburg, MS 39406-5053
F 601-266-6045

Prof. James R. Chelikowsky
University of Minnesota
Department of Chemical Engineering and Materials Science
151 Amundson Hall
421 Washington Avenue S.E.
Minneapolis, MN 55455-0132
T 612-625-4837; F 612-626-7246
jrc@msi.umn.edu

Dr. P. Y. P. Chen
University of New South Wales
School of Mechanical and Manufacturing Engineering
Sydney, NSW 2052, Australia
T 61-2-385-5162; F 61-2-633-1222

Prof. Weinong (Wayne) Chen
The University of Arizona
Department of Aerospace and Mechanical Engineering
1130 N. Mountain Avenue
Tucson, AZ 85721
T 520-621-6114; F 520-621-8191
wchen@allen.ame.arizona.edu

Prof. Alexander A. Chernov
Universities Space Research Assoc.
Mail Code SD47
Marshall Space Flight Center
MSFC, AL 35812
T 256-544-9196; F 256-544-8762
alex.chernov@msfc.nasa.gov

Prof. Michael Cima
Massachusetts Institute of Technology
Materials Processing Center
Bldg. 12-011
77 Massachusetts Avenue
Cambridge, MA 02139-4307
T 617-253-6877; F 617-258-6936
mjcima@mit.edu

Prof. Noel A. Clark
University of Colorado, Boulder
Department of Physics
Boulder, CO 80309-0390

Prof. Juan Pablo Claude
University of Alabama, Birmingham
Department of Chemistry
CHEM Building, Room 201
901 14th Street South
Birmingham, AL 35294-1240
T 205-975-2478; F 205-934- 2543
jpclaude@uab.edu

Dr. M. S. Clowdsley
NASA LaRC
MS 188 B
Hampton, VA 23681
F 757-864-8094

Dr. Sharon Cobb
NASA MSFC
Mail Code SD47
Marshall Space Flight Center
MSFC, AL 35812
T 256-544-7791; F 256-544-8762
sharon.cobb@msfc.nasa.gov

Prof. Carlos Coimbra
Drexel University
Philadelphia, PA 19104

Prof. Reid F. Cooper
University of Wisconsin, Madison
Department of Materials Science and Engineering
1509 University Avenue
Madison, WI 53706-1595
T 608-262-1133; F 608-262-8353
cooper@engr.wisc.edu

Dr. Sam R. Coriell
National Institute of Standards and Technology
100 Bureau Drive, MS 8555
Gaithersburg, MD 20899-8555
T 301-975-6169; F 301-975-4553
sam.coriell@nist.gov

Prof. Thomas H. Courtney
Michigan Technological University
Department of Materials Science and Engineering
1400 Townsend Drive
Houghton, MI 49931-1295
T 906-487-2036; F 906-487-2934
thc@mtu.edu

Prof. Gregory P. Crawford
Brown University
Division of Engineering
Box D
182 Hope Street
Providence, RI 02912
T 401-863-2858; F 401-863-912
Gregory_Crawford@brown.edu

Mr. Kevin Croat
Washington University
Physics Department
Box 1105
One Brookings Drive
Saint Louis, MO 63130
T 314-935-6379; F 314-935-6219
tkc@howdy.wustl.edu

Prof. Arne Croell
TU Bergakademie Freiberg
Inst. für NE-Metallurgie und Reinststoffe
Leipziger Str. 23
D-09599 Freiberg, Germany
T 49-3731-39-2017
F 49-3731-39-2268
arne.croell@inemet.tu-freiberg.de

Mr. Daniel Crunkleton
University of Florida
Department of Chemical Engineering
P.O. Box 116005
227 CHE
Gainesville, FL 32611
T 352 392-2420; F 352 392-9513
dcrunkle@che.ufl.edu

Dr. Francis A. Cucinotta
NASA JSC
Code SN
2101 NASA Road 1
Houston, TX 77058
T 281-483-0968; F 281-483-2696
fcucinot@ems.jsc.nasa.gov

Dr. Peter A. Curreri
NASA MSFC
Mail Code SD48
Marshall Space Flight Center
MSFC, AL 35812
T 256-544-7763; F 256-544-6660
peter.curreri@msfc.nasa.gov

Prof. Jonathan Dantzig
University of Illinois, Urbana
Department of Mechanical Engineering
MC-244
1206 W. Green Street
Urbana, IL 61801
T 217-333-4107; F 217-244-6534
dantzig@uiuc.edu

Prof. Delbert E. Day
University of Missouri, Rolla
Materials Research Center
1870 Miner Circle
Rolla, MO 65409-1170
T 573-341-4354; F 573-341-2071
day@umr.edu

Dr. Henry C. de Groh III
NASA GRC
Mail Stop 105-1
21000 Brookpark Road
Cleveland, OH 44135
T 216-433-5025; F 216-433-5033
henry.c.degroh@grc.nasa.gov

Prof. Graham D. de Vahl Davis
University of New South Wales
School of Mechanical and
Manufacturing Engineering
Sydney, NSW 2052, Australia
T 61-2-385-4099; F 61-2-633-1222
g.devahldavis@unsw.edu.au

Prof. Kenneth A. Debelak
Vanderbilt University
Department of Chemical Engineering
Box 1604, Station B
Nashville, TN 37235
T 615-322-2088; F 615-343-7951
kenneth.a.debelak@vanderbilt.edu

Prof. Jeffrey J. Derby
University of Minnesota
Department of Chemical Engineering and Materials Science
151 Amundson Hall
421 Washington Avenue, S.E.
Minneapolis, MN 55455-0132
T 612-625-1313; F 612-626-7246
derby@tc.umn.edu

Mr. G. Dhanaraj
State University of New York, Stony Brook
Department of Materials Science and Engineering
Stony Brook, NY 11794-2275

Prof. Alejandro R. Diaz
Michigan State University
Department of Mechanical Engineering
East Lansing, MI 48824
T 517-353-0825; F 517-353-1750
diaz@egr.msu.edu

Prof. Nikolaus Dietz
North Carolina State University
Department. of Materials Science
P.O. Box 7919
Raleigh, NC 27695-7919
T 919-515-8804; F 919-515-3419
ndietz@unity.ncsu.edu

Prof. B. Discher
University of Pennsylvania
Department of Chemical Engineering
BioEngineering and Mechanical Engineering
Philadelphia, PA 19104-6315

Prof. Dennis E. Discher
University of Pennsylvania
Department of Chemical Engineering
BioEngineering and Mechanical Engineering
Philadelphia, PA 19104-6315

Dr. Peter Dold
Universitat Freiburg
Kristallographisches Institut
Hebelstrasse 25
D-79106, Freiberg 1, Germany
T 49-761-203-6449; F 49-761-203-6434
pit@sgi3.krist.uni-freiburg.de

Dr. James Patton Downey
NASA MSFC
Mail Code SD48
Marshall Space Flight Center
MSFC, AL 35812
T 256-544-6432; F 256-544-2102
james.downey@msfc.nasa.gov

Prof. Edward L. Dreizin
New Jersey Institute of Technology
Department of Mechanical Engineering
University Heights
Newark, NJ 07102-1982
T 973-596-5751; F 973-642-4282
dreizin@njit.edu

Dr. Y. Du
Michigan Technological University
Department of Materials Science and Engineering
1400 Townsend Drive
Houghton, MI 49931-1295
F 906-487-2934

Prof. Paul Ducheyne
University of Pennsylvania
Department of BioEngineering
120 Hayden Hall, 3320 Smith Walk
Philadelphia, PA 19104-6315
T 215-898-8501; F 215-573-2071
ducheyne@seas.upenn.edu

Prof. Michael Dudley
State University of New York, Stony Brook
Department of Materials Science and Engineering
Stony Brook, NY 11794-2275
T 631-632-8500; F 631-632-8052
michael.dudley@sunysb.edu

Dr. T. Duffar
Centre d'Etudes Nuclaires Grenoble
85X Avenue des Martyrs
38041 Grenobel Cedex, France
F 33-76-88-51-18

Dr. Thierry Dumont
Université Lyon I
Laboratoire d'Analyse Numirique
Batiment 101
43 bd du 11 Novembre 1918
69622 Villeurbanne Cedex, France
F 33 4 72 44 80 53

Prof. Prabir K. Dutta
Ohio State University
Department of Chemistry
120 West Eighteenth Avenue
Columbus, OH 43210
T 614-292-4532; F 614-292-1685
dutta.1@osu.edu

Dr. Walter M. B. Duval
NASA GRC
Mail Stop 105-1
21000 Brookpark Road
Cleveland, OH 44135
T 216-433-5023; F 216-433-5033
walter.m.duval@grc.nasa.gov

Prof. M. Samy El-Shall
Virginia Commonwealth University
Department of Chemistry
1001 W. Main Street
Richmond, VA 23284-2006
T 804-828-3518; F 804-828-8599
selshall@hsc.vcu.edu

Mr. Peter Engel
Wyle Laboratories Inc., Florida Operations
Bldg. K7-569, Room 1142
Wyle-32
K7-569 Saturn Causeway
P.O. Box 21072
Kennedy Space Center, FL 32815
T 321-861-5158; F 321-861-6163
peterengle@hotmail.com

Dr. Edwin Ethridge
NASA MSFC
Mail Code SD47
Marshall Space Flight Center
MSFC, AL 35812
T 256-544-7767; F 256-544-1777
edwin.ethridge@msfc.nasa.gov

Prof. James W. Evans
University of California, Berkeley
Department of Materials Science and Engineering
Berkeley, CA 94720
T 510-642-3807; F 510-642-9164
evans@socrates.berkeley.edu

Dr. Rebecca L. A. Everman
University of Wisconsin, Madison
Department of Materials Science and Engineering
1509 University Avenue
Madison, WI 53706-1595
F 608-262-8353

Prof. Alexandre Fedoseyev
University of Alabama, Huntsville
CMMR
VBRH, Research Institute D-4
Huntsville, AL 35899
T 256-824-6889; F 256-824-6944
alex@cmmr.uah.edu

Prof. Robert S. Feigelson
Stanford University
Center for Materials Research
Press Warehouse
Stanford, CA 94305-4045
T 650-723-4007; F 650-723-3752
feigel@soe.stanford.edu

Dr. A. Ferrari
INFI
Milan, Italy

Dr. Shari Feth
University of Alabama in Huntsville
Mail Code SD47
Marshall Space Flight Center
MSFC, AL 35812
T 256-544-0519; F 256-544-8762
sheri.feth@msfc.nasa.gov

Dr. Merton C. Flemings
Massachusetts Institute of Technology
Materials Processing Center
77 Massachusetts Avenue, Rm. 8-407
Cambridge, MA 02139
T 617-253-3233; F 617-258-6886
flemings@mit.edu

Mr. David T. Frate
NASA GRC
Mail Stop 500-115
21000 Brookpark Road
Cleveland, OH 44135

Dr. Donald O. Frazier
NASA MSFC
Mail Code SD40
Marshall Space Flight Center
MSFC, AL 35812
T 256-544-7825; F 256-544-2102
don.frazier@msfc.nasa.gov

Dr. J. E. Frei
Rensselaer Polytechnic Institute
CII 9113
110 8th Street
Troy, NY 12180
F 518-276 2073

Prof. Andrienne C. Friedli
Middle Tennessee State University
Department of Chemistry
Box X076 MTSU
Murfreesboro, TN 37312
T 615-898-2071; F 615-898-5182
acfriedli@mtsu.edu

Dr. Archie Fripp Jr.
125 Little John Road
Williamsburg, VA 23185
T 757-253-2822
afripp@widomaker.com

Prof. Anup K. Gangopadhyay
Washington University, St. Louis
Department of Physics
Campus Box 1105
One Brookings Drive
St. Louis, MO 63130
T 314-935-4654; F 314-935-6379
Anup@howdy.wustl.edu

Dr. H. Gao
University of Pennsylvania
Department of Mechanical Engineering and
Applied Mechanics
Philadelphia, PA 19104-6315
F 215-573-6334

Dr. N. A. Gatsonis
Worcester Polytechnic Institute
100 Institute Road
Worcester, MA 01609-2280

Dr.Yi Ge
University of Illinois, Chicago
Department of Mechanical Engineering
M/C 251, 2039 ERF
842 West Taylor Street
Chicago, IL 60607-7022
F 312-413-0447

Dr. Georgi Georgiev
Tufts University
Department of Physics and Astronomy
Science and Technology Center
4 Colby Street, Room 208
Medford, MA 02155
F 617-627-3744

Prof. Randall M. German
The Pennsylvania State University
147 Research Bldg. West
University Park, PA 16802-6809
T 814-863-8025; F 814-863-8211
rmg4@psu.edu

Dr. Donald C. Gillies
NASA MSFC
Mail Code SD47
Marshall Space Flight Center
MSFC, AL 35812
T 256-544-9302; F 256-544-8762
donald.gillies@msfc.nasa.gov

Ms. Cindie Giummarra
Rensselaer Polytechnic Institute
CII 9113
110 8th Street
Troy, NY 12180
T 518-276 6130; F 518-276 2073
giummc@rpi.edu

Prof. Matthew Glaser
University of Colorado, Boulder
Department of Physics
Condensed Matter Lab.
Boulder, CO 80309-0390
T 303-492-3029; F 303-492-2998
glaser@bly.Colorado.edu

Prof. Martin E. Glicksman
Rensselaer Polytechnic Institute
Department of Materials Science and Engineering
Materials Research Center, Room 9111
110 8th Street
Troy, NY 12180
T 518-276-6721; F 518-276-2198
glickm@rpi.edu

Prof. Arun M. Gokhale
Georgia Institute of Technology
School of Materials Science and Engineering
778 Atlantic Drive
Atlanta, GA 30332-0245
T 404-894-2887; F 404-894-9140
arun.gokhale@mse.gatech.edu

Prof. Nigel D. Goldenfeld
University of Illinois, Urbana-Champaign
Beckman Institute
Loomis Lab, MC 704
1110 W Green
Urbana. IL 61801
T 217-333-8027
nigel@uiuc.edu
nigel@guava.physics.uiuc.edu

Dr. Vladimir D. Golyshev
All-Union Science Res. Inst. of Mineral
Raw Mat. Synthesis, VNIISIMS
Institutskaya str 1
Alexandrov-City 601600
Vladimirskaya Region; Russia
T 7-095-584-5816 or 7-(09244)92693
F 7-095-584-5816
post@thermo.vladimir.su

Dr. M. Gonik
All-Union Science Res. Inst. of Mineral
Raw Mat. Synthesis, VNIISIMS
Institutskaya str 1
Alexandrov-City 601600
Vladimirskaya Region, Russia
F 7-095-584-5816

Prof. Brian Grady
University of Oklahoma
School of Chemical Engineering and Materials Science
100 East Boyd, EC Rm. T-223
Norman, OK 73019-0628
T 405-325-4369; F 405-325-5813
bpgrady@mailhost.ecn.ou.edu

Prof. Alan R. Greenberg
University of Colorado, Boulder
Department of Mechanical Engineering
Campus Box 427
Boulder, CO 80309-0427
T 303-492-6613; F 303-492-4637
alan.greenberg@colorado.edu

Dr. Richard N. Grugel
NASA MSFC
Mail Code SD47
Marshall Space Flight Center
MSFC, AL 35812
T 256-544-9165; F 256-544-8762
richard.grugel@msfc.nasa.gov

Prof. Turgut M. Gür
Stanford University
Laboratory for Advanced Materials
McCullough Building, Room 135
476 Lomita Mall
Stanford, CA 94305-4045
T 650-723-6597; F 650-723-3044
turgut@stanford.edu

Prof. D. E. Gustafson
Vanderbilt University
Department of Chemical Engineering
P.O. Box 1604, Station B
Nashville, TN 37235

Mr. Robert J. Gustafson
Orbital Technologies Corp. (ORBITEC)
Space Center
1212 Fourier Drive
Madison, WI 53717
T 608-827-5000 Ext. 225
F 608-827-5050
gustafsonr@orbitec.com

Prof. Naomi J. Halas
Rice University
ECE Department - Mail Stop 366
6100 South Main
Houston, TX 77251
T 713-348-5611; F 713-348-5686
halas@rice.edu

Prof. Daniel A. Hammer
University of Pennsylvania
120 Hayden Hall
3320 Smith Walk
Philadelphia, PA 19104
T 215-573-6761; F 215-573-2071
hammer@seas.upenn.edu

Mr. Glen Haulenbeek
University of Alabama in Huntsville
Von Braun Research Hall, 34-M
Huntsville, AL 35899

Dr. Lawrence H. Heilbronn
Lawrence Berkeley National Laboratory
MS 74-197
One Cyclotron Road
Berkeley, CA 94720
T 510-486-4002; F 510-486-6949
LHHeilbronn@LBL.gov

Prof. John Heinbockel
Old Dominion University
Norfolk, VA 23529
jheinboc@odu.edu

Dr. J. C. Heinrich
University of Arizona
Department of Aerospace and Mechanical Engineering
Tucson, AZ 85721
T 520-621-6118
heinrich@zeus.ame.arizona.edu

Prof. William H. Hofmeister
Vanderbilt University
Department of Chemical Engineering
P.O. Box 1604, Station B
Nashville, TN 37235
T 615-322-7053; F 615-343-3202
hof@vuse.vanderbilt.edu

Dr. Dirk Holland-Moritz
Institut fur Raumsimulation
Deutsches Zentrum fur Luft -und Raumfahrt
Linder Hohe
D-51170 Cologne, Germany
T 49-0-2203-601 3292
F 49-0-2203-61768
dirk.holland-moritz@dlr.de

Prof. Mark D. Hollingsworth
Kansas State University
Chemistry Department
111 Willard Hall
Manhattan, KS 66506
T 785-532-2727; F 785-532-6666
mdholl@ksu.edu

Prof. George M. Homsy
Stanford University
Department of Chemical Engineering
Sauffer Building 3, Room113
Stanford, CA 94305
T 650-723-2419; F 650-723-9780
bud@chemeng.stanford.edu

Dr. Arlon J. Hunt
Lawrence Berkeley National Laboratory
Division of Environmental Energy Technologies
Mail Stop 70-108
One Cyclotron Road
Berkeley, CA 94720
T 510-486-5370; F 510-486-7303
ajhunt@lbl.gov

Dr. Robert W. Hyers
NASA MSFC
Mail Code SD47
Marshall Space Flight Center
MSFC, AL 358123
T 256-544-1683; F 256-544-8762
robert.hyers@msfc.nasa.gov

Dr. Ronald G. Iacocca
Pennsylvania State University
147 Research Building, West
University Park, PA 16802-6809
F 814-863-8211

Prof. Alexander F. Izmailov
Polytechnic University
Department of Chemical Engineering
Six Metrotech Center
Brooklyn, NY 11201
T 718-336-2835; F 718-336-2825
Izmailov@duke.poly.edu

Prof. Kenneth A. Jackson
University of Arizona
Arizona Materials Laboratory
Department of Materials Science and Engineering
4715 East Fort Lowell Road
Tucson, AZ 85712
T 520-322-2981; F 520-322-2993
kaj@aml.arizona.edu

Prof. Lyle Jalbert
University of Alabama, Huntsville
CMMR, Von Braun Research Hall
Huntsville, AL 35899
T 256-824-6963; F 256-824-6944
lyle.jalbert@teleionsolutions.com

Ms. Linda B. Jeter
NASA MSFC
Mail Code SD44
Marshall Space Flight Center
MSFC, AL 35812
T 256-544-7392; F 256-544-5892
linda.jeter@msfc.nasa.gov

Prof. David R. Johnson
Purdue University
School of Materials Engineering
1289 MSEE Building
West Lafayette, IN 47907-1289
T 765-494-7009; F 765-494-1204
davidjoh@ecn.purdue.edu

Dr. J. Jordan
Orbital Technologies Corp. (ORBITEC)
Space Center
1212 Fourier Drive
Madison, WI 53717
T 608-827-5000; F 608-827-5050

Dr. O. Jouravlev
Institute of Chemical Problems of Microelectronics
Vernadsky prospect 86
Moscow 117571, Russia
F 7-095-230-47-56

Dr. Frank Robert Juretzko
University of Alabama
Department of Metallurgical Engineering
Box 870202
Tuscaloosa, AL 35487-0202
T 205-348-1748; F 205-348-8574
juretzko@yahoo.com

Prof. Monica L. Kaforey
Case Western Reserve University
Department of Materials Science and Engineering
330 White Building
10900 Euclid Avenue
Cleveland, OH 44106
T 216-368-4219; F 216-368-3209
mlk14@po.cwru.edu

Ms. Natalie Kaiser
Universitat Freiburg
Kristallograph. Institute
Hebelstrasse 25
D-79104 Freiburg, Germany
T 49-761-203-6455; F 49-761-203-6434
natalie@sgi3.krist.uni-freiburg.de

Mr. Nam Hyun Kang
Pennsylvania State University
Applied Research Laboratory
150 MRI Building, Research Park
University Park, PA 16802
T 814-863-8558; F 814-863-2986
hhk105@psu.edu

Prof. David L. Kaplan
Tufts University
Department of Chemical Engineering
4 Colby Street
Medford, MA 02155
T 617-627-3251; F 617-627-3991
dkaplan1@emerald.tufts.edu

Prof. Alain S. Karma
Northeastern University
Department of Physics
111 Dana Research Center
360 Huntington Avenue
Boston, MA 02115
T 617-373-2929; F 617-373-2943
karma@neu.edu

Dr. Andrey V. Kartavykh
Institute for Chemical Problems of Microelectronics
Vernadsky prospect 86
Moscow 117571, Russia
F 7-095-230-47-56
ihpm@glas.arc.org
L22-icpm@mail.girmet.ru

Dr. Mohammad Kassemi
NTLC/NASA Glenn Research Center
Mail Stop 110-3
21000 Brookpark Road
Cleveland, OH 44135
T 216-433-5031; F 216-433-3793
mohammad.kassemi@grc.nasa.gov

Dr. Piotr Kaszynski
Middle Tennessee State University
Department of Chemistry
Box X076 MTSU
Murfreesboro. TN 37312
F 615-898-5182

Ms. Lara Keefer
Case Western Reserve University
10900 Euclid Avenue
White Building
Cleveland, OH 44106
T 216-368-0119; F 216-368-3209
lak5@po.cwru.edu

Prof. Kenneth F. Kelton
Washington University, St. Louis
Department of Physics
Campus Box 1105
One Brookings Drive
St. Louis, MO 63130
T 314-935-6228; F 314-935-6219
kfk@wuphys.wustl.edu

Prof. Tobias Kerle
University of Massachusetts
Department of Polymer Science
120 Governors Drive
Amherst, MA 01003
T 413-577-1535; F 413-577-1510
kerle@mail.pse.umass.edu

Dr. Ilyas I. Khayrullin
New Jersey Institute of Technology
Department of Electrical and Computer Engineering
University Heights
Newark, NJ 07102-1982

Dr. M.-H. Y. Kim
College of William and Mary
P.O. Box 8795
Williamsburg, VA 23187-8795

Prof. Shinwoo Kim
Hoseo University
Department of Materials Science and Engineering
Baebang Sechul-Ri Asan Chungnam
South Korea
T 82-418-540-5474
swkim@dogsur.hoseo.ac.kr

Mr. James D. Kinnison
The Johns Hopkins Applied Physics Laboratory
11100 Johns Hopkins Road
Laurel, MD 20723-6099
T 443-778-6169; F 443-778-6696
james.kinnison@jhuapl.edu

Dr. John P. Kizito
NCMR
21000 Brookpark Road
Cleveland, OH 44135
T 216-433-2275; F 216-433-3793
jpk5@po.cwru.edu

Prof. Kenneth J. Klabunde
Kansas State University
Department of Chemistry
111 Willard Hall
Manhattan, KS 66506
T 785-532-6849; F 785-532-6666
kenjk@ksu.edu

Prof. Manoochehr M. Koochesfahani
Michigan State University
Department of Mechanical Engineering
East Lansing, MI 48824
T 517-353-5311; F 517-353-7179
koochesf@egr.msu.edu

Prof. Matthew B. Koss
Rensselaer Polytechnic Institute
Materials Science and Engineering Department
CII 4225
110 8th Street
Troy, NY 12180-3590
T 518-276-2844; F 518-276-2198
kossm@rpi.edu

Prof. Sindo Kou
University of Wisconsin, Madison
Department of Materials Science and Engineering
1103 Engineering Research Building
1500 Engineering Drive
Madison, WI 53706
T 608-262-0576; F 608-262-8648
kou@engr.wisc.edu

Prof. Matthew John M. Krane
Purdue University
School of Materials Engineering
West Lafayette, IN 47907
T 765-494-4107; F 765-494-1204
krane@ecn.purdue.edu

Prof. William Krantz
University of Cincinnati
Department of Chemical Engineering
Cincinnati, OH 43221-0171
T 513-5564021 ; F 513-556-6741

Dr. Shankar Krishnan
Containerless Research, Inc.
906 University Place
Evanston, IL 60201
T 847-467-2678; F 847-467-2679
shanky@containerless.com

Prof. Anil D. Kulkarni
St. Louis University Medical Center
3635 Vista at Grand
St. Louis, MO 63110-0250
T 314-268-5274; F 314-268-5180

Mr. Jeffrey C. LaCombe
Rensselaer Polytechnic Institute
Materials Science and Engineering Department
CII Building, Room 4219
Troy, NY 12180
T 518-276-8068; F 518-276-2198
lacomj@rpi.edu

Dr. F.-C. Lai
University of Oklahoma
School of Aerospace and Mechanical Engineering
Room 212
865 Asp Avenue
Norman, OK 73019
F 405-325-1088

Prof. Ravindra B. Lal
Alabama A&M University
Department of Physics
P.O. Box 71
Normal, AL 35762
T 256-858-8148; F 256-851-5622
lal@caos.aamu.edu

Prof. David J. Larson Jr.
SUNY-SB/NASA Headquarters
Mail Code UM
Washington, DC 20546-0001
T 202-358-2237; F 202-358-2837
dlarson@hq.nasa.gov

Prof. C.-M. Lee
University of Pennsylvania
120 Hayden Hall
3320 Smith Walk
Philadelphia, PA 19104

Dr. Sandor L. Lehoczky
NASA MSFC
Mail Code SD40
Marshall Space Flight Center
MSFC, AL 35812
T 256-544-7758; F 256-544-8762
sandor.lehoczky@msfc.nasa.gov

Dr. R. A. Lemdiasov
Worcester Polytechnic Institute
100 Institute Road
Worcester, MA 01609-2280

Mr. Eddie Leonardi
University of New South Wales
School of Mechanical and Manufacturing Engineering
Sydney, NSW 2052, Australia
T 61-2-385-5162; F 61-2-633-1222
e.leonardi@unsw.edu.au

Dr. Fred W. Leslie
NASA MSFC
Mail Code SD47
Marshall Space Flight Center
MSFC, AL 35812
T 256-544-1633; F 256-544-6660
fred.leslie@msfc.nasa.gov

Prof. Jennifer A. Lewis
University of Illinois, Urbana-Champaign
Department of Materials Science and Engineering
Room 212A Ceramics Building
105 S. Goodwin Avenue
Urbana, IL 61801
T 217-244-4973; F 217-244-6917
jalewis@staff.uiuc.edu

Prof. Ben Q. Li
Washington State University
School of Mechanical and Materials Engineering
P.O. Box 642920
Pullman, WA 99164-2920
T 509-335-7386; F 509-335-4662
li@mme.wsu.edu

Prof. Fengcui Li
Clarkson University
International Center for Gravity, Materials Science and Applications
Potsdam, NY 13699-5700
F 315-268-3841

Mr. Chaowalit Limmaneevichitr
University of Wisconsin, Madison
Department of Materials Science and Engineering
1103 Engineering Research Building
1500 Engineering Drive
Madison, WI 53706
F 608-262-8648
limmanee@cae.wisc.edu

Prof. X.-M. Lin
Kansas State University
Department of Physics
111 Willard Hall
Manhattan, KS 66506

Prof. Z. Lin
University of Massachusetts
Polymer Science and Engineering Department
Amhurst, MA 01003-4530

Dr. Aleksey Lomakin
Massachusetts Institute of Technology
Room 13-2014
77 Massachusetts Avenue
Cambridge, MA 02139-4307
T 617-253-6804; F 617-225-2585
aleksey@critical.mit.edu

Dr. W. Loser
Institute of Solid State and Materials Research
Helmholtzstraße 20
D-01069 Dresden, Germany

Dr. Samuel A. Lowry
CFD Research Corporation
215 Wynn Drive
Huntsville, AL 35805-1958
T 256-726-4853; F 256-726-4806
sal@cfdrc.com

Dr. S. Z. Lu
Michigan Technological University
Department of Materials Science and Engineering
College of Enginering
1400 Townsend Drive
Houghton, MI 49931-1295
F 906-487-2934

Dr. Afina Lupulescu
Rensselaer Polytechnic Institute
Materials Science and Engineering Department
Materials Research Center
110 8th Street
Troy, NY 12180
T 518-276-2023; F 518-276-2073
lupula@rpi.edu

Mr. Paul Luz
NASA MSFC
Mail Code SD40
Marshall Space Flight Center
MSFC, AL 35812

Prof. Nancy Ma
University of Missouri, Rolla
Department of Mechanical and Aerospace
Engineering and Engineering Mechanics
1870 Miner Circle
Rolla, MO 65409-0050
T 573-341-4626; F 573-341-6899
ma@umr.edu

Dr. Allen K. MacKnight
Honeywell International Inc.
2525 W. 190th Street
M/S-36-1-93140
Torrance, CA 90504
T 310-512-3307; F 310-512-2246
al.macknight@honeywell.com

Prof. Jules Magda
University of Utah
Department of Chemical and Fuels Engineering
50 S. Central Campus Drive, Rm. 3290
Salt Lake City, UT 84112
T 801-581-7536; F 801-581-8692
jj.magda@m.cc.utah.edu

Ms. Diane C. Malarik
NASA GRC
Mail Stop 500-115
21000 Brookpark Road
Cleveland, OH 44135
T 216-433-3203; F 216-433-8660
diane.malarik@grc.nasa.gov

Dr. Jason T. Manka
Middle Tennessee State University
Department of Chemistry
Box X076 MTSU
Murfreesboro, TN 37312
F 615-898-5182

Prof. Carlos Marin
University of Alabama, Huntsville
CMMR, VBRH, D-29
Huntsville, AL 35899
T 256-824-6950; F 256-824-6944
marinc@email.uah.edu

Prof. Raquel Martin
Tufts University
Department of Chemical Engineering
4 Colby Street
Medford, MA 02155

Prof. Jonathan Masere
University of Southern Mississippi
Department of Chemistry and Biochemistry
P. O. Box 5043
Hattiesburg, MS 39406-5053
T 601-266-5899; F 601-266-6045
jonathan@wave.st.usm.edu

Mr. Larry W. Mason
Lockheed Martin
Mail Stop BO560
P.O. Box 179
Denver, CO 80201-0179
T 303-971-9067; F 303-971-0829
larry.w.mason@lmco.com

Dr. Douglas Matson
Massachusetts Institute of Technology
Materials Processing Center
77 Massachusetts Avenue, Room 8-409
Cambridge, MA 02139
T 617-253-3248; F 617-258-6886
matson@mit.edu

Prof. David H. Matthiesen
Case Western Reserve University
Department of Materials Science and Engineering
420 White Bldg., 10900 Euclid Avenue
Cleveland, OH 44106-7204
T 216-368-1366; F 216-368-3209
dhm5@po.cwru.edu

Prof. Richard J. Matyi
University of Wisconsin, Madison
Department of Materials Science and Engineering
1509 University Avenue
Madison, WI 53706
T 608-263-1716; F 608-262-8353
matyi@engr.wisc.edu

Prof. Richard H. Maurer
Johns Hopkins University
Applied Physics Laboratory
11100 Johns Hopkins Road
Laurel, MD 20723-6099
T 240-228-6482; F 240-228-6099
richard.maurer@jhuapl.edu

Prof. Jimmy W. Mays
University of Alabama at Birmingham
Department of Chemistry
Room 201
Birmingham, AL 35294
T 205-934-8101; F 205-934-8158
jmays@uab.edu

Dr. Sandip Mazumder
CFD Research Corporation
215 Wynn Drive, #501
Huntsville, AL 35805
T 256-726-4856; F 256-726-4806
sm@cfdrc.com

Dr. Konstantin Mazuruk
Universities Space Research Association
Mail Code SD47
Marshall Space Flight Center
MSFC, AL 35812
T 256-544-8633; F 256-544-8762
consty.mazuruk@msfc.nasa.gov

Ms. Sonya D. McCall
North Carolina State University
Materials Science and Engineering Department
Centennial Campus, Research Bldg. 1
Box 7919
Raleigh, NC 27695
T 919-515-8965; F 919-515-8967
sdmccall@unity.ncsu.edu

Dr. Geoffrey B. McFadden
National Institute of Standards and Technology
Computational and Mathematical
Sciences Division
Building 820, Room 365
100 Bureau Drive, Stop 8910
Gaithersburg, MD 20899-8910
T 301-975-2711; F 301-990-4127
mcfadden@nist.gov

Prof. John J. McGrath
Michigan State University
Department of Mechanical Engineering
A106 Research Complex - Engineering
East Lansing, MI 48824-1226
T 517-355-0299; F 517 355-7179
mcgrath@me.msu.edu

Prof. Michael McNallan
University of Illinois, Chicago
CME Department
M/C 246
842 W. Taylor Street
Chicago, IL 60607
T 312-996-2436; F 312-996-2426
mcnallan@uic.edu

Prof. Constantine Megaridis
University of Illinois, Chicago
Department of Mechanical Engineering
Mail Code 251
842 W. Taylor Street
Chicago, IL 60607-7022
T 312-996-3436; F 312-413-0447
cmm@uic.edu

Prof. Eckart Meiburg
University of California, Santa Barbara
Department Mechanical and Environmental Engineering
Santa Barbara, CA 93106
T 805-893-5278; F 805-893-5278
meiburg@Engr.ucsb.edu

Dr. Jack Miller
Lawrence Berkeley National Laboratory
One Cyclotron Road, MS 29-100
Berkeley, CA 94720
T 510-486-7130; F 510-486-7934
J_miller@lbl.gov

Dr. H. A. Mook
Oak Ridge National Laboratory
Neutron Scattering Group
P.O. Box 2008
Oak Ridge, TN 37831-6393
T 423-574-5242; F 423-574-6268
ham@ornl.gov

Dr. Shariar Motakef
CAPE Simulations Inc.
One Bridge Street, Suite 100
Newton, MA 02458
T 617-796-8882 x 101; F 617-796-7870
motakef@capesim.com

Mr. Sundeep Mukherjee
University of Alabama
Department of Metallurgical Engineering
Box 870202
Tuscaloosa, AL 35487-0202
T 205-348-1748; F 205-348-8574
mukhe001@bama.ua.edu

Prof. William W. Mullins
Carnegie Mellon University
Department of Materials Science and Engineering
5000 Forbes Avenue
Pittsburgh, PA 15213
T 412-268-2541; F 412-268-7696
wm06@andrew.cmu.edu

Prof. Bruce T. Murray
State University of New York, Binghampton
Mechanical Engineering Department
P.O. Box 6000
Binghampton, NY 13902-6000
T 607-777-6561; F 607-777-4620
bmurray@binghamton.edu

Dr. Allan S. Myerson
Illinois Institute of Technology
10 West 33rd Street
Chicago, IL 60616
T 718-260-3223; F 718-260-3125
myerson@iit.edu

Prof. Ralph E. Napolitano
Iowa State University
Ames Laboratory
104 Wilhelm Hall
Ames, IA 50011-3020
T 515-294-9101; F 515-294-4291
napolitano@ameslab.gov

Prof. Ranga Narayanan
University of Florida
Department of Chemical Engineering
Gainesville, FL 32611
T 352-392-9103; F 352-392-9513
ranga@che.ufl.edu

Prof. Robert J. Naumann
University of Alabama, Huntsville
Von Braun Research Institute M-43
Huntsville, AL 35899
T 256-824-6846; F 256-824-6919
naumannr@email.uah.edu

Prof. V. Nikolakis
University of Massachusetts, Amherst
Department of Chemical Engineering
Goessmann Laboratory
Amherst, MA 01003

Dr. Paul C. Nordine
Containerless Research, Inc.
910 University Place
Evanston, IL 60201
T 847-467-2678; F 846-467-2679
pnordine@containerless.com

Prof. E. A. O'Rear
University of Oklahoma
School of Chemical Engineering and Materials Science
100 East Boyd, EC Rm. T-223
Norman, OK 73019-0628
F 405-325-5813

Dr. Kinichi Ohsaka
University of Southern California
Aerospace and Mechanical Engineering
Los Angeles, CA 90089-1453
T 714 529-3544; F 714-529-3544

Dr. S. J. Oldenburg
Rice University
ECE Department and Department of Chemistry
Houston, TX 77005

Prof. Aleksandar G. Ostrogorsky
Rensselaer Polytechnic Institute
Department of Mechanical Engineering
JEC 2026
Troy, NY 12180
T 518-276-6975; F 518-276-6025
ostroa@rpi.edu

Dr. T. Peignier
University of Alabama, Huntsville
CMMR, VBRH, D-29
Huntsville, AL 35899
F 256-824-6944

Dr. Matthew R. Pekny
Intel Mask Operations
Mailstop SC2-12
3065 Bowers Avenue
Santa Clara, CA 95054-3202

Prof. John H. Perepezko
University of Wisconsin, Madison
Department of Materials Science and Engineering
1509 University Avenue
Madison, WI 53706-1595
T 608-263-1678; F 608-262-8353
perepezk@engr.wisc.edu

Prof. M. L. Peterson
Kansas State University
Department of Chemistry
311 CHEM-BIOCHEM
Manhattan, KS 66506
T 785-532-5419
mpeterso@ksu.edu

Mr. Vladimir Pines
NASA GRC
Mail Stop 105-1
21000 Brookpark Road
Cleveland, OH 44135

Prof. Lawrence S. Pinsky
University of Houston
Physics Department-5506
4800 Calhoun Blvd.
Houston, TX 77204-5506
T 713-743-3552; F 713-743-3589
pinsky@uh.edu

Dr. Y. B. Pithawalla
Virginia Commonwealth University
Department of Chemistry
1001 W. Main Street
Richmond, VA 23284-2006
F 804-828-8599

Prof. David R. Poirier
University of Arizona
Department of Materials Science and Engineering
P.O. Box 210072
Tucson, AZ 85721-0072
T 520-621-6072; F 520-621-8059
poirierd@u.arizona.edu

Prof. John A. Pojman
University of Southern Mississippi
Department of Chemistry and Biochemistry
P.O. Box 5043
Hattiesburg, MS 39406-5043
T 601-266-5035; F 601-266-6075
john.pojman@usm.edu

Prof. Dmitri Popov
Clarkson University
International Center for Gravity, Materials
Science and Applications
Potsdam, NY 13699-5700
T 315-268-7672; F 315-268-3841
popovdi@craft.comp.clarkson.edu

Mr. Timothée Pourpoint
University of Alabama, Huntsville
CMMR
Von Braun Research Hall
Huntsville, AL 35899
T 256-824-6960; F 256-824-6944
pourpot@email.uah.edu

Dr. David L. Price
Argonne National Lab.
MSD-223
9700 S. Cass Ave
Argonne, IL 60439

Prof. Shula Radin
University of Pennsylvania
Department of BioEngineering
3320 Smith Walk
Philadelphia, PA 19104
T 215-898-5140; F 215-573-2071
radin@seas.upenn.edu

Prof. Leo Radzihovsky
University of Colorado, Boulder
Department of Physics
Condensed Matter Laboratory
Boulder, CO 80309-0390
T 303-492-5436; F 303-492-2998
radzihov@lulu.colorado.edu

Prof. Miriam H. Rafailovich
State University of New York, Stony Brook
Department of Materials Science and Engineering
322 Old Engineering Building
Stony Brook, NY 11794-2275
T 631-632-8483; F 631-632-5764
miriam.rafailovich@sunysb.edu

Mr. Balaji Raghothamachar
State University of New York, Stony Brook
Department of Materials Science and Engineering
Stony Brook, NY 11794-2275
T 631-632-8501; F 631-632-8052
braghoth@ic.sunysb.edu

Dr. Valery V. Rakov
Institute for Chemical Problems of Microelectronics
Vernadsky prospect 86
Moscow 117571, Russia
T 7-095-239-9953; F 7-095-233-8869
ihpm@glas.apc.org

Dr. N. Ramachandran
Universities Space Research Assoc.
Mail Code SD47
Marshall Space Flight Center
MSFC, AL 35812
T 256-544-8308; F 256-544-8891
narayanan.ramachandran@msfc.nasa.gov

Prof. Ram Ramanathan
Clarkson University
International Center for Gravity, Materials
Science and Applications
Potsdam, NY 13699-5700
F 315-268-3841

Dr. Roger Rangel
University of California, Irvine
Department of Mechanical and Aerospace
Engineering
Engineering Gateway 4200
Irvine, CA 92697-3975
rhrangel@uci.edu

Dr. Nasser Rashidnia
NASA GRC
Mail Stop 500-102
21000 Brookpark Road
Cleveland, OH 44135
T 216-433-3622; F 216-433-3793

Mr. Thomas J. Rathz
University of Alabama, Huntsville
Mail Code SD47
Marshall Space Flight Center
MSFC, AL 35812
T 256-544-1409; F 256-544-1374
tom.rathz@msfc.nasa.gov

Prof. Chandra S. Ray
University of Missouri, Rolla
Materials Research Center
Martin E. Straumanis Hall
Rolla, MO 65409
T 573-341-6432; F 573-341-2071
csray@umr.edu

Prof. Liya L. Regel
Clarkson University
International Center for Gravity,
Materials Science and Applications
8 Clarkson Avenue
Box 5814
Potsdam, NY 13699-5700
T 315-268-7672; F 315-268-3833
regel@agent.clarkson.edu

Dr. Won-Kyu Rhim
Jet Propulsion Lab.
M/S 183-401
4800 Oak Grove Drive
Pasadena, CA 91109
T 818-354-2925; F 818-393-5039
won-kyu.rhim@jpl.nasa.gov

Dr. Eric E. Rice
Orbital Technologies Corp.
1212 Fourier Drive
Space Center
Madison, WI 53717
T 608 827-5000 x 230 F 608 827-5050
ricee@orbitec.com

Dr. Michael B. Robinson
NASA MSFC
Mail Code SD47
Marshall Space Flight Center
MSFC, AL 35812
T 256-544-7774; F 256-544-2176
mike.robinson@msfc.nasa.gov

Dr. Jan R. Rogers
NASA MSFC
Mail Code SD47
Marshall Space Flight Center
MSFC, AL 35812
T 256-544-1081; F 256-544-2102
jan.rogers@msfc.nasa.gov

Prof. Gregory S. Rohrer
Carnegie Mellon University
Department of Materials Science and Engineering
Roberts Engineering Hall
Room 143
5000 Forbes Avenue
Pittsburgh, PA 15213
T 412-268-2696; F 412-268-7596
gr20@andrew.cmu.edu

Prof. Christopher M. Roland
North Carolina State University
Department of Physics
Box 8202
Raleigh, NC 27695-8202
T 919-515-3170; F 919-515-7331
roland@gatubela.physics.ncsu.edu

Prof. Paul D. Ronney
University of Southern California
Department of Aerospace and Mechanical
Engineering; OHE 430H
Los Angeles, CA 90089-1453
T 213-740-0490; F 213-740-8071
ronney@usc.edu

Prof. David R. Roth
The Johns Hopkins University
Applied Physics Laboratory
11100 Johns Hopkins Road
Laurel, MD 20723-6099
T 240-228-4022; F 240-228-6696
david.roth@jhuapl.edu

Prof. John A. Roth
Vanderbilt University
Department of Chemical Engineering
Box 1604 B
Nashville, TN 37235
T 615-322-3517; F 615-343-7951
jar@vuse.vanderbilt.edu

Dr. M. Rushyniak
Virginia Commonwealth University
Department of Chemistry
1001 W. Main Street
Richmond, VA 23284-2006
F 804-828-8599

Prof. Thomas P. Russell
University of Massachusetts
Polymer Science and Engineering Department
Amherst, MA 01003-4530
T 413-577-1617; F 413-545-0082
russell@iskra.pse.umass.edu

Dr. Marie-Louise Sabougi
Argonne National Laboratory
MSD-223
9700 S. Cass Ave
Argonne, IL 60439

Prof. Albert Sacco, Jr.
Northeastern University
Center for Advanced Microgravity Material Processing
342 Snell Engineering Center
360 Huntington Avenue
Boston, MA 02115
T 617-373-7910; F 617-373-2209
asacco@coe.neu.edu

Prof. Satwindar S. Sadhal
University of Southern California
Department of Aerospace and Mechanical Engineering
Olin Hall - OHE 430
Los Angeles, CA 90089-1453
T 213-740-0492; F 213-740-8071
sadhal@usc.edu

Prof. Donald R. Sadoway
Massachusetts Institute of Technology
Department of Materials Science and Engineering
77 Massachusetts Avenue, Room 8-109
Cambridge, MA 02139-4307
T 617-253-3487; F 617-253-3487
dsadoway@mit.edu

Dr. Paola Sala
INFI
Milan, Italy

Prof. Rajiv Sampath
Cornell University
Sibley School of Mechanical and Aerospace Engineering
188 Frank H.T. Rhodes Hall
Ithaca, NY 14853-3801
F 607-255-9410

Prof. Paul G. Sanders
Harvard University
Division of Engineering and Applied Sciences
29 Oxford Street
Cambridge, MA 02138-2901
F 617-495-9837

Dr. Robert J. Schaefer
National Institute of Standards and Technology
Metallurgy Division
Materials (223), Room B268, Stop 8550
100 Bureau Drive
Gaithersburg, MD 20899-8550
T 301-975-5961; F 301-926-4553
robert.schaefer@nist.gov

Dr. Marcus Schweizer
Universities Space Research Assoc.
Mail Code SD47
Marshall Space Flight Center
MSFC, AL 35812
T 256-544-4167; F 256-544-8762
marcus.schweizer@msfc.nasa.gov

Prof. Rose Scripa
University of Alabama, Birmingham
Department of Materials Science and Engineering
1075 13th Street S
Birmingham, AL 35294
T 205-934-8453; F 205-934-8437
rscripa@Engr.uab.edu

Prof. Robert F. Sekerka
Carnegie Mellon University
Department of Physics
6416 Wean Hall
Pittsburgh, PA 15213-3890
T 412-268-2362; F 412-681-0648
rs07@andrew.cmu.edu

Dr. Subhayu Sen
Universities Space Research Assoc.
Mail Code SD47
Marshall Space Flight Center
MSFC, AL 35812
T 256-544-8264; F 256-544-8762
s.sen@msfc.nasa.gov

Dr. D. Sengupta
CFD Research Corporation
215 Wynn Drive
Huntsville, AL 35805-1958

Miss Brenda Serrano
University of Florida
Department of Chemical Engineering
P.O. Box 116005
227 CHE
Gainesville, FL 32611
T 352-392-2420; F 352-392-9513
besr@grove.ufl.edu

Dr. C. Seybert
University of California, Berkeley
Department of Materials Science and Engineering
Berkeley, CA 94720
F 510-642-9164

Prof. Mark Shavers
Loma Linda University/JSC
SN3
NASA Johnson Space Center
Houston, TX 77058
T 281-483-5899; F 281-483-5276
mshavers@ems.jsc.nasa.gov

Mr. In-Seok Shin
University of Alabama, Huntsville
VBRH, M-40
Huntsville, AL 35899
T 256-824-6630; F 256-824-6791
shini@email.uah.edu

Dr. J. L. Shinn
NASA LaRC
MS 188 B
NASA Langley Research Center
Hampton, VA 23681
F 757-864-8094

Dr. Laurent Sibille
Universities Space Research Assoc.
Mail Code SD48
Marshall Space Flight Center
MSFC, AL 35812
T 256-544-5221; F 256-544-6660
laurent.sibille@msfc.nasa.gov

Prof. Albert Sievers
Cornell University
Laboratory of Atomic and Solid State Physics
517 Clark Hall
Ithaca, NY 14853-2501
T 607-255-6422; F 607-255-6428
sievers@ccmr.cornell.edu

Prof. Jogender Singh
Pennsylvania State University
Applied Research Laboratory
Engineering Science and Mechanics Department
P.O. Box 30
University Park, PA 16802
T 814-863-9898; F 814-863-2986
jxs46@psu.edu

Dr. N. B. Singh
Northrop Grumman Corporation
Science and Technology Center
ESSS MS-3D14, ATL
1212 Winterson Road
Linthicum, MD 21090
T 410-765-1590; F 410-765-7652
narsingh_b_singh@md.northgrum.com

Dr. Robert C. Singleterry, Jr.
NASA LaRC
Materials Division
Environmental Interactions Branch
Mail Stop 188B
Hampton, VA 23681
T 757-864-1437; F 757-864-8094
r.c.singleterry@larc.nasa.gov

Dr. James Singletery, Jr.
Jet Propulsion Laboratory
4800 Oak Grove Drive
Mail Stop 302-306
Pasadena, CA 91109-8099
T 818-354-5046; F 818-393-4540

Dr. James S. Slepick
University of Illinois, Chicago
Department of Mechanical Engineering
M/C 251, 2039 ERF
842 West Taylor Street
Chicago, IL 60607-7022
F 312-413-0447

Dr. David D. Smith
NASA MSFC
Mail Code SD48
Marshall Space Flight Center
MSFC, AL 35812
T 256-544-7778; F 256-544-2102
david.d.smith@msfc.nasa.gov

Prof. Grant D. Smith
University of Utah
Materials Science and Engineering Department
122 S Central Campus Drive, Rm. 304
Salt Lake City, UT 84112-0560
T 801-585-3381; F 801-581-4816
gsmith2@geoffrey.emro.utah.edu

Prof. V. A. Snyder
Northwestern University
Department of Materials Science and Engineering
2225 North Campus Drive
Evanston, IL 60208-3108
F 847-491-7820

Prof. Kwang Jin Song
Yale University
Mason Lab M15
9 Hillhouse Avenue
New Haven, CT 06520
T 203-432-4342; F 203-432-7654
kwangjin.song@yale.edu

Prof. Christopher M. Sorensen
Kansas State University
Department of Physics
Manhattan, KS 66506
T 785-532-1626
sor@phys.ksu.edu

Prof. K. R. Sridhar
University of Arizona
NASA Ames Research Center
MS 239-23
Moffett Field, CA 94035-1000
T 650-604-1649; F 650-604-1092
sridhar@ares.ame.arizona.edu

Prof. Doru M. Stefanescu
University of Alabama
Department of Metallurgy and Materials Engineering
Solidification Laboratory
Room A-129 Bevill Bldg.
P. O. Box 870202
Tuscaloosa, AL 35487-0202
T 205-348-1748; F 205-348-8574
doru@coe.Engr.ua.edu

Dr. Ingo Steinbach
ACCESS
e.V.
Intzestr. 5
52072 Aachen, Germany
T 49-241-805899; F 49-241-38578
i.steinbach@access.rwth-aachen.de

Prof. S. Stoeva
Kansas State University
Department of Chemistry
111 Willard Hall
Manhattan, KS 66506

Dr. Ching-Hua Su
NASA MSFC
Mail Code SD47
Marshall Space Flight Center
MSFC, AL 35812
T 256-544-7776; F 256-544-8762
ching.hua.su@msfc.nasa.gov

Dr. Frank R. Szofran
NASA MSFC
Mail Code SD47
Marshall Space Flight Center
MSFC, AL 35812
T 256-544-7777; F 256-544-8762
frank.szofran@msfc.nasa.gov

Prof. Daniel R. Talham
University of Florida
Department of Chemistry
P.O. Box 117200
Gainesville, FL 32611-7200
T 352-392-9016; F 352-392-3255
talham@Chemicalufl.edu

Prof. Surendra N. Tewari
Cleveland State University
Department of Chemical Engineering
S.H. 464
Cleveland, OH 44115
T 216-523-7342; F 216-687-9220
tewari@csvax.egr.csuohio.edu

Dr. Sheila Ann Thibeault
NASA LaRC
Mail Stop 188B
Hampton, VA 23681-2199
T 757 864-4250
S.A.Thibeault@larc.nasa.gov

Dr. V. Timchenko
University of New South Wales
School of Mechanical and Manufacturing
Engineering
Sydney, NSW 2052, Australia
T 61-2-385-5162; F 61-2-633-1222

Dr. Padetha Tin
NASA GRC
NCMR
21000 Brookpark Road
Cleveland, OH 44135
T 216-433-8164; F 216-433-5033
padetha.tin@grc.nasa.gov

Dr. Paul Todd
SHOT Inc.
7200 Highway 150
Greenville, IN 47124
T 812-923-9591; F 812-923-9598
ptodd@shot.com

Prof. Lawrence W. Townsend
University of Tennessee
Nuclear Engineering Department
Knoxville, TN 37996-2300
T 865-974-5048; F 865-974-0668
ltownsen@utk.edu

Dr. Ram K. Tripathi
NASA LaRC
MS 188 B
NASA Langley Research Center
Hampton, VA 23681
T 757-864-1467; F 757-864-8094
r.k.tripathi@larc.nasa.gov

Prof. Rohit Trivedi
Iowa State University
Ames Laboratory
100 Wilhelm Hall
Ames, IA 50011-3020
T 515-294-5869; F 515-294-4291
trivedi@ameslab.gov

Dr. James D. Trolinger
MetroLaser Inc.
18010 Skypark Circle, # 100
Irvine, CA 92614-6428
T 949-553-0688; F 949-553-0495
jtrolinger@metrolaserinc.com

Dr. Miroslaw Trznadel
Middle Tennessee State University
Department of Chemistry
Box X076, MTSU
Murfreesboro, TN 37312
F 615-898-5182

Prof. Michael Tsapatsis
University of Massachussets, Amherst
Department of Chemical Engineering
159 Goessmann Laboratory
Amherst, MA 01003
T 413-545-0276; F 413-545-1647
tsapatsi@ecs.umass.edu

Dr. V. Tsvetivsky
All-Union Science Research Institute of Mineral
Raw Materials Synthesis
VNIISIMS
Institutskaya str 1
Alexandrov-City 601600
Vladimirskaya Region, Russia
F 7-095-584-5816

Dr. Dennis Tucker
NASA MSFC
Mail Code SD70
Marshall Space Flight Center
MSFC, AL 35812
T 256-544-2685; F 256-544-2659
dennis.tucker@msfc.nasa.gov

Dr. V. Ufimtsev
Institute for Chemical Problems of Microelectronics
Vernadsky prospect 86
Moscow 117571, Russia
F 7-095-230-47-56

Prof. Regina Valluzzi
Tufts University
Bioengineering Center
4 Colby Street
Medford, MA 02155
T 617-627-3136; F 617-627-3991
rv@marvin.tufts.edu

Prof. Peter G. Vekilov
University of Alabama, Huntsville
CMMR, VBRH, D-29
Huntsville, AL 35899
T 256-824-6892; F 256-824-6944
peter@cmmr.uah.edu

Prof. Dionisios G. Vlachos
University of Massachusetts, Amherst
Department of Chemical Engineering
159 Goessmann Laboratory
Amherst, MA 01003
T 413-545-6143; F 413-545-1647
vlachos@snail.ecs.umass.edu

Dr. Marcus Vlasse
NASA MSFC
Mail Code SD10
Marshall Space Flight Center
MSFC, AL 35812
T 256-544-7781; F 256-544-7128
marcus.vlasse@msfc.nasa.gov

Dr. Vitaly Volpert
Université Lyon I
Laboratoire d'Analyse Numirique
Batiment 101
43 bd du 11 Novembre 1918
69622 Villeurbanne Cedex, France
T 33 4 72 44 83 17; F 33 4 72 44 80 53
VOLPERT@LAN1.UNIV-LYON1.FR

Dr. Martin P. Volz
NASA MSFC
Mail Code SD47
Marshall Space Flight Center
MSFC, AL 35812
T 256-544-5078; F 256-544-8762
martin.volz@msfc.nasa.gov

Prof. Peter W. Voorhees
Northwestern University
Department of Materials Science and Engineering
2225 North Campus Drive
Evanston, IL 60208-3108
T 847-491-7815; F 847-491-7820
p-voorhees@northwestern.edu

Dr. Ljubomir Vujisic
CAPE Simulations Inc.
One Bridge Street, Suite 100
Newton, MA 01752
T 617-796-8882 x 103
F 617-796-7870
vujisic@capesim.com

Prof. John S. Walker
University of Illinois, Urbana
Mechanical and Industrial Engineering Department
140 Mechanical Engineering Building
1206 West Green Street
Urbana, IL 61802
T 217-333-7979; F 217-244-6534
jswalker@uiuc.edu

Dr. D. B. Wallace
Microfab Technologies
1104 Summitt Avenue
Plano, TX 75074

Dr. Y. Wang
Clarkson University
International Center for Gravity, Materials
Science and Applications
Box 5814
Potsdam, NY 13699-5814
F 315-268-3833

Prof. J. Douglas Way
Colorado School of Mines
Chemical Engineering and Petroleum Refining
Department
1500 Illinois Street
Golden, CO 80401-1887
T 303-273-3519; F 303-273-3730
dway@mines.edu

Dr. Richard Weber
Containerless Research, Inc.
906 University Place
Evanston, IL 60201-3149
T 847-467-2678; F 847-467-2679
weber@containerless.com

Prof. Francis C. Wessling
University of Alabama, Huntsville
CMDS, VBRH, M-65
301 Sparkman Drive
Huntsville, AL 35899
T 256-824-6620; F 256-824-6791
wessling@email.uah.edu

Dr. A. A. Wheeler
University of Southampton
Highfield
Southampton SO17 1BJ
United Kingdom

Prof. Joe B. Whitehead Jr.
University of Southern Mississippi
Department of Physics and Astronomy
Box 5046
Hattiesburg, MS 39406
T 601-266-4934; F 601-266-5149
Joe.Whitehead@usm.edu

Ms. Michaela E. K. Wiegel
Massachusetts Institute of Technology
77 Massachusetts Avenue
13-4150
Cambridge, MA 02139
T 617-253-2381; F 617-253-5827
wiegel@mit.edu

Prof. William R. Wilcox
Clarkson University
International. Center for Gravity, Materials
Science and Applications
Box 5814
Potsdam, NY 13699-5814
T 315-268-7672; F 315-268-3833
wilcox@clarkson.edu

Dr. Hermann Wilke
Institute for Crystal Growth
Rudower Chaussee 6
D-12489 Berlin – Adlershof
Germany

Prof. Donna Wilson
Tufts University
Department of Chemical Engineering
4 Colby Street
Medford, MA 02155

Dr. John W. Wilson
NASA LaRC
Materials Division
Mail Stop 188-B
8 West Taylor Street
Hampton, VA 23681-0001
T 757-864-1414; F 757-864-7730
john.w.wilson@larc.nasa.gov

Dr. Thomas L. Wilson
NASA JSC
Mail Code SN3
Houston, TX 77058
T 281-483-2147; F 281-483-5276
thomas.l.wilson@jsc.nasa.gov

Mr. William K. Witherow
NASA MSFC
Mail Code SD48
Marshall Space Flight Center
MSFC, AL 35812
T 256-544-7811; F 256-544-2102
bill.witherow@msfc.nasa.gov

Prof. August F. Witt
Massachusetts Institute of Technology
Department of Materials Science and Engineering
77 Massachusetts Avenue, Room 13-4138
Cambridge, MA 02139-4307
T 617-253-5303; F 617-253-5728
afwitt@mit.edu

Mr. Daniel Wolfe
Rice University
ECE Department and Department of Chemistry
Houston, TX 77005

Prof. Y.-Y. Won
University of Minnesota
Department of Chemical Engineering and Materials Science
Amundson Hall
421 Washington Avenue S.E.
Minneapolis, MN 55455-0132

Prof. Andrew Yeckel
University of Minnesota
Chemical Engineering and Materials Science
421 Washington Avenue SE
Minneapolis, MN 55455
T 612-626-9455; F 612-626-7246
yeckel@cems.umn.edu

Prof. Nicholas J. Zabaras
Cornell University
Sibley School of Mechanical and Aerospace Engineering
188 Frank H.T. Rhodes Hall
Ithaca, NY 14853-3801
T 607-255-9104; F 607-255-9410
zabaras@cornell.edu

Dr. J. Zaccaro
CNES
Laboratoire de Cristallographie
BP 166 38042
Grenoble cedex 09, France

Dr. Anvar A. Zakhidov
Honeywell Inc.
Honeywell Technical Center (HTC)
101 Columbia Road
Morristown, NJ 07962-1021
T 973-455-3935; F 973-455-5991
anvar.zakhidov@honeywell.com

Dr. J. Zartman
University of Colorado, Boulder
Department of Mechanical
Engineering
Campus Box 427
Boulder, CO 80309-0427
F 303-492-4637

Dr. Cary Zeitlin
Lawrence Berkeley National Laboratory
One Cyclotron Road
Mail Stop 29-100
Berkeley, CA 94720
T 510-486-5518; F 510-486-6949
cjzeitlin@lbl.gov

Dr. H. Zhang
Northrop Grumman Corporation
Science and Technology Center
ESSS MS-3D14, ATL
1212 Winterson Road
Linthicum, MD 21090
F 410-765-7652

Prof. Hui Zhang
State University of New York, Stony Brook
Department of Mechanical Engineering
Stony Brook, NY 11794-2300
T 631-632-8492; F 631-632-8544
Hui.Zhang@sunysb.edu

Prof. Evgenii V. Zharikov
Russian Academy of Sciences
General Physics Institute
Laser Materials and Technology Research Center
Vavilov Street 38, Build. D
117942 Moscow, Russia
T 7-095-135-8352; F 7-095-135-0270
zharikov@Isk.gpi.ru

Dr. Shen Zhu
Universities Space Research Assoc.
Mail Code SD47
Marshall Space Flight Center
MSFC, AL 35812
T 256-544-2916; F 256-544-8762
shen.zhu@msfc.nasa.gov

Prof. Maria I. Zugrav
University of Alabama, Huntsville
CMDS, VBRH D-29
301 Sparkman Drive
Huntsville, AL 35899
T 256-824-6650; F 256-824-6944
zugravm@email.uah.edu

REPORT DOCUMENTATION PAGE

Form Approved
OMB No. 0704-0188

1. AGENCY USE ONLY *(Leave Blank)*	2. REPORT DATE	3. REPORT TYPE AND DATES COVERED
	March 2001	Conference Publication

4. TITLE AND SUBTITLE
Microgravity Materials Science Conference 2000

5. FUNDING NUMBERS

6. AUTHORS
N. Ramachandran,* N. Bennett,* D. McCauley,** K. Murphy,***
S. Poindexter,* Editors

7. PERFORMING ORGANIZATION NAMES(S) AND ADDRESS(ES)
George C. Marshall Space Flight Center
Marshall Space Flight Center, AL 35812

8. PERFORMING ORGANIZATION REPORT NUMBER
M–1003

9. SPONSORING/MONITORING AGENCY NAME(S) AND ADDRESS(ES)
National Aeronautics and Space Administration
Washington, DC 20546–0001

10. SPONSORING/MONITORING AGENCY REPORT NUMBER
NASA/CP—2001–210827

11. SUPPLEMENTARY NOTES
Proceedings of a conference held at Huntsville, AL, June 6–8, 2000. *Universities Space Research Association, **University of Alabama in Huntsville, ***Morgan Research Corporation (all Huntsville, AL)

12a. DISTRIBUTION/AVAILABILITY STATEMENT
Unclassified-Unlimited
Subject Category 23
Standard Distribution

12b. DISTRIBUTION CODE

13. ABSTRACT *(Maximum 200 words)*

The 2000 Microgravity Materials Science Conference was held June 6–8 at the Von Braun Center, Huntsville, Alabama. It was organized by the Microgravity Materials Science Discipline Working Group, sponsored by the Microgravity Research Division (MRD) at NASA Headquarters, and hosted by NASA Marshall Space Flight Center and the Alliance for Microgravity Materials Science and Applications (AMMSA). It was the fourth NASA conference of this type in the microgravity materials science discipline. The microgravity science program sponsored ≈200 investigators, all of whom made oral or poster presentations at this conference. In addition, posters and exhibits covering NASA microgravity facilities, advanced technology development projects sponsored by the NASA Microgravity Research Division at NASA Headquarters, and commercial interests were exhibited. The purpose of the conference was to inform the materials science community of research opportunities in reduced gravity and to highlight the Spring 2001 release of the NASA Research Announcement (NRA) to solicit proposals for future investigations. It also served to review the current research and activities in materials science, to discuss the envisioned long-term goals, and to highlight new crosscutting research areas of particular interest to MRD. The conference was aimed at materials science researchers from academia, industry, and government. A workshop on in situ resource utilization (ISRU) was held in conjunction with the conference with the goal of evaluating and prioritizing processing issues in Lunar and Martian type environments. The workshop participation included invited speakers and investigators currently funded in the material science program under the Human Exploration and Development of Space (HEDS) initiative. The conference featured a plenary session every day with an invited speaker that was followed by three parallel breakout sessions in subdisciplines. Attendance was close to 350 people. Posters were available for viewing during the conference and a dedicated poster session was held on the second day. Nanotechnology, radiation shielding materials, Space Station science opportunities, biomaterials research, and outreach and educational aspects of the program were featured in the plenary talks. This volume, the first to be released on CD-Rom for materials science, is comprised of the research reports submitted by the Principal Investigators at the conference.

14. SUBJECT TERMS
microgravity research, materials science, in situ resource utilization, new technology, biomaterials research, radiation shielding

15. NUMBER OF PAGES
719

16. PRICE CODE
A99

17. SECURITY CLASSIFICATION OF REPORT	18. SECURITY CLASSIFICATION OF THIS PAGE	19. SECURITY CLASSIFICATION OF ABSTRACT	20. LIMITATION OF ABSTRACT
Unclassified	Unclassified	Unclassified	Unlimited